

RIKEN Accelerator Progress Report

1995

vol. **29**

理化学研究所
The Institute of Physical and Chemical Research (RIKEN)

RIKEN Accelerator Progress Report 1995
January-December
vol. **29**

理化学研究所
The Institute of Physical and Chemical Research (RIKEN)
Wako-shi, Saitama, 351-01 JAPAN

Editors

A. Goto T. Ichihara
T. Kambara T. Kobayashi
Y. Kobayashi T. Okada
I. Shimamura M. Takami
S. Yamaji F. Yatagai

All rights reserved. This report or any part thereof may not be reproduced in any form (including photostatic or microfilm form) without written permission from the publisher.

All reports are written on authors' responsibility and thus the editors are not liable for the contents of the report.

CONTENTS

	Page
I. PREFACE	1
II. OPERATION OF ACCELERATORS	
RRC and AVF Cyclotron Operation	3
Tandem Operation	5
RILAC Operation	6
III. RESEARCH ACTIVITIES	
1. Nuclear Physics	
Stochastic Variational Method with Realistic Potentials	7
Structure of the $A = 9$ System with Microscopic Cluster Model	8
Magnetic Moments of the Mirror Nuclei ${}^9\text{C}$ and ${}^9\text{Li}$	9
Magnetic Moment of ${}^{11}\text{Be}$	10
Direct Radiative Capture Process in the ${}^{12}\text{C}(n, \gamma){}^{13}\text{C}$ Reaction	11
Neutron Capture of Nuclei Far from Stability	12
Interaction Radii of Na-isotopes	13
Mechanism of the Inversion between 1d and 2s Single Particle Levels	14
A Systematic Study of Even-Even Mass Nuclei Up to the Drip Lines in Terms of the Relativistic Mean Field Theory	15
Systematics of Interaction Radii of Unstable Sd-Shell Nuclei	16
Nuclear Shell Energies and Deformations in Mass Formulas (1) Theory	17
Nuclear Shell Energies and Deformations in Mass Formulas (2) Results	18
Quantum Monte Carlo Diagonalization Method for Nuclear Shell Model	19
Extensive Hartree-Fock + BCS Calculation with Skyrme SIII Force	20
Do Soft Dipole States Exist in Light Nuclei?	21
Giant Resonance States in Neutron-Rich Nuclei	22
Double Giant Dipole Resonance States	23
Correlated Ground State and $E2$ Giant Resonance Built on It	24
Damping of Hot Giant Dipole Resonance as a Linear Irreversible Process	25
C_4 Symmetry in Superdeformation by Berry's Phase Analysis	26
Tilting Mechanism in ${}^{182}\text{Os}$	27
Estimation of Signature Splitting of TAR with GCM	28

3D Angular Momentum Projection of Tilted Axis Rotating States	29
Statistical Property of Molecular Dynamics with Wave Packets	30
Antisymmetrized Molecular Dynamics with Stochastic Incorporation of Vlasov Equation	31
Collisional Damping and the Temperature Dependence of Nuclear Dissipation	32
Dissipative Dynamics of Fission Studied with Three-Dimensional Langevin Equation .	33
Quenching of the Coulomb Sum Value	34
Symmetry Energy at Subnuclear Densities and the Layer of Non-spherical Nuclei in Neutron Star Crusts	35
Braking Index Changes from Neutron Star Glitches	36
Exotic Nuclear Deformation in the Neutron Star Crusts and the Origin of Glitches ...	37
A Study of Collision Frequency and Particle Density in Ultrarelativistic Nuclear Collisions by an Event Generator URASiMA	38
Gluon Distribution Function Using Bag Model and QCD Sum Rule	39
Lattice-QCD Calculations Using VPP500	40
Effective Potential Formalism for Dynamical Chiral-Symmetry Breaking in the Dual Ginzburg-Landau Theory	41
New α -Decaying Neutron-Deficient Isotopes ^{197}Rn and ^{200}Fr	42
New α -Decaying Neutron-Deficient Isotopes ^{196}Rn and ^{195}At	43
Study of α Decays from Evaporation Residues Produced by the $^{40}\text{Ar} + ^{232}\text{Th}$ Reaction	44
Nuclear Moments and Charge Radii of ^{175}Hf Determined by Laser Spectroscopy	45
Production of Neutron Deficient α -Decaying Hafnium Isotopes $^{161-157}\text{Hf}$ Using RIKEN GARIS/IGISOL	46
Measurement of Neutron Spallation Cross Sections	47
High-Spin States in ^{148}Tb	48
Life Time of High Charged States Isomer	49
Target Dependence of Production Rates of Projectile-like Fragments	50
Production and Identification of New Neutron Rich Nuclei ^{31}Ne and ^{37}Mg with $80 A \text{ MeV } ^{50}\text{Ti}$ Beam	51
Giant Dipole Resonance in Hot Rotating Nuclei	52
Entrance Channel Effect on the Pre-scission Time of Binary Decay for Medium Mass Nuclei (Mass ~ 110)	53
Temperature and Excitation Energy of Hot Nuclei Produced in $^{40}\text{Ar} + ^{116}\text{Sn}$ Reaction at $E/A=30$ and 37 MeV/nucleon	54
Measurement of the d - p Elastic Scattering at $E_d = 270 \text{ MeV}$	55
Elastic Scattering of Polarized Deuterons at $E_d = 270 \text{ MeV}$	56

Measurement of the $^{12}\text{C}(\vec{d}, \vec{d}')$ Reaction at $E_d = 270$ MeV	57
Precise Experiment on $\vec{n} + d$ Scattering at 12 MeV	58
Spin-Flip and Non-Spin-Flip Isovector Excitation Observed in the ($^{12}\text{C}, ^{12}\text{N}$) and ($^{13}\text{C}, ^{13}\text{N}$) Reactions at $E/A = 100$ – 135 MeV	59
Electromagnetic Moments of ^{13}O	60
Measurement of the Magnetic Moments of ^{14}B and ^{15}B Using Projectile Fragmentation Spin Polarization	61
Electric Quadrupole Moments of Neutron-Rich Nuclei ^{14}B and ^{15}B	62
Branching Ratios of the ^{14}B Beta Decay	63
Feasibility Test of Delayed Neutron Spectroscopy for Spin-Polarized Neutron-Rich Nuclei	64
States in ^{16}C Using the Transfer Reaction $^{15}\text{C}(d,p)^{16}\text{C}$	65
Measurement of β -Decay Branching Ratio of ^{17}Ne into the Ground and First Excited States of ^{17}F	66
Beta Decay of the Drip Line Nuclei ^{14}Be	67
Measurement of the Fusion Cross Section of Neutron-Rich Nuclei $^{29,31}\text{Al} + ^{197}\text{Au}$	68
Scattering of Radioactive Nuclei ^6He and ^3H by Proton	69
Spectroscopy of Halo Nucleus ^{11}Li	70
Effects of Neutron Skin and Halo in ^6He , ^8He , and ^{11}Li	71
Charge Exchange Reactions of ^{11}Li	72
Coulomb Dissociation of ^8B	73
Coulomb Dissociation Reaction and Neutron-Neutron Correlation in ^{11}Li	74
Coulomb Excitation of a Halo Nucleus ^{11}Be	75
Coulomb Excitation of ^{56}Ni	76
Neutron Skin of Na Isotopes Studied via Their Interaction Cross Sections	77
Interaction Cross Sections and Radii of Light Nuclei	78
Structure of ^{10}Li Studied by Pion Double Charge Exchange Reaction $^{10}\text{B}(\pi^-, \pi^+)^{10}\text{Li}$	79
RHIC Spin Project	80
Muon Pair Detector System for RHIC Spin Project	81

2. Atomic and Solid-State Physics

Resonances in Photodetachment of $\text{H}^-(2p^2, ^3P^e)$	83
Angular Distributions of Photoelectrons from Helium	84
Double Photoionization of Helium at Low Photon Energies	85
Scattering Angle Dependence of Electron Impact on O_2 and CO	86

Electron Energy Distribution Functions and Thermalization Time in Methane and in Argone-Methane Mixture	87
Correlation between the Carbon K-Shell X-Ray Emission Rates in Molecules	88
Charge Transfer Effect on Double Electron Excitation of Helium by Proton Impact ..	89
Electron Capture in Slow $O^+(^4S, ^2D, ^2P)$ -He Collisions: Effects of Metastable Ions ..	90
Electron Loss from H^- under Energetic, Highly Ionized Ion Impact	91
Close-Coupling Calculations of Electron Capture from Circular Rydberg States	92
Single- and Double-Charge-Exchange Cross Sections for $Ar^{q+} + H_2$ Collisions	93
Electron Capture in $H^+ + CH_4$ Collisions	94
Double and Single Ionization of Helium and Hydrogen Molecules by Slow Protons and Antiprotons	95
Muon-Transfer Reaction $t + d\mu(2s) \rightarrow t\mu(n = 2) + d$	96
Strong Induced-Dipole-Field Oscillations in an Excited $dt\mu$ Molecule above the $t\mu$ ($N = 2$) Threshold	97
Coincidence Measurement of Fragment Ions with Final Charge State of Projectile in Fast Ion $-C_{60}$ Collision	98
Three-Dimensional Recoil-Ion Momentum Analyses in 8.7 MeV O^{7+} -He Collisions ...	99
Intercombination Lines in Highly Charged Ions	100
Observation of a Systematic Deviation between Experimental and Theoretical Lifetimes for the $3s3p\ ^3P_1$ Level of High Z Mg-like Ions	101
Problems Caused by Beam-Related Electrons in Beam-Foil Lifetime Measurements ...	102
Beam-Foil Spectra of Highly Charged, Highly Excited Neon Ion in Visible Region	103
L X-Ray Emission Spectra of Copper	104
Angular Distribution Measurements of X-Rays from Multiply Ionized Atoms	105
Absolute Cross Sections for Charge Capture from Rydberg Targets by Slow Highly Charged Ions	106
Optogalvanic Diode-Laser Spectroscopy in Hf I	107
Measurement of the Isotope Shift in Fe by Resonance Ionization Spectroscopy	108
Knight Shift for ^{13}O Implanted in Pt	109
Effect of Ligand Distortion on the Hyperfine Magnetic Field of $^{61}Ni^{2+}$ Ions in the Spinel Chromites	110
In-Beam Mössbauer Study on Pure Iron Using $^{56}Fe(d, p)^{57}Fe$ Reaction	111
^{61}Ni Mössbauer Spectroscopy on Cubic Spinel Chromites	112
μ SR Study on $TlBa_2Y_{1-x}Ca_xCuO_y$	113
μ^\pm SR Measurement of $La_{2-x}(Ba,Sr)_xCuO_4$ around $x = 0.12$	114
μ^+ SR on $Fe_{1+x}Sb$	115

Quantum Diffusion of Positive Muon in Pure Tantalum	116
Spin Dynamics of μ Al Pseudo-Acceptor Centers in Si Probed by μ^- SR	117
μ SR Studies on Magnetic Correlations and Spin Dynamics in Kondo Semimetal CeNiSn	118
The Spin Dynamics of Polarons in Polyaniline Studied by μ^- SR	119
LF μ SR Studies on Reorientational Dynamics in Solid C ₇₀ Using the ARGUS Spectrometer	120
Single Event Effect in Power MOSFETs by High-Energy Heavy Ion	121
Heavy-Ion Irradiation Effects on the Single Crystal La _{1.85} Sr _{0.15} CuO ₄	122
Observation of Columnar Defects in ¹³⁶ Xe ⁺³¹ Bombarded Layered Materials	123
Laser Spectroscopy of Atoms and Molecules in Liquid Helium	124
Behaviour of Xe Atoms in Xe-Implanted Iron	125
3. Radiochemistry and Nuclear Chemistry	
Differential Recoil Ranges of Reaction Products in the Cu + ¹⁴ N, ⁴⁰ Ar Nuclear Reactions	127
Mass Transfer in the Heavy-Ion Reaction of ¹⁹⁷ Au Induced by ¹³⁶ Xe	128
Reaction of (^{14,15} N + ¹⁶⁵ Ho) and (⁴⁰ Ar, ¹⁴ N, + ¹⁴¹ Pr) Systems at Intermediate Energies	129
Multitracer Study on the Behavior of Various Elements in Atmosphere-Plant System .	130
Determination of Trace Elements in Ferns by Neutron Activation Analysis (I)	131
Determination of Trace Elements in Ferns by Neutron Activation Analysis (II)	132
Distribution Coefficients of Platinum Group Metals between Soil Solid and Liquid Phase	133
Group Separation of a Multitracer by Solvent Extraction	134
Group Separation of a Multitracer by Cation Exchange Column	135
Biodistribution Study of Antibodies Labeled with Multitracer in Mice	136
Study of Trace Elements Uptake by Tumor-Bearing Mice by the Multitracer Technique	137
Separation of a Multitracer from an Au Target Irradiated by Heavy Ions	138
Selective Separation and Reversed Phase Extraction of Zirconium and Hafnium from Multitracer Solution	139
Metabolism of Trace Elements in Marine Algae: A Study Using the Multitracer	140
Biodistribution of Gold Complexes in Mice	141
Metabolic and Biochemical Studies of Trace Elements in Zinc-Deficient Rats (1) Biochemical Properties of the Platinum-Group Elements	142
Metabolic and Biochemical Studies of Trace Elements in Zinc-Deficient Rats (2) Ionic Radius Dependence of Uptake of Rare-Earth Elements	143

<i>In Vivo</i> Behavior of Various Rare-Earth Elements in Lipogenous Diabetes Model Mice by Using the Multitracer Technique	144
Metabolic Studies of Various Trace Elements in Acute Alcoholic Mice	145
Research in Metabolic Physiology on Space Field by Using the Multitracer Technique-A Proposal	146
Preparation of a Multitracer from Heavy-Ion Irradiated Tin by Heating under Reduced Pressure	147
Time Dependence of Distribution of Trace Elements in Rats Using the Multitracer Technique	148
Multitracer Study on Distribution of Trace Elements in Vitamin D Overloaded Rats	149
Multitracer Study on Distribution of Trace Elements in Vitamin D Deficient Rats	150
Solvent Extraction Behavior of Multitracers by Di(2-ethylhexyl)phosphoric Acid	151
Multitracer Study on Stability Constants of Humate Complexes with Various Metal Ions	152
Metabolism of Various Trace Elements in LEC Rats Leading to Acute Hepatitis	153
Studies on the Ion Exchange Adsorption Behavior of Strongly Acidic Resin Nafion and Its Application to Analytical Chemistry	154
Uptake Behavior of Multitracers in LEC Rats before Jaundice Development	155
Biodistribution of Multitracers in Normal, Al-Overloaded and Cd-Overloaded Mice ..	156
Creating a New Design System Using a Cooled CCD Camera Multi Spectrum Imager	157
TDPAC of ⁹⁹ Ru Arising from ⁹⁹ Rh in α -Fe ₂ O ₃ and EuFeO ₃	158
Extraction of an Intense Slow Positron Beam Using He ⁺⁺ Beams from the AVF Cyclotron	159
Resistivity Dependence of Positron/Positronium Annihilation in Porous Silicon	160
Positron Annihilation Studies on the Interaction between Hydrogen and Defects in Nickel	161

4. Radiation Chemistry and Radiation Biology

Track-Depth Resolved Dynamics of Excited States in Ion Irradiated Rare Gases near Condensed Phases	163
Unusual Temperature-Dependent Decay of Self-Trapped Excitons Formed at High Density in Ion Irradiated BaF ₂	164
Effect of Heavy-Ion Beams during the Fertilization Cycle of Plants	165
Enhanced Cell Inactivation at Nonpermissive Temperature	166
Effects of Ne Ion Beams on the Survival of <i>Arabidopsis thaliana</i>	167
Dependence of Interphase-Death Induction on the LET of Accelerated Neon-Ions in CHO Cells	168
The Role of DNA Repair on Cell Killing by Neutron and Heavy-Ion Beams	169

Analysis of Mutations in the Human <i>HPRT</i> Gene Induced by Accelerated Heavy-Ion Irradiations (II)	170
Early Phase Histological Changes of Skin after Carbon Ion Slit-Beam Irradiation	171
Measurement of Potassium, Rubidium and Cesium Influx Rate into Rat Erythrocytes Using Multitracer Technique	172
Translocation of Radionuclides from Plant Leaf Surfaces	173
5. Instrumentation	
Computer Environment around the Accelerator Facility	175
Data Acquisition System for Segment-Ge Detector	176
Development of an On-line Laser Ion Source Using Resonance Ionization in an Ion Guide Chamber at RIKEN GARIS/IGISOL	177
Operation and Status of the RIKEN EBIS (REBIS)	178
Development of the Deuteron POLarimeter DPOL	179
Development of Polarized Xe Solid as a Means to Produce Spin Polarization in Stopped Unstable Nuclei	181
Development of the Detector for Sub-MeV β -Delayed Neutron	182
Slew Correction for Timing Signals from NaI(Tl) Scintillators	183
NaI(Tl) Detector Assembly for Low Intensity Radiation (DALI)	184
Summing Amplifiers for Heavy-Nucleus Search Experiments	185
Test of a High-Rate MWDC for Heavy-Ion Detection	186
Construction of a PPAC with High Position Resolution	187
Heavy Ion Beam Test of Cosmic Ray Telescope for the First Brazilian Scientific Satellite	189
Progress in Beam Optics for RIKEN-RAL Muon Facility	190
New Data Acquisition System for RIKEN-RAL μ CF Experiment	192
Installation of Tritium Gas Handling System for Muon Catalyzed Fusion Experiment at RIKEN-RAL Muon Facility	194
Development of a New μ SR Spectrometer ARGUS	196
Development of a Resonance Ionization Buffer Gas Cell for Laser Spectroscopy of Refractory Elements and Actinides	198
A New Beam Line for Material Irradiations in the Ring Cyclotron	199
6. Material Analysis	
RBS Study of Tb-Implanted Sapphire (II)	201
Sample Charging Effect on Satellite Spectra of Ion-Induced X Rays	202
Correlation between Seawater Temperature and Sr/Ca Ratios in Otoliths of Red Sea Bream <i>Pagrus major</i>	203
Whether Ion Beam Attracts Ions in Solutions or Not?	204

IV. NUCLEAR DATA

Status Report of the Nuclear Data Group	205
Measurements of Activation Cross Sections of Energy Up to 110 MeV for Several Neutron-Induced Reactions	206

V. DEVELOPMENT OF ACCELERATOR FACILITIES

Status of RIKEN 10 GHz ECRIS	207
Present Status and Future Plans of RIKEN 14.5 GHz Caprice	208
E-Field Injection for Extracting Much Faster Pulse Trains or for Enhanced CW Beams out of an ECRIS Potential-Well	209
Supporting Evidences of the LLPB Concept to Explain Enhanced High-Charge State Ion Beam-Current in ECRIS	211
Development of Polarized ^3He Gas Target	213
Development of a New Type of Single-Bunch Selector	214
Construction of a New Beam Line from the AVF Cyclotron	216
Improvement of the RF Control System for RILAC	217
Status of a New Injector System for RILAC	219
Development of RIKEN 18 GHz ECRIS	220
Development of a Variable-Frequency RFQ Linac for RILAC	221
Misalignment Effect of Vanes on Beam Transmission Efficiency in an RFQ Linac	223
Design Study of Siberian Snake Magnet for RHIC-Spin Project	225
Progress of RIKEN RI Beam Factory Project	226
Conceptual Design of a Frequency-Tunable IH Linac	228
Design Study of Sector Magnet of the Superconducting Ring Cyclotron (I)	230
Design Study of Sector Magnet of the Superconducting Ring Cyclotron (II)	232
Design Study of the Injection System of the Superconducting Ring Cyclotron (III) ...	234
Design of a Model Sector Magnet of the Superconducting Ring Cyclotron	236
Double Storage Rings for MUSES	238
Accumulator Cooler Ring and Booster Synchrotron Ring for MUSES	240
Design of Booster Synchrotron for MUSES	241
Computer Study of Magnet Power Supply for MUSES Booster Synchrotron (BSR) ...	242
Simulation of RF Stacking Injection at Accumulator Cooler Ring for MUSES	244
Electron Cooling at RI Beam Factory	246
Design of a Lattice of the DSR	248
Beam Current Limitations Due to Single-Beam Collective Effects at Double Storage Rings at MUSES	250

Merging Beam-Beam Interaction at DSR	252
Beam-Beam Interaction of Electrons and Ions at Double Storage Ring	254
Luminosity of Electron-Ion Collision in MUSES	256
An Undulator and the Photon Flux at MUSES	257
VI. RADIATION MONITORING	
Leakage Radiation Measurements in the Ring Cyclotron Facility	259
Dose Rates Due to Residual Activities in the Ring Cyclotron Facility	261
Routine Works for Radiation Safety in the Ring Cyclotron Facility	263
VII. LIST OF PUBLICATIONS	265
VIII. LIST OF PREPRINTS	271
IX. PAPERS PRESENTED AT MEETINGS	274
X. LIST OF SYMPOSIA	285
XI. LIST OF SEMINARS	286
XII. LIST OF PERSONNEL	289
AUTHOR INDEX	

I. PREFACE

The Report summarizes research activities at the RIKEN Accelerator Research Facility in the year of 1995. The research program at the Facility has been pursued under the framework of the project entitled Multi-disciplinary Researches on Heavy Ion Science. The program extends over a variety of fields; nuclear physics, atomic physics, nuclear chemistry, radiation biology, condensed matter physics in terms of accelerator or radiation, basic studies on energy production and accelerator cancer therapy, material characterization, application to space science, accelerator engineering, laser technology and computational technology.

The central facility is a heavy-ion accelerator complex consisting of the RIKEN Ring Cyclotron (RRC) and its subordinate accelerators, the energy-variable heavy ion linear accelerator (RILAC), and the $K = 70$ MeV AVF cyclotron. They have altogether delivered a beam time (on the target) of more than 8000 hours. Twelve laboratories at RIKEN and more than 400 researchers including outside users have participated in the program.

The Facility has marked a great milestone this year by starting two new projects; 1) R & D of the so called RIKEN Radioactive Beam Factory and 2) RIKEN-BNL collaboration program on spin structure functions. Having achieved approval of the two new projects, the Facility is moving towards a new stage of major development.

The project of the RIKEN Radioactive Beam Factory involves construction of a superconducting separate-sector cyclotron with K-number around 2400 MeV which serves as the energy booster upon the existing RRC. The beam energy of heavier elements is to become sufficiently high to produce projectile-fragment (PF) beams of a broadened range of unstable nuclei. The cyclotrons are to be accompanied with dual rings of synchrotron to enhance experimental perspectives. We anticipate that the Factory would make a central contribution to the development of next-generation radioactive beam (RIB) science. Most optimistically the Factory would be completed around 2002 or 2003.

Design works on the Factory are in progress to proceed to construction of a proto-type superconducting sector. Meanwhile a major development has been accomplished at the upstream end of the RILAC. A set of 18 GHz ECR ion source and a frequency-variable RFQ has been completed to significantly improve the beam output. The apparatus with the upgraded intensity is an important ingredient of the Factory project.

The Facility carries on an international research program on muon science in collaboration with the Rutherford-Appleton Laboratory. The muon beam fa-

cility at the proton synchrotron ISIS has started operation to accommodate versatile research programs using powerful pulsed muon beams.

The new project on relativistic-energy spin physics has been formulated as the 2nd international research program following the first on muon science. It is to be carried out in collaboration with Brookhaven National Laboratory. The program aims at investigation of spin related properties of nucleons in terms of the QCD framework. Spin-polarized proton beams will be developed and facilitated at RHIC, bringing a new opportunity of physics in the RHIC program. The construction of a muon arm has started as well as R & D work on Siberian snakes.

The base-line research program using the heavy-ion accelerator complex has maintained a steady development. Nuclear physics researches have been heavily associated with radioactive beam experiments. Studies on nuclear synthesis towards the drip lines and very heavy elements have continued, resulting in identification of new isotopes such as ^{31}Ne , ^{37}Mg , ^{197}Rn , and ^{200}Fr . Spectroscopy on extremely neutron rich nuclei has made a further progress: Inelastic scattering, charge exchange reactions and Coulomb dissociations have been extensively applied to study different excitation modes of halo (or skin) nuclei. The β - γ -neutron spectroscopy has been developed significantly. Reactions induced by unstable nuclei offered other unique opportunities. Sub-barrier fusion reactions with neutron rich nuclei have been measured to investigate plausible anomaly in cross sections. Measurements of reaction rates of astrophysical interest have continued. Among others the measurement of Coulomb dissociation cross section of ^8B has been elaborated in relation to the solar neutrino problem.

Development of the radioactive beams is crucial for the studies on unstable nuclei at the Facility. Uniquely the Facility provides three different types of radioactive beams: Firstly intermediate-energy RIB by means of projectile fragmentation has been most frequently used, amounting to about 40 % of the whole RRC beam time. The second type of RIB is the spin-polarized beam which is also produced via PF process. The beam has been used to determine nuclear moments (g -factor and Q) of a dozen of unstable nuclei including exotic nuclei such as ^{17}B . The third type of RIB is the high-spin isomer beam which is produced via reverse-kinematics fusion reactions. Beams of heavy isomers with spins close to $30 \hbar$ are obtained with considerable intensity. A study on secondary fusion reactions was initiated.

Spin-isospin response is another popular subject at

the Facility, where reactions ($d,^2\text{He}$) and ($d,d(0^+)$) as well as heavy-ion exchange reactions are primarily used. A simple direct-reaction mechanism characteristic of high-energy heavy-ion exchange reactions was proved to provide a useful means of the spectroscopy.

Atomic physics has been pursued, enjoying an extremely wide energy range of heavy ions covered by the set of the ECR ion source, RILAC and RRC. A method of recoil-ion momentum analysis in ion-atom collisions has been developed using a cold supersonic gas jet target. It allows determination of the final electronic state and resolves the small scattering angle in the range of 10^{-6} radian. The fragmentation of C_{60} molecules in collisions with heavy ions has been studied at the RILAC. A study on collisions between negative hydrogen ions and highly charged energetic ions has started. An international collaboration program on beam-foil spectroscopy of highly charged ions was further enhanced in collaboration with Lund University. A series of systematic lifetime measurements of Mg-like heavy ions has been extended to heavier elements up to Rh. Basic information for laser and plasma applications is gained.

In the domain of nuclear chemistry nuclear hyperfine studies have moved in a new phase of development for in-beam spectroscopy: The following three different approaches of in-beam Mössbauer spectroscopy were pursued. Firstly site occupation and atomic jump process of ^{57}Fe in solid rare gases were investigated using Coulomb-excited recoils. An alternative reaction of $^{56}\text{Fe}(d,p)^{57}\text{Fe}$ was used to study the dynamic behavior of interstitial ^{57}Fe atoms in a single crystal of Fe. An attempt to produce high-energy PF beam of the

short-lived ^{57}Mn isotope has been initiated to open a new domain of Moessbauer spectroscopy.

The multi-tracer technique originally developed at the Facility continuously cultivated new areas of application. Diabetic mice, LEC rats and atmosphere-plant systems were newly treated and influx rates of alkali metals into erythrocyte and labeling of antibodies with a multi-tracer were studied.

Heavy ion beams have offered a variety of means for material characterization including those facilitating PIXE, Rutherford scattering and channeling effect. Recently a project on slow positron spectroscopy using short lived isotopes was started at the AVF cyclotron.

Irradiation effects with heavy-ion beams are studied in several aspects. In the domain of radiation biology a striking effect was observed in irradiation of heavy ions on tobacco plants. A nitrogen beam elicited mutagenesis in the embryo of the plant when administered during the fertilization cycle and its effect was manifested in an extremely short period. Recently an intriguing application of radioactive beam was tested in relation to the cancer therapy. Use of a radioactive beam may offer a possibility to spot in real time the location of the stopped isotopes by means of positron tomography. A simulation experiment using a radioactive beam of ^{11}C was performed, demonstrating an encouraging perspective. Heavy-ion beams are also useful to modify the property of material in a controlled way. In this respect a study on the pinning effect of magnetic flux through high-Tc superconducting materials under the irradiation of high-energy heavy ions is in progress.

For the first time this issue presents a list of seminars held at the Facility.

Masayasu Ishihara
Director
RIKEN Accelerator Research Facility

II. OPERATION OF ACCELERATORS

RRC and AVF Cyclotron Operation

M. Kase, N. Inabe, A. Goto, T. Kageyama, I. Yokoyama, M. Nagase, S. Kohara, T. Nakagawa, K. Ikegami, O. Kamigaito, J. Fujita, H. Isshiki,* H. Akagi,* R. Ichikawa,* N. Tsukiori,* R. Abe,* K. Takahashi,* T. Maie,* T. Homma,* and Y. Yano

All beams, which were accelerated with the RIKEN Ring Cyclotron (RRC) in the one-year duration from Nov. 1994 to Oct. 1995, are listed in Table 1, together with fundamental acceleration parameters and a total time spent for experiments. In this period, a total of 35 kinds of beams, ranging widely in the energy and mass space, was used for experiments. Among of these, 13 kinds of beams, such as 80 MeV/n ^{50}Ti and 7 MeV/n

^{130}Te , were newly added to the list. A proton beam with the highest energy of 210 MeV, which had been accelerated only for a machine test in 1991, was firstly used for experiment.

The total beam time, which was used for experiments, amounts to 202 days. Most of it (86.7%) was devoted to nuclear physics experiments and the rest (13.3%) to experiments in many other fields, such as

Table 1. RRC beams accelerated during Nov. 1994–Oct. 1995.

Particle	Charge	RF F (MHz)	h in RRC	Injector	Energy (MeV/u)	Beam time (days)
H_2	1	26.2	5	AVF	80 [†]	1.8
	1	27.6	5	AVF	90	1.3
	1	29.0	5	AVF	100	1.3
	1	30.1	5	AVF	110	2.2
	1	30.5	5	AVF	113	2.5
	1	32.6	5	AVF	135	4.5
$\text{H}_2 \rightarrow \text{p}$	1	34.2	5	AVF	150 [†]	2.0
p	1	38.7	5	AVF	210	1.7
pol-d	2	32.6	5	AVF	135	18.9
^{12}C	6	32.6	5	AVF	135	17.6
^{13}C	6	29.0	5	AVF	100	13.2
^{14}N	6	32.7	9	RILAC	35	0.4
	7	32.6	5	AVF	135	3.3
^{16}O	8	32.6	5	AVF	135	6.7
^{18}O	7	35.2	9	RILAC	42 [†]	4.8
	8	29.0	5	AVF	100	24.9
^{20}Ne	10	32.6	5	AVF	135	7.8
^{22}Ne	10	24.6	5	AVF	70	4.3
	10	29.0	5	AVF	100	4.4
	10	30.1	5	AVF	110	5.9
^{36}Ar	6	18.8	11	RILAC	7.6	8.2
^{40}Ar	14	33.0	9	RILAC	37 [†]	0.5
	17	27.6	5	AVF	90 [†]	8.8
	17	28.1	5	AVF	95	2.6
^{48}Ti	7	18.8	11	RILAC	7.6 [†]	6.8
^{50}Ti	20	26.2	5	AVF	80 [†]	11.8
^{59}Co	24	26.2	5	AVF	80 [†]	1.9
^{58}Ni	25	28.1	5	AVF	95 [†]	5.9
^{84}Kr	21	28.1	10	RILAC	21 [†]	0.4
	23	28.0	9	RILAC	26	0.5
	25	32.7	9	RILAC	36	0.5
^{129}Xe	22	18.8	11	RILAC	7.6 [†]	2.8
^{136}Xe	31	28.0	9	RILAC	26	2.7
^{130}Te	22	18.0	11	RILAC	7 [†]	16.2
^{140}Ce	24	18.0	11	RILAC	7 [†]	3.6
Total						202.7

[†] New beams

* Sumijyu Accelerator Service, Ltd.

biology, medical science, radio-chemistry, health physics, and material science. The AVF-RRC operation was performed for 157 days (79%) and the RILAC-RRC operation for 42 days (21%).

It takes one day to prepare a beam on the average. However a beam tuning time longer than 1.5 days is sometimes necessary to meet user's special requirements on a strict single-turn extraction, a small beam spot on target, a well-separated single-bunched beam, and so on.

Stand-alone uses of the two injector have routinely been made during a time when the other injector is coupled with RRC. In Table 2 are listed the beams which were provided against users of the AVF cyclotron. A total of 44 days was spent additionally for various experiments on slow-positron beam production, in-beam Mössbauer spectroscopy, and RI production as well as nuclear physics.

In this one year, a total of 14 days of the scheduled machine time had to be canceled. Main reasons for

these unexpected shut-downs were relating to deflectors of both the AVF cyclotron and the RRC. They sometimes did not work sufficiently due to their unendurable leak currents. A periodic maintenance with opening a vacuum chamber is necessary in both the cases. Most of beam time which was canceled due to these troubles could be compensated by shortening maintenance time or holidays.

Recently a beam of 80 MeV/n ^{50}Ti was accelerated and used for an experiment. To get an enough intensity, we had to use an enriched-material, which is extremely expensive. To save the quantity of it, when it was charged to the 10 GHz ECR source, a thin alumina (Al_2O_3) pipe, a hole of which was filled with a small amount of powder of enriched (50%) TiO, was used in stead of a normal ceramic rod. It could supply an 80 MeV/n ^{50}Ti beam with an intensity of 8 pA on a target for a week at least.

A single-bunched beam is sometimes required by users as a time trigger for the measurement of time spectrum. A very compact single-bunch selector, which consists of a fast beam chopper and a sub-harmonic buncher, has been successfully developed. Both the devices are installed in a low-energy injection line of the AVF cyclotron. As long as a single-turn extraction is strictly achieved in each cyclotron, a pure single bunched beam with a repetition rate as high as 1 MHz is available.

In the spring of 1995, a beam line, E7e, was newly built in the E7 room for a stand-alone use of the AVF cyclotron in place of an old beam line E7b. As the result, the beam course E7b, which had been used for a muon spectrometer of Large Ω , was removed together with the experimental device. The new beam line was designed for the experiment using a polarized-deuteron beam. A new experiment on polarized-neutron scattering has just started using it.

Table 2. AVF beams which were used for experiments from Nov. 1994 to Oct. 1995.

Particle	RF F (MHz)	h in AVF	Ion source	Energy MeV/u	Beam time (days)
p	23.0	2	ECR	14.0	0.9
d	12.3	2	PIS	8.0	2.9
	13.2	2	PIS	9.1	17.8
	19.0	2	PIS	9.5	6.0
	23.0	2	PIS	14.0	1.9
α	15.5	2	ECR	25.0	9.3
	18.2	2	ECR	35.0	1.9
	17.2	2	ECR	32.0	0.3
^{27}Al	16.9	2	ECR	7.5	1.5
^{40}Ar	12.0	2	ECR	3.8	1.9
Total					44.4

Tandem Operation

E. Yagi, K. Ogiwara, T. Urai, and M. Iwaki

A 1.7 MV tandem accelerator has been newly installed and becomes available for experiment since April, 1995. A large portion of beam time is allotted to machine inspection and beam test. Additional beam lines are still under construction.

The experimental studies on the following subjects are being made.

- (1) Rutherford Backscattering Spectroscopy (RBS)
 - (a) Behaviour of Kr atoms implanted into aluminium by a channelling method (Muon Science Lab.).
 - (b) Behaviour of Xe atoms implanted into iron (Muon Science Lab.).
 - (c) RBS analysis of Tb-implanted sapphire crystals (Surface Characterization Centre).

(d) Characterization of oxide films grown on SrTiO_3 (Surface Chemistry Lab.).

(2) Nuclear Reaction Analysis (NRA)

(a) Lattice location of hydrogen in niobium alloys by a channelling method (Muon Science Lab.).

(3) Particle Induced X-ray Emission (PIXE)

(a) Application of PIXE to biomedical and material sciences: Trace element analysis using energy-dispersive X-ray spectrometry, and chemical state analysis using wave-dispersive X-ray spectrometry (Inorganic Chemical Physics Lab.).

(b) Development of an X-ray detector (Cyclotron Lab.).

RILAC Operation

E. Ikezawa, M. Hemmi, T. Chiba, S. Kohara, T. Aihara,* T. Ohki,* H. Hasebe,*
H. Yamauchi,* and Y. Miyazawa

RILAC has been in steady operation, and has supplied various kinds of ion beams for the experiments. Table 1 gives the statistics of operation from Jan. through Dec. 1995. One day of the scheduled beam time was cancelled owing to the damage of copper sheets for electric contact of the resonator No. 6: the thin copper sheets (10 cm wide, 7 cm long, and 0.3 mm thick) were melted with too high rf currents. This damage was extended in the region of about one meter in length. Table 2 summarizes the time sharing allotted for individual research groups. The percentage of the beam time for RRC was about 45% of the total: ions of ^{14}N , ^{18}O , ^{36}Ar , ^{40}Ar , ^{48}Ti , ^{84}Kr , ^{129}Xe , ^{130}Te , ^{136}Xe , ^{140}Ce , and ^{142}Ce were injected to RRC. Table 3 gives the statistics of ions used in this year. Among them, a $^{89}\text{Y}^{14+}$ beam at the acceleration frequency of 32 MHz is new. The percentage of the beam time for metallic ions amounted to about 36% of the total.

Table 1. Statistics of the operation from Jan. 1 through Dec. 31, 1995.

	Days	%
Beam time	174	47.7
Frequency change	15	4.1
Overhaul and improvement	52	14.2
Periodic inspection and repair	14	3.8
Machine trouble	1	0.3
Scheduled shut down	109	29.9
Total	365	100

Table 2. Beam time for individual research groups.

	Days	%
Atomic physics	60	34.5
Solid-state physics	6	3.4
Nuclear physics	6	3.4
Nuclear chemistry	2	1.1
Radiation chemistry	16	9.2
Accelerator research	6	3.4
Beam transportation to RRC	78	44.8
Total	174	100

Table 3. List of ions used in this year.

Ion	Mass	Charge state	Days
He	4	1	5
B	11	2, 3	8
C	12	2	6
N	14	3	2
O	16	2, 3, 5	5
O	18	4	7
Ne	20	3, 4	10
Si	28	5	1
Ar	36	6	6
Ar	40	5, 6, 8	39
Ti	48	7	9
Ni	58	6	2
Kr	84	10, 11, 13	13
Y	89	14	3
Zr	90	12	2
Zr	91	12	2
Nb	93	12	7
Xe	129	9	5
Te	130	9	13
Xe	136	9, 15	13
Ce	140	11	14
Ce	142	11	1
Pb	208	11	1

We carried out the following machine improvements: (1) In the rf system of six resonators, the servo motor controllers driving the capacitive trimmer were replaced with compact ones designed newly because they were worn out after many years operation. To get easy maintenance and stable operation, both automatic tuning and amplitude controllers were also replaced with newly designed ones;¹⁾ (2) The power supplies for the quadrupole magnets of the beam transport line were remodeled by replacing the obsolete power transistors with modern ones; and (3) The stainless-steel plates (159 sheets in total) mounted in three heat exchangers for RILAC cooling water were replaced with new ones because of deterioration after the fifteen-years use.

In the 8 GHz ECR ion source, we have tested to produce metallic ions by use of materials such as Gd_2O_3 and CaF_2 ; as a result, we obtained the beam intensity of 2 μA for Gd^{12+} and 6 μA for Ca^{6+} . The yield of Ca ions with a CaF_2 rod was lower than that with a CaO rod. So far, the ions of 10 kinds of gaseous elements and those of 42 kinds of solid elements have been produced by the 8 GHz ECR ion source.

References

- 1) S. Kohara et al.: This report, p. 217.

* Sumijyu Accelerator Service, Ltd.

III. RESEARCH ACTIVITIES

1. Nuclear Physics

Stochastic Variational Method with Realistic Potentials

Y. Ohbayasi,* Y. Suzuki, and K. Varga

[few-body systems, stochastic variational method, realistic potential.]

We have investigated the application of the stochastic variational methods (SVM)¹⁾ to the few-body problems what are treated as either multi-cluster or few-nucleon systems.²⁾ The results are obtained with ‘effective’ potentials.

Now we applied the SVM method to the system interacting via ‘realistic’ potentials, especially to the triton ground state ($E_{\text{Exp.}} = -8.4$ MeV). Since solving the nuclear many-body Schrödinger equation is difficult because of the complexity of the interaction and of the variety of nuclear motion, it is interesting to confirm whether our method is effective in such case.

Up to now, we selected Reid V8³⁾ and Eikemeier and Hackenbroich potential (EH)⁴⁾ as the ‘realistic’ potential. The former has the Yukawa function and the latter has the Gaussians. Both of them include the central, spin-orbit and tensor potentials. Because the potential has non-central parts, the needed channel becomes larger than that of the case with effective potential which has only central part. The orbital angular momentum channels included in the calculation are $(\ell_1, \ell_2)L = (0,0)0, (1,1)0, (2,2)0, (1,1)1, (2,2)1, (1,1)2, (0,2)2, (2,0)2$ and $(2,2)2$, and the total spin channels are $[(s_1, s_2) s_{12}, s_3]S = [(1/2, 1/2) 0, 1/2]1/2, [(1/2, 1/2) 1, 1/2]1/2$ and $[(1/2, 1/2) 1, 1/2]3/2$. We solved the triton ground state ($J^\pi = 1/2^+$) by selecting important basis functions on correlated Gaussians.

The application of the few-body problem to the triton system with the ‘realistic’ potential has already been investigated by GFMC, ATMS, and Feddeev groups.⁵⁾ In the case of Reid V8 potential, we get the energy of -7.6 MeV within 200 basis. Comparative results are: $-7.08(05)$ MeV [VMC], $-7.54(10)$ MeV [GFMC], -7.59 MeV [Faddeev]. We have confirmed that our method yields better results than the other with lower dimension of the basis functions. Figure 1 displays the energy convergence of triton for the different potentials.

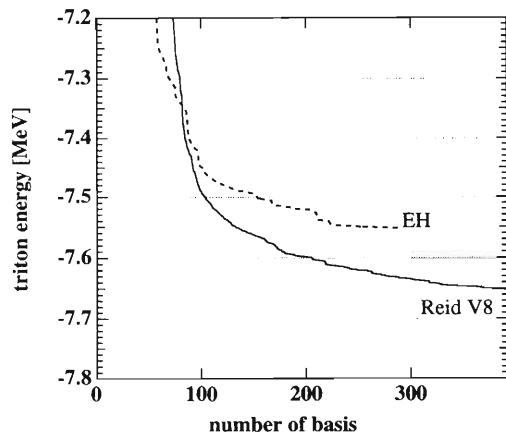


Fig. 1. The triton energy convergence of Reid V8 (Solid line) and Eikemeier and Hackenbroich (dashed line).

In summary, we applied the SVM to solve the triton ground state with the ‘realistic’ potentials. Our results give larger binding energy than the other methods. Thus we confirmed that our method is also useful for ‘realistic’ potential problems. For further application, we will extend to the system with more than three nucleons.

References

- 1) K. Varga, Y. Suzuki, and R. G. Lovas: *Nucl. Phys.*, **A571**, 447 (1994).
- 2) K. Varga, Y. Suzuki, and Y. Ohbayasi: *Phys. Rev.*, **C50**, 189 (1994); K. Varga, Y. Suzuki, and I. Tanihata: *ibid.*, **C52** (1995) in press; K. Varga and Y. Suzuki: *ibid.*, in press.
- 3) R. B. Wiringa and V. R. Pandharipande: *Nucl. Phys.*, **A317**, 1 (1979).
- 4) H. Eikemeier and H. H. Hackenbroich: *ibid.*, **A169**, 407 (1971).
- 5) See, e.g., J. Carlson, *Phys. Rev.*, **C38**, 1879 (1988).

* Graduate School of Science and Technology, Niigata University

Structure of the $A = 9$ System with Microscopic Cluster Model

K. Arai,* Y. Ogawa, Y. Suzuki, and K. Varga

[the mirror nuclei of ${}^9\text{Be}$ and ${}^9\text{B}$, the microscopic cluster model.]

Be isotopes, from ${}^8\text{Be}$ to the neutron drip-line ${}^{14}\text{Be}$, have very interesting properties because of the variety of binding mechanism and structure. ${}^8\text{Be}$ is well-known to have a 2α structure, and ${}^{11}\text{Be}$ and ${}^{14}\text{Be}$ have a neutron halo structure. Our purpose is to investigate the structure of Be-isotopes by a microscopic $2\alpha +$ valence neutrons model.

As the start of this investigation, we study ${}^9\text{Be}$ and its mirror nucleus ${}^9\text{B}$ with a $2\alpha + N$ three-body microscopic cluster model using the stochastic variational method.¹⁾

The two-nucleon interaction used in this calculation is Minnesota Pot. including the L-S force and the Coulomb Pot. The exchange-mixture parameter u in Minnesota Pot. is taken as 0.94 to reproduce the ground state binding energy of ${}^9\text{Be}$ from the three-body threshold. The calculated proton radius $r_p = 2.39[\text{fm}]$ is in good agreement with the experimental value derived from (e,e) data $r_p = 2.37[\text{fm}]$. Our result of the magnetic moment and electric quadrupole moment is also in very nice agreement with the experimental values. See Table 1. The probability of total angular momentum L in the ground state of the ${}^9\text{Be}$ (total spin and isospin are $S = \frac{1}{2}$, $T = \frac{1}{2}$) is about 85% for $L = 1$ and 15% for $L = 2$. This $L = 2$ component is important to reproduce the magnetic moment and Q-moment. The electron elastic longitudinal and transverse form factors were also calculated and found to reproduce experimental data very well. The calculated total reaction cross section for a carbon target at

800 MeV/nucleon is 850[mb], which is in fair agreement with the experimental value $806 \pm 9[\text{mb}]$.

Except for the ground state of ${}^9\text{Be}$, all the states of ${}^9\text{Be}$ and ${}^9\text{B}$ are above the three-body threshold. The complex scaling method was used to calculate these resonance states, and the interaction used here is the same as the ground state of ${}^9\text{Be}$. The calculated energy level and width of $\frac{5}{2}^-$, $\frac{1}{2}_1^-$, $\frac{7}{2}^-$ are in good agreement with the experimental ones. The investigation for the $\frac{1}{2}^+$ state is in progress.

Recently K. Varga et al. studied the structure of ${}^9\text{Li}$ and ${}^9\text{C}$ with $\alpha + (3N) + N + N$ four-body microscopic cluster model.²⁾ Because the ground state and the 2.43 MeV $\frac{5}{2}^-$ state of ${}^9\text{Be}$ are described well by the present model, the β decay of the ${}^9\text{Li}$ ground state to these states is expected to further test the accuracy of their wave functions or an available wave function of ${}^9\text{Li}$. The experimental value of $\log ft$ for the β decay to the ${}^9\text{Be}$ ground state is about 5.3,³⁾ indicating that the β -decay matrix element is fairly suppressed despite the allowed transition. In fact the Gamow-Teller (GT) matrix element, to any state of ${}^9\text{Be}$ which is described by the $\alpha + \alpha + n$ three-cluster model always vanishes regardless of the wave function of ${}^9\text{Li}$. This is most easily understood by acting the Hermitian conjugate of the GT operator on the ${}^9\text{Be}$ wave function and by noting that the spin-isospin part of the α -particle wave function is fully occupied. The break-up effect of the α particle is needed and we must extend the model space to reproduce experimental ft value. To see this effect, we extended the model space a little as a first test. One of the α particles is broken to triton and one proton, then the calculated $\log ft$ is about 6.1 and gets weak transition. A further investigation is being made.

Table 1. The matter, proton, neutron radius r_m, r_p, r_n and the magnetic moment: μ and the quadrupole moment: Q in the ground state of ${}^9\text{Be}$.

	cal.	exp. ³⁾
r_m (fm)	2.50	—
r_p (fm)	2.39	2.37
r_n (fm)	2.58	—
μ (μ_N)	-1.1689	-1.1778 \pm 0.0009
Q (e fm ⁻²)	5.13	5.3 \pm 0.3

References

- 1) K. Varga, Y. Suzuki, and R. G. Lovas: *Nucl. Phys.*, **A571**, 447 (1994).
- 2) K. Varga, Y. Suzuki, and I. Tanihata: *Phys. Rev.*, **C52**, 3013 (1995).
- 3) F. Ajzenberg-Selove: *Nucl. Phys.*, **A490**, 1 (1988).

* Graduate School of Science and Technology, Niigata University

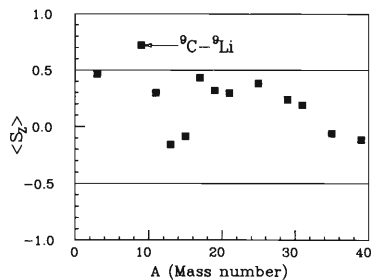
Magnetic Moments of the Mirror Nuclei ${}^9\text{C}$ and ${}^9\text{Li}$

N. Fukunishi and I. Tanihata

[NUCLEAR STRUCTURE, Magnetic moment, Shell model.]

The magnetic moment of a nucleus is one of the basic probes for the microscopic aspect of the nuclear structure, especially the spin structure of nuclei. Recently, K. Matsuta and his co-workers reported the magnetic moment of ${}^9\text{C}$,¹⁾ in which the proton number and the neutron number are highly asymmetric. With the previously determined value of the magnetic moment of ${}^9\text{Li}$, which is a mirror partner of ${}^9\text{C}$, they pointed out the anomalous behavior of unstable nuclei.

Under the assumption of the isospin symmetry and the use of free nucleon g-factors, the isoscalar magnetic moment (μ_{IS}) relates to the expected value of the total spin as $\mu_{IS} = J/2 + 0.38\langle S_Z \rangle$, where we choose the z-axis to be the quantized axis of the total angular momentum (J). Figure 1 shows $\langle S_Z \rangle$ for several mirror pairs whose mass number is odd. Roughly speaking, even numbers of like nucleons are usually coupled to give $J = 0$ due to the strong pairing correlation and the last unpaired nucleon mainly contributes to $\langle S_Z \rangle$. Thus, $\langle S_Z \rangle$ is usually less than $1/2$. The mirror pair ${}^9\text{C}$ and ${}^9\text{Li}$ exceed exceptionally this value.

Fig. 1. $\langle S_Z \rangle$ for several mirror pairs.

We analyzed this exotic phenomenon based on the conventional shell model. Our starting point is the p-shell model. Several effective interactions reproduce successfully properties of nuclei in this mass region.²⁾ We found in Fig. 2 that all of them failed to reproduce the present anomaly. The important point is that it does not mean that all effective interactions previously proposed have some shortcomings. We demonstrated that any effective interaction, even if it is unphysical, cannot reproduce simultaneously the isoscalar and the isovector magnetic moments (μ_{IV}) in this case. The reason is as follows. The nucleus ${}^9\text{C}$ has one active neutron and four active protons in the p-shell. Thus, possible combinations of the neutron and the proton spin are only two. The one is ($S_n = 1/2$, $S_p = 0$), where $S_n(S_p)$ is the neutron (proton) spin. The other

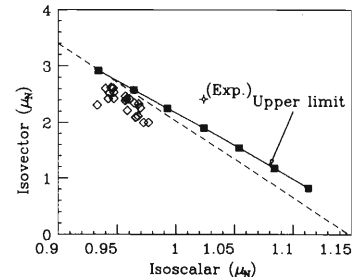


Fig. 2. The isoscalar and the isovector magnetic moments for the mirror pair ${}^9\text{C}$ and ${}^9\text{Li}$. The diamonds show the results of shell model calculation using several effective interactions. The solid line with black boxes shows the theoretical upper limit.

is ($S_n = 1/2$, $S_p = 1$). In this case, the broken pair of protons contribute $\langle S_Z \rangle$. To reproduce μ_{IS} , the latter component must contribute largely. It results in the strong reduction of μ_{IV} because the g-factors of the proton and the neutron have different sign. Thus, a maximum value of μ_{IV} exists for a given value of μ_{IS} as illustrated in Fig. 2. We found that the present experimental result exceeds this upper limit.

The previous discussions are based on three assumptions, that is to say, the isospin symmetry, the use of free nucleon g-factors, and the choice of the model space. We must investigate several effects that are believed to be small for light stable nuclei. We extended our calculation to include (1) two-particle type excitation from the p-shell to the sd-shell,³⁾ (2) effects of exchange currents and the tensor force with the use of effective g-factors,⁴⁾ (3) effects due to the coulomb force, the isospin-symmetry-breaking force and the charge-symmetry-breaking force. The last one explains qualitatively the discrepancy between theory and experiment, but these isospin-breaking effects can explain only 25% of the discrepancy quantitatively. We must mention that the present calculations do not include possible effects from loosely bound nucleons or clustering. In this sense, our analysis is incomplete. However, the present analysis revealed how exotic the magnetic moments of the mirror pair ${}^9\text{C}$ and ${}^9\text{Li}$ are.

References

- 1) K. Matsuta et al.: *Nucl. Phys.*, **A588**, 153c (1995).
- 2) They include, for example, the Cohen-Kurath interaction and the PSDT interaction recently proposed by Warburton and Brown.
- 3) The PSDWBP interaction is used.
- 4) A. Arima et al.: *Adv. Nucl. Phys.*, **18**, 1 (1987).

Magnetic Moment of ^{11}Be

T. Suzuki, T. Otsuka, and A. Muta

[Neutron halo, Magnetic moment.]

Magnetic moments of a neutron-halo nucleus, ^{11}Be , are investigated.¹⁾ The neutron halo is found to reduce the meson exchange current (MEC) contributions to the magnetic moment of ^{11}Be ($1/2_{g.s.}^+$). The calculated magnetic moment is found to be sensitive to the admixture of $|^{10}\text{Be}(2^+) \times d_{5/2}: 1/2^+ \rangle$ configuration in $^{11}\text{Be}_{g.s.}$. The measurement of the magnetic moment is highly recommended for the determination of the rate of the admixture of $|^{10}\text{Be}(2^+) \times d_{5/2}: 1/2^+ \rangle$ configuration in $^{11}\text{Be}_{g.s.}$.

As for the MEC, the pair, pionic and Δ_{33} -isobar currents due to one-pion exchanges are taken into account. We use a halo wave function for $\nu 1s_{1/2}$ -orbit obtained in a deformed Woods-Saxon (WS) potential ($\beta_2 = 0.7$) since the ground state is considered to be well deformed.²⁾ Calculated values of the MEC contributions to the magnetic moment for the pure $\nu 1s_{1/2}$ -state are $\delta\mu = -0.076$ (-0.117), 0.059 (0.098) and 0.019 (0.052) μ_N for the pair, pionic and Δ_{33} -isobar current, respectively, for the halo (harmonic oscillator (h.o.)) wave function. Reduction of the MEC contribution is found to be due to smaller overlap of a single-particle wave function of the halo orbit with those of core orbits. The net MEC contributions to the magnetic moment, which are small even without the halo effects, are reduced to 6% of the h.o. value for the deformed WS potential.

Now, we examine how the calculated magnetic moment depends on the rate of the admixture of the $|^{10}\text{Be}(2^+) \times d_{5/2}: 1/2^+ \rangle$ configuration. The ground state of ^{11}Be is assumed to have the following form:³⁾

$$|^{11}\text{Be}(1/2_{g.s.}^+) \rangle = \alpha |^{10}\text{Be}(0^+) \times \nu 1s_{1/2}: 1/2^+ \rangle + \beta |^{10}\text{Be}(2^+) \times \nu d_{5/2}: 1/2^+ \rangle \quad (1)$$

Calculated results of the magnetic moment with and without the MEC are shown in Fig. 1. As the configuration is free from the halo, the more the configuration is admixed, the less become the effects of the halo on the MEC contributions. We also carried out a calculation that takes into account the quenching effects from higher-order configuration mixing: $g_s^{\text{eff}} = 0.85 g_s^4$ (see Fig. 2). Calculated values of the magnetic moment depend almost linearly on $P(1s_{1/2}) = \alpha^2$. If the magnetic moment were measured, the probability of the admixture of the $|^{10}\text{Be}(2^+) \times d_{5/2}: 1/2^+ \rangle$ configuration in $^{11}\text{Be}_{g.s.}$ could be determined. It would also become apparent whether the quenching effects due to higher-order configuration mixing are important or not. $P(1s_{1/2})$ would be determined with an accuracy of $\sim 10\%$. The variational shell model (VSM),³⁾ for ex-

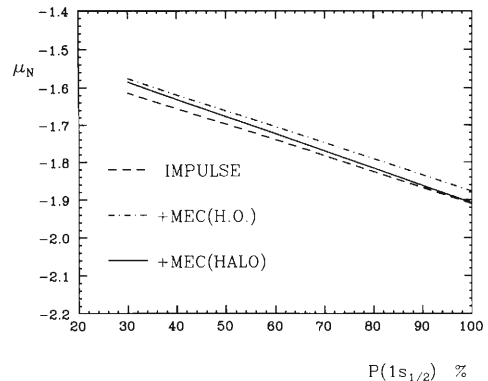


Fig. 1. Dependence of the calculated magnetic moment of $^{11}\text{Be}(1/2_{g.s.}^+)$ on $P(1s_{1/2})$. Dashed line denotes the impulse values while dash-dotted and solid lines include the MEC contributions obtained with h.o. and halo wave functions for the $1s_{1/2}$ orbit, respectively.

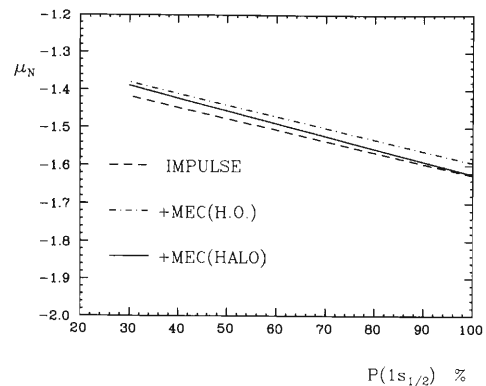


Fig. 2. The same as in Fig. 1 except that the effective isovector spin g-factor, $g_s^{\text{eff}} = 0.85 g_s$, is used.

ample, gives $P(1s_{1/2}) \sim 0.55$. A stripping reaction on $^{10}\text{Be}^5)$ yields a spectroscopic factor of 0.77. The measurement of the magnetic moment is now under plan⁶⁾ though it is a hard experiment.

References

- 1) T. Suzuki, T. Otsuka, and A. Muta: *Phys. Lett.* **B**, in press.
- 2) A. Muta and T. Otsuka: submitted to *Phys. Rev.* **C**.
- 3) T. Otsuka, N. Fukunishi, and H. Sagawa: *Phys. Rev. Lett.*, **70**, 1385 (1993).
- 4) W.-T. Chou, E. K. Warburton, and B. A. Brown: *Phys. Rev.*, **C47**, 163 (1993).
- 5) B. Zweiglin et al.: *Nucl. Phys.*, **A315**, 124 (1979).
- 6) K. Asahi: private communication.

Direct Radiative Capture Process in the $^{12}\text{C}(n,\gamma)^{13}\text{C}$ Reaction

A. Mengoni,* T. Otsuka, and M. Ishihara

[Neutron capture, neutron-rich nuclei, neutron halo.]

The neutron capture cross sections for the $^{12}\text{C}(n,\gamma)$ reaction leading to the four bound state of ^{13}C have been calculated¹⁾ in the framework of the direct radiative capture (DRC) model. The incident neutron energy region covered is $0.0253 \text{ eV} \leq E_n \leq 500 \text{ keV}$. A comparison with experimental results is made possible by the recent measurements performed at the Tokyo Institute of Technology.²⁾ A detailed description of the methodology for calculation is given elsewhere.¹⁾ The main results of the investigation can be summarized as:

1) The DRC model provides a reliable description of the capture process. In fact, in the energy region under consideration no compound nuclear state is observed (the first resonance is at $E_n = 2.1 \text{ MeV}$).

2) The role of incident p -wave neutrons is essential in the representation of the experimental results for the transitions leading to the $2s_{1/2}$ and to the $1d_{5/2}$ bound orbits in ^{13}C .

3) The calculated cross section due to incident s -wave neutrons is sensitive to the neutron-nucleus interaction.

4) The calculated cross section due to incident p -wave neutrons is essentially insensitive to the neutron-nucleus interaction.

Point 4), even though expected from a naive picture

of the neutron-nucleus collision process (in which the p -wave neutrons only interact peripherally with the target), is of particular relevance. In fact, on the one hand it sustains the reliability of the calculation and on the other hand it opens the possibility of using the (n,γ) reaction channel to derive information on the bound state wave functions. In fact, in the case of $p \rightarrow s$ transition the capture cross section depends essentially only on the matrix elements

$$Q_{i \rightarrow f}^{(1)} = \langle \Psi_f | \hat{T}^{E1} | \Psi_i \rangle$$

which, in turn, are sensitive only to the final state wave function. This result is being investigated in order to verify the possibility of directly extracting the radial component of the bound state wave function from the experimental (n,γ) cross section. In particular, using this technique it would be possible to directly verify the existence of exotic (e.g. halo) components in the wave function of excited nuclear states in stable and/or unstable neutron-rich nuclei.

References

- 1) A. Mengoni, T. Otsuka, and M. Ishihara: *Phys. Rev.*, **C52**, R2334 (1995).
- 2) T. Ohsaki, Y. Nagai, M. Igashira, T. Shima, K. Takeda, S. Seino, and T. Irie: *Astrophys. J.*, **422**, 912 (1994).

* Permanent address: Applied Physics Section, ENEA, Italy

Neutron Capture of Nuclei Far from Stability

A. Mengoni,* T. Otsuka, and M. Ishihara

[Neutron capture, neutron-rich nuclei, neutron halo, nucleosynthesis of heavy elements.]

It has been recently proposed^{1,2)} to use the neutron capture reaction channel (or its inverse, the coulomb dissociation) to study some peculiar structure properties of stable or near-stable nuclei. There are certain conditions which must be satisfied in order to apply this method. In particular, the condition that the density of levels has to be low enough to exclude the presence of nuclear compound states in the incident neutron energy region must be satisfied. The capture process which takes place under such conditions has been called the direct radiative capture (DRC) process. The DRC process of incident p -wave neutrons captured into bound s and d orbits is particularly suitable as an application of the method because for this particular case the matrix elements

$$Q_{i \rightarrow f}^{(1)} = \langle \Psi_f | \hat{T}^{E1} | \Psi_i \rangle$$

for the E1 γ -ray emitting transition $i \rightarrow f$ do not depend sensibly on the neutron-nucleus interaction. Therefore, the initial state wave function Ψ_i can be promptly calculated using simple potential models. Woods-Saxon or even square-well potential can be used to derive the radial component of the initial scattering state.³⁾ On the other hand, the final capturing state wave function, Ψ_f , directly enters in the matrix elements: hence, the role of the Ψ_f components on and outside the nuclear surface can be detected in a capture cross section measurement which provides

$$\sigma_{n,\gamma}(i \rightarrow f) = \frac{16\pi}{9\hbar} \bar{e}^2 k_\gamma^3 |Q_{i \rightarrow f}^{(1)}|^2.$$

Here, \bar{e} is the effective charge for neutrons and k_γ the emitted γ -ray wave number. Once that the calculation technique has been established and quantitatively tested for nuclei close to the stability line,^{2,3)} one can proceed further and apply the same method to unstable neutron-rich nuclei. In fact, as the neutron drip-line is approached, the neutron binding energy is drastically reduced making the level density low enough to strongly hinder the compound nucleus component of the capture process and making the DRC mechanism more likely to take place.

We have calculated the neutron capture reaction

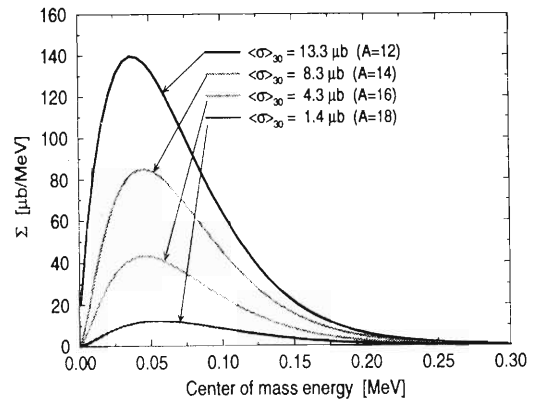


Fig. 1. Astrophysical Σ -factor for $n + {}^A\text{C}(n, \gamma)$ and $kT = 30$ keV.

rates for a chain of unstable neutron-rich carbon isotopes, in particular for applications in nuclear astrophysics, where we still must rely on model calculations for many of the required nuclear reaction rates needed for example in stellar and/or primordial nucleosynthesis calculations. In all of the cases considered the dominant reaction channel is an E1, DRC process with $p \rightarrow s$ and/or $p \rightarrow d$ as dominant transitions. The results are shown in the figure where the astrophysical Σ -factor

$$\Sigma_{kT}(E) \equiv \frac{2}{\sqrt{\pi}} \frac{1}{(kT)^2} E \sigma_{n,\gamma}(E) e^{-\frac{E}{kT}}$$

is shown for the $n + {}^{12,14,16,18}\text{C}(n, \gamma)$ reactions. The Maxwellian-averaged capture rates (equal to the integral of Σ), are also given in the figure.

References

- 1) T. Otsuka, M. Ishihara, N. Fukunishi, T. Nakamura, and M. Yokoyama: *Phys. Rev.*, **C49**, R2289 (1994).
- 2) A. Mengoni, T. Otsuka, and M. Ishihara: Proc. of the Workshop on Experimental Perspectives with Radioactive Nuclear Beams, Padova, 14-17, Nov., 1994, in press (1995).
- 3) A. Mengoni, T. Otsuka, and M. Ishihara: *Phys. Rev.*, **C52**, R2334 (1995).

* Permanent address: Applied Physics Section, ENEA, Italy

Interaction Radii of Na-isotopes

H. Sato

[Nuclear interaction radii.]

The determination of nuclear size and density distribution is one of the most important problems in nuclear physics, because these quantities give us quantitative idea of what is the nucleus and also give us a strong criterion for various nuclear structure calculations. In previous works, we studied the systematics of interaction radii in terms of the interaction cross section by performing the center of mass corrected Glauber model calculation including terms up to the second order of nucleon-nucleon profile function evaluated with the nuclear density distributions given by the density dependent Hartree-Fock type variational calculation,¹⁾ and found that the experimental interaction cross sections are nicely reproduced except for ¹¹Li.²⁾ We have pointed out that the interaction cross sections nicely satisfy the additivity relationship given by

$$\sigma(p, t) = \pi(R_p + R_t)^2,$$

where R_p and R_t are the interaction radii of the projectile and target nuclei, which are defined respectively by the interaction cross sections of identical nuclei, as

$$R_p = \sqrt{\sigma(p, p)/4\pi} \text{ and } R_t = \sqrt{\sigma(t, t)/4\pi}.$$

We also pointed out that the interaction radii R defined above can be understood as an energy independent characteristic nuclear radius in the nucleus-nucleus scattering like the charge radius in the electron scattering. In this work, we extend the study to the interaction cross sections of Na isotopes on a C target by employing Skyrme III (SKIII) interaction in the calculation of the nuclear radial distribution. The interaction cross sections and the interaction radii obtained are summarized in Table 1, and compared with experimental data.³⁾ Here we note that, though the

1f_{7/2} neutron state of ³²Na obtained is unbound by 0.087 MeV in this calculation, its radial wave function may not so differ from the real one because of a large centrifugal barrier in the potential. We find that the experimental values are nicely reproduced (except for ³²Na), and that the idea of the interaction radius defined through the cross section does also work nicely.

Table 1. The interaction cross sections and interaction radii of Na-isotopes (here the interaction radius of C is 2.595 fm).

A	σ_{exp} (mb)	σ_{cal} (mb)	R_A (fm)
20	1,086 (11)	1,075	3.250
21	1,100 (9)	1,090	3.295
22	1,092 (16)	1,110	3.345
23	1,147 (12)	1,130	3.395
24		1,150	3.450
25	1,185 (9)	1,170	3.510
26	1,211 (16)	1,205	3.600
27	1,229 (18)	1,235	3.690
28	1,265 (10)	1,275	3.780
29	1,281 (22)	1,300	3.845
30	1,318 (15)	1,325	3.905
31	1,358 (41)	1,350	3.970
32	1,395 (61)	(1,355)	(3.990)

References

- 1) H. Sato and Y. Okuhara: *Phys. Lett.*, **162B**, 217 (1985); *ibid.*, **168B**, 305 (1986); *Phys. Rev.*, **C34**, 2171 (1986).
- 2) I. Tanihata et al.: *Phys. Lett.*, **160B**, 380 (1985); *Phys. Rev. Lett.*, **55**, 2676 (1985).
- 3) T. Suzuki et al.: *Phys. Rev. Lett.*, **75**, 3241 (1995).

Mechanism of the Inversion between 1d and 2s Single Particle Levels

Y. Sugahara, K. Sumiyoshi, H. Toki, A. Ozawa, and I. Tanihata

[relativistic mean field theory, unstable nuclei.]

The physics of unstable nuclei attracts much attention. In nuclei far from the stability line, we have already found very interesting phenomena such as the formation of neutron halo and neutron skin. Near the drip lines, an interesting phenomenon was found recently. The experimental data indicate that $2s_{1/2}$ and $1d_{5/2}$ single particle levels could be inverted in some light nuclei. We study this phenomenon in the mean field picture.

First of all, in order to clarify the reason for the inversion of 2s and 1d levels, we consider a simple problem. Let us solve the radial Schrödinger equation with the Woods-Saxon potential, $V(r) = -V_0/(1 + \exp[(r - R)/a_c])$. By changing the diffuseness parameter a_c , we examine the relation between the shape of the potential and the inversion of the two levels. If we take a typical value, 0.6 fm for a_c , the potential has the normal shape as shown in Fig. 1(a). In this case, 2s and 1d levels appear in the normal order. When we increase a_c to 1.2 fm, the shape of the potential changes to the one in Fig. 1(b). The flat part near the center vanishes and the tail becomes larger. In this case, the inversion can happen as shown in Fig. 1(c).

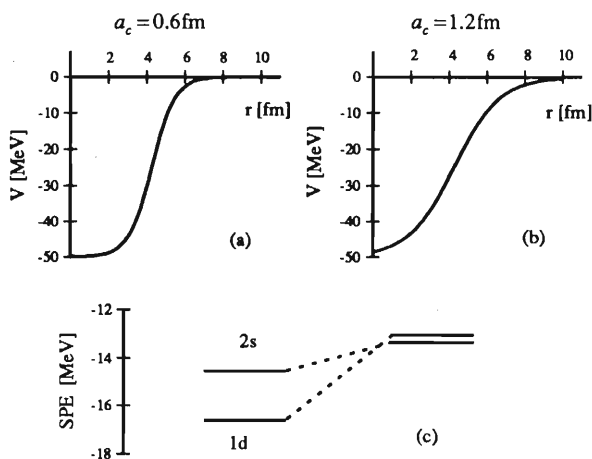


Fig. 1. Pictorial representation of the relation between the shape of the potential and the order of 2s and 1d levels. Here, the parameters for the Woods-Saxon potential are taken as $V_0 = -50$ MeV and $R = 4.3$ fm. The potential shown in (a) is for the case with the diffuseness $a_c = 0.6$ fm, while the one in (b) with $a_c = 1.2$ fm. The corresponding single particle energies of 2s and 1d levels are shown in (c); the left result corresponds to $a_c = 0.6$ fm and the right one to $a_c = 1.2$ fm.

What provides then such an enlarged tail and makes the flat part vanish? We find that the isovector potential plays an essential role. In the meson theory, the difference between the proton and the neutron densities creates the isovector potential. Therefore, the isovector potential has a peak near the surface if the proton and the neutron radii are different, where the difference between the proton and the neutron densities is the largest. On the other hand, the isoscalar potential has a similar shape to the total density. Hence, the addition of the isovector potential makes its flat part near the center vanish and the tail part enlarge as the case of the use of $a_c = 1.2$ fm.

In order to demonstrate the above discussion, we calculate the single particle energies for $2s_{1/2}$ and $1d_{5/2}$ levels of ^{14}C by the RMF theory with TM2 parameter set. In the RMF theory, ρ meson provides the isovector potential. Hence we change only the strength of the ρ -N coupling g_ρ , fixing other parameters. The calculated results are shown in Fig. 2. As g_ρ increases, 2s and 1d levels come close each other and the inversion occurs at $g_\rho \sim 5$. So far, we have discussed the effect of the isovector potential for the inversion only in the case of neutrons. The isovector potential acts also on protons. However, its influence is completely opposite to the case of neutrons. In fact as shown in Fig. 2, when g_ρ becomes large, the difference between 2s and 1d levels increases for protons.

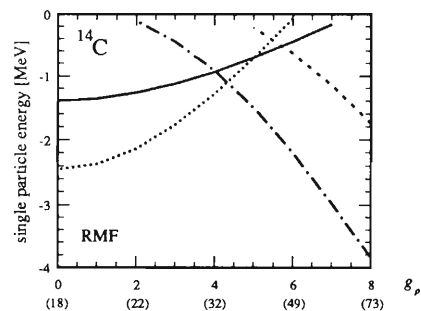


Fig. 2. The single particle energies for ^{14}C with the RMF theory as a function of g_ρ . The results for the neutron $2s_{1/2}$ and $1d_{5/2}$ levels are denoted by the solid and dotted curves, and those for the proton $2s_{1/2}$ and $1d_{5/2}$ levels are denoted by dashed and dash-dotted curves, respectively. As references, we show the corresponding symmetry energy for each value of g_ρ in the parentheses in unit of MeV.

A Systematic Study of Even-Even Mass Nuclei Up to the Drip Lines in Terms of the Relativistic Mean Field Theory

K. Sumiyoshi, D. Hirata, I. Tanihata, Y. Sugahara, and H. Toki

[nuclear structure, deformation, relativistic mean field theory.]

The recent advance at the radioactive nuclear beam facilities provides us with an explosive number of information on unstable nuclei. We are having the experimental data such as masses, radii and deformations of unstable nuclei in a wider region of the nuclear chart than before. The studies of exotic nuclei with such data have revealed the novel phenomena such as neutron halos¹⁾ and neutron skins²⁾ and bring new findings in nuclear physics.³⁾ Under this situation, we are eager to exploit the general feature of the nuclear properties using a reliable many body theory in the whole region of the nuclear chart.

We study the ground state properties of even-even mass nuclei up to the drip lines in the relativistic mean field (RMF) theory with axial deformation. The RMF theory, which is a phenomenological model based on the recent success of the relativistic Brueckner Hartree Fock theory,⁴⁾ has been successfully applied to the description of the properties of stable⁵⁾ and unstable nuclei.⁶⁾ Motivated by the recent RMF study on the shape coexistence and transitions of isotopes,⁷⁾ we extend further the study to the whole region of the nuclear chart in order to explore the systematics of nuclear properties.

We perform the constrained RMF calculations on the quadrupole moment and obtain all the possible ground state configurations from the energy curves using the supercomputer VPP500 at RIKEN. We adopt the TMA parameter set⁸⁾ and find that the total binding energies agree with the experimental data within 3 MeV when we select the deformation of the absolute minimum for each nuclide.

We show in Fig. 1 the calculated β deformation of even-even mass nuclei ranging from $Z = 8$ to $Z = 50$ up to the drip lines. We see the strong deformations around $Z = 38 \sim 42$ with $N = 38$ and 60 , which are suggested to be deformed magic numbers by the experiments.³⁾ It is interesting to remark the disappearance of the magic numbers $N = 20, 28,$ and 50 in

the neutron rich region. The thick neutron and proton skins are generally seen for nuclei far from the stability and its thickness can be large as 1 fm for very neutron rich nuclei.

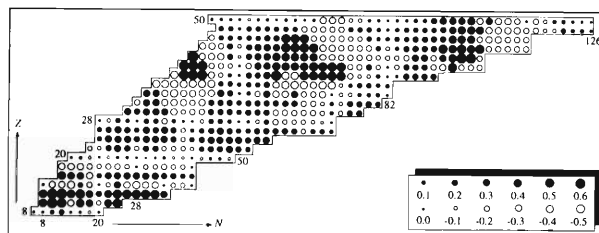


Fig. 1. The β deformation in the N-Z plane. The prolate and oblate shapes are denoted by closed and open circles, respectively, in the scale shown in the legend.

We are extending the analysis to the region beyond $Z = 50$ up to the super heavy region in order to explore the general trend in the nuclear chart.⁹⁾ Possible triaxial deformations are also being studied in the triaxial RMF code in the cases of the coexistence of prolate and oblate deformations observed in the present study.

References

- 1) I. Tanihata et al.: *Phys. Rev. Lett.*, **55**, 2676 (1985).
- 2) I. Tanihata et al.: *Phys. Lett.*, **B289**, 261 (1992).
- 3) J. H. Hamilton: *Treatise on Heavy Ion Science*, Vol. 8, ed. D. A. Bromley, Plenum, New York, p. 3 (1989).
- 4) R. Brockmann and R. Machleidt: *Phys. Rev.*, **C42**, 1965 (1990).
- 5) Y. K. Gambhir et al.: *Ann. Phys.*, **198**, 132 (1990).
- 6) D. Hirata et al.: *Phys. Rev.*, **C44**, 1467 (1991).
- 7) D. Hirata et al.: *Phys. Lett.*, **B314**, 168 (1993).
- 8) Y. Sugahara: Doctor thesis, Tokyo Metropolitan University (1995).
- 9) D. Hirata et al.: in preparation.

Systematics of Interaction Radii of Unstable Sd-Shell Nuclei

H. Sato

[Nuclear interaction radii.]

Recent study of the size of unstable nuclei with the use of the secondary unstable nuclear beams suggests that some extremely neutron rich nuclei, like ^{11}Li , can have a halo type neutron distribution. Here we report another possible type of peculiar behavior of the size of unstable nuclei: Thus far the nuclear size of a mass number A nucleus is believed to be proportional to $A^{1/3}$. However, the nuclear interaction radius of extremely neutron rich nuclei, which is defined by the interaction cross section of the identical nuclei of mass number A such as

$$R_A = \sqrt{\sigma(A, A)/4\pi},$$

can show possible degeneracy or reversion in its mass number dependence. In a previous work,¹⁾ we show that experimental interaction cross sections of Na-

isotopes on a C target²⁾ are nicely reproduced with the center of mass corrected Glauber model calculation including the terms up to the second order of a nucleon-nucleon profile function evaluated with the nuclear density distributions given by the density dependent Hartree-Fock type variational calculation.³⁾ We also pointed out that the interaction cross sections nicely satisfy the additivity relationship given by

$$\sigma(Na, C) = \pi(R_{Na} + R_C)^2.$$

We extend the study to the interaction cross sections of nuclei from O to Ca isotopes filling the neutron sd shell. Figure 1 shows the neutron number dependence of the interaction cross sections on a C target calculated with SKIII interaction. As shown in Fig. 1, we can expect possible reversion of the mass number

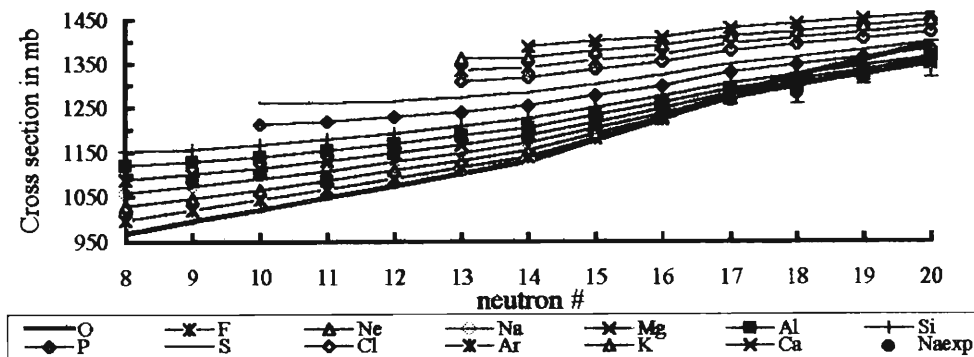


Fig. 1. The neutron number dependence of the interaction cross sections on a C target calculated with SKIII interaction.

dependence of nuclear interaction radii especially at around a neutron closed shell of $N = 20$. The size of ^{28}O is larger than that of ^{33}Al with SKIII. This kind of reversion is also found with many other types of interactions except SKV (SKV shows degeneracy of $R_O \doteq R_F \doteq R_{Ne}$). This kind of reversion is due to a small binding energy of the neutron $1d_{3/2}$ state and also to rather large binding energy dependence of the

size of the neutron $2s_{1/2}$ state having no centrifugal barrier.

References

- 1) H. Sato: This report, p. 13.
- 2) T. Suzuki et al.: *Phys. Rev. Lett.*, **75**, 3241 (1995).
- 3) H. Sato and Y. Okuhara: *Phys. Lett.*, **162B**, 217 (1985); *ibid.*, **168B**, 305 (1986); *Phys. Rev.*, **C34**, 2171 (1986).

Nuclear Shell Energies and Deformations in Mass Formulas

(1) Theory

M. Uno, H. Koura,* T. Tachibana,** and M. Yamada**

[shell-energy, deformation.]

A new method is devised, based on three assumptions, for estimating shell energies of deformed nuclei from spherical shell energies. The first assumption is on the relation between the shell energy and the occupation probabilities of *spherical* single-particle levels in the deformed nucleus. More specifically, we assume that the intrinsic shell energy comes only from the differences between the spherical single-particle levels and their structureless positions which are defined as a more uniform distribution of single-particle levels. Thus, we describe it as

$$E_{\text{in}}(Z, N) = \mu \sum_{\nu} w_{p\nu}(Z, N) (\varepsilon_{p\nu} - \bar{\varepsilon}_{p\nu}) + \mu \sum_{\nu} w_{n\nu}(Z, N) (\varepsilon_{n\nu} - \bar{\varepsilon}_{n\nu}), \quad (1)$$

where $\varepsilon_{j\nu}$ ($\nu = 1, 2, 3, \dots$, and $j = n$ or p) is a single-particle level in the spherical potential, $\bar{\varepsilon}_{j\nu}$ its structureless position, and $w_{j\nu}(Z, N)$ the occupation probability of the ν -th spherical single-particle state in the deformed nucleus (Z, N). The constant μ ($0 < \mu \leq 1$) is to take into account a possible reduction of the shell energies from the values of the extreme single-particle model.

The second is a possibility of expressing the occupation probabilities in the deformed nucleus as superpositions of those in appropriate spherical nuclei. From these assumptions we can derive the expression for the intrinsic shell energy of the deformed nucleus as

$$E_{\text{in}}(Z, N) = \sum_{Z'} W_p(Z'; Z, N) E_{0p}(Z', N) + \sum_{N'} W_n(N'; Z, N) E_{0n}(Z, N'). \quad (2)$$

Here, $E_{0p}(Z', N)$ and $E_{0n}(Z, N')$ are the proton and neutron shell energies of spherical nuclei, respectively, which are expected to be obtained by an appropriate method.¹⁾ Then, in order to determine the mixing weights $W_p(Z'; Z, N)$ and $W_n(N'; Z, N)$, we make the third assumption on the relation between the occupation probabilities and the radial nucleon distributions averaged over all directions. From this we can derive the expressions,

$$\rho_p(r; Z, N) = \sum_{Z'} W_p(Z'; Z, N) \rho_{0p}(r; Z', N), \quad (3a)$$

$$\rho_n(r; Z, N) = \sum_{N'} W_n(N'; Z, N) \rho_{0n}(r; Z, N'), \quad (3b)$$

where $\rho_j(r; Z, N)$ and $\rho_{0j}(r; Z, N)$ ($j = p, n$) are averaged distributions in deformed and spherical nuclei, respectively. These equations imply the possibility of determining the mixing weights by comparing averaged distributions in deformed and spherical nuclei. According to this inspection, we practically determine them by considering nuclear shapes as

$$W_n(N'; Z, N) = -\frac{1}{4\pi} \frac{d\Omega_{\text{occ}}(r(N'))}{dN'}. \quad (4)$$

Here, $\Omega_{\text{occ}}(r(N'))$ is the occupied solid angle (see Fig. 1). Equations (2) and (4) are sufficient to determine the intrinsic shell energy. Furthermore, an appropriate average deformation energy is prepared including, in addition to usual surface and Coulomb energies, two somewhat phenomenological energies: one related to the proton-neutron displacement, and the other to the favorableness for prolate shapes which may be understood as due to the part-time formation of clusters. The ground-state shell energy of the deformed nucleus and its equilibrium shape can be obtained by minimizing, with respect to changes of deformation parameters, the sum of the intrinsic shell energy and the average deformation energy. In our method we can also obtain the potential-energy surface plotted against deformation parameters. A more detailed explanation has been reported in Ref. 2.

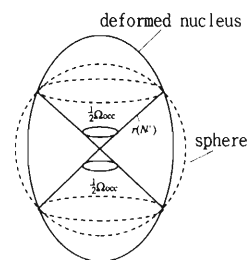


Fig. 1. Illustration of occupied solid angle $\Omega_{\text{occ}}(r(N'))$ in the case of prolate deformation.

References

- 1) M. Uno, T. Tachibana, M. Takano, H. Koura, and M. Yamada: *Nuclei Far from Stability 6 / Atomic Masses and Fundamental Constants 9*, Bernkastel-Kues, (IOP 132), p. 117 (1992); H. Koura, T. Tachibana, M. Uno, and M. Yamada: JAERI-Conf 95-008, p. 250 (1995); M. Uno, KURRI-TR-405, Research Reactor Institute, Kyoto Univ., p. 82 (1995).
- 2) H. Koura, M. Uno, T. Tachibana, and M. Yamada: Technical Report, No.95-25, Advanced Research Center for Science and Engineering, Waseda Univ., p. 1 (1995).

* Department of Physics and Applied Physics, Waseda University

** Advanced Research Center for Science and Engineering, Waseda University

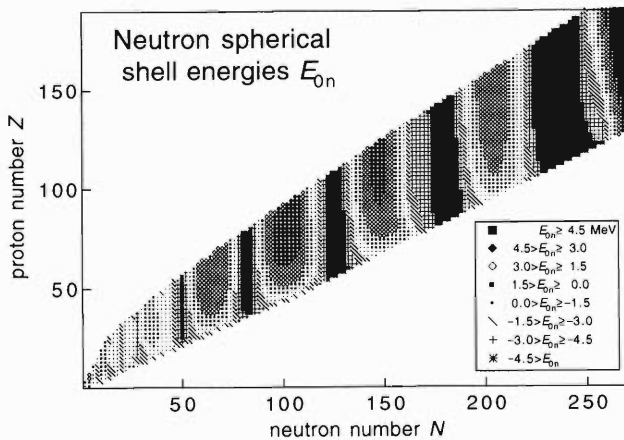
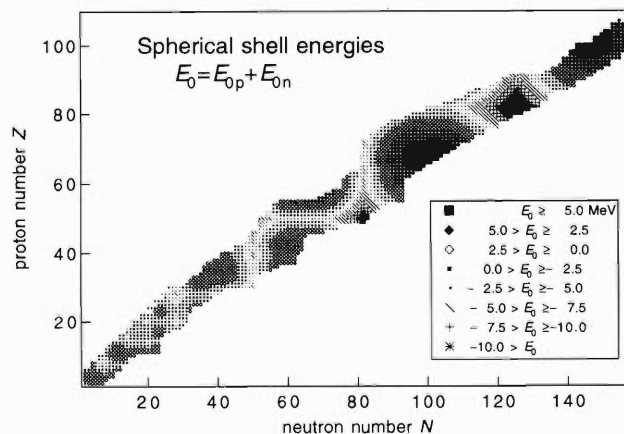
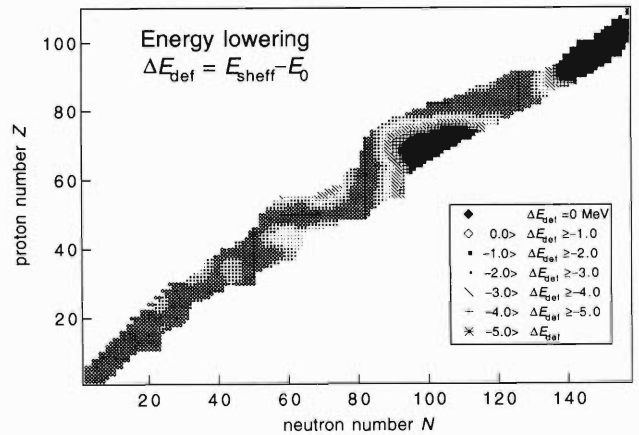
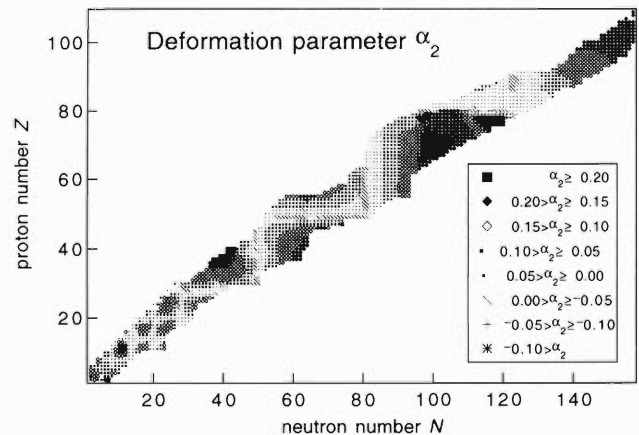
Nuclear Shell Energies and Deformations in Mass Formulas

(2) Results

M. Uno, H. Koura,* T. Tachibana,** and M. Yamada**

[shell-energy, deformation.]

According to the prescription explained in our preceding paper in this report, we numerically calculate ground-state shell energies of deformed nuclei and their equilibrium deformations. Here, we use the shell energies of spherical nuclei which have been obtained through a certain method with including up to pairing effects.¹⁾ They are roughly shown in Fig. 1 for neutron shell energies E_{0n} , and in Fig. 2 for total spherical shell energies $E_{0p} + E_{0n}$. We assume nuclear shapes as could be expressed within Y_2 and Y_4 deformations. In Fig. 3 is shown the energy lowering ΔE_{def} caused by deformation, that is, the difference between the shell energy of a deformed nucleus E_{sheff} and its spherical shell energy $E_{0p} + E_{0n}$. In Fig. 4 the deformation parameter α_2 is roughly shown.

Fig. 1. Neutron shell energies for spherical nuclei E_{0n} .Fig. 2. Total spherical shell energies $E_{0p} + E_{0n}$.Fig. 3. Energy lowering caused by deformation ΔE_{def} .Fig. 4. Deformation parameter α_2 .

It is noted that in Figs. 3 and 4 are shown the numerical results only for the existing nuclei without predictions, which is solely because of the problem of computational time. It is, except for the same problem, comparably easy in principle to extend our calculation to include higher-multipole deformations, Y_6 etc. We are now striving to get overall results which are available for prediction as well.

References

- 1) T. Tachibana, M. Takano, and M. Yamada: JAERI-M 91-032, p. 395 (1991); H. Koura, T. Tachibana, M. Uno, and M. Yamada: JAERI-Conf 95-008, p. 250 (1995); M. Uno: KURRI-TR-405 Research Reactor Institute, Kyoto Univ., p. 82 (1995).

* Department of Physics and Applied Physics, Waseda University

** Advanced Research Center for Science and Engineering, Waseda University

Quantum Monte Carlo Diagonalization Method for Nuclear Shell Model

T. Otsuka, T. Mizusaki, and M. Honma

[Nuclear Structure, Nuclear Shell Model, Quantum Monte Carlo Approach.]

Recently we advocated the quantum Monte Carlo diagonalization method,¹⁾ which is introduced as an approach having both the advantage of the quantum Monte Carlo method and that of the direct diagonalization of the Hamiltonian matrix. The present approach reduces drastically the basis-dimension problem of the direct diagonalization, and overcomes the intrinsic problems of the quantum Monte Carlo method,

i.e., *sign problem* etc. Up to now, we showed its validity by applying it to the Interacting Boson Model (IBM) and nuclear shell model. The formulation of the present theory is shown in Refs. 1 and 2. In the following Fig. 1, we show the typical results in the case of the nuclear shell model. This is the case of ^{24}Mg with the MSDI force. The dimension of entire Hilbert space is over 30,000, while in the QMCD calculation

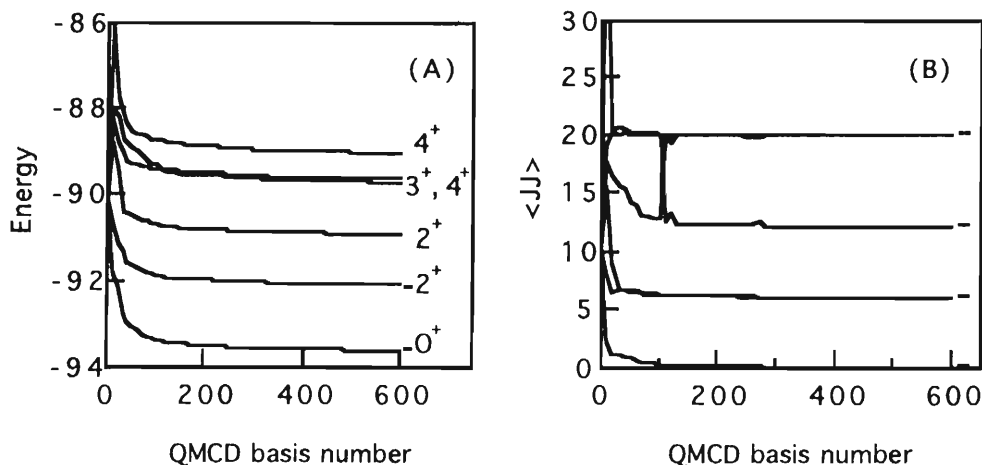


Fig. 1. (A) Energies and (B) expectation values of the angular momentum of low-lying states as functions of the QMCD basis dimension. The $M = 0$ space is considered. The exact values are shown by horizontal bars.

we can get well convergent eigenvalues within the 600 QMCD dimensions. Moreover, readers find that our method gives the excited states in contrast with the shell model Monte Carlo method.³⁾ These results show the promising future of the present method.

Now we are pursuing to investigate the huge shell model calculation with the realistic shell model interaction.

References

- 1) M. Honma, T. Mizusaki, and T. Otsuka: *Phys. Rev. Lett.*, **75**, 1284 (1995).
- 2) T. Mizusaki, M. Honma, and T. Otsuka: *Phys. Rev.*, **C**, submitted.
- 3) W. E. Ormand et al.: *ibid.*, **C49**, 1422 (1994); C. W. Johnson et al.: *Phys. Rev. Lett.*, **69**, 3147 (1992).

Extensive Hartree-Fock + BCS Calculation with Skyrme SIII Force

N. Tajima, S. Takahara,* and N. Onishi

[NUCLEAR STRUCTURE, $2 \leq Z \leq 114$, Skyrme-Hartree-Fock method,
SIII force, quadrupole moment, nucleon skin.]

We have done an extensive Hartree-Fock + BCS calculation with the Skyrme SIII force for 1029 even-even nuclei with $2 \leq Z \leq 114$ and N ranging from outside the proton drip line to beyond the experimental neutron-rich frontier (by a few neutrons).

The feature of our calculation is a three-dimensional Cartesian-mesh representation of single-particle wavefunctions, while most of the other methods for deformed nuclei express the single-particle wavefunctions by the expansion in a harmonic oscillator basis. An advantage of the mesh representation is the capability to treat nucleon skins and halos. On the other hand, they cannot be described efficiently in the oscillator-basis expansion because the asymptotic form of wavefunctions for large r is determined by the basis. Another advantage is that one can treat various shapes without preparing a basis specific to each shape. In contrast, with the oscillator expansion method, one has to adjust the oscillator frequencies ω_x , ω_y , and ω_z such that they are optimized for the shape and radius of the resulting solution.

We have utilized an HF + BCS code *EV8* developed by Bonche et al.¹⁾ In order to apply it to an extensive calculation, we have modified the code in several aspects, e.g., we have developed (1) a method to determine the pairing force strengths based on the continuous spectrum approximation, (2) a method to accelerate the convergence to the HF + BCS solution using an external quadrupole potential, and (3) a novel-form correction formula for the total energy due to the finite mesh size.

Comparing the resulting nuclear ground-state masses with experimental data and predictions by other mass models, we have found that the smooth behavior of the Skyrme SIII force is very good.

The electric axial quadrupole moments of our solutions agree well with the intrinsic moments deduced from experimental B(E2) \uparrow , except nuclei with small quadrupole moments. We have defined the deformation parameters a_{lm} for the HF + BCS solutions as those of the uniform-density sharp-surface liquid drop having the same monopole, quadrupole, and hexadecapole moments as our solution has. The magnitudes of thus-defined non-axial deformation parameters are very small ($|a_{22}|, |a_{42}| < 10^{-4}$, $|a_{44}| \sim 10^{-3}$) for all the ground and the first excited solutions. The difference of shapes (a_{20} and a_{40}) between protons and neutrons

is small, too. We have also calculated the energy difference between the oblate and the prolate solutions and found a clear difference between below and above the $N = 50$ shell magic.

We define the nucleon skin as in Ref. 2. We have found for our 1029 ground-state solutions that the skin grows monotonously and regularly as nucleons are added to the nucleus. On the other hand, the halo thickness grows very slowly except near the drip lines, where it changes the behavior completely and expands very rapidly. We have also observed that the neutron skin tends to make the density distribution more spherical.

All the results of the HF + BCS calculations reported in this paper are available electronically as an anonymous ftp service on the internet: nt1.c.u-tokyo.ac.jp. See a file read.me in the home directory for instructions. The available quantities are the binding energies, the Fermi levels, the pairing gaps, proton and neutron moments (r^2 , $r^2Y_{2,0}$, $r^2Y_{2,2}$, $r^4Y_{4,0}$, $r^4Y_{4,2}$, $r^4Y_{4,4}$), the skin thicknesses, the halo radii, the proton/neutron/mass deformation parameters (a_{20} , a_{22} , a_{40} , a_{42} , a_{44} , R_0 , ρ_0) of 1029 ground states and 758 first-excited local minima. Single-particle spectra and density distributions of protons and neutrons are also obtainable for each solution. Postscript figures displaying the results and some FORTRAN source codes to analyze the results are also provided.

The authors thank Dr. P. Bonche, Dr. H. Flocard, and Dr. P.-H. Heenen for providing the HF + BCS code *EV8*. They are also grateful to Dr. T. Tachibana for the TUYU mass formula code, to Dr. S. Raman for the computer file of the B(E2) \uparrow table, and to Dr. P. Möller for discussions on the results of the FRDM calculations. About 20% of the calculations for this paper were performed with a computer VPP500 at RIKEN, while the remainder were done at the Computer Center of the University of Tokyo with a financial support from RCNP, Osaka University, as RCNP Computational Nuclear Physics Project (No. 94-B-01). A detailed version of this paper has been submitted to Nuclear Physics **A** for publication.

References

- 1) P. Bonche et al.: *Nucl. Phys.*, **A443**, 39 (1985).
- 2) N. Fukunishi, T. Otsuka, and I. Tanihata: *Phys. Rev.*, **C48**, 1648 (1993).

* Institute of Physics, College of Arts and Sciences, University of Tokyo

Do Soft Dipole States Exist in Light Nuclei?

H. Kurasawa* and T. Suzuki

[NUCLEAR STRUCTURE soft dipole states.]

Recent experiments make it possible to study not only the ground states, but also the excited states of unstable nuclei. New modes peculiar to unstable nuclei are expected to be observed, and to provide new information on nuclear properties. One of them is a soft dipole mode,¹⁾ which is defined to be a harmonic vibration of the core nucleus against the excess neutrons. The dipole mode, unlike the giant dipole states of stable nuclei, may be excited without increasing the symmetry energy, so that the excitation energy would be very low, compared with that of GDR.

Recently, low lying dipole states have been observed in light unstable nuclei. For example, in ^{11}Li the excitation energy is about 1 MeV.²⁾ Those may be candidates of the soft mode, since their strength for electromagnetic excitation almost exhausts the molecular sum-rule value³⁾ as to the degrees of freedom between the core and the excess neutrons; in ^{11}Li the core is considered to be ^9Li . This fact, however, is not sufficient to draw a conclusion. Indeed, the post acceleration of the fragment observed in the Coulomb dissociation indicates that the lifetime of the excited states is too short for the dipole oscillation,⁴⁾ and that the reaction may be a direct breakup.⁴⁻⁶⁾

We have shown from the sum rule point of view that the soft dipole states with low excitation energy do not

exist in light nuclei.⁷⁾

First, we write the classical nuclear four-current according to the definition of the soft dipole mode. It is necessary for defining the amplitude of the dipole oscillation. Next, the microscopic nuclear four-current for the soft mode is derived from the model-independent sum rules. Comparing it with the classical current, we can obtain a constraint on the product of the amplitude and the excitation energy, which depends on the number of the excess neutrons and those of protons and neutrons in the core. If we use the experimental value of the excitation energy for ^{11}Li , the sum rule result yields the amplitude of the soft dipole state which is comparable with the nuclear size. This means that the observed state is not the soft dipole states. Such states are expected to appear only in heavy nuclei.

References

- 1) K. Ikeda: *Nucl. Phys.*, **A538**, 355c (1992).
- 2) T. Kobayashi et al.: *Phys. Lett.*, **B232**, 51 (1989).
- 3) Y. Alhassid et al.: *Phys. Rev. Lett.*, **49**, 1482 (1982).
- 4) K. Ieki et al.: *ibid.*, **70**, 730 (1993).
- 5) T. Nakamura et al.: *Phys. Lett.*, **B331**, 296 (1994).
- 6) S. Shimoura et al.: preprint RIKEN-AF-NP-177.
- 7) H. Kurasawa and T. Suzuki: *Prog. Theor. Phys.*, **94**, 931 (1995).

* Department of Physics, Faculty of Science, Chiba University

Giant Resonance States in Neutron-Rich Nuclei

H. Kurasawa* and T. Suzuki

[NUCLEAR STRUCTURE neutron-rich nuclei, giant resonance states.]

Stable nuclei have a dipole state which is an oscillation of protons against neutrons, and is called a giant dipole resonance state (GDR). In neutron-rich nuclei, the dipole state is expected to be decoupled into two modes.¹⁾ The one is called a skin dipole mode which is an oscillation of the excess neutrons against the core nucleons. In halo nuclei, this is called a soft dipole mode. The other is the core dipole state where neutrons of the core oscillate against the protons of the core. The excess neutrons do not participate in this oscillation.

The giant quadrupole states (GQR) of stable nuclei would be also decoupled into two modes in neutron-rich nuclei.²⁾ In the giant quadrupole states, all nucleons participate in the quadrupole oscillation. The one of the decoupled states is a neutron mode or skin mode which is a vibration of excess neutrons only. The core-nucleon density does not change the shape. The other is a vibration of the core nucleons only. The excess neutrons do not participate in the vibration.

We have studied whether or not the new modes provide us with more information on the nuclear effective force than GDR and GQR did.³⁾ For this purpose we have used a macroscopic model which shows the above classical pictures. The theoretical basis of the model is provided by the model-independent sum rules.

The macroscopic model makes it more transparent how each mode depends on the nuclear effective force, than microscopic models do.

We have shown that when using Skyrme force, the model gives analytic expressions of the excitation energies for the various modes. It is seen that each mode depends on the force parameters in a different way. For example, the excitation energies of the skin dipole modes are almost independent of the symmetry potential. This is because the energy-loss due to the oscillation of the protons against the excess neutrons is cancelled by the energy-gain due to the oscillation of the core-neutrons. It is also true in the skin quadrupole case, and those excitation energies are dominated by the isoscalar potential. The core modes are also studied and their dependence on the nuclear force is shown to be different from that of the giant resonance states in stable nuclei.

References

- 1) P. G. Hansen and B. Jonson: *Europhys. Lett.*, **4**, 409 (1987).
- 2) T. Otsuka: private communication.
- 3) H. Kurasawa and T. Suzuki: Proc. 3rd IN2P3-RIKEN Symp. on Heavy Ion Collisions, T. Motobayashi et al. (eds.), World Scientific, Singapore, p. 269 (1989).

* Department of Physics, Faculty of Science, Chiba University

Double Giant Dipole Resonance States

H. Kurasawa* and T. Suzuki

[NUCLEAR STRUCTURE double giant dipole states.]

In the last decade, pion double-charge exchange and relativistic heavy-ion reactions provided us with signatures on the existence of new giant resonance states in a wide range of nuclei.^{1,2)} Those are called the “double” giant dipole resonance states (DGDR), because the reactions are due to a multistep process and the observed excitation energy is close to twice (1.91 ± 0.02) that of the well-known giant dipole resonance states (GDR).¹⁾ The GDR is then called a “single” giant dipole resonance states. Resonance states are characterized, in addition to the excitation energy, by the width and the excitation strength. The width of DGDR is compared with that of GDR and observed to be by 1.60 ± 0.03 times wider than that of GDR.¹⁾ The strength is estimated with various models, but most of the calculations underestimate the experimental values.¹⁾

The folding model has been used extensively to analyze experimental data.¹⁾ Assuming independent phonon excitations of GDR, the model explains well the excitation energy and width of DGDR. The excitation energy is twice that of GDR, and the width, which is given by the square root of the variance of the strength function, is $\sqrt{2}$ times that of GDR. The excitation strength, however, is not explained in this model. Both pion and heavy ion reactions have observed the strength which is about twice that of the folding model.¹⁾

We have investigated the excitation energy, strength and width of DGDR as model-independently as we can.³⁾

We have shown that the strength of DGDR is de-

termined by model-independent sum rules. The sum rules give a relationship between the strengths of GDR and DGDR. If the mean excitation energy of DGDR is twice that of GDR, the DGDR strength is given by $2S^2$, where S denotes the GDR strength. Since the folding model, assuming DGDR to be independent excitations of GDR, satisfies the sum rules, the discrepancy between the folding model and experiments is not due to the model of the nuclear structure, but may be owing to assumptions for the reaction mechanism.

The mean excitation energy and width of DGDR are studied according to Tomonaga theory.^{4,5)} We can derive a rather model-independent relationship between the mean energies of DGDR and GDR, and also a relationship between the variances of their strengths. It is shown that the mean energy of DGDR is twice that of GDR, while the width of DGDR larger than $\sqrt{2}$ times that of GDR. These results are consistent with experiments, and obtained without assuming independent phonon excitations, in contrast with those of the folding model.

References

- 1) H. Emling: *Prog. Part. Nucl. Phys.*, **33**, 729 (1994).
- 2) Ph. Chomaz and N. Francaria: *Phys. Rep.*, **252**, 275 (1995).
- 3) H. Kurasawa and T. Suzuki: *Nucl. Phys.*, **A597**, 374 (1996).
- 4) S. I. Tomonaga: *Prog. Theor. Phys.*, **13**, 467; 482 (1955).
- 5) T. Suzuki: *J. de Phys.*, **45**, c4-251 (1984).

* Department of Physics, Faculty of Science, Chiba University

Correlated Ground State and $E2$ Giant Resonance Built on It

M. Tohyama

[Density matrix theory, correlated ground state, $E2$ giant resonance.]

Using the Lipkin model as a model hamiltonian, we have recently demonstrated¹⁾ that a stationary solution of a time-dependent density-matrix formalism (TDDM) can be obtained with an adiabatic method: starting with the Hartree-Fock (HF) ground state, we gradually turned on the residual interaction in time. The obtained stationary solution was a good approximation for the exact solution of the model. In this report we discuss the applicability of the adiabatic method to realistic nuclei taking ^{16}O as an example. We also study the effects of a consistent treatment of the initial ground state on the energy spectrum of the $E2$ giant resonance in ^{16}O .

TDDM determines the time evolution of a one-body density matrix ρ and a two-body density matrix ρ_2 , and consists of the following three coupled equations for a single-particle wave function ψ_α , an occupation matrix $n_{\alpha\alpha'}$ and a correlation matrix $C_{\alpha\beta\alpha'\beta'}$:

$$i\hbar \frac{\partial}{\partial t} \psi_\alpha(1, t) = h(1, t) \psi_\alpha(1, t), \quad (1)$$

$$i\hbar \dot{n}_{\alpha\alpha'} = \sum_{\beta\gamma\delta} [\langle \alpha\beta | v | \gamma\delta \rangle C_{\gamma\delta\alpha'\beta} - C_{\alpha\beta\gamma\delta} \langle \gamma\delta | v | \alpha'\beta \rangle], \quad (2)$$

$$i\hbar \dot{C}_{\alpha\beta\alpha'\beta'} = B_{\alpha\beta\alpha'\beta'} + P_{\alpha\beta\alpha'\beta'} + H_{\alpha\beta\alpha'\beta'}, \quad (3)$$

where $h(1, t)$ is the mean-field hamiltonian and v the residual interaction. The explicit expressions for $B_{\alpha\beta\alpha'\beta'}$, $P_{\alpha\beta\alpha'\beta'}$ and $H_{\alpha\beta\alpha'\beta'}$ have been presented in Ref. 2. To obtain a correlated ground state, we use the adiabatic method: we start with the HF ground state in which $1s$ and $1p$ single-particle states are fully occupied and make the residual interaction time dependent as

$$v = v_0(1 - e^{-t/\tau})\delta^3(\mathbf{r} - \mathbf{r}'), \quad (4)$$

where we choose $v_0 = -330 \text{ MeV fm}^3$. The correlation, HF and total energies thus calculated are shown in Fig. 1 as a function of time for two different values of τ : $\tau = 5 \times 10^{-23} \text{ s}$ (dotted line) and $\tau = 50 \times 10^{-23} \text{ s}$ (solid line). As shown in Fig. 1, the oscillations in the correlation and HF energies are drastically reduced when τ is increased from $5 \times 10^{-23} \text{ s}$ to $50 \times 10^{-23} \text{ s}$, and the total energy is almost saturated as a function of τ .

The $E2$ giant resonance built on the correlated ground state is excited by boosting the single-particle wave functions $\psi_\alpha(1)$ at $t = 5\tau$ where τ is $50 \times 10^{-23} \text{ s}$. The $E2$ strength distributions are shown in Fig. 2.

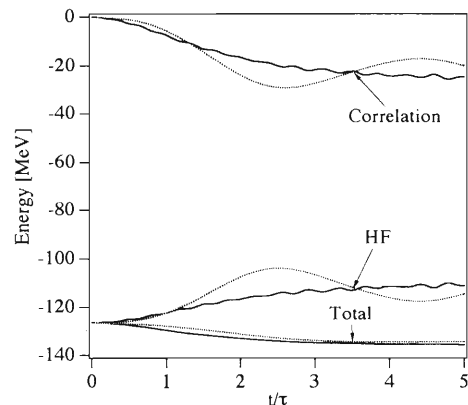


Fig. 1. Time evolution of the total energy, correlation energy and HF energy in TDDM.

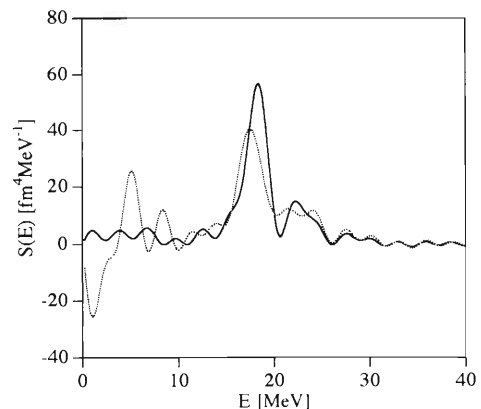


Fig. 2. $E2$ strength distributions in TDDM with the HF ground state (dotted line) and with the correlated ground state (solid line).

Solid line denotes the $E2$ resonance built on the correlated ground state and dotted line that on the HF ground state. Both distributions have a bump around 20 MeV but only the latter has a structure in the low energy region (below 10 MeV). We interpret this structure as an admixture of the $E2$ modes built on excited configurations. It is found that the mixing of spurious components in the $E2$ mode built on the HF ground state is eliminated with the use of the correlated ground state.³⁾

References

- 1) M. Tohyama: *Prog. Theor. Phys.*, **92**, L905 (1994).
- 2) M. Gong and M. Tohyama: *Z. Phys.*, **A335**, 153 (1990).
- 3) M. Tohyama: *Prog. Theor. Phys.*, **94**, L147 (1995).

Damping of Hot Giant Dipole Resonance as a Linear Irreversible Process

N. D. Dang* and F. Sakata**

[HOT NUCLEI, Giant Dipole Resonance, Nonequilibrium Statistical Mechanics.]

It is now well-established that the observed giant dipole resonance in hot nuclei (the hot GDR) has the apparent width, which increases strongly as the excitation energy goes up, and saturates at around 130 MeV in the case of Sn isotopes. Most theoretical studies in the last decade can reproduce the centroid energy of the hot GDR, but still give different, sometime controversial explanations regarding its width.

Recently we have developed a new approach,¹⁾ which treats explicitly the *irreversible* coupling between the collective degrees of freedom to the non-collective ones. In the case of the hot GDR, the collective degrees of freedom are the ph phonon states, while the pp and hh configurations consist only of non-collective degrees of freedom within the finite-temperature RPA. This irreversible coupling leads to the *thermal damping* of the collective ph phonon states, associated with the hot GDR, when these phonons are propagating through the heat bath. We show in this report the relation between this microscopic description and a macroscopic interpretation of the hot GDR. We consider the hot GDR as a statistical state, which is slightly deviated from the thermal equilibrium state under the influence of a temperature-dependent external perturbation. If one restricts the consideration to the evolution of a single collective phonon, responsible for the hot GDR excitation, the equation for the phonon propagation through the heat bath can be written as

$$[\eta - \omega_\nu - P_\nu(\eta)]G_\nu^-(\eta) = \frac{1}{2\pi}. \quad (1)$$

The polarization operator $P_\nu(\eta)$ arises at non-zero temperature in Eqn. (1) due to the irreversible coupling between the hot GDR and the heat bath via the noncollective pp and hh configurations. The imaginary part of its analytic continuation into the complex energy plane defines the thermal damping of the ph phonon as a function of energy η . The complex admittance can be expressed in terms of the Green function $G_\nu^{(-)}(\eta)$. The *normalized relaxation function* $\Psi(t)$, associated with the energy dissipation of the GDR to the heat bath, is derived from the Fourier transform of the complex admittance. If $\Psi(t)$ has good exponential decaying behavior $\Psi(t) \approx \exp(-t/\tau_c)$, the GDR thermal damping width can be extracted as the reverse of the relaxation time τ_c .

As an application we consider a simplest realization for the hot GDR in a system with mass $A = 112$, which is provided by a schematic model. It consists of four degenerate equidistant shells, which are symmetrically located at both sides of the Fermi level and interact via the separable dipole-dipole force. With increasing the temperature up to $T \approx 2.5$ – 3 MeV the relaxation time decreases drastically. However starting from $T \geq 2.5$ – 3 MeV it remains almost the same (Fig. 1). The analysis also shows that motional narrowing in hot GDR may occur if the thermal damping is small and, moreover, only at rather high temperature ($T \geq 4.6$ MeV, i.e. much higher than what has been predicted in Ref. 2), where the hot GDR is expected to disappear.³⁾

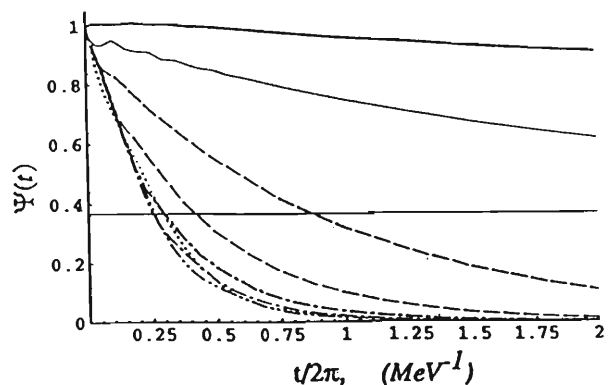


Fig. 1. Normalized relaxation function at finite temperature: $T = 0.5$ MeV (thick solid), $T = 1$ MeV (thin solid), $T = 1.5$ MeV (thick dashed), $T = 2$ MeV (thin dashed), $T = 2.5$ MeV (thick dash-dotted), $T = 3$ MeV (thin dash-dotted), $T = 4$ MeV (dash-double dotted), $T = 6$ MeV (dotted). The horizontal line is $1/e$.

References

- 1) N. Dinh Dang and M. Baldo: "Perspective of Nuclear Physics in the Late Nineties," Hanoi, March, 1994, World Scientific, Singapore, p. 212 (1995); N. Dinh Dang and F. Sakata: INS-Rep.-1079, INS, Univ. Tokyo, Dec. 1994, p. 28 (1994).
- 2) B. Lauritzen, R. A. Broglia, W. E. Ormand, and T. Døssing: *Phys. Lett.*, **B207**, 238 (1988).
- 3) J. Kasagi and K. Yoshida: *Nucl. Phys.*, **A569**, 195c (1994).

* On leave from the Institute of Nuclear Science and Technique, Vietnam Atomic Energy Commission, Hanoi, Vietnam

** Theory Division, INS, University of Tokyo

C₄ Symmetry in Superdeformation by Berry's Phase Analysis

K. Sugawara-Tanabe and K. Tanabe*

[C₄ symmetry, superdeformation, Berry's phase.]

Recently, C₄ symmetry has been observed for the superdeformed bands over the mass region of A ~ 130, 150 and 190. The energy levels show a bifurcation of $\Delta I = 4$ given by $E(I) = E_0(I) + (-)^{\alpha_4/2} C_0$, where $I = \alpha_4 \bmod 4$. Here we propose a new idea to produce $\Delta I = 4$ staggering without introducing the hexadecapole interaction.

At superdeformation both positive and negative parity levels are contained in a shell, which is a trigger to produce small γ softness. Then this very small asymmetry influences the stable rotation, although the axial symmetry is still preserved. Now the rotational frequency has the time-dependent component $\Delta\vec{\omega}(t)$ produced by this small asymmetry in addition to the original rotational frequency ω_0 along the rotational axis. We use the idea of a Berry's phase, i.e. the rapid variable (ω_0) is influenced by the slow variable ω_p , which is the average frequency of $\Delta\vec{\omega}(t)$. Then the eigenfunction in the body-fixed frame (b.-f.f.) is

given by $|\Phi\rangle = \exp(-i \int_0^t \Delta\vec{\omega}(t) \cdot \vec{I} dt') \exp(i\gamma_\alpha(t)) |\alpha\rangle$, where $|\alpha\rangle$ is the solution of the stationary rotation with frequency ω_0 in b.-f.f., and the Berry's phase $\gamma_\alpha(t)$ can be derived by $\dot{\gamma}_\alpha = \langle \alpha | \Delta\vec{\omega}(t) \cdot \vec{I} | \alpha \rangle$. Here we must remark that $\gamma_\alpha(n\tau_p) = 0$ where $\tau_p = 2\pi/\omega_p$ with integer n . We use the rigid triaxial rotor Hamiltonian, and then the small asymmetry term is given by $\frac{1}{8}(I_+^2 + I_-^2)(1/\mathcal{J}_2 - 1/\mathcal{J}_1)$. Classical mechanics gives the following relation between ω_p and ω_0 for a triaxial rotor: $(\omega_p/\omega_0)^2 = (\mathcal{J}_1 - \mathcal{J}_2)(\mathcal{J}_1 - \mathcal{J}_3)/(\mathcal{J}_1\mathcal{J}_2)$ for the case of $\mathcal{J}_1 \geq \mathcal{J}_2 \gg \mathcal{J}_3$. Now we consider the case of commensurable number η in $\omega_0/\omega_p = n + \eta$ (n integer) and adopt $\eta = \frac{1}{4}$ ($\eta = \frac{3}{4}$ gives the same results). The first order perturbation gives an energy shift ΔE in addition to E_0 , which has the order and the factor of $(-)^{\frac{I}{2}} \sqrt{I}$. This agrees with the experimental observation. We can apply the same technique to the case of $\eta = \frac{1}{3}$.

* Department of Physics, Saitama University

Tilting Mechanism in ^{182}Os

T. Horibata and N. Onishi

[tilted rotation, three-dimensional cranking, γ -deformation.]

Recently we demonstrated the existence of new states in ^{182}Os in which the nucleus is in stationary rotation about an axis tilted from the principal axes of the mass-quadrupole moment.¹⁾ Since the energies of the states are lower than those of the one-dimensional cranking states, our results suggest an interpretation for the backbending phenomena somewhat different from the standard model.²⁾ Therefore, it will be of great importance to make clear what mechanism is responsible for stabilizing the tilted axis rotation in this nucleus. This problem is elucidated by analyzing the respective roles of terms in the hamiltonian. In the case of $J = 14\hbar$ the energy takes minimum at $\psi = 27^\circ$ with its value $E = -208$ keV along the prime meridian, and hence the analysis is made intensively in the region of interval from $\psi = 0^\circ$ to 50° .

We plot the respective energies contributed from the one-body part (kinetic energy), the quadrupole-quadrupole interaction (Q - Q force), the pairing force and the total binding energy as a function of north-latitude in Fig. 1. Each energy is normalized to zero at $\psi = 0^\circ$, and only its variation is illustrated. While the total energy describes a rather gentle curve whose variation is small within less than ~ 1 MeV, the partial energies vary substantially by a typical value of ~ 3 MeV. The energy contribution from the Q - Q force is separately given by the $\mu = \pm 2$ and $\mu = 0$ terms.

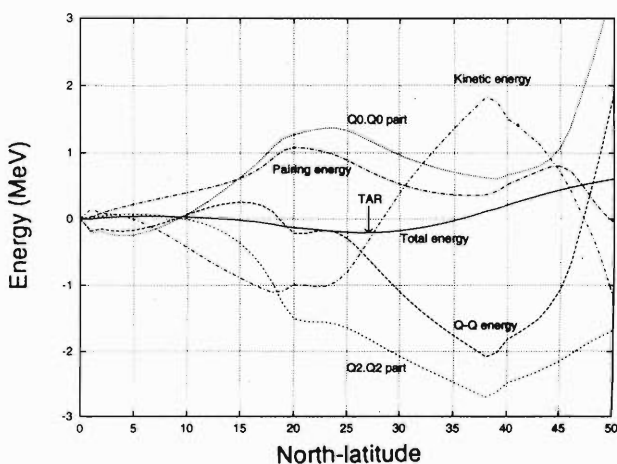


Fig. 1. The kinetic energy, the pairing energy, the energy contribution from the Q - Q force and the resultant total binding energy as a function of north-latitude angle at $J = 14\hbar$.

We divide the region into three intervals following their characteristics. In the first region from $\psi = 0^\circ$ to 20° , the rotation alignment of protons strongly suppresses their own pairing correlations and makes the moment of inertia large. Therefore the rotation of the protons carries a significant amount of angular momentum, and reduces the angular momentum of the neutrons. This results in the recovery of the pairing correlation of neutron. In this region the decrease of the kinetic energy acts as the counter force against the combined effect of the increase of the total pairing energy (reduce the pairing correlations) and the energy from the $Q_0.Q_0$ part of the interaction.

It is found from the calculation that the Q_2 components have a large fraction of partial contribution from the particles in the natural parity orbitals of either proton or neutron. The contribution from the particles in the natural parity orbital is particularly large in the first region, and the effect also appears in the behavior of " $Q_2.Q_2$ part" indicated in the figure in the same region. Especially, at the equilibrium point, the contribution of particles from the natural parity orbitals acts strongly as a driving force to make the tilted angle large.

In the second region in the interval from $\psi = 20^\circ$ to 40° , the pairing force and the Q - Q force play a role as the driving force to tilt the rotating axis while the rather rapid increase of the kinetic energy, which is the result of large γ -deformation due to increase of the $Q_2.Q_2$ part, pushes back the tilted angle as if it acts as a restoring force. In the third region, the triaxiality is reduced, and the nuclear shape rapidly changes toward the axially symmetric rotor.

The essential mechanism of the tilted axis rotation in our calculation is explained by the competition process between the kinetic energy and the energy of the Q - Q force, especially the force leading to the triaxiality. In the present calculation, the proton positive-parity states and the neutron negative-parity states, that is natural parity orbitals, turn out to be responsible for the occurrence of the TAR. Detailed discussions are given in the paper.³⁾

References

- 1) T. Horibata and N. Onishi: *Phys. Lett.*, **B325**, 283 (1994).
- 2) F. S. Stephens and R. S. Simon: *Nucl. Phys.*, **A183**, 257 (1972).
- 3) T. Horibata and N. Onishi: *ibid.*, **A596**, 251 (1996).

Estimation of Signature Splitting of TAR with GCM

T. Horibata, M. Oi, and N. Onishi

[tilted rotation, generator coordinate method, signature splitting.]

A self-consistent three-dimensional cranking calculation¹⁾ based on HFB for ^{182}Os has brought about an interesting result,²⁾ in which tilted axis rotating (TAR) states are more stable than the states rotating about the principal axis of mass-quadrupole moment (PAR). This fact implies that the intrinsic states become more stable through mixing of the *odd* angular momentum members in the wave functions. Namely the tilted axis rotation breaks the symmetry of signature³⁾ in the intrinsic states, which are composed of even and odd angular momentum states. This feature is quite favorable to a possible interpretation for the experimental fact that the energies of odd angular momentum members are very low; these states are considered to be the same members of the yrast band. The odd angular momentum members split upward from the even angular momentum members because of the signature splitting.

We estimate the signature splitting caused by the quantum tunneling between two wells located symmetrically with respect to the plane including two principal axes of the mass-quadrupole tensor, which will be called the equatorial plane. The tunneling is described in terms of the generator coordinate method (GCM),⁴⁾ in which the north-latitude ψ along the prime meridian is employed as a generator coordinate.

The generator wave function $f_\alpha(\psi)$ is determined by the variational equation of Hill-Wheeler.⁴⁾ The integral equation,

$$\int [H(\psi, \psi') - E_\alpha N(\psi, \psi')] f_\alpha(\psi') d\psi' = 0, \quad (1)$$

is solved to calculate the splitting energy, which is a difference of energy of the lowest anti-symmetric state from one of the lowest symmetric state.

The norm kernel is first diagonalized. We took 31 points of grid with 4° step from -60° to 60° for the numerical integration. All the eigenvalues should be positive and decrease rapidly as the node number n is increased. The discretized hamiltonian matrices are diagonalized again to obtain energy eigenvalues.

The energy eigenvalues of the five lowest states for $J = 14\hbar$ are depicted in Fig. 1 as a function of the number of states employed. We may choose a number by looking at the energy spectra which form a plateau vs. the increase of number of states. We found a very stable plateau for the lowest symmetric state (even an-

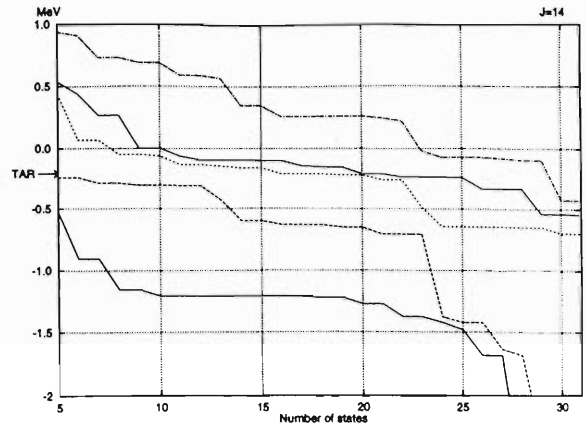


Fig. 1. The energy spectra for $J = 14\hbar$ in *g*-band as a function of the number of states employed in diagonalization. The energy is measured from the one for the PAR state for each J -value, and the arrows with “TAR” indicate the energy position of the local minima, i.e., TAR states.

gular momentum) and the first excited state of odd angular momentum. The signature splitting in *g*-band is expected to be in the range from 200 keV to 800 keV. On the other hand any significant energy separation could not be obtained in *s*-band in our calculation, though we could not judge where the truncation of states should be made. We can see two doublets whose energy differences are within 200 keV. In order to reproduce the experimental spectra, the depth of the double wells seems too deep in *s*-band.⁵⁾ The present calculation of GCM does not seem stable enough to draw a reliable value for the signature splitting, because the path of tunneling is restricted to the prime meridian.

References

- 1) A. K. Kerman and N. Onishi: *Nucl. Phys.*, **A361**, 179 (1981).
- 2) T. Horibata and N. Onishi: *Phys. Lett.*, **B325**, 283 (1994).
- 3) A. L. Goodman: *Nucl. Phys.*, **A230**, 466 (1974).
- 4) D. L. Hill and J. A. Wheeler: *Phys. Rev.*, **89**, 1102 (1953).
- 5) T. Horibata, M. Oi, and N. Onishi: *Phys. Lett.*, **B355**, 433 (1995).

3D Angular Momentum Projection of Tilted Axis Rotating States

M. Oi, N. Onishi, and T. Horibata

[NUCLEAR STRUCTURE Angular momentum projection, Tilted Axis Rotating States (TAR), generator coordinate method (GCM), overlap kernel.]

We have found the tilted axis rotating (TAR) solution in 3D Cranking Calculation based on HFB.¹⁾ We then solved the Hill-Wheeler equation;²⁾

$$\int [\mathcal{H}(\psi, \psi') - E_\alpha \mathcal{N}(\psi, \psi')] f_\alpha(\psi') d\psi' = 0, \quad (1)$$

the energy and norm kernels are defined as;

$$\begin{pmatrix} \mathcal{H}(\psi, \psi') \\ \mathcal{N}(\psi, \psi') \end{pmatrix} = \langle \Phi(\psi) | \begin{pmatrix} \hat{H} \\ 1 \end{pmatrix} | \Phi(\psi') \rangle, \quad (2)$$

and, the many-body wave function is written as,

$$|\Psi\rangle = \int d\psi f_\alpha(\psi) |\Phi(\psi)\rangle, \quad (3)$$

where $|\Phi(\psi)\rangle$ represents the TAR solution labeled by a tilting angle ψ being a generator coordinate.

A weight function $f(\psi)$, is expanded³⁾ by the orthonormalized set that diagonalizes \mathcal{N} ;

$$f(\psi) = \sum_{k, n_k \neq 0} \frac{g_k}{\sqrt{n_k}} u_k(\psi), \quad (4)$$

where $u_k(\psi)$ and n_k are determined by

$$\int d\psi' \mathcal{N}(\psi, \psi') u_k(\psi') = n_k u_k(\psi). \quad (5)$$

Practically, we truncate the expansion in finite terms. When the weight function $f(\psi)$ is truncated at the $(\alpha + 1)$ -th order, it is written as “ $f_\alpha(\psi)$ ”.

Energy eigenvalues, $\{E_\alpha\}$, depend on the number of the terms, but it is expected that the eigenvalues converge as the number increases. In our results, the convergence of the eigenvalues depends on the constrained angular momentum. While we obtained a wide plateau in the energy-vs.-number curve for a certain angular momentum, we had a gentle down-slope for another. The latter causes a fatal deficiency for the calculation, because it is a sensitive problem to determine where we should truncate the expansion.

The angular momentum projection is one way to get rid of this shortcoming. Since our solution of TAR was obtained by the HFB equation that violates the rotational symmetry, the angular momentum is not a good quantum number. Only its expectation value is what we know. When the width of the angular momentum distribution is large, the constraint on the angular momentum seems insufficient.

First, we calculate the norm and energy overlap kernels; \mathcal{N} and \mathcal{H} . The kernels are multi-valued functions because they involve square root. To determine the branch of \mathcal{N} , we use helpful formulae;⁴⁾ the loga-

$$\epsilon(\Omega) \equiv \ln \langle \Phi(\psi) | \hat{R}(\Omega) | \Phi(\psi) \rangle \quad (6)$$

$$= \frac{1}{2} \text{Tr}[\ln(U^\dagger R^\dagger(\Omega)U + V^\dagger R^T(\Omega)V)], \quad (7)$$

rithmic overlap is evaluated as; where U and V are the so-called uv-matrices in HFB theory, and $\Omega = (\theta, \phi, \chi)$. (θ, ϕ) represents the direction of the rotation axis, and χ is the rotation angle.

Then, we consider the derivative of ϵ , $i \frac{\partial}{\partial \chi} \epsilon(\Omega)$. On one hand, it is calculated approximately, that is,

$$i \frac{\partial}{\partial \chi} \epsilon(\theta, \phi, \chi) \simeq \frac{\epsilon(\theta, \phi, \chi + \Delta\chi) - \epsilon(\theta, \phi, \chi)}{\Delta\chi} + O(\Delta\chi), \quad (8)$$

which still contains the ambiguity of the branch. But, the derivative is expressed without ambiguity;⁴⁾

$$i \frac{\partial}{\partial \chi} \epsilon(\Omega) = \text{Tr}[j(\theta, \phi) \rho(\Omega)], \quad (9)$$

where $j(\theta, \phi)$ is a one-body angular momentum matrix about the rotation axis, and $\rho(\Omega)$ is a density matrix.

After these formulae are compared with each other, it is feasible to set the proper branch in $\epsilon(\Omega)$.

Next, the projection matrix is calculated⁵⁾

$$P_{MK}^I(\psi) = \frac{2I+1}{8\pi^2} \int d\Omega D_{MK}^{I*}(\Omega) \langle \Phi(\psi) | \hat{R}(\Omega) | \Phi(\psi) \rangle, \quad (10)$$

where $D_{MK}^I(\Omega)$ is the Wigner's d-function and $\hat{R}(\Omega)$ is the rotation operator.

It is, then, feasible to evaluate the probability of the states with a certain angular momentum in the cranking solutions, which contain the TAR and PAR (principal axis rotating) states. The trace of the projection matrix gives the probability.⁶⁾ It is expected that in the PAR states even numbers of angular momentum have major fraction compared with odd ones, while more odd states are included in the TAR states.

Finally, we are planning to solve again the Hill-Wheeler equation with the help of the projected TAR states, which are obtained⁵⁾ as;

$$|\Phi_M^I(\psi)\rangle = \sum_K g_K \hat{P}_{MK}^I(\psi) |\Phi(\psi)\rangle. \quad (11)$$

References

- 1) T. Horibata and N. Onishi: *Phys. Lett.*, **B325**, 283 (1994).
- 2) T. Horibata et al.: *ibid.*, **B353**, 433 (1995).
- 3) P. Ring and P. Schuck: *The Nuclear Many-Body Problem* (1980).
- 4) T. Horibata and N. Onishi: *Prog. Theor. Phys.*, **46**, 1650 (1980).
- 5) K. Hara et al.: *Nucl. Phys.*, **A385**, 14 (1982).
- 6) S. Islam et al.: *ibid.*, **A326**, 161 (1979).

Statistical Property of Molecular Dynamics with Wave Packets

A. Ono and H. Horiuchi

[antisymmetrized molecular dynamics, statistical property, nucleon-emission, wave packet.]

Recently, there is a controversy^{1,2)} on the statistical property of molecular dynamics models with wave packets such as the antisymmetrized molecular dynamics³⁾ (AMD) which are developed in nuclear physics. We first clarify that there coexist mutually opposite two statistics in the AMD framework: One is the classical statistics of wave packet centroids and the other is the quantum statistics of the motion of wave packets which is described by the AMD wave function.

We examine the statistical property of wave packet centroids by using the framework of microcanonical ensemble of the nuclear system with realistic effective two-nucleon interaction. The calculated relation between the excitation energy E and the temperature T_c has turned out to be just the linear relation $E/A = 3T_c$, which means that the statistical property of the wave packet centroids is completely classical. This is a rather natural result because the dynamics of the wave packet centroids is governed only by the equation of motion of AMD which has a classical form.

It should be reminded that we are treating the AMD wave functions and the calculation of observables is made for these wave functions. For example, we can consider the occupation probability of the single-particle level for the harmonic oscillator mean field case. Assuming that the wave packet centroids obey the classical canonical statistics with the temperature T_c , the occupation probability $P'_n(T_c)$ for the n th level is calculated numerically (or analytically for the case of distinguishable particles) by taking account of the spread of wave packets. On the other hand, the usual quantum relation of the occupation probability is denoted by $P_n(T)$ as a function of the temperature T . By the calculation it is proved that $P'_n(T_c) = P_n(T)$ is satisfied for any n if we relate T_c and T by a certain relation. This result just means that the statistical property of wave packets is quantum and there is nothing to be complained about the AMD description of the statistical property of the internal motion of nuclei. It is emphasized that the temperature T_c of the classical statistics of wave packet centroids is different from the temperature T of the quantum statistics of wave packets.

However, the statistical property of AMD for the nucleon-emission process is classical because it is described only by the motion of wave packet centroid. This defect of AMD is clearly proved by the calculation of the liquid-gas phase equilibrium realized for a many-nucleon system confined in a large potential wall. In Fig. 1, we show the completely classical relation be-

tween the excitation energy of the liquid nucleus and the temperature of the system which is calculated from the kinetic energy of the gas nucleons.

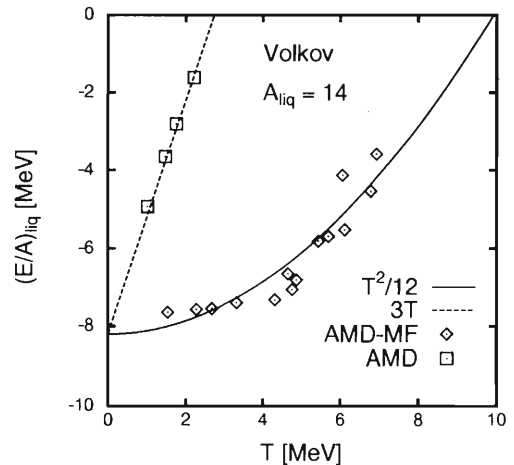


Fig. 1. The statistical property of the excited nucleus calculated with the usual AMD and the AMD-MF. Lines of $(E/A)_{\text{liq}} = 3T + \text{const.}$ and $T^2/(12 \text{ MeV}) + \text{const.}$ are drawn for the comparison.

The reason of the above result is that the nucleon cannot go out of the nucleus unless the centroid can, while the high momentum component should be allowed to go out in the exact quantum description. In order to solve this problem, we propose to introduce a new stochastic process into AMD by giving the momentum fluctuation to the wave packet according to its momentum distribution. This extension enables the wave packet to split stochastically into several parts and therefore the high momentum part can go out of the nucleus. This extended AMD is called AMD-MF (AMD with momentum fluctuation). The calculated statistical property of AMD-MF for the nucleon-emission process is also shown in Fig. 1, which proves that the quantum statistical property for the nucleon-emission process has been recovered by the new stochastic process.

References

- 1) A. Ohnishi and J. Randrup: *Nucl. Phys.*, **A565**, 474 (1993).
- 2) J. Schnack and H. Feldmeier: preprint GSI-95-34 (1995).
- 3) A. Ono, H. Horiuchi, Toshiki Maruyama, and A. Ohnishi: *Prog. Theor. Phys.*, **87**, 1185 (1992).

Antisymmetrized Molecular Dynamics with Stochastic Incorporation of Vlasov Equation

A. Ono and H. Horiuchi

[antisymmetrized molecular dynamics, wave packet, Vlasov equation,
heavy-ion reaction, fragmentation, $^{40}\text{Ca} + ^{40}\text{Ca}$ at 35 MeV/nucleon.]

An important fact which we learned in the study of the statistical property of AMD is that the origin of the problem is the simple single-particle motion, and we have improved the nucleon-emission process by taking account of the splitting of the wave packet according to its momentum width in AMD-MF (AMD with momentum fluctuation). This extension of AMD should be generalized for the application to nuclear reactions because the spreading and/or the splitting of wave packets is important in various processes as well as the nucleon-emission process.

The general method, called AMD-V (AMD with Vlasov equation), is formulated as follows. At each time t_0 , the time evolution of each Gaussian wave packet with the physical coordinate being its centroid is calculated with the Vlasov equation which is a semi-classical approximation of time-dependent Hartree-Fock (TDHF) equation and therefore does not have any restriction on the wave packet shape. The wave packet at $t_0 + \delta t$ which has diffused to some directions in phase space is represented by a sum of Gaussian wave packets with the same width as that of the Gaussian wave packet at t_0 and then one of these Gaussian wave packets is chosen stochastically according to its weight. In other words, a stochastic displacement is given to the wave packet centroid so that the ensemble-averaged time evolution of the one-body distribution function is equivalent to the solution of Vlasov equation for the diffusing directions.

As explained above, AMD-V has introduced the stochastic branching process. It should be emphasized that the future time evolution of each branch is independent of other branches. This situation corresponds to the linear combination of wave functions of channels in truly quantum description. On this point, AMD-V is different from TDHF (or Vlasov) equation though they are equivalent for the instantaneous time evolution of one-body distribution function. Especially, the fluctuation of the mean field among branches (or channels) is described in AMD-V, which enables the description of the fragmentation.

In order to see the important effects of the incorporation of Vlasov equation in heavy-ion collisions, we have calculated $^{40}\text{Ca} + ^{40}\text{Ca}$ reaction at 35 MeV/nucleon with AMD and AMD-V using Fujitsu VPP500 of RIKEN. In the calculation of AMD, most events have turned out to be binary with very excited ($E^*/A \sim 5$ MeV) projectile-like and target-like fragments whose decay is very slow. The yield of light intermediate

mass fragments (IMFs) is very small. Few α particles (0.2 \sim 0.3 per event) are produced in the dynamical stage, while the yield of protons is overestimated. On the other hand, in AMD-V many IMFs are produced in the dynamical stage of reaction ($t \lesssim 200$ fm/c). Their excitation energies are already small ($E^*/A \sim 2$ MeV) and therefore the effect of the statistical decay is not important. The multiplicity of dynamical α particles is about 2-3 and the overestimation of proton yield is not so large. As shown in Fig. 1, we have obtained very good reproduction of the data of charge distribution as well as other features of the fragmentation. These data have never been reproduced so well by any other microscopic models and statistical models.

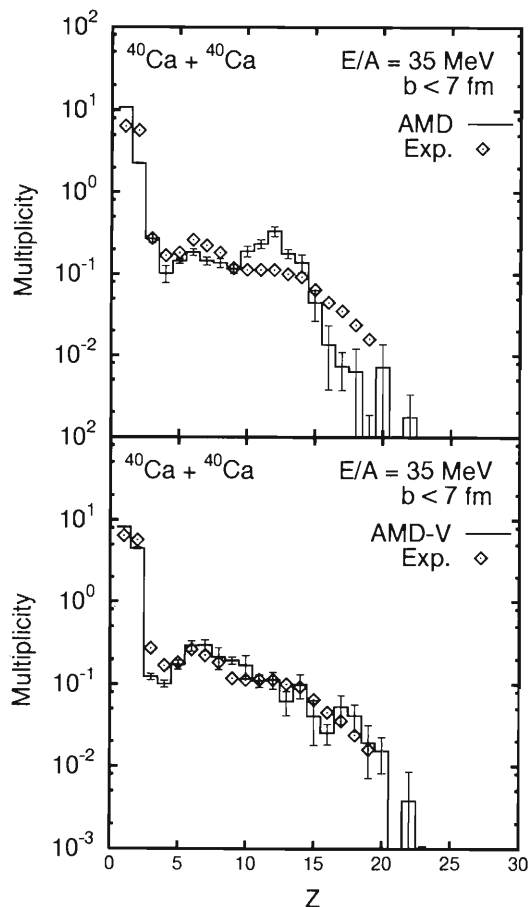


Fig. 1. Charge distribution of fragments produced in $^{40}\text{Ca} + ^{40}\text{Ca}$ collisions at 35 MeV/nucleon calculated with AMD (upper) and AMD-V (lower). Experimental filter has been applied.

Collisional Damping and the Temperature Dependence of Nuclear Dissipation

H. Hofmann,* F. A. Ivanyuk,** and S. Yamaji

[large scale collective motion, linear response theory.]

To date the nature of nuclear dissipation is still an unresolved problem. For isoscalar modes at finite excitations the best information available at present comes from fission experiments, when comparing the decay rate of fission with the ones for emission of light particles or gamma rays. Nowadays it seems not only possible to deduce numbers for the effective damping rate η at the barrier,¹⁾ but to gain information about its temperature dependence.²⁾ In our notation $\eta = \gamma/(2\sqrt{M|C|})$, with γ , M , C being the coefficients for friction, inertia and stiffness. The authors of Ref.2 find an η which increases markedly with T , at small to moderately large values of the temperature.

Such behavior is hard to understand, neither on the basis of two body viscosity nor on the wall formula.³⁾ In the first case friction should decrease with T like T^{-2} , in the second it would practically stay constant. In principle, the other two transport coefficients appearing in η , namely M and C , must be expected to change with temperature, too. But such dependence will be weak, as long as they are evaluated within the macroscopic models.³⁾ Therefore, the observed increase of η with T shows us strong evidence for the necessity for a microscopic theory.

In this report we want to concentrate on temperatures where the influence of self-consistency on friction is small.⁴⁾ Then we may apply the zero frequency limit, which gives

$$\gamma(0) = - \int \frac{d\hbar\Omega}{4\pi} \frac{\partial n(\Omega)}{\partial \Omega} \sum_{jk} \left| F_{jk} \right|^2 \varrho_k(\Omega) \varrho_j(\Omega), \quad (1)$$

denoting by F_{jk} the matrix elements of \hat{F} in the mean field. Here, $n(x)$ is the Fermi function determining the occupation of the single particle levels. The $\varrho_k(\omega)$ represents the distribution of the single particle strength over more complicated states and can be written as

$$\varrho_k(\omega) = \frac{\Gamma(\omega, T)}{(\hbar\omega - \epsilon_k - \Sigma'(\omega, T))^2 + \left(\frac{\Gamma(\omega, T)}{2}\right)^2} \quad (2)$$

For $\Gamma(\omega, T)$ the following form has been used

$$\Gamma(\omega, T) = \frac{1}{\Gamma_0} \frac{(\hbar\omega - \mu)^2 + \pi^2 T^2}{1 + \frac{1}{c^2} [(\hbar\omega - \mu)^2 + \pi^2 T^2]} \quad (3)$$

with μ being the chemical potential. The factor $1/\Gamma_0$ represents the strength of the ‘‘collisions’’. The cut-off parameter c allows one to account for the fact that

the imaginary part of the self-energy does not increase indefinitely when the excitations get away from the Fermi surface.

In Fig. 1 we show the temperature dependence of friction. They have been obtained for a system of 138 particles by using an infinitely deep square well for the single particle potential. At low temperatures, we see a marked increase. At higher temperatures, we see $\gamma(0)$ to reach some maximal value of the same order of magnitude as the one of the wall formula, shown here by the horizontal line.

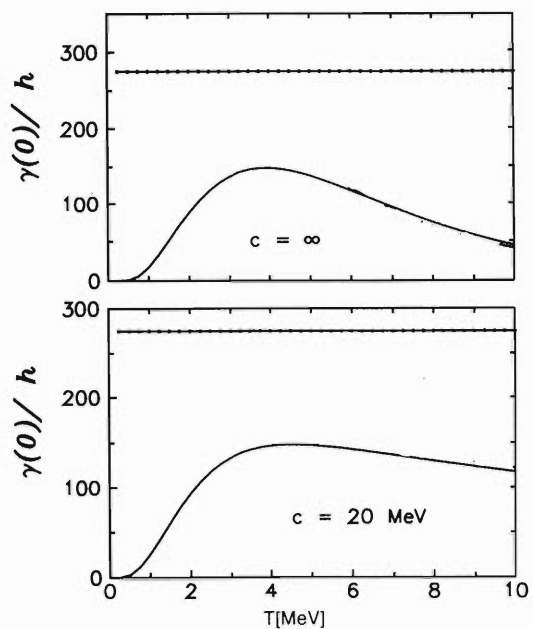


Fig. 1. The friction coefficient $\gamma(0)$ as a function of T .

Comparing the upper and lower figures, we observe a pronounced sensitivity of the T -dependence of friction on the cut-off parameter c . Within the mere ‘‘relaxation time approximation’’, i.e. for $c \rightarrow \infty$, friction drops like T^{-2} , as expected for hydrodynamic modes.

References

- 1) D. Hilscher and H. Rossner: *Ann. Phys. Fr.*, **17**, 471 (1992).
- 2) P. Paul and M. Thoennessen: *Ann. Rev. Part. Nucl. Sci.*, **44**, 65 (1994).
- 3) W. J. Swiatecki: *Nucl. Phys.*, **A574**, 233c (1994).
- 4) S. Yamaji et al.: *ibid.*, **A475**, 487 (1988).

* Physik-Department der Technischen Universität, Germany
 ** Institute for Nuclear Research of the Ukrainian Academy, Russia

Dissipative Dynamics of Fission Studied with Three-Dimensional Langevin Equation

T. Wada, S. Yamaji, and Y. Abe

[Fission, Langevin equation, mass asymmetry, precission neutron, fragment kinetic energy.]

Fission phenomenon induced by heavy ions provides a good field to study nuclear dissipative dynamics in high excitation. The collective fissioning mode interacts frequently with the thermalized nucleons. We can consider it as a Brownian particle interacting with a heat bath of nucleons. Langevin equation is expected to be useful for a phenomenological description.

As is well known, fission is a multi-dimensional phenomenon: a number of macroscopic collective degrees of freedom have to be taken into account, *e.g.*, a distance between future fragments, fragment deformation, necking, mass asymmetry, *etc.* In particular, the mass-asymmetric degree of freedom is very important because the fragment mass distribution can be measured directly. To consider the mass-asymmetric degree of freedom, we have to treat at least three-dimensional collective space, which requires a lot of computations. Recent rapid increase of the computer power has enabled us to extend the Langevin approach to the three-dimensional case.¹⁾

In a previous study, two-dimensional Langevin equation was applied to the symmetric fission of ^{200}Pb .²⁾ Including the particle evaporation in the continuous limit, we calculated the precission multiplicities of neutrons as well as the kinetic energy distribution of fission fragments at the same time. The calculated precission neutron multiplicity (ν_{pre}) and the mean value of the fragment kinetic energy (TKE) coincide with the experimental ones.³⁾ The calculated variance of the kinetic energy (σ_{TKE}), however, is too small to reproduce the experiment. The small σ_{TKE} may indicate that the two-dimensional description of the nuclear shape is not sufficient to describe all possible scission configurations.

In view of the importance of the mass-asymmetric degree of freedom, three-dimensional calculation has been performed for the same system including the mass-asymmetric degree of freedom. For this case, we adopt the shape parametrization by Maruhn and Greiner.⁴⁾ The neck parameter ε is fixed to 0.4 in the present calculation. We have treated z_0 (distance between the two potential centers), α (mass asymmetry parameter), and δ (fragment deformation parameter) as 3 collective parameters to be described by the

Langevin equation.

The results of two- and three-dimensional calculations with one-body (wall-and-window) friction is given in Table 1 for $E^* = 195.8$ MeV and for several values of the spin of the compound nucleus (ℓ). The mean values of the fragment kinetic energy in the three-dimensional case are slightly smaller than the corresponding two-dimensional ones. Three-dimensional σ_{TKE} 's are larger than the corresponding two-dimensional ones by about 20%, which turns out to be compatible with the experiment.³⁾ One should notice that the precission neutron multiplicity differs very little between two- and three-dimensional calculations, which means that the time scale of fission does not change in the two cases. The effect of inclusion of the mass asymmetric degree of freedom is that it acts to reduce the mean value of the fragment kinetic energy compared with that in symmetric fission and acts to increase the variance by allowing more flexible scission configurations.

The computer work has been performed on FUJITSU VPP500, RIKEN.

Table 1. Comparison between the results of two- and three-dimensional Langevin calculations.

ℓ (\hbar)	3DIM			2DIM		
	σ_{TKE} (MeV)	TKE (MeV)	ν_{pre}	σ_{TKE} (MeV)	TKE (MeV)	ν_{pre}
30	13.2	142.6	8.06	10.7	147.2	7.96
50	14.1	142.8	6.97	11.6	148.5	6.74
70	15.4	143.2	5.74	12.5	150.0	5.45

References

- 1) T. Wada: Proc. Tours Symp. on Nucl. Phys. II, World Scientific, Singapore, p. 470 (1995).
- 2) T. Wada, Y. Abe, and N. Carjan: *Phys. Rev. Lett.*, **70**, 3538 (1993).
- 3) D. J. Hinde et al.: *Nucl. Phys.*, **A452**, 550 (1986); D. J. Hinde et al.: *Phys. Rev.*, **C45**, 1229 (1992).
- 4) J. Maruhn and W. Greiner: *Z. Phys.*, **251**, 431 (1972); K. Sato et al.: *ibid.*, **A288**, 383 (1978).

Quenching of the Coulomb Sum Value

H. Kurasawa* and T. Suzuki

[NUCLEAR STRUCTURE electron scattering, Coulomb sum.]

Sum rules are one of the most important touchstones of nuclear models. If experiments show the sum rules not to be satisfied, it means a breakdown of the model, and new models or new degrees of freedom are required. For example, the sum of the Gamow-Teller strength should be given by $\sim (N - Z)$, when nucleonic degrees of freedom only are taken into account. In a (p,n) reaction, however, the quenching of the sum value has been observed. This fact implies a contribution from other degrees of freedom like Δ 's. For the sum of the photo-absorption strength, on the other hand, the nuclear current provides the sum rule value $\sim NZ/A$. Experiments have shown, however, enhancement of the strength, which indicates the existence of the meson exchange current in nuclei.

In electron scattering, the sum rule on the longitudinal response function is known, which is called the Coulomb sum rule. This is derived for a nonrelativistic nucleon system. Experiments on the sum rule have been performed at Saclay,^{1,2)} Bates,³⁾ and SLAC,⁴⁾ and shown that the sum rule value is quenched by 20–50% in medium heavy and heavy nuclei.

We have studied what kind of new degrees of freedom is required in the electron scattering.⁵⁾ The Coulomb sum value has been calculated in nonrelativistic and relativistic models. It has been shown that particle-hole correlations within the Fermi sea explain

a part of the quenching observed in medium heavy and heavy nuclei, but they are not enough to explain the data both in relativistic and nonrelativistic models. If we include antinucleon degrees of freedom in the particle-hole correlations, the relativistic model can reproduce the available data. The relationship among the antinucleon's effects, modification of the nucleon size and the effective mass of mesons is also discussed. New experimental data on the Coulomb sum are required at the momentum transfer between 0.6 and 1 GeV, in order to confirm the prediction of the present relativistic model.

References

- 1) P. Barreau et al.: *Nucl. Phys.*, **A402**, 515 (1983); Z. E. Meziani et al.: *Phys. Rev. Lett.*, **52**, 2130 (1984); Z. E. Meziani et al.: *ibid.*, **54**, 1233 (1985).
- 2) A. Zghiche et al.: *Nucl. Phys.*, **A572**, 513 (1994).
- 3) M. Deady et al.: *Phys. Rev.*, **C33**, 1897 (1986); C. Blatchley et al.: *ibid.*, **C34**, 1243 (1986); T. C. Yates et al.: *Phys. Lett.*, **B312**, 382 (1993).
- 4) J. P. Chen et al.: *Phys. Rev. Lett.*, **66**, 1283 (1991); Z. E. Meziani et al.: *ibid.*, **69**, 41 (1992).
- 5) H. Kurasawa and T. Suzuki: Proc. the Korea-Japan Joint Symp. on Recent Developement of Nuclear Study using Electron and Photon Beams, I-Tong Cheon (ed.), Global Publication Services, Singapore, p. 39 (1995).

* Department of Physics, Faculty of Science, Chiba University

Symmetry Energy at Subnuclear Densities and the Layer of Non-Spherical Nuclei in Neutron Star Crusts

K. Oyamatsu, K. Sumiyoshi, Y. S. Mochizuki, and H. Toki

[relativistic field theory, equation of state, neutron stars, unstable nuclei, neutron skins.]

The structure of neutron-star crusts is one of the most important part of neutron stars because all we can observe from the earth are limited to phenomena which occur at neutron-star surfaces (crusts). The crustal matter itself is also interesting because of its extreme neutron richness which can never be produced in laboratories. Furthermore, one of the present authors (K.O.) showed that the stable nuclear shape in the inner crust matter is not necessarily spherical, and that it should change from sphere, to cylinder, slab, cylindrical hole and spherical hole with increase of density before the nuclei finally dissolve into uniform matter.¹⁾ These exotic nuclear shapes are now being investigated from the viewpoints of their implications in the structure and evolution of neutron stars.²⁻⁶⁾

Recently, Sumiyoshi, Oyamatsu and Toki⁷⁾ performed the Thomas-Fermi calculation of the crustal matter with an equation of state (EOS) in the relativistic Brueckner Hartree-Fock (RBHF) theory and found that the layer of the non-spherical nuclei is much thinner than those calculated with non-relativistic EOS's. In Fig. 1, we compare the RBHF results with a non-relativistic result with model IV in Ref. 1 (hereafter referred to as oya4). In these two models, the energies due to the gradients of local nucleon densities are nearly the same. Therefore, this discrepancy is expected to stem from the bulk properties of the EOS. We note here that the shell effects are too small at the densities of interest to change results of the semiclassical calculations.⁸⁾

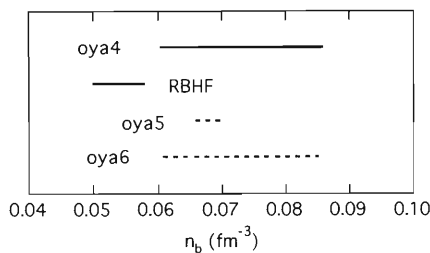


Fig. 1. The density region of the non-spherical nuclei calculated with various models.

In the present study, we focus on the effects due to the symmetry energy and perform the Thomas-Fermi calculation of the inner crust matter with two energy density functionals, oya5 and oya6, which are the same as oya4 except for the density dependence of the symmetry energy. The symmetry energy of oya5, having the same value as oya4 at nuclear density, is a nearly linear function of density as those of most of relativistic EOS's are. On the other hand, oya6 has similar density dependence to oya4 but its value is much smaller (by 13%). As shown in Fig. 1, the density region of the non-spherical nuclei is quite sensitive to the density dependence of the symmetry energy (oya5), rather than to the value of the symmetry energy at saturation density (oya6). This implies that properties of the matter in the inner crust with extreme neutron-richness should be investigated with due consideration of the symmetry energy at subnuclear densities. We also note that the density dependence at subnuclear densities affects its high density-part of the EOS which is crucially important to determine bulk properties of neutron stars, such as mass and size. We may extract some information from careful investigations on properties of unstable nuclei, especially from neutron skins, and this line of study is now being carried out.

References

- 1) K. Oyamatsu: *Nucl. Phys.*, **A561**, 431 (1993).
- 2) Y. Mochizuki and T. Izuyama: *Astrophys. J.*, **440**, 263 (1995).
- 3) G. Lazzari and F. V. De Blasio: *Nuovo Cim.*, **A107**, 1423 (1994).
- 4) G. Lazzari and F. V. De Blasio: *Z. Phys.*, **A350**, 117 (1994).
- 5) F. V. De Blasio and G. Lazzari: *Phys. Rev.*, **C52**, 418 (1995).
- 6) G. Lazzari and F. V. De Blasio: *Z. Phys.*, **A353**, 13 (1995).
- 7) K. Sumiyoshi et al.: *Nucl. Phys.*, **A595**, 327 (1995).
- 8) K. Oyamatsu and M. Yamada: *ibid.*, **A578**, 181 (1994).

Braking Index Changes from Neutron Star Glitches

Y. S. Mochizuki

[Neutron stars.]

Pulsars are rotating neutron stars with very strong magnetic fields. We know their rotational states through observing pulsating radio signals from them. Pulsars usually undergo a slowdown according to a simple power law, $\dot{\Omega}_c = -k\Omega_c^n$, where Ω_c is the angular velocity of the observed crust of a pulsar, k is a constant, and n is called the braking index. In principle, the braking index is defined as $n = \Omega_c \ddot{\Omega}_c / \dot{\Omega}_c^2$. For magnetic dipole braking, $n = 3$. Measured index values so far include $n = 2.51$ for the Crab pulsar, $n = 2.84$ for PSR B1509-58, and $n = 2.01$ for PSR B0540-69. It has been reported recently, however, that some pulsars have abnormal braking indices; the index of PSR B1757-24 has decreased from ~ 41 to ~ 22 in less than 1 year. A possible explanation on the anomalous braking indices is based on glitches.

Glitches are unpredictable sudden spinups of pulsars. The size of a glitch is defined as $\Delta\Omega_c/\Omega_c$, where $\Delta\Omega_c$ is a change in Ω_c brought about by a glitch. In the Vela pulsar, for example, the glitch size is of the order of 10^{-6} . After a glitch, the increased angular velocity decays towards almost the extrapolation of the preglitch values with a larger deceleration rate than before. Therefore, in the postglitch relaxation phase, the braking index can become large and change in the time scales of the relaxation. Although glitches have not been observed in PSR B1757-24, it possibly glitched before the beginning of observation, and may be in its recovery state from the glitche.

The physical origin of glitches is a long standing open problem since a glitch was first observed in Vela in 1969, whereas the postglitch relaxation has been explained by means of the vortex creep model.¹⁾ The vortex creep model describes coupling states between the observed neutron star crust and neutron superfluid, which is rotating at Ω_s in the star interior. In this model, the two components are assumed to be decoupled at the time of a glitch, and the postglitch relaxation is regarded as a recoupling process between the two. Here, the braking index changes from glitches were simulated under a reasonable range of neutron star models, glitch sizes, and the vortex creep model parameters. The results were applied to the case observed in PSR B1757-24.

Figure 1 shows the braking index changes corresponding to various glitch sizes for the neutron star model constructed by stiff (PS) equation of state and the vortex creep model parameter $\omega_{cr} = \Omega_s - \Omega_c = 0.1 \text{ rad s}^{-1}$. We see that a larger glitch produces a larger maximum of the braking index.

Now we are going to discuss about the case of PSR

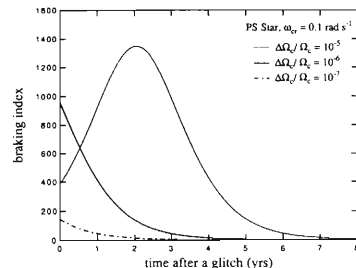


Fig. 1. Evolution curves of braking index after a glitch.

B1757-24. The observation of this pulsar has started in January 1990. Figure 2 shows the observed change of the braking index²⁾ and its fitting by the above model of the glitch size 10^{-6} . Since PSR B1757-24 and the Vela pulsar are of almost the same age, the size 10^{-6} is also preferable for PSR B1757-24. From Fig. 2 we see that the observed index decrease can be explained as the interglitch behavior, and a glitch of $\sim 10^{-6}$ size would have taken place about 2 years before the beginning of the observation.

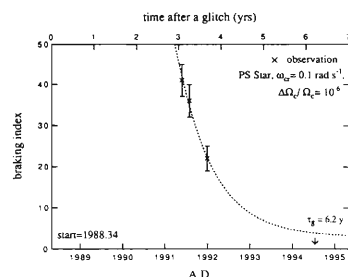


Fig. 2. Best fitting for observed braking indices of PSR B1757-24.

In the vortex creep model, we can roughly estimate the glitch interval as $\tau_g = 10^{-2}/|\dot{\Omega}_c| = 6.2$ years for PSR B1757-24 under the assumption that it experiences Vela-like glitches. If PSR B1757-24 is really a glitching pulsar, this means that it will glitch again around 1994. Based on the above estimation by the author, the timing behavior of PSR B1757-24 was further analyzed, and it was recently confirmed that the pulsar actually had glitched in February 1994.³⁾ Namely, the abnormal braking indices are significant as an indicator of glitching pulsars.

References

- 1) M. A. Alpar et al.: *Astrophys. J.*, **409**, 345 (1993).
- 2) V. M. Kaspi: private communication.
- 3) A. G. Lyne et al.: in preparation (1995).

Exotic Nuclear Deformation in the Neutron Star Crusts and the Origin of Glitches

Y. S. Mochizuki, K. Oyamatsu, and T. Izuyama

[Neutron stars, Coulomb lattice potential, Nuclear fusion.]

The inner crust of a neutron star consists of the lattice of neutron rich nuclei and the superfluid neutrons. These are imbedded in the degenerate Dirac electron gas. Since the neutron superfluid is rotating, there exist many quantized vortices. The vortex lines are expected to be nearly parallel to the axis of rotation. Each superfluid vortex line possesses a normal fluid core over a distance ζ , the coherence length of the superfluid. In the vortex core the pairing energy of the neutron Cooper pair is lost. To simplify, we assume that the Cooper pair formation is prohibited in nuclei. Then clearly the most energetic position of a vortex core is achieved by maximum overlap of a vortex and nuclei. Hence the vortex line is expected to be pinned along a line of nuclei.

In the major part of the inner crust the nuclei are expected to be spherical. In the vicinity of the stellar core, however, the nuclear materials in the crust may take exotic forms. These are the lattice of nuclear rods and the multi-layer of plate-like nuclear matter.^{1,2)} This was derived from energetic considerations; the stable nuclear shape is determined by minimizing $W_S + W_C$, where W_S is the surface energy and W_C the Coulomb energy. This argument holds for the vortex free region.

The nuclear shapes inside and in the vicinity of the vortex core lines are accomplished by minimizing $(W_S + W_C) + [\text{the pairing energy in the neutron superfluid}]$. In the inner crust there exists a region where the pairing energy plays an important role in this minimization and hence the nuclear materials pinning the vortex core line may not be a series of spherical nuclei. A novel nuclear material may be constructed by absorbing some nuclei into the vortex core. In this way the pairing energy will be gained at the expense of the Coulomb energy. From the energetic point of view, we have confirmed³⁾ that a vortex core line can induce a nuclear rod along itself (Fig. 1). Significantly, this pinning-induced nuclear rod will strongly trap the vortex line. This self-trapping may be a crucial mechanism for the pulsar glitches, *i.e.*, sudden spin-ups of neutron stars.³⁾ The nuclear rod formation requires a nuclear fusion.

How high is the Coulomb energy barrier? Here, we investigated the Coulomb barrier for the initiation of the fusion, in which one of the nuclei is absorbed from the neighborhood into the vortex core. We considered cubic boxes made up of many (up to $\sim 10^3$) nuclei with periodic boundary conditions. The electrostatic interaction is considered by Fourier analysis. We found that the barrier is definitely less than 3.1 MeV. Note that the Coulomb energy of the nearest neighbor nuclear pair is 80 MeV if we adopt 30 fm for the nuclear separation and 40 for the proton number of a nucleus, the suggested value in previous papers. There are two reasons for the dramatic reduction of the barrier. The first reason is the electron screening. The second is a small value, 22, of the proton number in a nucleus adopted here, which is a recent result from the equation of state based on relativistic Brueckner-Hartree-Fock theory.⁴⁾

When the considered nucleus is absorbed into the vortex core, the other nuclei were assumed to be fixed at their lattice sites. Actually the nuclear positions must be relaxed. We therefore expect a substantially lower Coulomb barrier than 3.1 MeV.

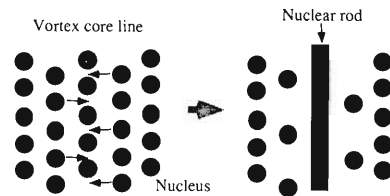


Fig. 1. A naive sketch of deformation from spherical to rod-like nuclear matter, induced by a vortex line.

References

- 1) K. Oyamatsu and M. Yamada: *Nucl. Phys.*, **A578**, 181 (1994).
- 2) C. J. Pethick et al.: *ibid.*, **A584**, 675 (1995).
- 3) Y. Mochizuki and T. Izuyama: *Astrophys. J.*, **440**, 263 (1995).
- 4) K. Sumiyoshi et al.: *Nucl. Phys.*, **A595**, 327 (1995).

A Study of Collision Frequency and Particle Density in Ultrarelativistic Nuclear Collisions by an Event Generator URASiMA

S. Daté, K. Kumagai,* O. Miyamura, H. Sumiyoshi, and X-Z. Zhang**

[high energy reaction, quark-gluon plasma, event generator.]

It is a basic problem for creating QGP in laboratories to what extent nuclear matter is compressed and whether or not the thermalization is accomplished in ultrarelativistic nucleus-nucleus (A-A) collisions. To answer the problem, we have studied local collision frequencies of hadrons produced in ultrarelativistic A-A collisions by employing an event generator URASiMA. It turns out that a thermalized high density local system is achievable in the CERN-SPS energy region although its size is not always large.

The event generator URASiMA describes A-A collisions in a conventional hadronic level employing the multi-chain model (MCM)¹⁾ for generation of multi-particle final states. The generator traces trajectories of particles which are treated as straight lines between interaction points in full 1 + 3 dimensional space-time. Interactions between two particles are treated as point-like so that the problem of ambiguous time ordering is avoided.

The produced particles suffer secondary cascade collisions after the formation time in their hadronic environment. URASiMA takes into consideration full generations of cascade collisions although interaction channels are limited, at the moment, to inelastic and elastic nucleon-nucleon (N-N), π -N interactions, and elastic π - π interaction via ρ meson. The inelastic π -N interaction is included as a channel $\pi N \rightarrow \pi \Delta \rightarrow \pi \pi N$.

The validity of the model has been checked by comparing the output of URASiMA with several experimental data on the global quantities and, newly for this time, with the experimental data on Sulphur + Nucleus collisions at 200 GeV/nucleon.²⁾

As the process of a collision evolves, decelerated nucleons and produced hadrons form a collision complex. We may estimate the nucleon and pion density in a sphere of volume V located in the center of the complex from the local collision frequency as

$$\rho_N = \frac{\left(\frac{dN_C^{\pi N}}{dt}\right)^2 \langle v \sigma_{\pi \pi} \rangle}{\sqrt{\left(\frac{dN_C^{\pi \pi}}{dt}\right)^2 2 \langle v \sigma_{\pi N} \rangle^2 V}}$$

$$\rho_\pi = \frac{\left(\frac{dN_C^{\pi N}}{dt}\right)^2 \langle v \sigma_{NN} \rangle}{\sqrt{\left(\frac{dN_C^{NN}}{dt}\right)^2 2 \langle v \sigma_{\pi N} \rangle^2 V}}$$

Note that we are counting only the number of these particles which are involved in collisions and contribute to thermalization of the system.

Figure shows the dependence of the particle number density on the stopping power of nuclei and on the nuclear mass numbers. Refer to Ref. 3 for details.

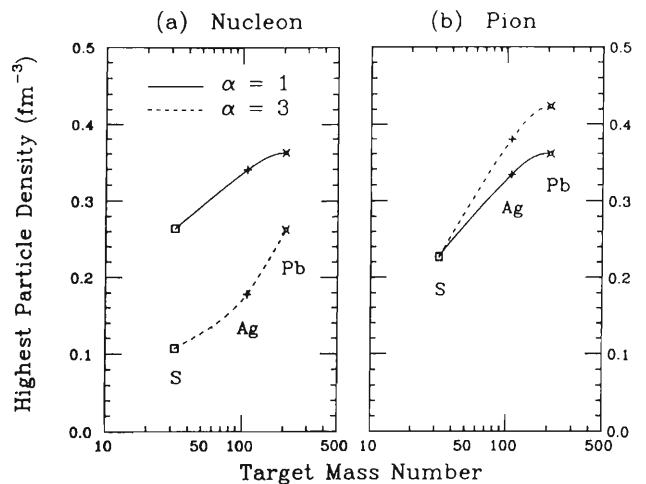


Fig. 1. Target mass number dependence of the highest (a) nucleon- and (b) pion-density inside the central sphere for $\alpha = 1$ (solid curve) and $\alpha = 3$ (dashed curve).

References

- 1) K. Kinoshita, A. Minaka, and H. Sumiyoshi: *Prog. Theor. Phys.*, **61**, 165 (1979); *ibid.*, **63**, 928 (1980).
- 2) WA80 Collab., R. Albrecht et al.: *Z. Phys.*, **C55**, 539 (1992).
- 3) S. Daté, K. Kumagai, O. Miyamura, H. Sumiyoshi, and X-Z. Zhang: *J. Phys. Soc. Jpn.*, **64**, 766 (1995).

* Department of Physics, Hiroshima University

** China Institute of Atomic Energy

Gluon Distribution Function using Bag Model and QCD Sum Rule

H. Kitagawa

[polarized gluon, bag model, QCD sum rule.]

Deep inelastic scattering experiments using high energy leptons have disclosed the structure of hadrons, which are composed of “quarks” and “gluons”. Most of the theoretical models of hadrons assume that hadrons are composed only of quarks. Experimental data, however, have shown that the quarks do not carry all of the momentum of hadron, then gluons are pointed out to play an important role. One of the main purposes of the RHIC-SPIN project (polarized proton-proton collider) is to investigate the polarization of gluons in the proton, and to give an answer to the “proton spin problem”.

Bag model is one of the effective tools to study the properties of nucleons. Nucleon is made of three quarks inside the bag, which is considered to represent the gluon condensation. MIT bag model is the simplest one, and is employed here. Results of calculations are shown in Fig. 1. In this model, perturbative gluons are obtained by the Maxwell equation with the source term of quarks. Non-perturbative part, “bag”, contributes to them indirectly through quarks. Bag model, hence, is not suitable for the discussion of absolute values

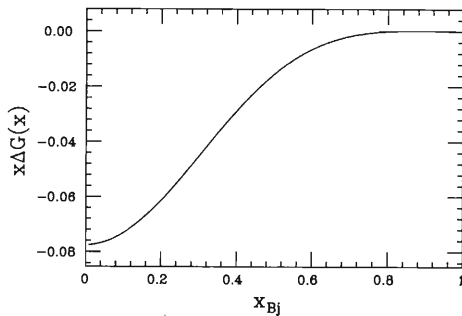


Fig. 1. Polarized gluon fraction calculated using the MIT bag model.

of observables, though it is useful to study the global structure, i.e. x -distribution.

QCD sum rule is a useful method to evaluate absolute values. This is complementary to the result of bag models, and is applied to the gluon “spin” contribution, i.e. the expectation value of gluon distribution, or the second moment of distribution:

$$\langle S_G \rangle = \int_0^1 x \Delta G(x) dx. \quad (1)$$

Belyaev and Blok applied this method to the spin-unpolarized gluon in Ref. 1, which is followed here. Second moments of quark and gluon appear in the response of constant external fields, which are introduced by the following lagrangian terms,

$$\Delta \mathcal{L}_q = -i\bar{\phi} D_\mu \gamma_\nu \phi S^{\mu\nu} \quad (2)$$

$$\Delta \mathcal{L}_G = -G_\mu^\lambda G_{\lambda\nu} S^{1\mu\nu} \quad (3)$$

where ϕ and G represent the quark and gluon respectively, and S and S^1 are the tensor external fields. Their forms are determined by the operator product expansion (OPE). In the spin-polarized case, following lagrangian terms are derived by OPE.

$$\Delta \mathcal{L}_q^{\text{pol.}} = -i\bar{\phi} D_\mu \gamma_5 \gamma_\nu \phi S_{\text{pol.}}^{\mu\nu} \quad (4)$$

$$\Delta \mathcal{L}_G^{\text{pol.}} = -(1/2)\epsilon_\mu^{\lambda\rho\sigma} G_{\rho\sigma} G_{\lambda\nu} S_{\text{pol.}}^{1\mu\nu}. \quad (5)$$

Second moments of the distributions of the polarized quark and polarized gluon are obtained using the above lagrangian terms. Calculations are now in progress.

References

- 1) V. M. Belyaev and B. Yu. Blok: *Z. Phys.*, **C30**, 279 (1986).

Lattice-QCD Calculations Using VPP500

S. Kim and S. Ohta

[lattice quantum chromodynamics, parallel computer.]

We are calculating the mass of light hadrons in quenched lattice quantum chromodynamics (QCD) with staggered quarks.¹⁾ The new vector-parallel supercomputer of RIKEN,²⁾ VPP500, allows us to do such a calculation on the largest-ever lattice size of $48^3 \times 64$ at the finest-ever lattice spacing of $a^{-1} \sim 4\text{GeV}$ (or equivalently the inverse-squared lattice coupling of $\beta = 6/g^2 = 6.5$). The physical lattice volume of about $(2.4\text{ fm})^3$ is large enough for extrapolation to remove the errors from finite volume. The lattice spacing is fine enough for extrapolation to remove such a discretization artifact like the flavor symmetry breaking. We are also able to use such light quark mass like $m_q = 0.00125a^{-1} \sim 5\text{ MeV}$, i.e. we no longer have to make extrapolation from very heavy values like $m_q \sim 100\text{ MeV}$. Being free from these systematic errors simultaneously for the first time, we are ready to study another type of systematic error arising from the quenched approximation itself. There are suggestions³⁾ and possible evidence⁴⁾ that the chiral ($m_q \rightarrow 0$) limit of quenched QCD differs from that of full QCD in regard of the divergent “quenched chiral log” term, $\ln m_q$. In the latter works,⁴⁾ however, the former three types of systematic error were studied separately. In contrast the present work simultaneously addresses all of them. Also in the current study the chiral limit should be approached more reliably than before since the flavor symmetry violation is smaller.

Our preliminary results using 50 gauge configurations are summarized in the Edinburgh plot in Fig. 1. In contrast to earlier studies, all the points, except for the left-most point for the lightest quark mass, lie below the guiding lines. This means that the ground-state nucleon is less squeezed on the current lattice than before. At the lightest quark mass of $m_q = 0.00125$, we now see the ratio m_π/m_ρ as low as ~ 0.3 . This suggests that our lattice is big enough even down to such light quark mass. Thus pushing the quark mass even smaller and reaching the region where $m_\pi/m_\rho \simeq 0.2$ and $m_\pi \simeq 0.04$ are now viable. Extrapolation to small m_q will soon be unnecessary. Also the current result shows approximate flavor symmetry restoration: the mass of Nambu-mode pion and that of non-Nambu-mode pions agree with each other. All these attractive features of the current results suggest that the chiral limit of our data will be more interesting. However, we think that the investigation on the

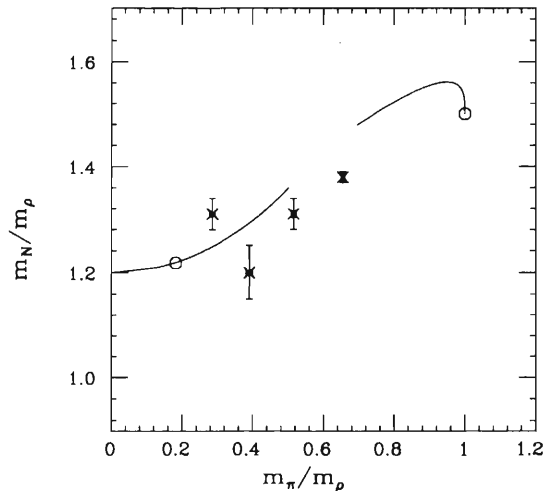


Fig. 1. Edinburgh plot at $\beta = 6.5$ on $48^3 \times 64$ lattice for quark mass $m_q = 0.01, 0.005, 0.0025$ and 0.00125 . The two circles are the experimental point (left) and naive quark model prediction (right).

quenched chiral log in the pion mass and chiral condensate requires a still higher statistics of at least 100 gauge configurations and perhaps more. We already gathered 100 configurations and their full analysis is under way.

Using the same supercomputer, SO is also involved in the development of the “Self-Test Monte Carlo” method for a reliable frame work of numerical Monte Carlo calculations in general, and SK is involved in projects on the over-improved cooling method and 3D Thirring model respectively concerning some features of lattice QCD.

References

- 1) S. Kim and S. Ohta: in Proc. “Lattice’95,” *Nucl. Phys. B*, (Proc. Suppl.), to be published.
- 2) S. Kim and S. Ohta: in Proc. “Lattice’94,” *Nucl. Phys. B*, (Proc. Suppl.), **42**, 920 (1995).
- 3) S. R. Sharpe: *Phys. Rev.*, **D46**, 3146 (1992); C. W. Bernard and M. F. L. Golterman: *ibid.*, **D46**, 853 (1992).
- 4) S. Kim and D. K. Sinclair: *Phys. Rev.*, **D48**, 4408 (1993); *Nucl. Phys. B* (Proc. Suppl.), **34**, 347 (1994); *Phys. Rev.*, **D52**, R2614 (1995).

Effective Potential Formalism for Dynamical Chiral-Symmetry Breaking in the Dual Ginzburg-Landau Theory

S. Umisedo,* H. Suganuma,** and H. Toki

[QCD, color confinement, chiral symmetry, effective potential, monopole condensation.]

Recent progress in the lattice gauge theory¹⁾ clarifies the central role of QCD-monopole condensation²⁻⁵⁾ in color confinement, which was firstly conjectured by Nambu.²⁾ The important correlation between QCD-monopole condensation and dynamical chiral-symmetry breaking (D χ SB) was firstly pointed out by Suganuma-Sasaki-Toki²⁾ solving the Schwinger-Dyson (SD) equation in the Dual Ginzburg-Landau (DGL) theory, and was discovered by Miyamura also in the lattice QCD.⁶⁾

We study D χ SB in the DGL theory using the effective potential formalism instead of the SD equation to extract the contribution of confinement to D χ SB directly. Within the ladder approximation, the SD equation is generated from the effective potential $\Gamma_{\text{eff}}[S]$ up to the two-loop diagram by imposing the extreme condition on the quark propagator $S(p)$.⁷⁾ Using the non-perturbative gluon propagator $D_{\text{DGL}}^{\mu\nu}(p)$ in the DGL theory,³⁻⁵⁾ the effective potential can be expressed as

$$\Gamma_{\text{eff}}[S] = -i\text{Tr} \ln(SG^{-1}) - i\text{Tr}(SG^{-1}) + \int \frac{d^4p}{(2\pi)^4} \frac{d^4q}{(2\pi)^4} \frac{\vec{Q}^2 e^2}{2} \text{tr}(\gamma_\mu S(p)\gamma_\nu S(q)D_{\text{DGL}}^{\mu\nu}(p-q)),$$

where $G(p)$ is the bare quark propagator, and $S(p)$ the interacting quark propagator including the gauge interaction effect, $G^{-1}(p) = \not{p} + i\epsilon$, $S^{-1}(p) = \not{p} - M(p) + i\epsilon$ in the chiral limit. For the energetic argument for D χ SB, it is useful to examine the effective potential $V_{\text{eff}}(M(p^2)) = -\Gamma_{\text{eff}}(S)$, which corresponds to the vacuum energy density as a function of the dynamical quark mass $M(p^2)$.

Figure 1 shows $V_{\text{eff}}(M(p^2))$ as a function of the infrared quark mass $M(0)$ using the quark-mass ansatz,

$$M(p^2) = \frac{M(0)p_c^2}{(p^2 + p_c^2)} \left\{ \frac{\ln p_c^2}{\ln(p^2 + p_c^2)} \right\}^{1 - \frac{N_c^2 - 1}{2N_c} \cdot \frac{9}{11N_c - 2N_f}},$$

which is suggested by the renormalization group analysis.⁷⁾ One finds the clear double-well structure in $V_{\text{eff}}(M(p^2))$, which has a nontrivial minimum at $M(0) \simeq 0.4\text{GeV}$.

The nonperturbative gluon propagator is separated

into two parts responsible to the linear potential and the Yukawa potential, respectively,³⁻⁵⁾ $D_{\text{DGL}}^{\mu\nu}(p) = D_{\text{linear}}^{\mu\nu}(p) + D_{\text{Yukawa}}^{\mu\nu}(p)$. Hence, by examining these two parts separately, the importance of the confinement effect to D χ SB can be studied quantitatively. We find that the main driving force for D χ SB is brought from the confinement part, $D_{\text{linear}}^{\mu\nu}(p)$.

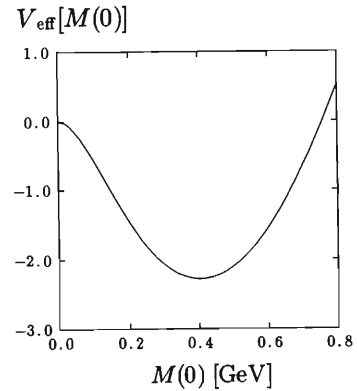


Fig. 1. The effective potential V_{eff} as a function of the infrared quark mass $M(0)$ in the dual Ginzburg-Landau theory.

References

- 1) Proc. of Lattice 94, Nucl. Phys. (Proc. Suppl.), **B42**, (1995).
- 2) Y. Nambu: *Phys. Rev.*, **D10**, 4264, (1974).
- 3) H. Suganuma, S. Sasaki, and H. Toki: *Nucl. Phys.*, **B435**, 207, (1995).
- 4) S. Sasaki, H. Suganuma, and H. Toki: *Prog. Theor. Phys.*, **94**, 373 (1995).
- 5) H. Suganuma, S. Sasaki, and H. Toki: Proc. of Int. Conf. on Quark Confinement and Hadron Spectrum, Como, Italy, World Scientific, p. 238 (1995); S. Sasaki, H. Suganuma, and H. Toki: *ibid.*, p. 241.
- 6) O. Miyamura and S. Origuchi: Proc. Int. Workshop on Color Confinement and Hadrons, RCNP, Osaka, World Scientific, (1995) in press.
- 7) K. Higashijima: *Prog. Theor. Phys. Suppl.*, **104**, 1, (1991) and references cited therein.

* Tokyo Metropolitan University

** Research Center for Nuclear Physics, Osaka University

New α -Decaying Neutron-Deficient Isotopes ^{197}Rn and ^{200}Fr

K. Morita, Y. Pu, T. Nomra, Y. Tagaya, T. Uchibori, K. Lee, K. Uchiyama, M. Kurokawa,
T. Motobayashi, H. Ogawa, M. Hies, J. Feng, A. Yoshida, S. Jeong, S. Kubono, M. Wada, K. Sueki,
T. Ishizuka, Y. Fujita, H. Miyatake, T. Shimoda, T. Shinozuka, H. Kudo, Y. Nagai, and S. Shin

[new isotope, $^{166}\text{Er}(^{36}\text{Ar},5\text{n})^{197}\text{Rn}$, $^{169}\text{Tm}(^{36}\text{Ar},5\text{n})^{200}\text{Fr}$, $E_{\text{lab}} = 186, 200 \text{ MeV}$.]

New neutron-deficient isotopes, ^{197}Rn , $^{197\text{m}}\text{Rn}$, and ^{200}Fr , have been produced and identified on the basis of genetic correlations in the $^{166}\text{Er}(^{36}\text{Ar},5\text{n})^{197}\text{Rn}$ ($E_{\text{lab}} = 186, 200 \text{ MeV}$) and $^{169}\text{Tm}(^{36}\text{Ar},5\text{n})^{200}\text{Fr}$ ($E_{\text{lab}} = 186 \text{ MeV}$) reactions. The results have already been published in *Z. Physik A*.¹⁾ See Ref. 1 for the details of data analysis and discussions. Here we present only a brief description of the experiment together with summarization of the results.

The 273.6 MeV ^{36}Ar pulsed beam (10 ms on / 10 ms off) supplied from the RIKEN Ring Cyclotron and degraded to 186 MeV or 200 MeV with aluminum foils was used to bombard a 1.4 mg/cm^2 ^{166}Er target (enriched to 96.3%) electrodeposited onto a thin aluminum foil or a self-supporting 2 mg/cm^2 ^{169}Tm target. Reaction products recoiling out of the target were separated from the beam by using a gas-filled recoil

separator (GARIS).²⁾ A two-dimensionally position-sensitive silicon detector (PSD: $64 \text{ mm} \times 64 \text{ mm}$) was set at the focal plane of the GARIS. A large-area micro-channel plate assembly (MCP) was set about 60 cm upstream from the PSD to measure time of flights of the reaction residues between the MCP and the PSD. The implantation signal as well as the subsequent α -decay signals were then recorded event by event with a CAMAC based on-line data taking system. A search of time and position correlation of the events enables us to identify decay chains like: evaporation residues \rightarrow first α -decay \rightarrow second α -decay. Consequently, new α -decaying isotopes can be identified if the corresponding daughter nuclei are known to be α -emitters. A summary of the measured α -decay energies and half-lives are shown in Table 1.

Table 1. The alpha energies E_α and half-lives $T_{1/2}$ measured in the present work.

Isotope	E_α (keV) (present work)	$T_{1/2}$ (ms)	Reaction Channel	E_α (keV)	$T_{1/2}$ (ms) (literature)	Ref.	$T_{1/2}(\text{ms})^{\text{a)}$ (systematics)
^{197}Rn	7261 ± 30	51^{+35}_{-15}	$^{166}\text{Er}(^{36}\text{Ar}, 5\text{n})$	—	—		45
^{193}Po	6946 ± 30	182^{+146}_{-56}	Daughter of ^{197}Rn	6940 ± 20	360 ± 50	[3]	110
$^{197\text{m}}\text{Rn}$	7370 ± 30	18^{+9}_{-5}	$^{166}\text{Er}(^{36}\text{Ar},5\text{n})$	—	—		19
$^{193\text{m}}\text{Po}$	6991 ± 30	154^{+106}_{-44}	Daughter of $^{197\text{m}}\text{Rn}$	7000 ± 20	260 ± 20	[3]	68
$(^{196}\text{Rn})^{\text{b)}$	(7428)	(5) ^{c)}	$^{166}\text{Er}(^{36}\text{Ar},6\text{n})$	—	—		12
$(^{192}\text{Po})^{\text{b)}$	(7211)	(32) ^{d)}	Daughter of ^{196}Rn	7170 ± 20	34 ± 3	[3]	17
^{200}Fr	7500 ± 30	570^{+270}_{-140}	$^{169}\text{Tm}(^{36}\text{Ar},5\text{n})$	—	—		16
^{196}At	7053 ± 30	320^{+220}_{-90}	Daughter of ^{200}Fr	7055 ± 7	300 ± 100	[4]	100

a): Calculated by the systematics for even-even nuclei reported in Ref. 5. The Q_α values used are those determined in this work for the mother nuclei and those reported in the literature for the daughter nuclei.

b): Only one decay chain was observed. c): Time difference between ER - $\alpha 1$. d): Time difference between $\alpha 1$ - $\alpha 2$.

References

- 1) K. Morita et al.: *Z. Physik*, **A352**, 7 (1995).
- 2) K. Morita et al.: *Nucl. Instrum. Methods Phys. Res.*, **B70**, 220 (1992).

- 3) M. Leino et al.: *Phys. Rev.*, **C24**, 2370 (1981).
- 4) V. Treytl et al.: *Nucl. Phys.*, **A97**, 405 (1967).
- 5) B. A. Brown: *Phys. Rev.*, **C46**, 811 (1992).

New α -Decaying Neutron-Deficient Isotopes ^{196}Rn and ^{195}At

Y. Pu, K. Morita, T. Nomura, Y. Tagaya, T. Uchibori, T. Minemura, K. Lee,
T. Motobayashi, M. Hies, T. Ariga, A. Yoshida, K. Sueki, and S. Shin

[α -decay, new isotopes, ^{166}Er ($^{36}\text{Ar},6n$) ^{196}Rn , $E_{\text{lab}} = 208$ MeV, ^{164}Er ($^{36}\text{Ar},p4n$) ^{195}At , $E_{\text{lab}} = 183, 199$ MeV.]

As a continuation of our previous experiment¹⁾ of synthesizing new neutron-deficient isotopes such as ^{197}Rn and ^{200}Fr , experiments have been performed to synthesize more neutron-deficient radon and astatine isotopes. Compared with the previous set-up, the detection efficiency for α -decays has been improved from about 50 to 80% of 4π solid angle by installing 4 solid state detectors (SSD: 64 mm \times 64 mm) around the large position sensitive detector (PSD: 64 mm \times 64 mm).²⁾ The experiment was carried out at E1 cave of the ring cyclotron lab of RIKEN. A 273.6 MeV ^{36}Ar pulsed-beam (5ms on–5ms off) from the ring cyclotron was degraded in energy by using aluminum foils to 208 MeV to bombard a 1.4 mg/cm² ^{166}Er (enriched to 96.3%) target and to energies of 183 and 199 MeV to bombard a 1.2 mg/cm² ^{164}Er (enriched to 62%) target respectively. The beam intensity was about 1.3×10^{11} pps. Evaporation residues (ER) were separated from the beam by using the gas-filled recoil separator GARIS³⁾ and were subsequently implanted onto the PSD located at the focal plane after traversing a large micro-channel-plate (MCP) set. The energy calibration for both the PSD and SSDs is based on α -decays from the implanted known ^{200}Rn isotope and its daughter ^{196}Po . For the beam-on period, an α -decay signal is

distinguished from an implantation signal by the absence of an MCP signal. A true α -decay chain of the type of ER- $\alpha 1$ (first α -decay)- $\alpha 2$ (second α -decay) is identified with those events whose positions coincide with each other and the time differences between them are within reasonably short time intervals. (1) ^{196}Rn : In an analysis of the data obtained in the bombardment of ^{166}Er with ^{36}Ar -ion at $E_{\text{lab}} = 208$ MeV, three α -decay chains of the type ER- $\alpha 1$ - $\alpha 2$ have been observed. The number of accidental events has been estimated to be about 1×10^{-5} . Because the measured $\alpha 2$ -decay energy and its half-life agree well with the known α -decay of ^{192}Po as shown in Table 1, the three $\alpha 1$ decays of the observed decay chains are assigned to that of new isotope ^{196}Rn . See Table 1 for the measured α -decay energy and half-life. The systematics of half-lives listed in the last column of Table 1 are obtained according to the formula in Ref. 6 by using the measured $E\alpha$ values. (2) $^{195\text{m,g}}\text{At}$: In a similar analysis of the data obtained in the bombardment of ^{164}Er with ^{36}Ar ions at $E_{\text{lab}} = 199$ MeV, three kinds α -decay chains have been observed. From the observed $\alpha 2$ energies, half-lives and their excitation functions they can be assigned to those of the poorly-known isotopes $^{195\text{m}}\text{At}$ (4 events) and ^{195}At ⁵⁾ (40 events) re-

Table 1. The measured α -decay energies and half-lives of identified isotopes in the present work in comparison with previous findings.

Isotope	$E\alpha$ (keV)	$T_{1/2}$ (ms)	Reaction Channel	$E\alpha$ (keV)	$T_{1/2}$ (ms)	Ref.	$T_{1/2}(\text{ms})^{6)}$
	(present work)			(literature)			(systematics)
^{196}Rn	7492 ± 30	3^{+7}_{-2}	$^{166}\text{Er}(^{36}\text{Ar},6n)$	7428 ± 30	$3^{\text{a)}$		12
^{192}Po	7196 ± 30	34^{+80}_{-20}	Daughter of ^{196}Rn	7170 ± 20	34 ± 3	[4]	17
$^{195\text{m}}\text{At}$	7179 ± 30	32^{+32}_{-10}	$^{164}\text{Er}(^{36}\text{Ar},p4n)$	---	---		37
$^{191\text{m}}\text{Bi}$	6882 ± 30	98^{+98}_{-32}	Daughter of $^{195\text{m}}\text{At}$	6876 ± 20	150 ± 15	[4]	77
$^{195\text{g}}\text{At}$	7072 ± 30	55 ± 25	$^{164}\text{Er}(^{36}\text{Ar},p4n)$	---	---		89
$^{191\text{g}}\text{Bi}$	6318 ± 30	9 ± 4 (s)	Daughter of $^{195\text{g}}\text{At}$	6310 ± 20	13 ± 1 (s)	[4]	12 (s)
$(^{195}\text{At})^{\text{b)}$	7152 ± 30	47 ± 28	$^{164}\text{Er}(^{36}\text{Ar},p4n)$	7190 ± 30	140 ± 50	[5]	49
$(^{191}\text{Bi})^{\text{b)}$	6317 ± 30	4 ± 2 (s)	Daughter of $(^{195}\text{At})^{\text{b)}$	6290 ± 30	13 ± 1 (s)	[5]	12 (s)
$^{195}\text{At}^{\text{b,c)}$	7135 ± 30	135 ± 30	$^{164}\text{Er}(^{36}\text{Ar},p4n)$	7125 ± 30	150 ± 30	[5]	53

a) Only one decay chain was observed in our previous work.¹⁾ b) Only tentatively assigned and partially based on the excitation function behavior and reaction Q-value arguments. c) α - α correlation was not observed.

spectively using similar genetic correlation arguments described above. See Table 1 for the observed α -decay energies and half-lives.

References

- 1) K. Morita et al.: *Z. Phys.*, **A352**, 7 (1995).
- 2) M. Kurokawa: Proc. of the Tours Symp. on Nucl. Phys.

- II, Aug.30–Sept.2, p. 428 (1994).
- 3) K. Morita et al.: *Nucl. Instr. Methods Phys. Res.*, **B70**, 220 (1992).
- 4) A. Ritz: *Atom. Dat. Nucl. Dat. Tab.*, **47**, 215 (1991).
- 5) M. Leino: Univ. of Helsinki, Rep. Series in Phys. HU-P-D37 (thesis, unpublished)
- 6) G. Brown: *Phys. Rev.*, **C46**, 811 (1992).

Study of α Decays from Evaporation Residues Produced by the $^{40}\text{Ar} + ^{232}\text{Th}$ Reaction

M. Kurokawa, T. Nomura, T. Motobayashi, H. Murakami, Y. Iwata, T. Uchibori, T. Kikuchi, S. Jeong, Y. Tagaya, M. Wada, N. Ikeda, S. Kubono, I. Katayama, K. Morita, Y. Pu, A. Yoshida, Y. Nagai, H. Kudo, K. Sueki, H. Nakahara, T. Shinozuka, M. Fujioka, H. Miyatake, Y. Fujita, T. Shimoda, and M. Tanikawa

[NUCLEAR REACTION, $^{232}\text{Th}(^{40}\text{Ar}, \alpha 3n)^{265}106$, $E = 5.08$ A MeV; measured reaction products, α decays, time and position correlations; gas-filled separator.]

To examine possible enhancement of (HI, αxn) reaction in producing superheavy elements,¹⁾ evaporation residues (EVRs) produced by the $^{40}\text{Ar} + ^{232}\text{Th}$ reaction were measured by the delayed coincidence method.

An ^{40}Ar beam was accelerated to 7.6 A MeV by RIKEN Ring Cyclotron and was degraded to about 5.08 A MeV at the center of a ThO_2 target in order to bombard the target with an optimum energy for $^{232}\text{Th}(^{40}\text{Ar}, \alpha 3n)^{265}106$ channel. The irradiated dose was calculated from the counts of elastically scattered ^{40}Ar particles, which were detected by a silicon detector set at 45° . The produced EVRs were roughly separated from other light reaction products by a gas-filled recoil ion separator (GARIS) with a large angular acceptance. The selected EVRs were implanted into a position sensitive silicon detector (PSD) with good position resolution²⁾ placed at the focal point of the GARIS. The PSD detected the EVRs themselves, the α decays from the EVRs and the decays from their descendant nuclei. For the EVRs and their α decays, the data were recorded independently. Decay chains, consisting of $\text{EVR} \rightarrow \alpha_1 \rightarrow \alpha_2$ events, were constructed by relating the positions and the times of the events. Besides the PSD, four silicon detectors surrounding the PSD were used to detect α particles escaped from the PSD. Also a time pickup detector using a micro channel plate was mounted about 60 cm upstream of the PSD for rough measurement of the EVR's mass from the time-of-flight information.

The number of the extracted decay chains was six. Figure 1 shows the α -decay energies for the chains and they are all assigned to the decay chains from $^{265}106$. For the hatched area of the figure, the expected number for the accidental chain, which is formed by the accidentally correlated events, was evaluated to be 0.24 under the same position and time conditions employed to extract the six chains. The cross section of the

$^{232}\text{Th}(^{40}\text{Ar}, \alpha 3n)^{265}106$ reaction is 610_{-250}^{+350} pb, where the errors are statistic ones. The systematic uncertainty is estimated to be a factor of three. The value is larger than the cross section 2 pb for the $^{238}\text{U}(^{34}\text{S}, 5n)^{267}108$ reaction, which forms the same compound nucleus. The results suggest larger survival probability of the (HI, αxn) reaction. Some improvements and developments, construction of a rotating target system and a modification of the PSD design for example, are now in progress to reduce the accidental correlation.

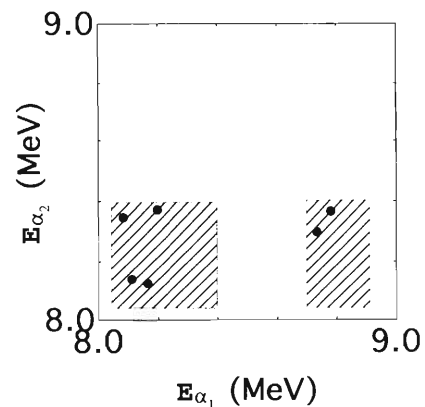


Fig. 1. The three-fold coincident events, found for the EVR- α_1 - α_2 combination. The horizontal axis represents the energy of α_1 and the vertical one is for α_2 .

References

- 1) T. Nomura: Proc. Int. Symp. on Heavy-ion Physics and its Application Lanzhou, Oct. 1990, eds. W. O. Shen, Y. X. Luo, and J. Y. Liu, World Scientific, Singapore, p. 349 (1991).
- 2) M. Kurokawa: Proc. Tours Symposium on Nuclear Physics II Tours, France, Aug.-Sept. 1994, eds. H. Utsunomiya, M. Ohta, J. Galin, and G. Mützenber, World Scientific, Singapore, p. 428 (1995).

Nuclear Moments and Charge Radii of ^{175}Hf Determined by Laser Spectroscopy

W. G. Jin, M. Wakasugi, M. Hies, T. T. Inamura, T. Murayama, T. Ariga,
T. Wakui, H. Katsuragawa, T. Ishizuka, J. Z. Ruan, and I. Sugai

[NUCLEAR REACTION $^{175}\text{Lu}(\text{d}, 2\text{n})^{175}\text{Hf}$, nuclear moments μ and Q , charge radii $\delta\langle r^2 \rangle$.]

To study the isotope shift and hyperfine structure (hfs) of refractory elements, we developed a laser spectroscopic method with an Ar-sputtering atomic beam source.¹⁾ Using this powerful technique, we have started a systematic study for Hf and Ta as well as other refractory elements.²⁾ This paper reports a new result on the long-lived ($T_{1/2} = 70$ d) unstable isotope ^{175}Hf .

^{175}Hf isotope with a nuclear spin $5/2$ is very interesting from the nuclear-structure viewpoint because it is in a well deformed region. However, even the sign of the nuclear magnetic dipole moment is not known and no information has been reported on the nuclear deformation of ^{175}Hf .

We produced the radioactive isotope ^{175}Hf by the $^{175}\text{Lu}(\text{d}, 2\text{n})$ reaction using a 19 MeV d beam from the RIKEN AVF Cyclotron. About 10^{15} atoms of ^{175}Hf were obtained in an area of 6 mm in diameter. The radioactive isotope ^{175}Hf was set into our off-line chamber. The atomic beam of ^{175}Hf was produced using

the Ar-sputtering method. Fluorescence induced by a cw ring dye laser pumped with an Ar-ion laser was measured with a cooled photomultiplier.

Figure 1 shows a measured hyperfine spectrum of the 555-nm transition for ^{175}Hf . A peak from ^{174}Hf isotope produced simultaneously by the $^{175}\text{Lu}(\text{d}, 3\text{n})$ reaction was also observed. From the hyperfine spectrum of ^{175}Hf , the hfs constants for the atomic ground state 3F_2 were determined: $A = 121(4)$ MHz and $B = 495(15)$ MHz. The magnetic dipole and electric quadrupole moments were derived as $\mu = -0.604(18)$ μ_N and $Q_S = 2.66(8)$ b. Accuracy of these values is improved by a factor of 5 compared with the previous values.^{3,4)} It is shown for the first time that the magnetic dipole moment has a negative value.

The isotope shift between ^{175}Hf and ^{174}Hf was also obtained as 124 MHz. Changes in mean square nuclear charge radii $\delta\langle r^2 \rangle$ were then derived for ^{175}Hf and are plotted in Fig. 2 together with other data of Hf. A systematic trend can be found from Fig. 2.

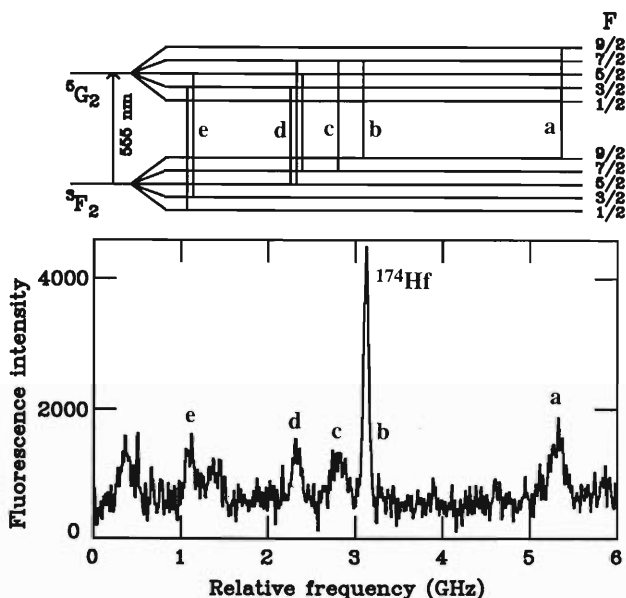


Fig. 1. Measured hyperfine spectrum of the 555-nm transition for ^{175}Hf . The peaks labeled with a-e are the hyperfine peaks of ^{175}Hf . Hyperfine splittings and transition scheme for ^{175}Hf are shown in the upper part.

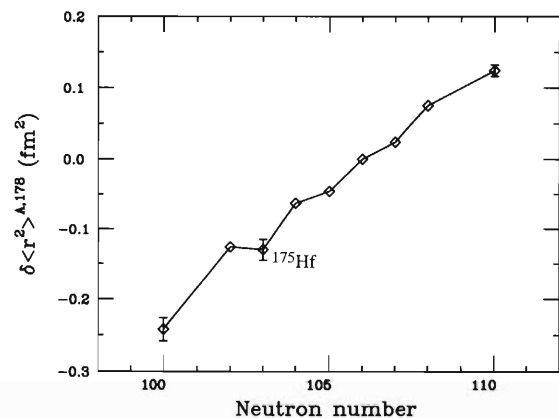


Fig. 2. Systematics of changes in mean square nuclear charge radii $\delta\langle r^2 \rangle$ for Hf isotopes.

References

- 1) M. Wakasugi et al.: *Rev. Sci. Instrum.*, **64**, 3487 (1993).
- 2) W. G. Jin et al.: *Phys. Rev.*, **A52**, 157 (1995), and references therein.
- 3) P. Herzog et al.: *Z. Phys.*, **B63**, 241 (1986).
- 4) G. Kaindl et al.: *Phys. Lett.*, **B46**, 62 (1973).

Production of Neutron Deficient α -Decaying Hafnium Isotopes $^{161-157}\text{Hf}$ Using RIKEN GARIS/IGISOL

M. Hies, T. Ariga, T. T. Inamura, W. G. Jin, H. Kunz*, K. Morita, T. Murayama, Y. Pu,
and M. Wakasugi

[nuclear reaction $^{\text{nat}}\text{Sn}+^{48}\text{Ti}$; 5.5 AMeV; production of α -decaying Hf isotopes;]
[gas filled recoil separator.]

To investigate unstable nuclei in the refractory element region by means of laser spectroscopy¹⁾ the production of neutron deficient α -decaying hafnium isotopes has been performed using the gas filled recoil separator GARIS.²⁾ The recoils are produced via the $^{\text{nat}}\text{Sn}(^{48}\text{Ti},\text{xn})$ nuclear reaction using a 7.6 AMeV ^{48}Ti -beam with the intensity of 10 pA. The target consists of natural tin (0.9 mg/cm²) evaporated on 15 μm aluminum backing. The titan beam was energy degraded through the GARIS entrance window (10 μm aluminum) and the target backing down to 5.5 AMeV. Due to the large variety of stable tin isotopes, the calculated cross sections results in a broad excitation function (see Fig. 1) giving access to all α -decaying Hf isotopes without changing the beam energy. The total production rate of α -decaying Hf recoils, using these calculated cross sections and the α -decay branching ratios is calculated at 265 MeV incident primary beam energy to 64 Hf- α -counts per sec and per pA primary beam current. The recoils are separated with GARIS from the primary beam and are implanted in an open PIN-photo diode detector (Hamamatsu S3590, 1 cm², 300 μm Wafer), where the α -decay energy and the recoil energy are measured.

A typical measured α -spectrum is shown in Fig.

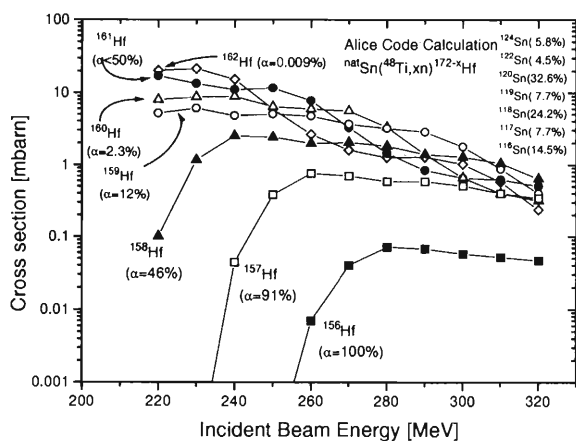


Fig. 1. Calculation of cross section for the nuclear reaction $^{\text{nat}}\text{Sn}(^{48}\text{Ti},\text{xn})\text{Hf}$ as a function of the incident titan beam energy.

2. All reaction channels could be assigned using the xn,pxn, α xn-channels and the nuclear decay daughters. A total Hf α -count rate of 4.0 counts per sec and per pA was determined at the position of the IGISOL chamber with a recoil beam diameter of about 4 cm. The recoil energy in the middle of the IGISOL chamber was degraded to 4 MeV using a 5 μm aluminum ion guide entrance foil. The helium gas pressure inside the cell was 220 mbar. The production rate can be explained by the calculated cross sections assuming a GARIS efficiency in the order of 10%. Further experiments are planned to increase the production rate by improving the focusing and collection efficiency of GARIS or using different enriched target-beam combinations like $^{144}\text{Sm}(^{20}\text{Ne},\text{xn})$ -reactions or α xn-reactions. However, even with such a low production rate a laser spectroscopic experiment can be performed, if using the radioactive decay measurement is used to detect the resonance ionization in a buffer gas.³⁾

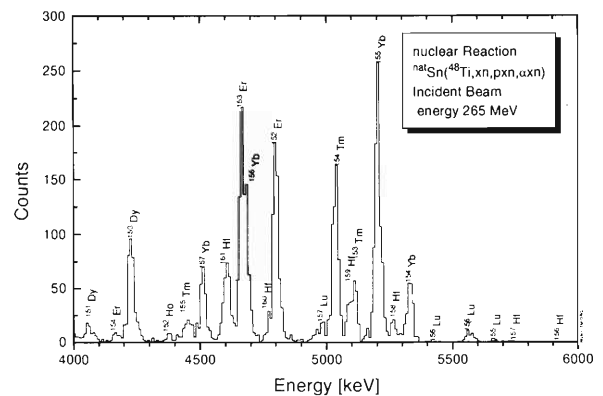


Fig. 2. Measured α -spectrum for an incident titan beam energy of 265 MeV.

References

- 1) M. Hies et al: This report, p. 177
- 2) K. Morita et al: *Nucl. Instr. Methods Phys. Res.*, **B70** 220 (1992).
- 3) H. Backe et al: *Hyperfine Interact.*, **74**, 47 (1992).

* University of MAINZ Institute of Physics, Germany

Measurement of Neutron Spallation Cross Sections

T. Nakamura, E. Kim, A. Konno, M. Imamura, N. Nakao,
T. Shibata, Y. Uwamino, N. Nakanishi, S. Fujita, and J. Nakajima

[neutron spallation reaction, ^{209}Bi (n,xn) reactions.]

Neutron reaction data in the energy range above 20 MeV are very poor and no evaluated data file exists at present. In this study, we measured the neutron spallation cross sections of C, Al, Co, Cu and Bi using a quasi-monoenergetic p-Li neutron field at the E4 experimental room of the separate sector ring cyclotron. The proton beams having energies of 80, 90, 100, 110, 120, 135, 150, and 210 MeV were injected on a 10 mm thick Li target through a beam swinger. Protons passed through the target were cleared out by a magnet and absorbed in a spectrograph. Neutrons produced at 0 deg were transported through an iron-concrete collimator of 20 cm by 20 cm aperture and 120 cm long. The neutron spectra were measured with the TOF method using a BC501A organic liquid scintillator and the absolute neutron fluence was measured with the Li activation method using the ^7Be activity from the ^7Li (p,n) ^7Be reaction.

The gamma-ray activities of the irradiated samples were counted by using a Ge detector and the reaction rates of identified radioisotopes were obtained after correction of the sum-coincidence effect and self absorption.

We could identify the produced radionuclides down to ^{196}Bi from the ^{209}Bi (n,14n) reaction for 150 and 210 MeV p-Li neutron. The spallation cross section data were obtained from the neutron spectra and the reaction rates.

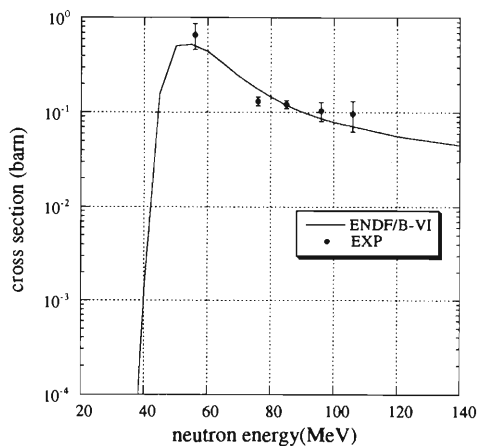


Fig. 1. ^{209}Bi (n,6n) reaction cross section.

We are now analyzing the measured results. As examples, Fig. 1 to 3 give the cross section data of ^{209}Bi (n,6n), (n,8n) and (n,10n) reactions, respectively, compared with ENDF/B-VI high energy file data calculated by the ALICE code.¹⁾ Our experimental results show good agreement with them.

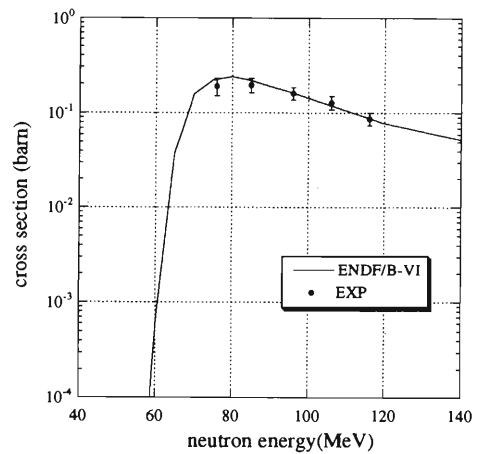


Fig. 2. ^{209}Bi (n,8n) reaction cross section.

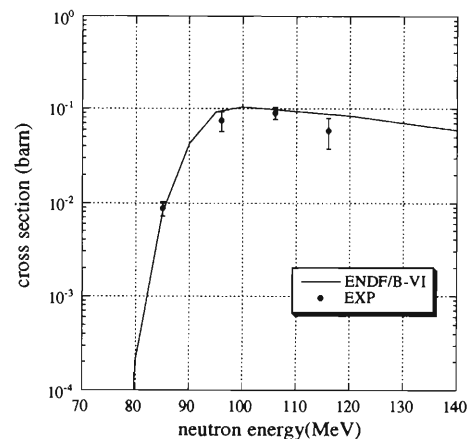


Fig. 3. ^{209}Bi (n,10n) reaction cross section.

References

- 1) National Nuclear Data Center, Brookhaven National Laboratory, "Evaluated Nuclear Data File", ENDF/B-VI (1990).

High-Spin States in $^{148}\text{Tb}^\dagger$

E. Ideguchi, Y. Gono, S. Mitarai, T. Morikawa, A. Odahara, M. Kidera, M. Shibata, H. Tsuchida, K. Miyazaki, M. Oshima, Y. Hatsukawa, S. Hamada,* H. Iimura,* M. Shibata,* T. Ishii,* T. Murakami, H. Kusakari, M. Sugawara, T. Kishida, K. Morita, H. Kumagai, and M. Ishihara

[Nuclear reactions, $^{141}\text{Pr}(^{13}\text{C},6n)^{148}\text{Tb}$, $^{27}\text{Al}(^{130}\text{Te},9n)^{148}\text{Tb}$.]

The high-spin isomers found systematically in $N=83$ isotones¹⁻⁶⁾ show similar features. The excitation energies and half-lives are almost the same, i.e. ~ 8 MeV and ~ 1 μs , respectively, except for those of ^{146}Eu and ^{149}Dy . Among these isotones the level structure of ^{147}Gd was most extensively studied experimentally⁴⁾ and theoretically.⁷⁾ The configuration and the excitation energy of the high-spin isomer were reproduced well by the deformed independent particle model (DIPM) calculation.⁷⁾ Recently it was reported⁸⁾ that the level structure of ^{145}Sm could be understood within the framework of DIPM. It is interesting to study whether this model could be applied to interpret the level structure of the odd-odd nucleus ^{148}Tb to the same extent as those of the odd mass nuclei ^{147}Gd and ^{145}Sm .

The decay scheme of the high-spin isomer in ^{148}Tb was studied by the recoil-catcher method using $^{27}\text{Al}(^{130}\text{Te},9n)^{148}\text{Tb}$ reaction at RIKEN. The excitation energy of the high-spin isomer reported previously⁵⁾ was revised to be 8.620 MeV. The half-life of the isomer was determined to be 1.310 ± 0.007 μs .

The level structure above the high-spin isomer was extended up to the spin (31) state at 11.8 MeV by in-beam γ -ray spectroscopic techniques using $^{141}\text{Pr}(^{13}\text{C},6n)^{148}\text{Tb}$ reaction at the JAERI tandem accelerator facility.

The excited states below the (24^-) state were understood as resulted from the weak couplings of $\pi h_{11/2}$ and $\nu f_{7/2}$ to those states of ^{147}Gd and ^{147}Tb ,⁹⁾ respectively. The same coupling argument did not work for the states above the (24^-) state of ^{148}Tb . They were, however, reproduced well by the DIPM calculation.⁷⁾ The configuration of the isomer was given to be $[\pi h_{11/2}^2 d_{5/2}^{-1} \nu f_{7/2} h_{9/2} i_{13/2}]_{27+}$ which corresponds to that of ^{147}Gd after filling one proton in the $\pi(d_{5/2}^{-2})_0$ orbits.

The deformation parameters β were also calculated by DIPM for the yrast states of ^{148}Tb . The results exhibited the abrupt increase of the deformation at the high-spin isomer from spherical to oblate in the same way as reported⁸⁾ for odd-A isotones, ^{147}Gd and ^{145}Sm .

The average moments of inertia of $N=83$

isotones^{4,8,10)} were estimated by plotting the excitation energies of yrast states as a function of $I(I+1)$ in Fig. 1. They seem to have values between 77 and 96 MeV^{-1} up to the highest spin state known experimentally. Those values are smaller than the rigid body values, i.e. ~ 110 MeV^{-1} , for these nuclei. The detail structure of convex shapes in Fig. 1 may be attributed to the residual interactions¹¹⁾ among the valence particles.

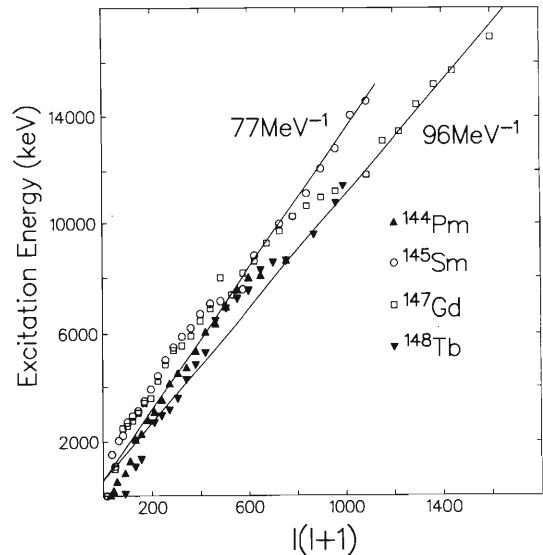


Fig. 1. Comparison of the experimental yrast states of ^{148}Tb with those of ^{144}Pm ,¹⁰⁾ ^{145}Sm ,⁸⁾ and ^{147}Gd .⁴⁾

References

- 1) T. Murakami et al.: *Z. Phys.*, **A345**, 123 (1993).
- 2) A. Ferragut et al.: *J. Phys. Soc. Jpn.*, **62**, 3343 (1993).
- 3) E. Ideguchi et al.: *Bull. Phys. Soc. Jpn.*, p. 108 (1993).
- 4) M. W. Drigert et al.: *Nucl. Phys.*, **A515**, 466 (1990), and references therein
- 5) R. Broda et al.: Symp. on High Spin Phenomena in Nucl., Argonne, March, p. 397 (1979).
- 6) A. M. Stefanini et al.: *Nucl. Phys.*, **A258**, 34 (1976).
- 7) T. Døssing et al.: *Phys. Scr.*, **24**, 258 (1981).
- 8) A. Odahara et al.: *Z. Phys.*, **A350**, 185 (1994).
- 9) Z. Meliani et al.: *J. Phys.*, **G20**, L7 (1994).
- 10) Y. Zhang et al.: *RIKEN Accel. Prog. Rep.*, **27**, 32 (1993).
- 11) J. P. Schiffer and W. W. True: *Rev. Mod. Phys.*, **48**, 191 (1976).

[†] Condensed from the articles in *Z. Phys.*, **A352**, 363 (1995).

* Japan Atomic Energy Research Institute

Life Time of High Charged States Isomer

H.-Y. Wu, T. Kishida, M. Ishihara, and E. Ideguchi

[Isomer State, Half Life, Internal Conversion, Charged States, Energy level Shift.]

Changes of atomic environment can affect the nuclear reaction and decay processes. Even a nuclear process with no electron participation, is affected by the change of screening for ejected particle. The process that involves an electron is directly affected by the electronic cloud near nuclear surface, such as electron capture (EC) and internal conversion (IC). The variation of transition rate is essentially proportional to the change of electron density available at the nucleus. Another effect is due to the atomic energy level shift. For example, the binding energy of a K-shell electron is shifted to an excitation energy higher than the threshold of the IC for the isomer state of ^{125}Te , which strongly affects the life time of the isomer (Table 1).

Table 1. Comparison of the observed and calculated life time of isomer state of ^{125}Te , with 35.49 keV of the transition energy.

charge state	config.	Exp.	calc ^{a)}	$T_{1/2}$ (ns) calc ^{b)}	calc ^{c)}	E_B^K (keV) Ref ^{d)}	Ref ^{e)}	this work
0	(neutral)	1.49	1.49	1.49	1.49	31.81	31.81	31.81
40	($3s^2$)			2.1	1.50		35.27	34.17
44	($2s^2 2p^4$)		1.5	2.8	1.53		35.58	35.09
45	($2s^2 2p^3$)	> 2	8.0	3.3	1.54	35.61	35.58	35.33
46	($2s^2 2p^2$)	> 2	8.3	3.9	1.58	35.91	35.91	35.56
47	($2s^2 2p^1$)	6 ± 1	8.5	15.1	10.0	36.26	36.26	35.81
48	($2s^2$)	11 ± 2	10.3	40.3	10.2	36.60	36.60	36.04
49	($2s^1$)			55.8	13.9			36.28
50	($1s^2$)			90.3	21.9			36.53

a),d),e) From Ref. 3 and its reference. b) This work, M1 and E2 mixture type transition Ref. NNDC. c) This work, M1 type transition.

The IC coefficient α is given by non-trivial order of perturbation theory. The electron wave function is given by a set of coupled Dirac differential equations for a central potential $V(r)$, that includes the screening and exchange effects. The electron wave function was calculated using the WKB screening approximation¹⁾ for different charge states. The α , for nuclei with nuclear charge Z and electron number Q , can be deduced as

$$\alpha^{(Q)} = \sum_{\sigma} \left[\alpha_{\sigma} \left(\frac{P'W}{PW'} \right)_{\sigma} \left(\frac{N_{\sigma}^{(Q)}}{N_{\sigma}^{(Z)}} \right) \right],$$

where W and P are energy and momentum of IC electron for sub-shell σ , the prime denotes the quantity with screening correction, and $N_{\sigma}^{(Z)}$ and $N_{\sigma}^{(Q)}$ are numbers of σ shell electrons for neutral and charged states, respectively. The screening effect for W' and P' is calculated by using Thomas-Fermi model.²⁾

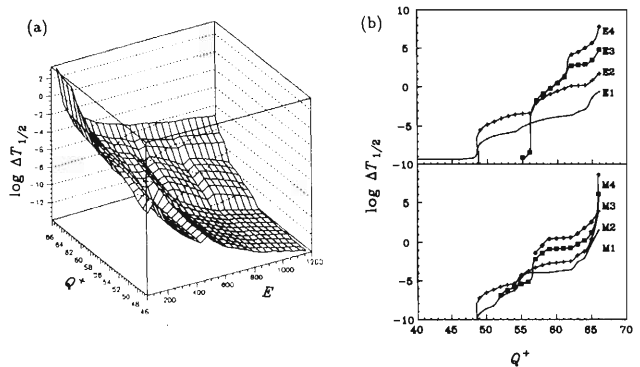


Fig. 1. Relationship between the half life change and charged states of ^{149}Dy for different transition type (Energy=50 keV) (a) and for different energy (E_2) (b).

Figure 1 shows the results of calculations. The α is a function of transition energy, the type of transition, and charged states. For the ionization process, the change of life time is larger when the transition energy is smaller. The change becomes also larger for a transition with higher multipolarity. Magnetic transitions are more affected than the electric transitions. The life time of excited states in highly charged atoms is increased extremely because it is determined only by the γ transition without internal conversion. All the figures show the structure of shell and sub-shell. The changes of life time are mainly contributed by 1s and 2s orbits.

In an isomer beam with energy greater than 10 MeV/nucleon, where the atoms are nearly bare, some isomer states for a special transition type may have a long life time.³⁾ At a beam energy lower than 10 MeV/nucleon or a transition with higher energy than 400 KeV, the change of life time is relatively small. Although the changes of the isomer life time are at most 1% in the case of the present high spin isomer beam line of RIKEN,⁴⁾ this effect will become very important for RIKEN RI Beam Factory, where isomer beams with higher energies may be involved.

References

- 1) M. E. Rose: *Phys. Rev.*, **49**, 727 (1936).
- 2) W. R. Garrett et al.: *Z. Physik*, **198**, 453 (1967).
- 3) F. Attallah et al.: *Phys. Rev. Lett.*, **75**, 1715 (1995).
- 4) T. Kishida et el.: *RIKEN Accel. Prog. Rep.*, **28**, 50 (1995).

Target Dependence of Production Rates of Projectile-like Fragments

M. Notani, H. Sakurai, N. Aoi, M. Hirai, H. Kobinata, Y. Watanabe, T. Nakamura, A. Yoshida, Y. Watanabe, T. Kubo, T. Nakagawa, N. Inabe, H. Kumagai, A. Goto, and M. Ishihara

[NUCLEAR REACTIONS ${}^9\text{Be}$, ${}^{181}\text{Ta}({}^{50}\text{Ti}, X)$, $E({}^{50}\text{Ti}) = 80\text{A MeV}$;]
 [Target Dependence of Fragment Production Rate.]

Radioactive ion beams produced by the projectile fragmentation reactions are a very useful tool in nuclear physics. The production mechanism of projectile-like fragments at intermediate energies (10~100 A MeV) has been investigated to understand the mechanism itself, then to make precise prediction of the secondary beam intensity for designing experiments. It was reported that the production yields of the neutron-rich isotopes with 44A MeV ${}^{48}\text{Ca}$ beam are strongly dependent on the N/Z ratio of the target.¹⁾ Here we present our results on the target dependence with a higher energy beam, 80A MeV ${}^{50}\text{Ti}$.

We used two energy-loss-equivalent targets, ${}^9\text{Be}$ and ${}^{181}\text{Ta}$, with thickness of 289 and 435 mg/cm², respectively. Details of the experiment are described elsewhere.²⁾ We accumulated data with $B\rho=3.45\text{Tm}$ setting of the RIPS spectrometer. Figure 1 shows production yields of projectile-like fragments for ${}^{17-22}\text{N}$, ${}^{19-24}\text{O}$, ${}^{21-27}\text{F}$, ${}^{24-30}\text{Ne}$, ${}^{27-33}\text{Na}$, ${}^{30-36}\text{Mg}$, and ${}^{33-38}\text{Al}$. We found that ${}^{181}\text{Ta}$ can earn several times larger yields of the neutron-rich nuclei with $A/Z\sim 3$ than ${}^9\text{Be}$.

Figure 2 shows the experimental cross sections and predicted ones by the INTENSITY code.³⁾ This code is based on the participant spectator models, taking into account only the fragmentation mechanism, and has been widely used in designing experiments. The experimental cross sections were obtained from comparisons between the experimental yields and predicted ones.

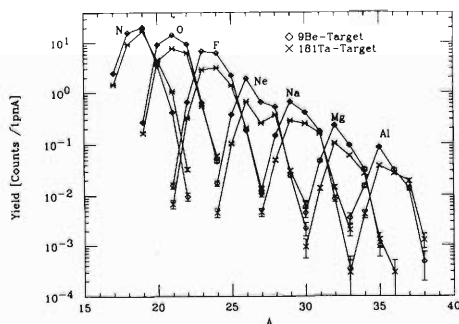


Fig. 1. Production yields for the isotopes of N, O, F, Ne, Na, Mg, and Al obtained with targets of ${}^9\text{Be}$ and ${}^{181}\text{Ta}$ in the reactions with ${}^{50}\text{Ti}$ beam at 80A MeV. The thickness of two targets was energy-loss-equivalent for the incident beam.

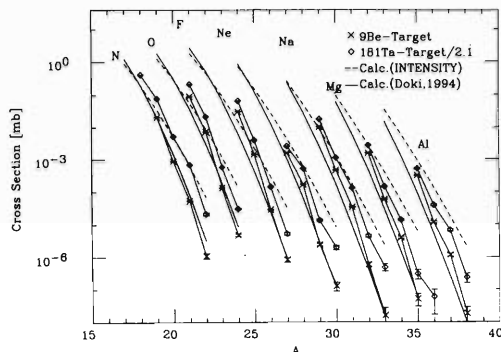


Fig. 2. Production cross sections of projectile-like fragments for ${}^9\text{Be}$ and ${}^{181}\text{Ta}$ targets, compared with the cross sections calculated by the INTENSITY code and by the modified one. The cross sections for ${}^{181}\text{Ta}$ targets are divided by a factor of 2.1; thus one prediction curve for each isotope presents the cross sections for two targets at once.

To minimize ambiguities of the INTENSITY parameter set for the cross section evaluation, we chose the isotopes with their momentum acceptance of more than 0.1%. As seen in Fig. 2, the INTENSITY cannot predict well the experimental cross sections for very neutron-rich nuclei.

An attempt to improve the INTENSITY prediction by tuning parameters was made for projectile-like fragments from 93.6A MeV ${}^{40}\text{Ar}+{}^9\text{Be}$ reactions.⁴⁾ This modified INTENSITY by use of the new parameters describes fairly well the production cross sections for ${}^{50}\text{Ti}+{}^9\text{Be}$ reactions, but underestimates the cross sections of neutron-rich nuclei for a ${}^{181}\text{Ta}$ target (see Fig. 2). This discrepancy cannot be explained in terms of only the fragmentation reaction and suggests that the transfer reaction plays a significant role even at this beam energy.

References

- 1) D. Guillemaud-Mueller et al.: *Phys. Rev.*, **C41**, 937 (1990).
- 2) H. Sakurai et al.: This report, p. 51.
- 3) J. A. Winger, B. M. Sherrill, and D. J. Morrissey: *Nucl. Instrum. Methods Phys. Res.*, **B70**, 380 (1992).
- 4) Y. Doki: JAERI-M 94-028, p. 70; Master thesis, Tokyo University (1994).

Production and Identification of New Neutron Rich Nuclei ^{31}Ne and ^{37}Mg with 80 A MeV ^{50}Ti Beam

H. Sakurai, T. Nakamura, M. Notani, T. Kubo, A. Yoshida, H. Kumagai, Y. Watanabe, T. Nakagawa, A. Goto, N. Inabe, N. Aoi, M. Hirai, Y. Watanabe, H. Kobinata, and M. Ishihara

[NUCLEAR REACTIONS $^{181}\text{Ta}(^{50}\text{Ti},\text{X})$, $E(^{50}\text{Ti}) = 80$ A MeV; deduced fragment]
[production rate vs mass and Z; evidence for ^{31}Ne , ^{37}Mg .]

An attempt to synthesize new neutron rich nuclei in $10 \leq Z \leq 13$ region can be made by means of the Riken Projectile Fragment Separator (RIPS).¹⁾ The total effective acceptance of such nuclei at RIKEN is about two orders of magnitude higher than at the GANIL-LISE.²⁾ Here, we report the first production and identification of new neutron rich nuclei ^{31}Ne and ^{37}Mg with 80 A MeV ^{50}Ti beam.

^{50}Ti ions provided by the ECR were accelerated in the AVF and RING Cyclotron to an energy of 80 A MeV. At the ECR, 60% enriched ^{50}Ti -oxide powder was used as the ion source material. The oxide powder was contained into a ceramic rod which was moved toward the plasma by about 100 μm step every hour, and the average beam intensity was ~ 2 pnA. From the study on target dependence of fragment yields,³⁾ we used a 435 mg/cm² thick ^{181}Ta target.

Reaction products were analyzed with the RIPS spectrometer operated in the achromatic mode.¹⁾ The particle identification of our experiment was performed event-by-event in a more redundant way than that of the GANIL experiment,⁴⁾ by means of measurements of magnetic rigidity, time-of-flight, energy deposit (ΔE) and kinetic energy (E). At the momentum dispersive focal plane F1, a Parallel Plate Avalanche Chamber (PPAC) was mounted for $B\rho$ measurements. At the final focal point F3, all other detectors were located; a 0.5 mm thick plastic scintillation counter (PL), two 0.3 mm surface barrier type silicon detectors, and two 3 mm thick lithium drift silicon detectors. The time-of-flight of fragments was obtained from the PL timing and RF signal of the cyclotron. The ΔE measured by use of the first three silicon detectors leads to three independent determinations of Z with accuracy of 0.1% (r.m.s.) for $Z \sim 10$ nuclei. The mass to charge state ratio, A/Q , of fragments was determined from the magnetic rigidity and time-of-flight, and the mass A from the E and time-of-flight, hence finally $Q - Z$ was reduced for the fragments which stopped at the final silicon detector. The accuracy of A/Q and Q was about 0.2% in r.m.s. This method can resolve uncertainty of charge states as backgrounds against neutron rich nuclei, and provide a very clean particle identification. Taking into account energy loss in the target for both the beam and fragments with $A/Z \sim 3.1$, the magnet rigidity of the RIPS spectrometer was set to be 3.6 Tm. We accumulated data for 4 days to search for new neutron rich isotopes.

After piling-up rejections and requiring a fully stripped condition for fragments, we obtained the two dimensional plot, A/Z versus Z , as seen Fig. 1. We have observed new isotopes ^{31}Ne (23 events) and ^{37}Mg (3 events). The previous GANIL experiment⁴⁾ reported that no events associated with ^{31}Ne were found, and concluded that ^{31}Ne was unbound. This discrepancy could be caused by less statistics and/or less feasible separation of fragments at the GANIL, where $B\rho$ measurements were not involved in particle identification. We observed nine events of ^{32}Ne , while the GANIL people had four events. In addition, for the particle stable nucleus ^{34}Na , we had fifteen events, but they had no events.

For the first time, this experiment produced and identified the new neutron rich nuclei ^{31}Ne and ^{37}Mg , and showed that those nuclei are particle-stable nuclei.

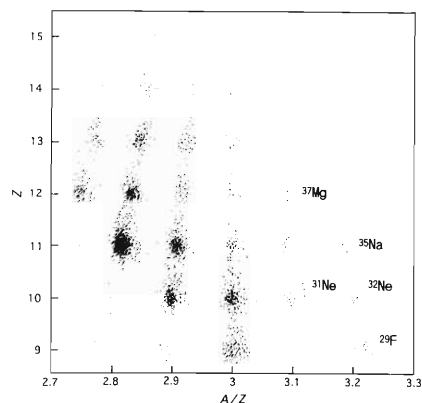


Fig. 1. Two-dimensional A/Z versus Z plot obtained in the fragmentation reaction of the ^{50}Ti beam at 80 A MeV on a 435 mg/cm² tantalum target during a 4-day run with magnetic rigidity $B\rho=3.6$ Tm of the RIPS spectrometer. The ^{31}Ne isotope (23 counts) and ^{37}Mg (3 counts) are clearly visible.

References

- 1) T. Kubo et al.: *Nucl. Instrum. Methods Phys. Res.*, **B70**, 309 (1992).
- 2) R. Anne, A. C. Möller, J. C. Jacmart, and M. Langevin: *ibid.*, **A257**, 215 (1987).
- 3) M. Notani et al.: This report, p. 50.
- 4) D. Guillemaud-Mueller et al.: *Phys. Rev.*, **C41**, 937 (1990).

Giant Dipole Resonance in Hot Rotating Nuclei

Y. Aoki, R. Sasaki, T. Ohtsuki, J. Kasagi, K. Yuasa-Nakagawa,
K. Furutaka, Y. Futami, K. Yoshida, T. Nakagawa, and T. Suomijarvi*

[NUCLEAR REACTIONS: $^{40}\text{Ar} + ^{92}\text{Mo}$, ^{116}Sn , ^{124}Sn and $^{\text{nat}}\text{Ni}$ at $E = 7/\text{MeV}/\text{nucleon}$,
Heavy ion fusion reaction, Giant dipole resonance, γ -ray multiplicity.]

In order to understand the mechanism of broadening of the GDR width in hot nuclei, it is very important to separate the effect of angular momentum from that of the temperature. We measured high energy γ -rays emitted from hot compound nuclei formed in the $^{40}\text{Ar} + ^{92}\text{Mo}$, ^{116}Sn , ^{124}Sn and $^{\text{nat}}\text{Ni}$ reactions together with the γ -ray multiplicity which is a measure of the angular momentum. The experiments were performed at RIKEN Ring Cyclotron Facility. Self supporting metallic foils were bombarded with ^{40}Ar beams at $E = 7 \text{ MeV}/\text{nucleon}$. High energy γ -rays from the compound nucleus were detected with 2 sets of high energy γ -ray detectors placed at 90° and 130° with respect to the beam direction. Each detector consisted of 7 BaF_2 scintillators; only the center one was irradiated to improve the detector response. γ -ray multiplicities were measured with a γ -ray multiplicity filter composed of 62 BaF_2 scintillators covering $1/3$ of 4π . The TOF method and the pulse shape analysis were used to reject the events due to neutrons or charged particles.

Compound nuclei formed in the heavy ion reactions have high angular momenta. The estimated critical angular momenta for complete fusion are about $75 \hbar$ for $^{40}\text{Ar} + ^{92}\text{Mo}$, ^{116}Sn and ^{124}Sn reactions, and $70 \hbar$ for $^{40}\text{Ar} + ^{\text{nat}}\text{Ni}$ reaction. We analyzed the events with $M_\gamma \geq 5$ for a Ni target (M_γ is the number of the fired detectors) which corresponds to $60 \hbar$ of the averaged angular momentum, for with $M_\gamma \geq 8$ which corresponds to $70 \hbar$ for other reactions. By selecting these high angular momentum events, γ -rays from the nuclei excited by deep-inelastic collisions which bring the angular momentum up to $30 \hbar$ are discriminated from the fusion events.

Figure 1(a) is the γ -ray energy spectra obtained in the $^{40}\text{Ar} + ^{124}\text{Sn}$ reaction for $M_\gamma \geq 8$; solid circles are γ -rays detected at 90° and open circles are at 130° . The data at 130° are corrected for the Doppler shifts. Broad bumps due to the decay of GDR are clearly seen for $E_\gamma > 10 \text{ MeV}$ and the spectral shapes are very similar for both angles. In order to see the difference between these two spectra more clearly, the ratio of the spectra, $W(130^\circ) / W(90^\circ)$, is plotted in Fig. 1(b), which shows more or less isotropic except for $8 < E_\gamma < 12 \text{ MeV}$. The spectra measured in the $^{40}\text{Ar} + ^{\text{nat}}\text{Ni}$ reaction for $M_\gamma \geq 5$ are shown in Fig. 2

together with the ratio of their spectra. In contrast to the case of the $^{40}\text{Ar} + ^{124}\text{Sn}$ reaction, the spectrum observed at 130° shows an enhancement to the one at 90° at around $E_\gamma \cong 20 \text{ MeV}$; this is clearly seen in Fig. 2(b). These observations can be interpreted as the effect of deformation and rotation of the compound nucleus since anisotropy of the GDR decay γ -rays from deformed rotating nuclei depends strongly on the γ -ray energy.¹⁾ More quantitative analysis is now in progress.

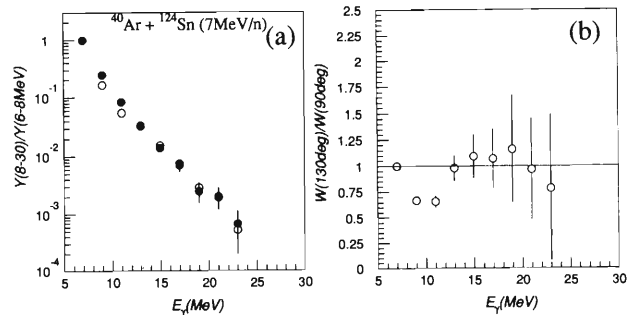


Fig. 1 (a) γ -ray energy spectra obtained in $^{40}\text{Ar} + ^{124}\text{Sn}$ reaction at $E = 7 \text{ MeV}/\text{nucleon}$ for $M_\gamma \geq 8$. Open circles show the spectrum obtained at 130° and closed circles the spectrum obtained at 90° . (b) Ratio of the 2 spectra in (a).

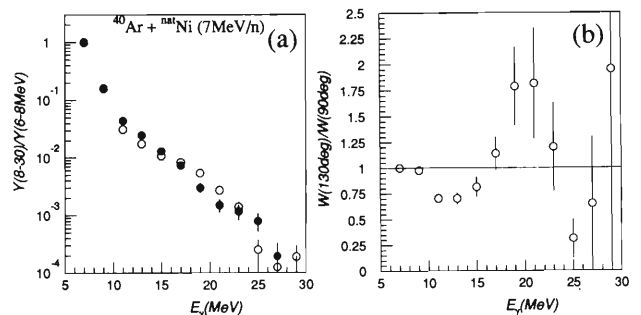


Fig. 2 (a) γ -ray energy spectra obtained in $^{40}\text{Ar} + ^{\text{nat}}\text{Ni}$ reaction at $E = 7 \text{ MeV}/\text{nucleon}$ for $M_\gamma \geq 5$. The notations are the same as those in Fig. 1(a). (b) Ratio of the 2 spectra in (a).

References

- 1) P. Thiroff et al.: *Nucl. Phys.*, **A482**, 93c (1988).

* Institute de Physique Nucléaire, IN2P3-CNRS

Entrance Channel Effect on the Pre-scission Time of Binary Decay for Medium Mass Nuclei (Mass ~ 110)[†]

K. Yuasa-Nakagawa, T. Nakagawa, K. Furutaka, K. Matsuda,* Y. Futami,
K. Yoshida, J. Kasagi, S. M. Lee, T. Suomijärvi,** W. Q. Shen, and T. Matsuse

[NUCLEAR REACTIONS: Binary decay fragments, Pre- and post-scission charged particle multiplicities, Pre-scission time, Entrance channel effect, Average angular momentum.]

In the heavy ion reactions at low to intermediate energies, the dynamics of a binary decay process is considered to be one of the most interesting topics. It provides an excellent ground to test nuclear many-body theories. In such reactions the angular momentum brought into the system has proven to play a vital role in the characterization of various decay processes and it also contributes to the interaction time of the reactions.

We have studied the dependence of interaction time on the entrance channel mass asymmetries and angular momenta for a medium mass system using pre-scission charged particle multiplicities.

The experiment was performed using the large scattering chamber (ASCHRA). The multiplicities of protons and α particles have been measured in coincidence with a binary decay fragment in the reactions of $^{84}\text{Kr} + ^{27}\text{Al}$ and $^{58}\text{Ni} + ^{56}\text{Fe}$ at the incident energies of 10.6 and 10.0 MeV/nucleon, respectively. These two systems lead to similar composite systems with almost the same excitation energy. Heavy fragments were detected at 10 degrees by a time-of-flight counter telescope consisting two channel plate detectors and a large solid state detector. Light charged particles were detected with the 3π multi-detector system which is composed of 120 phoswich detectors that cover the angular range between 10 to 160 deg. in the laboratory angle. A phoswich detector consists of a thin plastic scintillator and a thick BaF_2 crystal. It can identify not only light charged particles but also neutrons and γ -rays.

The obtained energy spectra of protons and α particles were fitted by three source analysis and the pre- and post-scission charged particle multiplicities were extracted.

To evaluate a pre-scission time of the composite system, we made a statistical calculation using two statistical models. In the GEMINI,¹⁾ the pre-scission time was calculated by introducing the fission delay time. In the extended Hauser-Feshbach Method (EHFM),²⁾ we have introduced the cut-off of the excitation energy of two fission fragments. The results obtained by two calculations match one another within 20% discrepancy.

In Fig. 1(a) the obtained pre-scission time is plotted by closed circles as a function of entrance channel mass

asymmetries. The result of $^{16}\text{O} + \text{Ag}$ is taken from Ref. 3. In Fig. 1(b) the pre-scission time is plotted as a function of the average angular momentum of binary decay.

As shown in the figures, it is clear that the difference of the entrance channel makes a great contribution to the pre-scission time. Dynamics of the entrance channel should be considered in the calculation of pre-scission time. We have applied the method proposed in Ref. 4, i.e., the combination of the code HICOL⁵⁾ and a statistical calculation. The calculated results with entrance channel dynamics are shown by open circles in the figures. The slope in the Fig. 1(b) became gentler than that of the statistical calculation, however, the tendency is not changed, i.e., the pre-scission time increases as the average angular momentum decreases. This is comprehensible because the larger angular momentum which leads to the larger centrifugal force helps the system to make a binary decay.

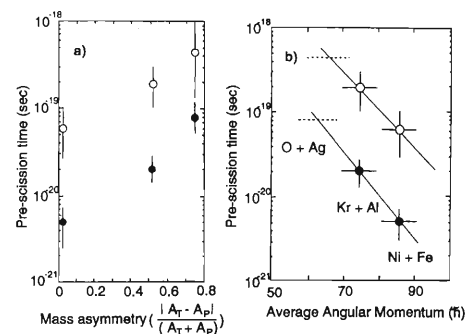


Fig. 1. (a) The extracted statistical pre-scission time and the result of the calculation with entrance channel dynamics are plotted as a function of the entrance channel mass asymmetry. (b) The extracted pre-scission times are plotted as a function of average angular momentum for binary decay of the systems. For both figures, the closed circles show the pre-scission time deduced by the statistical calculations and the open circles are the results of the calculation with entrance channel dynamics.

References

- 1) R. J. Charity et al.: *Nucl. Phys.*, **A483**, 371 (1988).
- 2) T. Matsuse et al.: Proc. Int., Symp. NIKKO '91, Y. Abe et al. (eds.), AIP, New York, p. 112 (1991).
- 3) D. J. Hinde et al.: *Phys. Rev.*, **C45**, 1229 (1992).
- 4) K. Siwek-Wilczynska et al.: *ibid.*, **C51**, 2054 (1995).
- 5) H. Feldmeier: *Rep. Prog. Phys.*, **50**, 915 (1987).

[†] Condensed from the article in *Phys. Lett.*, **B351**, 77 (1995)

* Mitsubishi Electric, Co.

** Institut de Physique Nucléaire, Orsay, France

Temperature and Excitation Energy of Hot Nuclei Produced in $^{40}\text{Ar} + ^{116}\text{Sn}$ Reaction at $E/A=30$ and 37 MeV/nucleon

K. Furutaka, K. Yoshida, A. Yajima,* Y. Akeboshi,** K. Matsuda,** T. Murakami, J. Kasagi, T. Nakagawa, K. Yuasa-Nakagawa, Y. Futami, A. Galonsky, and G. Bizard

[NUCLEAR REACTIONS: $^{40}\text{Ar} + ^{116}\text{Sn}$ at $E/A = 30, 36.4$ MeV/u; measured neutron, proton and α particle energy spectra and angular distributions; moving source analysis.]

Properties of hot nuclei produced in intermediate energy ($10 \leq E/A \leq 100$ MeV) heavy ion reaction have attracted much interests in recent years. Among them, the relation between temperature and excitation energy, i.e. the level density parameter, of the hot nuclei has been of a great interest. In light charged particle measurements, a decrease of the level density parameter a from $A/8$ to $A/13$ (A : mass number) was observed,^{1,2)} while experiments in which neutrons were detected showed that their spectra were well reproduced by the statistical model calculations with $a = A/8$.³⁻⁵⁾ To resolve these contradictory results, a series of experiments were performed in which neutrons, protons and alpha particles emitted in $^{40}\text{Ar} + ^{116}\text{Sn}$ reactions at $E/A = 30$ and 37 MeV were measured in coincidence with heavy evaporation residues(ER).

Self-supporting foil of ^{116}Sn (about $1\text{mg}/\text{cm}^2$) was bombarded with 30 and 36.4 MeV/u ^{40}Ar beams. Neutrons were detected with 22 liquid scintillation detectors and their energies were measured through the Time-of-flight (TOF) method. TOF lengths ranged from 0.8 m to 2.4 m. Detection angles were between 30 and 155 deg. Overall time resolution was about 1.5ns (FWHM) for prompt gamma rays. Protons and alpha particles were measured in the separate run with 80 phoswich detectors composed of a BaF_2 crystal and a thin plastic scintillator. Heavy residues were detected with 4 stacks of a MCP-MCP-Si detector array placed at 10 deg. with respect to the beam direction. Mass A_{ER} and velocity V_{ER} of the residues were deduced.

Events were divided into 4 groups according to V_{ER} as a measure of energy and momentum transferred to the hot composit system, and thermal excitation energies E_{th} were deduced for each group. Firstly, slope parameters (or apparent temperatures) τ_i and multiplicities M_i of the particles were deduced through the moving source analysis of the spectra, in which two isotropic emission sources with the Maxwellian shape were assumed. One source corresponds to the emission from a pre-equilibrium-like source with $\sim 1/2$ beam velocity, while the other describes the equilibrated hot nuclei which are assumed to be moving with V_{ER} . Surface type Maxwellian emission was assumed for all sources except for the equilibrium neutron source, for which volume emission was used. Then average energies of the particles emitted from the equilibrium com-

ponent $E_{i,eq}$ were calculated from τ_{eq} . After that, E_{th} s were calculated by using the following relation

$$E_{th} = \sum_{i=n,p,\alpha} [M_{i,eq}(E_{i,eq} + E_{i,C} + B_i)] + E_{\gamma}, \quad (1)$$

instead of a traditional calculation method using V_{ER} based on the massive transfer model. E_C and B_i stand for Coulomb energy and binding energy of a particle i , respectively. E_{γ} is the energy removed through the γ -ray emission process.

In Fig. 1 extracted apparent temperatures of the hot nuclei (the equilibrium sources) were plotted against the thermal excitation energies deduced from Eqn. (1). Dotted lines were the results of statistical model calculations using the code CASCADE⁶⁾ with level density parameters from $A/8$ to $A/13$. From the figures it can be said that the excitation energy dependence of the temperature parameters of the hot nuclei produced in these reactions is well described by using the level density parameter $a \sim A/8$ to $A/10$ and the parameters are almost the same for all particles.

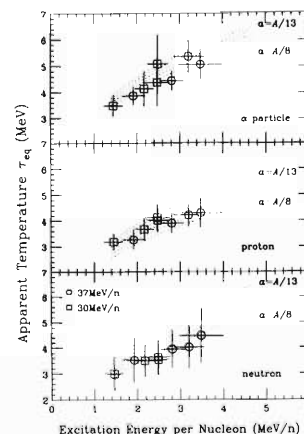


Fig. 1. Apparent temperatures were plotted against the thermal excitation energies deduced from Eqn. (1). Dotted lines are the results of the statistical model calculations with a from $A/8$ to $A/13$.

References

- 1) D. Fabris et al: *Phys. Lett.*, **B196**, 429 (1987).
- 2) R. Wada et al: *Phys. Rev.*, **C39**, 497 (1989).
- 3) E. Holub et al: *ibid.*, **C28**, 252 (1983).
- 4) D. Hilscher et al: *ibid.*, **C36**, 208 (1987).
- 5) K. Yoshida et al: *ibid.*, **C46**, 961 (1992).
- 6) F. Pühlhofer: *Nucl. Phys.*, **A280**, 267 (1977).

* Present address: Toshiba Electric, Co.

** Present address: Mitsubishi Electric, Co.

Measurement of the d - p Elastic Scattering at $E_d = 270$ MeV

N. Sakamoto, H. Okamura, T. Uesaka, S. Ishida, H. Otsu, T. Wakasa, Y. Satou,
T. Niizeki, K. Hatanaka, Y. Koike,* and H. Sakai

[NUCLEAR REACTIONS $^1\text{H}(\text{polarized } d, d)$, $E = 270$ MeV; measured $\sigma(\theta)$,
 $A_y(\theta)$, $A_{yy}(\theta)$, $A_{xx}(\theta)$, and $A_{xz}(\theta)$; Faddeev calculations.]

In this report we present new data of the differential cross sections for the d - p elastic scattering at $E_d^{\text{lab}} = 270$ MeV and a comparison between predictions of a Faddeev calculation and the experimental data of the differential cross sections and all components of the analyzing powers.¹⁾

The differential cross sections have been measured in the same angular range of the analyzing power measurement.¹⁾ The deuteron beam which was accelerated up to 270 MeV by the RIKEN Ring Cyclotron bombarded the polyethylene film with a thickness of 40 mg/cm². The data were taken by a kinematical coincidence method in order to discriminate the d - p elastic scattering from other scattering processes such as the elastic scattering by carbon or the deuteron break-up process. The contribution of the $^{12}\text{C}(d, dp)^{11}\text{B}$ knock-out reaction whose final products are indistinguishable from those of the d - p elastic scattering has been measured at an angle $\theta_{\text{c.m.}} = 86.6^\circ$ by using a carbon

target and found to be less than 1%. The total uncertainties in the final cross sections are statistical error of $\pm 1\%$ and a systematic error of $\pm 6\%$.

The analyzing powers and the differential cross sections are compared with predictions of a Faddeev calculation in Fig. 1 and Fig. 2, respectively. The Faddeev calculation was made by using a separable expansion method²⁾ employing the Argonne v_{14} potential. The solid and dashed curves are the results of the Faddeev calculations with the Argonne v_{14} NN partial wave interactions of $j \leq 4$ and $j \leq 3$, respectively. All components of the analyzing powers are well reproduced. In contrast, the fit to the differential cross sections is poor. The calculated cross sections are 30% smaller than the experimental values at angles around $\theta_{\text{c.m.}} = 120^\circ$ where the cross sections have a minimum. Inclusion of the $j = 4$ higher partial wave does not improve the fit. This might imply that a tuning of the Argonne v_{14} potential is needed although the analyzing powers are described well.

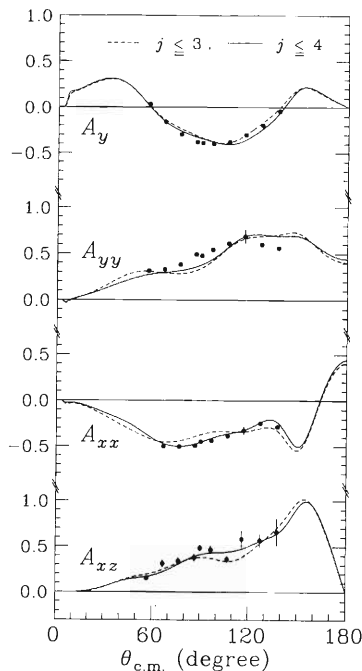


Fig. 1. The analyzing powers for the d - p elastic scattering at $E_d = 270$ MeV. The error bars are statistical ones only. Dashed and solid curves are the results of Faddeev calculations with the Argonne v_{14} NN interaction for $j \leq 3$ and $j \leq 4$, respectively.

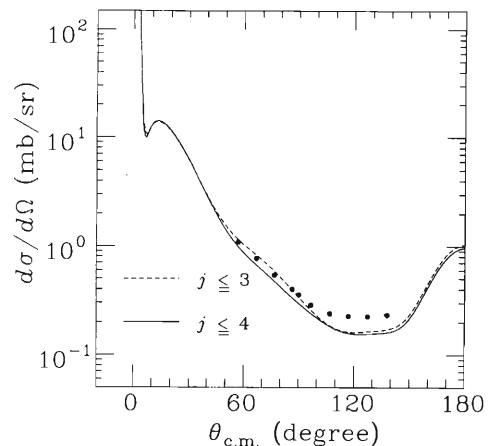


Fig. 2. The differential cross sections for the d - p elastic scattering at $E_d^{\text{lab}} = 270$ MeV. The systematic errors are not shown in the figure. Solid and dashed curves are the same as in Fig. 1.

References

- 1) N. Sakamoto et al.: *RIKEN Accel. Prog. Rep.*, **27**, 39 (1993).
- 2) Y. Koike et al.: *Phys. Rev.*, **C42**, R2286 (1990).

* Department of Physics, Hosei University

Elastic Scattering of Polarized Deuterons at $E_d = 270$ MeV

T. Ohnishi, H. Okamura, S. Ishida, H. Otsu, N. Sakamoto, T. Uesaka, T. Wakasa,
Y. Satou, S. Fujita, T. Nonaka, and H. Sakai

[NUCLEAR REACTION ^{12}C , ^{40}Ca , ^{90}Zr , and $^{208}\text{Pb}(d, d)$; measured $\sigma(\theta), A_y(\theta), A_{yy}(\theta), A_{xx}(\theta)$.]

We have measured the differential cross sections and the vector and tensor analyzing powers, A_y and A_{yy} , for the elastic scattering of polarized deuterons at $E_d^{\text{lab}} = 270$ MeV from ^{12}C , ^{40}Ca , ^{90}Zr and ^{208}Pb targets. We also measured A_{xx} and A_{xz} for the ^{40}Ca target, because these quantities are useful for the study of the tensor interaction.¹⁾ To measure A_{xx} and A_{xz} , it is necessary to control the angle of quantization axis with respect to the beam direction. In a previous experiment,²⁾ only the tensor analyzing power A_{xx}^* , which is a combination of A_{xx} , A_{yy} and A_{xz} , was measured. We established a new method of controlling the direction of quantization axis using a Wien filter at RIKEN.³⁾ The

present data is the first measurement of the complete set of the analyzing powers at intermediate energies.

The vector and tensor polarized deuteron beams were provided by the polarized ion source and accelerated up to 270 MeV by the RIKEN Ring Cyclotron. The scattered deuterons were analyzed by the spectrometer, SMART. The energy resolution was 200 keV (FWHM).

The angular distributions of the differential cross sections are plotted in ratio to Rutherford cross section in Fig. 1. Figures 2, 3, and 4 show the angular distributions of the analyzing powers, A_y , A_{yy} , A_{xx} and A_{xz} . The error bars are statistical only. The optical model analysis is in progress.

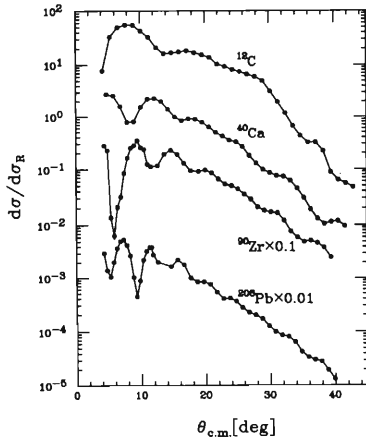


Fig. 1. Angular distributions of cross section for the deuteron elastic scattering from ^{12}C , ^{40}Ca , ^{90}Zr , and ^{208}Pb at $E_d^{\text{lab}} = 270$ MeV.

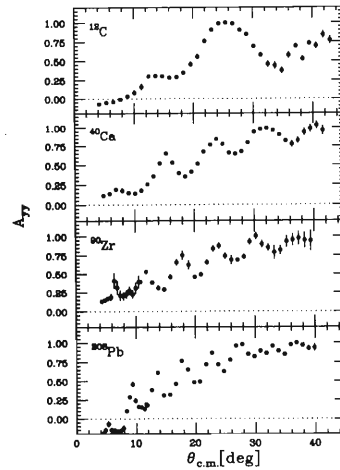


Fig. 3. Angular distributions of analyzing power A_{yy} .

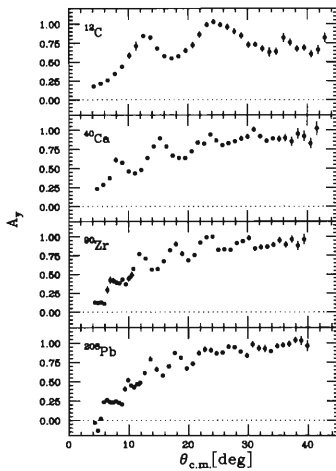


Fig. 2. Angular distributions of analyzing power A_y .

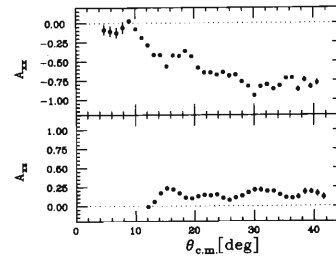


Fig. 4. Angular distributions of analyzing powers A_{xx} and A_{xz} from ^{40}Ca .

References

- 1) Y. Iseri et al.: *Nucl. Phys.*, **A533**, 574 (1991).
- 2) T. Uesaka et al.: *RIKEN Accel. Prog. Rep.*, **27**, 40 (1993).
- 3) H. Okamura et al.: *AIP Conf. Proc.*, **343**, 123 (1995).

Measurement of the $^{12}\text{C}(\vec{d}, \vec{d}')$ Reaction at $E_d = 270$ MeV

Y. Satou, S. Ishida, H. Okamura, N. Sakamoto, H. Otsu, T. Uesaka, T. Wakasa, S. Fujita, T. Ohnishi, T. Nonaka, H. Sakai, T. Ichihara, T. Niizeki, N. Nishimori, and K. Hatanaka

[NUCLEAR REACTION, deuteron inelastic scattering, $E_d = 270$ MeV.]

The study of spin excitation in nuclei is one of the most interesting issues in nuclear physics today. In recent years $\Delta S=1$ strength has been located in several nuclei by measuring spin-flip probability in the (\vec{p}, \vec{p}') reaction. For $\Delta S=1$ transitions induced by proton, however, the isovector ($\Delta T=1$) part of the N-N effective interaction mainly contributes to the excitation of the nucleus. Hence very little is known about the isoscalar ($\Delta T=0$) $\Delta S=1$ strength except for some cases.¹⁾ To study the isoscalar spin strength in nuclei by using the (\vec{d}, \vec{d}') reaction, we have newly developed the Deuteron POLarimeter DPOL which can determine all the vector and tensor polarization components of scattered deuterons simultaneously by utilizing $^{12}\text{C}(d, d)$, $^1\text{H}(d, ^2\text{He})$ and $^1\text{H}(d, d)$ reactions.²⁾

The measurement of the $^{12}\text{C}(\vec{d}, \vec{d}')$ reaction was carried out by using a 270 MeV polarized deuteron beam from the RIKEN Ring Cyclotron. This was the first polarization transfer measurement making use of the DPOL. Details of the polarized deuteron beam are described elsewhere.³⁾ Inelastically scattered deuterons were momentum analyzed by a magnetic spectrograph SMART and their positions were determined by a multiwire drift chamber (MWDC) located at the second focal plane (FP-2). Elastically scattered deuterons were stopped by a 5 cm-thick lead slit placed at the first focal plane (FP-1). The energy resolution was about 200 keV (FWHM) with a natural carbon target of 87.2 mg/cm² thick. Two plastic trigger counters, which were placed downstream of the MWDC and accompanied with a 2.5 cm-thick polyethylene plate, were used as polarization analyzer targets. Scattered particles from the analyzer targets were detected by the plastic counter hodoscope system DPOL.²⁾

Measurements were performed for excitation energies ranging from 2 to 25 MeV and for angles between 2° and 8°. This angular range corresponds to the angular acceptance of SMART. Figure 1 shows the

excitation energy spectra of ^{12}C at 3° and 5°. The unnatural parity states at 12.7 (1⁺) and 18.3 (2⁻) MeV are clearly excited as well as the natural parity states at 4.44 (2⁺), 7.65 (0⁺) and 9.64 (3⁻) MeV. The known broad states at 10.3 (0⁺) and 15.4 (2⁺) MeV and several unknown structures above 20 MeV are also observed. The 1⁺ $T = 1$ state at 15.1 MeV which is prominent in the (p, p') reaction is absent because of the isoscalar nature of the (d, d') reaction.

Further analysis to separate the spin and non-spin transitions by extracting spin-flip probability is now in progress.

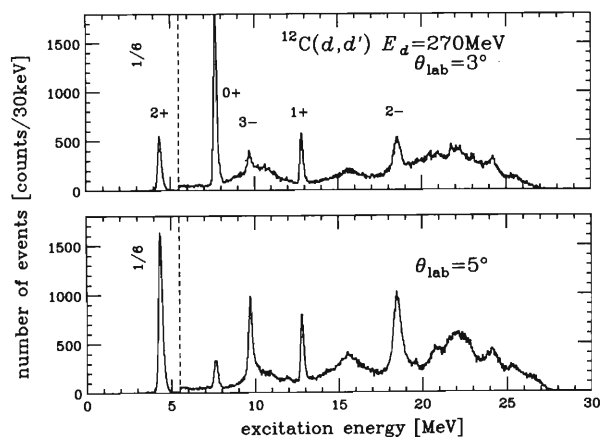


Fig. 1. Excitation energy spectra of ^{12}C at 3° and 5° (lab).

References

- 1) S. Ishida et al.: *Phys. Lett.*, **B314**, 279 (1993); M. Morlet et al.: *ibid.*, **B247**, 228 (1990); B. N. Johnson et al.: *Phys. Rev.*, **C51**, 1726 (1995).
- 2) S. Ishida et al.: *AIP Conf. Proc.*, **343**, 182 (1995).
- 3) H. Okamura et al.: *ibid.*, p. 123.

Precise Experiment on $\bar{n} + d$ Scattering at 12 MeV

N. Nishimori, K. Sagara, T. Fujita, H. Akiyoshi, F. Wakamatsu, K. Maeda, H. Nakamura, and T. Nakashima*

[NUCLEAR REACTION, $D(\bar{n},n)D$, Polarized-Neutron Beam, $E_n = 12$ MeV, Charge Symmetry Breaking.]

The analyzing power $A_y(\theta)$ of nucleon-deuteron (N-d) scattering at a low energy region is very sensitive to the P-state nucleon-nucleon (NN) interaction. Therefore the $A_y(\theta)$ difference between n-d and p-d scattering is a suitable observable to study the charge symmetry breaking (CSB) in the P-state NN interaction.

To study the CSB, the following four items are necessary. (1) A rigorous 3N calculation for n-d scattering. Such calculations based on realistic NN potentials have been extensively made in the Faddeev formalism. (2) Precise $A_y(\theta)$ data of \bar{p} -d scattering. They have been already measured at $E_p = 2$ -18 MeV within an accuracy of 1%.^{1,2)} (3) Precise $A_y(\theta)$ data of the \bar{n} -d scattering. Existing \bar{n} -d $A_y(\theta)$ data have experimental errors of about 3%. More accurate data are necessary to investigate CSB. Hence we planned to make an \bar{n} -d experiment with an accuracy compatible with that of a \bar{p} -d experiment. (4) A rigorous 3N calculation for p-d scattering. Coulomb force should be treated exactly. So far such a calculation has been made only below the deuteron breakup threshold, $E_p \leq 3.3$ MeV.³⁾

The present $\bar{n} + d$ experiment at 12 MeV was made at a new E7 course using \bar{d} -beam from the AVF cyclotron. As described in Ref. 4, 12 MeV \bar{n} -beam was produced by $D(\bar{d},\bar{n})$ reaction at 0° using 9 MeV \bar{d} -beam. The \bar{d} -beam polarization (p_d^y) was measured throughout the experiment using ${}^3\text{He}(\bar{d},p)$ reaction. The $1 \mu\text{A}$ \bar{d} -beam of $p_d^y = 0.7$ produced about 1×10^6 neutrons/sec of $p_n^y = 0.6$ on the target. The \bar{n} -d $A_y(\theta)$ was measured simultaneously at eight angles using two targets of deuterated scintillators (NE230 and NE213d) and four-pair (left and right) neutron counters (NE213).

The preliminary \bar{n} -d $A_y(\theta)$ data are shown by squares in Fig. 1, together with our \bar{p} -d data¹⁾ obtained at Kyushu University Tandem Accelerator Laboratory (KUTL). Though the present data agree with those of Triangle University National Laboratory (TUNL),⁵⁾ the statistical accuracy is twice improved. The accuracy of the absolute scale of the present data is about 1%, due to the fact that the p_n^y has been precisely determined by a separate experiment using ${}^4\text{He}(\bar{n},n)$ scattering at KUTL.

The differences of A_y maxima between \bar{n} -d and \bar{p} -d scattering are shown in Fig. 2. Our preliminary data is twice more accurate than TUNL data at 12 MeV. The data disagree with the approximate Coulomb calculation⁶⁾ in which only the long-range part of Coulomb force is taken into account. When

an exact Coulomb calculation is made at 12 MeV, a definite conclusion will be obtained about the charge symmetry breaking in NN force, especially in the P-wave part.

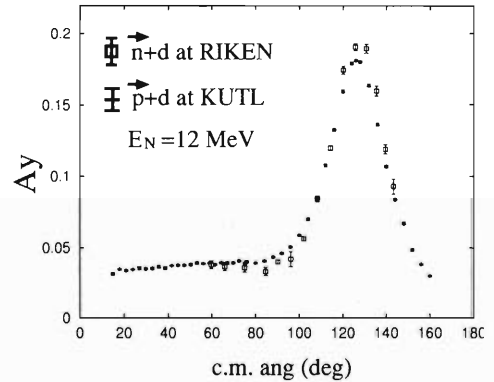


Fig. 1. $A_y(\theta)$ of N-d scattering at 12 MeV. The squares are the present preliminary \bar{n} -d data. The crosses are \bar{p} -d data obtained at KUTL.

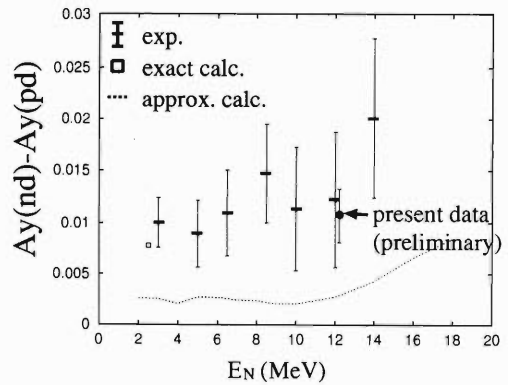


Fig. 2. Energy dependence of $A_y(\theta)$ difference between \bar{n} -d and \bar{p} -d scattering at their peaks. The diamonds are experimental data. The closed circle is the present preliminary data. The square shows an exact Coulomb calculation. The dotted line indicates an approximate Coulomb calculation.

References

- 1) K. Sagara et al.: *Phys. Rev.*, **C50**, 576 (1994).
- 2) S. Shimizu et al.: *ibid.*, **C52**, 1193 (1995).
- 3) G. H. Berthold et al.: *ibid.*, **C41**, 1365 (1990).
- 4) K. Sagara et al.: *RIKEN. Accel. Prog. Rep.*, **28**, 121 (1995).
- 5) C. R. Howell et al.: *Few Body Systems*, **2**, 19 (1987).
- 6) T. Takemiya: *Prog. Theor. Phys.*, **86**, 975 (1991).

* Department of Physics, Kyushu University

Spin-Flip and Non-Spin-Flip Isovector Excitation Observed in the $(^{12}\text{C},^{12}\text{N})$ and $(^{13}\text{C},^{13}\text{N})$ Reactions at $E/A = 100\text{--}135$ MeV

T. Ichihara, T. Niizeki, S. Ishida, Y. Satou, T. Uesaka, H. Okamura, K. Katoh, Y. Fuchi,
S. Kubono, M. H. Tanaka, H. Ohnuma, and M. Ishihara

[charge exchange reaction $(^{13}\text{C},^{13}\text{N})$, $(^{13}\text{C},^{13}\text{N})$, isovector excitation, giant dipole resonance.]

The charge-exchange reactions of $(^{12}\text{C},^{12}\text{N})$ at $E/A = 135$ MeV and $(^{13}\text{C},^{13}\text{N})$ at $E/A = 100$ MeV have been studied for ^9Be , $^{12,13}\text{C}$, $^{24,25,26}\text{Mg}$, ^{27}Al , ^{28}Si , $^{54,56}\text{Fe}$, $^{56,58}\text{Ni}$, ^{90}Zr , ^{120}Sn and ^{208}Pb with the spectrograph SMART.¹⁾ Cathode-readout drift chambers (CRDC)²⁾ were used to measure the position of the analyzed particles.

The $(^{12}\text{C},^{12}\text{N})$ reactions have a selectivity of $\Delta S = 1$ and $\Delta T = 1$, while the $(^{13}\text{C},^{13}\text{N})$ reactions have a selectivity of $\Delta S = 0, 1$ and $\Delta T = 1$. Several DWBA calculations and recent experimental study¹⁾ indicated that these reactions are dominantly one-step processes in the $E/A > 100$ MeV region. It was reported that the $\Delta S = 0$ components dominate over the $\Delta S = 1$ components in the $(^{13}\text{C},^{13}\text{N})$ reactions at $E/A = 50$ MeV, while the contribution of the two-step process affects angular distributions to remove the diffractive pattern.³⁾ The advantage in measuring the $(^{13}\text{C},^{13}\text{N})$ reaction at $E/A = 100$ MeV is the dominance of the one-step process, while the disadvantage is the possible

decreasing ratio of the $\Delta S = 0$ to $\Delta S = 1$ components. However, the combination of the $(^{12}\text{C},^{12}\text{N})$ and $(^{13}\text{C},^{13}\text{N})$ reactions in this higher energy domain would be exploited to isolate the $(\Delta S, \Delta T) = (1, 1)$ and $(0, 1)$ excitations.

Following Fig. 1 shows the preliminary sample of Q-value spectra for ^{12}C and ^{28}Si targets. The broad peak at $Q_t = 22$ MeV ($Ex = 7.5$ MeV) observed in the $^{12}\text{C}(^{12}\text{C},^{12}\text{N})^{12}\text{B}$ reaction is considered to be mainly $\Delta S = 0$ giant dipole resonance (GDR) while that in the $^{12}\text{C}(^{13}\text{C},^{13}\text{N})^{12}\text{B}$ reaction is $\Delta S = 1$ spin dipole resonance. Strong GDR excitation was observed in the $(^{13}\text{C},^{13}\text{N})$ reaction in the $12 < A < 28$ region for the measured target nuclei. But in the heavier region of $54 < A$, the GDR is not clearly observed.

In the medium heavy nuclei such as $^{54,56}\text{Fe}$, $^{56,58}\text{Ni}$, ^{90}Zr , ^{120}Sn and ^{208}Pb , we also observed the $2\hbar\omega$ resonances in the $(^{13}\text{C},^{13}\text{N})$ reaction. The nature of these $2\hbar\omega$ resonances is under investigation.

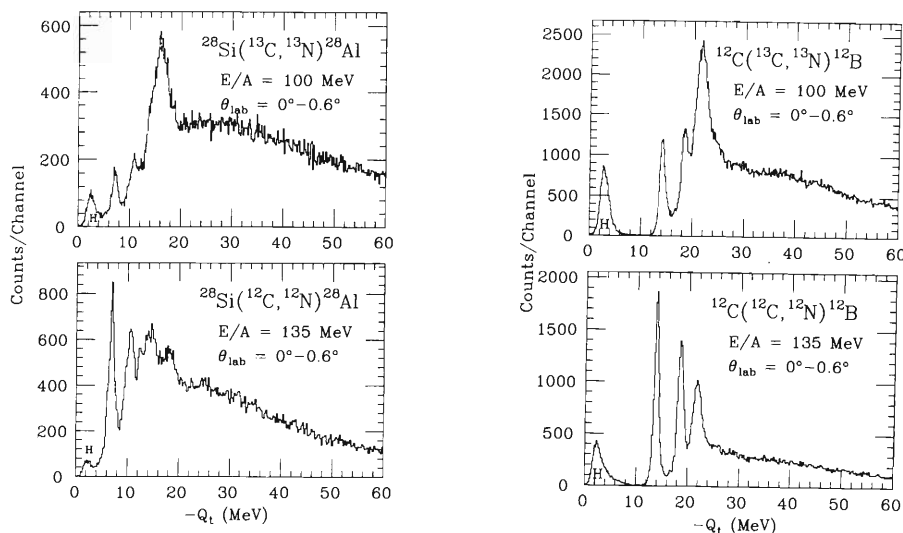


Fig. 1. Sample Q-value spectra for the $(^{12}\text{C},^{12}\text{N})$ and $(^{13}\text{C},^{13}\text{N})$ reactions for ^{12}C and ^{28}Si targets.

References

1) T. Ichihara et al.: *Phys. Lett.*, **B323**, 278 (1994); *Nucl. Phys.*, **A583**, 109 (1995).

2) Y. Fuchi et al.: *Nucl. Inst. Methods. Phys. Res.*, **A362**, 521 (1995).

3) C. Benat et al.: *Nucl. Phys.*, **A555**, 455 (1993).

Electromagnetic Moments of ^{13}O

K. Matsuta, M. Tanigaki, M. Fukuda, T. Minamisono, Y. Nojiri, M. Mihara, K. Minamisono, T. Fukao,
K. Sato, Y. Matsumoto, T. Ohtsubo, S. Fukuda, S. Momota, K. Yoshida, A. Ozawa, T. Kobayashi,
I. Tanihata, J. R. Alonso,* G. F. Krebs,* and T. J. M. Symons*

[NUCLEAR REACTION $^{16}\text{O} + \text{Be}$, $E = 130$ MeV/nucleon; measured β -ray asymmetry of ^{13}O , nuclear magnetic resonance; deduced magnetic moment and quadrupole moment of ^{13}O ground state.]

Nuclear magnetic moments of mirror nuclei provide us with information on nuclear structure and non-nucleonic degrees of freedom in nucleus. The electric quadrupole moment is a good probe for the proton halo in proton rich nuclei because it depends on the radial wave function of the valence proton. As a step towards the systematic studies on the nuclear structure of the mirror nuclei and on the proton halo in proton rich nuclei, we have measured the magnetic moment and the electric quadrupole moment of ^{13}O ($I^\pi = 3/2^-$, $T_{1/2} = 8.6$ ms) for the first time, through the combined technique of polarized radioactive nuclear beam and the β -NMR detection. The ^{13}O is a mirror partner of ^{13}B , thus the present experiment completes the mirror moment measurements for the pair in the $T = 3/2$ quartet of $A = 13$.

^{13}O nuclei were produced through the 130 MeV/nucleon $^{16}\text{O} + ^9\text{Be}$ collision at RIKEN Ring Cyclotron, and were separated by RIPS (RIKEN Projectile Fragment Separator). Polarization was obtained by selecting their emission angles. Thus polarized nuclei were then slowed down by an energy degrader and were implanted in an MgO single-crystal catcher (or TiO_2 for Q-moment measurement). The catcher was placed in a strong magnetic field of $H_0 \sim 4$ kOe (or 8 kOe for Q moment) for maintaining the polarization and for NMR. H_0 was monitored by proton NMR throughout the measurement and was maintained in a high stability. Beta rays were detected by two sets of scintillation counter telescopes placed above and below the catcher relative to the polarization axis. NMR spectra were detected through the β -ray asymmetry change in these counters.

An NMR spectrum was obtained as shown in Fig. 1. From the spectrum, the magnetic moment of ^{13}O was obtained as $|\mu(^{13}\text{O})| = (1.3891 \pm 0.0003) \mu_N$ with a correction for the chemical shift. The sign should be negative because the Schmidt value and all predictions are negative. With the known magnetic moment of the mirror partner ^{13}B , spin expectation value (σ) is obtained to be 0.76, using the scalar moment relation; $\mu(T_Z = +3/2) + \mu(T_Z = -3/2) = J + 0.380\langle\sigma\rangle$. The $\langle\sigma\rangle$ value of ^{13}O is consistent with the systematics from $T = 1/2$ pairs, making contrast with the $\langle\sigma\rangle$ value of ^9C , which is unusually large $\langle\sigma\rangle =$

1.44.¹⁾

A ν_Q spectrum was obtained as shown in Fig. 2. From the ν_Q spectrum, the quadrupole coupling constant was obtained as $|eqQ(^{13}\text{O in TiO}_2)/h| = (1900 \pm 100)$ kHz, with the asymmetry parameter $\eta = 0.868$ known for ^{17}O in TiO_2 .²⁾ Combined with the known $|eqQ(^{17}\text{O in TiO}_2)/h|$ and the known $Q(^{17}\text{O})$, the preliminary result for the quadrupole moment of ^{13}O was obtained as $|Q(^{13}\text{O})| = (33 \pm 4)$ mb.

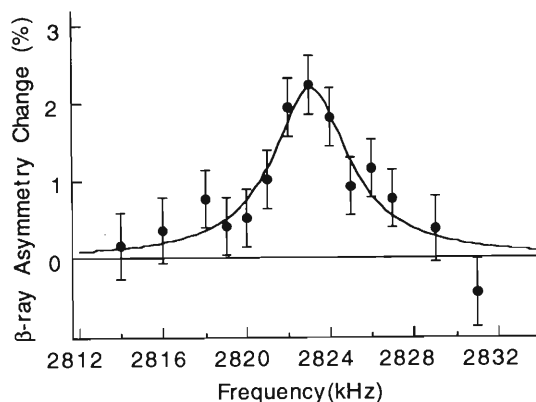


Fig. 1. NMR spectrum of ^{13}O in MgO

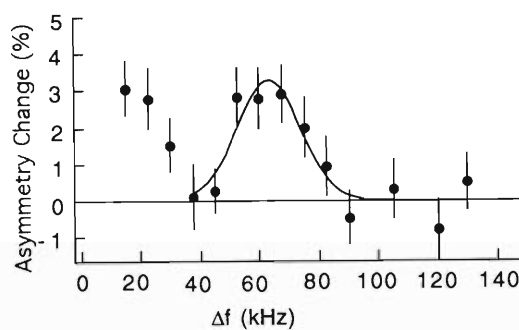


Fig. 2. ν_Q spectrum of ^{13}O in TiO_2 .

References

- 1) K. Matsuta et al.: *Nucl. Phys.*, **A588**, 153c (1995).
- 2) Ch. Gabathuler et al.: *Proc. XVII Congress Ampere*, p. 499 (1973).

* LBL, Berkeley

Measurement of the Magnetic Moments of ^{14}B and ^{15}B Using Projectile Fragmentation Spin Polarization[†]

H. Okuno, K. Asahi, H. Ueno, H. Izumi, H. Sato, M. Adachi, T. Nakamura, T. Kubo, N. Inabe, A. Yoshida, N. Fukunishi, T. Shimoda, H. Miyatake, N. Takahashi, W.-D. Schmidt-Ott, and M. Ishihara

[NUCLEAR STRUCTURE, Magnetic moment of the ground state of ^{14}B and ^{15}B ,
Analysis using OXBASH code.]

By making use of spin polarization in the projectile fragmentation reaction, the magnetic moments of ^{14}B and ^{15}B have been determined by the β -NMR measurement. The experimental procedure and the preliminary results have been reported previously.¹⁾ The final results were obtained as $\mu(^{14}\text{B}) = (1.185 \pm 0.005) \mu_N$ and $\mu(^{15}\text{B}) = (2.659 \pm 0.015) \mu_N$, where μ_N stands for the nuclear magnetron.

The results for ^{14}B were compared with the PSDMK calculation²⁾ in Fig. 1(a). The calculation depends on the energy difference ε between the $s_{1/2}$ and $d_{5/2}$ single-particle states. The standard value ε_{std} is obtained by reproducing the negative parity states of ^{16}O .²⁾ When ε is taken as $\varepsilon = \varepsilon_{\text{std}}$, the calculation yields a μ value which is significantly smaller than the experimental result, indicating the overestimation of the $[\pi p_{3/2}, \nu d_{5/2}]^{2-}$ component. On the

other hand the agreement with experiment is significantly improved when ε is lowered by about 1 MeV from the standard value ε_{std} . At the same time, this lowered ε value better reproduces the low-lying energy levels of ^{14}B , as shown in Fig. 1(b). These observations suggest that the neutron $s_{1/2}$ state shifts downwards with respect to the $d_{5/2}$ state in ^{14}B .

In Fig. 2, we compare the observed magnetic moments of odd mass B isotopes with several theoretical predictions. The A dependence of the Λ -like behavior in Fig. 2 mainly arises from those configurations in which two neutrons in the sd -shell couple to form $J^\pi = 2^+$. The shell model calculations tend to underestimate the quenching effect at $A = 15$. This is more apparent with the PSDWBP interaction, indicating a significant underestimate of the neutron 2^+ configurations.

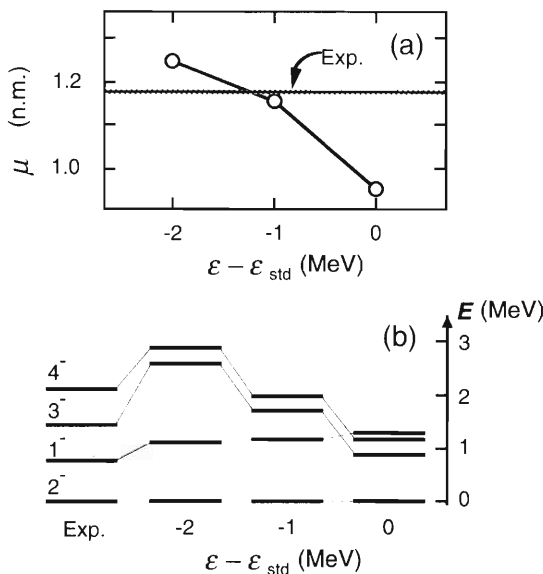


Fig. 1. Magnetic moments (a) and low-lying energy levels (b) of ^{14}B calculated with three different values of the $s_{1/2}$ single particle energy ε . ε_{std} stands for the value which is normally adopted for the OXBASH calculations.²⁾ Experimental values are also shown.

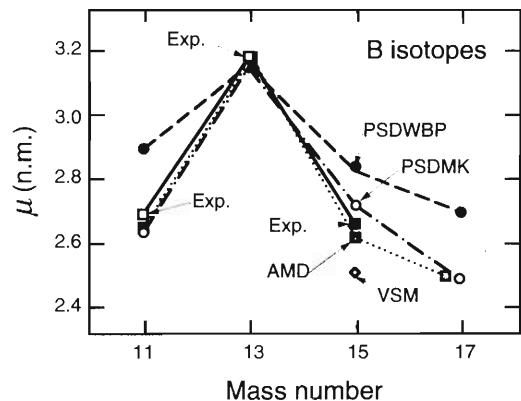


Fig. 2. Comparison of experimental and theoretical magnetic moments for the odd-mass B isotopes. A filled square indicates the μ value obtained in this work. The circles represent theoretical values calculated with a shell model code OXBASH.²⁾

References

- 1) H. Okuno et al.: *RIKEN Accel. Prog. Rep.*, **25**, 41 (1991).
- 2) B. A. Brown, A. Etchegoyen, and W. D. M. Rae: MSUCL Report, No. 524, p. 1 (1988).

[†] Condensed from an article in *Phys. Lett.*, **B354**, 41 (1995).

Electric Quadrupole Moments of Neutron-Rich Nuclei ^{14}B and ^{15}B

H. Izumi, K. Asahi, H. Ueno, H. Okuno, H. Sato, K. Nagata, Y. Hori, M. Adachi,
N. Aoi, A. Yoshida, G. Liu, N. Fukunishi, and M. Ishihara

[NUCLEAR REACTION ^{93}Nb (^{18}O , $^{14,15}\text{B}$), $E/A = 70$ MeV/nucleon; spin-polarized radioactive beams;
measured β -NMR frequency; deduced quadrupole moments, ^{14}B , ^{15}B .]

Spin-polarized fragments¹⁾ ^{14}B and ^{15}B produced in intermediate-energy projectile fragmentation reactions were implanted in a Mg single crystal, and the electric quadrupole coupling constants for ^{14}B and ^{15}B were determined by the β -NMR spectroscopy.²⁾ In this report, we present the results of final analysis and discussion. In Fig. 1 the NMR spectra obtained for ^{14}B and ^{15}B are presented. In the figure the observed β -ray up/down ratio is plotted as a function of eqQ/h .

The coupling constants for ^{14}B and ^{15}B in a Mg single crystal were determined to be $|eqQ(^{14}\text{B})/h| = 106.03 \pm 1.15$ kHz and $|eqQ(^{15}\text{B})/h| = 135.04 \pm 2.05$ kHz. Taking the ratios of the respective values to the ^{12}B result $|eqQ(^{12}\text{B})/h| = 46.933 \pm 0.578$ kHz and using the reported values $|Q(^{12}\text{B})| = 13.21 \pm 0.26$ mb³⁾, Q -moments for ^{14}B and ^{15}B were determined as $|Q(^{14}\text{B})| = 29.84 \pm 0.75$ mb and $|Q(^{15}\text{B})| = 38.01 \pm 1.08$ mb.

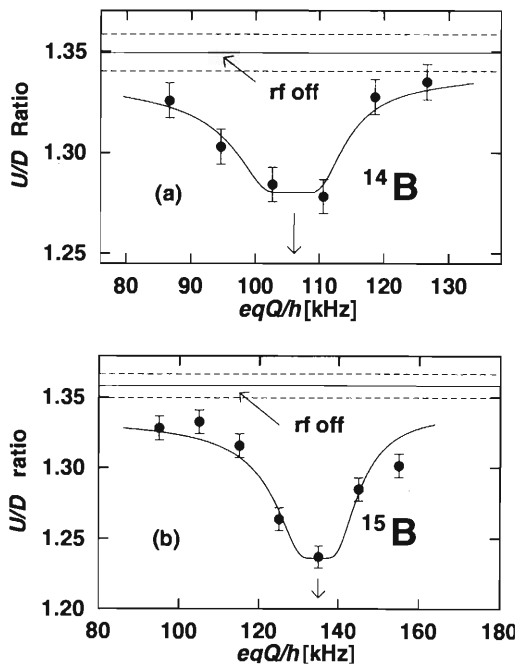


Fig. 1. The up/down ratio of β -ray intensities is plotted as a function of eqQ/h , observed for (a) ^{14}B and (b) ^{15}B implanted in a Mg crystal. The curves represent results of the least-squares fittings of the line shape to the data.

The experimental Q -moment for ^{15}B is plotted in Fig. 2 together with those for the other odd-mass B isotopes. Shell-model calculations with $0\hbar\omega$ model space, using effective charges commonly accepted in this mass region, predict values about 40% larger than the experimental $Q(^{15}\text{B})$. The large overestimation of $Q(^{15}\text{B})$ by the shell model is removed if the neutron effective charge is taken to be as small as $e_n = 0.1$. It may suggest an interesting notion that the core polarization induced by excess neutrons in neutron-rich nuclei is much smaller than in stable nuclei.

The $Q(^{14}\text{B})$ sensitively reflects small admixture of the $d_{3/2}$ neutron configuration and, when combined with the previously obtained data for the magnetic moment,⁴⁾ determines reliably the ground state wave function of ^{14}B .

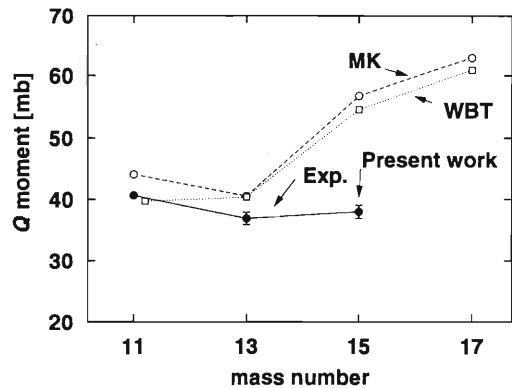


Fig. 2. Comparison of the experimental and theoretical quadrupole moments for the odd-mass B isotopes. Exp: Experimental data. MK and WBT: $0\hbar\omega$ shell model calculations the effective interactions of PSDMK and PSDWBT, respectively, in Ref. 5

References

- 1) H. Okuno et al.: *Phys. Lett.*, **B335**, 29 (1994).
- 2) K. Asahi et al.: *RIKEN Accel. Prog. Rep.*, **27**, 42 (1993).
- 3) T. Minamisono et al.: *Phys. Rev. Lett.*, **69**, 2058 (1992).
- 4) H. Okuno et al.: *Phys. Lett.*, **B354**, 41 (1995).
- 5) Shell model code OXBASH, B. A. Brown et al.: *MSUCL Report*, **524**, 1 (1988).

† Condensed from the article in *Phys. Lett.*, **B**, to be published.

Branching Ratios of the ^{14}B Beta Decay

H. Ogawa, N. Aoi, K. Asahi, M. Adachi, M. Ito, H. Izumi, H. Ueno, K. Nagata,* A. Yoshida,
H. Okuno, G. Liu, S. Mitsuoka, and M. Ishihara
[RADIOACTIVITY $^{14}\text{B}(\beta^-)$; measured β spectrum, β -delayed γ spectrum.]

The neutron-rich nucleus ^{14}B , in which the last neutron resides in the sd shell while the valence protons are in the p shell, provides a useful testing ground for models of the effective interaction connecting the p and sd shells. In fact, Millner and Kurath¹⁾ have applied their first successful model to the β decay of ^{14}B . Experimentally, the total rate of the ^{14}B β decay is known, but its branching ratios have been measured only for the allowed transitions to the 1^- and 3^- states of ^{14}C .²⁾ In this report the observation of the unique first-forbidden β -decay branch to the ^{14}C ground state is presented.

Fragments ^{14}B ($J^\pi = 2^-$, $T_{1/2} = 13.8$ ms, $Q_\beta = 20.64$ MeV) were produced through the fragmentation of ^{22}Ne projectiles at $E/A = 110$ MeV/nucleon on a 832 mg/cm²-thick Be target. The fragments emitted from the target were isotopically separated by the projectile fragment separator RIPS, and the beam of ^{14}B thus purified was stopped in an active stopper made of a 7 mm-thick plastic scintillator located at the final focus. The β rays were detected with a plastic scintillation telescope consisting of a 4 mm-thick ΔE counter and a 130 mm-thick E counter. Furthermore the β -delayed γ rays were detected by a NaI(Tl) scintillation counter which was placed on the other side of the stopper.

The energy spectrum of β rays detected in coincidence with the β signals from the active stopper is shown in Fig. 1. The spectrum is dominated by a major component of the allowed shape with an endpoint energy around 14.6 MeV, which in fact is considered as the sum of contributions from a few allowed branches to the excited states, as shown in Fig. 2. In the portion with $E_\beta > 14.6$ MeV, however, contribution of another component with a much higher endpoint energy is evident. This component proves to be absent in a spectrum taken in coincidence with the γ -ray detector. The spectrum in Fig. 1 was fitted with a theoretical function assuming that the high-energy component stems from the ground state branch. The result yielded the relative intensity of the high-energy component. As a matter of fact, however, the high-energy portion should be contaminated by the signal summing effect between the β rays from the excited-state branches and their coincident γ rays. After correcting for this effect based on the Monte Carlo simulation code EGS4,³⁾ we tentatively obtain the branching ratio $R_{g.s.} = 1.4 \pm 0.8\%$ for the first-forbidden transition to the ^{14}C ground state. We plan to make a final measurement with a reduced

solid angle for the β counter, so that the summing effect becomes negligible.

We also observed in a γ -ray spectrum taken in coincidence with the β events a clear evidence for a new branch to the 2^- state. More extended analysis of the γ -ray spectrum is now in progress.

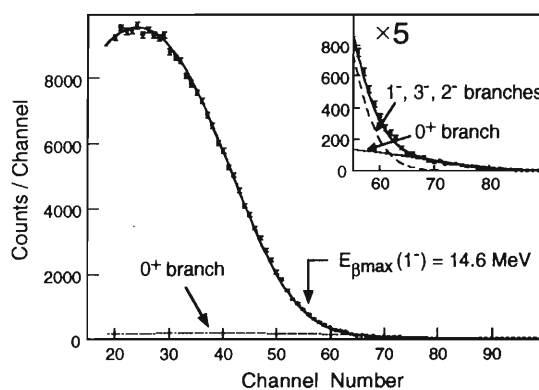


Fig. 1. The β -ray energy spectrum from ^{14}B obtained with a plastic scintillation counter. The inset shows the high-energy portion in an expanded ordinate scale.

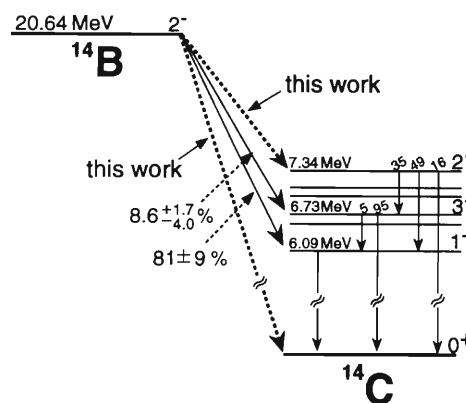


Fig. 2. The decay scheme of ^{14}B and the energy levels of the daughter nucleus ^{14}C . The known β branching ratios of the transitions to the 1^- and 3^- states are taken from Ref. 2.

References

- 1) D. J. Millener et al.: *Nucl. Phys.*, **A255**, 315 (1975).
- 2) D. E. Alburger et al.: *Phys. Rev.*, **C10**, 912 (1974).
- 3) W. R. Nelson et al.: Stanford Linear Accelerator Center Report, SLAC-265 (1985).

* Nippon Telegraph and Telephone Corporation

Feasibility Test of Delayed Neutron Spectroscopy for Spin-Polarized Neutron-Rich Nuclei

H. Miyatake, M. Sasaki, H. Ueno, T. Shimoda, N. Aoi,
T. Shirakura, K. Asahi, H. Izumi, H. Ogawa, G. Liu, and A. Yoshida

[RADIOACTIVITY $^{15}\text{B}(\beta^-)$, measured β -delayed neutron and J^π of excited states in ^{15}C .]

Nuclei near the neutron drip-line decay into various highly excited states in daughter nuclei because of the large Q_β -values. Since most of the final states locate higher than the neutron separation energy, the unbound neutron decays immediately after the β -decay. It, therefore, is possible to identify the individual β -transitions by detecting the delayed neutrons. This method has been widely used as the "delayed particle spectroscopy". It is to be noted that more spectroscopic information can be deduced, if the parent nucleus is spin-polarized, as described below.

The angular distribution of the β -rays in an allowed transition from the polarized nucleus is expressed with the asymmetry parameter (A) and the polarization (P) of the parent nucleus. The A is described as a function of spins and parities of both the initial and final states. Since the AP values for individual transitions can be experimentally obtained, the J^π for unknown transitions can be assigned by comparing the AP values with those for the known transitions.

In order to study the feasibility of this method, we measured the β -rays from polarized ^{15}B in coincidence with the delayed neutrons. The polarized ^{15}B was obtained in the same manner as that used by Ueno et al.¹⁾ Fragments of ^{15}B emitted at angles from 1.5 to 2.5 degrees with respect to the beam axis were separated and focused by using RIPS. The β -rays from ^{15}B were detected by a pair of β -ray counter telescopes placed perpendicular to the reaction plane, and the asymmetry in β -decay was observed by the β -NMR method. The time-of-flight of delayed neutrons was measured by seven plastic counters ($\Omega = 1.1$ sr.) placed 1.5 m away from the stopper to identify the final states of the β -transitions.

Polarization of ^{15}B was determined as $P = -10.7 \pm 1.6\%$ from the most intense transition to the 3.103 MeV state in ^{15}C . This transition is assigned by the 1.77 MeV delayed neutron peak as shown in Fig. 1. The A values for other allowed transitions were then deduced as listed in Table 1. Since the ground state of ^{15}B is known as $J^\pi = 3/2^-$, possible asymmetry parameters of allowed transitions are -1.0 , -0.4 and $+0.6$, and the J^π values of final states are thus assigned as listed in Table 1. These assignments are consistent

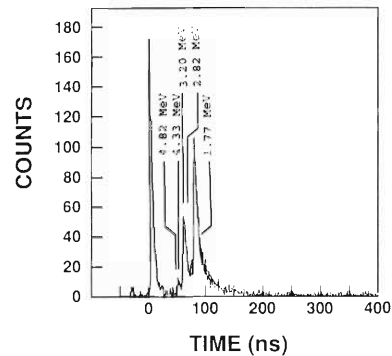


Fig. 1. A part of neutron time of flight spectra with start signals of β -rays detected by the up-counter telescope during the β -NMR off-resonance period.

Table 1. Summary of ^{15}B decay. The J^π values assigned and log ft-values in this experiment are consistent with those in Ref. 2

E_B^{lab} (MeV)	$E_x(^{15}\text{C}; \text{MeV})$	$AP(\%)$	$A(\%)$	J^π	$I_\beta(\%)$	logft	I^π (Ref. 2)
4.82(6)	6.372(20)	-25.2(75)	2.5(8)	$3/2^-$	4.1(6)	5.05(7)	...
4.33(4)	5.866(8)	93.0(81)	-8.7(15)	$1/2^-$	2.6(4)	5.33(7)	$1/2^-$
3.20(1)	4.657(9)	5.9(26)	-0.5(2)	$3/2^-$	23.3(34)	4.56(6)	$3/2^-$
2.82(2)	4.220(3)	-4.3(47)	0.4(4)	$3/2^-$	7.0(10)	5.15(7)	$3/2^-$
1.77(1)	3.103(4)	10.7(16)	-1	$3/2^-$	63.1(90)	4.34(6)	$3/2^-$

with the reported values.²⁾

In the present work, it was successfully shown that the delayed neutron spectroscopy combined with polarized unstable nuclei can be a unique tool to determine J^π of the highly excited states in nuclei far from stability, where spectroscopic information is hardly accessible otherwise. It should be pointed out that this method can be applied not only to delayed neutrons but also to delayed charged particles or γ -rays.

As the next step of the present work, we will soon apply this method to ^{17}B in order to study the decay scheme of ^{17}B , on which only little information has been obtained.³⁾

References

- 1) H. Ueno et al.: *RIKEN Accel. Prog. Rep.*, **28**, 41 (1995).
- 2) R. Harkewicz et al.: *Phys. Rev.*, **C44**, 2365 (1991).
- 3) G. Raimann et al.: *ibid.*, **C53**, 453 (1996).

States in ^{16}C Using the Transfer Reaction $^{15}\text{C}(\text{d},\text{p})^{16}\text{C}$

G. Raimann, M. J. Balbes, R. N. Boyd, J. Feng, M. Fujimaki, K. Kimura, S. Kubono, T. Kobayashi, A. Korshennikov, E. Yu Nikolskii, A. Ozawa, I. Tanihata, J. Vandegriff, and K. Yoshida

[NUCLEAR REACTIONS, radioactive nuclear beam, CD_2 , $\text{D}(^{15}\text{C},\text{p})$, $E/A = 65$ MeV.]

The inhomogeneous models of Big Bang nucleosynthesis suggest various branch points in the mass flow to heavier elements (mass 20 and greater). We have investigated two such points recently,^{1,2)} using β -delayed neutron breakup. The mass 15 branch point results from the competition between ^{15}C β -decay and the $^{15}\text{C}(\text{n},\gamma)^{16}\text{C}$ reaction. The $\text{D}(^{15}\text{C},\text{p})^{16}\text{C}$ reaction was used to study the neutron capture reaction strength. This transfer reaction is sensitive to levels in ^{16}C , both above and below the $^{15}\text{C} + \text{n}$ threshold. If high enough proton energy resolution is achieved, spectroscopic factors can be calculated from the measured angular distribution of the protons.

In the experiment, a 65 A MeV ^{15}C beam was produced from a 100 A MeV primary ^{22}Ne beam. Two thin plastic scintillators (1 mm) at F2 and F3 of the beam line and TOF were used to identify ^{15}C ions. Each ^{15}C ion was tracked in x and y-direction by two MWPCs, after which it entered a scattering chamber. There it hit a CD_2 -target (3 mg/cm²) and subsequently left the chamber through an exit window. Four silicon detector telescopes were mounted at backward scattering angles to detect protons (these protons in inverse kinematics correspond to forward-scattered protons in the center-of-mass).

Each detector telescope consisted of two thin position-sensitive silicon strip detectors and one thick (3 mm) silicon detector to stop the protons. The thicknesses of the ΔE -detectors were 250 μm (1 mm pitch)

and 400 μm (5 mm pitch). The 1 mm-pitch detectors were operated with charge division to reduce the number of readout signals.

The most critical issue was to achieve high enough energy resolution to identify states in ^{16}C . The resolution was mostly determined by the beam TOF, the thickness of the CD_2 -target, the position resolution of the MWPCs and the energy resolution of the E -detectors. The overall uncertainty was estimated to be between 300 and 400 keV proton energy. Unfortunately, one of the two MWPCs broke during the first hours of the experiment, and one of the timing scintillators was instead used to obtain position information along at least one coordinate direction and with less precision.

An extremely strong background contribution from particles elastically back-scattered from the exit foil was observed in all of the detector telescopes. In fact, due to the proximity of the exit foil to the target and to the detector assembly, the "background" has been found to be so strong in the data analysis done to date that no evidence for the proton events of interest has been seen. More restrictive data cuts are presently being tried to isolate the events of interest.

References

- 1) A. Ozawa et al.: *Nucl. Phys.*, **A592**, 244 (1995).
- 2) G. Raimann et al.: *Phys. Rev.*, **C53**, 453 (1996).

Measurement of β -Decay Branching Ratio of ^{17}Ne into the Ground and First Excited States of ^{17}F

A. Ozawa, M. Fujimaki, S. Fukuda, S. Ito, T. Kobayashi, G. Kraus,
S. Momota, G. M \ddot{u} nzenberg, T. Suzuki, I. Tanihata, and K. Yoshida

[RADIOACTIVITY $^{17}\text{Ne}(\beta^+\gamma)$; measured β and β -delayed γ and deduced branching ratios.]

Recently, a large radius of ^{17}Ne compared to the ones of ^{17}F and ^{17}N has been observed by measuring interaction cross sections at a relativistic energy.¹⁾ This anomalous radius can be explained by the anomalous structure of ^{17}Ne , i.e., reversal of s-d orbitals.¹⁾ In this assumption, the configuration of the ^{17}Ne ground state is abnormally given by $(1p_{1/2})^{-\nu}(2s_{1/2})^{2\pi}$ and that of the ^{17}N ground state is normally given by $(1d_{5/2})^{2\nu}(1p_{1/2})^{-\pi}$. In order to prove this anomaly it is crucial to observe asymmetry of ft values given by the quantity $\delta = (ft)^+/(ft)^- - 1$. Since δ will be zero in complete symmetry, deviation from zero will show the asymmetry in ground states of initial nuclei and/or in states of final nuclei. In the present case, ^{17}Ne and ^{17}N decay to states in ^{17}F and ^{17}O , respectively. Since ^{17}F and ^{17}O are doubly closed shell plus one nucleon nuclei, their ground and first excited states are simple and well known, i.e., $(1d_{2/5})$ and $(2s_{1/2})$ respectively. Thus, δ 's into the ground and first excited states are crucial for the proof of anomaly in ^{17}Ne . However, δ into the ground states has not been obtained until now due to no observation of β -decay branching ratio of ^{17}Ne into the ground state in ^{17}F . Furthermore, only one measurement is known for the β -decay branching ratio of ^{17}Ne into the first excited state of ^{17}F .²⁾ Thus, we propose to measure β -decay branching ratio of ^{17}Ne into the ground and first excited states of their daughter nuclei.

^{17}F has only one bound excited state. Thus, if we measure the number of ^{17}F produced from ^{17}Ne , we can obtain the sum of branching ratio into the first and ground states. Since their half-lives are different so much, it is possible to obtain the sum of branching ratio by measuring the β -decay time spectrum. Fur-

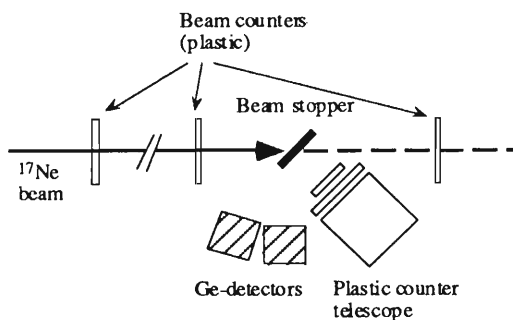


Fig. 1. Experimental setup.

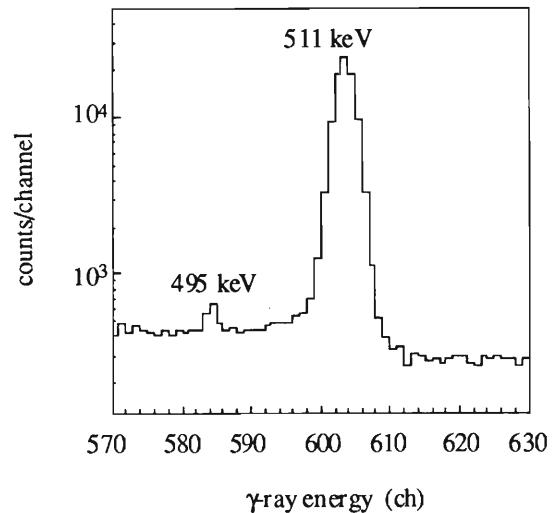


Fig. 2. Typical γ -ray energy spectrum following the β -decay of ^{17}Ne .

thermore, it is also possible to measure the branching ratio into the first excited state by detecting 495 keV γ -ray emitted from the first excited state and the number of ^{17}Ne . Thus, subtracting the branching ratio into first excited state from the sum, we can obtain one into the ground state.

Experimental setup is shown in Fig. 1. A ^{17}Ne beam of about 30 A MeV was produced by the projectile fragmentation of a primary beam ^{20}Ne accelerated by Ring Cyclotron and separated by the RIPS facility. Major contaminant was ^{15}O with the ratio of 1 by 1. The beam was stopped in a thin plastic plate tilted by 45° to the beam axis at the front of a plastic counter telescope and two Ge detectors. The number of implanted nuclei was counted by the scintillators located on beam line. These counters were also used to identify the passing nuclei by dE and TOF measurements. A β -ray emitted from stopped ^{17}Ne was detected by a plastic counter telescope consisted of dE - dE - E counters. A delayed γ -spectra emitted from the stopped ^{17}Ne was detected by the two Ge detectors. A typical energy spectrum of the Ge detectors is shown in Fig. 2. An energy peak of 495 keV, that corresponds to the γ -ray emitted from the first excited state of ^{17}F , is clearly visible in the figure. Analysis is now in progress.

References

- 1) A. Ozawa et al.: *Phys. Lett.*, **B334**, 18 (1994).
- 2) M. J. G. Borge et al.: *ibid.*, **B317**, 25 (1993).

Beta Decay of the Drip Line Nuclei ^{14}Be

N. Aoi, K. Yoneda, H. Miyatake, H. Ogawa, Y. Yamamoto, E. Ideguchi,
T. Kishida, T. Nakamura, M. Notani, H. Sakurai, T. Teranishi,
S. S. Yamamoto, Y. Watanabe, A. Yoshida, and M. Ishihara

[RADIOACTIVITY $^{14}\text{Be}(\beta^-)$, measured β -delayed neutron, deduced $\log ft$, and deduced E_x in ^{14}B .]

We reported in the reference¹⁾ on the measurement of the β -decay of neutron drip line nucleus ^{14}Be . In the energy spectrum of the delayed neutron, we found a strong peak at the energy of 283(2) keV with the branching ratio of 63(15)%. This decay is very fast for the β^- -decay, suggesting an unusual nuclear structure of the drip line nuclei. However, in the last experiment, we had an ambiguity in the decay energy and in the branching ratio mainly due to the difficulties in determining the neutron detection efficiency for such low energy neutrons. We have carried out an alternative experiment focusing on the measurement of the β -decay to low-lying excited states of ^{14}B . We measured neutrons by a newly developed detector²⁾ for the neutrons of the energy between 100 keV and 1 MeV. We also detected the β -ray total energy and delayed γ rays in order to determine the relevant β -decay schemes clearly.

A ^{14}Be beam was provided by RIKEN Projectile-fragment Separator (RIPS) using projectile fragmentation of 100 MeV/nucleon ^{18}O . The ^{14}Be ions were implanted into a 1 mm thick Si detector located at the final focal plane (F3) of RIPS. The emitted β rays were detected by thin plastic scintillators placed upside and downside of the beam stopper. Behind these detectors, we set thick plastic scintillators in order to measure the total energy of β rays from ^{14}Be (Q_β of ^{14}Be is 16.2 MeV). The energy of the neutron was measured by means of the TOF method. The flight path of the neutron was set to be 50cm. γ rays were detected by Ge detectors.

The obtained neutron TOF spectrum is shown in Fig. 1. The sharp peak around 0ns corresponds to the prompt γ rays. The huge peak near 70 ns corresponds to the transition mentioned above. The mean energy of this peak and its branching ratio are determined tentatively to be 288(6) keV and 73(15)%, respectively. The decay curve of the events gated by this neutron peak showed that this neutron peak was originated from the delayed neutron of ^{14}Be . The decay branch was determined from the maximum energy of the β rays which coincided with the neutrons. The precise decay energy was obtained from the neutron energy taking the recoil energy into account. Then, the relevant decay was found to be the transition to the unknown excited state of ^{14}B ($E_x = 1.28$ MeV) and that the neutron was emitted via the following process,



Using the branching ratio and decay energy obtained by this work and the half life measured by Dufour et al.,³⁾ the $\log ft$ value is calculated to be 3.73(9) which is one of the smallest values for β^- -decay. From the small $\log ft$ value, this transition was determined to be a Gamow-Teller transition and the J^π of the final state is 1^+ . It is unusual that an abnormal parity state is located in such a low energy region (J^π of $^{14}\text{B}(\text{g.s.})$ is 2^-). This state may be described as the excitation of the neutron sitting at $1p_{1/2}$ in the ground state of ^{14}B to $2s_{1/2}$ in a different major shell. Thus, this excitation energy after being corrected for the residual interaction between a valence neutron and a proton is considered as the energy difference between $1\nu p_{1/2}$ and $2\nu s_{1/2}$. Assuming that the residual interaction between a neutron in $2\nu s_{1/2}$ or $1\nu p_{1/2}$ and a proton in $\pi 1p_{3/2}$ is the same for ^{14}B and ^{12}B , the energy difference is calculated to be around 1.5 MeV. This value is about one half of that of the nuclei near the stability line. It is well-known that the energy of the single particle neutron orbital of $2\nu p_{1/2}$ decreases as the proton number decreases in $N = 7$ nuclei as in the case of ^{11}Be .⁴⁾ The present work showed for the first time that the same phenomenon happens in $N = 9$ nuclei.

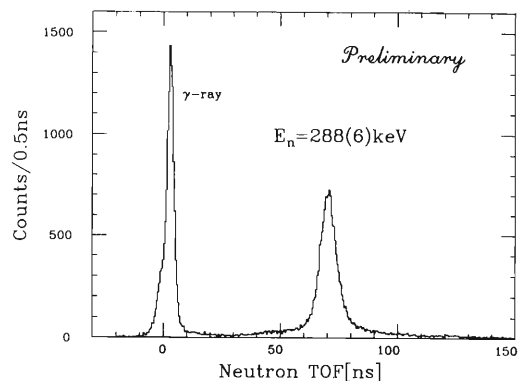


Fig. 1. TOF spectrum of neutron from ^{14}Be . The sharp peak around 0 ns corresponds to the prompt γ ray. The peak around 70 ns corresponds to the neutron with energy of 288(6) keV.

References

- 1) N. Aoi et al.: *RIKEN Accel. Prog. Rep.*, **28**, 38 (1995).
- 2) K. Yoneda et al.: This report, p. 182.
- 3) J. P. Dufour et al.: *Phys. Lett.*, **B206**, 195 (1988).
- 4) I. Talmi and I. Unna: *Phys. Rev. Lett.*, **4**, 469 (1960).

Measurement of the Fusion Cross Section of Neutron-Rich Nuclei $^{29,31}\text{Al} + ^{197}\text{Au}$

Y. Watanabe, T. Fukuda, A. Yoshida, Y. Watanabe, Y. Mizoi, J. Nakano, M. Hirai,
H. Sakurai, H. Kobinata, Y. Pu, K. Kimura, and M. Ishihara

[NUCLEAR REACTIONS $^{197}\text{Au}(^{29}\text{Al}, \text{F})$, $E_{\text{CM}} = 95\text{-}165 \text{ MeV}$;
 $^{197}\text{Au}(^{31}\text{Al}, \text{F})$, $E_{\text{CM}} = 95\text{-}165 \text{ MeV}$; measured fission cross section.]

It is established that the fusion cross section of heavy ions is strongly enhanced in the energy region near and below the Coulomb barrier as compared to the calculations based on the one-dimensional barrier penetration model.¹⁾ This phenomenon is expected to become more remarkable in the fusion reaction with neutron-rich nuclei, because of a possibility that excess neutrons favor penetration. In order to investigate this possibility, the systematic fusion cross section measurements of $^{27,29,31}\text{Al} + ^{197}\text{Au}$ were performed, measuring fusion-fission reactions. The measurements for a stable nucleus, $^{27}\text{Al} + ^{197}\text{Au}$, and details of the detector performance have been reported elsewhere.²⁾ In this paper, we report the fusion cross section measurements for two systems, $^{29,31}\text{Al} + ^{197}\text{Au}$.

The neutron-rich RI beams, $^{29,31}\text{Al}$, were produced via a fragmentation process of ^{40}Ar primary beam which impinged on a Be production target with 2.5 mm thickness. The energy and intensity of the primary beam were 90 MeV/nucleon and 40 pA. They were then separated by the projectile fragment separator RIPS. Since the secondary beam energy was still high (~ 40 MeV/nucleon), it was reduced with an Al degrader plate with 0.98 mm and 0.85 mm thickness for $^{29,31}\text{Al}$ beams, respectively. The intensity of ^{29}Al and ^{31}Al beams after the degrader was 5×10^5 cps and 2×10^5 cps, respectively. The energy of ^{29}Al and ^{31}Al beams after the degrader was 180 MeV (ranging from 160 to 232 MeV) and 170 MeV (ranging from 133 to 199 MeV), respectively. Because the energy distributions of the secondary beams were wide spread, the time of flight (TOF) between a plastic scintillator and an MCP detector was measured in order to determine the energy of the secondary beams one by one. The purity of the $^{29,31}\text{Al}$ beam was 99% and 94%, respectively. The other impurities were rejected in the analysis using the TOF and the RF timing from the cyclotron.

The Al beams impinged on a stack of ten thin Au targets ($\sim 380 \mu\text{g}/\text{cm}^2$) which was surrounded by two pairs of MWPC walls. The compound nucleus produced through a fusion reaction results in a fission and two fission fragments are detected by these MWPC's. The energy and spot size of Al beams at every target were measured with PSD, separately. The fusion-fission events were identified from a subset of the events

that hit one MWPC and had a coincident fragment in the opposite side MWPC. By selecting the energy loss through MWPC's and the opening angles of two fragments, fusion-fission events were clearly separated from backgrounds due to the elastic scattering.

Making use of the wide energy distributions of the secondary beams and the energy loss through the MWPC gases (helium 40 mbar and isobutane 10 mbar), fusion cross sections for the wide energy range were obtained all at once. Figure 1 shows measured fusion excitation function for the systems of $^{27,29,31}\text{Al} + ^{197}\text{Au}$. The fusion cross sections for three systems were determined by taking into account the efficiency of MWPC, which was estimated by a simulation calculation. The X-error bars indicate the size of binning at the analysis which is determined so that each bin has a sufficient yield. The Y-error bars include only statistical errors. We have not yet fully estimated the error in the absolute values, but the relative value of the fusion cross sections between three systems, $^{27,29,31}\text{Al} + ^{197}\text{Au}$, and among each energy is well established.

As shown in Fig. 1, the fusion cross section for neutron-rich nuclei, $^{29,31}\text{Al}$, is enhanced below the barrier as compared to that for the stable nucleus, ^{27}Al .

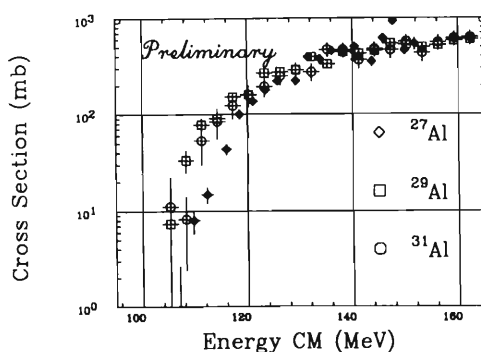


Fig. 1. A preliminary result of the fusion cross section.

References

- 1) M. Beckerman: *Phys. Rep.*, **129**, 145 (1985).
- 2) A. Yoshida et al.: *RIKEN Accel. Prog. Rep.*, **27**, 114 (1993).

Scattering of Radioactive Nuclei ${}^6\text{He}$ and ${}^3\text{H}$ by Proton

A. A. Korshennikov, E. Yu. Nikolskii,* T. Kobayashi, A. Ozawa, S. Fukuda, E. A. Kuzmin,*
S. Momota, B. G. Novatskii,* A. A. Ogloblin,* V. Pribora,* I. Tanihata, and K. Yoshida

[NUCLEAR REACTIONS, radioactive nuclear beam, $p({}^6\text{He},p)$, $p({}^6\text{He},p{}^4\text{He})$,
E/A = 71 MeV, $p({}^3\text{H},p)$, E/A = 73.5 MeV.]

Structure of such exotic extremely neutron rich nuclei at the neutron drip line as ${}^{11}\text{Li}$, ${}^{11}\text{Be}$, ${}^8\text{He}$ was studied by the cross sections' measurements, fragmentation experiments and by elastic scattering, while the related nucleus ${}^6\text{He}$ was experimentally studied much less. We performed an investigation of scattering ${}^6\text{He}+p$ together with a study of proton scattering by the radioactive nucleus ${}^3\text{H}$.

We used beams of ${}^6\text{He}$ (71 A MeV) and ${}^3\text{H}$ (73.5 A MeV) produced by the RIPS and studied collisions ${}^6\text{He}+p$ and ${}^3\text{H}+p$ (targets CH_2 or C) by the missing mass method detecting recoil protons both in an inclusive way and in coincidence with other emitted particles. Protons were measured by two telescopes of solid state detectors. Particles from a projectile breakup were measured by a charge fragment detectors (dipole magnet+drift chamber+plastic scintillators) and neutron walls.

The measured spectra of protons show the ground states of ${}^6\text{He}$ and ${}^3\text{H}$ and the known excited state of ${}^6\text{He}$ at $E^* = 1.8$ MeV. The obtained angular distributions for elastic scattering ${}^6\text{He}+p$ and ${}^3\text{H}+p$ are presented in Fig. 1 as a ratio to the Rutherford cross section. It is seen that the experimental points correspond mainly to the nuclear scattering. Cross sections

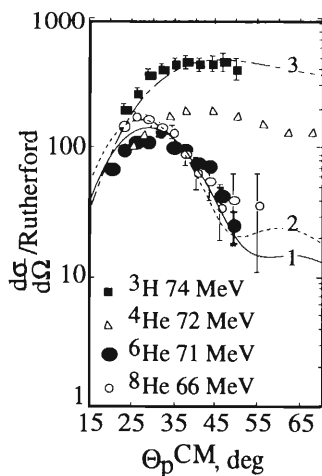


Fig. 1. Angular distributions in a ratio to the Rutherford cross section for the proton scattering by ${}^3\text{H}$, ${}^6\text{He}$, ${}^8\text{He}$, and ${}^4\text{He}$. Curves show optical model calculations.

$d\sigma/d\Omega_{cm}$ are shown in Fig. 2. Both figures also show data for scattering ${}^8\text{He}+p$, which we measured previously, and data for ${}^4\text{He}+p$ ¹⁾ at the center-of-mass energies close to that for ${}^6\text{He}+p$. The measured ${}^6\text{He}+p$ data is compared with the $p+{}^6\text{Li}$ data²⁾ at almost the same energy of 72 MeV on the bottom of Fig. 2. Data for scattering $p+{}^3\text{He}$ at 85 MeV³⁾ is compared with the ${}^3\text{H}+p$ data on the top of Fig. 2.

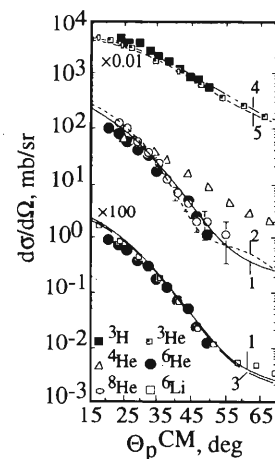


Fig. 2. Cross sections for the proton scattering by ${}^3\text{H}$, ${}^3\text{He}$, ${}^4\text{He}$, ${}^6\text{He}$, ${}^8\text{He}$, and ${}^6\text{Li}$. Curves present the optical model calculations.

An analysis of these proton scattering data demonstrates that (1) results for ${}^6\text{He}$ and ${}^8\text{He}$ are very similar to each other and differ essentially from that for ${}^4\text{He}$ reflecting that ${}^6\text{He}$ and ${}^8\text{He}$ have close matter radii and contain the density components extended beyond α -particle; (2) angular distributions for the proton scattering by ${}^6\text{He}$ and ${}^6\text{Li}$ are almost identical showing resemblance between gross-characteristics of density distributions in ${}^6\text{He}$ and ${}^6\text{Li}$; and (3) results for ${}^3\text{H}$ and ${}^3\text{He}$ are in an intimate agreement one with another in consistency with the belonging of these nuclei to the same isospin doublet.

References

- 1) S. Burzynski et al.: *Phys. Rev.*, **C39**, 56 (1989).
- 2) R. Henneck et al.: *Nucl. Phys.*, **A571**, 541 (1994).
- 3) L. G. Votta et al.: *Phys. Rev.*, **C10**, 520 (1974).

* Kurchatov Institute, Moscow, Russia

Spectroscopy of Halo Nucleus ^{11}Li

A. A. Korshennikov, E. Yu. Nikolskii,* T. Kobayashi, A. Ozawa, S. Fukuda, E. A. Kuzmin,* S. Momota, B. G. Novatskii,* A. A. Ogloblin,* V. Pribora,* I. Tanihata, and K. Yoshida

[NUCLEAR REACTIONS, radioactive nuclear beam, $p(^{11}\text{Li},p)$, $p(^{11}\text{Li},p^{11,9,8,7}\text{Li})$, $p(^{11}\text{Li},pn^{9,8,7}\text{Li})$, $E/A = 75$ MeV, $p(^8\text{He},p)$, $E/A = 66$ MeV.]

The neutron rich nucleus ^{11}Li presents one of the most exciting problems in nuclear physics. However, reflecting experimental difficulties, number of spectroscopic studies of ^{11}Li is restricted by two papers only Refs. 1 and 2. In Ref. 1, a weak peak corresponding to the ^{11}Li state at $E^* = 1.2 \pm 0.1$ MeV was observed. In Ref. 2 this state was not observed, but three other excited states were reported: at $E^* \sim 2.47, 4.85$ and 6.22 MeV. We performed a new study of ^{11}Li by means of scattering $^{11}\text{Li}+p$. The key point of the experiment was a correlational measurement of emitted particles.

We used the ^{11}Li beam produced by the RIPS and studied collisions $^{11}\text{Li}+p$ (targets CH_2 or C) by the missing mass method detecting recoil protons both in an inclusive way and in coincidence with particles from the breakup of ^{11}Li . Protons were measured by two telescopes of solid state detectors. Particles from the dissociation of ^{11}Li ($^9,8,7\text{Li}$ and neutrons) were measured using a charge fragment detection system (dipole magnet, drift chamber, and hodoscope of scintillators) and neutron walls. Note that in this experiment we studied the $^8\text{He}+p$ scattering also.

The inclusive spectrum of protons shows a strong peak corresponding to the ^{11}Li ground state as well as two weak peculiarities at $E^* \sim 4.9$ and 6.4 MeV, consistent with the results of Ref. 2. In addition, the inclusive spectrum of protons demonstrates a peak at ~ 1.25 MeV in agreement with Ref. 1. This state of ^{11}Li is clearly seen with obvious statistical significance in Fig. 1, where the solid histogram presents the proton spectrum detected in coincidence with ^9Li . The same state of ^{11}Li is also seen in proton spectra from the processes $p(^{11}\text{Li},p^{9,8,7}\text{Li})$ and $p(^{11}\text{Li},pn^{9,8,7}\text{Li})$. The observed width of the state is close to the experimental resolution.

In Fig. 1, a group on the right side from the 1.25-MeV peak attracts attention. If this is one more excited state of ^{11}Li , it is located at a higher energy ~ 3.0 MeV than the state at ~ 2.47 MeV reported in Ref. 2, and we suppose that two peaks at ~ 1.25 and ~ 3.0 MeV were not resolved in Ref. 2. One more tentative group might be distinguished in Fig. 1 at ~ 4.9 MeV. At last, note a structure at ~ 11.3 MeV in Fig. 1. It is interesting that the corresponding peak is seen in the spectrum measured in Ref. 2.

All obtained data about the ^{11}Li states are summarized in Fig. 2.

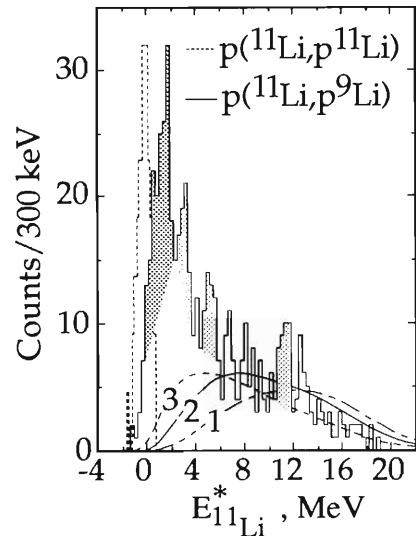


Fig. 1. Proton spectra from the processes indicated on the figure. Curves show physical backgrounds.

$p(^{11}\text{Li}, p)$ present experiment	$^{11}\text{Be}(\pi^-, \pi^+)$ T. Kobayashi <i>et al</i> [1]	$^{10}\text{Be}(^{14}\text{C}, ^{13}\text{N})$ $^{14}\text{C}(^{14}\text{C}, ^{17}\text{F})$ H.G. Bohlen <i>et al</i> [2]
11.3 ± 0.35		
6.4 ± 0.25	6.396	6.22 ± 0.07
4.9 ± 0.25	$^7\text{Li}+4n$	4.85 ± 0.07
3.0 ± 0.2	4.36	
1.25 ± 0.15	$^8\text{Li}+3n$	2.47 ± 0.07
	0.34	
	$^9\text{Li}+2n$	
	1.2 ± 0.1	
	^{11}Li	^{11}Li

Fig. 2. Levels of ^{11}Li .

References

- 1) T. Kobayashi: *Nucl. Phys.*, **A538**, 343c (1992).
- 2) H. G. Bohlen *et al.*: *Z. Phys.*, **A351**, 7 (1995).

* Kurchatov Institute, Moscow, Russia

Effects of Neutron Skin and Halo in ${}^6\text{He}$, ${}^8\text{He}$, and ${}^{11}\text{Li}$

A. A. Korshennikov, C. A. Bertulani,* and I. Tanihata

[Neutron halo, neutron skin, few-body model, eikonal calculation, proton elastic scattering.]

One of the most exciting events in nuclear physics of recent years is a discovery of extended neutron distributions in exotic neutron rich nuclei. Peculiarities of density shape sometimes are used for classification of extended neutron distributions into two groups, skins and halos. During last years experimental studies in RIKEN formed a bank of data on the proton elastic scattering by exotic nuclei ${}^{11}\text{Li}$, ${}^8\text{He}$, and ${}^6\text{He}$. We performed a comparative analysis of these data. It turns out that proton feels valence neutrons in ${}^6\text{He}$ and ${}^8\text{He}$ and does not feel them in ${}^{11}\text{Li}$.

Figure 1 shows the data for scattering ${}^8\text{He}+p$, ${}^6\text{He}+p$, and ${}^{11}\text{Li}+p$ at different energies^{1,2)} as well as data for $p+{}^6\text{Li}$,³⁾ which were included in our analysis, because ${}^6\text{Li}$ can be considered as an α -core plus an extended $n+p$ distribution. We used the eikonal approach, which has no fitting parameters and provides connection with densities.

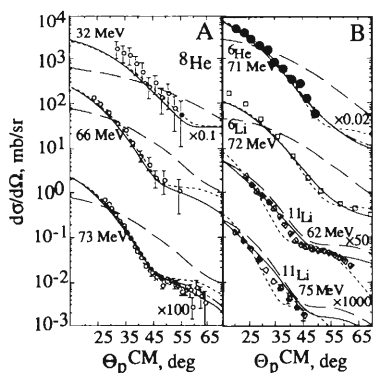


Fig. 1. Proton scattering by ${}^8,{}^6\text{He}$, ${}^6,{}^{11}\text{Li}$.

Calculations with the “realistic” densities, which correspond to the experimental matter radius, R^{mat} , of ${}^8,{}^6\text{He}$ or ${}^6,{}^{11}\text{Li}$ and contain the skin or the halo, are shown in Fig. 1 by solid curves and are in a good agreement with all data. Calculations with the “non-halo” densities, which correspond to R^{mat} , but neglect a difference between proton and neutron radii, are shown by dotted curves. For all cases except for ${}^{11}\text{Li}$ these curves are close to the solid curves. The dashed curves, which correspond to the “core-like” densities where the skin or the halo is neglected and R^{mat} is replaced by the radius of the core, differ drastically from the experimental data for ${}^6\text{He}$, ${}^8\text{He}$ and ${}^6\text{Li}$. Such regularities are different for scattering ${}^{11}\text{Li}+p$: the solid curves are

more similar to the dashed curves than to the dotted ones.

Such a distinction of ${}^{11}\text{Li}$ from ${}^8\text{He}$ and ${}^6\text{He}$ remains at high energy proton scattering (Fig. 2). Calculations for ${}^{11}\text{Li}+p$ at 800 A MeV show that the solid curve (the “realistic” density) is close to the dashed curve (the “core-like” density) and both of them differ from the dotted curve. In the scattering by ${}^6\text{He}$ and ${}^8\text{He}$ at angles $\leq 10^\circ$ the solid curves are close to the dotted ones and differ from the dashed curves. At larger angles all three curves have distinctive behaviors (inserts in Fig. 2) showing a possibility of extracting detailed information about densities of ${}^8\text{He}$ and ${}^6\text{He}$.

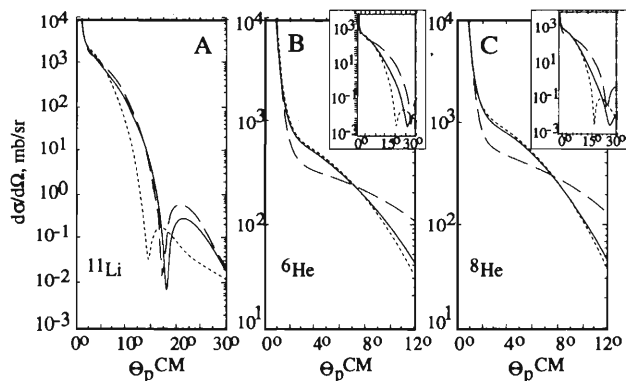


Fig. 2. Calculations of high energy proton scattering by ${}^{11}\text{Li}$, ${}^6,{}^8\text{He}$.

Summarizing, (1) the scattering of ${}^6,{}^8\text{He}$ and ${}^6\text{Li}$ at low energies (and at small angles at high energies) is not sensitive to a difference in the neutron and proton distributions, but it is sensitive to the matter radius of these nuclei and feels the density extension beyond the α -particle; and (2) on the contrary, the elastic scattering ${}^{11}\text{Li}+p$ is mainly determined by the proton scattering on the ${}^9\text{Li}$ -core and is not sensitive to the neutron halo extended beyond the ${}^9\text{Li}$ -core. These results form a basis for distinction between the neutron skin (${}^6,{}^8\text{He}$) and the neutron halo (${}^{11}\text{Li}$).

References

- 1) A. Korshennikov et al.: *Phys. Lett.*, **B343**, 53 (1995); *ibid.*, **B316**, 38 (1993); to be published in *Phys. Rev.*, **C53**, (1996).
- 2) C. B. Moon et al.: *ibid.*, **B297**, 39 (1992).
- 3) R. Henneck et al.: *Nucl. Phys.*, **A571**, 541 (1994).

* Universidade Federal do Rio de Janeiro, Brazil

Charge Exchange Reactions of ^{11}Li

T. Teranishi, S. Shimoura, Y. Ando, M. Hirai, M. Ishihara, N. Iwasa, T. Kikuchi,
S. Moriya, T. Motobayashi, H. Murakami, T. Nakamura, T. Nishio, H. Sakurai,
T. Uchibori, Y. Watanabe, and Y. Yanagisawa

[NUCLEAR REACTIONS: $p(^{11}\text{Li}, ^{11}\text{Be}^*)n$, $d(^{11}\text{Li}, ^{11}\text{Be}^*)nn$, 63 MeV/nucleon.]

We have studied Fermi and Gamow-Tellar (GT) transitions of the halo nucleus ^{11}Li by the charge exchange reactions $p(^{11}\text{Li}, ^{11}\text{Be}^*)n$ and $d(^{11}\text{Li}, ^{11}\text{Be}^*)nn$. One of our interests is to study the isobaric analogue state (IAS) of ^{11}Li , which has never been observed. The IAS's for stable nuclei have been studied well so far by (p,n) reactions. They have narrow widths, and their Coulomb displacement energies are well approximated by the following expression:¹⁾

$$\Delta E_C = 1.44(Z + 0.5)/A^{1/3} + 1.13 \text{ [MeV]}. \quad (1)$$

In the case of the ^{11}Li nucleus, the IAS may have different properties from those of stable nuclei, because of the unusual nucleon distribution in the ^{11}Li nucleus.

We utilized inverse kinematics reactions of (p,n)- and (d,2n)-type, namely $p(^{11}\text{Li}, ^{11}\text{Be}^*)n$ and $d(^{11}\text{Li}, ^{11}\text{Be}^*)nn$, since ^{11}Li is provided as a secondary beam. Proton and deuteron targets were used to distinguish the type of the transition (Fermi or GT). Fermi and GT transitions are allowed for the proton target. On the other hand, only GT transition is allowed for the deuteron target provided that the relative energy between two neutrons in the final state is small. Most of the final states $^{11}\text{Be}^*$ are particle unbound and decay into more than two particles. For the IAS, only the decay channel $^9\text{Li}+p+n$ is allowed by the isospin selection rule, namely the isospin of the IAS ($T = 5/2$) can be constructed from the $^9\text{Li}+p+n$ ($T = 3/2, 1/2$, and $1/2$) combination only. The excitation energy of $^{11}\text{Be}^*$ was determined by reconstructing the invariant mass from momentum vectors of outgoing particles. Since the outgoing particles are kinematically focused due to the characteristics of inverse kinematics, relatively high efficiency of the coincidence detection is achieved.

A 63 MeV/nucleon ^{11}Li beam from the RIPS facility at RIKEN was used to bombard $(\text{CH}_2)_n$ and $(\text{CD}_2)_n$ targets (200 mg/cm²). The final state particles emitted from $^{11}\text{Be}^*$ were detected by ΔE - and E - hodoscopes which consisted of 13 and 33 plastic scintillators, respectively. Charged particles were identified by combining ΔE -, E - signals with time-of-flight (TOF) information between the target and hodoscopes. Particles which produced signals in E -hodoscope (12 cm thick), but not in ΔE -hodoscope (0.5 cm thick), were identified as neutrons. The momentum vector of a par-

ticle was obtained by the TOF and position information of the hodoscopes. The invariant masses of the final states $^{11}\text{Be}^*$ were constructed from the momentum vectors. Carbon-target runs were also performed in order to estimate the background contribution.

The relative energy spectra of the $^9\text{Li}+p+n$ channel with H and D targets are shown in Fig. 1. A peak at $E(^9\text{Li}+p+n) \sim 1.0$ MeV ($E_X(^{11}\text{Be}) \sim 21.2$ MeV) was found in the spectrum for the H target, while no sharp peak was found for the D target. Thus, the peak can be regarded as the IAS of ^{11}Li . The Coulomb displacement energy ΔE_C is about 1.3 MeV, consistent with a value $\Delta E_C = 1.1$ MeV of the formula (1). Taking into account the resolving power of the relative energy in the present detector system, the natural width of the peak was deduced to be about 0.5 MeV (FWHM). The width is somewhat larger than those of IAS's for stable nuclei. Two theoretical predictions^{2,3)} show that the width is sensitive to the configuration of the valence neutrons in ^{11}Li . The scattering angle distributions of $^{11}\text{Be}^*$ for $^9\text{Li}+p+n$ channel with H and D targets indicate that the dominant component of the angular momentum transfer Δl is zero. Analysis for channels related to the GT transitions ($^9\text{Li}+d$, $^8\text{Li}+t$, $^6\text{He}+^4\text{He}+n$, and so on) is now in progress.

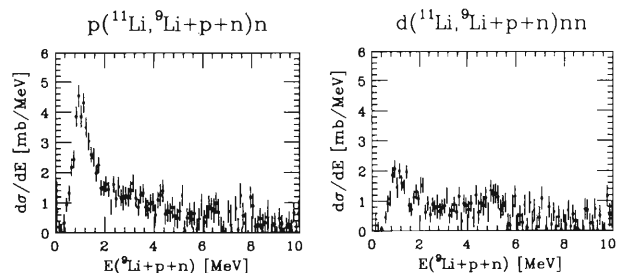


Fig. 1. Relative energy spectra for $^9\text{Li}+p+n$ channel with H (left) and D (right) targets.

References

- 1) J. D. Anderson et al.: *Phys. Rev.*, **138**, B615 (1965).
- 2) Y. Suzuki and K. Yabana: *Phys. Lett.*, **B272**, 173 (1992).
- 3) M. V. Zhukov et al.: preprint NORDITA-95/32 N.

Coulomb Dissociation of ${}^8\text{B}$

T. Kikuchi, T. Motobayashi, N. Iwasa,^{*1} S. Moriya, Y. Ando, H. Murakami, S. Shimoura, T. Teranishi, Y. Yanagisawa, T. Nishio, T. Uchibori, T. Nakamura, M. Hirai, Y. Watanabe, H. Sakurai, S. Kubono, M. Gai, R. H. France III,^{*2} K. I. Hahn,^{*} C. Michotte,^{*3} P. Lipnik,^{*3} and T. Delbar^{*3}

[${}^{208}\text{Pb}({}^8\text{B}, p){}^7\text{Be}$] ${}^{208}\text{Pb}$; Coulomb Dissociation.]

The first experiment of Coulomb dissociation of ${}^8\text{B}$ ¹⁾ showed the usefulness of the Coulomb dissociation method in studying the ${}^7\text{Be}(p, \gamma){}^8\text{B}$ reaction at low energies. At the same time, it showed some problems of this method and one of the most important was in the estimation of the multipolarity.

For the Coulomb dissociation of ${}^8\text{B}$, $E1$ excitation is dominant and some mixture of $E2$ excitation is possible. For the setup of the first experiment, $E2$ contribution was estimated at 15% of the $E1$ amplitude at 1 MeV using a theoretical calculation of the cross section for the ${}^7\text{Be}(p, \gamma){}^8\text{B}$ reaction at low energies.²⁾ However, we could not distinguish the $E2$ excitation from the $E1$ experimentally.

Since the $E2$ excitation becomes dominant at large angles, it is important to cover a wide angular range to distinguish $E2$ from $E1$. Recently, we performed the second experiment with a new setup covering a wider angular range. Additionally, we improved energy and angular resolution in the setup.

The experiment was performed at RIKEN using RIPS. A ${}^8\text{B}$ radioactive beam of 52 MeV/nucleon was used with a ${}^{208}\text{Pb}$ target of 50 mg/cm². The typical intensity of the beam was 2×10^4 /sec. The dissociation products, proton and ${}^7\text{Be}$, were measured by a plastic scintillator hodoscope placed at 3.1 m downstream from the target. A helium bag was inserted between the target and the hodoscope to reduce the dissociation in the air. The hodoscope covers the area of 1×1 m² and it consists of 13 strips of ΔE counters (5 mm thick) and 18 strips of E counters (6 cm thick). Surrounding the target position, 56 NaI (Tl) scintillators were located to detect the γ rays from the excited ${}^7\text{Be}$ nuclei, which are associated with another possible channel of the dissociation process. Hitting positions in the hodoscope and the TOF between the target and the hodoscope were measured. From this information, we constructed the p - ${}^7\text{Be}$ relative energy and the scattering angle of the p - ${}^7\text{Be}$ center-of-mass.

The experimental results for the relative energy spectrum and angular distribution are shown in Fig. 1. The solid curves show the results of Monte-Carlo

simulation calculations with a constant $S_{17} = 22$ eV-b assuming pure $E1$ transition. Note that the calculations take account of the detector efficiency. The angular distribution is integrated over the energy range of $E_{rel} = 0.5$ – 3.0 MeV. Both distributions show good agreement with the simulation results. Especially, the angular distribution at large angles suggests that the mixture of $E2$ transition is rather small. Further analysis is now in progress.

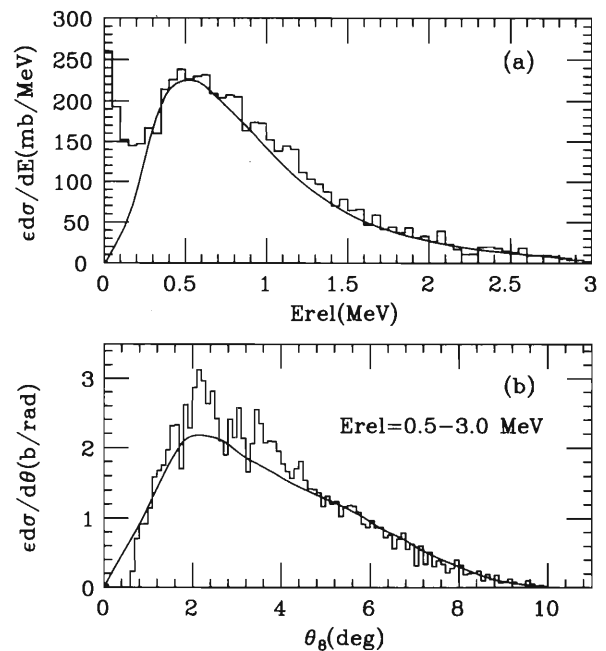


Fig. 1. (a) Measured p - ${}^7\text{Be}$ relative energy spectrum. (b) Yields plotted versus angles of the p - ${}^7\text{Be}$ center-of-mass that are integrated over the energy range $E_{rel} = 0.5$ – 3.0 MeV. The solid curves show the results of Monte-Carlo simulation.

References

- 1) T. Motobayashi et al.: *Phys. Rev. Lett.*, **73**, 2680 (1994).
- 2) K. H. Kim et al.: *Phys. Rev.*, **C35**, 363 (1987).

^{*1} GSI, Germany

^{*2} Department of Physics, Yale University, U.S.A.

^{*3} Institut de Physique Nucléaire, Université Catholique de Louvain, Belgium

Coulomb Dissociation Reaction and Neutron-Neutron Correlation in $^{11}\text{Li}^\dagger$

S. Shimoura, T. Nakamura, M. Ishihara, N. Inabe, T. Kobayashi, T. Kubo, R. H. Siemssen,*
I. Tanihata, and Y. Watanabe

[NUCLEAR REACTIONS heavy-ion collision, radioactive beam, Coulomb dissociation,]
Pb(^{11}Li , $^9\text{Li}+2\text{n}$)X, soft $E1$ mode.

We have performed a full exclusive measurement of the Coulomb dissociation reaction, Pb(^{11}Li , $^9\text{Li} + 2\text{n}$)X, at an incident energy of 43 A MeV. An excitation energy spectrum of ^{11}Li deduced from the invariant mass of the three body system, $^9\text{Li} + 2\text{n}$, shows a prominent peak around 1 MeV with a large tail towards higher excitation energies (Fig. 1). The relative energy spectrum between the observed two neutrons shows a peak with very small energy below 100 keV, which is much smaller than the excitation energy of $^{11}\text{Li}^*$ (Fig. 2). These characteristics are well reproduced by a direct breakup model with an extended

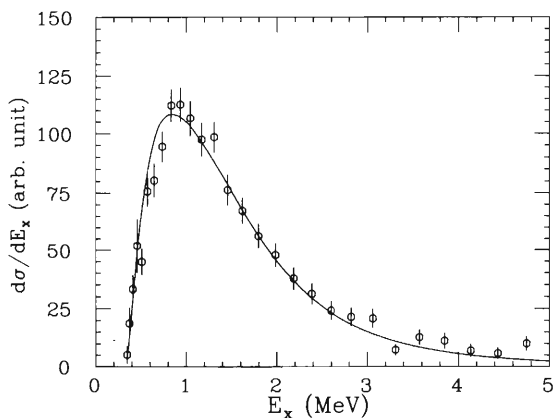


Fig. 1. Excitation energy spectrum of ^{11}Li spectrum. Solid lines represent the prediction of the direct up model.

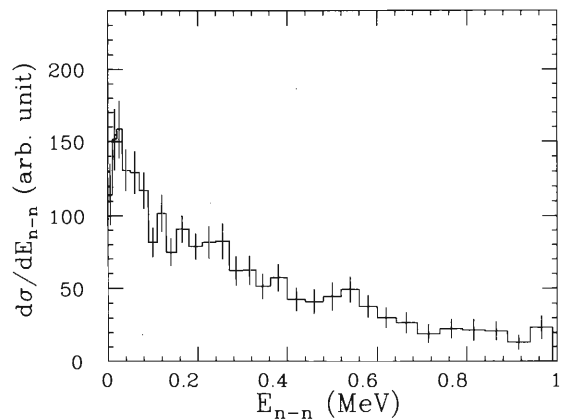


Fig. 2. Relative energy spectrum of the observed two neutrons.

di-neutron cluster model, where the ground state of the ^{11}Li nucleus consists of the core and the di-neutron with a distributed mass spectrum. Taking into account the final state interaction between the two halo neutrons, the *rms* of the neutrons is deduced to be 5.1 fm, whereas the *rms* of the distance between the two neutrons is 7.0 fm. The correlation between the halo neutrons, $\langle \vec{r}_1 \cdot \vec{r}_2 \rangle / \sqrt{\langle r_1^2 \rangle \langle r_2^2 \rangle}$ is deduced to be close to zero, where \vec{r}_1 (\vec{r}_2) denotes the radial vector of each neutron with respect to the *c.m.* of the ^{11}Li nucleus. In terms of the shell-model description this result is compatible with the situation where the two neutrons move almost independently or the correlated two particles are attributed to a fairly pure configuration $[j^2]_{J=0}$ with a particular *j*-value.

[†] Condensed from the article in Phys. Lett., **B348**, 29 (1995)

* KVI, University of Groningen, The Netherlands

Coulomb Excitation of a Halo Nucleus ^{11}Be

T. Nakamura, T. Motobayashi, H. Sakurai, S. Shimoura, T. Teranishi, Y. Yanagisawa, and M. Ishihara

[NUCLEAR REACTION $^{11}\text{Be} + ^{208}\text{Pb}$, $E(^{11}\text{Be}) = 64$ MeV/u, Coulomb excitation neutron halo, $B(E1)$.]

Coulomb excitation reaction using an intermediate energy radioactive nuclear beam has been proven to be a useful tool in investigating the structures of nuclei far from the stability. One advantage is that the reaction mechanism is comparatively well understood. Extraction of the relevant reduced matrix element may be made by the equivalent photon method based on the first order perturbation or by a simple coupled-channel calculation. However, the validity of these methods is in some cases questioned due to the ambiguities caused by the higher order excitations or by the nuclear excitation contribution.

The present experiment investigates the ^{11}Be Coulomb excitation to its first excited state ($E1: 1/2^+ \rightarrow 1/2^-$, $E_x = 320$ keV) in order to perform a rigorous test of our understanding of the Coulomb excitation process. Its inverse transition was formerly studied by measuring the life time,¹⁾ so that we may compare the deduced $B(E1)$ strength with that obtained in the life-time measurement. On the other hand, the previous result on the Coulomb excitation of ^{11}Be at GANIL²⁾ provided a result contradictory to the life-time measurement. It is, thus, of importance to examine the relevant Coulomb excitation via an independent experiment.

The experiment was performed at RIKEN Ring Cyclotron. A secondary ^{11}Be beam was almost purely (over 98%) separated via the fragment separator RIPS. The beam with a mean energy of 64 MeV/u impinged upon a ^{208}Pb target with thickness of 350 mg/cm². The Coulomb excitation cross section was obtained by measuring the de-exciting γ rays in coincidence with the scattered ^{11}Be particles. The γ rays were detected with 54 NaI(Tl) plastic scintillators, each of which is of rectangular shape with size of $6 \times 6 \times 12$ cm³, surrounding the target from 66 to 154 degrees in the laboratory frame. The inelastically scattered ^{11}Be particles were detected and identified with a $\Delta E - E$ plastic scintillator telescope located 3.1 m downstream of the target. The maximum scattering angle detectable with the telescope was 9.0 degree, which is much larger than the grazing angle 3.7 degree for the relevant reaction.

Figure 1 shows the obtained γ -ray energy spectrum in the $^{11}\text{Be} + ^{208}\text{Pb}$ inelastic scattering, where the Doppler shifts caused by the source velocity ($v = 0.35 c$) were corrected according to the angle of each detector. Accidental coincidence events were subtracted in Fig. 1 by using the data obtained by setting a gate at the region beside the true-coincidence peak in the timing spectrum of γ rays. As clearly seen in the figure, only one photo-peak at 320 KeV corresponding

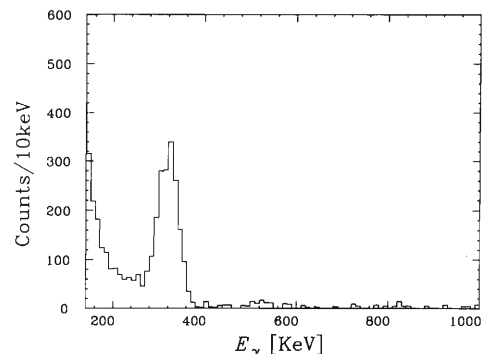


Fig. 1. De-excitation γ -ray energy spectrum in the inelastic scattering of $^{11}\text{Be} + ^{208}\text{Pb}$ measured by NaI(Tl) counters. Doppler shifts are corrected in the spectrum.

to the $1/2^- \rightarrow 1/2^+$ transition was observed. Since the 320 KeV state is the only one bound state of the ^{11}Be nucleus, this de-excitation γ rays have to be fed only via the excitation of the ^{11}Be ground state to the $1/2^-$ state. The excitation cross section was obtained to be 302 ± 8 (statistical) ± 30 (systematic) mb.

Utilizing the equivalent photon method, the $B(E1)$ value for the relevant excitation was extracted. As a cutoff impact parameter, we adopted 12.3 fm, which was determined from the impact parameter dependence observed in the Coulomb dissociation of ^{11}Be .³⁾ The obtained $B(E1)$ amounts to 0.099 ± 0.010 e²fm². We also analyzed the angular distribution of scattered ^{11}Be particles. The distribution was compared with the calculated distribution obtained by a coupled channel calculation code ECIS incorporating the finite energy- and angular spreads of the beam, angular resolution of the detector, and the multiple scattering effect by a Monte-Carlo simulation. The best fit deformation parameter β was obtained to be 0.124 ± 0.007 (statistical) ± 0.007 (systematic), which corresponds to $B(E1) = 0.100 \pm 0.017$ e²fm².

The present results in both analysis procedures are in good agreement with the value 0.116 ± 0.012 e²fm² obtained from the life-time measurement. This fact demonstrates the validity of the Coulomb excitation at intermediate energies. The higher order effects and nuclear excitation contribution were found to be as small as about 10%, if any.

References

- 1) D. J. Millener et al.: *Phys. Rev.*, **C28**, 497 (1983).
- 2) R. Anne et al.: *Z. Phys. A*, in press.
- 3) T. Nakamura et al.: *Phys. Lett.*, **B331**, 296 (1994).

Coulomb Excitation of ^{56}Ni

Y. Yanagisawa, T. Motobayashi, S. Shimoura, K. Ieki, Y. Ando, T. Nishio,
S. Moriya, Y. Iwata, T. Kikuchi, T. Uchibori, T. Nakamura, M. Notani,
N. Aoi, T. Teranishi, H. Sakurai, M. Ishihara, and J. Péter*

[$^{208}\text{Pb}(^{56}\text{Ni}, ^{56}\text{Ni} \gamma)^{208}\text{Pb}$, Coulomb excitation, deduced $B(E2)$.]

Recently, Coulomb excitation at several tens MeV/nucleon has been studied using unstable beam.¹⁾ From the spectroscopic view point, the electromagnetic excitations are properties useful in studying basic structures of the nuclei. We studied the Coulomb excitation of double magic nucleus ^{56}Ni using a 70.7 MeV/nucleon ^{56}Ni beam provided by the RIPS facility of the Riken Ring Cyclotron. A ^{208}Pb target of 350 mg/cm² thickness was set in the air at the focal point of the RIPS, and was bombarded by a ^{56}Ni beam with 500 s⁻¹ intensity.

Scattered ^{56}Ni nuclei were detected by a counter telescope placed at 15 cm from the target after passing through a 25 μm thick mylar window. The telescope consisted of two surface barrier silicon detectors. The first detector has a 60 \times 60 mm² effective area and 400 μm thickness, and the second is of octagon shape with 36 cm² effective area and 1 mm thickness. The detected charged particle was identified by the ΔE -E method. The excitation to the 2⁺ state of ^{56}Ni was identified by measuring the γ -ray deexcitation of the 2⁺ state in coincidence with the scattered ^{56}Ni particles.

Sixty NaI(Tl) scintillators were placed around the target to detect the γ rays. Each scintillator crystal is of rectangular shape with size 6 \times 6 \times 12 cm³ coupled with a 5.1 cm ϕ photomultiplier tube. Their energy resolution was typically 7.5% for the 662 keV γ ray. A 0.5 mm thick plastic scintillator was placed in front of the silicon detector telescope to obtain a timing signal providing the coincidence condition with the γ -ray detector.

Figure 1 shows the γ -ray spectrum for the $^{56}\text{Ni} + ^{208}\text{Pb}$ inelastic scattering after the doppler shift correction. As clearly seen in Fig. 1, a full-energy peak at 2.7 MeV corresponding to the 2⁺ \rightarrow 0⁺ transition was observed. The excitation cross section was extracted with photo-peak efficiency calculated by a simulation code GEANT. The calculated spectrum was in good agreement with the experimental one around the

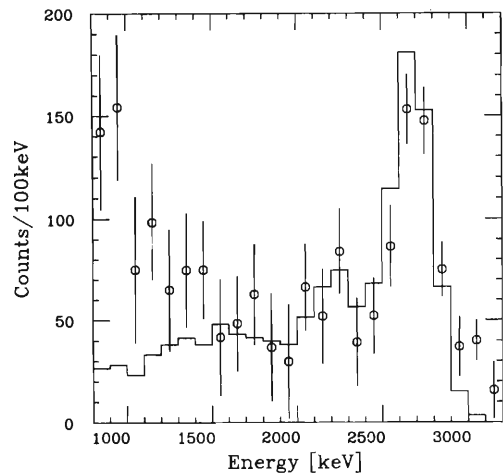


Fig. 1. Doppler-corrected spectrum for γ -ray energy emitted from the $^{56}\text{Ni} + ^{208}\text{Pb}$ inelastic scattering at $E_{in} = 70.7$ MeV/nucleon incident energy. The histogram shows the simulation result. (see the text)

peak. (See, Fig. 1)

An experimental deformation parameter β_C was extracted by comparing the predicted cross section obtained by a coupled channel calculation code ECIS with the experimental one. Since the parameter β_C is directly related to $B(E2)$, a preliminary $B(E2)$ value for the ^{56}Ni 2⁺ excitation was obtained. The result, $B(E2 : 0^+ \rightarrow 2^+) = 510 \pm 100 \text{ e}^2\text{fm}^4$, agrees with the values deduced from an analysis of the $^{56}\text{Ni} + \text{p}$ inelastic scattering²⁾ within errors. Note that the error quoted above contains systematic uncertainties. An effort to reduce the uncertainties is in progress.

References

- 1) T. Motobayashi et al: *Phys. Lett.*, **B346**, 9 (1995).
- 2) G. Kraus et al: *Phys. Rev. Lett.*, **B264**, 1773 (1994).

* Laboratoire de Physique Corpusculaire, IN2P3-CNRS, ISMRA and Université de Caen, France

Neutron Skin of Na Isotopes Studied via Their Interaction Cross Sections

T. Suzuki, H. Geissel,* O. Bochkarev,** L. Chulkov,** M. Golovkov,** D. Hirata, H. Irnich,* Z. Janas,* H. Keller,* T. Kobayashi, G. Kraus,* G. Münzenberg,* S. Neumaier,* F. Nickel,* A. Ozawa, A. Piechaczek,* E. Roeckl,* W. Schwab,* K. Suemmerer,* K. Yoshida, and I. Tanihata

In order to obtain more direct information concerning the neutron skin, we measured σ_I , determined the effective root-mean-square (*rms*) matter radii ($\tilde{r}_m \equiv \langle r_m^2 \rangle^{1/2}$), and deduced the rms neutron radii ($\tilde{r}_n \equiv \langle r_n^2 \rangle^{1/2}$) for a chain of Na isotopes in the mass range from $A = 20$ to 32 comparing with the *rms* charge radii ($\tilde{r}_c \equiv \langle r_c^2 \rangle^{1/2}$) determined by isotope-shift measurements.¹⁾

The experiment²⁾ was performed at the projectile FRagment Separator (FRS) facility at GSI. We applied the optical limit of the Glauber model to obtain the effective *rms* radii (\tilde{r}_k). Suffix k denotes $p(c)$ for the proton (charge) distribution and $n(m)$ for the neutron (matter) distribution, respectively. As for the form of the density distribution of projectiles, we used the Fermi-type distribution for both protons and neutrons. Namely, the density $\rho k(r)$ at a distance r is given by

$$\rho k(r) = \rho k(0) / [1 + \exp((r - R_k)/d_k)]$$

where the parameter R_k is the half-density radius and d_k is the surface diffuseness. Suffix k indicates a proton or neutron. It was found that the Fourier transformation of the longitudinal form factor ($|F_L(q)|$), measured in elastic electron scattering on ^{23}Na ,³⁾ could be well fitted by the above equation for $r < 4.0$ fm, while the covered range of the momentum transfer (q) was limited as $0.25 < q < 2$ fm⁻¹. The fitted parameters for the proton distribution in ^{23}Na ($R_p = 3.137$ fm, $d_p = 0.564$ fm) gave the value $\tilde{r}_p = 2.829$ fm, which agrees with \tilde{r}_p obtained from the experimental value of \tilde{r}_c . There are four parameters ($R_p, R_n, d_p,$ and d_n) in these distributions. On the other hand, only two quantities were experimentally determined. Therefore, we have to assume further conditions between the parameters in order to deduce the density distribution or the effective *rms* radius. To see the sensitivity of the assumption to the final results, we applied two extreme assumptions: a) $R_n(^A\text{Na}) = r_0 N^{1/3}$, and $R_p(^A\text{Na}) = R_n(^{23}\text{Na}) = 3.137$ fm (the value obtained for ^{23}Na) and b) $d_p(^A\text{Na}) = d_n(^A\text{Na}) = 0.564$ fm (the value obtained at ^{23}Na). In assumption a), the densities are considered to change only due to changes in the surface diffuseness, except for the $N^{1/3}$ dependence of R_n . On the other hand, all changes are put into changes of R_k in assumption b). We consider that

a realistic change would be in between these two assumptions.

In the following we restrict ourselves to a discussion based on the result from case b), however, the discussion does not differ if we use case a). In Fig. 1 ΔR is plotted against the difference between the neutron and proton separation energy or the Fermi-energy difference ($S_p - S_n$). For nuclei having an even neutron number, we took S_n as half of the two-neutron separation energy. It can be seen that ΔR has a strong correlation with $S_p - S_n$, for the first time. Such a correlation has been predicted by the RMF model,⁴⁾ and is shown by the shadow in Fig. 1. The experimental data agree well with the prediction.

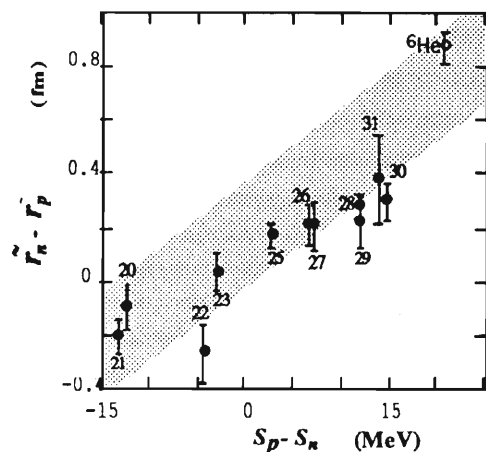


Fig. 1. The two-dimensional plot of the difference between the proton separation energy and that of a neutron ($S_p - S_n$) versus the thickness of the neutron skin ($\tilde{r}_n - \tilde{r}_p$). The corresponding mass number is indicated at each data point. The shaded area shows the calculated correlation for various isotopes ranging from helium up to lead.

References

- 1) G. Huber et al.: *Phys. Rev.*, **C18**, 2342 (1978).
- 2) T. Suzuki et al.: *Phys. Rev. Lett.*, **75**, 3241 (1995).
- 3) R. P. Singhal et al.: *J. Phys.*, **G8**, 1059 (1982).
- 4) I. Tanihata et al.: *Phys. Lett.*, **B289**, 261 (1992).

* Gesellschaft für Schwerionenforschung, Germany

** Kurchatov Institute, Russia

Interaction Cross Sections and Radii of Light Nuclei

A. Ozawa, T. Kobayashi, Y. Sugahara, I. Tanihata, O. Yamakawa,*¹
K. Omata, K. Sugimoto,*² D. Olson,*³ W. Christie,*³ and H. Wieman*³

[NUCLEAR REACTIONS Be,C,Al,(¹⁵B, ¹⁵B)X, Be,C,Al,(⁹C, ⁹C)X, Be,C,Al,(¹⁰C, ¹⁰C)X,
Be,C,Al,(¹⁵C, ¹⁵C)X, Be,C,Al,(¹³N, ¹³N)X, Be,C,Al,(¹³O, ¹³O)X, Be,C,Al,(¹⁴O, ¹⁴O)X,
Be,C,Al,(¹⁵O, ¹⁵O)X, $E/A = 730$ MeV; measured interaction cross sections σ_I , deduced
root mean square radii.]

The recent development of radioactive nuclear beams provides new measurements of the radii of unstable light nuclei at the relativistic energy.¹⁻⁶ In these papers, isotope, isospin, and energy dependence of the radii are shown.^{3,4,6} Furthermore, combining the recent development in measurements of quadrupole moments, some interesting systematics was shown.⁵ To extend the stream of the study, we have to know the unknown radii of other light nuclei.

The secondary beams of radioactive isotopes ¹⁵B, ⁹C, ¹⁰C, ¹⁵C, ¹³N, ¹³O, ¹⁴O, and ¹⁵O were produced through the projectile fragmentation of ¹²C (for ⁹C), ¹⁸O (for ¹⁵B and ¹³N), ²⁰Ne (for ¹⁰C, ¹⁵C, ¹³O, and ¹⁴O), and ²²Ne (for ¹⁵O) primary beams (800 A MeV) accelerated by the Bevalac at the Lawrence Berkeley Laboratory. The secondary beams produced in a Be target were separated by their rigidity using a beam transport line, and the interaction cross section (σ_I) was measured by means of a transmission method with Be, C, and Al targets at a mean energy of around 730 A MeV, using a large acceptance spectrometer (HISS) as described in previous papers.^{1,2} The ¹⁵B values in this work are consistent with the previous values³ but have much better accuracy. The effective root-mean-square (RMS) radii of the nucleon distribution have been deduced from the σ_I 's using Glauber model calculations, of which the details are described in Ref. 2. The RMS radii were deduced from the σ_I 's by use of the Harmonic-Oscillator (HO) type density distributions.

Figure 1 shows the effective RMS matter radii as a function of the isotopes in B, C, N, and O. In the figure, the RMS matter radii calculated from the observed RMS charge radii are also shown for the stable nuclei. In the calculation, we used HO type density distributions and determined the RMS matter radii to reproduce the observed RMS charge radii. In the C, N, and O isotopes, the radii of the most proton-rich nuclei (⁹C, ¹²N, ¹³O) are larger than the ones of their neighbors. The observed global tendency of isotope dependence can be quantitatively reproduced by relativistic mean field (RMF) calculations.

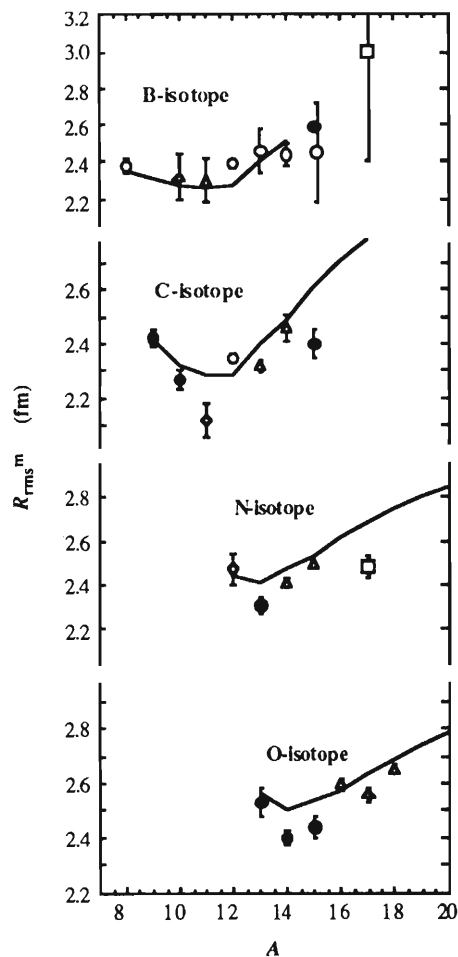


Fig. 1. The effective RMS matter radii (R_{rms}^m) for B, C, N and O isotopes. Closed circles are data points obtained in the present work, open circles are from Ref. 3, open squares from Ref. 4, open rhombuses from Ref. 5, and the lines are calculated radii by RMF. Open triangles are the radii calculated from the observed RMS charge radii.

References

- 1) I. Tanihata et al.: *Phys. Lett.*, **B160**, 380 (1985).
- 2) I. Tanihata et al.: *Phys. Rev. Lett.*, **55**, 2676 (1985).
- 3) I. Tanihata et al.: *Phys. Lett.*, **B206**, 592 (1988).
- 4) A. Ozawa et al.: *ibid.*, **B334**, 18 (1994).
- 5) A. Ozawa et al.: *Nucl. Phys.*, **A583**, 807 (1995).
- 6) T. Suzuki et al.: *Phys. Rev. Lett.*, **75**, 3241 (1995).

*¹ Fukui Prefectural University

*² Osaka University

*³ LBL, Berkeley, U.S.A.

Structure of ^{10}Li Studied by Pion Double Charge Exchange Reaction $^{10}\text{B}(\pi^-, \pi^+)^{10}\text{Li}$

T. Kobayashi, K. Tanaka,* D. Smith,** R. Ivie,** P. Hui,** and T. Fortune**

[NUCLEAR REACTIONS $^{10}\text{B}(\pi^-, \pi^+)$, $E(\pi^-) = 160$ MeV, deduced positions of ground and excited states.]

The structure of ^{11}Li , which is known to have a neutron halo, is most commonly treated as a 3-body system of $^9\text{Li} + n + n$ by various theoretical groups. In this case, the interaction of $^9\text{Li} + n$, i.e., ^{10}Li resonance, becomes important. There were several experiments on ^{10}Li in the past, however, results are not consistent with each other. In the isotope with a neutron number 7, the relative position of $\nu p_{1/2}$ and $\nu 2s_{1/2}$ orbitals is becoming closer from oxygen to boron, and the $\nu 2s_{1/2}$ orbital becomes a ground state in ^{11}Be . In ^9He , however, a $\nu p_{1/2}$ state becomes again a ground state. Therefore, it is an interesting question whether the ground state of ^{10}Li , which is located between ^9He and ^{11}Be , is a neutron p-wave or s-wave state.

The measurement was performed using the EPICS spectrometer at LAMPF. The pion-induced double charge exchange reaction, $^{10}\text{B}(\pi^-, \pi^+)^{10}\text{Li}$, was measured at a laboratory angle of 5° and at an incident energy of 164 MeV. The spectrum is shown in Fig. 1. The resolution in the Q-value spectrum was tested by the elastic scattering, $^{10}\text{B}(\pi^-, \pi^-)^{10}\text{B}$, and it was about 0.4 MeV FWHM. It can be seen that there are structures near the threshold and around 5 MeV.

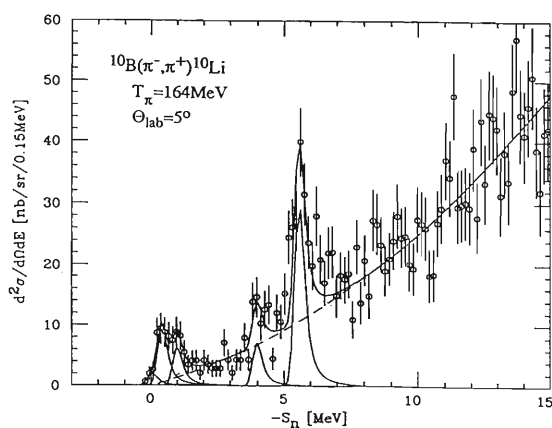


Fig. 1. Spectrum of $^{10}\text{B}(\pi^-, \pi^+)^{10}\text{Li}$ at 164 MeV.

If the structure near the threshold is analyzed assuming a single peak, the width of the peak becomes 0.8 MeV. It is too narrow for an s-wave, and too wide for a p-wave. The peak was then fitted assuming a doublet using an elastic line shape, and peaks at 0.33, 0.93, 3.98, and 5.56 MeV were found. Then the fit-

ting was repeated taking into account the width of the states. The width of the first 2 peaks is about 0.4 MeV, and that of the second 2 peaks is about 0.8 MeV. These widths are consistent with p-wave and d-wave, respectively.

For a possible s-wave resonance near the threshold, a small amount of deviation from the fitting is observed on the left side of the peak if the peak is fitted as a doublet. The fitting is repeated assuming a triplet. The energy of the 1st peak, corresponding to the possible s-wave resonance, is very close to the threshold: about 0.02 MeV. But the existence of this peak is not conclusive since there is no appreciable decrease of chi square in the fitting. Observed states are summarized in Fig. 2.

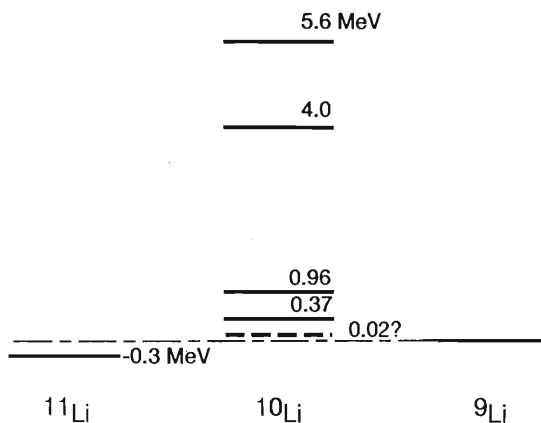


Fig. 2. States in ^{10}Li from the present measurement.

Our measurement agrees with that by H.G. Bohlen, who concluded that there are p-wave doublets at 0.42 and 0.8 MeV. When the spectrum by Young, who concluded that there is only one peak around 0.54 MeV, is checked closely, there is a deviation from the fitting on the left side of the peak. There may be still a possibility that their spectrum can be fitted with a doublet. From the present measurement, we believe that it is conclusive that there are two p-wave states within 1 MeV from the threshold.

References

- 1) H. G. Bohlen et al.: *Z. Phys.*, **A344**, 381 (1993).
- 2) B. M. Young et al.: *Phys. Rev.*, **C49**, 271 (1994).

* Physical Division, KEK

** Physical Division, University of Pennsylvania, U.S.A.

RHIC Spin Project

H. En'yo, K. Hatanaka, T. Ichihara, K. Imai, T. Katayama, A. Masaike, M. Okamura, N. Saito, Y. Sakemi, T.-A. Shibata, H. Sato, Y. Watanabe, H. Wu, M. Yosoi, and M. Ishihara

[*pp* interaction, structure function, spin, asymmetry, polarized beam.]

We promote the high energy spin physics project, the RHIC spin project, utilizing the Relativistic Heavy Ion Collider (RHIC) at Brookhaven National Laboratory (BNL) in collaboration with BNL. One of the major goals of the project is to solve so-called proton spin crisis. The project will open a new field combining the high-energy hadron physics and nuclear physics.

The project consists of two major parts, (1) acceleration of the polarized protons at RHIC and (2) construction of a muon-pair detector system. In this paper, the overview of the project is described. Following two papers present the conceptual designs of those experimental apparatus and the spin control devices for polarized beam acceleration.

The study of spin-dependent effects in deep inelastic scattering (DIS) has renewed the interest of the structure of the proton. The result of European Muon Collaboration experiment¹⁾ was interpreted as a very small quark contribution to the proton spin. Possible solutions of this problem are an unexpectedly polarized gluon or a sea-quark in the proton. In the process of the DIS, however, a gluon does not participate at the leading order and the sea-quark contribution cannot be separated from the quark contribution. In the case of proton-proton collision, gluon contents can be probed by high- p_T prompt photon production and heavy quark production at the leading order; an anti-quark can be tagged in W -production and Drell-Yan process. Thus such an experiment will provide completely new information on the spin structure of the proton.

The physics goals of the RHIC spin project are to elucidate the spin structure of the proton, and to test the standard model mainly via the parity violating process.

The RHIC complex for polarized proton beam acceleration is shown in Fig. 1. The polarized source, linac, booster, and AGS exist. To maintain the proton polarization during its acceleration, the partial siberian snake should be installed in AGS, and the full siberian snakes should be installed in the RHIC main ring. The full siberian snakes will be constructed by RIKEN.

The energy of the polarized proton beam will be variable from 25 to 250 GeV, where the center-of-mass energies are 50 and 500 GeV, respectively. The luminosity is expected to reach to $2 \times 10^{32} \text{ cm}^{-2} \text{ sec}^{-1}$. At the highest energy, 500 GeV, production of weak bosons is copious. Thus it is suitable to study parity violating effects. The variability of the beam energy

will allow us the study of Q^2 -dependence of the polarized structure functions, and the precision test of QCD is possible.

There are two major experiments, PHENIX and STAR. The STAR has the TPC-based detector system which covers the pseudo rapidity region, $|\eta| < 1.2$. The PHENIX, which we participate in, has two parts; a central arm covering $|\eta| < 0.35$; a muon-pair detector system which covers $1.2 < |\eta| < 2.4$. The latter part is going to be constructed by RIKEN. The PHENIX is advantageous in the capability of the particle identification and a powerful trigger system. Two experiments are complimentary.

The construction of both of the accelerator devices and experimental apparatus is scheduled to be completed until the end of March, 1999. The first collision is expected on April 1, 1999.

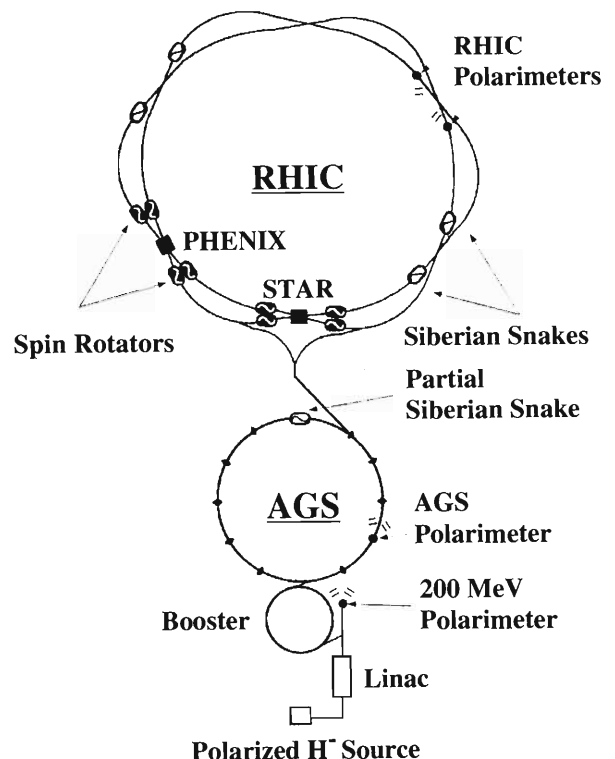


Fig. 1. Schematic representation of the RHIC accelerator complex.

References

- 1) J. Ashman et al.: *Phys. Lett.*, **B264**, 306 (1988).

Muon Pair Detector System for RHIC Spin Project

H. En'yo, T. Ichihara, K. Imai, A. Masaïke, N. Saito, Y. Sakemi, T.-A. Shibata,
Y. Watanabe, M. Yosoi, and M. Ishihara

[pp interaction, structure function, spin, asymmetry, polarized beam.]

We are constructing a muon-pair detector system for the RHIC Spin Project at Brookhaven National Laboratory (BNL). It is a part of the PHENIX detector system for Relativistic Heavy Ion Collider (RHIC).¹⁾

The detection of the muons with high momentum resolution is the key to making the physics outputs maximal. For example, we are going to detect muons with a high transverse momentum from W^\pm decays. The momentum of such a muon provides a good measure of the momentum fraction, x , which is carried by the initial quarks. Thus measurements of the muon momentum with high resolution leads to good resolution of x .

Figure 1 shows the muon-pair detector system schematically. Other components are not shown for clarity. The muon-pair detector system covers the pseudo rapidity region, $1.2 < |\eta| < 2.4$. It consists of three parts: a muon magnet, muon tracking chambers, and a muon identifier.

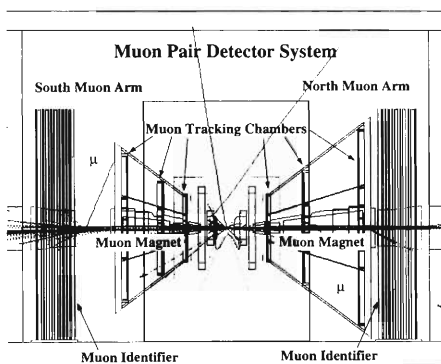


Fig. 1. Plan view of the muon-pair detector system. Overlaid is a typical event of Z^0 production in pp collision at $\sqrt{s} = 500$ GeV.

The muon magnet is to analyze the momentum of a muon with high resolution. The integrated magnetic field is about 7500 and 2500 Gauss \times m at $\theta = 15^\circ$ and 30° , respectively.

The tracking chamber system utilizes Cathode Strip Readout Chamber technology and comprises three stations. Each station has the three gas volumes with the structure of fine cathode plane, anode wire plane, and coarse cathode plane. The spatial resolution of the fine cathode plane is expected to be 100 microns.

The muon identifier consists of six layers of muon detectors and five layers of hadron absorbers inserted between the muon detectors. The muon detector is a

plastic proportional tube. The cell size of the tube is 0.9 cm and eight separate cells are in one counter. The counter is about 5 m long and 8.3 cm wide.

Each layer has two x and y planes with one staggered to the other by a half cell to eliminate the geometrical inefficiency of a single plane.

The performance of the muon tracking system has been studied utilizing GEANT²⁾ based simulation. Inclusive production of Z^0 in pp collision at $\sqrt{s} = 500$ GeV has been simulated with PYTHIA³⁾ for this purpose. A typical event is displayed in Fig. 1. In this simulation the detector response has been fully simulated, i.e. the signals in the tracking chambers have been simulated and momentum reconstruction has been performed.

Resulting dimuon mass resolution at Z^0 is shown in Fig. 2. The spectrum has been fitted to Breit-Wigner form smeared with Gaussian resolution. The mass resolution of 5.3 GeV/ c^2 has been obtained. With the requirements of muon penetration up to the 6-th layer of the muon identifier, the Z^0 identification efficiency is 96%.

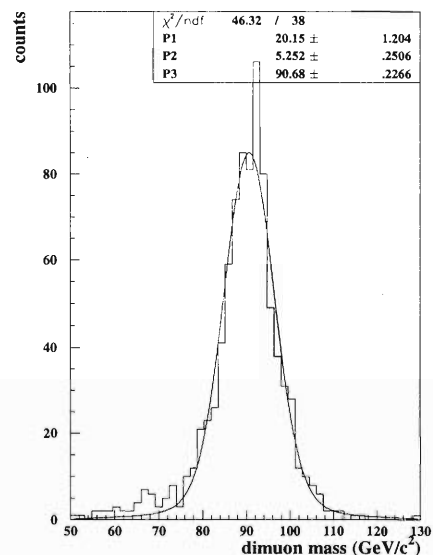


Fig. 2. Dimuon mass spectra in Z^0 production in pp collision at $\sqrt{s} = 500$ GeV.

References

- 1) H. En'yo et al.: This report. p. 80.
- 2) GEANT: CERN Library Long Write-up, W5013.
- 3) H.-U. Bengtsson and T. Sjöstrand: *Comput. Phys. Commun.*, **46**, 43 (1987); CERN-TH. 6488/92 and references therein.

2. Atomic and Solid-State Physics

Resonances in Photodetachment of $H^-(2p^2, 3P^e)$

J.-Z. Tang, C.-D. Lin,* B. Zhou,* and I. Shimamura

The cross sections for the photodetachment from the second bound state of a negative hydrogen ion, namely, the $H^-(2p^2 3P^e)$ state, at photon energies above the $H(n=2)$ threshold are calculated using a hyperspherical close-coupling method.¹⁻³⁾ The energy of this state lies in the continuum $H(1s) + e$, but this state is parity forbidden to autoionize into $H(1s) + e$, and is therefore a true bound state. The present study was carried out for the following reasons.

First, to study the effect of the extremely weak binding of $H^-(2p^2 3P^e)$, or of its diffuse wave function, on the photodetachment cross sections and their resonance structures. The binding energy with respect to the $H(n=2)$ threshold is 0.01 eV, which is much smaller than the binding energy 0.75 eV of the ground state $H^-(1s^2 1S)$. For reliable calculations of dipole transition matrix elements at energies close to the $n=2$ threshold, the wave function of the extremely diffuse initial state has to be calculated extremely accurately.

Second, to compare the photodetachment cross sections with those calculated by Jacobs et al.⁴⁾ using three-state close-coupling wave functions for the final continuum states, and with the recent results of Du et al.,⁵⁾ who calculated the cross sections at low energies using a semi-empirical adiabatic hyperspherical approximation. We found that the partial cross sections for leaving the hydrogen atom in the $2s$ and $2p$ excited states are in good agreement with the close-coupling calculations of Jacobs et al.⁴⁾ in a low-energy region. At even lower energies than those covered by Jacobs et al., the photodetachment cross sections drop rapidly toward the $H(n=2)$ threshold in agreement with the results of Du et al.⁵⁾

Third, to locate and identify many shape (or potential) resonances and Feshbach resonances of H^- associated with high- n thresholds. We also extended the calculations to higher energies to analyze resonances near the $H(n=3)$ threshold. We found two series of Feshbach resonances of $3P^o$ symmetry, one series of Feshbach resonances of $3D^o$ symmetry, and one shape resonance each of these symmetries. The calculated positions and widths of these resonances are listed in Table 1. The existence of shape resonances just

Table 1. Energies E_r and widths Γ (in a.u.) of resonance states of H^- lying close to the $H(n=3)$ threshold. $3.15[-5] = 3.15 \times 10^{-5}$.

	Present		Complex coordinate ⁷⁾	
	$-E_r$	Γ	$-E_r$	Γ
$H^-(3P^o)$				
1. Feshbach	0.06791	1.65[-3]	0.06791	1.71[-3]
2. Feshbach	0.05743	3.04[-4]	0.05742	3.03[-4]
3. Feshbach	0.05640	4.15[-6]	0.05638	4.00[-6]
4. Feshbach	0.05592	6.42[-5]	0.05591	5.65[-5]
5. Feshbach	0.05563	1.33[-5]	0.05562	1.20[-5]
6. Shape	0.05478	8.92[-4]	0.05475	8.5[-4]
$H^-(3D^o)$				
1. Feshbach	0.05578	3.15[-5]	0.05577	3.8[-5]
2. Shape	0.05555	2.46[-4]	0.05550	2.8[-4]

above high- n excitation thresholds appears to be quite common in H^- . Using diabatic hyperspherical potential curves, we have assigned a set of commonly used correlation quantum numbers⁶⁾ to these Feshbach and shape resonances. The calculated resonance positions and widths are in good agreement with the variational results obtained by Ho and Bhatia⁷⁾ using the complex-coordinate rotation method as shown in the table. The details of the work have been reported elsewhere.⁸⁾

References

- 1) J.-Z. Tang, S. Watanabe, and M. Matsuzawa: *Phys. Rev.*, **A46**, 2437 (1992).
- 2) J.-Z. Tang and I. Shimamura: *ibid.*, **A50**, 1321 (1994).
- 3) J.-Z. Tang and I. Shimamura: *RIKEN Accel. Prog. Rep.*, **28**, 62; 63 (1995).
- 4) V. L. Jacobs, A. K. Bhatia, and A. Temkin: *Astrophys. J.*, **202**, 1278 (1980).
- 5) N.-Y. Du, A. F. Starace, and M.-Q. Bao: *Phys. Rev.*, **A50**, 4365 (1994).
- 6) C. D. Lin: *ibid.*, **A29**, 1019 (1984); *Adv. At. Mol. Phys.*, **22**, 77 (1986).
- 7) Y. K. Ho and A. K. Bhatia: *Phys. Rev.*, **A48**, 3720 (1993); Y. K. Ho (private communication).
- 8) J.-Z. Tang, C. D. Lin, B. Zhou, and I. Shimamura: *Phys. Rev.*, **A51**, 4694 (1995).

* Kansas State University, U.S.A.

Angular Distributions of Photoelectrons from Helium

J.-Z. Tang and I. Shimamura

Photoionization of helium, a seemingly simple two-electron problem, has been attracting more and more theoretical and experimental interest recently. Experimentally, the recent high-resolution measurements have revealed rich structures in the spectra of total (TCS) and partial (PCS) photoionization cross sections and the angular distributions of photoelectrons.^{1,2)} Theoretically, powerful computational methods have been developed recently and they produce results that agree very well with each other and with experiments on the TCS and the resonance parameters for doubly excited states converging to low- n thresholds. However, there are significant discrepancies among theoretical results³⁾ on the photoelectron angular distributions or the differential cross sections (DCS), and hence on the asymmetry parameter often denoted by β . The TCS and PCS depend only on the absolute values of the dipole transition amplitudes, while the DCS depends also on the relative phases of these amplitudes. This implies that the DCS and β contain more physical information than the TCS and PCS and are more sensitive than the latter to the details of the effects considered in a particular calculation.

In this work, we apply the hyperspherical close-coupling (HSCC) method^{4,5)} to study the DCS for photoionization of He in the energy range between the $n = 2$ and 4 thresholds. This method has proved to be quite powerful in reproducing the experimental TCS and PCS measured with high resolution; see, e.g., Ref. 6. Therefore it is expected to lead also to reliable results on the angular distributions and asymmetry parameters. The wave function for the total two-electron system is expanded in terms of hyperspherical basis functions,^{4,5)} set up *ab initio*. This expansion is found to converge rapidly. At some point of the hyperradius, the wave function is connected smoothly to an outer-region wave function in independent-electron coordinates, as explained before.^{4,5)}

We have found in the DCS and in β not only the resonances clearly seen in the TCS but also those narrow resonances that are hardly recognized in the TCS. Some differences between the present theory and experiments have been attributed to the estimation of the experimental background and to the particularly strong influence of the finite experimental resolution on β . After making corrections for them, the calculated

spectra Gaussian convoluted with an experimental resolution agree quite well with the experimental data in Ref. 1, unlike previous theoretical results.³⁾ The Fig. 1 compares the present results for the DCS with the data from Ref. 1 at 0° and 90° between the $n = 3$ and 4 thresholds. Part of this work has been published in Ref. 2.

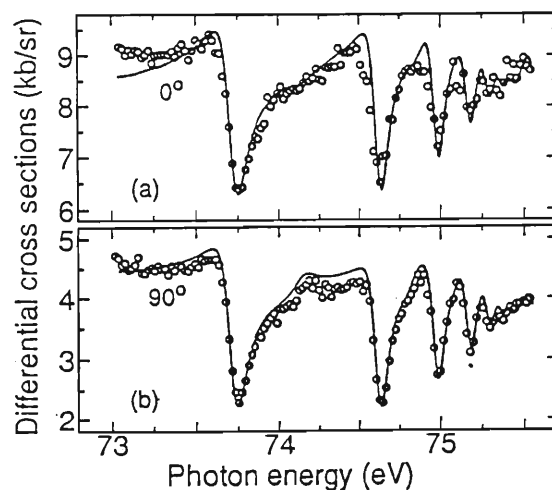


Fig. 1. The differential cross sections at (a) 0° and (b) 90° for photoionization of He: $h\nu + \text{He} \rightarrow e + \text{He}^+(n = 2)$. Solid curve: present result convoluted with a resolution of 60 meV. Circles: experimental results of Ref. 1 corrected in this work for a linear background.

Further results of the present calculations agree well with recent high-resolution measurements, as is discussed in detail elsewhere in a joint experimental-theoretical paper.²⁾

References

- 1) M. Zubek et al.: *J. Phys. B*, **24**, L337 (1991).
- 2) A. Menzel et al: *Phys. Rev. Lett.*, **75**, 1479 (1995).
- 3) I. Sanchez and F. Martin: *Phys. Rev.*, **A48**, 1243 (1993), and the references cited therein.
- 4) J.-Z. Tang, S. Watanabe, and M. Matsuzawa: *Phys. Rev.*, **A46**, 2437 (1992).
- 5) J.-Z. Tang and I. Shimamura: *RIKEN Accel. Prog. Rep.*, **28**, 62; 63 (1995).
- 6) J.-Z. Tang and I. Shimamura: *Phys. Rev.*, **A50**, 1321 (1994).

Double Photoionization of Helium at Low Photon Energies

J.-Z. Tang and I. Shimamura

Theoretical calculations of double photoionization (DPI) are quite difficult in general, partly because one has to deal with double continua involving the two emitted electrons, and partly because the cross section is as small as several percent of the single-photoionization (SPI) cross section at most. The single-photon DPI never occurs if the electron-electron correlations are ignored, and this correlation is strong especially in the low-energy region, i.e., for photon energies from the double-ionization threshold to several hundred eV. In the present work, we carried out accurate calculations of DPI of a prototype atom, He, in the low-energy region by extending the hyperspherical close-coupling (HSCC) method.¹⁾ The details of the work have been reported elsewhere.²⁾

Among the existing *ab initio* computational schemes for DPI, the many-body perturbation theory (MBPT)³⁾ and the eigenchannel *R*-matrix method⁴⁾ have been most successful. The first method, MBPT, treats the electron-electron interaction in a perturbative way and is expected to be a better approximation at high energies³⁾ than at low energies. The *R*-matrix method of Ref. 4 is a close-coupling approach using pseudostates to represent the continuum. The DPI cross sections calculated by these methods depended on the adopted form of the dipole operators, which is an indication of the inaccuracy of the calculations.

Compared with the MBPT method, the present one is non-perturbative and the electron-electron correlation effect is more accurately included. The present method is a close-coupling-type approach just as the *R*-matrix method and uses, in the outer region (where one of the electrons lies far from the rest of the system), asymptotic solutions for an electron interacting with He⁺ in discretized pseudostates that simulate the continuum states of He⁺ and that are similar to the pseudostates used in Ref. 4. In the inner region (where all the three particles in the system lie close together), however, the wave function of the total system is expanded in terms of hyperspherical basis functions¹⁾ in the present method, and close-coupling equations in the hyperradius are numerically solved. This results in faster convergence than the expansion in terms of basis functions in independent-electron coordinates, like those used in Refs. 3 and 4.

The calculated DPI cross sections are compared in Fig. 1 with those obtained by the MBPT and the *R*-matrix method. The present results were obtained by using 175 basis functions and by matching the inner-

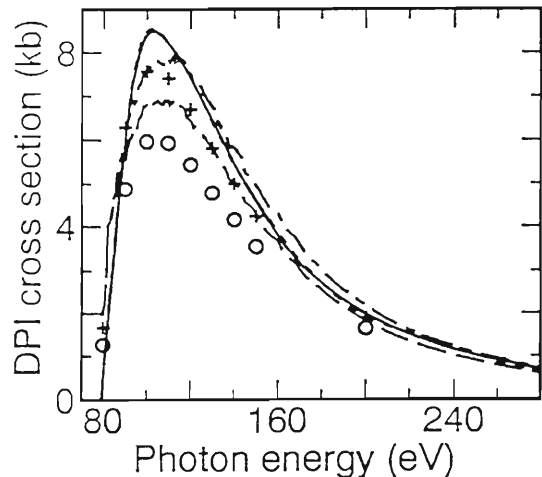


Fig. 1. Double photoionization cross sections for He. Solid and short-broken curves: A (acceleration) and L (length) forms, present method. Dot-dash and long-broken curves: A and V (velocity) forms, *R*-matrix method.⁴⁾ + and o: A and L forms, MBPT.³⁾

region and outer-region wave functions at a hyperradius of 30 a.u. The convergence of the SPI cross section within 3 significant digits and of the DPI cross section within several percent has been confirmed. An outstanding feature of the present results is that the cross sections obtained in the length and acceleration forms agree very well with each other. This fact, together with the good convergence of each cross section, guarantees the accuracy of the present results. The calculated ratio of the cross sections for double to single photoionization is smaller than most experimental data, but is in excellent agreement with a very recent accurate measurement.⁵⁾ We note finally that the DPI cross sections, obtained in Ref. 6 by a new method based on an integral form of the amplitude function for DPI, are close to the present results.

References

- 1) J.-Z. Tang, S. Watanabe, and M. Matsuzawa: *Phys. Rev.*, **A46**, 2437 (1992).
- 2) J.-Z. Tang and I. Shimamura: *ibid.*, **A52**, 2437 (1995).
- 3) K. Hino et al.: *ibid.*, **A48**, 1271 (1993).
- 4) K. W. Meyer and C. H. Greene: *ibid.*, **A50**, R3573 (1994).
- 5) R. Dörner et al.: preprint.
- 6) M. Pont and R. Shakeshaft: *J. Phys.*, **B28**, L571 (1995).

Scattering Angle Dependence of Electron Impact on O₂ and CO

M. Kimura, M. A. Dillon,* R. J. Buenker,** G. Hirsch,** Y. Li,** and L. Chantranupong**

Intensity distributions of electronic transitions in O₂ and CO within a vibrational progression resulting from electron impact excitation are studied theoretically and experimentally. The multireference single- and double- excitation configuration-interaction (MRD-CI) method is used to elucidate details of selected electronic transitions. Figure 1 illustrates adiabatic potential curves for CO obtained by the MRD-CI. In particular, the adiabatic MRD-CI approach can account for the variation of the Franck-Condon envelop with scattering angle that has been reported for the $B^1\Sigma^+ \leftarrow X^1\Sigma^+$ transition in CO and also was recently observed in the $B^3\Sigma^- \leftarrow X^3\Sigma^-$ transition of O₂. This behavior contrasts with the relative stabil-

ity of the intensity distribution observed within the CO: $A^1\Pi \leftarrow X^1\Sigma^+$ vibrational progression as exemplified in Fig. 2. In the former case, the excited state undergoes changes in its character with internuclear separation because of the presence of an avoided crossing. Since a transition from the zeroth vibrational level in the ground electronic state to an individual vibrational level in the excited electronic state tends to select a particular internuclear distance (R-centroid), each vibrational band may behave as a transition to a separate electronic level. This happens because the excited state wavefunction undergoes a compositional change with internuclear separation between the adiabatic partners of the avoided crossing. The details have been published elsewhere.¹⁾

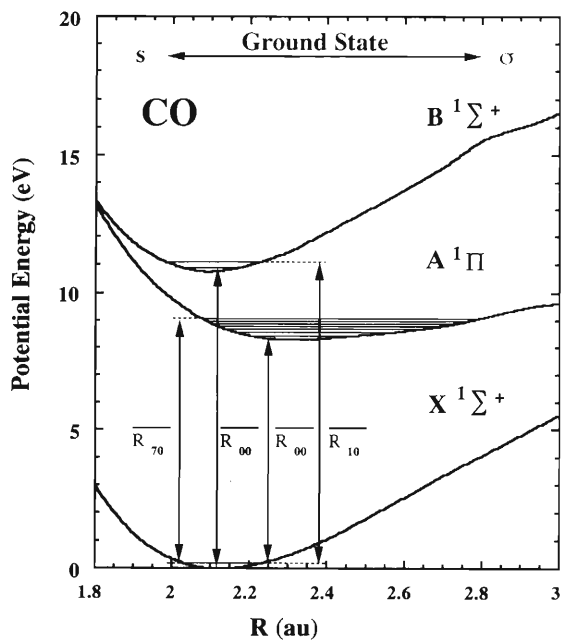


Fig. 1. Adiabatic potential curves for the CO molecule.

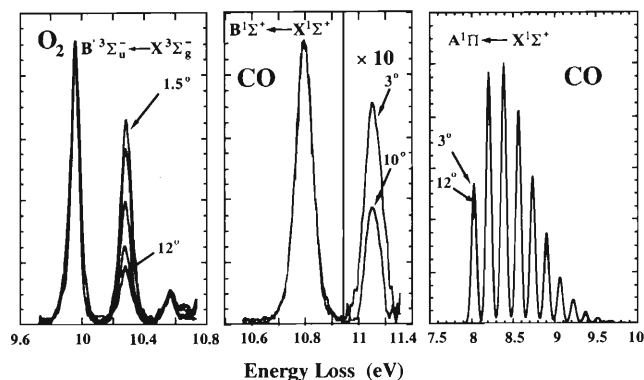


Fig. 2. Electron energy loss spectra for $B^3\Sigma^- \rightarrow X^3\Sigma^-$ transition in O₂ and $B^1\Sigma^+ \rightarrow X^1\Sigma^+$ transition in CO.

References

- 1) M. A. Dillon, M. Kimura, R. J. Buenker, G. Hirsch, Y. Li, and L. Chantranupong: *J. Chem. Phys.*, **102**, 1561 (1995).

* Argonne National Laboratory, Argonne, U.S.A.

** Theoretisch Chemie, Bergische Universität-Gesamthochschule Wuppertal, Germany

Electron Energy Distribution Functions and Thermalization Time in Methane and in Argone-Methane Mixture

M. Kimura, I. Krajcar-Bronic,* and I. Shimamura

Electron energy distribution and thermalization in methane and argone-methane mixtures are studied by using the Boltzmann equation. Suppose that the medium consists of two species at number densities N_A and N_B atoms or molecules with mass M_A and M_B . If no external field is applied and spatial spherical symmetry of the initial electron distribution is assumed, then electron distribution function $f(v, t)$ of speed v at time t satisfies the Boltzmann equation,

$$\frac{\partial f(v, t)}{\partial t} = J_{el} + J_{inel}, \quad (1)$$

where J_{el} and J_{inel} are the elastic and inelastic collision operators. The calculated condition for the thermalization of electrons is: the initial electron energy is 1 eV in CH_4 and Ar gases at $T = 300$ K and $p = 1$ atm. The presence of low-lying vibrational excited states in methane significantly changes electron energy distribution functions and relaxation time. We found that (1) the mean electron energy just below the first vibrational excited state is reached faster by 1000 times when the vibrational states are taken into account, and (2) electron energy distribution functions have distinct peaks at energy intervals equal to the vibrational threshold energies. Both these effects are due to a large vibrational stopping cross section. The thermalization time in mixtures of argone-methane without vibrational states smoothly changes as the mixture composition varies, and no significant difference in the electron energy distribution function is observed. When the vibrational excited states are taken into account, the thermalization is almost completely defined by CH_4 , even at very low fractional concentrations of CH_4 . The sensitivity of the electron energy distribution functions on the momentum transfer cross sections used in calculation on the thermalization is tested and it is found that in the present range of deviation in momentum transfer cross sections, the effect is not significant. Figure 1 shows electron collision cross sections for both momentum transfer and vibrational excitations for CH_4 and momentum transfer cross section for Ar used in the calculation. Figure 2 illustrates electron energy distribution functions (time-evolution) in Ar- CH_4 mixtures when only momentum transfer cross

sections for CH_4 are included in the calculation. The details can be found elsewhere.¹⁾

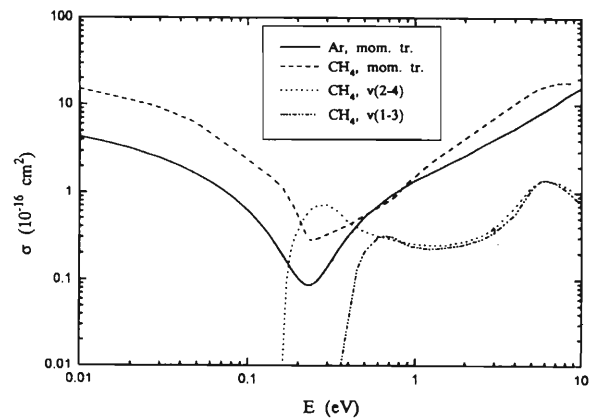


Fig. 1. Electron collision cross sections for both momentum transfer and vibrational excitations for CH_4 and momentum transfer cross sections for Ar.

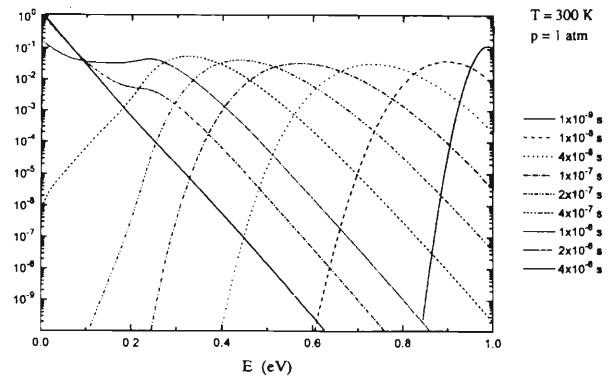


Fig. 2. Electron energy distribution functions (time evolution) in Ar- CH_4 mixtures, when only momentum transfer cross sections for CH_4 are included in the calculation.

References

- 1) I. Krajcar-Bronic, M. Kimura, and I. Shimamura: to be submitted in *J. Chem. Phys.*

* Rudjer Boskovic Institute, Croatia

Correlation between the Carbon K-Shell X-Ray Emission Rates in Molecules

M. Kimura

A clear correlation is shown between carbon K-shell X-ray emission rates from molecules that contain carbon atoms and their π bond orders. This correlation is based on the present calculation for C_2H_2 , C_2H_4 and C_2H_6 and previous calculations of Larkins¹⁾ for CO, CO_2 , HCN and CH_3OH . Because the π bond order has an inverse linear relationship with the bond length, the C K-shell X-ray emission rate correlates with the bond length as well. Some rationale for the findings based on electronegativity and charge distribution is given. The correlation manifests itself in a chemical effect on the C K-shell X-ray emission rate. Figure 1 displays the present C X-ray emission rates and Fig. 2 shows the Auger transition rates as a function of the valence electron density in carbon together with the data obtained by Larkins.¹⁾ As Fig. 1 shows

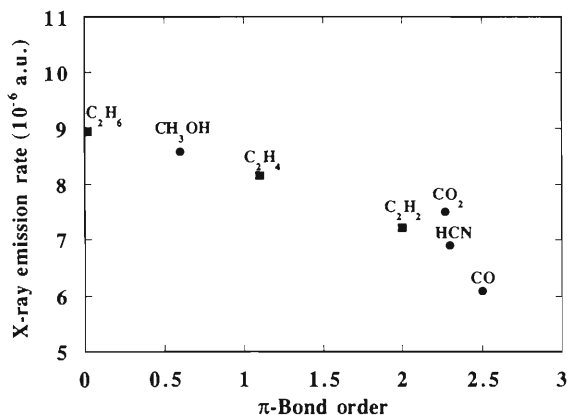


Fig. 1. X-ray emission rates for a variety of carbon-containing molecules as a function of π bond order. Present work: solid square; Larkins: solid circle.

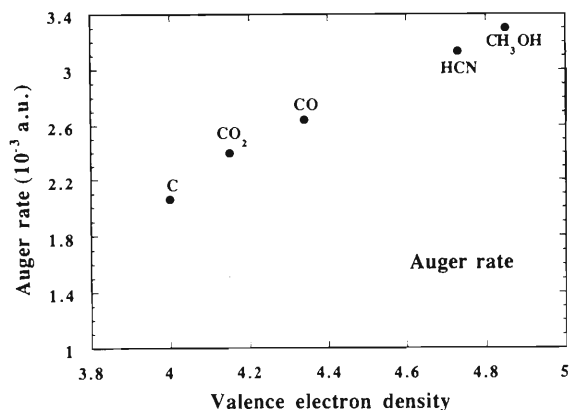


Fig. 2. Auger transition rate as a function of valence electron density. All data are from Larkins.¹⁾

for C_2H_6 , in which no π orbital exists, the π bond order is very small. All valence electrons in this molecule are in σ orbitals that are well-localized near inner shell orbitals resulting in a large X-ray emission rate. As seen in Fig. 2, the Auger transition rate appears to increase linearly as the electron density increases. For the Auger transition, the electron correlation operator is the source of the dynamics and hence, the total coupling strength depends on the electron density in a molecule. As the electron density increases, the overall coupling strength per molecule increases, leading to a larger Auger rate. The details have been published elsewhere.²⁾

References

- 1) F. P. Larkins: *J. Electron Spectrosc. Relat. Phenom.*, **51**, 115 (1990).
- 2) M. Kimura: *Chem. Phys. Lett.*, **200**, 524 (1992).

Charge Transfer Effect on Double Electron Excitation of Helium by Proton Impact

N. Fukushima,* T. Morishita,* K. Hino, S. Watanabe, and M. Matsuzawa

We report an autoionizing electron emission cross section from a doubly-excited helium in the $N = 2$ manifold produced by proton impact. The electron emission process by proton and anti-proton impact in the MeV-energy region has been intensively studied these few years to analyse sensitive dependence of resonance profiles on a sign of projectile charge due to interference among several partial waves of the ejected electron.^{1,2)} Theories have well reproduced experimental findings regarding both backgrounds and doubly-excited resonances. When the incident energy decreases down to a hundred keV-region, special attention has to be paid to the following two important effects on the excitation process; that is, the charge transfer and the post-collision interaction contributions to an electron emission cross section. In this report, only the first issue will be taken into consideration. This takes effect only to the case of proton impact.

Ab initio close-coupling method is employed in the impact parameter representation. Basically, we adopt a one-center atomic orbital expansion in terms of helium wave functions obtained by the hyperspherical close-coupling method.³⁾ The hyperspherical method is known to be one of the excellent ways to take into account a strong electron correlation effect in a two-electron atom. Instead, as a price to be paid, the adoption of it causes a numerical difficulty in calculating a coupling matrix element between a projectile-centered atomic wave function and a (target-centered) hyperspherical wave function. This difficulty hampers a straightforward application of an additional projectile-centered atomic orbital expansion to the present close-coupling scheme to evaluate a charge transfer channel. The manipulation adopted here to remedy this difficulty is the following. First, relevant coupling matrix elements for a charge transfer channel are evaluated using a (target-centered) Hartree-Fock wave function instead of a hyperspherical one, since it is thought that the electron correlation effect on a one-electron charge transfer would be small. Such one-electron matrix elements are relatively tractable. Next, the scattering matrix elements for a charge transfer are calculated using these coupling matrix elements by the method pertinent to the incident-energy region concerned here, for instance, by the first-Born approximation or the

distorted-wave Born approximation if necessary. Finally, these predetermined matrix elements are introduced into the two-electron close-coupling equation as inhomogeneous terms expressing a coupling between a direct channel and a transfer channel.

Figure 1 shows our preliminary result for the electron emission spectrum ascribable to the $(2s)^2\ ^1S^e$ state induced by the 150 keV proton bombardment. This calculation includes only a 1s-1s charge transfer channel obtained by the first-Born approximation. Here, for simplicity, a screened hydrogenic wave function has been used for evaluating a transfer scattering matrix element in place of a Hartree-Fock one. There is little difference between spectral profiles with and without considering the charge transfer effect. Extended calculations including more charge transfer channels are in progress.

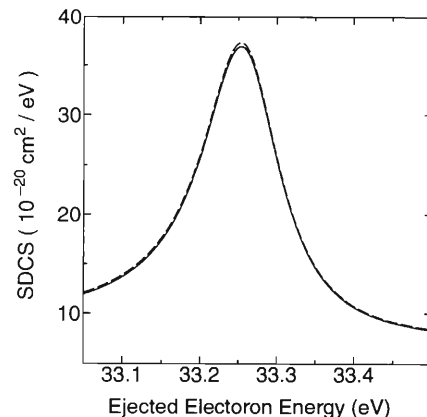


Fig. 1. The electron emission cross section (SDCS, single differential cross sections in energy) from the $(2s)^2\ ^1S^e$ doubly excited state of helium by 150 keV proton impact. The solid and the dashed lines stand for calculations with and without considering a charge transfer channel, respectively.

References

- 1) T. Morishita et al.: *J. Phys. B: At. Mol. Opt. Phys.*, **27**, L287 (1994).
- 2) T. Morishita et al.: to be submitted in *Phys. Rev. A*, Other references therein.
- 3) J. Z. Tang et al.: *Phys. Rev.*, **A46**, 2437 (1992).

* Department of Applied Physics and Chemistry, University of Electro-Communications

Electron Capture in Slow $O^+(^4S, ^2D, ^2P)$ -He Collisions: Effects of Metastable Ions

M. Kimura, J. P. Gu,* G. Hirsch,* R. J. Buenker,* and A. Dalgarno**

Recently reports appeared on two experimental attempts by Kusakabe et al.¹⁾ and Wolfrum et al.²⁾ to study the single-electron capture in collisions of O^+ ions with He atoms in the keV regime. The results have led to two conflicting conclusions: Kusakabe et al. predicted larger cross sections when metastable ions were present, whereas Wolfrum et al. found no contribution from metastable ions. The processes they dealt with are the following with respect to asymptotic energy defects and the corresponding adiabatic potential curves are shown in Fig. 1:

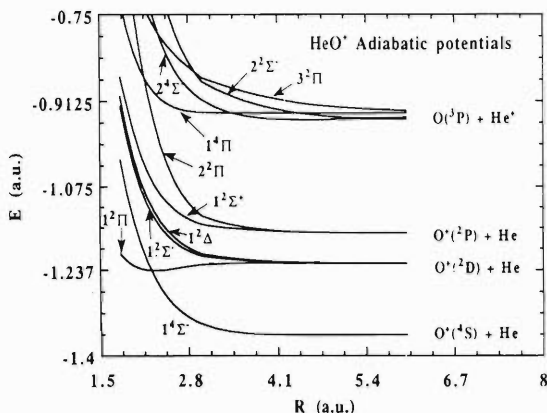
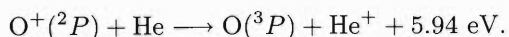
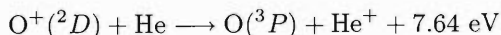
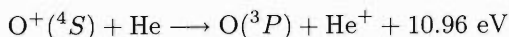


Fig. 1. Adiabatic potentials of the HeO^+ system. The energy is given relative to -76.0 a.u.

The present cross sections for electron capture by the ground $O^+(^4S)$ state and metastable $O^+(^2D, ^2P)$ states are presented in Fig. 2. The cross sections clearly show that the electron capture by the metastable ions is more probable by an order of magnitude than that by the ground state. Kusakabe et al.

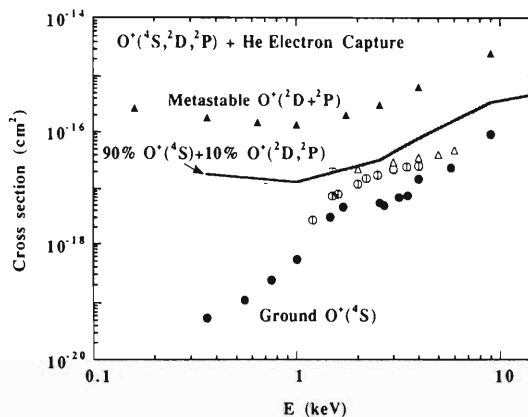


Fig. 2. Electron capture cross section above 100 eV. Present work: ●, $O^+(^4S)$; ▲, $O^+(^2D, ^2P)$. Experiment: ○, $O^+(^4S)$; □, capture by mixed ground and metastable O^+ ions, Kusakabe¹⁾ et al. and Wolfrum et al.²⁾

used a technique of electron impact ionization of the CO_2 molecule to generate O^+ ions, but the fraction of metastable-state ions is not known. Wolfrum et al. on the other hand, used a similar technique on the H_2O molecule and reported that in their 130-eV electron impact, the ions produced were 47% $O^+(^4S)$, 40% $O^+(^2D)$ and 13% $O^+(^2P)$. In contrast, for 30-eV electron impact, only the ground state of O^+ ions was produced (100%). As Hughes and Tiernan reported,³⁾ the appearance potentials for $O^+(^2D)$ and $O^+(^2P)$ ions are 26.5 and 28.3 eV, respectively. Hence, a mixture of a small fraction of metastable O^+ ions could well be expected when 30 eV electrons are used. Therefore, we suspect that metastable $O^+(^2D, ^2P)$ ions were actually present in all experiments in the work of Wolfrum et al. The details have been published elsewhere.⁴⁾

References

- 1) T. Kusakabe et al.: *J. Phys. Soc. Jpn.*, **59**, 1987 (1990).
- 2) E. Wolfrum et al.: *Phys. Rev.*, **A45**, R4218 (1992).
- 3) M. Hughes and T. O. Tiernan: *J. Chem. Phys.*, **55**, 3419 (1971).
- 4) M. Kimura et al.: *Phys. Rev.*, **A49**, 3131 (1994).

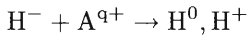
* Theoretisch Chemie, Bergische Universität-Gesamthochschule Wuppertal, Germany

** ITAMP, Harvard-Smithsonian Center for Astrophysics, U.S.A.

Electron Loss from H^- under Energetic, Highly Ionized Ion Impact

H. Tawara, T. Tonuma, H. Kumagai, and T. Matsuo

Electron loss processes from negative hydrogen ions under collisions of ions,



are important in various fields such as the development of powerful ion sources and plasma apparatus. In particular, much attention has recently been paid to their applications to fusion plasma research relevant to neutral plasma heating. Though their importance has been noted in many years, only limited experimental investigations have been reported until now because of technical difficulties.¹⁻⁶⁾

In the present work, the electron loss processes from H^- ions under energetic (MeV/nucleon) highly ionized heavy ion impact is planned to be investigated. 2.5 keV H^- ion beams, extracted from an off-centered duoplasmatron ion source with ferrite permanent magnets and purified through two electrostatic deflectors, are crossed at 45 degrees with 1–2 MeV/nucleon A^{q+} ($q = 6-30$) ions provided from RIKEN linear accelerator, as shown in Fig. 1. Typical beam-overlapping shapes, which are the most important in ion-ion collision experiments, are shown in Fig. 2.

In ion-ion collision experiments, as the target ion densities are generally very low compared with those

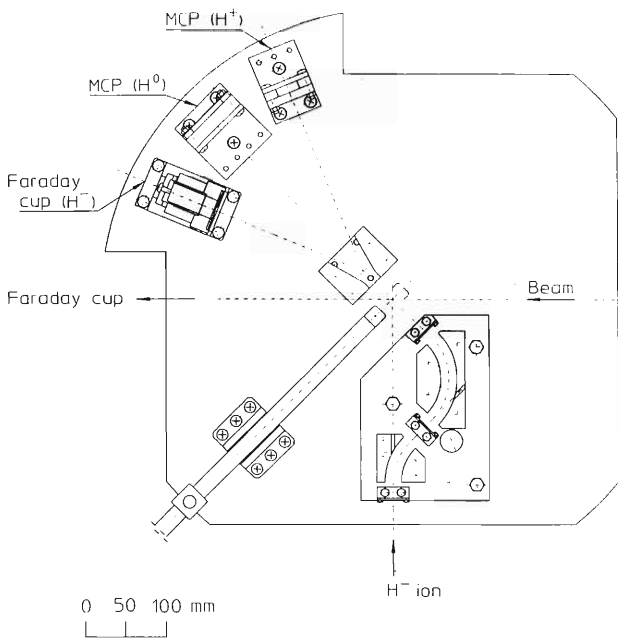


Fig. 1. Schematic experimental apparatus.

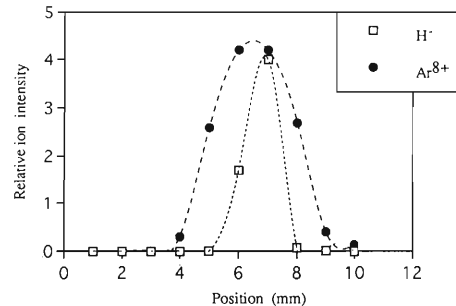


Fig. 2. Overlapping shapes of 1.5 MeV/nucleon Ar^{6+} beam and 2.5 keV H^- ions.

of residual gas atoms, both of the colliding ion beams have to be chopped in order to improve the signal-to-noise (S/N) ratios. In the present experiment, we have tried to use the unique time-structures of the accelerated ion beams from the LINAC, which are known to be short-bunched at the accelerating frequency. We have found that careful RF-tuning is necessary in order to minimize the tails of the bunched beams which are expected to significantly influence S/N ratios, just as that in the beam-chopping technique. This is expected to increase S/N ratios by a factor of about 20 at the bunched beam width of 1.5 ns at 33 MHz. It has been found experimentally that the tails of the time-structures of ion beams can be also reduced significantly through proper adjustment of the beam collimating slits, though some fraction of ion beams may be lost.

In the present collision energies, the electron loss from H^- ions is expected to be dominated by the pure ionization under the influence of the strong Coulomb field of projectile ions.

Now we are trying to measure the cross sections mentioned above and also to look into the detailed mechanisms in electron loss processes involving H^- ions under highly ionized MeV/nucleon ion impact.

References

- 1) E. Salzborn: *J. de Phys.*, Suppl., **50**, C1-207 (1989).
- 2) K. Dolder and B. Peart: *Rep. Prog. Phys.*, **48**, 1283 (1985).
- 3) F. Melchert et al.: BNL Symp., p. 789 (1992).
- 4) F. Melchert et al.: *Phys. Rev. Lett.*, **74**, 888 (1995).
- 5) L. P. Presnyakov, H. Tawara, and D. B. Uskov: *Nucl. Instrum. Methods Phys. Res.*, **B98**, 332 (1995).
- 6) G. D. Alton, R. A. Sparrow, and R. E. Olson: *Phys. Rev.*, **A45**, 5957 (1992).

Close-Coupling Calculations of Electron Capture from Circular Rydberg States

M. F. V. Lundsgaard,* N. Toshima, and C. D. Lin*

In a recent letter¹⁾ Hansen *et al.* reported electron capture cross sections from circular Rydberg states as a function of the angle, φ , between the ion velocity and the angular momentum of the circular orbital. They studied the collision of 2.5 keV $^{23}\text{Na}^+$ on the Rydberg state of Li with $n=25$, $l=n-1$ and $m=+l$, where m is defined relative to a weak, external magnetic field. It was found that the electron capture cross section depends strongly on the angle φ , with the maximum occurring at $\varphi = 90^\circ$ and decreases rapidly with decreasing φ . Attempts have been made by Hansen, with limited success, to interpret this φ -dependence in terms of higher order perturbation theories and in terms of results obtained for lower n states ($n=10$) calculated using the classical trajectory Monte Carlo (CTMC) method.²⁾ In this report, we show that the observed φ -dependence is consistent with the known propensity rule for electron capture from low-lying excited states. This propensity rule has been proved based on the results from elaborate close-coupling calculations³⁾ and from experiments for collisions of protons on oriented $\text{Na}(3p)$ states.⁴⁾ We carry out close-coupling calculations to determine the φ dependence for electron capture from a circular $\text{H}(4f)$ state by protons at the same scaled collision velocity (the ratio of the projectile velocity to the initial orbital velocity of the electron), and show that the calculated φ -dependence is nearly identical to the measured result for the $n=25$ circular state by Hansen *et al.*

To specify the collision more precisely, we first define the “natural frame” of reference. In this frame the collision plane is the $x'y'$ halfplane where y' is positive and $+x'$ is the direction of the incident beam. The quantization axis ($+z'$ direction) is perpendicular to the scattering plane such that $x'y'z'$ forms a right-handed coordinate system. A circular Rydberg state $|i\rangle_B = |n, l = n-1, m_i = l\rangle_B$, where m_i is given with respect to the z_B -axis, can be obtained from rotating the circular state $|n, l = n-1, m_i = l\rangle'$ defined with respect to the natural frame $x'y'z'$ by two successive rotations,

$$|i\rangle_B = \sum_q \sum_m \mathcal{D}_{qm_i}^{(l)}(0, -\varphi, 0) \mathcal{D}_{mq}^{(l)}(\eta + \pi/2, \pi/2, \pi) |nlm\rangle. \quad (1)$$

In the equation above, \mathcal{D} is the rotation matrix and η is the rotation angle of the scattering plane $x'y'$ with respect to the space fixed xz plane ($z=x'$). The amplitude $a_{fi}^B(\varphi, b, \eta)$ for the transition $|i\rangle_B \rightarrow |f\rangle$ depends on the angles φ , η , and the impact parameter b . This amplitude can be expressed as a coherent sum of amplitudes defined with respect to the natural frame,

$$a_{fi}^B(\varphi, b, \eta) = \sum_q \sum_m i^q (-1)^m \times \exp(iq\eta) d_{mq}^{(l)}(\pi/2) d_{m_i q}^{(l)}(\varphi) a'_{fm}(b), \quad (2)$$

where d is the reduced rotation matrix.

We obtain the cross section by integrating the transition probabilities over the impact parameter plane and summing over all the final states,

$$\sigma_{cap}(\varphi) = \sum_q (d_{m_i q}^{(l)}(\varphi))^2 \times \sum_m \sum_{m'} d_{mq}^{(l)}(\pi/2) d_{m' q}^{(l)}(\pi/2) \rho'_{mm'}, \quad (3)$$

where

$$\rho'_{mm'} = \sum_f 2\pi \int_0^\infty a'_{fm}(b) a'^*_{f m'}(b) b db. \quad (4)$$

The results are shown in Fig. 1, together with the data of Hansen.¹⁾ Interestingly, the agreement between the calculations for the circular state for $n=4$ and the experimental results for the circular state for $n=25$ is amazingly good. This suggests that the observed φ -dependence is insensitive to the principal quantum number of the initial Rydberg state. Further details of the calculations are given elsewhere.⁵⁾

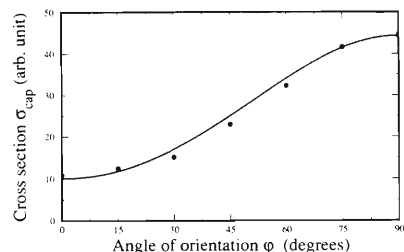


Fig. 1. Comparison between the experimental cross sections (dots) for electron capture from a circular Rydberg state ($n=25$, $l=24$, $m=24$) and the theoretical cross sections (solid line) for capture from a ($n=4$, $l=3$, $m=3$) circular state. The collision velocity is 1.66 times of the average electron velocity in both cases.

References

- 1) S. B. Hansen, T. Ehrenreich, E. Horsdal-Pedersen, K. B. MacAdam, and L. J. Dubé: *Phys. Rev. Lett.*, **71**, 1522 (1993).
- 2) G. A. Kohring, A. E. Wetmore, and R. E. Olson: *Phys. Rev.*, **A28**, 2526 (1983).
- 3) N. Toshima and C. D. Lin: *ibid.*, **A46**, 2564 (1992).
- 4) A. Dubois, S. E. Nielsen, and J. P. Hansen: *J. Phys.*, **B26**, 705 (1993).
- 5) M. F. V. Lundsgaard, N. Toshima, and C. D. Lin: *Phys. Rev.*, **A51**, 1347 (1995).

* Department of Physics, Kansas State University, U.S.A.

Single- and Double-Charge-Exchange Cross Sections for $\text{Ar}^{q+} + \text{H}_2$ Collisions

M. Kimura, I. Shimamura, and N. Shimakura

The cross sections for single-electron capture, including transfer ionization, and for double-electron capture, have been measured recently for $\text{Ar}^{q+} + \text{H}_2$ collisions for $q = 6, 7, 8, 9$, and 11 with projectile energies from q eV to q keV.¹⁾ For understanding the physics underlying these processes, theoretical calculations have been made for Ar^{6+} and Ar^{8+} impact using a molecular-state expansion method in the energy region from 240 eV to 80 keV,¹⁾ and good agreement has been found with the experimental results. Here, the theoretical part of the work is briefly described. The details of the whole work involving both experiment and theory have been published elsewhere.¹⁾

A semiclassical molecular-state expansion method, which is believed to be valid for collision energies above a few 10 eV/u, has been used. Molecular states of the system $(\text{ArH}_2)^{q+}$ were obtained by the configuration-interaction (CI) method with Slater-type orbitals. In this CI calculation, the two H_2 electrons were treated explicitly, while the effect of the more tightly bound electrons of Ar ions was represented by Gaussian-type pseudopotentials. These pseudopotentials were determined so as to reproduce the energy levels of $\text{Ar}^{(q-1)+}$. The H_2 molecules were approximated by atoms having an average first- and second-ionization potentials of 15.8–16.1 and 31.7 eV, respectively, average meaning that over the vibrational wave function squared.

Several sets of coupled-channel calculations using

straight-line trajectories for the heavy-particle motion, including different molecular states were carried out to assess the convergence and to identify dominant collision mechanisms or reaction paths. A typical set included (1) the initial channel $\text{Ar}^{q+} + \text{H}_2$, (2) representative single-electron-transfer channels $\text{Ar}^{(q-1)+}(n = 3, 4) + \text{H}_2^+$, and (3) some double-electron-transfer channels $\text{Ar}^{(q-2)+}(n = 3, n' = 3, 4, 5) + 2\text{H}^+$.

For Ar^{6+} impact, the molecular-state expansion calculation produced cross sections that are about 50% below the experimental values for both single and double capture. For Ar^{8+} impact, the calculation is in better agreement with experiment for both single and double capture. Because of the extra two electrons in Ar^{6+} in comparison with Ar^{8+} , the quality of molecular-state calculations was somewhat lower for Ar^{6+} impact, giving less satisfactory agreement with the experiment. The general trends of the cross sections agree quite well with each other between the experiment and the theory.

See Ref. 1 for further details of comparison between theory and experiment and discussion of the dynamics of the measured and calculated processes.

References

- 1) S. Kravis, H. Saitoh, K. Okuno, K. Soejima, M. Kimura, I. Shimamura, Y. Awaya, Y. Kaneko, M. Oura, and N. Shimakura: *Phys. Rev.*, **A52**, 1206 (1995).

Electron Capture in $H^+ + CH_4$ Collisions

M. Kimura, Y. Li,* G. Hirsch,* and R. J. Buenker*

Electron capture and direct elastic scattering in collisions of H^+ ions with CH_4 molecules are studied by using a molecular representation within fully quantum-mechanical approaches below 1.5 keV. Calculations are carried out at two different molecular configurations: (1) C_{3v} symmetry, in which H^+ approaches along the direction of a C-H in CH_4 , and (2) C_{2v} symmetry, in which H^+ approaches along a bisector of an H-C-H bond angle. Figure 1 shows adiabatic potential curves for C_{2v} symmetry. We find that the electron capture in the C_{2v} symmetry configuration takes place preferentially over that in the C_{3v} symmetry configuration at scattering angles below 15° at 1.5 keV, and that the situation reverses at larger scattering angles. Hence, interferences arising from these molecular configurations on differential cross sections for the electron capture and elastic scattering processes are present but weak, except for angles near the crossing. Accord-

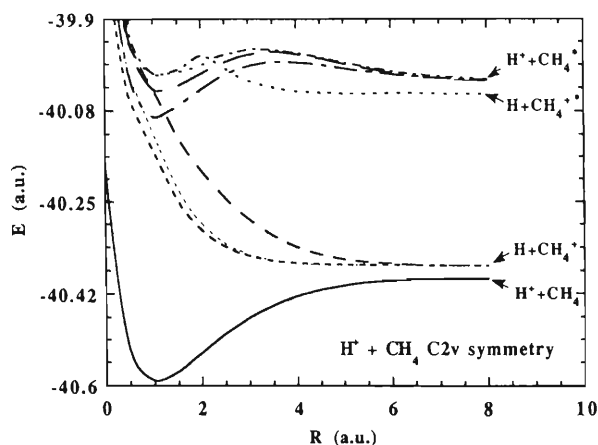


Fig. 1. Adiabatic potential energies for $H^+ + CH_4$ C_{2v} symmetry.

ingly, the total cross section for the C_{2v} symmetry is larger by more than an order of magnitude, because in this symmetry H^+ can penetrate deep inside the electron distribution of a CH_4 molecule, causing a strong interaction. The present differential cross section from 0.01 to 1.0 degrees at 1.5 keV is shown in Fig. 2 along with experimental data.¹⁾ In addition, the angular dependence in the differential cross section is quite different for the two molecular configurations at all energies studied. The details have been published elsewhere.²⁾

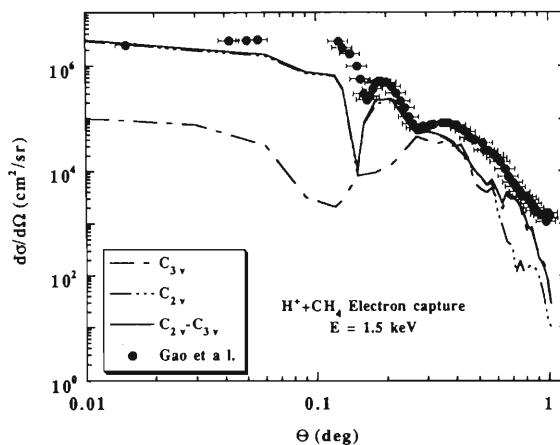


Fig. 2. Differential cross section from 0.01° to 1.0° at 1.5 keV. The solid line shows the averaged result, the dashed-dotted line the result for C_{3v} , and dashed three-dot line the result for C_{2v} . The \bullet symbols represent the experimental data of Gao et al.¹⁾

References

- 1) R. S. Gao et al.: *Phys. Rev.*, **A41**, 5929 (1990).
- 2) M. Kimura, Y. Li, G. Hirsch, and R. J. Buenker: *Phys. Rev.*, **A52**, 1196 (1995).

* Theoretisch Chemie, Bergische Universität-Gesamthochschule Wuppertal, Germany

Double and Single Ionization of Helium and Hydrogen Molecules by Slow Protons and Antiprotons

M. Kimura, I. Shimamura, and M. Inokuti*

The first series of atomic collision experiments using an antiproton beam of energy above 0.5 MeV was carried out in the low-energy antiproton ring (LEAR) at CERN.¹⁾ In these experiments, the ratio $R_S = \sigma^{++}/\sigma^+$ between double- and single-ionization cross sections, σ^{++} and σ^+ of He for antiproton impact was found to be larger by a factor of two than that for proton impact. Some theoretical attempts have been made to understand the conspicuous difference between p-impact and p-impact double ionization.²⁻⁵⁾ The studies have shed light on the limitations of the independent-particle model and on the importance of electron correlation in these processes.

Recently, Hvelplund et al.⁶⁾ have carried out experiments in a much lower energy regime down to 10 keV and found that the ratio for protons decreased sharply as the energy decreased, while the ratio for antiproton increased nearly monotonically. We have investigated the double and single ionization of He and H₂ for protons and antiprotons by using a semiclassical molecular-state representation.⁷⁾ In this method, the electron motion is described quantum mechanically as a two-center molecular-state problem and the relative motion between the two heavy nuclei is described classically. Discrete molecular electronic states were determined by the configuration-interaction method with the use of Slater-type orbitals as basis functions. Singly ionized continuum electronic states were obtained in the fixed-nuclei static-exchange approximation for elastic electron scattering from the neutral molecule or the molecular ions (HeH)⁺⁺ and (H₂)⁺. The internuclear distance for H₂ was fixed. Those for doubly ionized states were constructed by using a perturbation method in which the interelectronic Coulomb potential is the perturbation and the terms up to the first order in the wave function are retained. For H₂, the nuclear motion was frozen in the calculation. The adiabatic wave-packet approach,

which spans electronic continuum locally, was taken. A discretized sampling procedure, based on the Gauss quadrature, was used to select continuum states for the molecular state expansion method. The number of channels included in the calculations was 200–300. The results of the ratios for proton and antiproton impacts for He were reported earlier⁷⁾ and our results successfully reproduced the experimental findings for both systems. The theoretical rationales for dynamics were: (1) for the antiproton impact, the electronic binding energy decreases, which is the main mechanism for single ionization. The electron-electron interaction in the presence of antiprotons is of primary importance in the emission of two electrons, (2) for the proton impact, the ladder-climbing mechanism is a main mechanism for single and double ionization. Once one electron is ionized, the second electron feels more stronger attraction from a He nucleus and it is less likely to lead to double ionization, hence resulting a decreasing ratio as energy decreases. For H₂, when an antiproton approaches perpendicular with respect to the molecular axis of H₂, the double ionization probability was found to be a maximum, but when it approaches parallel to the molecular axis, the double ionization probability was minimized. These features closely relate to the electron charge distribution of H₂ molecule.

References

- 1) L. H. Andersen et al.: *Phys. Rev. Lett.*, **57**, 2147 (1986).
- 2) H. Knudsen and J. F. Reading: *Phys. Rep.*, **212**, 107 (1992).
- 3) L. Ford and J. F. Reading: *J. Phys.*, **B21**, L685 (1988).
- 4) J. McGuire: *Phys. Rev. Lett.*, **49**, 1153 (1982).
- 5) D. R. Schultz, R. E. Olson, and C. O. Reinhold: *J. Phys.*, **B24**, 521 (1991).
- 6) P. Hvelplund et al.: *ibid.*, **B27**, 925 (1994).
- 7) M. Kimura, I. Shimamura, and I. Inokuti: *Phys. Rev.*, **A49**, R4281 (1994).

* Argonne National Laboratory

Muon-Transfer Reaction $t + d\mu(2s) \rightarrow t\mu(n=2) + d$

A. Igarashi, I. Shimamura, T. Shirai,* and N. Toshima

The muon-transfer reaction between hydrogen-like muonic atoms in excited states,



is crucial in determining the fraction q_{1s} of $d\mu$ in the ground state in a mixture of deuterium D_2 and tritium T_2 .¹⁾ The physical situation of the muon transfer reaction is quite different depending on whether the $d\mu$ atom is initially in the ground state or in an excited state, and the theoretical treatment of the muon transfer between excited states is much more difficult for the following reasons.

The degeneracy of excited states requires a much larger expansion basis set for the scattering wave function, and leads to an extremely long-range potential that decays as the second inverse power of the distance between the charge and the muonic atom. The fact that the muon transfer is most important at low energies, where fully quantum mechanical treatment is necessary, is another cause of the difficulty. All work devoted so far to reaction (1) involving excited states is based on the semiclassical treatment in contrast to the case of a transfer between the ground states, for which reliable cross sections are available.

We have developed the hyperspherical coupled-channel or close-coupling (HCC) method and have demonstrated its efficiency for the ground-state muon transfer process.²⁾ The greatest advantage of this method for rearrangement collisions is that it can treat different arrangement channels on equal footing. Here, we report full-quantal calculations for the process (1) in the case of $n=2$ by solving the Schrödinger equation directly with the HCC method. The calculations are carried out at five energies between 0.001 and 0.1 eV. The hyperspherical channels, defined for each fixed value of the hyperradius R , that converge to $d\mu(n=1-3)$ and $t\mu(n=1-3)$ in the asymptotic R region are used to expand the wave function for the total system. For some values of the total angular momentum J , an enlarged calculation with the channels converging to the $d\mu(n=4)$ and $t\mu(n=4)$ states included are performed to confirm the convergence of the cross sections with the size of the basis set. The cross sections change little, which proves a good convergence. The scattering equations in the HCC method are solved for $J=0-10$, and this is sufficient for the converged transfer cross sections. The higher-partial-wave contributions to the elastic cross sections are calculated using an expansion in terms of atomic orbitals of $d\mu(n=1-2)$, and the continuity of the results from the two methods is good.

The elastic and transfer cross sections in the HCC method are presented in Fig. 1, and are compared with

other theoretical transfer cross sections calculated in semiclassical approximations. For the elastic cross section, there is no reported work and the comparison is not made. The HCC elastic and transfer cross sections have similar values at an energy of 0.001 eV, and the elastic cross section shows a weaker decrease with increasing energy. The transfer results differ considerably between different methods.

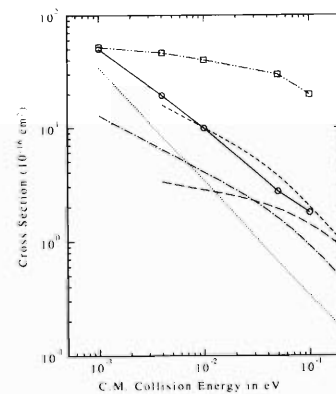


Fig. 1. Cross sections for elastic scattering $t + d\mu(2s) \rightarrow t + d\mu(2s)$ and for muon transfer $t + d\mu(2s) \rightarrow t\mu(n=2) + d$. Elastic: open squares, present calculation. Muon transfer: open circles, present calculation; dotted curve, Solov'ev;³⁾ dot-dashed curve, Menshikov et al.;⁴⁾ dashed curve, Czapliński et al. without electron screening;⁵⁾ long-dashed curve, Czapliński et al. with electron screening.⁵⁾

In the actual experimental system for the study of muon-catalyzed fusion, the triton in the initial channel in reaction (1) is embedded in a molecule T_2 or DT . In other words, the actual processes of experimental interest are



and



Thus the muon-transfer reaction (1) occurs under the screening of charges by two electrons. A comparison of the transfer cross sections of Czapliński et al.⁵⁾ with and without the electron-screening effect reveals that the effect becomes more pronounced as the collision energy is lowered. A realistic calculation including it requires a further study.

References

- 1) L. I. Ponomarev: *Contemporary Phys.*, **31**, 219 (1990).
- 2) A. Igarashi et al.: *Phys. Rev.*, **A50**, 4951 (1994).
- 3) E. A. Solov'ev: *Yad. Fiz.*, **43**, 138 (1986).
- 4) L. I. Menshikov et al.: *Z. Phys. D*, **2**, 1 (1986).
- 5) W. Czapliński et al.: *Phys. Rev.*, **A50**, 518 (1994).

* Department of Reactor Engineering, Japan Atomic Energy Research Institute

Strong Induced-Dipole-Field Oscillations in an Excited $dt\mu$ Molecule above the $t\mu$ ($N = 2$) Threshold

K. Hino and J. H. Macek*

Investigations on elementary atomic processes for a $dt\mu$ molecule are quite important to disentangle complicated phenomena underlying the muon catalyzed fusion (μCF) and to understand the general Coulomb three-body problem beyond the validity of the infinite nuclear mass approximation. Recently, of special interests are Feshbach resonances and muon transfer processes in the manifolds of $N \geq 2$, which are thought to play decisive roles in μCF . Such atomic processes relevant to an excited $dt\mu$ molecule are characterized by a long-range nature of an attractive dipole interaction $-\alpha/R^2$, where α is associated with a dipole moment of a $t\mu$ ($d\mu$) atom induced by a collision partner d (t) and R is an internuclear distance. The most remarkable peculiarity of the dipole interaction manifests itself in the existence of the infinite number of bound or resonance states below a threshold and in the appearance of oscillations of cross sections above the threshold. The latter effect is called the Gailitis-Damburg (GD) oscillation.¹⁾ The strong GD oscillation is expected in $dt\mu$ since the magnitude of α measured in the muon atomic unit is about ten times greater than that of a hydrogen negative ion H^- gauged in the usual atomic unit. In this report, we concern ourselves with this intriguing effect.

We employ the hyperspherical method to analyze the Coulomb three-body system of $dt\mu$ since it enables us to apply straightforward to any three-body system irrespective of its mass and charge ratios. The S-matrix (S'), amenable to the Stark representation, is obtained by a usual matching procedure. This matrix is furthermore transformed into the S-matrix (S) in the hydrogenic representation by $S = V^{(+)}S'V^{(-)\dagger}$ with $V^{(\pm)}$ unitary.¹⁾

In Figs. 1 and 2, we show squared T-matrices corresponding to S' and S for the elastic and inelastic collisions within the $N = 2$ manifold of $t\mu$ from extremely low energy region to relatively higher energy region. The partial wave for these collisions is limited to the S-wave and the Lamb shift contribution is taken into no account. The quantities of $|T'_{f',i'}|^2$ of Fig. 1 exhibit oscillating structures nearly above 1 eV. The oscillations are thought to result from interference of the dipole-oscillation phase pertaining to the attractive dipole channel of $t\mu$ with several phases belonging to the upper attractive channels, especially, to the nearest channel of $d\mu$. As a result of the above-mentioned transformation, the T-matrices of $T'_{f',i'}$ in the Stark representation are mixed up one another to show the

strong GD oscillations of $|T_{f,i}|^2$ in Fig. 2.

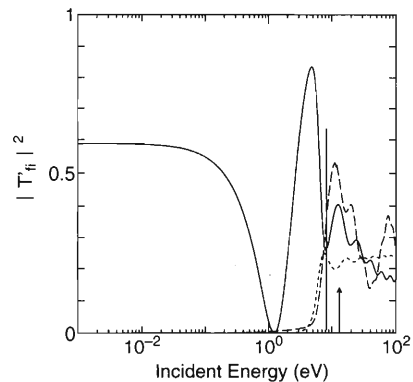


Fig. 1. The squared T-matrix of $|T'_{f',i'}|^2$ versus the incident energy in the center-of mass frame measured from the $t\mu$ ($N = 2$) threshold. The solid line, the dashed line and the dot line mean $|T'_{+,+}|^2$, $|T'_{-,-}|^2$ and $|T'_{+,-}|^2$, respectively, where $+$ and $-$ stand for the lower and the higher Stark states within the $t\mu$ ($N = 2$) manifold. The arrow at 12.01 eV indicates the threshold of $d\mu$ ($N = 2$). The vertical line at 8.24 eV is the Feshbach resonance supported by the attractive dipole potential of $d\mu$ ($N = 2$).

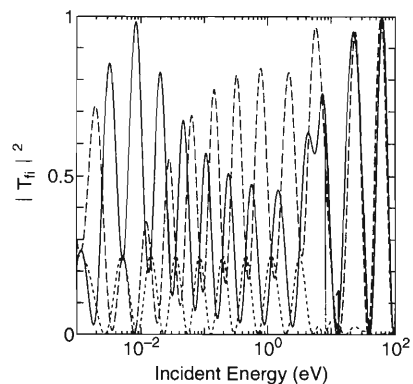


Fig. 2. The squared T-matrix of $|T_{f,i}|^2$ versus the incident energy in the center-of mass frame measured from the $t\mu$ ($N = 2$) threshold. The solid line, the dashed line and the dot line mean $|T_{2s,2s}|^2$, $|T_{2p,2p}|^2$ and $|T_{2s,2p}|^2$, respectively, where $2s$ and $2p$ stand for the excited states of $t\mu(2s)$ and $t\mu(2p)$, respectively. The arrow and the vertical line are the same as in Fig. 1.

* Department of Physics and Astronomy, University of Tennessee and Oak Ridge National Laboratory, U.S.A.

References

- 1) M. Gailitis and R. Damburg: *Proc. Phys. Soc.*, **82**, 192 (1963).

Coincidence Measurement of Fragment Ions with Final Charge State of Projectile in Fast Ion -C₆₀ Collision

Y. Nakai, A. Itoh, T. Kambara, Y. Bitoh, and Y. Awaya

The interest in the fragmentation of C₆₀ induced by the collision with ions, electrons, and photons is recently increasing.¹⁻⁶⁾ LeBrun *et al.* measured the fragment distribution for the collision of fast Xe ions with gaseous C₆₀.¹⁾ They discussed the fragment ion distribution by a bond-percolation model which is often used for nuclear multifragmentation. The small size fragments come from the multifragmentation phenomena of C₆₀. The multifragmentation is caused by the large energy transfer and multiple ionization. It is expected the large energy transfer events can be selected using coincidence fragment distribution measurements with a projectile final charge state because projectile charge transfer occurs when the projectile trajectory has an overlap with C₆₀ in fast collision. We performed selective measurements of the fragment ion distributions at such overlap collisions using the coincidence measurement method with projectile charge transfer.

We used the time-of-flight (TOF) method for fragment ion distribution measurements. The carbon ion beam of 1.3 MeV/u from RILAC passed through C₆₀ vapor formed by a heated oven at 420–450°C. The mass-to-charge ratio(m/q) of fragment ions was analyzed by a TOF spectrometer located at 90° with respect to the incident beam. The TOF spectra were obtained using a multi-hit time-to-digital-converter (TDC). The final charge states of projectile ions were analyzed by a bending magnet downstream from the target area, and projectile ions were detected by a parallel plate avalanche counter (PPAC).

In Fig. 1 we present the total TOF spectrum for initial charge state 5+ without coincidence. It is similar to the TOF spectrum by LeBrun *et al.* It has the peaks for C₆₀⁺, the peaks for C_{60-2n}⁺, which are thought to be residual cluster ions after evaporation of carbon dimers, and the peaks for small fragments whose size n is up to n = 15. In the small size fragment, the odd-numbered peaks are more intense than the even-numbered peaks up to n = 9 and the peaks corresponding to n = 11 and 15 are also intense as seen in the other fragmentation experiments and small cluster formation experiments. For the other initial charge state of projectile, we got the similar TOF spectra even though the intensities of small fragments are more intense with increasing an initial charge state of projectile.

Figure 2 shows the TOF spectra in coincidence with the final charge state in the cases of projectile K-shell electron loss (C⁴⁺ to C⁵⁺ and C⁵⁺ to C⁶⁺) and electron capture by projectiles with K-shell electron vacancies (C⁵⁺ to C⁴⁺ and C⁶⁺ to C⁵⁺). Little or no

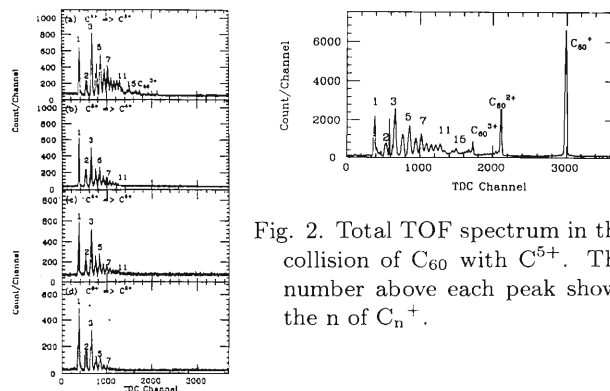


Fig. 1. TOF spectra in the coincidence measurement with a final charge state of projectile.

parent-like heavy fragment ions can be seen here. Only for the electron loss from projectile C⁴⁺, we can see weak peaks corresponding to multiple charged parent-like fragment ions. The odd-even oscillation can be also seen here though these TOF spectra are quite different from the total TOF spectra without coincidence.

In the case of electron capture in our energy region, a predominant process is that a 1s-electron localized around a carbon nuclei of C₆₀ is captured to K or L-shell of the projectile ion. So, the 1s-vacancy is created inside C₆₀ and it decays through the Auger process. The Auger process causes the emission of a few electrons, which is recently shown by photo-excitation and photo-ionization of 1s-electron.⁶⁾ Moreover, the projectile ions can excite and ionize other electrons because the projectile trajectory overlaps with the electron cloud of C₆₀. Thus, the electron capture process causes multiple ionization and excitation of C₆₀ enough for multifragmentation. In the projectile K-shell electron loss, the ionization and excitation of electrons of C₆₀ also occur. And the projectile K-shell electron loss process may produce the 1s-vacancy of C₆₀ because most of such K-electron losses seems to occur close to a carbon nuclei of C₆₀ at our incident energy. So, the projectile K-shell electron loss process can also cause multifragmentation. The fragment ion distributions seem to depend only on the initial charge state of projectile.

References

- 1) T. LeBrun *et al.*: *Phys. Rev. Lett.*, **72**, 3965 (1994).
- 2) P. Hvelplund *et al.*: *ibid.*, **69**, 1915 (1992).
- 3) B. Walch *et al.*: *ibid.*, **72**, 1439 (1994).
- 4) D. Ding *et al.*: *ibid.*, **73**, 1084 (1994).
- 5) H. Hohmann *et al.*: *ibid.*, p. 1919.
- 6) S. Aksela *et al.*: *ibid.*, **75**, 2112 (1995)

Three-Dimensional Recoil-Ion Momentum Analyses in 8.7 MeV O⁷⁺-He Collisions

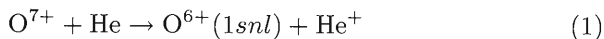
T. Kambara, J.-Z. Tang, Y. Awaya, B. D. DePaola, O. Jagutzki, Y. Kanai, M. Kimura, T. M. Kojima, V. Mergel, Y. Nakai, H. W. Schmidt-Böcking, and I. Shimamura

We have measured the final electronic state distributions and differential cross sections of single-electron capture and target single-ionization processes for 8.7 MeV O⁷⁺-He collisions as functions of scattering angle, using high resolution recoil-ion momentum spectroscopy.¹⁾ Information on the final electronic state is obtained from the longitudinal momentum component $p_{\parallel R}$ (parallel to the projectile direction) of the recoil ions and that on the projectile scattering angle from the transverse momentum component $p_{\perp R}$. The details of the work have been reported elsewhere.²⁾

The setup and the preliminary results were reported previously.³⁾ A collimated 8.7 MeV O⁷⁺ beam from the RILAC was intersected with a target of supersonic He jet from a pre-cooled gas. Performing a recoil-projectile coincidence, we have determined the three-dimensional recoil-ion momentum for selected final projectile and recoil charge states.

The experimental resolution of the longitudinal momentum component was about ± 0.5 a.u. and that of the transverse component was about ± 0.2 a.u. which corresponds to an angular resolution of about $\pm 1.5 \times 10^{-6}$ rad for the projectile scattering angle.

For the pure single-electron capture



the $p_{\parallel R}$ distribution is displayed in Fig. 1(a) and the differential cross sections $d\sigma/dp_{\perp R}$ is displayed in (b). In single-electron capture, the dominant contributions to capture were found to be those from the $n = 4$ and higher states. Figure 1(b) shows the corresponding transverse momentum distribution integrated over the whole peak structure in Fig. 1(a).

A semiclassical molecular-state-expansion method was used to calculate the electron capture cross sections. The recoil momentum distribution was obtained by using the WKB approximation for the heavy particle motion. We carried out five-channel calculations, the results of which are included in Fig. 1. The cross section for transfer to the $n = 5$ state is found to be dominant, whereas the $n \leq 4$ states are not much populated. The differential cross section convoluted by the experimental resolution qualitatively agrees with the present experimental cross section, although the absolute value of the maximum differential cross section is larger than the experimental value by a factor of about 2.5.

The transfer ionization process

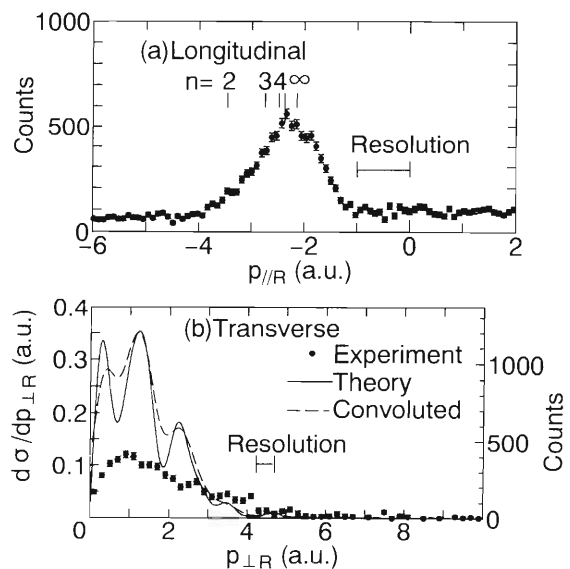
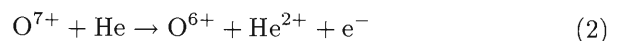


Fig. 1. Measured recoil-ion momentum distribution for the pure single-capture reaction channel: (a) displays the longitudinal momentum $p_{\parallel R}$ distribution and (b) the differential cross section as a function of the transverse momentum $p_{\perp R}$. The n -values in (a) correspond to the final principal quantum number in O⁶⁺($1snl$). Solid line in (b) shows the results of the close-coupling calculations and dashed line shows the results convoluted by the experimental resolution.



was found to proceed through the single-electron capture accompanied by a single target ionization which mainly populates final $n = 2$ to $n = 4$ states. The contribution of another possible process, the double-electron capture followed by auto-ionization of the projectile, is relatively small. It was also found that the differential cross section (transverse momentum distribution) differs significantly from the pure single capture cross section.

References

- 1) J. Ullrich, R. Dörner, V. Mergel, O. Jagutzki, L. Spielberger, and H. Schmidt-Böcking; *Comments At. Mol. Phys.*, **30**, 285 (1994).
- 2) T. Kambara et al.: *J. Phys. B: At. Mol. Opt. Phys.*, **28**, 4593 (1995).
- 3) T. Kambara et al.: *RIKEN Accel. Prog. Rep.*, **28**, 75 (1995).

Intercombination Lines in Highly Charged Ions

P. Bengtsson, K. Ando, T. Kambara, Y. Kanai, T. M. Kojima, Y. Nakai, Y. Awaya, L. Engström, R. Hutton, I. Kink, I. Martinson, and B. Nyström

The spectra of heavy and highly charged ions are often line-rich making analyses of such spectra complicated. Most of the levels in such ions are very short-lived, that is the lifetimes are in the order of ps. The beam-foil technique offers a possibility to study the ions excited by the foil at well-defined distance from the excitation point. Since the ions are moving with a well-defined velocity, that distance is equivalent to a time after the excitation. The distance can be chosen such that all the fast transitions have almost completely decayed and thus they have become weak. Thus only lines originating from long-lived levels, mostly so-called intercombination lines, which are lines originating from transitions where the initial and final state have different spins, remain in the spectrum. Such a spectrum is referred to as delayed spectrum.¹⁾

The work reported here concerns ions of Kr, Y, Zr and Nb. The energy of these ions were 1.67 and 2 MeV/u and they were obtained from RILAC. Measurements of the spectra were made at a delay-time of approximately 500 ps. All the intercombination lines we have been concentrating our attention on, the Mg-like intercombination line $3s^2\ ^1S_0-3s3p\ ^3P_1$, the Al-like $3s^23p\ ^2P_{1/2}-3s3p^2\ ^4P_{1/2}$ and $3s^23p\ ^2P_{3/2}-3s3p^2\ ^4P_{5/2}$ lines and the Si-like $3s^23p^2\ ^3P_1-3s3p^3\ ^5S_2$ and $3s^23p^2\ ^3P_2-3s3p^3\ ^5S_2$, appear within a wavelength region of approximately 20 Å for these elements.

The relative intensities of each line in the spectra at the two different energies depend on the charge state distribution of the element at that particular beam energy. The lines we observe in these “delayed spectra” are most likely intercombination lines or other forbidden lines exhibiting a substantially longer lifetime than the so-called allowed transitions. These two features are used to support the identifications.

Our observations of Mg-, Al- and Si-like intercombination lines agree well with the observations in the sequence for the Mg- and Al-like ions; that is, the wavenumbers follow a smooth trend. However they

seem to disagree with the transition energy reported for the Si-like $3s^23p^2\ ^3P_1-3s3p^3\ ^5S_2$ and $3s^23p^2\ ^3P_2-3s3p^3\ ^5S_2$ lines in Mo,²⁾ see Fig. 1. The earlier observations have been based on comparison with Ref. 3 and have been approaching agreement with the calculated values. Our observations disagree with both Ref. 2 and 3. Even though not involving the theoretical values in the discussion, it is clear that something is not right. The observations in Ti IX-Br XXII in the plot are done by Träbert et al.^{4,5)} This will be subject to further investigation for higher Z elements.

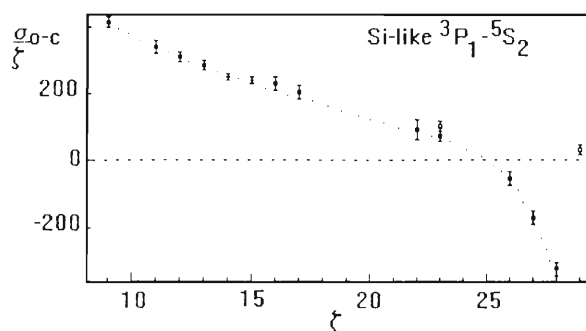


Fig. 1. Isoelectronic comparison of wavenumbers reduced by the theoretical value by Huang.³⁾ The dotted line is to guide the eye. ζ is the effective core charge seen by the jumping electron. σ_{o-c} is the difference between observed and calculated wavenumbers. The wavenumbers are in cm^{-1} .

References

- 1) E. Träbert: *Physica Scripta*, **48**, 699 (1993).
- 2) C. Jupén et al.: *ibid.*, **44**, 562 (1991).
- 3) E. Träbert et al.: *J. Opt. Soc. Am.*, **B5**, 2173 (1988).
- 4) E. Träbert: *Phys. Rev.*, **A47**, 3805 (1993).
- 5) K.-N. Huang: *At. Data Nucl. Data Tables*, **32**, 503 (1985).

Observation of a Systematic Deviation between Experimental and Theoretical Lifetimes for the $3s3p\ ^3P_1$ Level of High Z Mg-like Ions

R. Hutton, L. Engström, S. Hultdt, B. Nyström, I. Martinson, K. Ando, P. Bengtsson, T. Kambara, Y. Kanai, T. M. Kojima, Y. Nakai, and Y. Awaya

In a previous report¹⁾ we discussed beam-foil measurements of the $3s3p\ ^3P_1$ lifetime for Mg-like Zr and Nb. We hinted at a possible discrepancy with the currently available theoretical values. During the recent year measurements have been made on a number of other Mg-like ions and this discrepancy has been con-

Table 1. Comparison of the experimental $3s3p\ ^3P_1$ lifetimes with those calculated by Curtis.⁴⁾

Ion	τ_{exp} [ns]	τ_{theory} [ns]
Ni XVI	10.8 ± 0.2	12.5
r XXV	1.24 ± 0.05	1.54
Y XXVIII	0.72 ± 0.07	0.878
Zr XXIX	0.55 ± 0.03	0.0743
Nb XXX	0.45 ± 0.025	0.637

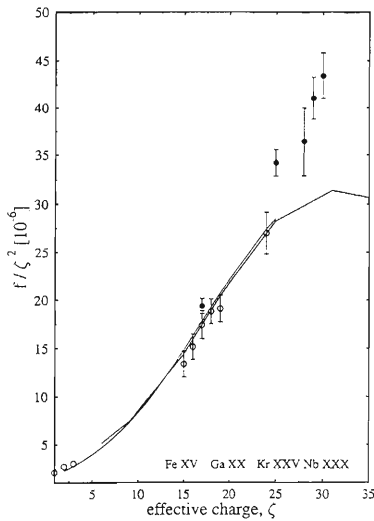


Fig. 1. This shows a comparison of the experimental and theoretical scaled oscillator strengths for $3s^2\ ^1S_0$ - $3s3p\ ^3P_1$ spin-forbidden transition in Mg-like ions. The filled circle data points are measured at RIKEN. The two theoretical curves are those reported by Huang and Johnson⁵⁾ and Cheng and Johnson.⁶⁾ Cheng and Johnson present calculations for a few elements over a large range of atomic numbers, and with larger intervals. ζ is the effective core charge seen by the jumping electron.

firmed. Measurements have been performed for Mg-like Ni, Kr and Y and we have re-measured the Zr and Nb cases. The measurements were done using beams of 0.7 MeV/u Ni and 2 MeV/u Kr, Y, Zr and Nb provided by the RILAC accelerator. The beam-foil set up described earlier²⁾ was modified to account for background problems from beam-related electrons as discussed by Hutton et al.³⁾ Table 1 shows a comparison of our $3s3p\ ^3P_1$ lifetimes with the values obtained by Curtis.⁴⁾ The deviation between experiment and theory is clearly seen in Fig. 1 where our scaled oscillator strength is shown along with the theoretical values of Huang and Johnson⁵⁾ and Cheng and Johnson.⁶⁾

References

- 1) R. Hutton et al.: *RIKEN Accel. Prog. Rep.*, **28**, 69 (1995).
- 2) K. Ando et al.: *J. Spectr. Soc. Jpn.*, **41**, 370 (1992).
- 3) R. Hutton et al.: to be published.
- 4) L. J. Curtis: *Physica Scripta*, **43**, 137 (1991).
- 5) K.-N. Huang et al.: *Nucl. Instrum. Methods Phys. Res.*, **B9**, 503 (1985).
- 6) K. T. Cheng et al.: *Phys. Rev.*, **A16**, 263 (1977).

Problems Caused by Beam-Related Electrons in Beam-Foil Lifetime Measurements

R. Hutton, L. Engström, S. Huldt, B. Nyström, I. Martinson, K. Ando, P. Bengtsson, T. Kambara, Y. Kanai, T. M. Kojima, Y. Nakai, and Y. Awaya

During our studies of the $3s3p\ ^3P_1$ lifetime for Mg-like ions¹⁾ we have found a number of problems caused by beam-related electrons. For example the cusp-electrons for the 2 MeV/u beams of Kr, Y, Zr and Nb used will have an energy of 1.066 KeV and the binary-encounter peak will be at 4.264 keV. It appears that when such electrons hit the entrance slit of the 2.2 m grazing incidence spectrometer a high photon background is generated. This rate depends on the position of the foil with respect to the entrance slit. We could remove the background by applying a magnetic field over the spectrometer slits, see Fig. 1. We have also used an auxiliary slit arrangement fixed on the spectrometer slit to eliminate this background problem. The 2nd problem, related to these electrons, is that of beam normalisation. As the foil is moved away from the Faraday cup the fraction of electrons in the beam will change (angular distribution, scattering etc.). This means that a constant current from the accelerator will not give constant data acquisition times for different foil positions. We have studied this during periods of stable accelerator operation. Through these studies we could generate a correction function. We have also eliminated the problem by using a secondary fixed foil in front of the Faraday cup. In the cases where we have used both methods to measure a decay curve the extracted lifetimes have agreed. There is a 3rd background problem which is not yet solved. This is a very intense but short lived background at or close to the foil. It is assumed that this is generated either by electrons hitting the spectrometer slit or X-rays from the foil. We will attempt to reduce this by putting a bias ring in front of the slits and by tilting the foil holders.

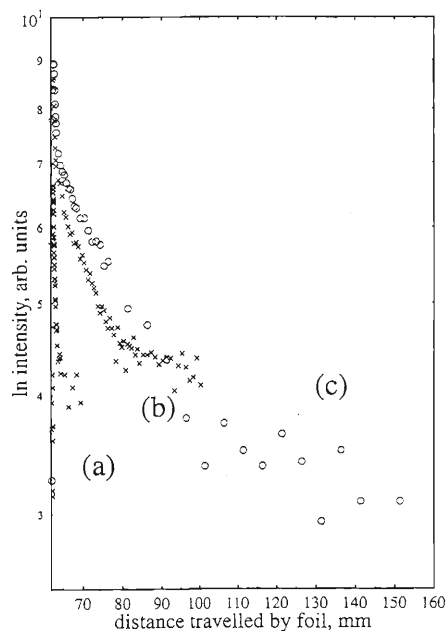


Fig. 1. Decay curves for the $3s^2\ ^1S_0-3s3p\ ^3P_1$ transition in Nb^{29+} (197.68 Å). Curve (a) shows the intensity decay of prompt background near the foil, recorded at a position where no spectral lines were observed. Curves (b) and (c) are taken from lifetime measurements without or with the external magnetic field, respectively. In the latter case the background is reduced to practically the detector dark rate.

References

- 1) R. Hutton et al.: to be published.

Beam-Foil Spectra of Highly Charged, Highly Excited Neon Ion in Visible Region

K. Ishii, Y. Kimura, T. Nishida, and K. Ando

Atomic structure and spectra of highly charged rare gas ions have received increasing interest from the viewpoint of diagnostics of fusion-oriented high temperature plasma. The low lying allowed transitions have been well studied in the conventional discharge sources. However, there is still a lack of information on the spectra of high lying and/or multiply excited transitions. The beam-foil method is efficient for producing these states.

The beam-foil spectra of Ne ion at energy of 0.5 and 1.0 MeV/u from the linear accelerator RILAC were recorded in the range between 2000 and 5500 Å. Photons emitted from the Ne ion beam were viewed in the perpendicular direction of the beam, dispersed by a monochromator ($f = 25$ cm) and detected by a photomultiplier. Higher spectral resolution was achieved by the refocusing method. Most of the lines are classified due to the transitions of high n, ℓ -levels. The most intense lines in each line groups are those with possible highest ℓ transitions. Some of the satellite lines are classified as multiply excited state transitions.

We have first calculated wavelengths from the hydrogenic term energy for n, ℓ -level given as

$$T_H = -\frac{R\zeta^2}{n^2} \left\{ 1 + \frac{\alpha^2\zeta^2}{n^2} \left(\frac{n}{j+1/2} - \frac{3}{4} \right) \right\}$$

where R is the Rydberg constant and ζ is the ion charge. The transition probabilities were also calculated.¹⁾ The wavelength thus obtained with the highest possible ℓ value is in good agreement with the most intense line in each observed line group. As the next step we have taken into account the core polarization effects.²⁾ Finally both energy levels and transition probabilities were computed by use of the atomic structure calculation code (HXR).³⁾

In Fig. 1(a) a partial spectrum of 0.5 MeV/u beam immediate downstream of the foil is shown. The lines are classified to the transition of $1s^22s7\ell-1s^22s8\ell$ as indicated, where ℓ ranges from 3 to 7. The lower Fig. 1(b) shows the spectrum calculated by the HXR method. In the calculation the following configurations were included together with the configuration interactions in Be-like Ne VII:

$$2s6\ell + 2s7\ell + 2s8\ell + 2s9\ell + 2p4\ell + 2p5\ell.$$

The levels with $\ell \leq 6$ in $n = 8$ manifold are largely perturbed with the nearby lying configuration $2p5\ell$ levels, and the lines of the transition $2s7\ell'-2s8\ell$ with $\ell' \leq 5$ and $\ell \leq 6$ are shifted appreciably from the line of the

yrast transition $2s7i-2s8k$. A line at 3681 Å is classified to $n = 10 - n = 12$ transition in He-like Ne IX. A few weak lines on the larger wavelength side of the $2s7i-2s8k$ line are probably due to multiply excited transitions. Two lines around 3750 Å are $2s7f-2s8g$, $2s7d-2s8f$ or $2s7g-2s8f$.

Most of the intense lines covered in the present work are identified as transitions between high n, ℓ -levels with $\Delta n = 1$, where n is ranging from 6 to 10 in Ne VII, Ne VIII, Ne IX and Ne X. Detailed analysis will be given elsewhere.⁴⁾

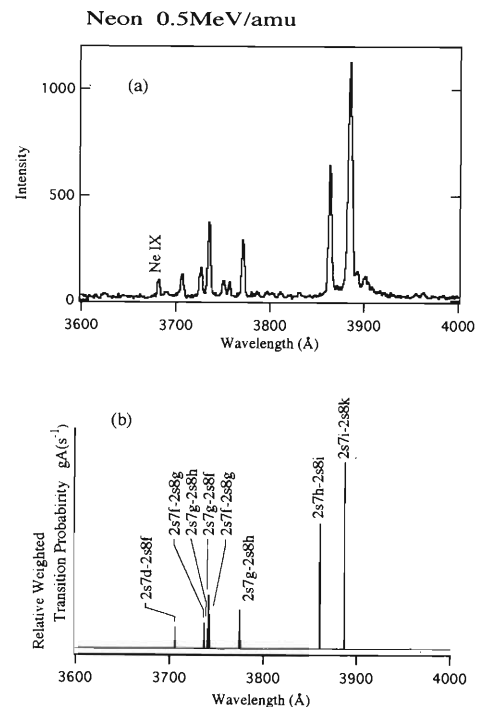


Fig. 1. Partial spectrum of Ne ion. (a) Observed and (b) calculated.

References

- 1) H. A. Bethe and E. E. Salpeter: *Quantum Mechanics of One- and Two-Electron Atoms*, Springer-Verlag, Germany (1957).
- 2) B. Edlén: in *Handbuch der Physik*, Vol. 27, ed. S. Flügge, Springer-Verlag, Germany, p. 80 (1964).
- 3) R. D. Cowan: *The Theory of Atomic Structure and Spectra*, University of California Press, U.S.A. (1981).
- 4) K. Ishii, Y. Kimura, T. Nishida, and K. Ando: to be submitted in *Physica Scripta*.

L X-Ray Emission Spectra of Copper

K. Kawatsura, R. Takahashi, H. Kageyama, T. Kambara, M. Oura,
T. Papp, Y. Kanai, and Y. Awaya

The structure of the K X-ray diagram emission lines of the 3d transition elements has been the subject of numerous studies. Recently, we have reported that broad satellite peaks are observed on the high-energy side of the L X-ray diagram emission lines in 3d transition metals (Cr, Mn, Fe and Co) by 1.1 MeV N- and 0.85 MeV Ne-ion impacts and the $L\alpha_{1,2}$ lines are significantly shifted to lower energies.¹⁾

In this report we present the results of the high-resolution measurement of L X-ray emission spectra from a Cu target produced by 0.73 MeV/nucleon He, Si and Ar ions at the RILAC. A well collimated beam ($< 1 \times 1 \text{ mm}^2$) was incident on a Cu foil target of 0.2-2 μm thickness. The L X-ray spectra were measured by using a broad-range crystal spectrometer with a flat RbAP crystal ($2d = 2.612 \text{ nm}$).²⁾

Figure 1 shows L X-ray spectra from a Cu foil target by 0.73 MeV/nucleon He^{2+} , Si^{5+} and Ar^{6+} ions, respectively. Since the $L\eta$ and $L\iota$ lines are found to be relatively weak, we focused our attention on the energy region of the $L\alpha_{1,2}$ and $L\beta_1$ lines. The peak energies of L X rays obtained at the RILAC with heavy ions were calibrated with those produced by H- and He-ion impacts at the JAERI-TIARA.

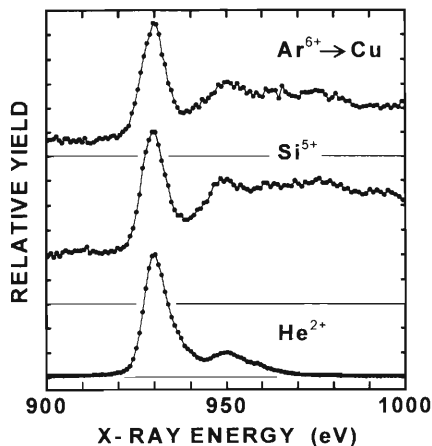


Fig. 1. L X-ray spectra of Cu produced by 0.73 MeV/nucleon He^{2+} , Si^{5+} , and Ar^{6+} ion impacts.

In cases of Si- and Ar-ion impacts, we found a very weak and broad band at the low-energy side of the $L\alpha_{1,2}$ line, and found more complicated structures at the high-energy side of $L\alpha_{1,2}$ and $L\beta_1$ lines. We also found broadening of the $L\alpha_{1,2}$ line to a lower energy, but no shift of the peak energy. The weak band

(900–923 eV) was attributed to the radiative Auger effect (RAE) or radiative electron rearrangement (RER). These are frequently observed in the K X-ray transition spectra, but have not been observed in the L X-ray transition. We consider that the complicated structures above $L\alpha_{1,2}$ and $L\beta_1$ lines are the satellite and hypersatellite lines due to multiple L- and M-shell ionization.

Full understanding of the origin of the broadening of the $L\alpha_{1,2}$ line to a lower energy is difficult and awaits for future studies. However, we have tried to compare the experimental spectra with the calculated ones based on the multiconfiguration Dirac-Fock method (GRASP code).³⁾ Table 1 shows the resulting peak centroid energies of calculated transitions of $L\alpha_{1,2}$ and $L\beta_1$ X-ray diagram and satellite lines for a Cu free atom. It is noted that the centroid energy of $L\alpha_{1,2}$ satellite lines with one 3d electron vacancy shifts by 1.6 eV to a lower energy than the diagram lines. This explains the broadening to lower-energy side in the $L\alpha_{1,2}$ spectrum produced by heavy-ion impacts. The transition energy with initial two 3d vacancies is the same as the energy of the diagram line. A larger energy shift in $L\beta_1$ X-ray transition was found in the calculation; -1.9 and -1.0 eV for one and two 3d vacancies, respectively. However, it is difficult to discuss $L\beta_1$ spectra observed, since the Cu L_3 and L_2 absorption edges lie at 933 and 951 eV, respectively, and $L\alpha_{1,2}$ satellite lines are overlapped in this energy region. They seem to hide the low-energy shift of the $L\beta_1$ lines.

Table 1. Averaged centroid energies in eV for Cu $L\alpha_{1,2}$ and $L\beta_1$ X-ray diagram and satellite lines calculated by Dyall et al.³⁾ using the MC-DF method (GRASP code).

X-ray	Transition	Number of 3d electron vacancy		
		0	1	2
$L\alpha_{1,2}$	$2p_{3/2}-3d_{3/2,5/2}$	930.0	928.4	930.1
$L\beta_1$	$2p_{1/2}-3d_{3/2}$	950.1	948.2	949.1

References

- 1) K. Kawatsura, K. Ozawa, M. Terasawa, K. Komaki, and F. Fujimoto: *Nucl. Instrum. Methods Phys. Res.*, **B75**, 28 (1993).
- 2) A. Hitachi, H. Kumagai, and Y. Awaya: *ibid.*, **195**, 631 (1982).
- 3) K. G. Dyall, I. P. Grant, C. T. Johnson, F. A. Parpia, and E. P. Plummer: *Comput. Phys. Commun.*, **55**, 425 (1989).

Angular Distribution Measurements of X-Rays from Multiply Ionized Atoms

T. Papp, Y. Awaya, T. Kambara, K. Kawatsura, T. M. Kojima, Y. Nakai, and M. Oura

In heavy-ion impact the dominant process is the multiple ionization of target atoms. To calculate the ionization cross sections for the L-shells two competing methods are used,¹⁾ namely the ECPSSR-BC theory and the coupled channel calculation method. However, in the determination of ionization cross sections the knowledge of decay parameters, like fluorescence yields, X-ray branching ratios and Coster-Kronig transition probabilities are necessary ingredients.¹⁾ The available information on these parameters is very limited and strongly depends on the distributions of the vacancies on various shells.²⁾ A series of measurements was carried out to study the L-shell X-ray spectra of medium and heavy elements by Si(Li) detectors, having moderate resolution compared to crystal diffraction spectrometers. The presence of many satellite lines makes the analysis of X-ray spectra complicated, which indicates a need for high resolution measurements. Generally, in the case of multiply ionized atoms the magnetic substate population of the initial state of the X-ray transition is nonstatistical. This may result in the anisotropic angular distribution of the L_1 and L_2 X-rays. Additionally in the case of the L_3 subshell both the initial and final state can be aligned; as a consequence some X-ray transitions are expected to have large polarization and anisotropy in angular distribution.³⁾ We have developed a formalism to describe the angular distribution and polarization of X-ray transitions between aligned initial and aligned final states.

To study this possibility, and to measure the L-shell X-ray yield ratios, an angular distribution measurement was carried out on a terbium target. The experimental arrangement was similar to an earlier measurement reported in Ref. 4. The target atoms were ionized by Ar ions from the RILAC, at 13.2, 29.4, 52, and 80 MeV incident energies. The target X-rays were diffracted by LiF(200) and (220) crystals and a position sensitive proportional counter was used to detect the X-rays. Reference spectra were also recorded following X-ray excitation from an X-ray tube and with 28 MeV N projectile from the RILAC as well. The relative intensity of the X-rays differs largely from the X-ray excited case. Typical spectra are presented for the N and Ar projectile impact in Fig. 1. The L_γ complex was hardly discernible as an indication of the strong multiple outer shell ionization.

In the evaluation of the X-ray spectra difficulties arose from the determination of the spectrometer

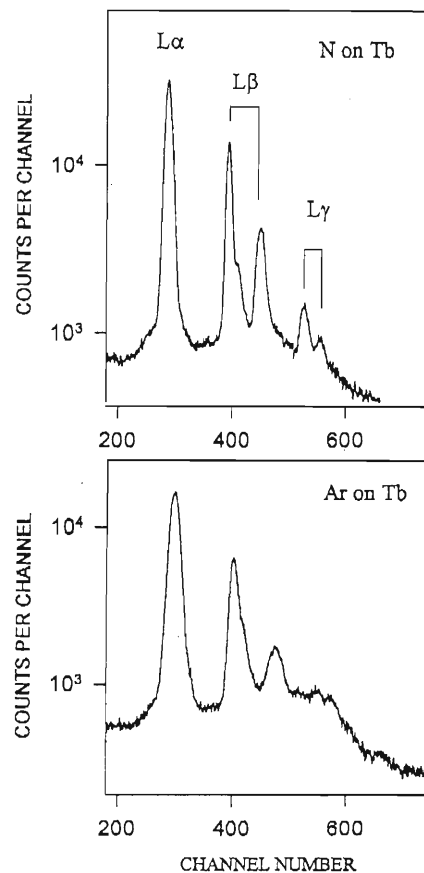


Fig. 1. The L X-ray spectra of terbium following 28 MeV N (upper part) and 80 MeV Ar (lower part) ion impact.

transmission function, and the polarization sensitivity of the apparatus. A method for the determination of the polarization sensitivity was developed. It is based on the strong energy dependence of the largely polarized bremsstrahlung radiation of an X-ray tube. The evaluation of the data is in progress.

References

- 1) R. Mehta et al.: *J. Phys.*, **B28**, 1187 (1995).
- 2) D. F. Anagnostopoulos et al.: *ibid.*, p. 47.
- 3) T. Papp and L. Kocbach: *J. de Physique*, **C9**, 245 (1987).
- 4) T. Papp, Y. Awaya, A. Hitachi, T. Kambara, Y. Kanai and T. Mizogawa: *RIKEN Accel. Prog. Rep.*, **24**, 47; 48 (1990); T. Papp, Y. Awaya, A. Hitachi, T. Kambara, Y. Kanai, T. Mizogawa, and I. Török: *J. Phys.*, **B24**, 3797 (1991).

Absolute Cross Sections for Charge Capture from Rydberg Targets by Slow Highly Charged Ions

B. D. DePaola, M.-T. Huang,* S. Winecki,* M. P. Stöckli,* Y. Kanai,
S. R. Lundeen,** C. W. Fehrenback,** and S. A. Arko*

We measured absolute charge capture cross sections in collisions of slow highly charged xenon ions with laser excited Rydberg Rb(10f) atoms.¹⁾ The cross sections were measured for scaled projectile velocities ν_p/ν_e from 1.0 to 6.0, and for projectile charge of 8, 16, 32, and 40, where ν_p is the projectile velocity and ν_e the orbital velocity of the Rydberg electron. The experimental setup is schematically shown in Fig. 1. A collimated beam of xenon ions from the Kansas State University Cryogenic Electron Beam Ion Source (KSU CRYEBIS) intersects a thermal beam of excited Rb(10f) atoms in a collision chamber. After interacting with a Rb target, the ion beam is electrostatically deflected by a pair of parallel plates onto a two-dimensional position-sensitive detector (PSD).

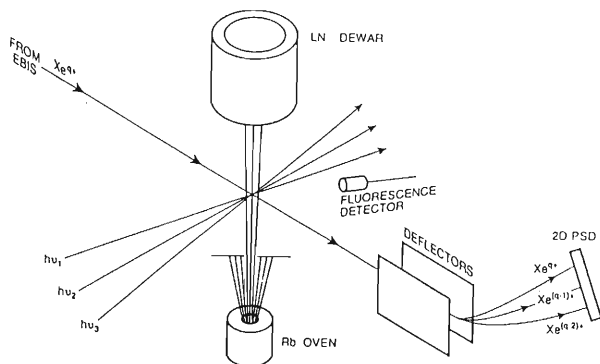


Fig. 1. Simplified overview of the experimental apparatus.

A resistively heated oven at the bottom of the collision chamber produces a beam of Rb atoms. The collimated beam passes into the region where collisions with the ions take place and is then collected on a surface cooled by liquid nitrogen. In the interaction region, the Rb beam is stepwise excited to high Rydberg states by three cw lasers; (1) a single mode tunable diode laser at 780 nm, (2) a Nd:YAG pumped F-center laser at 1530 nm, and (3) an Ar-ion laser-pumped Ti:sapphire laser at 755 nm.

Obtained absolute capture cross sections are shown in Fig. 2. Error bars show the relative error in Fig. 2. Absolute uncertainty is about a factor of 3. The cross sections seem to reach a plateau at the lowest velocities and drop rapidly as the velocity is increased. These

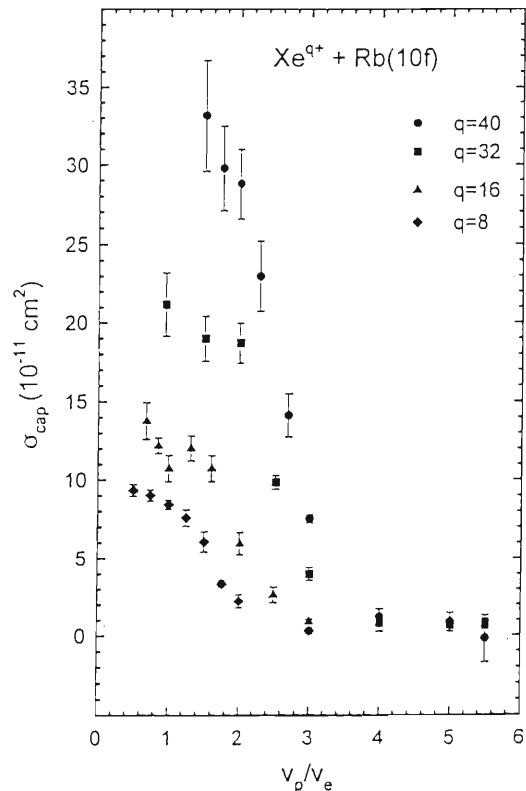


Fig. 2. Absolute charge capture cross sections as a function of scaled projectile velocity (ν_p/ν_e). Error bars are relative. Absolute uncertainty is about a factor of 3.

behaviors are explained qualitatively by a classical theory such as the Bohr-Lindhard model. In the Bohr-Lindhard model,²⁾ a capture cross section is given by

$$\sigma = 16\pi q n^4 \text{ for } V_s < (4q)^{1/4}$$

$$\sigma = \pi q^3 n^4 V_s^{-7} \text{ for } V_s > (4q)^{1/4}$$

where q is the projectile charge, n is the principal quantum number of the target electron, $V_s = \nu_p/\nu_e$, and the cross section is expressed in atomic units. Our results are in good agreement with this model.

References

- 1) B. D. DePaola et al.: *Phys. Rev.*, **A52**, 2136 (1995).
- 2) J. S. Briggs: Proc. Niels Bohr Centennial Conference, North-Holland, Amsterdam, p. 183 (1985).

* Department of Physics, Kansas State University, U.S.A.

** Department of Physics, Colorado State University, U.S.A.

Optogalvanic Diode-Laser Spectroscopy in Hf I

W. G. Jin, T. Minowa, H. Uematsu,* H. Katsuragawa, and M. Hies

Laser spectroscopy has been proved to be a powerful technique to study nuclear deformation and moments.¹⁾ Using RIKEN cyclotron facility, now we are performing a systematic laser spectroscopic study of Hf unstable isotopes. However, spectroscopic information about stable isotopes is necessary for unstable nuclear spectroscopy. Since Hf is a refractory element, it is difficult to produce its atomic beam. Therefore, it is particularly of challenge from the viewpoint of laser spectroscopy to introduce a simple method for producing Hf atomic beam and develop convenient laser spectroscopy, for instance, using a diode-laser rather than an expensive and complicated ring dye laser. This paper reports convenient optogalvanic diode-laser spectroscopy in Hf I.

A Hf galvatron was used in this experiment. Hf atoms were produced by Ar and Ne-ion sputtering in a galvatron. We used a 785-nm single-mode diode laser with a power of 3 mW. Temperature and current of the diode laser were controlled by a controller. The frequency scanning was achieved by modulation of the current. The laser beam was chopped at a frequency of about 500 Hz by a mechanical chopper. The laser-induced optogalvanic signal was detected and fed into a lock-in amplifier. Laser frequency calibration was made by recording the transmission peaks through a home-made confocal Fabry-Perot interferometer with a free spectral range of 300 MHz.

Figure 1 shows a measured optogalvanic spectrum of the 784.5-nm transition from $5d^26s^2\ ^1D_2$ to $5d6s^26p$

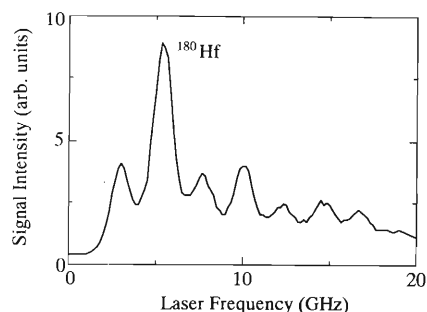


Fig. 1. Measured optogalvanic spectrum of the 784.5-nm transition in Hf I. A peak of ^{180}Hf is labeled with the isotopic symbol and others are the hfs peaks of ^{177}Hf and ^{179}Hf .

3P_1 in Hf I. The FWHM of peaks is about 700 MHz, mainly from the Doppler broadening. The peaks of ^{180}Hf and ^{178}Hf isotopes are overlapped and this shows that the isotope shift is smaller than 700 MHz for the isotope pair of 180-178. This result agrees with that measured for other d - p transitions.²⁾ The hfs peaks of the odd-isotopes, ^{177}Hf and ^{179}Hf with the nuclear spin 7/2 and 9/2, respectively, are clearly observed. This is the first optogalvanic diode-laser spectroscopy in Hf I.

References

- 1) W. G. Jin et al.: *Phys. Rev.*, **A52**, 157 (1995).
- 2) D. Zimmermann et al.: *ibid.*, **A50**, 1112 (1994).

* Tokyo Gakugei University

Measurement of the Isotope Shift in Fe by Resonance Ionization Spectroscopy

T. Minowa, K. Hamada,* H. Uematsu,** W.-G. Jin, and H. Katsuragawa

Optical measurement of the isotope shift in an element allows us to obtain information on nuclear deformation of the element. In a previous report we described resonance ionization spectroscopy of Fe and mass separation of three stable isotopes of Fe using a two-stage acceleration time-of-flight mass spectrometer.¹⁾ As a next step we have measured the isotope shift in Fe and determined the relative changes in mean square nuclear charge radii $\delta \langle r^2 \rangle$.

Fe atomic beam was generated by laser ablation of an Fe target in a vacuum chamber. The second harmonic radiation of a YAG laser (Quanta-Ray GCR-11) was used for laser ablation. Continuous cleaning of the surface of the Fe target with a small polisher was carried out for stable supply of the atomic beam.

Fe atoms were ionized by focused radiation of a dye laser tuned to the $z^5D_4^o - a^5D_4$ transition of Fe (385.991 nm). Generated Fe ions were accelerated and mass-separated through the drift region of the mass separator, resolving power of which was about 400. Mass-separated Fe ions were detected with a ceratron. Outputs of the ceratron detector were amplified and acquired with a digital oscilloscope (Hewlett Packard 54522A) triggered by radiation of a XeCl excimer laser which pumped the dye laser. The waveform acquired with the 54522A was sent to a computer through the GPIB bus and recorded as TOF spectrum.

Resonance ionization spectra of the three stable isotopes, ^{54}Fe , ^{56}Fe , and ^{57}Fe , were obtained as follows. In isotope shift measurements the computer functioned as a set of three multi-channel scalers which counted ^{54}Fe , ^{56}Fe , and ^{57}Fe isotopes, respectively. Because the dye laser scan was controlled by the computer, the channels of the scalers correspond to the wavelength steps of the dye laser radiation.

Figure 1 shows the resonance ionization spectrum of ^{56}Fe . Peak wavelengths of the spectra were determined by the least-squares fitting. The normal mass shift was subtracted from the observed isotope shift in Fe. The relative $\delta \langle r^2 \rangle$ was calculated from the residual isotope shift. The residual isotope shift contained the specific mass shift and the field shift. Although it was reported that the specific mass shift in Fe is small compared with the field mass shift, the former causes uncertainties in the relative $\delta \langle r^2 \rangle$.

The relative $\delta \langle r^2 \rangle$ is plotted against the mass number of Fe (Fig. 2). The solid line denotes the value calculated by the droplet model. Good agreement be-

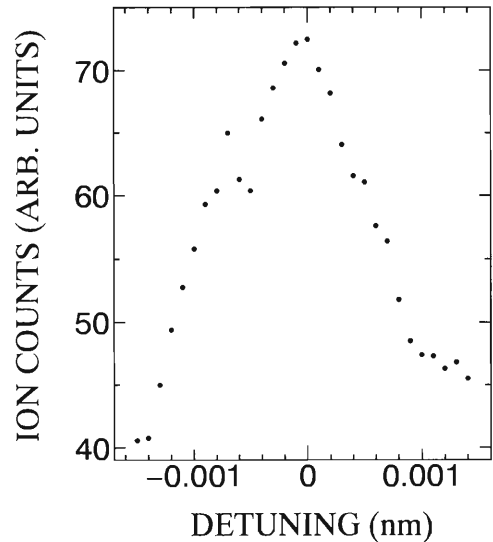


Fig. 1. Resonance ionization spectrum of ^{56}Fe .

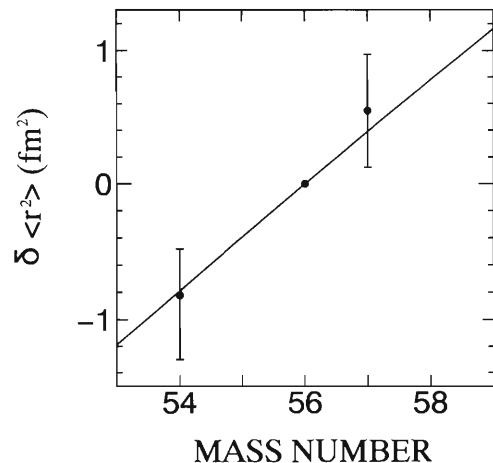


Fig. 2. The relative changes in mean square nuclear radii $\delta \langle r^2 \rangle$ in Fe are plotted against the mass number of Fe.

tween the two suggests that nuclei of the stable isotopes of Fe are scarcely deformed.

References

- 1) H. Katsuragawa et al.: *RIKEN Accel. Prog. Rep.*, **27**, 70 (1993).

* Faculty of Science, Toho University

** Tokyo Gakugei University

Knight Shift for ^{13}O Implanted in Pt

K. Matsuta, M. Tanigaki, M. Fukuda, T. Minamisono, Y. Nojiri, H. Akai,* M. Mihara, K. Minamisono,
T. Fukao, K. Sato, Y. Matsumoto, T. Ohtsubo, S. Fukuda, S. Momota, K. Yoshida, A. Ozawa,
T. Kobayashi, I. Tanihata, J. R. Alonso,** G. F. Krebs,** and T. J. M. Symons**

The Knight shift K and the spin relaxation time T_1 for interstitial impurities implanted in metals are important clues to the electronic structure of the metals. Among the metals, Pt is known to be unique having a very low local electron density around the Fermi level for interstitial impurities, and therefore, having long T_1 and small K . Pt is often used for the magnetic moment measurements because of this advantage. It is important to measure Knight shifts systematically for better understanding of the electronic structure inside metals. Because of the recent development of the technique of polarized radioactive nuclear beams, the choice of probe nuclei now becomes much wider. In the present experiment, we measured the Knight shift and the relaxation time of the proton drip-line nucleus ^{13}O ($I^\pi = 3/2^-, T_{1/2} = 8.6$ ms) through the combined technique of polarized beams and the β -NMR detection.

Polarized ^{13}O nuclei were produced through the 130 MeV/nucleon $^{16}\text{O} + ^9\text{Be}$ at the RIKEN Ring Cyclotron and were separated by the RIPS (RIKEN Projectile Fragment Separator). Thus purified nuclei were then slowed down by an energy degrader and were implanted in a Pt foil placed in a strong magnetic field $H_0 = 4.0$ kOe to maintain the polarization created in the collision. NMR of ^{13}O was observed by means of asymmetric β -ray emission. Polarization effect is recorded as a function of time in order to measure T_1 . To measure Knight shift K , NMR spectrum was also observed for ^{13}O in an ionic crystal MgO.

As a result, a preliminary value of T_1T was obtained for ^{13}O in Pt to be (2.90 ± 0.65) Ks. A preliminary value of Knight shift was obtained from the NMR Spectra shown in Fig. 1 to be $K = +(4.23 \pm 0.14) \times 10^{-3}$. The T_1T for ^{13}O in Pt is unusually small compared with other impurities in Pt. As expected from the unusually small T_1T , the K for ^{13}O is also unusually large. The present results strongly suggest that the electronic structure around ^{13}O in Pt is unusual compared with other cases and the local density at Fermi level must be huge.

In order to explain the present results, the electronic structure was calculated for the second-period main group elements in Pt in the framework of the local spin density approximation of the density functional theory, using the super-cell method in the Korringa-Kohn-Rostoker (KKR) band-structure

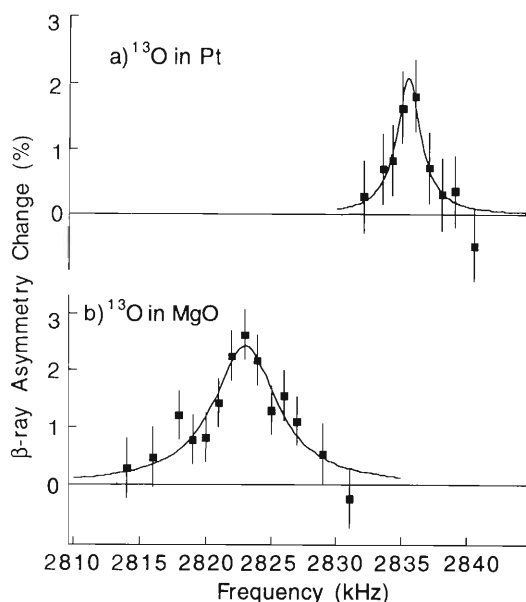


Fig. 1. NMR spectra of ^{13}O implanted in Pt and MgO.

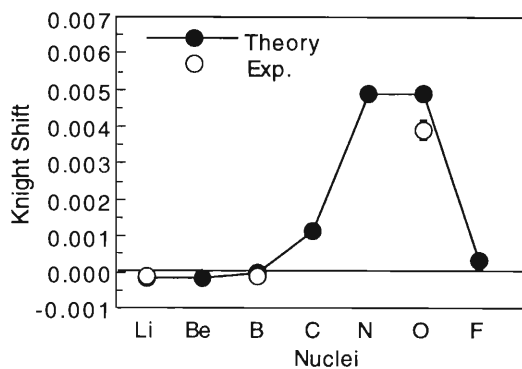


Fig. 2. Experimental and theoretical Knight shifts for interstitial impurities in Pt.

calculation. The theoretical values are shown in Fig. 2 with the experimental Knight shifts. Although the calculation is still preliminary, agreement with the present data is remarkable. It is concluded that the short T_1 and the large K for ^{13}O in Pt can be understood by the large local electron density around the Fermi level, which is well reproduced theoretically by the KKR band-structure calculation.

* School of Science, Osaka University

** Lawrence Berkely Laboratory, U.S.A.

Effect of Ligand Distortion on the Hyperfine Magnetic Field of $^{61}\text{Ni}^{2+}$ Ions in the Spinel Chromites[†]

Y. Kobayashi, T. Okada, Y. Noro,* J. Nakamura, and H. Kitazawa**

We have applied ^{61}Ni Mössbauer spectroscopy to the spinel-type chromites $M_{0.9}\text{Ni}_{0.1}\text{Cr}_2\text{O}_4$ ($M = \text{Mn}, \text{Co}, \text{Cu}, \text{and Zn}$), in which Ni^{2+} ions were substituted for a part of M^{2+} at the A -sites.^{1,2} These Mössbauer spectra measured at 5 K presented symmetric and resolved hyperfine structures, typically observed in the cases of a pure hyperfine magnetic interactions. The derived $|H_{\text{hf}}|$ of Ni^{2+} ions at the A -sites are 800, 540, 510, and 390 kOe for Cu-, Co-, Zn-, and Mn-chromite, respectively. We summarize our present results of $|H_{\text{hf}}|$ against the c/a ratio as the ligand distortion in Fig. 1 together with the previous results of NiCr_2O_4 ³) and the system of $\text{NiFe}_x\text{Cr}_{2-x}\text{O}_4$.⁴) It is indicated that the $|H_{\text{hf}}|$ of Ni^{2+} at the A -sites depends linearly on the Jahn-Teller distortion c/a . We will discuss the mechanism and the origin of the large $|H_{\text{hf}}|$ in consideration of the relation between the electronic state of a Ni^{2+} ion and the ligand distortion.

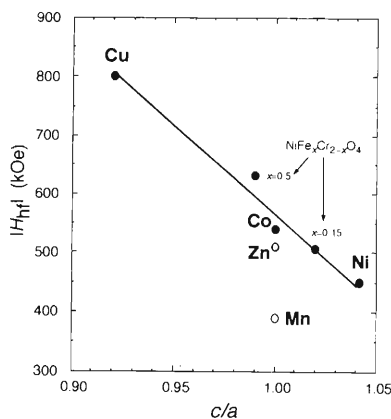


Fig. 1. Ligand distortion c/a dependence of the hyperfine magnetic field of Ni^{2+} ions at the A -sites of the spinels.

The magnitude of H_{hf} at a nucleus can be calculated by the sum of the Fermi contact term, the field caused by the orbital angular momentum, and the dipole magnetic field.⁵) The first term is estimated to be around -270 kOe for Ni^{2+} ions and the third to be very small.⁶) However, the observed $|H_{\text{hf}}|$ in this paper are much larger than the values of the Fermi contact term. So, the contribution of the orbital angular momentum is expected to be dominant in the total $|H_{\text{hf}}|$ in this system.

The energy level of the ground state of d^8 ions at cubic tetrahedral A -sites is a triply degenerate $^3\text{T}_{1u}$. The degeneracy at the A -sites could be removed by ligand distortion arising from the Jahn-Teller effect. The energy level of the ground state of Ni^{2+} ions should be split into a singlet and a doublet. The ground state in NiCr_2O_4 becomes a singlet due to the Jahn-Teller distortion of $c/a > 1$. It means that this $L_z^* = 0$ state has no effective orbital angular momentum. However, an appreciable orbital angular momentum should be induced as a second-order perturbation by the exchange interaction and the spin-orbit interaction in spite of a singlet state. In contrast, the ground state in Cu-chromite ($c/a < 1$) is doubly degenerate and corresponds to $L_z^* = \pm 1$, so that the orbital angular momentum arises from the first-order perturbation. The difference between the energy levels in both cases can be reflected in the magnitude of H_{hf} through the induced orbital angular momentum.

In the effects of ligand distortion, $c/a < 1$ stabilizes the $L_z^* = \pm 1$ states and splits the $L_z^* = 0$ far above the $L_z^* = \pm 1$. The spin-orbit interaction connects the $L_z^* = \pm 1$ states and the $L_z^* = 0$ state by the selection rule. As a result, the Jahn-Teller interaction and the spin-orbit interaction cooperate to enhance the orbital angular momentum. This situation is realized only under the condition $c/a < 1$ (CuCr_2O_4 and $\text{NiCr}_{1.5}\text{Fe}_{0.5}\text{O}_4$). For $c/a > 1$, the ligand distortion results in an opposite effect for inducing orbital angular momentum; a larger distortion results in a smaller $|H_{\text{hf}}|$.

It is believed that the symmetry of the ligands of Ni^{2+} ions is not cubic in Co- and Zn-chromites, so that $|H_{\text{hf}}|$ must be smaller than that of $\text{NiCr}_{1.5}\text{Fe}_{0.5}\text{O}_4$ but larger than that of NiCr_2O_4 . The observed $|H_{\text{hf}}|$ of $\text{Mn}_{0.9}\text{Ni}_{0.1}\text{Cr}_2\text{O}_4$ with $c/a = 1$ is discussed in another report.⁷⁾

References

- 1) T. Okada et al.: *RIKEN Accel. Prog. Rep.*, **28**, 80 (1995).
- 2) T. Okada et al.: *Phys. Lett. A*, **209**, 241 (1995).
- 3) H. Sekizawa et al.: *J. de Physique*, **32**, C1-326 (1971).
- 4) J. C. Love and F. E. Obenshain: *AIP Conf. Proc.*, **18**, 513 (1973).
- 5) E. Fermi and E. Segre: *Z. Physik*, **8**, 729 (1933).
- 6) A. Okiji and J. Kanamori: *J. Phys. Soc. Jpn.*, **19**, 908 (1964).
- 7) T. Okada et al.: This report, p. 112.

[†] Condensed from the article in *Phys. Lett. A*, **209**, 241 (1995)

* Hitachi Multimedia Systems R&D Division

** National Research Institute for Metals

In-Beam Mössbauer Study on Pure Iron Using $^{56}\text{Fe}(d, p)^{57}\text{Fe}$ Reaction

Y. Yoshida, Y. Kobayashi, J. Nakamura, F. Ambe, E. Yagi,
R. Sielemann,* T. Grund,** and A. Seeger**

Iron is one of the largest industrial productions and most widely used among all other metals in the world. However, the nature of point defects in pure iron is still a large open question. There have been controversial interpretations on the recovery stages for vacancies and self-interstitials. In order to study the nature of point defects in pure iron from an atomistic point of view, we use an in-beam Mössbauer technique,¹⁻⁴⁾ which appears to provide information not only on the structure and the stability of point defects, but also on their jump processes.

Although it is rather difficult to detect the point defects in pure iron because of the very low concentration of defects, two Mössbauer experiments have been performed so far: A conventional source experiment on ^{57}Co doped iron, which was irradiated by neutrons and electrons at low temperatures,⁵⁾ showed recovery stages after annealing in the total area intensity, the hyperfine splitting and the line width as well. Furthermore, in an in-beam Mössbauer experiment using Coulomb-excitation and recoil-implantation⁶⁾ two stages were found around 300 and 650 K in the same Mössbauer parameters as in the source experiment.

In an in-beam Mössbauer experiment using $^{56}\text{Fe}(d, p)^{57}\text{Fe}$ reaction, a pulsed deuteron beam is used to produce ^{57}Fe nucleus in the target of pure iron. The Mössbauer probe of ^{57}Fe is excited to the nuclear level of 14.4 keV and simultaneously ejected from lattice sites with the average recoil energy of several hundreds keV. The recoils of ^{57}Fe stop on different lattice sites in the specimen within the time of a few picoseconds. Subsequently the emitted γ -rays are measured using a parallel-plate-avalanche counter (PPAC) between deuteron pulses. Accordingly, this in-beam technique provides a possibility to study both the final lattice sites of ^{57}Fe atoms "internally" implanted in pure iron and their jump processes at elevated temperatures. In order to determine the jump vectors of implanted ^{57}Fe atoms on different sites, one has to measure the angular dependence of Mössbauer spectrum at different crystal orientations. Since the active area irradiated by deuterons is rather small (5×10 mm), the measuring geometry in the present method is much

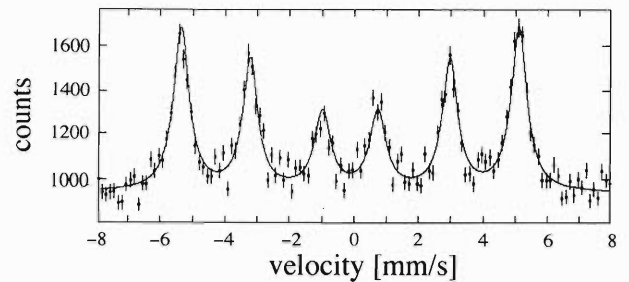


Fig. 1. Mössbauer spectrum of ^{57}Fe in pure iron after $^{56}\text{Fe}(d, p)^{57}\text{Fe}$ reaction measured at 35 K.

superior than that of the in-beam Mössbauer technique using Coulomb-excitation and recoil-implantation.⁶⁾

The energy and the intensity of deuteron beam from the AVF cyclotron were 8 MeV and 200 nA, respectively. We measured a polycrystal iron and also a single crystal at different temperatures from 35 to 300 K. Figure 1 shows the Mössbauer spectrum of a polycrystal iron at 35 K. No satellite component due to defects can be seen in all spectra. However, the line width and the hyperfine splitting at 35 K are slightly different from the values obtained in an absorber experiment⁷⁾ on pure Fe. In addition, these Mössbauer parameters show unusual temperature dependence at around 300 K, which may originate from a jump process of defects.

References

- 1) Y. Yoshida, M. Menningen, B. Keck, G. Vogl, G. Weyer, and K. Schröder: *Phys. Rev. Lett.*, **61**, 195 (1988).
- 2) Y. Yoshida: *Hyperfine Interact.*, **47**, 95 (1989).
- 3) R. Sielemann and Y. Yoshida: *ibid.*, **68**, 119 (1991).
- 4) B. Keck, R. Sielemann, and Y. Yoshida: *Phys. Rev. Lett.*, **71**, 4178 (1993).
- 5) Y. Yoshida, S. Nasu, and F. E. Fujita: Proc. Yamada Conf. 5th on Point Defects and Defects Interactions in Metals and Alloys, eds. J. Takamura, M. Doyama and M. Kiritani, p. 199 (1982).
- 6) Y. Yoshida, D. Tuppinger, G. Vogl, B. Keck, and R. Sielemann: *HMI-B. Annual Rep.*, **490**, 112 (1990).
- 7) R. S. Preston, S. S. Hanna, and J. Heberle: *Phys. Rev.*, **128**, 2207 (1962).

* Hahn-Meitner-Institute, Berlin, Germany

** Max-Planck-Institute für Metalforschung & Max-Planck-Institute für Physik, Stuttgart, Germany

^{61}Ni Mössbauer Spectroscopy on Cubic Spinel Chromites

T. Okada, Y. Noro,* Y. Kobayashi, J. Nakamura, H. Kitazawa,** and F. Ambe

In pervious papers,^{1,2)} we reported that, in ^{61}Ni Mössbauer spectroscopy, the hyperfine magnetic field H_{hf} of ^{61}Ni ions in the A sites of spinel chromite $\text{Cu}_{0.9}\text{Ni}_{0.1}\text{Cr}_2\text{O}_4$ was found to be 800 kOe, which is the largest ever reported for ^{61}Ni . The magnitude of H_{hf} of $^{61}\text{Ni}^{2+}$ ions in the A sites of various spinel chromites has been shown to be linearly dependent on the ligand distortion of the crystal. Calculation of the orbital angular momentum caused by the ligand distortion accounts for the above characteristics.³⁾ It means that the orbital angular momentum is the main origin of the large H_{hf} .

In this report, ^{61}Ni Mössbauer measurements of three cubic spinel chromites $\text{M}_{0.9}\text{Ni}_{0.1}\text{Cr}_2\text{O}_4$ (M=Mn, Co, and Zn) are made to clarify in detail the H_{hf} of $^{61}\text{Ni}^{2+}$ ions on the basis of the orbital angular momentum.

The single line source of ^{61}Cu (\rightarrow ^{61}Ni) was produced in the RIKEN AVF cyclotron. Powdered specimens were prepared by the conventional ceramic sintering method. The source and absorber were kept at the same temperature, 5 K, in a liquid helium cryostat. Experimental procedure was reported in detail in Ref. 2.

Mössbauer spectra of $\text{Co}_{0.9}\text{Ni}_{0.1}\text{Cr}_2\text{O}_4$, $\text{Zn}_{0.9}\text{Ni}_{0.1}\text{Cr}_2\text{O}_4$ and $\text{Mn}_{0.9}\text{Ni}_{0.1}\text{Cr}_2\text{O}_4$ taken at 5 K are shown in Fig. 1. Each spectrum consists of broad and spread lines. Twelve straight solid lines at the bottom of the figure are the calculated positions and intensities of the absorption peaks caused by H_{hf} . The values of H_{hf} amount to 390 kOe for $\text{Mn}_{0.9}\text{Ni}_{0.1}\text{Cr}_2\text{O}_4$, 540 kOe for $\text{Co}_{0.9}\text{Ni}_{0.1}\text{Cr}_2\text{O}_4$ and 510 kOe for $\text{Zn}_{0.9}\text{Ni}_{0.1}\text{Cr}_2\text{O}_4$, respectively. The values of 540 and 510 kOe are expected by calculation of the orbital angular momentum under the cubic symmetry ($c/a = 1$) when the direction of the orbital angular momentum lies in the c plane. The value of 390 kOe for $\text{Mn}_{0.9}\text{Ni}_{0.1}\text{Cr}_2\text{O}_4$ is considerably smaller

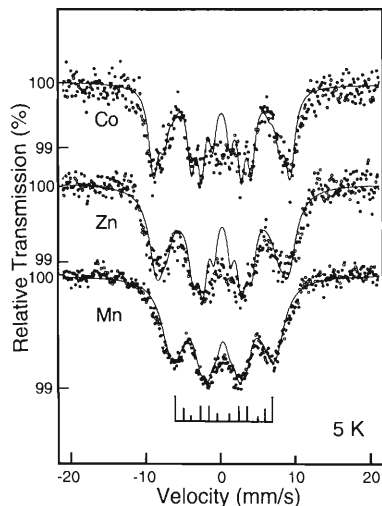


Fig. 1. ^{61}Ni Mössbauer spectra of cubic spinel chromites at 5 K. Co: $\text{Co}_{0.9}\text{Ni}_{0.1}\text{Cr}_2\text{O}_4$, Zn: $\text{Zn}_{0.9}\text{Ni}_{0.1}\text{Cr}_2\text{O}_4$, and Mn: $\text{Mn}_{0.9}\text{Ni}_{0.1}\text{Cr}_2\text{O}_4$.

than the others. The specimen MnCr_2O_4 has a ferromagnetic spiral structure below 20 K. The spin direction for MnCr_2O_4 rises from the c plane toward the c axis.⁴⁾ Then, the orbital angular momentum which has the maximum value in the c plane is deduced by raising the spin from the c plane. Therefore, H_{hf} for $\text{Mn}_{0.9}\text{Ni}_{0.1}\text{Cr}_2\text{O}_4$ is smaller than the others. This confirms that the orbital angular momentum is the main origin of the large H_{hf} .

References

- 1) T. Okada et al.: *RIKEN Accel. Prog. Rep.*, **28**, 80 (1995).
- 2) T. Okada et al.: *Phys. Lett. A*, **209**, 241 (1995).
- 3) Y. Kobayashi et al.: This report, p. 110.
- 4) J. M. Hastings and L. M. Corliss: *Phys. Rev.*, **126**, 556 (1962).

* Hitachi Multimedia Systems R&D Division

** National Research Institute for Metals

μ SR Study on $\text{TlBa}_2\text{Y}_{1-x}\text{Ca}_x\text{Cu}_2\text{O}_y$

I. Watanabe, S. Nakajima,* and K. Nagamine

The Tl-system cuprate is one of the hole-doped high- T_c cuprates which show the highest transition temperature, T_C . The hole density of $\text{TlBa}_2\text{Y}_{1-x}\text{Ca}_x\text{Cu}_2\text{O}_y$ which is the so-called 1212 system and one of the Tl-families can be changed by the substitution of Ca^{2+} for Y^{3+} . The crystal structure is inserted in Fig. 1. The system shows the insulating behavior at $x = 0$. The electric conductivity of the system increases with increasing x . The SC appears $x > 0.5$.¹⁾ T_C grows up suddenly and shows a maximum ($T_C \approx 100$ K) around $x = 0.6$. By the analogy with other hole doped cuprates, some magnetically ordered states of Cu spins are expected to appear near $x = 0$; however, there has been no study in the insulator region near $x = 0$. To investigate the magnetic state of the system, the μ SR measurement is a powerful technic because the injected muon ($S = 1/2$) interacts with electrons and nuclei in the crystal only through magnetic interactions. In this paper, we report the first observation of the AF ordered state of the Cu spins in the Tl-1212 system by the μ SR measurement.

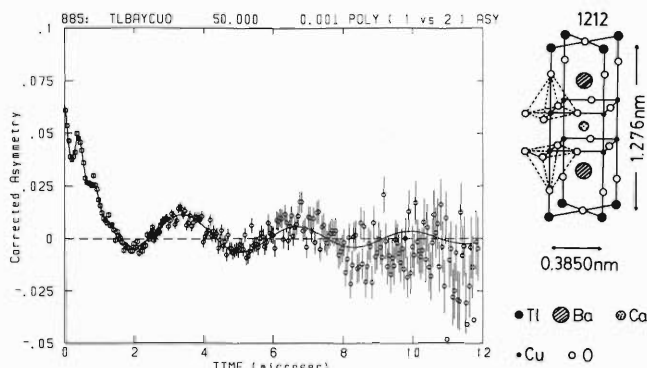


Fig. 1. Time evolution of the positive surface muon spin asymmetry taken under the zero field at 49 K. The crystal structure of the Tl-1212 system is also shown.

The μ SR measurement has been done at RIKEN-RAL Muon Facility, which has started to work from the beginning of 1995 at Rutherford-Appleton Lab. in UK,²⁾ under the zero field condition by using the surface muon beam with a momentum of 27 MeV/c.

The time evolution of the muon spin asymmetry for $x = 0$ at 49 K is shown in Fig. 1. Two precession components are observed. The existence of the precession of asymmetry means that a unique internal magnetic field which is due to the magnetic ordering of the system exists at each muon site. Thus, this finding in the

zero field measurement shows clearly the existence of the magnetically ordered state of the Cu-spins. Because there are two components of the precession frequency, there are at least two sites at which the injected muons stop in the crystal. The saturated internal field at each muon site is about 170 and 23 Gauss, respectively.

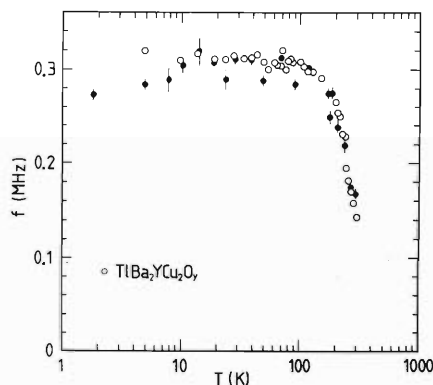


Fig. 2. Temperature dependence of the frequency of the slow precession component in the muon spin asymmetry of $\text{TlBa}_2\text{Y}_{1-x}\text{Ca}_x\text{Cu}_2\text{O}_y$. The open circles are for $x = 0$ and the closed circles are for $x = 0.5$.

Figure 2 shows the temperature dependence of the frequency of the slow precession component for $x = 0$ (open circles). The frequency is constant below 100 K and decreases with increasing temperature above 100 K. The precession is still observed at room temperature indicating the existence of the magnetic ordered state. The estimated magnetic transition temperature, T_N , is about 400 K.

Similar measurements have been done on this system changing x up to 0.5 by 0.1 step. In each sample similar two precession components were observed. The temperature dependence of the frequency of slow precession component for $x = 0.5$ is shown in Fig. 2 (closed circles). No difference in the saturated internal fields at the muon sites and no difference in T_N 's were observed among all samples, indicating that there is no change in the electronic state of the Cu-O₂ plane even though Y^{3+} is substituted by Ca^{2+} up to 50%, which operation is expected to induce holes in the Cu-O₂ plane. The more detailed analysis and the measurement in the SC state are going on now.

References

- 1) S. Nakajima et al.: *Physica*, **C182**, 89 (1991).
- 2) K. Nagamine et al.: *Hyperfine Interact.*, **87**, 1091 (1994).

* Department of Chemistry, Tohoku University

μ^\pm SR Measurement of $\text{La}_{2-x}(\text{Ba,Sr})_x\text{CuO}_4$ around $x = 0.12$

I. Watanabe, K. Kumagai,* and K. Nagamine

The high- T_C superconductivity (SC) in $\text{La}_{2-x}\text{Ba}_x\text{CuO}_4$ and $\text{La}_{2-x}\text{Sr}_x\text{CuO}_4$ disappears within a narrow range of the dopant concentration around $x = 0.12$.¹⁾ When the concentration of doped holes in the system is changed by substituting Li for Cu²⁾ or by substituting Th for La,³⁾ the value of x at which the SC is most suppressed is shifted, showing that the suppression of the SC strongly correlates with the hole concentration in the system.

In the La-Ba system, the transition from the orthorhombic (LTO) to the tetragonal (LTT) structure occurs below 60 K for $x = 0.125$ ⁴⁾ and this structural transition affects transportation phenomena of the system.⁵⁾ The LTO-LTT transition has not been observed in the La-Sr system; when La is substituted by Nd (La-Nd-Sr system); however, the LTO-LTT transition occurs and the SC is suppressed.⁶⁾

From the zero-field μ^+ SR measurement using the pulsed surface muon beam, an antiferromagnetic (AF) order of Cu-spins was observed in the La-Sr and the La-Ba systems around $x = 0.12$ ⁷⁾ at low temperatures. Figure 1 shows the x -dependence of the magnetic transition temperature, T_N . In both systems, T_N shows its maximum when the SC is most suppressed, showing that the AF ordered state of Cu-spins competes with the SC state.⁷⁾ Because of no big difference in the magnetically ordered states, a similar ordered state of Cu-spins to the one observed in the La-Ba system appears in the La-Sr system.

Recently, it is reported from the neutron diffraction measurement on the La-Nd-Sr system that the SC is suppressed by the stripe structure of the spin density wave (SDW) and the charge density wave (CDW)

which is stabilized by the LTO-LTT transition.⁸⁾

It has been believed that the magnetic ordered state of the Cu-spins suppresses the SC; however it is still in controversy why the magnetic ordered state can be stabilized within the narrow range of $x = 0.12$. To clarify the driving origin of the magnetic ordered state, a μ^- SR experiment was performed at the RIKEN-RAL Muon Facility⁹⁾ at which the worldwide strongest pulsed μ^- beam is available.

Figure 2 shows the time evolution of the μ^- spin asymmetry of the La-Sr system in zero field for $x = 0.115$ at 1.5 K. The time spectrum is well fitted by the exponential type relaxation function, indicating that fluctuations of the magnetic field which are induced by the magnetically ordered state of Cu-spins, exist at the oxygen site.¹⁰⁾ The temperature dependence of the zero field measurement is now in progress and it is expected that more detailed information of the electronic state of CuO_2 plane will be obtained in the near future.

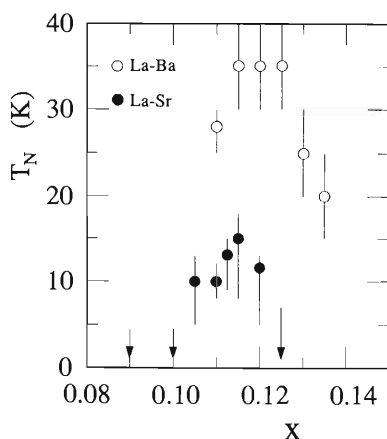


Fig. 1. x -dependence of T_N of the La-Ba and the La-Sr system around $x = 0.12$.

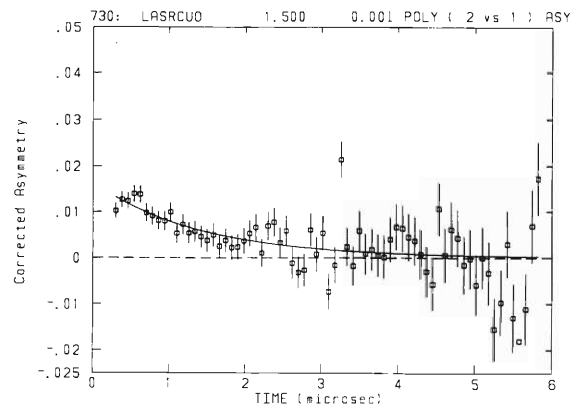


Fig. 2. Time evolution of the negative muon spin asymmetry in the La-Sr system for $x = 0.115$ at 1.5 K. The AF ordered state appears in the system at this temperature.

References

- 1) K. Kumagai et al.: *Physica C*, **235**–240, 1715 (1994).
- 2) S. Shamoto et al.: *Solid State Commun.*, **76**, 923 (1990).
- 3) Y. Maeno et al.: *Phys. Rev.*, **B44**, 7753 (1991).
- 4) J. D. Axe et al.: *Phys. Rev. Lett.*, **62**, 2751 (1989).
- 5) M. Sera et al.: *Solid State Commun.*, **69**, 851 (1989).
- 6) M. K. Crawford et al.: *Phys. Rev.*, **B44**, 7749 (1991).
- 7) I. Watanabe et al.: *Hyperfine Interact.*, **86**, 603 (1994).
- 8) J. M. Tranquada et al.: *Nature*, **375**, 561 (1995).
- 9) K. Nagamine et al.: *Hyperfine Interact.*, **87**, 1091 (1994).
- 10) R. S. Hayano et al.: *Phys. Rev.*, **B20**, 850 (1979).

* Department of Physics, Faculty of Science, Hokkaido University

μ^+ SR on Fe_{1+x}Sb

J. Nakamura, I. Watanabe, K. Asai, F. Ambe, and K. Nagamine

The NiAs-type intermetallic compound, $\text{Fe}_{1.15}\text{Sb}$, was studied using pulsed 27 MeV/c μ^+ -beam under zero-field condition in the temperature range of 6 ~ 280 K at RIKEN-RAL Muon Facility.¹⁾

According to early studies, magnetization, polarized neutron diffraction (PND) and ^{57}Fe Mössbauer effect measurements of $\text{Fe}_{1.14}\text{Sb}$, Fe atoms on the regular sites in NiAs-type crystal structure possess the magnetic moment of $\sim 0.9 \mu_B$, and their magnetic moments are ordered below 105 K with a triangular spin arrangement in the c -plane.^{2,3)} The temperature dependence of the hyperfine magnetic field, H_{hf} , at the regular site ^{57}Fe reveals the Néel temperatures, T_N , of 200 and 140 K at $x = 0.15$ and 0.25 of Fe_{1+x}Sb , respectively.⁴⁾ There is no anomaly around T_N in the temperature dependence of the magnetization, but a broad cusp is observed at ~ 10 K. It is considered that a large magnetic susceptibility of the interstitial site Fe atoms, which are ordered below the cusp temperature, buries the anomaly at T_N . Because of no magnetic Bragg peaks in PND pattern for the interstitial Fe atoms, their magnetic moments are considered to be frozen into a spin-glass state, but the detailed magnetic property is not clarified yet. The purpose of the present study is to obtain information on the magnetic properties of the regular and interstitial Fe atoms by means of μ^+ SR.

A polycrystalline sample of $\text{Fe}_{1.15}\text{Sb}$ was prepared by melting appropriate weight of the powdered raw materials in an evacuated quartz tube. The ingot was powdered and submitted to the measurements. The concentration was confirmed to be $x = 0.15$ from the lattice constants.

Figure 1(a) shows the temperature dependence of the initial asymmetry of the muon-spin polarization assuming a single component of the exponential decay. The initial asymmetry drastically decreases with decreasing temperature around 200 K, showing that a magnetically ordered state of the regular site Fe atoms sets in below this temperature ($T_N \sim 200$ K). On further cooling, the initial asymmetry recovers up to 1/3 of the full asymmetry, indicating the appearance of a static random field.⁵⁾ This "1/3-tail" decreases gradually below 50 K because of dynamical spin fluctuations of Fe spins. The temperature dependence of the depolarization rate λ is shown in Fig. 1(b). That of λ possesses a divergence around 140 K, which means a very large magnetic fluctuation of the regular site Fe atoms below T_N . Furthermore, the value of λ increases with decreasing temperature below 50 K according to the increase of the susceptibility, which shows the cusp at ~ 10 K.

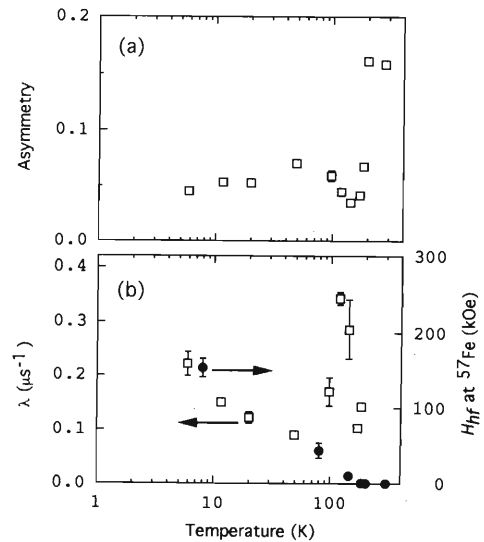


Fig. 1. The temperature dependence of the initial asymmetry (a) and the depolarization rate λ (b). The hyperfine magnetic field H_{hf} at ^{57}Fe derived from the Mössbauer spectroscopy is also shown in (b) with solid circle.

The present result of μ^+ SR suggests gradual slowing-down of the magnetic fluctuation of the interstitial site Fe atoms below 50 K. The result is consistent with that of the previous Mössbauer study, in which H_{hf} at ^{57}Fe at the interstitial sites appears gradually from a relatively higher temperature than the cusp temperature [see the solid circle in Fig. 1(b)].⁴⁾ In ^{57}Fe Mössbauer spectra, it is difficult to separate the component of interstitial site Fe atoms from that of the regular site Fe and to distinguish dynamical effects from the static distribution of H_{hf} . The present result shows that the pulsed μ^+ SR method is useful for the compound having plural kinds of magnetic moments with different dynamical fluctuations.

In order to clarify the magnetic properties below 50 K, experiments at much lower temperatures (below 6 K) and those in a longitudinal magnetic field are proposed to obtain further information on the fluctuations of Fe-spins.

References

- 1) K. Nagamine et al.: *Hyperfine Interact.*, **87**, 1091 (1994).
- 2) K. Yamaguchi et al.: *J. Phys. Soc. Jpn.*, **33**, 1292 (1972).
- 3) T. Yashiro et al.: *ibid.*, **34**, 58 (1973).
- 4) J. Nakamura et al.: *Nuovo Cimento D*, in press.
- 5) R. S. Hayano et al.: *Phys. Rev.*, **B20**, 850 (1979).

Quantum Diffusion of Positive Muon in Pure Tantalum

R. Kadono, I. Watanabe, and K. Nagamine

Quantum diffusion is an interesting phenomenon in crystalline solids where light interstitial particles like protons and muons migrate by tunneling under the potential barrier between adjacent sites. Because of the light mass the tunneling amplitude of implanted muons is expected to be greatly enhanced and thereby dominate their diffusion property. The characteristic of the quantum tunneling diffusion emerges as a hopping rate proportional to the *negative* power of temperature i.e., $\nu \propto T^{-\alpha}$, where the value of α depends on the property of a dissipative bath coupled to the tunneling particle. Such a power-law has been clearly observed both in metals with $\alpha \simeq 0.6^{1)}$ and in ionic crystals with $\alpha \simeq 3 \sim 7.^{2-6)}$

One of the most interesting aspects of the diffusion in metals is the idea that the cloud of normal conduction electrons around a charged particle (e.g., positive muon) cannot follow the motion of the particle adiabatically, as a consequence of the orthogonality catastrophe originating from divergent infrared couplings to the electrons. This non-adiabatic behavior of particle-electron polaronic state leads to a much smaller power (i.e., $0 < \alpha < 1$)^{7,8)} as seen for the muon diffusion in metals compared with that in insulators where particle-phonon interaction is explicit. Moreover, it is theoretically predicted that this particle-electron coupling can be directly tested by looking into the effect of superconductivity on muon diffusion: The superconducting energy gap introduces a cut-off to the infrared couplings and thereby the adiabaticity of particle-electron polaronic state must be restored.⁷⁾

The first step for testing the above prediction is to look for a suitable system; there are several candidates of simple metals showing superconductivity and sufficiently large nuclear moments (which is necessary to observe the motional effects by μ SR), including V, Nb, Ta, In, and Al. Recently we have measured the muon hopping rate in pure Ta (99.997%) by the ARGUS spectrometer at the newly completed RIKEN-RAL Muon Facility and obtained a very promising result. Namely, unlike in other bcc metals, the hopping rate seems to be relatively slow ($< 10^6 \text{ s}^{-1}$) and virtually not affected by the residual impurities during the muon lifetime ($=2.2 \mu\text{s}$). This is further evidenced by the temperature dependence of the hopping rate

shown in Fig. 1, where the hopping rate increases with decreasing temperature below about 30 K ($\alpha \sim 2$ for 15–25 K then $\alpha \sim 0.2$ for 5–15 K), showing turnover near 4 K and decreases with decreasing temperature.

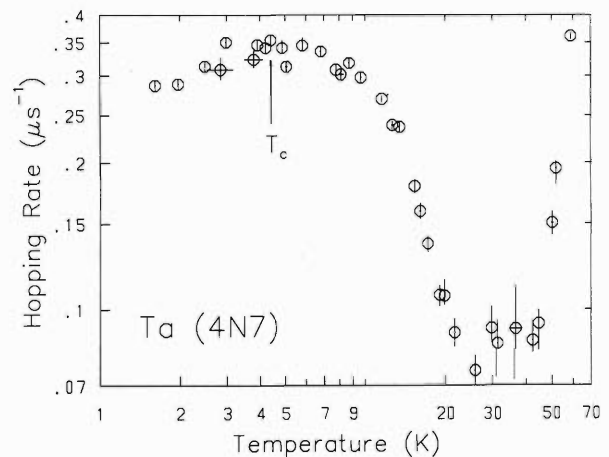


Fig. 1. Temperature dependence of muon hopping rate in pure Ta (99.997%). The T^{-2} dependence is due to the damping of tunneling by muon-phonon interaction whereas $T^{-0.2}$ is due to the strong electronic damping. The T -dependence below 4 K is yet to be elucidated in comparison with the data in normal state Ta.

This result indicates that we are going to have an opportunity for the first time in the past two decades to study the effect of superconductivity on quantum diffusion in an intrinsic system.

References

- 1) See, for example, G. M. Luke et al.: *Phys. Rev.*, **B43**, 3284 (1991), and references therein.
- 2) R. F. Kiefl et al.: *Phys. Rev. Lett.*, **62**, 792 (1989).
- 3) R. Kadono et al.: *ibid.*, **64**, 665 (1990).
- 4) J. W. Schneider et al.: *ibid.*, **68**, 3196 (1992).
- 5) R. Kadono et al.: *Phys. Rev.*, **B50**, 1999 (1994).
- 6) V. Storchak et al.: *Phys. Rev. Lett.*, **72**, 3056 (1994).
- 7) J. Kondo: *Physica*, **125B**, 279 (1984); *ibid.*, **126B**, 377 (1984); *Hyperfine Interact.*, **31**, 117 (1986).
- 8) K. Yamada: *Prog. Theor. Phys.*, **72**, 195 (1984); K. Yamada et al.: *ibid.*, **73**, 1342 (1985).

Spin Dynamics of μAl Pseudo-Acceptor Centers in Si Probed by μ^- SR

R. Kadono, F. L. Pratt, I. Watanabe, and K. Nagamine

The negative muon (μ^-) has a unique feature that it is captured by an atom with a charge number Z upon implantation to form a "muonic atom" with a reduced charge number $Z - 1$. This is due to the effective shielding of the nuclear charge by μ^- which has about 200 times shorter Bohr radius compared with that of a 1s electron. When the initial μ^- is spin-polarized, it partially preserves the polarization during atomic transitions between muonic orbits, maintaining about 1/6 of the initial polarization at the muonic 1s state (when the nuclear spin is zero) to form a polarized "pseudo-nucleus ($Z - 1$)". The atomic process including the Auger electron emission is complete within 10^{-9} s which is much shorter than the time scale probed by the μSR technique. Thus, the polarized muonic atom can be applied to the study of condensed matter in a similar fashion as positive muons, despite some technical difficulties that it has shorter lifetime for the larger atomic charge number Z with a small electron decay asymmetry ($< (1/3) \times (1/6) \sim 5\%$), and that the technique is virtually limited to those with no nuclear spins. For example, μ^- O probe has been used to study the high- T_c superconductors and their parents compounds.¹⁾

It is known that the electron paramagnetic resonance (EPR) signal associated with acceptor centers is hardly observed in elemental semiconductors due to fast electron spin relaxation,²⁾ which has been the serious obstacle to the study of electronic structure of active centers. The implanted negative muon forms a spin-polarized acceptor center and thereby the μ^- SR may serve as a complementary technique to provide microscopic information. Recently, some results of μ^- SR study in crystalline silicon were reported,^{3,4)} although there remains some disagreement with each other. In this short note we report our preliminary results of μ^- SR study in crystalline silicon in comparison with those by other groups.

The experiment was conducted at the port-2 channel of the newly completed RIKEN-RAL Muon Facility in the Rutherford Appleton Laboratory. A negative muon beam with a momentum of 50 MeV/c was implanted into the sample consisting of 10 intrinsic c-Si wafers ([111], resistivity $\simeq 2.2$ k Ω cm, total ~ 3 mm thick) and time-differential TF- μSR spectra were obtained by the ARGUS spectrometer.⁵⁾ The applied magnetic field was 4.0 mT, which is considerably lower than those reported in Refs. 3 and 4 (see below). The long-lived background rate was such that the electrons from μ^- Si muonic atoms (lifetime ~ 0.8 μs) were clearly observed over 6 μs range.

Figure 1 shows the observed electron decay asymmetry and spin relaxation rate of μ^- Si ($\equiv \mu\text{Al}$) versus temperature. The asymmetry decreases as temperature is lowered below 40 K, disappearing almost completely at 10 K. This result is qualitatively in good agreement with Ref. 3. On the other hand, the reduction of asymmetry is in accordance with the increase of spin relaxation rate, which is also in line with the result reported in Ref. 4. The change of asymmetry observed at 4.0 (this work) and 40 mT³⁾ is absent at 80 mT⁴⁾ and thereby suggesting that the hyperfine field from the electron shell at the μAl core may be $10^{1.5}$ mT. The relatively slow relaxation observed below 40 K may be due to the spin-exchange interaction with quasi-localized holes near μAl acceptor centers. More detailed experiment is in progress.

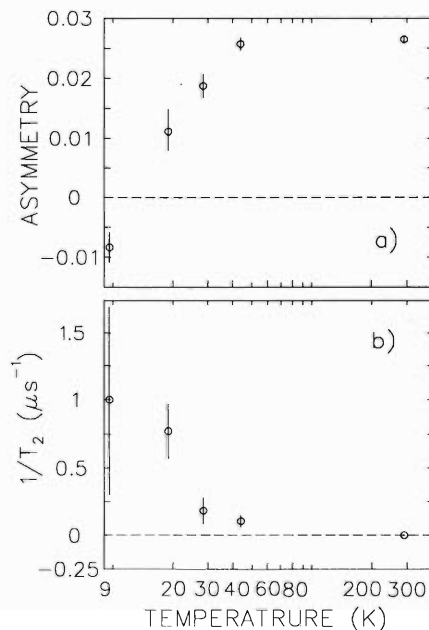


Fig. 1. Temperature dependence of a) μ -e decay asymmetry and b) spin relaxation rate for the μAl acceptor centers in c-Si.

References

- 1) N. Nishida: *Hyperfine Interact.*, **79**, 823 (1993).
- 2) See, for example, G. W. Ludwig, and H. H. Woodbury: *Electron Spin Resonance in Semiconductors*, Academic Press, New York (1962).
- 3) M. Koch et al.: *Hyperfine Interact.*, **65**, 1039 (1990).
- 4) T. N. Mamedov et al.: *ibid.*, **86**, 717 (1994).
- 5) R. Kadono et al.: This report, p. 196.

μ SR Studies on Magnetic Correlations and Spin Dynamics in Kondo Semimetal CeNiSn

S. Flaschin, A. Kratzer, G. M. Kalvius, R. Kadono, I. Watanabe, and K. Nagamine

The system CeT₂Sn, where T stands for a *d* transition element like Ni (3*d*), Pd (4*d*) or Pt (5*d*), has attracted considerable interest within the field of highly correlated electron systems. We study the series CeT₂Sn and related materials with μ SR to gain information on the development of magnetic correlations and on the spin dynamical behavior at very low temperatures.

The most interesting compound within this series is CeNiSn. It led to the definition of a “new” class of materials termed “Kondo semiconductors”¹⁾ since it exhibits Kondo lattice behavior at more elevated temperatures, yet possesses in addition a very narrow gap (≈ 1 K) in the density of states at the Fermi surface. Neutron diffraction shows the gap to be open only in certain directions of reciprocal space²⁾ and recent heat capacity and resistivity data established basically metallic behavior at very low temperatures.³⁾ Hence the name “Kondo-semimetal” appears more appropriate.

μ SR studies showed that magnetic correlations exist at temperatures well below the gap formation.^{4,5)} The muon spin relaxation rate λ first rises with decreasing temperature in a fashion typical for the relaxation behavior in a paramagnet near the magnetic transition temperature but then saturates at temperatures below ≈ 100 mK. From longitudinal field decoupling data it is apparent that the electronic spin correlations responsible for the muon depolarization are of dynamic nature even at lowest temperatures. The moment of the Ce ions is very low due to the Kondo effect.

From transport measurements and bulk magnetic studies⁶⁾ we know that magnetic correlations become stronger by doping CeNiSn with Cu. This leads to a transition from a valence fluctuating semiconductor via a heavy fermion state into an antiferromagnetic Kondo state. The latter is reached in CeNi_{1-x}Cu_xSn for a Cu-concentration of $x \geq 0.13$. The gap is closed for a concentration of $x \geq 0.10$.

We want to learn how magnetic correlations are changing in these samples. As a first step we did μ SR investigations on CeNi_{0.9}Cu_{0.1}Sn. Preliminary results showed, as expected, the influence of the nuclear moments of Cu. Below 10 K a change in the relaxation behavior could be detected. There were strong hints that for $T < 4$ K a second fast damping signal appears.

Our experiment at the RIKEN beamline at RAL should give more insight into the relaxation behavior. We did zero field and longitudinal field experiments in a temperature range from 1.7 K to 10 K using the VARIOX cryostat.

From the decoupling data in low longitudinal fields

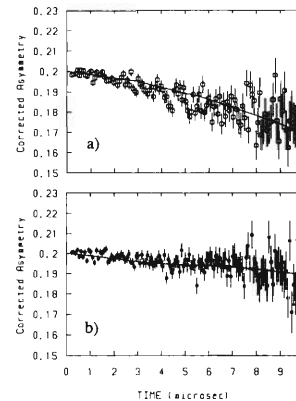


Fig. 1. Decoupling of the nuclear damping of Cu. Zero field (a) and longitudinal field of 10 G (b) at 10 K are shown as an example.

(see Fig. 1) we could conclude that the Cu ions are homogeneously distributed within the Ni matrix. This conclusion could be drawn from comparison with Monte-Carlo simulations.

Furthermore, the results showed that the former data have to be reinterpreted as a change in signal shape instead of assuming an additional strongly damped signal. From these data we concluded that a further change in spectral shape could be expected at even lower temperatures. Since this temperature range is not accessible at the RIKEN beamline we continued our experiment at the MUSR beamline using the dilution refrigerator. We found spin-glass like behavior.^{7,8)} We assume that the Cu ions induce a moment at the Ce neighbors. This phenomenon was seen before in so called “induced moment spin glasses” as PrP⁹⁾ or ScTb.¹⁰⁾ Thus, we have high moments at Ce statistically distributed in a Ce matrix with very low moments. At the lowest reachable temperature (40 mK) the field distribution appears to be static in contrast to CeNiSn.

References

- 1) T. Takabatake et al.: *Phys. Rev.*, **B41**, 9607 (1990).
- 2) T.E. Mason et al.: *Phys. Rev. Lett.*, **69**, 490 (1992).
- 3) G. Nakamoto et al.: *Physica B*, **206 & 207**, 840 (1995).
- 4) A. Kratzer et al.: *Europhys. Lett.*, **19 (7)**, 649 (1992).
- 5) G.M. Kalvius et al.: *Physica B*, **206 & 207**, 807 (1995).
- 6) T. Takabatake et al.: *J. Magn. Magn. Mat.*, **76 & 77**, 87 (1988).
- 7) Y. J. Uemura et al.: *Phys. Rev.*, **B39**, 4729 (1989).
- 8) I. A. Campbell et al.: *Phys. Rev. Lett.*, **72**, 1291 (1994).
- 9) S. K. Hasanain et al.: *Phys. Rev.*, **B24**, 5165 (1981).
- 10) H. Yoshizawa et al.: *ibid.*, **B27**, 448 (1983).

The Spin Dynamics of Polarons in Polyaniline Studied by μ^- SR

F. L. Pratt, A. Monkman,* K. Ishida, I. Watanabe, R. Kadono, and K. Nagamine

Conducting polymers such as polyaniline have been a source of considerable scientific and technological interest since the discovery of high metallic conductivity in doped polyacetylene and further discoveries of interesting electro-optical properties such as large optical nonlinearity and electroluminescence in various conjugated polymer systems. Fundamental to the understanding of these conducting polymers are the nature and properties of their charge and spin excitations, which take the form of polarons and solitons. The muon is a particularly sensitive probe of these excitations, as the muon implantation process itself generates an excitation whose dynamical properties can be studied via the evolution of the muon spin polarisation. This was first demonstrated in polyacetylene using μ^+ SR¹⁾ and subsequent studies were reported for a range of conducting polymers.²⁾ We report here an extension of these studies using the μ^- SR technique, which has been made possible following the recent completion of the RIKEN-RAL Pulsed Muon Facility at the Rutherford Appleton Laboratory.

Measurements were made using negative muons with a momentum of 60 MeV/c at RIKEN-RAL Port 2 (μ SR port). The polyaniline (emeraldine base) sample consisted of an array of seven pressed discs each 2–3 mm thick and 12 mm in diameter with 3 mm of silver before the sample acting as a degrader. The muon spin rotation was first checked in weak transverse fields to measure the diamagnetic amplitude and then the longitudinal relaxation was studied as a function of longitudinal field. Measurements were made at 10 and 300 K.

In contrast to positive muon implantation in undoped conducting polymers, where muonium is formed initially, which then rapidly reacts with the polymer, negative muon implantation leads to the formation of muonic atoms, where the nuclear charge becomes shielded by the muon to form an atom with effective atomic number $Z-1$. Polyaniline consists mostly of carbon which will be converted to boron-like atoms by this process. This leaves a spare electron in the form of a polaron which is free to diffuse away from the implantation site. The spin diffusion process can be monitored by the relaxation of the muon spin and in particular the longitudinal field dependence of the relaxation rate provides important information about the spectral dimension of the diffusion process.

Figure 1 shows the measured relaxation rate as a function of field. Very different behaviour can be seen at high and low temperatures. At 10 K the power-law field dependence indicates low-dimensional spin diffusion in a regime where interchain transport is relatively slow. In contrast the weakness of the field dependence at 300 K indicates fast interchain transport and 3D spin diffusion.

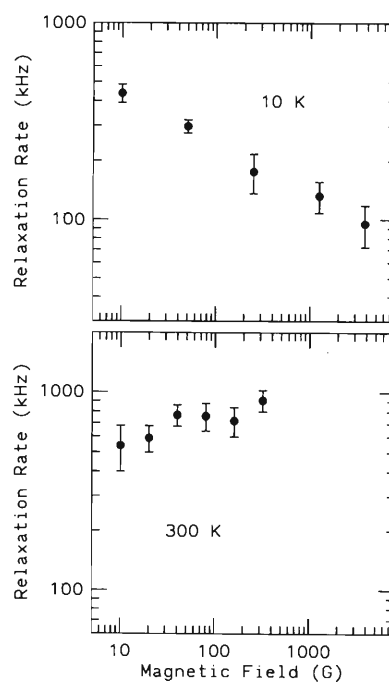


Fig. 1. μ^- longitudinal spin relaxation rate in Polyaniline (Emeraldine base) as a function of applied magnetic field at 10 and 300 K.

μ^- SR is expected to be particularly useful in systems with slow nuclear capture i.e. with low atomic number, as found in organics, and these initial results demonstrate that μ^- SR in conducting polymers can provide a valuable complementary technique to μ^+ SR and other magnetic probes.

References

- 1) K. Nagamine et al.: *Phys. Rev. Lett.*, **53**, 1763 (1984).
- 2) F. L. Pratt et al.: *Synthetic Metals*, **55**, 677 (1993).

* University of Durham, U.K.

LF μ SR Studies on Reorientational Dynamics in Solid C₇₀ Using the ARGUS Spectrometer

R. M. Macrae, R. Kadono, F. L. Pratt, K. Tanigaki,* and K. Nagamine

Muon techniques have proved valuable in the study of reorientational dynamics and electronic structure in the pure fullerenes C₆₀ and C₇₀, and in particular in elucidating the motional differences between them produced by the presence or absence of 10 C atoms.^{1,2)} The dynamics of C₇₀ have been found to be rather complex, and discussion of the microscopic mechanism involved is by no means over.

When positive muons are implanted into fullerenes two distinct hyperfine probes are generated. During its deceleration process from MeV energies μ^+ picks up an electron to form Mu, a light isotope of atomic H. Inside the fullerene spheroid this atom is stable over the muon's microsecond-scale lifetime, and has hyperfine parameters close to their vacuum values. On the fullerene *exterior* Mu reacts very rapidly to form a radical with a reduced hyperfine interaction anisotropic in the molecular frame. The interaction of this anisotropy with reorientational motional anisotropy as a function of temperature is a "handle" on microscopic molecular dynamics.

In C₇₀ there are five distinct sites for radical-forming chemical addition, labelled A to E from pole to equator. Studies by time-integral avoided level-crossing μ SR²⁾ showed the presence of reorientational anisotropy up to 370 K, proving muons a more sensitive probe of this anisotropy than neutrons or NMR. The behaviour was modelled pseudostatically in terms of an *effective* axial anisotropy $D_{\parallel}(T)$, and the energetics were considered within a simple thermodynamic model involving four dynamical populations X_i undergoing different types of motion.

The present experiments use the technique of time-resolved LF μ SR spectroscopy to extend these dynamical explorations. The decay asymmetry measured as a function of field shows a recovery pattern dependent on the hyperfine tensor components. In particular, the hyperfine anisotropy is revealed in the very low field part of the repolarisation pattern. (See Fig. 1.) The yields and isotropic parameters of all 5 radical adducts are known from transverse field experiments,³⁾ while zero-field measurements reveal that the most important radicals have similar static anisotropies. Hence it should be possible to reconstruct from the polarisation pattern as a function of T a set of thermodynamic parameters comparable to that extracted from ALC- μ SR.

Measurements were carried out using the ARGUS spectrometer over 4 decades of field range from 0.5 G to 3800 G. (See Fig. 2). Other techniques show

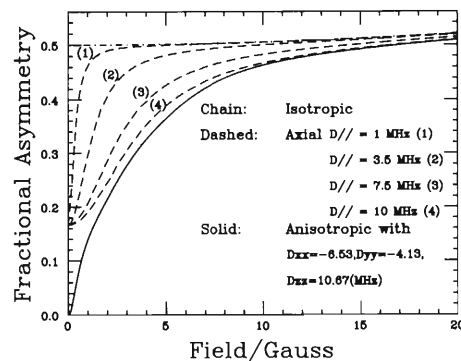


Fig. 1. Calculated low-field repolarisation pattern for several effective anisotropies of a radical with isotropic coupling $A_{\mu} = 275$ MHz.

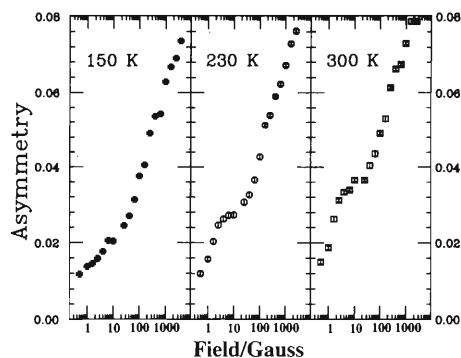


Fig. 2. ARGUS results for C₇₀.

that at 150 K the reorientational motion is completely frozen, while 230 K is just above the onset of uniaxial reorientation and at 300 K (between the two macroscopic phase transitions) the unique axis is itself moving. However, the observed dependences are the *opposite* of what would be expected within the simple static model. This indicates that the data contain extra dynamical information not available from time-integral techniques, relating to incomplete averaging over the occupied motional modes on the μ SR timescale. A crude model in which the anisotropic hyperfine parameters have a gaussian width while the isotropic coupling is held constant suggests the hf *anisotropy* is statically broadened at low temperatures and narrows as motion becomes more rapid.

References

- 1) E. Roduner et al.: *Chem. Phys.*, **192**, 231 (1995).
- 2) R. M. Macrae et al.: *J. Phys. Chem.*, **98**, 12133 (1994).
- 3) A. Lappas et al.: *J. Chem. Soc., Chem. Commun.*, **1994**, 2743.

* Fundamental Research Laboratories, NEC Corporation

Single Event Effect in Power MOSFETs by High-Energy Heavy Ion

S. Matsuda, T. Akutsu, T. Hada, J. Aoki, T. Hirose, H. Ohira, Y. Nagai, T. Kohno, N. Inabe, M. Kase, A. Goto, and Y. Yano

Power MOSFETs (Metal- Oxide- Semiconductor Field Effect Transistors) perform excellently as power switching devices. However, power MOSFETs have a possible catastrophic failure mode known as Single Event Burnout (SEB) phenomenon which is caused by turn-on of the parasitic transistor with the electric charge generated by penetration of a fast heavy ion. It is important to consider this phenomenon in application of electronic devices in space.

The detailed mechanism of SEB was observed experimentally by the EPICS (Energetic Particle Induced Charge Spectroscopy) measurement system.^{1,2)} The experimental results were also confirmed with the numerical simulation technique.

RIKEN Ring Cyclotron was used for the heavy ions irradiation. The selected ions were Kr and Xe, and their characteristics are shown in Table 1. To avoid contaminant ions, irradiation was made using a defocused beam without a scatterer such as an Au foil. The incident beam was monitored by an SSD just adjacent to the sample device.

Table 1. Characteristics of the ions used in this study.

Ions	Energy [MeV]	LET [MeV/(mg/cm ²)]	Range [μ m(Si)]
⁸⁴ Kr	2184	17.4	385
¹³⁴ Xe	3536	33.7	339

The sample device for this study was a Fuji Electric Corps Power MOSFET 2SK725. Its maximum drain-source voltage rating (V_{DS}) was 500 V. The high voltage rating requires a relatively thick active layer ($\sim 40 \mu\text{m}$ of epi-layer). However, Kr and Xe have length ranges larger than the thickness of the active region.

Kuboyama et al. reported the experimental results only about normally incident irradiation to the test sample.^{1,2)} In our experiment, the angle of incident heavy ion beam was changed by turning the target, because the Power MOSFETs will receive the cosmic rays coming from every direction of the universe.

Figure 1 shows the SEB occurrence rate for each angle (0° , 15° , 30° , and 45°) with respect to the incident beam. This figure shows that as the angle becomes larger, the applied voltage, at which the SEB occurs, becomes larger. This figure also shows that the results of Xe and Kr are different. The reason for the

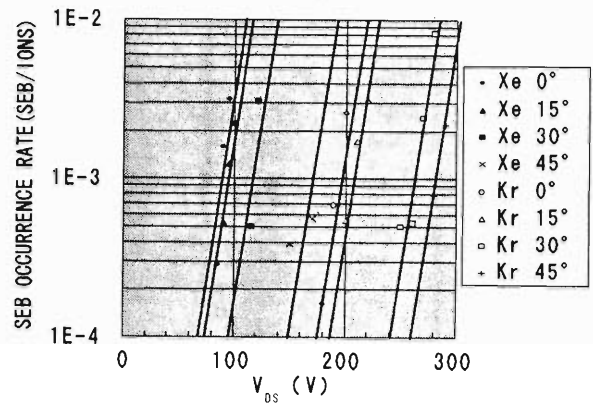


Fig. 1. SEB occurrence rate (2SK725).

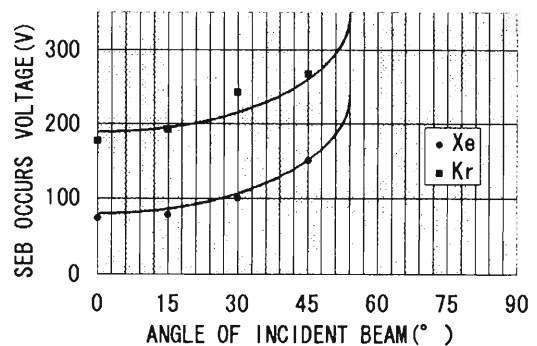


Fig. 2. SEB occurs vs. angle of incident beam.

different results for Xe and Kr is the difference of the LET (Linear Energy Transfer). To analyze each experimental result, we compared the applied voltages when the SEB occurs at 1 time per 10^4 ions. Figure 2 shows the result of the comparison. In case of a Xe ion, when the angle of incident beam is smaller than 30° , the voltage at which the SEB occurs is smaller than 100 V. If the Power MOSFET is used at the applied voltage smaller than 100 V for space application, it will be affected by $(1 - \cos 30^\circ) \cong 0.134$ portion of total cosmic beams. This result is a most important concern for future work.

References

- 1) S. Kuboyama et al.: *IEEE Trans. Nucl. Sci.*, **NS-39**, 1698 (1992).
- 2) S. Kuboyama et al.: *ibid.*, **NS-41**, 2210 (1994).

Heavy-Ion Irradiation Effects on the Single Crystal $\text{La}_{1.85}\text{Sr}_{0.15}\text{CuO}_4$

M. Matsuda, G. Tatara, K. Katsumata, T. Kambara, Y. Awaya, T. Mitamura, M. Terasawa,
Y. Endoh,* K. Yamada,* and S. Hosoya**

It has been reported that heavy ions irradiation on superconductors produces columnar defects which consist of continuous amorphous tracks.¹⁻³⁾ The columnar defects are very efficient pinning centers for vortices. The columnar defects not only enhance the critical current density J_C , but they also cause new phases, such as Bose-glass phase in the H-T phase diagram.^{4,5)}

We have studied heavy ions irradiation effects on the superconducting properties of $\text{La}_{1.85}\text{Sr}_{0.15}\text{CuO}_4$ single crystals. The crystals were grown by a traveling solvent floating zone (TSFZ) method. The typical dimension of the sample was about $5(l) \times 4(w) \times 0.1(t)$ mm³. The unirradiated samples show a sharp superconducting transition T_C at 37 K. The samples were irradiated with 3×10^{10} cm⁻² 3.4 GeV Xe³¹⁺ ions from the Ring Cyclotron at room temperature. The ion beam was aligned parallel to the c-axis. It is estimated that most of the heavy-ion beams penetrate through the sample. The magnetization and magnetic susceptibility were measured by using a SQUID magnetometer.

We have observed remarkable irradiation effects on the magnetization (M-H) curve as seen in Fig. 1 without degradation of T_C . The critical current density

J_C is estimated from the maximum value of the magnetization. The presence of columnar defects increases J_C by a factor of 10 (5 K, 0.1 T) and 4 (25 K, 0.1 T). Figure 2 shows preliminary results of the temperature dependence of the irreversibility line (H_{irr}) where the hysteretic behavior appears in the M-H curve. The line is to be identified with the melting line of the vortex lattice. The line is shifted to higher temperature due to the columnar defects, which indicates that the vortex lattice becomes harder in the presence of strong pinning. More detailed measurements of DC and AC susceptibility are required to identify the new phase (Bose-glass phase) in La-Sr-Cu-O system.

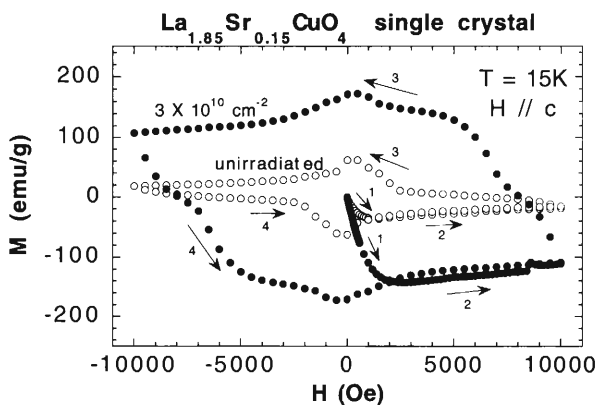


Fig. 1. M-H curves of the $\text{La}_{1.85}\text{Sr}_{0.15}\text{CuO}_4$ crystal before (open circles) and after (closed circles) irradiation with 3×10^{10} Xe³¹⁺/cm² (3.4 GeV).

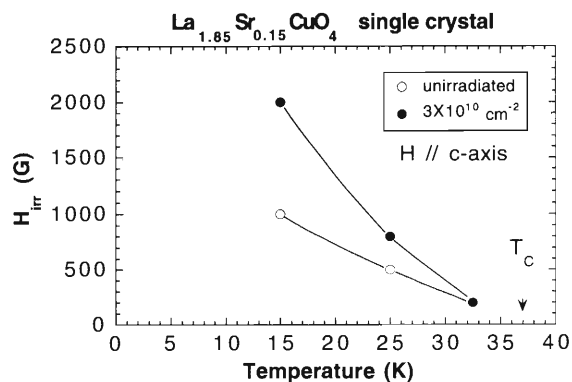


Fig. 2. The irreversibility lines of the $\text{La}_{1.85}\text{Sr}_{0.15}\text{CuO}_4$ crystal before (open circles) and after (closed circles) irradiation with 3×10^{10} Xe³¹⁺/cm² (3.4 GeV).

References

- 1) S. Behler et al.: *Phys. Rev. Lett.*, **72**, 1750 (1994).
- 2) H. W. Zandbergen et al.: *GSI Scientific Report*, p. 213 (1993).
- 3) M. Terasawa et al.: *Physica C*, **235/240**, 2805 (1994).
- 4) L. Krusin-Elbaum et al.: *Phys. Rev. Lett.*, **72**, 1914 (1994).
- 5) C. J. van der Beek et al.: *ibid.*, **74**, 1214 (1995).

* Department of Physics, Tohoku University

** Institute of Inorganic Synthesis, Faculty of Engineering, Yamanashi University

Observation of Columnar Defects in $^{136}\text{Xe}^{+31}$ Bombarded Layered Materials

N. Nishida, H. Sakata, K. Satoh, S. Kaneko, H. Sawada, T. Kambara, and Y. Awaya

In copper-oxide high- T_c superconductors, pinning effects are weak due to the short coherence length (~ 30 Å) and anisotropic nature of the superconductivity. It is essential to find how to increase pinning effects for various applications of high- T_c superconductors. In some materials high energy heavy ions generate columnar defects which are linear damage tracts of ~ 100 Å diameter along the tracks of heavy ions. These columnar defects have been found to be effective to pin vortices of high- T_c superconductors in high magnetic fields. Therefore, it is interesting and important to study how columnar defects are generated and what the electronic states are around them. In order to study influences of columnar defects on the surrounding electronic states and generation mechanisms of columnar defects, we have installed a newly designed target chamber at E5a beam line from RIKEN Ring Cyclotron and bombarded 3.4 GeV $^{136}\text{Xe}^{+31}$ (26 MeV/nucleon) ions through single

crystals of several layered materials; $\text{Bi}_2\text{Sr}_2\text{CaCu}_2\text{O}_x$, 1T-TaS₂, 2H-NbSe₂ and graphite (HOPG). $^{136}\text{Xe}^{+31}$ ions of 3.4 GeV have high enough energy to penetrate our samples of about 0.1 mm thickness. They were observed by a transmission electron microscope (TEM) and a scanning tunneling microscope (STM) at Tokyo Institute of Technology. In $\text{Bi}_2\text{Sr}_2\text{CaCu}_2\text{O}_x$, columnar defects have been observed by TEM as shown in Fig. 1a and 1b. However, in 1T-TaS₂ and highly oriented pyrographite (HOPG) columnar defects have not been observed as shown in Fig. 1c and 1d. The reason why these differences are brought about is under consideration. At present the studies of $\text{Bi}_2\text{Sr}_2\text{CaCu}_2\text{O}_x$ are in progress by using a scanning tunneling spectroscopic microscope which can be operated at low temperature (2.2 K) and in high magnetic fields (14.5 T). We acknowledge professor N. Yamamoto (TIT) for taking TEM photographs of our samples.

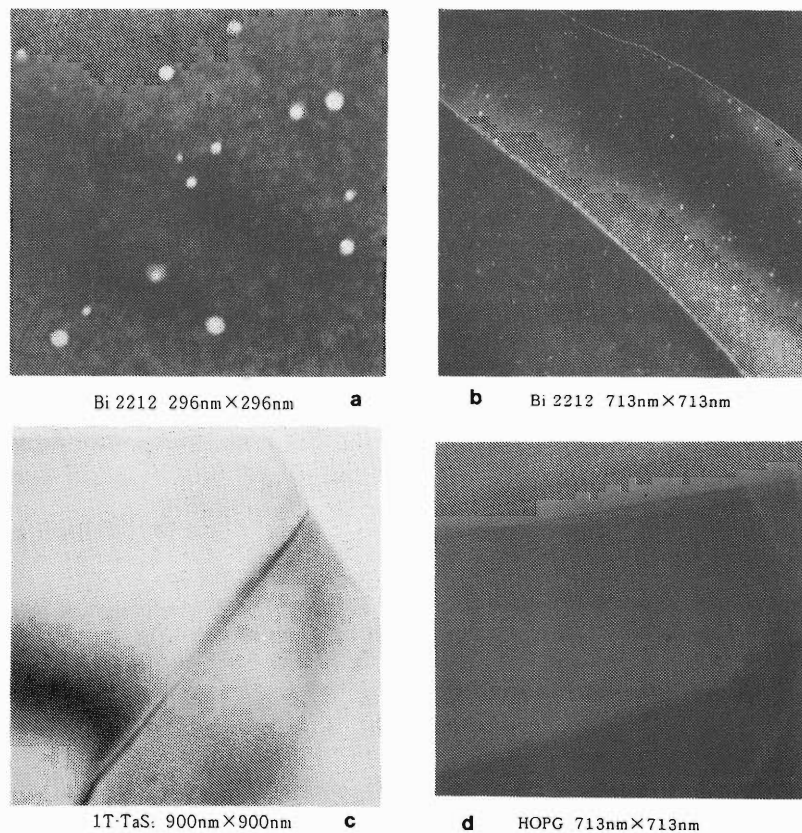


Fig. 1. Columnar defects observed by TEM in $\text{Bi}_2\text{Sr}_2\text{CaCu}_2\text{O}_x$ (a), (b), in 1T-TaS₂ (c), and in HOPG (d). The defects are seen as white spots in (a) and (b), but not in (c) and (d).

Laser Spectroscopy of Atoms and Molecules in Liquid Helium

M. Nakamura, Q. Hui, J. L. Persson, Z. Jakubek, Y. Kasai, M.-P. Coquard, and M. Takami

We are currently studying the physical properties of neutral atoms and molecules in liquid helium. One of the objectives of this work is to find the feasibility of applying this technique to the on-line spectroscopic study of unstable nuclei produced by RRC and to other fundamental physics. For the first application, we are studying the optical spectra of neutral atoms (impurity particles) in liquid helium.^{1,2)} A neutral atom is known to be trapped in a bubble-like cavity due to a strong repulsive force between the impurity and surrounding helium atoms.³⁾ The coupling of the cavities with the trapped atoms induces a large shift and broadening of the atomic spectra. Spectroscopic study of atomic ions in liquid helium, which is more suitable for the study of unstable nuclei, is also in progress.

For the second application, the measurement of electric dipole moment in a neutral heavy atom trapped in solid helium has been proposed. Our interest is to use diatomic molecules containing heavy atoms to carry out a similar measurement. As a first step, we studied electronic spectra of metal dimers and trimers in liquid helium.⁴⁾ A schematic diagram of the experimental set up and conditions were described in a previous report.⁵⁾

Neutral molecules are dispersed in HeII by laser ablation of solid metal samples immersed in HeII. A second YAG laser beam, with a few ms delay after the ablation, dissociated the particles to disperse metal molecules in HeII. A pulsed dye laser was used to excite the molecules with a 50 ns–10 ms delay time after dissociation. The emission from the molecules was detected by a photomultiplier through a 25 cm monochromator.

So far we studied electronic spectra of Ca_2 , Cu_2 , and Ag_3 in liquid helium. The absorption and emission spectra of S-S transitions of Ca_2 and Cu_2 showed vibrational structures. The Cu_2 emission spectrum is shown in Fig. 1 as an example. The emission has been observed only from the lowest vibrational states, reflecting rapid relaxation of the dimer vibration in liquid helium. Vibrational frequencies and spacing of Cu_2 were slightly different from those in free space.

For the applications discussed above, high resolution measurements of atomic/molecular spectra are indispensable. Feasibility of optical pumping for high resolution radiofrequency spectroscopy among the hyperfine and Zeeman sublevels has been demonstrated already.⁶⁾ One important result in the present work is the finding of rapid vibrational relaxation in

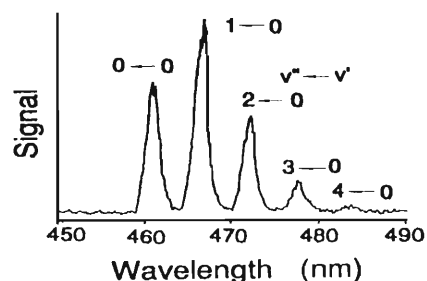


Fig. 1. $B^1\Sigma_u^+ - X^1\Sigma_g^+$ emission band of Cu_2 .

liquid helium because this will allow optical pumping to produce non-thermal population distribution among hyperfine and Zeeman sublevels in diatomic molecules. For efficient production of non-thermal population distribution, many cycles of optical absorption and emission are necessary. In molecules, this is in general almost impossible because the optically excited molecules has little chance to come back to the same level due to the existence of many rotational/vibrational levels. In liquid helium, the rapid vibrational relaxation and low temperature (typically lower than 1.7 K) will allow a molecule repeated transitions between specific levels through absorption and emission of photons. The experimental confirmation of this technique is in progress.

In addition to stable diatomic molecules, we recently succeeded in observing the emission from AgHe_2 exciplex. When the D2 line of Ag atom was excited in liquid helium, a broad and red-shifted emission band was observed in addition to the atomic D1 line. This broad band has been assigned to the emission from the AgHe_2 complex in HeII formed by the attractive potential between the $P_{3/2}$ state of Ag and ground state He atom. The assignment has been confirmed by simulation of the band profile based on an *ab-initio* AgHe pair potential.

References

- 1) J. H. M. Beijersbergen et al.: *Phys. Lett.*, **A181**, 393 (1993).
- 2) Q. Hui et al.: *Laser Chem.*, **15**, 221 (1995).
- 3) H. Bauer et al.: *Phys. Lett.*, **A146**, 134 (1990).
- 4) J. L. Persson et al.: *Phys. Rev.*, **A52**, 2011 (1995).
- 5) M. Nakamura et al.: *RIKEN Accel. Prog. Rep.*, **28**, 77 (1995).
- 6) T. Kinoshita et al.: *Phys. Rev. Lett.*, **B49**, 3648 (1994).

Behaviour of Xe Atoms in Xe-Implanted Iron

E. Yagi and M. Hacke*

It has been known that heavy inert gas atoms (Ar, Kr and Xe) implanted into metals at ambient temperature precipitate into micro-cluster, and that for high implantation doses they are in a solid phase (solid inert gas bubbles) epitaxially aligned to matrices and in a high pressure state.

In previous channelling studies on Kr-implanted Al crystals (an fcc crystal), we have demonstrated that at the initial stage of implantation small complexes such as KrV_4 and KrV_6 consisting of Kr atoms and implantation-introduced Al vacancies (V) are formed, and act as nucleation centres for the subsequent bubble formation.¹⁻⁴⁾

For comparison of the behaviour of inert gas atoms between fcc crystals and bcc crystals, we made channelling experiments on Xe-implanted Fe crystals (a bcc crystal). Xe atoms were implanted into Fe single crystals at room temperature at an energy of 150 keV up to a dose of $1 \times 10^{16}/\text{cm}^2$. Rutherford backscattering-channelling experiments were performed at room temperature with a He beam of 1.5 MeV for $\langle 100 \rangle$, $\langle 110 \rangle$ and $\langle 111 \rangle$ channels. The channelling angular profile obtained for He ions backscattered by Xe atoms exhibits a simple shallow dip having the same angular halfwidth as that of the channelling angular profile (channelling dip) for He ions backscattered by host Fe atoms for each of these three channels. The relative depth of the Xe dip with respect to the host Fe dip was approximately 17%. As an example the result for the $\langle 100 \rangle$ channel is shown in Fig. 1. This result indicates that approximately 17% of the Xe atoms are located at substitutional sites and the remaining 83% are at random sites, i.e. in the form of bubbles. For the

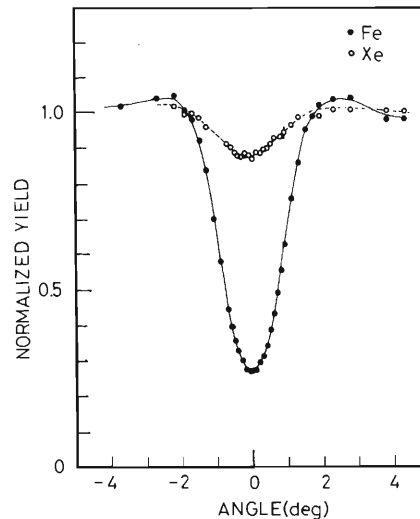


Fig. 1. $\langle 100 \rangle$ channelling angular profiles obtained for a $1 \times 10^{16} \text{Xe}/\text{cm}^2$ implanted Fe specimen. The solid curve and the broken curve are drawn only to guide the eye.

study of bubble nucleation, experiments on the specimens implanted with lower doses are being carried out.

References

- 1) E. Yagi: *Phys. Stat. Sol.*, (a)**104**, K13 (1987).
- 2) E. Yagi: *Nucl. Instrum. Methods Phys. Res.*, **B39**, 68 (1989).
- 3) E. Yagi, I. Hashimoto, and H. Yamaguchi: *J. Nucl. Mater.*, **169**, 158 (1989).
- 4) E. Yagi: *Phys. Rev. Lett.*, **67**, 3804 (1991).

* Present address: Institut für Schicht- und Ionen-Technik (ISI2), Forschungszentrum Jülich GmbH, Germany

3. Radiochemistry and Nuclear Chemistry

Differential Recoil Ranges of Reaction Products in the Cu + ^{14}N , ^{40}Ar Nuclear Reactions

M. Furukawa, A. Shinohara, T. Muroyama, S. Kojima, K. Mukai, A. Yokoyama, T. Saito, Y. Ohkubo, and F. Ambe

Recoil range distributions were measured for the heavy-ion (^{14}N and ^{40}Ar) nuclear reaction of natural copper with a radiochemical technique. The experiments were performed at the E3b course of the RIKEN Ring Cyclotron. The target was self-supporting 0.30–0.45 mg/cm² Cu metal foil and was set at the center of a Lucite cylindrical chamber. In the interior of the chamber, the catcher foil stack consisting of 10 sheets of Mylar films of 3.5–23 μm in thickness was put on to catch the recoil products. The ions used were 35 and 95 MeV/nucleon ^{40}Ar and 35, 70, and 135 MeV/nucleon ^{14}N . The irradiation was done for 3 to 4 hours in the beam current ranging from 50 to 200 nA. Each catcher foil was subjected to the off-line γ -ray spectrometry.

The activity distributions of the recoil products were obtained from the main γ -ray intensities observed in the individual catcher foils. Differential ranges obtained from the activity-per-thickness were presented

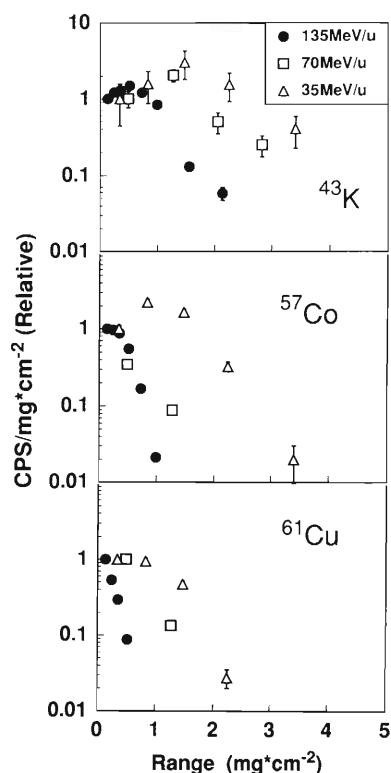


Fig. 1. Differential recoil ranges of typical recoil products in the Cu + ^{14}N systems.

in Fig. 1 for ^{43}K , ^{57}Co , and ^{61}Cu in the Cu + ^{14}N systems. The recoil range and its width are extremely small for the target-like product; those for the spallation products increase with the decrease of the product mass. They also decrease with the increase of the projectile energy, as described previously.¹⁾ The quantitative discussion on the momentum distribution will be given after conversion of the recoil range to the recoil momentum or energy.

We assumed that the peak position of the range distribution is equivalent to the longitudinal momentum transfer and the width corresponds to the isotropic velocity of the product. Figure 2 shows the correlation between the longitudinal momentum per product mass ($P_{//}/A$) and the isotropic velocity (V) of the typical products (^{43}K , ^{51}Cr , and ^{61}Cu), which was deduced from the recoil range data based on the above assumption. The latter is the measure of the excitation energy in the precursor of the spallation process following the collision step. One can see an approximately linear relation between $P_{//}/A$ and V . The reaction mechanism will be discussed from the collision kinematics obtained here in addition to the systematic data about the average recoil ranges and product yields measured previously.

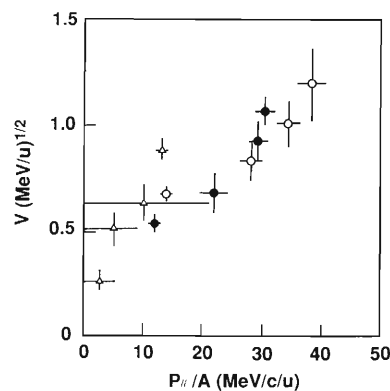


Fig. 2. Correlation between the longitudinal momentum per product mass ($P_{//}/A$) and the isotropic velocity (V) of the recoil product. \circ : ^{43}K , \bullet : ^{51}Cr , and \triangle : ^{61}Cu .

References

- 1) E. Taniguchi et al.: *Radiochim. Acta*, **62**, 163 (1993).

Mass Transfer in the Heavy-Ion Reaction of ^{197}Au Induced by ^{136}Xe

A. Yokoyama, T. Saito, H. Baba, A. Shinohara, M. Furukawa, and Y. Ohkubo

Deep inelastic reaction is an important process in the heavy-ion-induced reaction especially for the energy region above 10 MeV/u, where the other processes such as fragmentation also have substantial cross sections. It is difficult to predict the complicated processes of heavy systems such as gold plus xenon since the nuclear fusion process is hindered by Coulomb repulsion for the heavy systems. It is reported in Ref. 1 that the three-body interaction contributes to the reaction mechanism of a gold plus xenon system. It is also reported in Refs. 2 and 3 that a deep inelastic reaction plays an important role in the above system.

In the present study, we measured the mass distribution and the differential ranges of the products from a reaction of ^{197}Au with 23 MeV/u ^{136}Xe ions by using a radiochemical method in order to investigate the reaction mechanism of the relevant system and add further information to it.

The experiments were carried out at the RIKEN ring cyclotron (RRC) facility. The targets of Au metal foils were of 18.81 mg/cm² in thickness. The target was sandwiched by three Al foils of 25 μm in thickness and one Al foil of 50 μm in thickness for the measurement of short-lived nuclides. Two of the Al catcher foils were replaced by 50 μm Kapton[®] foils for the measurement of long-lived nuclides. The projectile energy of the ions was 26 MeV/u and the energy at the center of the target foil was 23 MeV/u. The details of the experiment are the same as described elsewhere.⁴⁾

Figure 1 shows the yields of the product nuclei observed in each foil of the stack of a target and catchers. The observed products are widely distributed in the mass range between 30 and 200 in atomic mass unit for the target foil and a forward foil (Au3). The yields of products of masses near the mass of the target or the projectile nuclide are increased. It may be due to the contribution of a peripheral reaction such as a mechanism of nearly grazing trajectory. A lot of products with masses less than 120 amu are observed in the most downstream foil and consequently have long ranges. They are considered to be produced via a fission process and multifragmentation. The distribution of the mass region between 150 and 190 exhibits the characteristics of the target fragmentation. Many neutron deficient nuclides are concentrated in the mass

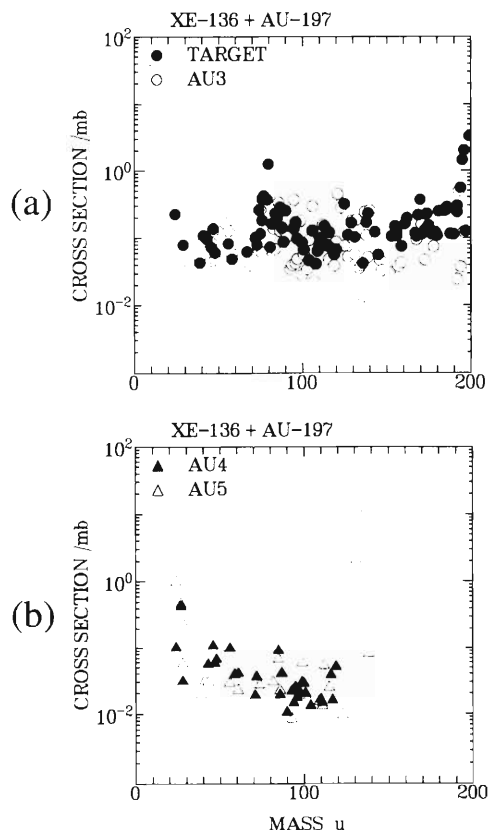


Fig. 1. Formation cross sections of the products in each foil of the stack for the ^{197}Au and 23 MeV/u ^{136}Xe system. The foils of Au3, Au4, and Au5 are forward catchers in order of the distance from the target foil.

region around 100 amu. It means that these nuclides are produced via a system which has a large excitation energy and causes evaporation of many nucleons. The results support the possibility of a three-body process following the substantial dissipation of the projectile kinetic energy.

References

- 1) O. Granier et al.: *Nucl. Phys.*, **A481**, 109 (1988).
- 2) A. Yokoyama et al.: *Phys. Rev.*, **C46**, 647 (1992).
- 3) W. Loveland et al.: *Phys. Lett.*, **B312**, 53 (1993).
- 4) H. Kusawake et al.: *Radiochim. Acta*, **69**, 65 (1995).

Reaction of ($^{14,15}\text{N} + ^{165}\text{Ho}$) and ($^{40}\text{Ar}, ^{14}\text{N}, + ^{141}\text{Pr}$) Systems at Intermediate Energies

K. Mukai, A. Yokoyama, T. Saito, H. Baba, Y. Ohkubo, A. Shinohara, and M. Furukawa

In the heavy ion reaction studies many reaction mechanisms have been proposed for a wide variety of projectile-target combinations and beam energies. We have studied complete and incomplete fusion for the reactions of ^{165}Ho with 35, 70, 135 MeV/nucleon ^{14}N , and ^{141}Pr with 35 MeV/nucleon ^{14}N and 10, 25, 38, 59, 95 MeV/nucleon ^{40}Ar beams using the thick-target, thick-catcher recoil range techniques.

In the present work we carried out angular distribution experiments for the (35, 70 MeV/nucleon $^{14,15}\text{N} + ^{165}\text{Ho}$) system in order to investigate precisely the incomplete fusion mechanism in each mass region. We performed the experiments at the RIKEN Ring Cyclotron E3b course using the radiochemical method. A cylindrical box made of Lucite was set in an irradiation chamber of the course. A ^{165}Ho target, which was inclined to 23.7° with respect to the beam direction, was bombarded by ^{14}N ions for about two hours. The ^{165}Ho targets were made by spattering on the $30 \mu\text{g}/\text{cm}^2$ carbon backing. The target thicknesses were $0.10 \text{ mg}/\text{cm}^2$ for the 35 MeV/nucleon experiment and $0.26 \text{ mg}/\text{cm}^2$ for the 70 MeV/nucleon experiment. Mylar films with $14.3\text{--}100 \mu\text{m}$ in thickness were attached to the inside wall of the cylindrical box. The beam spot was narrowed with two slits and the beam intensity was monitored with a Faraday cup. After irradiation, the catcher foils were splitted into seven pieces and assayed by Ge γ -ray spectrometers.

In the previous experiments the longitudinal momenta transferred (LMT) along the beam direction were determined from the measured cross sections and average forward ranges (FW). The details of calculation are described elsewhere.¹⁾ There are considerable discrepancies between observed values and Leray's systematics,²⁾ which is often referred to explaining incompleteness of the system irrespective of the projectile-target combination. It was found that the averaged value of $P_{//}/P_{\text{cn}}$ of the $^{14}\text{N} + ^{165}\text{Ho}$ system was comparable to that of the $^{14}\text{N} + ^{141}\text{Pr}$ system, and that the target mass seems to have little influence on the entrance channel dependence of the incomplete fusion process. The discrepancy is concluded to reveal the effect of the energy and angular momentum of the projectile.

Differential cross sections for $^{87}\text{Y}^m$, $^{111}\text{In}^g$, $^{135}\text{Ce}^g$, ^{160}Er are shown in Figs. 1 and 2. From the distribution in 35 MeV/nucleon and 70 MeV/nucleon ^{14}N experiments the angular distributions are observed to be

more forward peaking as the mass number increases. The distribution of $^{87}\text{Y}^m$, which would be a fission fragment, extends to larger angles compared to other products. Interpretation of these angular distributions is in progress.

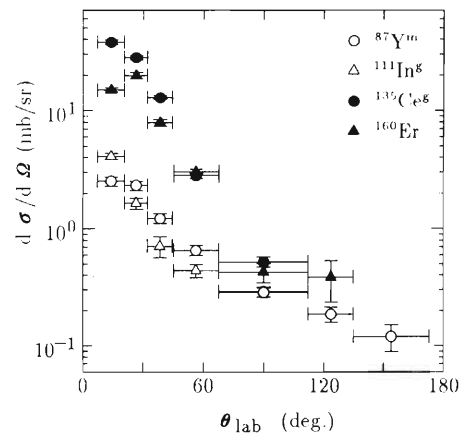


Fig. 1. The angular distributions of the products in the 70 MeV/nucleon ^{14}N experiment.

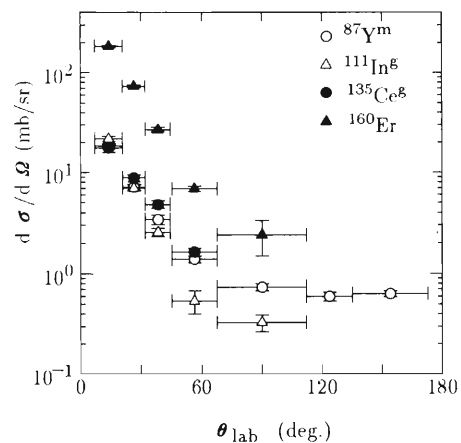


Fig. 2. The angular distributions of the products in the 35 MeV/nucleon ^{14}N experiment.

References

- 1) K. Mukai et al.: *OULNS Ann. Rep.*, p. 115 (1993).
- 2) S. Leray: *J. Phys. C*, **4**, 275 (1986).

Multitracer Study on the Behavior of Various Elements in Atmosphere-Plant System

T. Shinonaga,* S. Ambe, S. Enomoto, H. Maeda, M. Iwamoto, T. Watanabe, and I. Yamaguchi

Many works have been done on the pollution of plants with airborne elements and the importance of airborne elements in health physics was demonstrated. However, most of the previous studies did not clearly distinguish between the absorption via roots and that via leaves. Here, we studied the direct absorption of atmospheric elements by soybean plants using the radioactive multitracer technique.

A radioactive multitracer was prepared from an Au target irradiated with 135 MeV/nucleon ^{14}N at the RIKEN Ring Cyclotron. Soybean seedlings were cultivated in a box where multitracer-adsorbed cellulose powders were floating in air. Detailed experimental procedures were described in a previous report.¹⁾

Monitors were placed beside the soybean plants for determination of distribution of the multitracer in the box. They were constructed of glass fiber paper with a structure similar to that of the soybean plant.

Amounts of absorbed elements are expressed in relative values by dividing the peak area in γ -spectra of 1 g of dry samples by the corresponding peak area of a given portion of the multitracer. About 0.2% of the multitracer was absorbed by the soybean, of which 80% was found in the leaves, and 10% each in beans and stems.

Relative amounts of elements in the monitors were almost the same irrespective of the position. This indicates that the radioisotopes were uniformly distributed in the box. The relative amounts of elements in the leaves, beans and stems markedly differ depending on the element.

Distributions of elements in green and brown leaves originating from the middle node are shown in Fig. 1(a) and (b) together with relative values of the monitor. It is remarkable that Se was accumulated in large amounts in both green and brown leaves, although the value for green leaves was lower than that for brown leaves. Relative amounts of Sc, Y, Eu, Gd, Yb, and Ir were several-fold higher in brown leaves than in green leaves. The relative amounts of Co, As, Se, and Hf were 2- to 3-fold higher in brown leaves than in green leaves. However, there was little difference in the relative amounts of Mn, Rb, and Sr between green leaves and brown leaves.

The tendency for high Se accumulation also occurs

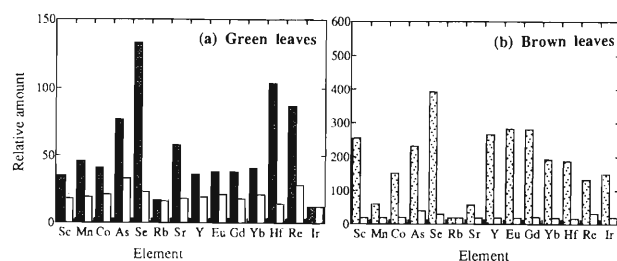


Fig. 1. Relative amounts of elements in (a) green leaves and (b) brown leaves. White bars indicate the values of monitor.

in the beans and this appears more clearly in the seeds than in the pods as shown in Fig. 2(a). It is interesting to note that although the seeds were not physically exposed to the multitracer-adsorbed cellulose powders during growth, high amounts of Co, Se, and Rb were observed in the seeds. Scandium, Y, Eu, Gd, Hf, and Ir were not observed in the seeds.

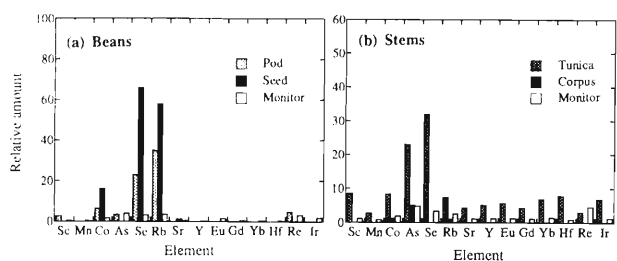


Fig. 2. Relative amounts of elements in (a) beans and (b) stems.

Since the soil was covered with films, there was little absorption of the elements by the soil, and no γ -ray peaks were observed in the root. These results offer evidence that the elements observed in the leaves were directly absorbed from air and that the elements observed in beans are due to transport from the leaves after their absorption through the leaf cuticle.

References

- 1) T. Shinonaga et al.: *RIKEN Accel. Prog. Rep.*, **28**, 85 (1995).

* Present address: Institute of Heavy Ion Physics, Peking University, China

Determination of Trace Elements in Ferns by Neutron Activation Analysis (I)

T. Ozaki, S. Enomoto, Y. Minai, S. Ambe, F. Ambe, and T. Tominaga

Importance of trace elements in life systems was first recognized more than one hundred years ago. However, accumulation of trace elements in ferns has not been studied well because ferns are regarded as the species somewhat backward in evolution as compared with the angiosperms or the gymnosperms. It is noteworthy that pteridophytes also have become abundant and diverse in evolution after diverging from other plants. Studies on accumulation of trace elements in pteridophytes should reveal an unexpected phenomenon because specialization in evolution often reaches extraordinary features. In this article, we report accumulation of lanthanides in ferns. Accumulation of other elements will be summarized in a following paper in this volume.

About 70 kinds of fern samples have been analyzed by means of the neutron activation analysis. The fern samples were collected at the Koishikawa Botanical Garden, School of Science, University of Tokyo. Several kinds of the ferns were sampled at the same place twice or three times over a year to examine seasonal variations in their elemental compositions. The plant samples were immediately packed in polyethylene bags at the sampling location. The samples were rinsed gently with distilled water and then with ultrapurified water. Their bodies were divided into mesophylls and leafstalks for analysis. When the samples could not be divided into these two parts, as in the case of *Psilotum nudum* (a whisk fern) or *Equisetum ramosissimum* (a scouring rush), the whole bodies were used. The samples were air-dried for one week at room temperature. 100–150 mg of each sample was sealed in a small polyethylene bag for irradiation. Neutron irradiation was carried out at the TRIGA-II reactor at Atomic Energy Institute, Rikkyo University. Gamma-ray spectra were measured twice by an HPGc detector coupled with a 4096 multichannel analyzer after 1 week and 2 weeks of cooling.

Concentrations of lanthanides in plant tissues are generally very low.¹⁾ However, the concentrations (dry weight base) in most samples were higher (Fig. 1) than those in the ordinary plants (e.g., 0.003–5 ppm).²⁾ In particular, the fern samples accumulated lighter lanthanides (La and Ce). Lanthanum was found to be most abundant in the fern samples (more than 20 ppm) except for some cases where Ce showed higher concentrations than La.

Here, we define concentration ratio (Ri) as follows:

$$R_i = C_{i,(fern)} / C_{i,(soil)}$$

where $C_{i,(fern)}$ and $C_{i,(soil)}$ represent concentrations of

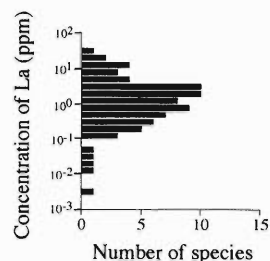


Fig. 1. Concentration distribution of La in fern samples.

an element i in a fern and the surrounding soil, respectively. The concentration ratio indicates the degree of accumulation of each element in the ferns. The concentration ratio varied regularly with the atomic number of the lanthanides, except for Ce (Fig. 2). Cerium tends to occur as tetravalent in the environment. The difference in oxidation state between Ce and other lanthanides may cause the anomaly in the plot.

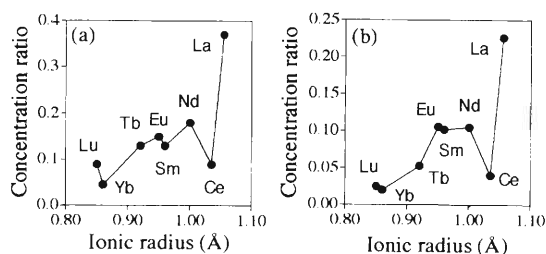


Fig. 2. Concentration ratios of lanthanides in (a) *Crytomium fortunei* and (b) *Dryopteris yakusilvicola*.

In recent years, special attention has been paid to biological roles of rare earth elements. It has been reported that many plants can discriminate against lanthanides.^{3,4)} On the other hand, there are many reports concerning beneficial effects of rare earths on the production of plants even though no evidence has been revealed that they are essential elements. A multitracer from an Au target irradiated in RIKEN Ring Cyclotron contains many kinds of radionuclides of lanthanides. Application of the multitracer technique should be useful for the elucidation of uptake mechanisms of lanthanides and their roles in growth of ferns.

References

- 1) P. Linsalata et al.: *Health Phys.*, **33**, 56 (1989).
- 2) M. Koyama et al.: *J. Radioanal. Nucl. Chem.*, **112**, 789 (1987).
- 3) N.A. Campbell et al.: *J. Exp. Bot.*, **25**, 61 (1974).
- 4) K. K. Harmet: *Plant Physiol. (Bethesda)*, **64**, 1094 (1979).

Determination of Trace Elements in Ferns by Neutron Activation Analysis (II)

T. Ozaki, S. Enomoto, Y. Minai, S. Ambe, F. Ambe, and T. Tominaga

As presented in a preceding paper, ferns tend to accumulate lanthanides (in particular, La and Ce). The analytical results indicated that some of other trace elements were also accumulated in ferns. In this report, we summarize accumulation of trace elements found in the analysis, except for lanthanides described in the preceding report.

Neutron activation analysis was employed to determine Ca, Sc, Cr, Fe, Co, Zn, Rb, Cs, Ba, La, Ce, Sm, Eu, Yb, and Lu. Experimental procedures were described in the preceding paper.

The accumulator species newly found in this work are summarized in Table 1. The concentration of Sc in ordinary plants reported by Koyama and his co-workers ranges from 0.002 to 0.01 ppm,¹⁾ whereas *Stegnogramma griffithii* showed about 4 ppm Sc in the

present work. While any role of Sc in life systems has not been reported, the extraordinarily high concentration suggests that Sc is involved in some biological activities in some ferns. It is noteworthy that Sc accumulator species tend to concentrate Cr, Fe, and Co. This is indicative of similarity in the uptake mechanism for those elements. Although Cr is usually toxic to living bodies, the species listed in Table 1 showed high concentrations of Cr. Those species possibly have special mechanisms for utilizing Cr or for neutralizing its toxicity. Zinc was found to be very abundant in some species: more than 1000 ppm in *Asplenium cheilosorum* and *Lygodium japonicum*. Since it was reported that the Zn concentration ranged from 2 to 100 ppm in ordinary plants,¹⁾ those species could be regarded as an accumulator of Zn.

Table 1. Accumulator species for each element found in this work.

Element	Species	Genus	Concentration (ppm)	Concentration range for ordinary plants (ppm) ¹⁾
Sc	<i>Stegnogramma griffithii</i>	<i>Stegnogramma</i>	3.9	0.002 - 0.01
	<i>Asplenium trichomanes</i>	<i>Asplenium</i>	2.0	
	<i>Selaginella tamariscina</i>	<i>Selaginella</i>	1.5	
Cr	<i>Stegnogramma griffithii</i>	<i>Stegnogramma</i>	25	0.02 - 1.0
	<i>Asplenium trichomanes</i>	<i>Asplenium</i>	12	
	<i>Selaginella tamariscina</i>	<i>Selaginella</i>	6.4	
	<i>Hymenophyllum barbatum</i>	<i>Hymenophyllum</i>	6.4	
Fe	<i>Stegnogramma griffithii</i>	<i>Stegnogramma</i>	870	20 - 200
	<i>Psilotaceae</i>	<i>Psilotum nudum</i>	530	
	<i>Asplenium trichomanes</i>	<i>Asplenium</i>	470	
	<i>Selaginella tamariscina</i>	<i>Selaginella</i>	380	
Co	<i>Stegnogramma griffithii</i>	<i>Stegnogramma</i>	4.0	0.005 - 1.0
	<i>Asplenium trichomanes</i>	<i>Asplenium</i>	2.2	
	<i>Selaginella tamariscina</i>	<i>Selaginella</i>	1.3	
Zn	<i>Asplenium cheilosorum</i>	<i>Asplenium</i>	1900	2 - 100
	<i>Lygodium japonicum</i>	<i>Lygodium</i>	1100	
	<i>Asplenium hondoense</i>	<i>Asplenium</i>	580	
Ba	<i>Dicranopteris linearis</i>	<i>Dicranopteris</i>	380	10 - 100
	<i>Asplenium hondoense</i>	<i>Asplenium</i>	330	
	<i>Blechnum niponicum</i>	<i>Blechnum</i>	240	
La	<i>Dryopteris erythrosora</i>	<i>Dryopteris</i>	32	0.003 - 5
	<i>Asplenium cheilosorum</i>	<i>Asplenium</i>	23	
	<i>Asplenium trichomanes</i>	<i>Asplenium</i>	21	
	<i>Asplenium hondoense</i>	<i>Asplenium</i>	14	

Tracer technique is very useful to deduce uptake and accumulation mechanisms of trace elements in the living organisms. A carrier-free multitracer produced in RIKEN Ring Cyclotron by irradiation of an Ag target contains many kinds of radionuclides of essential elements for plants and some other elements whose biological roles are unknown. This technique should

provide a clue to the elucidation of mechanisms concerning the uptake process and accumulation of the elements in ferns.

References

- 1) M. Koyama et al.: *J. Radioanal. Nucl. Chem.*, **112**, 789 (1987).

Distribution Coefficients of Platinum Group Metals between Soil Solid and Liquid Phase

H. Yasuda, S. Ambe, and S. Uchida*

In these days, high-tech industries are developing and producing new materials by synthesizing selected elements and considerable amounts of some rare metals are released to the environment. For evaluating and preventing the adverse health effect to humans, behavior of those metals in a real environment needs to be accurately traced. However, little information on the environmental behavior of selected rare metals, particularly platinum group metals, is available for this purpose.¹⁾ Then, in this study, distribution coefficients (K_{ds}) of three platinum group metals (Rh, Ir, and Pt) were measured for Japanese agricultural soils using a multitracer technique. The K_d is defined as a concentration ratio between soil solid and liquid phase and generally used in radiological environmental impact assessments for representing radionuclide sorption characteristics onto soil.

The radioisotopes of platinum group metals (^{101}Rh , ^{189}Ir , and ^{191}Pt) were produced by irradiating a thin gold foil with a ^{14}N beam (135 MeV/nucleon) in RIKEN Ring Cyclotron. The isotopes generated were separated from the Au target and the pH was adjusted finally to 0.05 M HCl. The contact solution was a rainwater (pH 4.5, electric conductivity 0.065 mS cm^{-1}) collected using a stainless steel bottle placed outdoors at Tokaimura, Japan; it was filtered through a $0.45 \mu\text{m}$ membrane filter and kept in a refrigerator. As samples of solid phase, sixteen agricultural soils were collected from cultivated lands in Japan; the soils sampled were passed through a 2 mm sieve, and dried at room temperature for about one month. The soils were analyzed for 8 chemical properties: cation exchange capacity (CEC), anion exchange capacity (AEC), exchangeable potassium content (exch.K), exchangeable Ca content (exch.Ca), activated aluminum content (activ.Al), activated iron content (activ.Fe), total carbon content (total C), and total nitrogen content (total N). The probability distributions of these chemical properties showed log-normal type distributions.²⁾

The K_{ds} were measured by a batch technique. Plastic bottles (50 mL) containing 3 g of each soil received 30 mL of the contact solution (rainwater) with 0.2 mL of the multitracer solution. The bottles were shaken at 100 rpm keeping the temperature at $21 \text{ }^\circ\text{C}$. After 20 hrs, each bottle was centrifuged at 3500 rpm and the supernatant solution was passed through a $0.45 \mu\text{m}$ membrane filter and measured for the γ -ray intensity with a Ge-detector (Ortec, GEM-30185) coupled with a multichannel analyzer (Seiko, EG&G 7800). The K_d

[L kg^{-1}] was calculated by the difference of radionuclide concentration in the supernatant.

The K_{ds} obtained here were examined for their variational characteristics, i.e. probability distribution types and correlations with the soil properties. The cumulative probability distribution of each nuclide K_d is shown in Fig. 1. The platinum K_{ds} were larger than those of other two metals and the rhodium K_{ds} showed larger variability compared to the iridium K_{ds} . The results of Shapiro-Wilk test indicated that the probability distributions of these nuclide K_{ds} were not normal type distribution but log-normal one. In the results of correlation analyses between the K_{ds} for rhodium and iridium and the soil properties (Table 1), adequate correlations were observed with the selected properties relating to the amount of clay, i.e. activated aluminum and activated iron contents. The platinum K_{ds} did not show a positive correlation with any chemical property of soil.

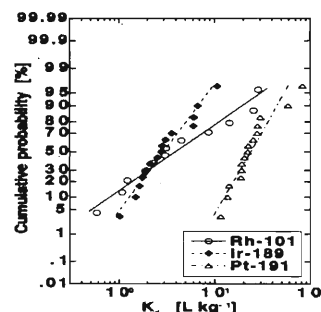


Fig. 1. Cumulative probability distributions of the K_{ds} of ^{101}Rh , ^{189}Ir , and ^{191}Pt obtained for 16 Japanese agricultural soils.

Table 1. Spearman correlation coefficients between the K_{ds} and the chemical properties of the soils.

nuclide	n	CEC	AEC	exch. K	exch. Ca	activ. Al	activ. Fe	total C	total N
^{101}Rh	12	0.80*	0.66	0.29	0.56	0.87*	0.83*	0.90*	0.88*
^{189}Ir	15	0.54	0.53	0.07	0.13	0.89*	0.71	0.53	0.48
^{191}Pt	15	-0.18	-0.12	-0.11	-0.32	-0.09	-0.11	-0.21	-0.25

*The coefficient value is larger than 0.80.

In future researches, it is desired to confirm the sorption equilibria and to clarify the effects of other environmental factors such as temperature, co-existing ion concentrations, and oxidation state.

References

- 1) A. Kabata-Pendias et al.: "Trace Elements in Soils and Plants", CRC Press, Boca Raton, p. 293 (1992).
- 2) H. Yasuda et al.: *Water Air Soil Pollut.*, **83**, 85 (1995).

* Division of Radioecology, National Institute of Radiological Sciences

Group Separation of a Multitracer by Solvent Extraction

B. Liu, S. Ambe, S. Enomoto, H. Maeda, R. G. Weginwar, and F. Ambe

1. Solvent Extraction of REE

In the course of the multitracer studies, we obtained interesting results on distributions of rare earth elements (REE) in rats and mice. For these studies, using only REE tracers was found to be more convenient than using the whole multitracer. The multitracer contains radioisotopes of Sc, Y and lanthanides from Ce to Lu.¹⁾ We studied the conditions for the simultaneous extraction of REE from the multitracer solution and their back extraction in order to obtain a group of tracers consisting of only REE (Hereafter, the tracer elements are denoted by the symbols of the elements with an asterisk. Note that they are all in the carrier-free state).

Di(2-ethylhexyl)orthophosphoric acid (HDEHP) was used for extraction of REE from the multitracer solution.²⁾ Extraction was first carried out using 0.02 mol dm⁻³ HDEHP-toluene, since the REE are present in trace amounts. In this case, the extraction efficiency was about 0% for Ce*, 50% for Eu*, and 100% for Lu*. When the concentration of HDEHP was increased, the extraction efficiency of Ce* increased with the concentration of HDEHP, as shown in Fig. 1. It was found that n-heptane gave higher extraction yields than toluene when used as a diluent. Although the difference in the extraction efficiency was small between HDEHP-toluene and -n-heptane at a low concentration of 0.1 mol dm⁻³ HDEHP, heptane yielded higher efficiency exceeding 90% at 0.4 and 0.5 mol dm⁻³ HDEHP (Fig. 1). Under the optimum conditions found in this study, practically all the REE in the multitracer were extracted. Namely, we used 0.4 mol dm⁻³

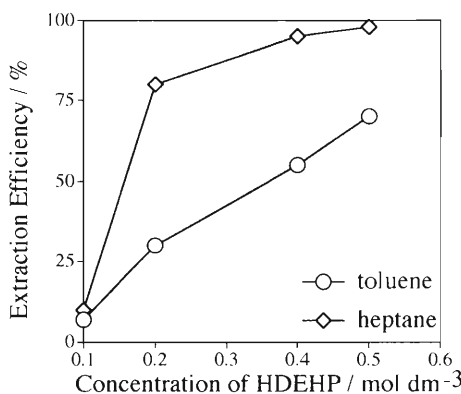


Fig. 1. Extraction efficiency of Ce(III) from 0.05 mol dm⁻³ HCl with HDEHP.

HDEHP-heptane for extraction of REE from 0.05 mol dm⁻³ HCl. All of Zr* and Hf*, 60% of Fe* and 40% of Zn* were co-extracted with 0.4 mol dm⁻³ HDEHP-n-heptane. Back extraction was carried out with an equal volume of 8 mol dm⁻³ HCl after the organic phase was diluted by adding the same volume of heptane. Yttrium*, Ce*, Eu*, and Gd* were completely back-extracted and for Yb* and Lu*, the back-extraction efficiency was 95 and 90%, respectively. Iron* and Zn* were also back-extracted completely. In contrast, Zr* and Hf* were not appreciably back-extracted even with either conc. HCl or conc. HNO₃.

2. Solvent Extraction of Tc and Re

Nowadays, technetium and rhenium have become very important for use in environmental and medical studies. Although Tc* and Re* were produced by irradiation of an Au target, they were evaporated and trapped together with an acidic solution in a cooling flask during the dissolution of the Au foil and the evaporation of the resulting solution. With an aim to include these two elements in the multitracer, we also studied how to collect Tc* and Re* from the trapped solution.

Two cm³ of a highly acidic solution of Tc* and Re* collected in the cooling flask of the evaporator was adjusted with NaOH to pH higher than 12, and then a few drops of H₂O₂ were added. The solution was warmed with a water bath for 10 min. Then Tc* and Re* were extracted with an equal volume of MEK. After phase separation, the organic phase was diluted with CCl₄ and shaken with the same volume of distilled water twice. Both elements were back-extracted into the aqueous phase.

Because only Re(VII) and Tc(VII) are extracted by MEK, the extraction efficiency was relatively low in the absence of H₂O₂. Only about 70% and about 50% of Tc* and Re*, respectively, were extracted into the organic phase. After the addition of H₂O₂, however, the extraction efficiency for Tc* increased to about 100% and that for Re* to greater than 80%. This is thought that the presence of H₂O₂ prevents the reduction of Tc(VII) and Re(VII) by MEK or some organic impurity in it. As regards the back extraction, more than 90% of Tc* and Re* in the solvent were back-extracted after two extractions with an equal volume of the aqueous phase.

References

- 1) S. Ambe et al.: *Anal. Sci.*, **7**, Suppl., p. 317 (1991).
- 2) K. Kimura: *Bull. Chem. Soc. Jpn.*, **33**, 1038 (1960).

Group Separation of a Multitracer by Cation Exchange Column

B. Liu, S. Ambe, S. Enomoto, H. Maeda, R. G. Weginwar, and F. Ambe

From an Au target, a multitracer solution containing a large number of radioisotopes of elements from Be to Hg was obtained.¹⁾ The multitracer solution gave complex γ -ray spectra consisting of more than 400 lines, resulting in overlapping of peaks and peaks hidden by the background. Previously, we used the whole multitracer without further separation. However, we soon realized that the overlapping of peaks is serious and reduction of the number of radioisotopes can increase the number of those effectively used as tracers. There are also specific demands for tracers containing a relatively small number of radioisotopes such as those of alkaline metals and of the platinum group. Among them, there are some carrier-free radioisotopes such as those of Rb and As, which are not commercially available, especially in a carrier-free state. In response to these demands, we studied the separation of the multitracer into several small groups by the methods of cation exchange. We aim at the development of separation methods to yield carrier-free and salt-free radioisotope tracers for further application of the multitracer technique to chemical and biological studies (Hereafter, the tracer elements are denoted by the symbols of the elements with an asterisk. Note that they are all in the carrier-free state).

A multitracer solution was evaporated to dryness and the residue was dissolved in 10 cm³ of a 0.5 mol dm⁻³ HCl solution. The solution was then poured on a chromatographic column filled with Dowex W50-X8 (100-200 mesh, H⁺ form, 15 cm high and 0.8 cm I.D.) previously equilibrated with distilled water and washed with 0.5 mol dm⁻³ HCl. Two elution procedures were performed. Procedure I: The column was washed with 20 cm³ of 0.5 mol dm⁻³ HCl, 40 cm³ of 2 mol dm⁻³ HNO₃, and 40 cm³ of 6 mol dm⁻³ of HNO₃ successively, as shown in Fig. 1. Every 2 cm³ of the eluate was collected in a test tube and was subjected to γ -ray spectrometry. Procedure II: The column was eluted with 20 cm³ of 0.5 mol dm⁻³ HCl, 20 cm³ of 0.1 mol dm⁻³ H₂C₂O₄ solution in 0.5 mol dm⁻³ HCl, 40 cm³ of 2 mol dm⁻³ HNO₃ and finally 40 cm³ of 6 mol dm⁻³ HNO₃, as is also shown in Fig. 1.

In the first 0.5 mol dm⁻³ HCl elution common to Procedures I and II, Pt*, Ir*, Rh*, Ag*, Re*, As*, and Se* radioisotopes were eluted from the cation-exchange column. It is considered that Pt*, Ir*, and Ag* exist as chloro complexes and As*, Re* and Se* as oxyanions. In the second elution of Procedure I with 2 mol dm⁻³ HNO₃, In*, V*, (Na*, K*, Rb*, Cs*), (Be*, Mg*, Ca*, Sr*, Ba*), Mn*, Co*, Cu*, Zn*, and Ga*

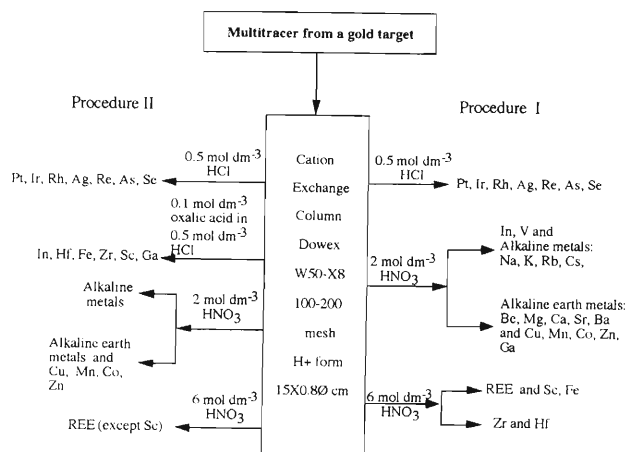


Fig. 1. Elution chart of group separation from the multitracer by cation exchange.

were successively eluted. By collecting the eluate in small portions, they were divided into alkaline metal, alkaline earth metal and other divalent and trivalent metal groups. Finally, with 6 mol dm⁻³ HNO₃, REE were eluted out. It was found that Sc* and Fe* were also eluted out with lanthanides. Zirconium* and Hf*, which were strongly adsorbed on the resin, were eluted out after REE with substantial tailing and the recoveries of these two elements were poor. A very small part of the radioisotopes of Ir also appeared in other fractions, which indicates the complicated chemical forms of Ir*.

The difference of Procedure II from I is that, in the former, 0.1 mol dm⁻³ oxalic acid solution in 0.5 mol dm⁻³ HCl was used as the second eluting solution. The merit of procedure II is that Zr* and Hf* are eluted completely from the resin. This method is therefore recommended when recoveries of Zr* and Hf* are necessary. A 0.1 mol dm⁻³ oxalic acid solution in 0.5 mol dm⁻³ HCl was used for the removal of Fe and Sc interferences from geological materials.²⁾ We found that In*, Zr*, Hf*, and Ga* were also eluted besides Fe* and Sc* using this eluent, while the other elements remained strongly adsorbed on the resin.

References

- 1) S. Ambe et al.: *Anal. Sci.*, **7**, Suppl., p. 317 (1991).
- 2) S. Meloni et al.: *J. Radioanal. Nucl. Chem.*, **71**, 429 (1982).

Biodistribution Study of Antibodies Labeled with Multitracer in Mice

B. Liu, S. Enomoto, S. Ambe, and F. Ambe

In the field of radiopharmaceutical science, radioactive metal ions chelated to small molecules, peptides, or proteins such as monoclonal antibodies have been used clinically for diagnosis of cancers and for basic studies on functions of various organs. In the selection of suitable isotopes for radiopharmaceutical uses, we usually label a compound with different isotopes one by one and compare their *in vitro* and *in vivo* behavior, which involves tedious work. Moreover, slight changes of conditions are inevitable in these separate experiments. In the multitracer technique developed at RIKEN, a large number of radioisotopes produced by high-energy heavy-ion irradiation of a metal target are simultaneously used as tracers. This is a great advantage for biological, pharmaceutical and medical studies. With the multitracer technique, we can obtain much information at one time and under strictly identical experimental conditions.

In this work, labeling of antibodies, immunoglobulin G (IgG) with a multitracer was investigated and the metabolism of the labeled antibodies was studied.¹⁾

A carrier- and salt-free multitracer solution in 0.05 mol-dm⁻³ hydrochloric acid was prepared. Diethylenetriaminepentaacetic acid (DTPA) was conjugated to IgG by the cyclic dianhydride method. After the multitracer solution was added to the IgG-DTPA solution, IgG-DTPA-multitracer was separated from free multitracer ions by means of a molecular-cut filter. To determine the *in vitro* stability of incorporated isotopes, the labeled IgG preparations were dialyzed against saline and 0.1 mmol-dm⁻³ EDTA solutions and the radioactivity remaining in the dialysis bags was measured with an HpGe detector. As a control, the same labeling procedure was performed with another IgG solution without conjugation with DTPA. In animal experiments, the antibodies labeled with multitracer were injected intraperitoneally into mice. The mice were sacrificed at 3, 24, and 48 hr after injection. Different organs were dissected, weighed, and counted with HpGe detectors. The biodistribution data were computed as percentage of injected dose (ID) per gram of organs.

It was found that the stability constant of the metal DTPA complex was a main factor in determining the labeling efficiency. Labeling efficiency of the metal ions in the multitracer solution increased with the stability constant of the DTPA complex. For the control sample without DTPA, the amounts of radioisotopes combined with IgG were lower than the detection limit. No obvious loss of the radioisotopes from the labeled IgG-DTPA was detected during 48 h of dialysis in saline and EDTA solutions. This indicates that once metal

ions combine with IgG-DTPA, the chelates are stable under the conditions studied.

The *in vivo* properties of multitracer-labeled IgG show that the stability constant of the DTPA-metal complex is only one of the factors that affect the biodistribution of radioisotopes. The property of the metal ion is also very important. Figure 1 shows the biodistribution of 10 radiotracers which were labeled on IgG. The metabolism rate of rare earth elements which can form very stable complexes with DTPA such as Y, Eu, Gd, and Yb was slow in blood, which is a metabolic characteristic of macro molecular IgG. Although the stability constants of Zr and Hf DTPA complexes are also very high, they did not show high stability *in vivo*. These two elements kept dissociating from the antibodies in blood and accumulated in bones. The rare earth elements showed similar behavior to each other. However, it seems that the *in vivo* stability of Ce was less than that of Y, Eu, Gd, and Yb. Here maybe the nature of the DTPA complex plays an important role. From Fig. 1, we can also see that the accumulation targets of the broken-down radioisotopes were different. Dissociated Ce had high accumulation in liver, while Zr and Hf accumulated largely in bones.

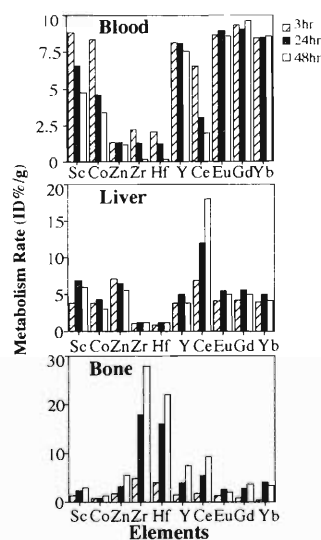


Fig. 1. Distribution of multitracer labeled IgG in some organs.

References

- 1) B. Liu et al.: *J. Radioanal. Nucl. Chem. Lett.*, **201**, 273 (1995).

Study of Trace Elements Uptake by Tumor-Bearing Mice by the Multitracer Technique

B. Liu, S. Enomoto, S. Ambe, R. G. Weginwar, and F. Ambe

A variety of radioisotopes injected intravenously show a higher concentration in tumor than in normal tissues.¹⁾ Some of these isotopes have been used for detecting the location of tumors, although the uptake mechanism of the isotopes by tumors is still not so clear. Taking the advantages of the multitracer technique, we determined the bio-distribution of radioactive elements in tumor bearing mice and compared the uptake of the diverse elements by the tumor.

In the multitracer technique developed at RIKEN, a number of radioisotopes useful in biological research are produced by irradiation of different targets with high-energy heavy ions. The irradiated target is dissolved in an appropriate medium and the target material is chemically removed leaving the radioisotopes to be used as radioactive tracers in a solution. The merits of multitracer technique lie in its high efficiency and its reliable comparison among each element used as tracer due to the identity of experimental conditions.

For the production of multitracer, a plate of gold was irradiated with the 135 MeV/nucleon ¹²C beam from the RIKEN Ring Cyclotron. The Au target containing various kinds of radioisotopes was dissolved in aqua regia. The solution was evaporated to near dryness under a reduced pressure in a rotary evaporator. The residue in the evaporation flask was dissolved in 3 mol dm⁻³ HCl. Gold ions were completely removed by extraction with ethyl acetate, leaving the radioisotopes as a multitracer in carrier- and salt-free states. In this study, the radioisotopes of the following 16 elements found in the multitracer were used as tracers: Be, Sc, Zn, Rb, Y, Zr, Te, Ba, Hf, Ir, Pt, Ce, Eu, Gd, Yb, and Lu.

The experimental mice underwent implantation of sarcoma in the thigh. One week later, a multitracer solution in saline was administered intravenously to the tumor-bearing mice. At 3, 24, and 48 hr after injection, the mice were sacrificed and the activity of radioactive elements in the organs was measured using HpGe detectors coupled with an MCA. As a comparison, a group of tumor-bearing mice, which were administered with a multitracer solution in 0.5 mol dm⁻³ sodium citrate, pH 5.0, were sacrificed at 24 hr after intravenous injection. The distribution data were given as injected dose %/g tissue of tumor/injected dose %/g tissue of muscle (Tumor/Muscle ratio).

Table 1 shows the Tumor/Muscle ratio of 16 elements at 3, 24, and 48 hr after injection in tumor bear-

Table 1. Tumor/muscle ratio of multitracer elements at 3, 24, and 48 hr after injection.

	3 hr		24 hr		48 hr	
	Saline	Saline	Saline	Citrate	Saline	Saline
Be	1.48	3.07	3.94	3.94	3.21	3.21
Sc	0.65	3.42	6.98	6.98	3.71	3.71
Zn	0.24	1.51	4.16	4.16	1.73	1.73
Rb	0.78	0.61	1.28	1.28	0.59	0.59
Y	2.60	17.27	30.86	30.86	10.89	10.89
Zr	0.58	0.24	6.74	6.74	0.34	0.34
Te	0.69	0.86	4.12	4.12	0.95	0.95
Ba	1.04	1.98	3.82	3.82	2.22	2.22
Hf	0.32	0.43	5.67	5.67	0.73	0.73
Ir	0.85	2.72	3.19	3.19	3.00	3.00
Pt	0.66	2.29	2.82	2.82	2.33	2.33
Ce	0.86	2.54	11.00	11.00	3.69	3.69
Eu	1.06	4.55	14.88	14.88	6.61	6.61
Gd	2.32	4.40	8.70	8.70	7.50	7.50
Yb	1.57	6.19	24.09	24.09	10.38	10.38
Lu	1.67	6.81	32.00	32.00	10.44	10.44

ing mice. Generally speaking, alkaline metals such as Rb and divalent cations such as alkaline earth metals and Zn showed a low Tumor/Muscle ratio. While the rare earth elements revealed a high tumor-uptake. On the other hand, Zr, Hf, Pt, and Ir showed low Tumor/Muscle ratio. The mechanism of accumulation of inorganic elements in tumor is complicated. For reason of the high uptake of the trivalent cations, partly, it was presumed that hard acids of trivalence would replace calcium in the calcium salts of hard bases (calcium salts of acid mucopolysaccharides, etc.) present in tumor tissue. Although Zr and Hf are hard tetravalent cations, these two elements may bind to chloride and therefore gave a lower Tumor/Muscle ratio. Also as shown in Table 1, the citrate solution gave a little higher Tumor/Muscle ratio for most of the elements studied. It is still not clear whether the citrate helps to form a certain complex as a ligand in serum and then results in high tumor-uptake.

References

- 1) A. Ando et al.: *Int. J. Nucl. Med. Biol.*, **12**, 115 (1985).

Separation of a Multitracer from an Au Target Irradiated by Heavy Ions

R. G. Weginwar, Y. Kobayashi, S. Ambe, B. Liu, S. Enomoto, and F. Ambe

The radiochemical solvent extraction procedure for the extraction of Au(III) from a solution of an Au target irradiated with an N-14 ion beam has been developed. It is based on the extraction of Au(III) with ethyl acetate or isobutyl methyl ketone from 3M HCl in the presence of 2% sodium citrate solution as a masking agent leaving behind a carrier-free multitracer in an aqueous medium. From the organic phase Au(III) tracer with carrier is then back extracted by 2-amino-2-hydroxymethyl-1,3-propanediol in an aqueous medium. Various conditions, such as pH, HCl concentration, various solvents, and coextraction of other elements, in the extraction of Au have been studied.

A piece of gold foil was irradiated with 135 MeV/nucleon N-14 ion beam at RIKEN Ring Cyclotron. After cooling, the foil was dissolved in aqua regia and this solution was evaporated to dryness under reduced pressure and the residue was dissolved in 3M HCl.^{1,2)} An appropriate amount of this tracer solution was taken in a funnel containing 3M HCl and 2% sodium citrate solution as a masking agent and was extracted with an equal amount of ethyl acetate or isobutyl methyl ketone. After equilibration, the yellow-colored organic phase containing an Au tracers with carrier was separated out from the carrier-free multitracer aqueous phase. Then, the organic phase was back extracted by 2-amino-2-hydroxymethyl-1,3-propanediol in an aqueous medium. Each phase was counted on 4k MCA coupled with an HPGe detector to calculate percent extraction of radionuclides.

Several aqueous systems were prepared in acidic range and extractions were carried out with ethyl acetate and isobutyl methyl ketone. From Fig. 1(a) and (b) it is observed that Au(III) was extracted up to 98% with ethyl acetate and isobutyl methyl ketone at 2-4 M HCl. Maximum extraction was about 95% at pH 1 and as pH increased the percent extraction decreased. Similarly various other organic solvents were examined for Au(III) extraction. But only ethyl acetate, isobutyl methyl ketone and diethyl ether were found to be suitable for extraction of Au(III) with the percent extraction up to 98% at 3M HCl.

In the coextraction study, it is observed that the coextraction trend of Fe, Re and Sc is similar, i.e., those elements give almost the same percent extraction with both the solvents. Fe yields the maximum coextraction at 6 M HCl, while Sc shows small dependence on the HCl concentration. In case of Re, the percent coextraction is much higher with isobutyl methyl ketone than that with ethyl acetate, and shows a maximum at 4 and 3 M HCl respectively with both the solvents. The coextraction of rare earth elements (REE), transition elements and many other elements is being in the

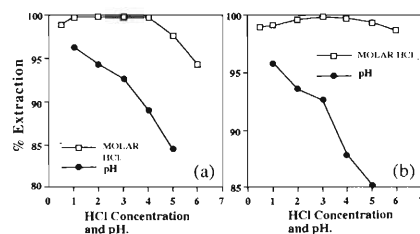


Fig. 1. Variation of % extraction of Au(III) by (a) ethyl acetate and (b) isobutyl methyl ketone with HCl concentration and pH.

range of 2-5%.

The major coextraction of Re, Fe and Sc is up to 20-35%, while the coextraction of Na is about 12% and that of As and Ru is about 4-5%. Suppression of the coextraction using a masking agent was also studied and it was found that the coextraction of Re, Fe, Sc and Na was depressed to 10-20% and that of REE and transition elements to 2-5%.

It was also observed that in the absence of Au(III) the percent coextraction of all these elements is almost negligible except for Fe and Re. However, as the concentration of Au(III) increases, the coextraction of Re and Fe sharply increased but that of Ru, Rb, As, Te also increased marginally. It was also observed that the percent coextraction attained a plateau for all these elements examined beyond 100 mg/ml of Au(III) concentration in the system. We also studied the percent coextraction variation for Sc and Na with increasing concentration of Au(III). The percent coextraction was almost negligible in the absence of Au(III), but with the increase in Au(III) concentration up to 50 mg/ml, the coextraction increased to about 19% for Sc and 12% for Na. These observations are considered to be due to the formation of strong ion association complexes of these elements with chloroauric acid in ethyl acetate or isobutyl methyl ketone in the presence of HCl. Thus at lower concentrations of Au(III) in the extracting system, the percent coextraction of various radio elements are depressed down. Except for Re, Fe and Sc there is no serious coextraction with ethyl acetate as well as with isobutyl methyl ketone. Thus the method can be safely used for the extraction of Au(III) to get a carrier-free multitracer solution which can be conveniently used for most of the biological and chemical applications.

References

- 1) S. Ambe et al.: *J. Radioanal. Nucl. Chem. Articles*, **195**, 297 (1995).
- 2) F. Ambe: *RIKEN Rev.*, No. 4, p. 31 (1994).

Selective Separation and Reversed Phase Extraction of Zirconium and Hafnium from Multitracer Solution

R. G. Weginwar, B. Liu, S. Ambe, S. Enomoto, H. Maeda, and F. Ambe

The extraction behaviour of Zr and Hf was studied in the systems of HClO_4 -TTA-benzene and HNO_3 - and HCl -TTA-xylene.^{1,2)} These studies provide little information on the coextraction of other elements. With the aim to use pure and carrier-free Zr and Hf in the multitracer for the biological study, we have developed selective solvent extraction of Zr and Hf from the multitracer using 2-thenoyltrifluoroacetone (TTA) in decahydro-naphthalene (decalin).

The simultaneous radiochemical separation of Zr and Hf from a solution of an Au target irradiated by an N-14 ion beam has been developed. It is based on the extraction of Zr and Hf with TTA in decalin from the multitracer solution containing carrier free Zr and Hf, and the extraction of other elements from 2 M of HCl and HNO_3 . The reversed phase extraction of Zr and Hf is also developed by using aqueous EDTA solution at pH range of 8.5-10. Various parameters, such as effects of pH, HCl and HNO_3 concentration, equilibration time, concentration of TTA, various solvents, and coextraction of other elements on the extraction of Zr and Hf, have been optimized.

Separation of the multitracer from an Au target irradiated by an N-14 ion beam is already described in a previous report.³⁾ A carrier-free multitracer solution in an aqueous phase was used in this study.

Typically, 1 ml of a carrier-free multitracer solution was taken in a beaker containing 8.5 ml of 2 M HCl or HNO_3 and 0.5 ml of H_2O_2 , the contents were warmed slightly with stirring. After cooling, the contents were transferred to a separating funnel containing 10 ml of 0.2 M TTA in decalin, and the funnel was shaken for about 15 minutes using a mechanical shaker. After equilibration, the separated organic phase was transferred to another separating funnel and 5 ml of a buffer solution of pH range 8.5-10 and 5 ml of 0.20 M aqueous EDTA solution were added to it. The solutions were shaken for about 5 min for back extraction of Zr and Hf. All activities were counted on an HPGe detector and 4 k MCA.

The effect of HCl and HNO_3 concentration on percent extraction of Zr and Hf was studied. It was observed that the extraction behaviour of both the elements is almost the same up to 5 M concentration.

Almost complete extraction occurred at 2 M HCl and HNO_3 . The percent extraction was decreased as the acid concentration increased. At higher HCl concentrations, complex formation of Zr and Hf with chloride ions in the aqueous phase lowers the extraction efficiency. Also the optimum pH for the maximum extraction of Zr and Hf was found to be 3 and then the extraction efficiency decreased at higher pH, which may be due to formation of hydroxides.

Several aqueous media were prepared in 2 M HCl and HNO_3 acid and extraction was carried out with TTA and various organic solvents. We found that the decalin gives the highest extraction yield of Zr and Hf amongst the other 14 solvents studied. Extraction was quantitative only with decalin and moderate with xylene. Other solvents were also effective but extraction was below 90% for both the elements. Also it was observed that the percent extraction of Zr and Hf is more effective in HCl medium than in HNO_3 medium in all the solvents.

The reagent concentration was also important in Zr and Hf extraction study. At lower concentrations of the reagent, the percent extraction is less and as the concentration of the reagent increased from 0.05 to 0.2 M the percent extraction increased sharply and then it remained constant for both the elements.

In the coextraction study, Rb, Sr, Nb and Sc are coextracted but coextraction of Sr and Rb is about 3% and 5% respectively. However, the coextraction of Nb is about 11% and that of Sc is about 15%. The other elements present in the multitracer are not coextracted at all. Therefore, except Sc and Nb there is no serious coextraction. The carrier-free Zr and Hf were back extracted using aqueous EDTA at pH 8.5-10 which lowers the coextraction of interfering elements by about 2-5%, and back extracted carrier-free Zr and Hf can be used for a further study of animal and plants.

References

- 1) F. L. Moore: *Anal. Chem.*, **26**, 997 (1956).
- 2) R. E. Connick and W. H. McVey: *J. Am. Chem. Soc.*, **71**, 3182 (1949).
- 3) R. G. Weginwar et al.: This report, p. 138.

Metabolism of Trace Elements in Marine Algae: A Study Using the Multitracer

R. G. Weginwar, M. Katayama, S. Ambe, S. Enomoto, B. Liu, and F. Ambe

The behaviour of various trace elements in marine algae is being studied by the multitracer technique. In recent years, pollution in marine environment has become a serious problem for human lives. These problems are mainly due to industrial waste as well as waste from human life. Another problem is the radioisotopes emitted from nuclear testings and accidentally leaked from nuclear plants into the ocean. These wastes may influence human bodies possibly through the food chains. Therefore, the mechanism of the incorporation of trace elements from sea water into plants and animals is important for our own health.

In this study, the incorporation of various trace elements in the marine algae (*Chactoceros* sp.) is experimentally investigated using a radioactive multitracer. As the first step, the relative amount of elements incorporated in the marine algae is determined.

For the production of a multitracer, an Au target irradiated with N-14 ion beam at the RIKEN Ring Cyclotron was dissolved in aqua regia and Au(III) was finally removed from 3 M HCl solution by extraction with ethyl acetate, and a carrier-free multitracer solution in artificial sea water was prepared.

The algae were grown in a normal medium¹⁾ under 2700 lux light from fluorescent lamps at 26°C on a rotary shaker for several weeks and then transferred to a new medium without phosphate salts. Four ml of a culture solution was transferred to a sterilized tube and centrifuged at 2000 rpm for about 5 min. and the aqueous phase was discarded. The cells left in the tube were mixed with 4 ml artificial sea water and 0.5 ml of the multitracer solution. After specific time intervals (5, 10, 20, 50 min.), 1 ml of the culture solution

was withdrawn and washed with 1 ml of sea water (3 times); finally the cell fraction and all the washing fractions were collected in separate tubes and counted on an HPGe detector and 4k MCA. Some preliminary results of incorporated elements in the cells are shown in Fig. 1. From Fig. 1, it is evident that the rate of incorporation of Se, Rb, As, Co, Fe, and Zn is quite similar. A further work is being carried out on incorporation as well as excretion of trace elements in marine algae in order to understand the detailed mechanism of incorporation of these elements.

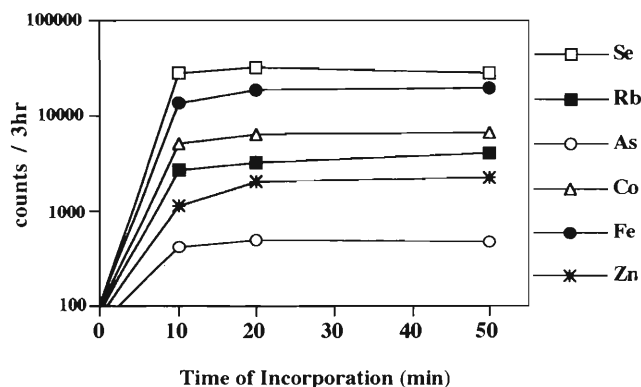


Fig. 1. Incorporation of carrier-free radio nuclides in marine alga cells.

References

- 1) M. Katayama, Y. Sugawa-Katayama, and A. A. Benson: *Appl. Organomet. Chem.*, **4**, 213 (1994).

Biodistribution of Gold Complexes in Mice

R. G. Weginwar, S. Enomoto, B. Liu, S. Ambe, and F. Ambe

Many gold compounds are highly toxic to animals, especially chloroauric acid and its salts, largely because of their oxidising ability.¹⁾ Gold and its compounds have a long history of medical applications. A few gold compounds have been used very successfully, in the treatment of rheumatoid arthritis, as an antitumor agent, etc. Very little is known about the mechanism in which the gold containing drugs act. The purpose of this paper is to study the biodistribution of Au(III) ions and Au(III) complexes in mice. It is thought that gold(III) would be more suitable than gold(I) for certain purposes. Gold(III) is isoelectronic with platinum(II), and forms similar square planar complexes. However, many gold(III) complexes are readily reduced to gold(I) or gold metal, which means that they would never reach the desired site and would instead be toxic. It is necessary to choose the ligands very carefully to prevent this.

In the present study, the uptake and distribution of radioactive gold(III) ions and gold(III) complexes in various tissues, organs and blood of normal mice were examined to clarify the behavior and role of gold(III) in animals.

A piece of gold foil was irradiated with 135 MeV/nucleon C-12 ion beam at RIKEN Ring Cyclotron. After cooling, the foil was dissolved in aqua regia and this solution was evaporated to dryness under reduced pressure and the residue was dissolved in 3M HCl. An appropriate amount of the solution was taken in a funnel containing 5 cm³ of 3M HCl was extracted with an equal amount of ethyl acetate. After equilibration, the yellow-colored organic phase containing Au tracers with carrier was separated out. Then the organic phase was back extracted with an equal volume of 0.1 M, 2-amino-2-hydroxymethyl-1,3-propandiol in an aqueous medium. Similarly, the organic phase was back extracted with 0.1 M sodium diethyl dithiocarbamate in parallel. Also, a Au(III) tracer with carrier was prepared in saline water. These solutions were injected i.p. (12 mg Au(III) / kg of mice) to normal ddY mice which were 10 weeks old. The mice were sacrificed after 3, 24, 48 hrs and the tissues, organs and blood were weighed and the activities were determined

by gamma-ray spectrometry. The results are given in percentage of i.p. dose and weight of tissues, organs and blood (Uptake rate %/g).

Figure 1 shows the distribution of the amino complex of Au(III) in mice. It is seen from Fig. 1 that the uptake in kidney, testes, liver, blood and spleen is high. In case of kidney, the uptake rate of the amino complex is about 4 times higher at 48 hrs after injection than that at 3 hrs after injection. While in case of muscle, uptake is almost twice at 48 hrs than that at 3 hrs after injection, it is reversed in case of blood and testes, namely, accumulation of the complex is about 5 and 3 times more at 3 hrs than at 48 hrs after injection, respectively. In case of liver, spleen and intestine, uptake is almost comparable in both the cases.

The measurement has been finished and the analysis is now being carried out for the diethyl dithiocarbamate complex and the tracer with no complexing agent in saline water at 3, 24, and 48 hrs after injection.

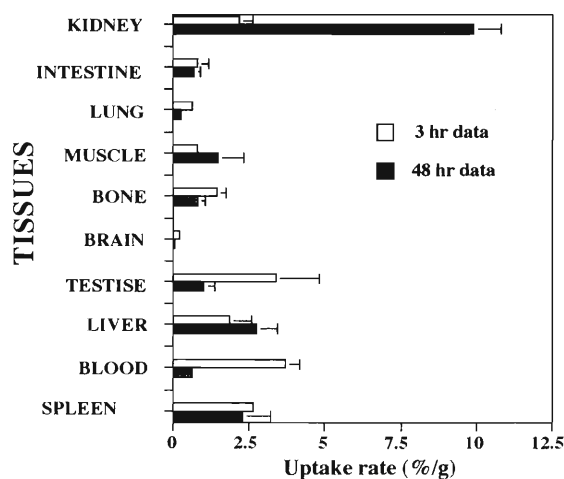


Fig. 1. Uptake rate (%/g) 2-amino-2-hydroxymethyl-1,3-propandiol complex of Au(III) in various tissues, organs and blood of normal mice.

References

- 1) R. V. Parish and S. M. Cottrill: *Gold. Bull.*, **20**, 3 (1987).

Metabolic and Biochemical Studies of Trace Elements in Zinc-Deficient Rats (1) Biochemical Properties of the Platinum-Group Elements

S. Enomoto, M. Yanaga, R. Hirunuma, K. Endo, S. Ambe, and F. Ambe

A new multitracer technique developed by us can be used to analyze the metabolism and behavior of a number of elements in living bodies simultaneously. We were able to reproduce a wide range of results on the behavior of various elements obtained in individual experiments performed by other researchers in a single run using this technique. At the same time, we could reveal the behavior and interaction of many other trace elements which other researchers have not included in their analysis.

Zinc is the second most abundant transition element in animals, following iron and plays an important role in many metabolic processes in living organisms.

In the present study, the uptake and distribution of radioactive isotopes in various tissues, organs and body fluids of normal and zinc-deficient rats were examined by means of the multitracer technique to clarify the behavior and roles of various trace elements.¹⁾

A multitracer was prepared from a gold target irradiated with a 135 MeV/nucleon heavy ion beam. A saline solution containing the multitracer was prepared and was injected intravenously to normal and zinc deficient male Wistar rats. The chemical forms of tracers on administration were assumed to be Sc^{3+} , VO_2^+ , Mn^{2+} , Co^{2+} , Zn^{2+} , Rb^+ , Sr^{2+} , Y^{3+} , Ce^{3+} , Eu^{3+} , Gd^{3+} , Tm^{3+} , Yb^{3+} , Lu^{3+} , ReO_4^- , $[\text{IrCl}_6]^{2-}$, and $[\text{PtCl}_6]^{2-}$.

The amount of zinc accumulated in the skin, testicles, and bones of the zinc-deficient rats was smaller than that accumulated in the same tissues of the normal rats; however, the amount of zinc accumulated in other tissues including the blood was larger in the former than in the latter rats. Bone and skin are organs in which zinc is known to store. The results of neutron activation analysis suggested a decrease in the amount of zinc accumulated in these organs in zinc-deficient rats compared with normal one (unpublished). The amount of zinc accumulated in the testicles was also found to be smaller in zinc-deficient rats than in normal one. As a major symptom of zinc deficiency, a decrease in reproductive ability is reported. Therefore, our results regarding zinc accumulation in zinc-deficient rats may indicate decrease in reproductive ability.

Figure 1 shows the uptake of Pt and Ir in normal and zinc-deficient rats. The amount of Pt accumulated in the kidneys and plasma was significantly larger than that of Ir. However, when we administered Pt and Ir to zinc-deficient rats, the amount of Ir accumulated in kidneys and plasma was larger than that of Pt by a factor of about 2–5.

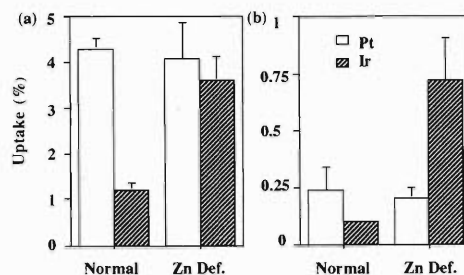


Fig. 1. Uptake (%) of the platinum group elements in normal and zinc-deficient rats. (a) kidneys and (b) plasma.

In general, Pt and Ir are classified into a group of elements exhibiting similar behavior in normal rats (the platinum group). The present results on Pt and Ir in normal rats agree well with the previous reports.

The chemical forms of Pt and Ir in the dosage solution and the body fluids were $[\text{PtCl}_6]^{2-}$ and $[\text{IrCl}_6]^{2-}$, respectively. However, the distributions of Pt and Ir in zinc-deficient rats are quite different from those in normal rats. Accordingly, the differences in the rate of uptake of these elements in zinc-deficient rats are regarded to be a result of differences in binding proteins or protein affinity.

Therefore, we carried out SDS-PAGE for plasma of normal and zinc-deficient rats. Pt-binding proteins in normal rats were found also to bind to Ir, but to have much greater affinity for Pt. On the other hand, in the zinc-deficient state, the Pt-binding affinity of a Pt-binding protein was less, and the Ir-binding affinity of a Pt-binding protein increased. Proteins which specifically bind to Ir exist in the plasma. These proteins which have a specific Ir-binding fraction have a molecular weight of approximately 66 kDa. However, we must examine this protein in more detail. The metallothionein activities in the kidneys and skeletal muscle of zinc-deficient rats were increased approximately 32 and 42%, respectively, by Ir. In other words, in the zinc-deficient state, Ir induced metallothionein activities which were stronger than those induced by Pt.

These results suggest that zinc deficiency contributes to conformational changes or affinity changes of transport proteins or enzymes which are involved in the uptake of Pt and Ir.

References

- 1) S. Enomoto et al.: *J. Radioanal. Nucl. Chem.*, in press.

Metabolic and Biochemical Studies of Trace Elements in Zinc-Deficient Rats (2) Ionic Radius Dependence of Uptake of Rare-Earth Elements

S. Enomoto, M. Yanaga, R. Hirunuma, K. Endo, S. Ambe, and F. Ambe

We have developed a multitracer technique which enables simultaneous analysis of the behavior of a number of elements in various chemical and biological systems. Significant features of the technique are as follows. (1) The broadness of the elements covered. (2) High efficiency. (3) The behavior of a number of elements can be compared under identical experimental conditions. (4) Serendipity. (5) Carrier-free and often salt-free radioisotopes can be used. (6) Many isotopes which are not readily available as single tracers are included.

In the present study, the uptake and distribution of rare-earth elements (REE) in various tissues, organs and body fluids of normal and zinc-deficient rats were examined by means of the multitracer technique to clarify the behavior and role of different trace elements.¹⁾

The amount of REE taken up in various tissues, such as liver and kidney, was found to be correlated with the ionic radius of the REE. Figure 1 shows the dependence of the amount of uptake in liver (Fig. 1(a)) and bone (Fig. 1(b)) on the REE ionic radius. The amount of uptake of "light" REE (Ce and Eu) in liver increased with increasing ionic radius; however, that of "heavy" REE (Lu, Yb, Y, Tm, Tb, and Gd) in liver showed no marked tendency to ward change with change in ionic radius. These results suggest that the uptake of light REE, whose ionic radii are similar to that of calcium, is interrelated with the calcium transport proteins in the cytoplasmic membrane.

Therefore, we measured the binding activity of the purified Ca channels of Ce, Eu, Y, Yb, and Lu with primary-culture hepatic cells. The binding activity was found to decrease in the following order: Ce > Ca > Eu >>> Y > Yb = Lu. We also measured the binding activities of Ca²⁺-ATPase and REE and calculated the binding ratio of REE vs. calcium to Ca²⁺-ATPase. The binding ratios of Ca²⁺-ATPase for Ce and Eu were similar to that of Ca. However, the affinities of Ca²⁺-ATPase for Y, Yb, and Lu were smaller to that of Ca. The above results of the binding activity measurements of both proteins indicate that the membrane transport of the light REE involves transport proteins such as various Ca channels and Ca²⁺-ATPase and that cytoplasmic accumulation requires the presence of Ca²⁺-ATPase in the endoplasmic reticulum.

In contrast, the amount of uptake of REE in bone was different from that in other tissues (Fig. 1(b)). The heavy REE were accumulated in bone to a greater ex-

tent than the light REE. The amount of uptake of light REE decreased with increasing ionic radius. These results indicate that heavy REE are adsorbed on hydroxyapatite that reacts with enzymes such as alkaline phosphatase and that light REE are non-specifically adsorbed on connective tissue on bone surface.

As shown in Fig. 1(a) and (b), the distributions of various REE exhibited similar behavior in normal and zinc-deficient rats. These results indicate that the calcium transport system does not involve Zn-regulated proteins.

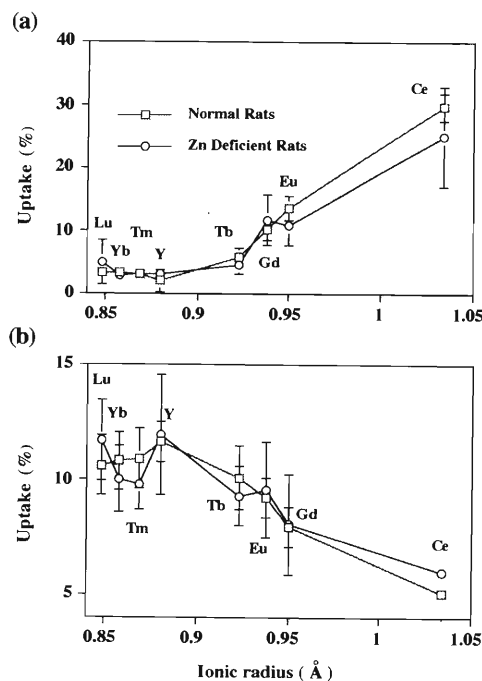


Fig. 1. Dependence of the amount of uptake (%) in liver (a) and bone (b) on ionic radii.

The levels of various biotrace elements can reflect various disease states. In certain diseases, some elements become a reliable source of information for diagnosis.

In conclusion, when we applied to a given biological system, the multitracer technique is a powerful tool to obtain information on the behavior of trace elements and the multidimensional interdependence of various elements in various tissues, organs and body fluids.

References

- 1) S. Enomoto et al.: *J. Radioanal. Nucl. Chem.*, in press.

In Vivo Behavior of Various Rare-Earth Elements in Lipogenous Diabetes Model Mice by Using the Multitracer Technique

S. Enomoto, B. Liu, R. G. Weginwar, R. Amano, S. Ambe, and F. Ambe

Radioactive-tracer method is a useful technique in science, technology, medicine and other various fields. Recently, a new 'multitracer technique' has been developed at RIKEN. A multitracer solution contains a number of radioactive isotopes employed for tracing. The multitracer enables us to determine the characteristic behavior of various elements under an identical condition. Diabetes is one of the most general and intractable diseases of adult people, which has a lot of complications. In the present study, the multitracer technique was applied to an investigation of the *in vivo* behavior of trace elements in lipogenous diabetes model mice in comparison with normal mice.

A gold foil was irradiated with C-12, N-14 or O-16 beam of 135 MeV/nucleon from RIKEN Ring Cyclotron. The Au foil was dissolved in aqua regia. After Au ions were removed by extraction with ethyl acetate, the rare-earth elements (REE) were extracted from a HCl-multitracer solution by di(2-ethylhexyl) phosphoric acid solution in heptane and were back-extracted with HCl.¹⁾ The REE multitracer solution was kept to dryness and dissolved in a saline solution before experiments. The solution was injected intraperitoneally to diabetes model (KKAy/Ta Jcl) and normal mice (male). The mice were sacrificed several hours after injection. The tissues, organs and body fluids were weighed and their radioactivities were determined by γ -ray spectrometry. Identification and determination of isotopes were done on the basis of their energies, half-lives and peak areas. The results are given in percentage of intraperitoneally injected dose of tissues, organs and body fluids (uptake %).²⁾

From the analysis of γ -ray spectra, distributions of Y, Ce, Eu, Gd, Yb, and Lu were determined. When intraperitoneally injected, various REE exhibited quite different distributions in both normal and diabetes mellitus model mice. The uptake of REE in the livers of both kinds of mice shown in Fig. 1 was correlated with changes in the ionic radius of REE. The uptake of "light" REE increased with increasing ionic radius; however, there was no marked tendency in that of "heavy" REE. The quantities of accumulation of REE in diabetes mice liver were larger than that of normal mice by a factor of about 2–5. Triglyceride and blood sugar concentrations in blood serum of diabetes mice were found to be relatively higher than those of normal mice as shown in Table 1. The results of pathologic diagnosis in a diabetes mouse liver by a microscope revealed hepatic steatosis. The uptake

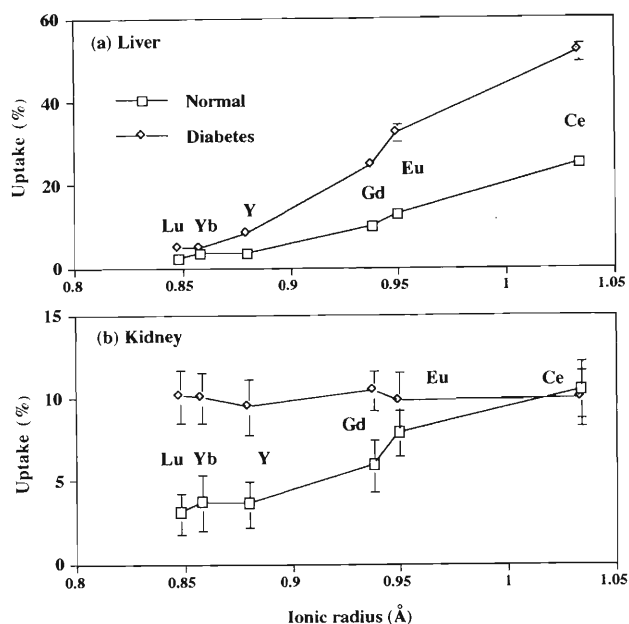


Fig. 1. Uptake dependence on ionic radii in liver (a) and kidney (b).

Table 1. Biochemical data of diabetes model and normal mice serum.

	Diabetes model	Normal (ddY)
Blood sugar value (GLK/G6PDH)	250.3±1.6 mg/dl	121.4±16.9 mg/dl
Triglyceride	242.8±14.3 mg/dl	95.1±22.7 mg/dl

of the REE in a normal mouse kidney, is correlated with changes in the ionic radius of the REE. However, the uptakes in diabetes mice do not depend on the REE ionic radii. The results of pathologic diagnosis in a diabetes mouse kidney revealed diabetic nephrosclerosis. Mesangial cells become the vitreous structures and show the tuberos lesion. These results indicated that REE are accumulated in adipose tissue of liver in the case of diabetes mice and that REE are stored in renal corpuscles.

References

- 1) B. Liu et al.: *Bull. Chem. Soc. Jpn.*, in press.
- 2) S. Enomoto et al.: *J. Inorg. Biochem.*, **59**, 353 (1995).

Metabolic Studies of Various Trace Elements in Acute Alcoholic Mice

S. Enomoto, B. Liu, R. G. Weginwar, R. Amano, M. Yanaga, S. Ambe, and F. Ambe

Bio-trace elements are concerned with many physiological functions and their concentration changes reflect various kinds of diseases. It has also become clear that many of them are important in maintenance of *in vivo* metabolic functions.

Alcoholics is illness characterized by insufficient nutrition, dyspepsia and abnormal absorption of nutrients. Alcoholics is easy to produce abnormality in metabolism of bio-trace elements merging with liver or pancreas obstruction. Ingested alcohol is metabolized in the liver. When alcohol is taken by excess, alcohol metabolism in the liver is selectively accelerated and, therefore, whole metabolism in the liver system suffers a drastic disorder.

Principally, alcohol ingested in the liver is dehydrogenated by alcohol dehydrogenase (ADH) in hepatic cell and becomes acetaldehyde. Furthermore, this acetaldehyde receives dehydrogenation by aldehyde dehydrogenase and becomes acetic acid. This acetic acid is used in synthesis of acetyl CoA, and it is utilized by the TCA cycle.

When alcohol is taken in surplus, the creation of NADH increases. Therefore, the NADH/NAD ratio becomes large, and this co-enzymatic system in hepatic cells inclines to the reduction type. On this account, the concerned reaction system in hepatic cells goes to a direction of restoring this conditions. That is to say, metabolism in the liver system is led to a general change.

Besides the ADH enzymatic system, there are three non-alcohol dehydrogenase systems (non-ADH) as follows; microsome-ethanol enzymatic system, NADPH-oxidase-catalase system and xanthine oxidase-catalase system. These metabolism systems usually take approximately 25% of all alcohol metabolism. The continuous dosage of alcohol activates non-ADH systems. As a result, non-ADH systems be come to share around 50% in quantity of all the alcohol metabolism. The liver is the leading organ for metabolism of chemicals including trace elements and drugs besides alcohol. The dramatic change of liver function by alcohol described above gives big influence to the metabolism. As a characteristic of biochemical changes of the alcoholics liver obstruction, hepato-secretary proteins such as albumin and transferrin accumulate in inner hepatic

cells. Albumin and transferrin are important proteins participating in the first reception and transportation process of trace elements. Therefore, it can be predicted that alcoholics give large influence on the bio-behavior of trace elements, too.

In the literature, certain influence of alcohol on the metabolism of copper, selenium, iron, and magnesium is described. However, the nutritional influence given to alcohol metabolism of other trace elements is not yet studied at all. Therefore, it was assumed that detailed investigation is required.

In this work, we carried out studies on the metabolic abnormality of trace elements in acute alcoholics, with the multitracer technique.

Three ddY mice were treated intraperitoneally with alcohol at 3 hr before and at 3, 11, 19, 27, 35, 43, 51, 59, 67 and 71 hrs after the multitracer solution injection described below. Each mice received 0.025 ml/g body weight of 25 (V/V)% alcohol each time. The injection schedule is shown in detail in Table 1. A multitracer

Table 1. The experimental schedule of ethanol (E), the multitracer solution (M) injection, and sacrifice (S).

group	-3	0	3	11	19	27	35	43	51	59	67	71	hr.
(a)	E	M	S										
(b)	E	M	E	E	E	S							
(c)	E	M	E	E	E	E	E	E	S				
(d)	E	M	E	E	E	E	E	E	E	E	E	S	

Ethanol of concentration 0.025 ml/g (25% Ethanol /saline solution) is intraperitoneally injected. The multitracer saline solution (0.1 ml/ each mice) is intraperitoneally injected.

was prepared from a silver target irradiated with a 135 MeV/nucleon heavy ion beam, and 11 radioisotopes served as tracers. A saline solution containing the multitracer was prepared and injected intraperitoneally to the above acute alcoholic mice. After sacrificed, the mice were subjected to the examination of the uptake and distribution of radioactive tracers in their various organs. The measurements have been finished and the data analysis is now being carried out. Detailed data and discussion will be reported later.

Research in Metabolic Physiology on Space Field by Using the Multitracer Technique – A Proposal

S. Enomoto, H. Maeda, S. Ambe, and F. Ambe

The creatures on the earth fit themselves to various kinds of environment, and evolve and prosper. In recent years, it has been realized that mankind utilizes universal space. Information concerning changes of homeostasis of a creature in universal space is still much limited. Detailed physiological studies on this problem are a pressing need. Bio-trace elements can be an index reflecting various kinds of diseases. In certain diseases, some elements become a reliable source of information for diagnosis. The multitracer technique, a tracer technique developed by us, can analyze metabolism and behavior of different elements in the living bodies simultaneously. We proved that this method is a powerful tool to obtain information on the behavior of bio-trace elements.^{1,2)}

In this article, we describe the usefulness of the multitracer technique in the studies of trace elements in living bodies and discuss possibility of its application to metabolic physiology in universal space environments such as low or zero gravity, low oxygen concentration, radioactive rays exposure and low atmospheric pressure.³⁾

The multitracer method excels in following points in comparison to the current method. (1) The broadness of the elements covered. At present, fifty-two elements have been traced with the technique. Information about around 10 from 50 kinds of elements is provided in a single experiment. (2) Information is completely provided under the same condition. Because of differences of sample and individual are large in the living body, it is extremely important in each elemental mutual comparison and interacting studies that data about many elements are provided under the completely same conditions. (3) When we utilize a usual radioisotope as a tracer, a very small amount of it is sufficient. However, in the case of (n, γ) reaction,

the quantity of a stable isotope contained in the radioisotope product cannot be ignored. On the contrary, each element in a multitracer solution is carrier-free and therefore consideration of its toxicity is completely needless. A quantity of one element is approximately pico gram order or less. (4) Because we can measure the behavior of many elements simultaneously, there is the possibility that we can discover a new fact about the trace elemental behavior and role that is not intended. (5) We can get various kinds of elements in the periodic table as a tracer by selecting a target. (6) The multitracer contains a precious radioisotope even as a single tracer (Mg-28, Ca-47 etc.).

From these points of view, the multitracer technique is quite suitable for the space experiment with only a limited chance and period. For instance, at our bone, the obstruction of calcium absorption occurs in a low gravity space environment. Besides this, a change of various kinds of physiological situations that are not clear occurs, too. It is considered in this connection that we can make the behavior of bio-trace elements clear, in particular dynamics of bone seeking elements by application of a multitracer. Undoubtedly, these experiments will give basic and useful information about physiology and biochemistry of the creatures to use the universal space in future.

References

- 1) S. Enomoto, M. Yanaga, R. Hirunuma, K. Endo, S. Ambe, and F. Ambe: *J. Radioanal. Nucl. Chem.*, in press.
- 2) B. Liu, S. Ambe, S. Enomoto, and F. Ambe: *J. Radioanal. Nucl. Chem., Lett.*, **201**, 273 (1995).
- 3) S. Enomoto, S. Ambe, and F. Ambe: *Proc. of 12th Space Utilization Symp.*, **12**, 91 (1995).

Preparation of a Multitracer from Heavy-Ion Irradiated Tin by Heating under Reduced Pressure

M. Iwamoto, H. Maeda, and F. Ambe

A separation method of multitracers by heating under reduced pressure from a heavy-ion irradiated target was established.¹⁻³⁾ We previously chose gold, silver, and copper as targets, and in this report an experiment on tin is described. Tin has a very low vapor pressure in spite of its lower melting point (231.8 °C) than ordinary metals.

A tin target was irradiated with a 135 MeV/nucleon

¹⁴N beam or ¹²C beam. After irradiation, the target was heated up to a fixed temperature under a reduced pressure in a quartz tube for 1 hour. A sample was heated up to 600 °C and after that up to 800 °C. Two other samples were heated up to 1000 and 1100 °C, respectively. It was found that some kinds of nuclides were driven out of the target and trapped on a cold part of the tube. They were easily dissolved by warm

Table 1. Activity of the nuclides.

Heating temperature activity	600 °C (cps)	800 °C (cps)	1000 °C (cps)	1100 °C (cps)
Be-7		0.705	0.386	
Sc-47		0.113	0.0132	0.477
Cr-51			0.0082	0.2034
Mn-54	0.072	5.67	0.0246	0.2087
Cu-67				0.5933
Zu-65	0.108	0.404	0.0956	0.2208
As-77	0.0404	0.164	0.0042	0.0336
Se-75	0.37	30	0.232	1.5156
Rb-83	0.719	7.89	0.54	0.5107
Rb-84	0.298	0.303	0.1547	0.1669
Y-88		0.022	0.0024	0.0027
Zr-88		0.097	0.0082	0.1875
Ag-105			0.0054	1.7629
Ag-106m				0.2888
Cd-109	0.723	0.883	0.0916	0.5481
In-111	1.352	1.147		2.5228
In-114m	0.696	0.618	0.006	2.955
Sn-117m		3.605	0.0132	0.4771
Sb-120				0.155
Te-119m		0.0729	0.0014	0.0662
Te-121	0.099	0.133	0.0181	0.1271
Te-121m		0.157	0.0217	0.191

6M HCl. Heating time and dissolving time were the same. Table 1 shows the amount of activity of some nuclides with comparatively long half-lives. Some elements (Zn, As, Se, Rb, Cd, In) were expelled from the target even at a low temperature and some other elements (Sc, Ag, Sb, Te) only at a high temperature.

References

- 1) M. Iwamoto et al.: *RIKEN Accel. Prog. Rep.*, **24**, 72 (1990).
- 2) M. Iwamoto et al.: *ibid.*, **25**, 97 (1991).
- 3) M. Iwamoto et al.: *ibid.*, **26**, 85 (1992).

Time Dependence of Distribution of Trace Elements in Rats Using the Multitracer Technique

K. Endo, R. Hirunuma, M. Yanaga, M. Tozawa,* S. Enomoto, S. Ambe, and F. Ambe

Previously, the uptake and distribution of radioactive isotopes in various tissues, organs, and body fluids of rats were examined by means of the multitracer technique.^{1,2)} The present study aimed to examine the time dependence of tissue distributions of radioactive isotopes for a time range of one to six days. The experimental procedures are the same as reported previously.²⁾

The tissue distributions of radioisotopes of Rb, Mn, Co, Zn, As, Rb, Pt, and Ir were measured in the time range of one to six days after oral administration. The results on Rb, Zn, Co, and As are described in the following. Figure 1 shows the results on the tissue

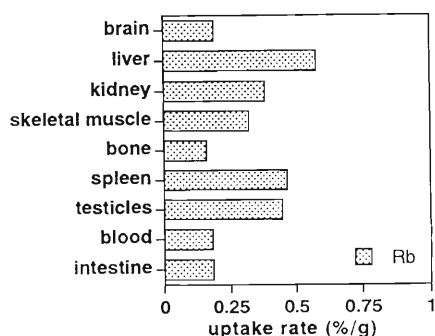


Fig. 1. Tissue distribution of rubidium in rats 3 days after administration.

distribution of Rb expressed in % dose/g for each tissue three days after administration. The data represent average values of three rats. Rb was distributed in every tissue and high concentrations (% dose/g) of it were found in liver (0.58), spleen (0.48), and testicles (0.45), and low concentrations in intestine (0.18), blood (0.18), and bone (0.16). Figure 2 shows the time dependence of Rb concentrations for eight tissues and blood. A general trend was found that the tissue distri-

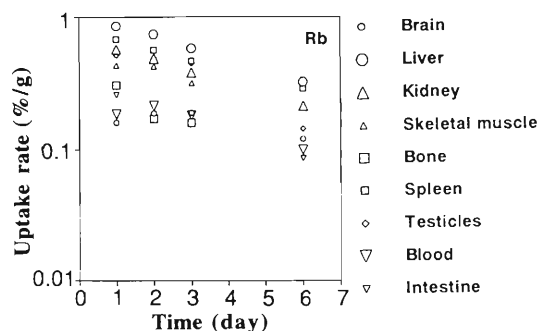


Fig. 2. Time dependence of rubidium concentration (% dose/g) in eight tissues and blood.

butions of Rb decreased in every tissue examined with time elapsing after administration. Variation range of the tissue concentration of Rb one day after administration is estimated to be a factor of 4.4, taking the ratio of the highest (0.88 in liver) to the lowest concentration (0.20 in bone). The variation was found to be 3.7 after six days; namely, it tends to be smaller with time elapsing after administration. A similar trend was observed for all the radioactive isotopes used in this study, although the variation range and the decay rate were characteristic of each radioisotope and tissue.

Zn was also found in all the tissues. The distribution of radioactive Zn one day after administration ranged from 1.4 in liver to 0.03% dose/g in blood, whereas it changed to 0.19 in liver and 0.03% dose/g in blood 6 days after administration. The variation of the RI concentration among the eight tissues and blood was over a factor of 40 one day after administration, and narrowed to a factor of 6.3 after six days. It is to be additionally remarked that the Zn concentration in blood was kept almost constant, i.e., 0.03, 0.04, and 0.03% dose/g for 1, 3 and 6 days after administration. The time dependence of the concentration of Zn in brain and testicles was also small. In the case of Co, high concentrations (% dose/g) were found in kidney (0.69) and liver (0.47), and low concentrations in skeletal muscle (0.006), and testicles (0.02) one day after administration. The range of the variation in concentration among the eight tissues and blood was greater than two order of magnitude. After six days, the concentration was found to be 0.07% dose/g in kidney, 0.06% dose/g in liver, 0.02% dose/g in skeletal muscle, and below the detection limit in testicles.

Arsenic showed the following characteristic behavior, i.e., (1) the variation in tissue concentration is the largest among the elements investigated, and (2) the apparent dwell time in each tissue is long. The uptake and distribution of As one day after administration was found to be 6.3% dose/g in blood (the highest), and 0.05 in skeletal muscle (the lowest), which corresponds to a variation range of 126. The % dose/g concentrations were 0.36 in blood and 0.04 in intestine after six days. The variation range was estimated to be about one order of magnitude.

References

- 1) M. Yanaga, S. Enomoto, R. Hirunuma, R. Furuta, K. Endo, A. Tanaka, S. Ambe, F. Ambe, M. Tozawa, and F. Ambe: *RIKEN Accel. Prog. Rep.*, **28**, 86 (1995).
- 2) S. Enomoto, M. Yanaga, R. Hirunuma, K. Endo, S. Ambe, and F. Ambe: *ibid.*, p. 93.

* Dept. Chem., The Jikei University School of Medicine

Multitracer Study on Distribution of Trace Elements in Vitamin D Overloaded Rats

R. Hirunuma, K. Endo, M. Yanaga, S. Enomoto, B. Liu, S. Ambe, and F. Ambe

It is well-known that Vitamin D (VD), used for therapy of rickets, osteoporosis and renal failure, affects the metabolism of Ca and P. Recently, it is also used for therapy of malignant tumor and psoriasis. However, the effects of VD on the metabolism of various trace elements have scarcely been studied. In the present study, effects of VD on the behavior of various elements in rats were examined by the multitracer technique, which can be used to determine the behavior of various elements under the same experimental conditions.

A multitracer solution containing various radioisotopes was prepared from a Ge or Au target irradiated with N-14 beam of 135 MeV/nucleon from RIKEN Ring Cyclotron. A half ml (0.25 μg as alfacalcidol) of a VD solution was orally administered to each male Wistar rat every day for a week. A tenth ml of a saline solution containing the multitracer was injected intravenously in the tail vein of each rat. Then 0.2 ml (0.1 μg as alfacalcidol) of the VD solution was injected intraperitoneally every day until sacrifice. As a reference, three normal rats were used. Urine was collected at each proper time after injection. The VD-overloaded and normal rats were sacrificed and the radioactivities of tissues and body fluids were determined by γ -ray spectrometry. The observed γ -rays were assigned to each radioisotope on the basis of their energies and half-lives. The behavior of Be, Ca, Sc, V, Cr, Mn, Fe, Co, Ni, Zn, Ga, As, Rb, Sr, Ba, Ir, Pt, Ce, Eu, and Gd was examined. There were little individual differences in each group of rats.

In order to examine the physiological condition of the rats fed with excess VD, the concentrations of alkaline phosphatase, acid phosphatase and Ca in their plasma were examined. The values of the alkaline phosphatase for the VD-overloaded and normal rats were found to be 12 ± 2 Bessey-Lowry Unit (B-L U) and 17 ± 1 B-L U, respectively. There was little difference between the values of acid phosphatase of the normal and the VD-overloaded rats. The Ca concentrations were found to be 9.2 ± 0.5 mg/dl and 11.6 ± 0.1 mg/dl, respectively, for the normal and the VD-overloaded ones. The low concentration of alkaline phosphatase and the high concentration of Ca for the VD-overloaded rats prove that they were really overloaded with VD.

The amounts of Be and Sc excreted in urine from the VD-overloaded rats were much less than those from the normal rats. The uptake of Be in almost all the tissues of the VD-overloaded rats was smaller than that of the normal ones. The excretion in feces may have been

increased by the VD-overloading, although the excretion was not measured in the present experiment. It is thought that the accumulation (and also toxicity) of Be was restrained by the excess VD. In various tissues of VD-overloaded rats, a remarkable increase in uptake of Sc was observed.

Calcium was not detected in the urine of the normal rats, which is explained by reabsorption of the element into the distal tubules of kidney. However, in the VD-overloaded rats, the excretion rate of Ca in urine at twelve hours after injection was as high as $9 \pm 2\%$. The Ca concentration was high in blood of the VD-overloaded rats. The excess Ca was not reabsorbed, but excreted into urine to keep the homeostasis of Ca concentration in blood. The only tissue in which Ca was detected was bone. In the bone, Ca exists as hydroxyapatite and is resorbed from the bone by parathyroid hormone and VD, and the uptake in the bone is promoted by calcitonin. The Ca concentration in the body is kept by the homeostasis. In the bone, the uptake of Ca decreased slightly in case of the VD-overloaded rats, which could be ascribed to the effects of VD on the promotion of osteoclast. The uptake of Be, Sr, and Ba by the VD-overloaded rats also decreased slightly. The metals belonging to alkaline earth elements behaved similarly to Ca.

In the intestine and testicles, the larger uptake of almost all the elements examined was found by the VD-overloaded rats. Although VD is known to enhance the absorption of Ca from small intestine, it was found in the present experiment that VD also raised the absorption of other cations. Testosterone is known to affect the absorption of divalent cations into testicles. The present results on the enhancement of the uptake in testicles of the VD-overloaded rats strongly support that VD increases the function of testosterone for the uptake of trace elements in the organ.

The distribution of all the elements was much larger in the skin of VD-overloaded rats than that of the normal ones. However, if the skin was washed with water, the difference in the distribution of each element was not remarkable; i.e., the distribution of each element in the skin of the VD-overloaded rats decreased by washing and it was found to be similar to that of the normal rats. This suggests that the excretion of trace elements into perspiration through sweat glands is more active in VD-overloaded rats.

The present study clearly demonstrates that VD also affects the metabolism of essential elements other than Ca and P.

Multitracer Study on Distribution of Trace Elements in Vitamin D Deficient Rats

R. Hirunuma, K. Endo, M. Yanaga, S. Enomoto, B. Liu, S. Ambe, and F. Ambe

Vitamin D (VD) behaves as a hormone of Ca control functioning to small intestine, bone, kidney and accessory thyroid gland. VD increases the ability of Ca absorption from the small intestine and Ca concentration in blood. VD has a wide effect on the metabolism of Ca in the body, while parathyroid hormone mainly controls Ca concentration in the body. The effects of VD on the metabolism of trace elements other than Ca and P have scarcely been studied. This report describes the application of the multitracer technique to the study of uptake and the distribution of various elements in VD-deficient rats. A similar study in VD-overloaded rats is described in a separate report.¹⁾

Preparation of the multitracer and injection of its saline solution to the rats were performed as described elsewhere.¹⁾ Vitamin D deficient rats were fed with mother rats, and the mother being fed with VD deficient diet after giving birth children. As a reference, three normal rats were used. Urine was collected at each twelve hours after injection. The rats were sacrificed on four days after injection and the radioactivities of tissues and body fluids were determined by γ -ray

spectrometry. Using the multitracer solution obtained from a Ge-target, the behavior of Be, V, Ca, Cr, Mn, Fe, Co, Zn, and As was examined.

In order to study the physiological condition of the rats fed with VD-deficient food, the concentration of alkaline phosphatase, acid phosphatase, and Ca in their plasma was examined. The concentration of alkaline and acid phosphatase was determined based on the Bessey-Lowry method. The values of the alkaline phosphatase for the normal and VD deficient rats were found to be 17 ± 1 Bessey-Lowry Unit (B-L U) and 32 ± 6 B-L U. There was little difference in the value of acid phosphatase between the normal and the VD deficient rats (the value of normal rats was 2.9 ± 0.2 B-L U and that of VD deficient rats was 3.1 ± 0.3 B-L U). The Ca concentration in plasma was determined based on the OCPC method, and found to be 9.2 ± 0.5 mg/dl (normal rats) and 5.7 ± 0.7 mg/dl (VD deficient rats). The high concentration of alkaline phosphatase and the low concentration of Ca for the VD deficient rats prove that they were really deficient with VD.

The amounts of various elements in excretion of the

Table 1. Excretion rate of various elements after 4 days from injection.

Elements	Urine (%)		Feces (%)	
	Normal rats	VD deficient rats	Normal rats	VD deficient rats
Be	23	25	7	7
V	29	32	11	10
Cr	42	49	8	9
Mn	0	0	24	28
Fe	0	0	8	6
Co	58	87	6	9
Zn	0.8	0.7	14	18
As	31	13	1.3	0.9

VD deficient rats after 4 days from injection are shown in Table 1. The result indicates that there was little difference in distribution for the excretion of the elements between the normal and the VD deficient rats in general. However, the amounts of As in urine of the VD deficient and normal rats were 13 and 31%, respectively, 4 days after injection. Arsenic was little excreted into feces of both groups of rats. The uptake of As in the VD deficient and the normal rats is shown in Fig. 1. The distribution of As in the blood of the VD deficient rats was estimated to be 9% dose/g whereas that to be 3.2% dose/g in the normal rats. Arsenic is bound to a globin part of hemoglobin in erythrocytes. It is thought that VD affects the behavior of As in the body.

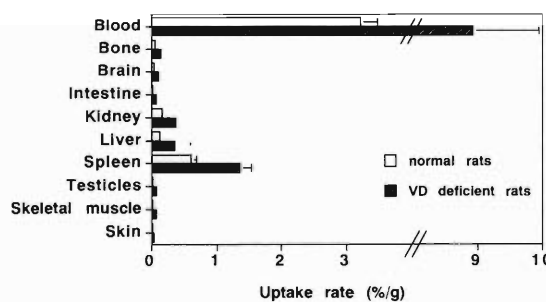


Fig. 1. Distribution of As in the VD deficient and normal rats on 4 days after injection.

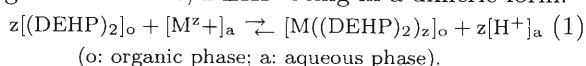
References

- 1) R. Hirunuma et al.: This report, p. 149.

Solvent Extraction Behavior of Multitracers by Di(2-ethylhexyl)phosphoric Acid

Y. Takahashi, Y. Minai, S. Ambe, H. Maeda, F. Ambe, and T. Tominaga

Di(2-ethylhexyl)phosphoric acid (DEHP) has been widely employed as a solvent extraction reagent, especially for selective extraction of lanthanides(III).¹⁻⁴ If the extraction mechanism by DEHP was understood, it could be used to determine stability constants of metal complexes.^{5,6} The extraction equilibrium of a z-valent metal ion (M^{z+}) in the aqueous phase, in general, can be given as follows, DEHP being in a dimeric form:⁴



The extraction constant (K_{ex}) is defined as

$$K_{ex} = ([M((DEHP)_2)_z]_o [H^+]_a^z) / ([M^{z+}]_a [(DEHP)_2]_o^z). \quad (2)$$

In this study, the multitracer technique was applied to reveal the extraction behavior of various metal ions under the identical experimental conditions.

Multitracers were prepared by irradiating Au and Ag targets with ¹²C or ¹⁴N ions in RIKEN Ring Cyclotron.^{7,8} The multitracer solutions were spiked into the mixture of a DEHP toluene solution and a HClO₄-NaClO₄ aqueous solution (I = 0.02). The concentration of (DEHP)₂ in toluene and pH varied from 0.5 to 0.01 M and from 0.8 to 2.5, respectively. After shaking, both phases were separated to record γ -ray spectra by a pure Ge detector. The photopeak intensities of radionuclides of elements including Be, Sc, V, Cr, Mn, Fe, Co, Zn, Ga, As, Se, Rb, Sr, Y, Zr, Tc, Ba, Ce, Eu, Gd, Tb, Tm, Yb, Lu, Hf, Re, Ir, and Pt were determined with a routine. The extraction coefficient D was obtained as the ratio of photopeak intensities of both phases after correction for the decay.

In Fig. 1 is shown the dependence of logD on pH and on log[(DEHP)₂], respectively, for some ions. Under the conditions we examined, As, Rb, Tc, and Re were never extracted, since Rb⁺ is an alkali metal ion and the others form oxoanions in the aqueous phase.

As for Be, Sc, V, Cr, Mn, Fe, Co, Zn, Ga, Sr, Y, Ba, Ce, Eu, Gd, Tb, Tm, Yb, and Lu, each logD was linearly related to pH and log[(DEHP)₂]. Since the

extraction of the tracers will not influence [(DEHP)₂]_o, this allows Eqn. (2) to be converted to

$$\log D = z \text{pH} + z \log[(DEHP)_2] + \log K_{ex}. \quad (3)$$

The slopes of logD against pH and log[(DEHP)₂] were identical to 2 for alkaline earth metals and 3 for rare earth elements, respectively, as expected from the relations shown in Eqn. (3). The slopes also indicated that Mn, Co, and Zn were divalent, while Cr, Fe, and Ga were trivalent under the condition examined. However, the slopes for V changed from 2 at about pH 1 to 1 at pH > 1.8, suggesting that VO²⁺ and VO₂⁺ were stable at the respective pH region.⁹ The logK_{ex} obtained by least squares fitting for Eqn. (3) were listed in Table 1. The values enable us to determine stability constants of the complexes with these ions by the solvent extraction method.¹⁰ Regarding rare earth elements and alkaline earth metals, logK_{ex} decreased with the increase in ionic radii. This demonstrates the higher stability of a DEHP complex of the smaller ion in the organic phase.

Table 1. Extraction constants (K_{ex}) for the elements studied.

Element	Charge	logK _{ex}	Element	Charge	logK _{ex}	Element	Charge	logK _{ex}
Be	2	1.1	Zn	2	-1.3	Eu	3	0.1
Sc	3	8.8	Ga	3	-0.8	Gd	3	0.3
Cr	3	-5.8	Sr	2	-4.5	Tb	3	0.7
Mn	2	-3.6	Y	3	1.6	Tm	3	2.0
Fe	3	3.2	Ba	2	-5.1	Yb	3	2.9
Co	2	-5.1	Ce	3	-1.5	Lu	3	3.1

The logD dependence on pH and on log[(DEHP)₂] for Zr, Hf, Se, Ir, and Pt was different from that expected from Eqn. (3). This indicates that species not shown in Eqn. (1) were formed for those elements in the solvent extraction system. For instance, most of Zr and Hf should have been hydrolyzed in the pH region we studied.⁹ Further studies are needed to understand the extraction behavior of those elements.

References

- 1) D. F. Peppard et al.: *J. Inorg. Nucl. Chem.*, **4**, 141 (1957).
- 2) K. Kimura: *Bull. Chem. Soc. Jpn.*, **33**, 1038 (1960).
- 3) K. Kimura: *ibid.*, **34**, 63 (1960).
- 4) C. F. Baes, Jr.: *J. Inorg. Nucl. Chem.*, **24**, 707 (1962).
- 5) P. M. Shanbhag et al.: *ibid.*, **43**, 3319 (1981).
- 6) Y. Takahashi et al.: *J. Radioanal. Nucl. Chem., Lett.*, **186**, 129 (1994).
- 7) S. Ambe et al.: *Chem. Lett.*, **1991**, 149.
- 8) S. Ambe et al.: *Anal. Sci.*, **7**, 317 (1991).
- 9) C. F. Baes et al.: *The Hydrolysis of Cations*, Krieger Rub. Com., Florida (1986).
- 10) Y. Takahashi et al.: This report, p. 152.

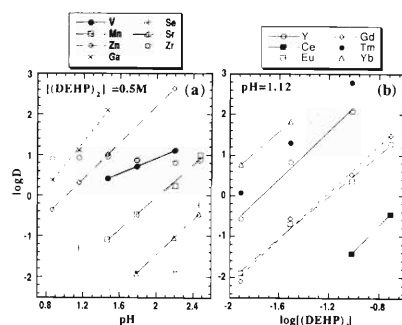


Fig. 1. Dependence of distribution coefficient D on pH (a) and log[(DEHP)₂] (b).

Multitracer Study on Stability Constants of Humate Complexes with Various Metal Ions

Y. Takahashi, Y. Minai, S. Ambe, H. Maeda, F. Ambe, and T. Tominaga

Humic acid is regarded as an important factor controlling the behavior of metal ions in natural aquifer system¹⁾ due to its high affinity with cations. Humic acid is a naturally-occurring polyacid having a variety of functional groups in a macromolecule.²⁾ The stability constants of humate complexes reported in literature scatter over a wide range, partly owing to the different experimental methods and complexation models employed in each work.³⁾ For the mutual comparison of stabilities of humate complexes with various metal ions, a particular method and model should be applied.

The multitracer technique has been applied to study the mutual differences in behavior of a number of elements. We can obtain information on the behavior of those elements under strictly identical experimental conditions. Employing the multitracer technique to obtain stability constants of humate complexes with various ions, we can eliminate any bias in the determination for their mutual comparisons.

Stability constants were determined by solvent extraction with di(2-ethylhexyl)phosphoric acid (DEHP) as an extractant.^{4,5)}

Stability constants (β) of the humate complexes with divalent and trivalent cations are shown in Fig. 1. As a whole, $\log\beta$ increased with increasing pH, or degree of the ionization of humic acid, since increased negative charge on the humic acid molecule with the increase in pH enhances the interaction between a metal ion and humic acid. The slope of $\log\beta$ of a divalent ion against pH was twice as that of pK_a , whereas the slope for a trivalent ion was three times larger than that of pK_a (Fig. 1). It has been reported that the electrostatic interaction dominates the metal-humate formation.⁶⁾ This implies that the increment of $\log\beta$ or pK_a with

increasing pH should be proportional to the charge of the cation, as observed. This also explains the higher stability of a humate complex with a trivalent ion than that with a divalent ion.

On the basis of the pH dependence, $\log\beta$ at neutral pH as in natural water was estimated by extrapolation. Assuming the concentration of humic acid,⁴⁾ the estimated $\log\beta$ values give proportions of the humate species relative to free ions in the natural water system (Table 1). The proportions of carbonate and hydroxide complexes were also calculated (Table 1). Based on such a speciation calculation, the humate complexes are considered to be predominant in dissolved species of rare earth elements in a natural aquifer system at neutral pH. It is notable that a significant fraction of alkaline earth metals can be dissolved as humate complexes, whereas carbonates are dominant as dissolved species of divalent transition metal ions such as Mn, Co, and Zn. About Fe and Ga, hydrolyzed species dominate their dissolved species in the solution system.

Table 1. Ratios of concentration of dissolved complex (ML) to free ion (M) in a land water system at pH = 0.02 and I = 0.02 ([L]: concentration of ligands in land water; $\log\beta$ (HA, pH = 7): estimated stability constant of humate at pH = 7; hydrolysis constants and stability constants of carbonates in literature⁷⁾ were employed in the calculation).

Ligand	[L](M)	$\log([ML]/[M])$										
		Be	Sr	Ba	Mn	Co	Zn	Cr	Fe	Ga	Sc	Ln
CO ₃ ²⁻	5E-7		-3.5	-3.5	0.5	0.5	0.5					-0.8
OH, i=1 ^f	1E-7	1.6	-6.2	-6.4	-3.6	-2.7	-2.0	3.5	4.8	4.4	2.7	-1.5
OH, i=2 ^f	1E-7	0.4				-5.6	-2.9		8.3	8.1	4.3	-14.0
OH, i=3 ^f	1E-7	-2.2				-11.3	-7.4		9.0	10.7	4.9	-21.0
OH, i=4 ^f	1E-7								6.4	11.4	2.0	-28.0
HA	1E-7(eq/l)	5.0	-0.5	-0.5	-0.5	-1.0	-1.5	5.0	11.0	10.0	16.0	6.0
$\log\beta$ (HA, pH=7)		12	6.5	6.5	6.5	6	5.5	12	18	17	23	13

^fOrder of hydrolysis.

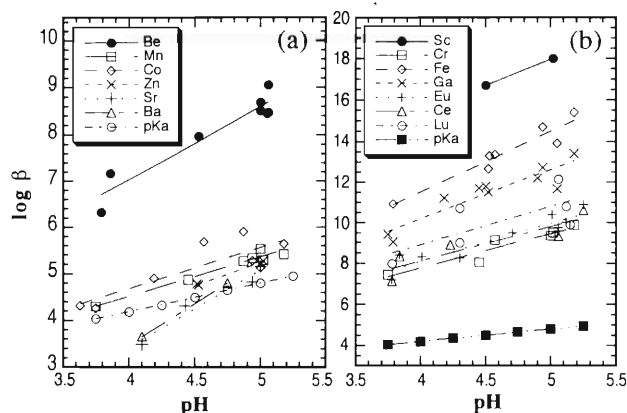


Fig. 1. The pH dependences of pK_a of humic acid and stability constants of humate complexes with divalent ions (a) and trivalent (b) ($C_s = 0.02$).

References

- 1) W. Stumm et al.: Aquatic Chemistry, Wiley, New York (1981).
- 2) F. J. Stevenson: Humus Chemistry, J. Wiley and Sons, New York (1982).
- 3) Y. Minai et al.: Proc. 3rd Int. Symp. Adv. Nucl. Ener. Res., p. 521 (1991).
- 4) R. A. Torres et al.: *Radiochim. Acta*, **35**, 143 (1984).
- 5) Y. Takahashi et al.: This report, p. 151.
- 6) T. Miyajima: Ion Exchange and Solvent Extraction, Marcel Dekker, Inc., Chap. 12 (1995).
- 7) A. E. Martell et al.: Critical Stability Constants, Plenum Press, New York (1982).

Metabolism of Various Trace Elements in LEC Rats Leading to Acute Hepatitis

M. Yanaga, S. Enomoto, R. Hirunuma, B. Liu, K. Endo, S. Ambe, M. Tozawa,*
H. Nakahara, and F. Ambe

Previously, we reported that the multitracer technique has excellent reliability and versatility for a comparative study of the uptake and distribution of many different elements in rats.^{1,2)} In the present work, this technique was applied to an investigation of the uptake and distribution of trace elements in LEC (Long-Evans Cinnamon) rats. The LEC rat is one of the two inbred strains selected by coat colour which were isolated from a closed colony of Long-Evans rats at the Center for Experimental Plants and Animals, Hokkaido University.³⁾ The rat spontaneously develops fulminant hepatitis and severe jaundice at 4–6 months of age and finally develops hepatocellular carcinoma from 12 to 18 months after birth.⁴⁾

A physiological saline solution of multitracer was obtained from a silver target irradiated with a ¹⁴N-ion beam accelerated by the RIKEN Ring Cyclotron. The solution was injected intravenously to five 16-week-old male LEC rats and three 16-week-old male SD rats. Two days after injection, the rats were sacrificed and 8 organs and tissues besides blood corpuscles and plasma were removed. They were brain, liver, kidney, spleen, stomach and intestine, skeletal muscle, testis and bone. The organs and tissues were placed in polyethylene bottles and weighed, and subjected to γ -ray spectrometry using pure Ge detectors. Identification and determination of nuclides were done on the basis of their energies, half-lives and peak areas.

Figures 1 and 2 show uptake of various trace elements in liver and kidney, respectively. As shown in Fig. 1, uptakes of Sc, Mn, Fe and Zn in the liver of LEC rats were much larger than those of SD rats. Although weight of LEC rats and SD rats used in this study was 195–270 g and 470–560 g, respectively, the difference of uptake percent per unit weight of these elements

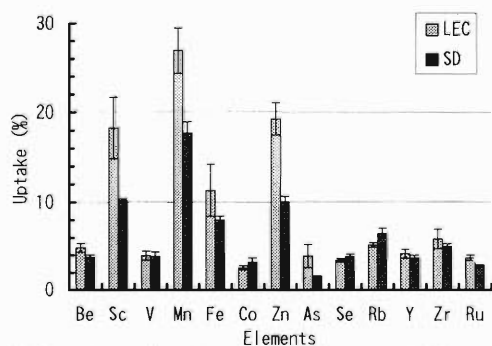


Fig. 1. Uptakes of various trace elements in liver of LEC and SD rats.

between LEC rats and SD rats was larger than the difference of weight of rats. Copper was not detected in the multitracer solution used in this experiment, although it is well known that abnormal accumulation of copper is found in the liver of LEC rats and this causes the acute hepatitis and hepatoma.⁵⁾ However, a possibility of abnormal metabolism of Sc and Mn in the stage examined was first found in the present work. It seems that the trends of Fe and Zn are in agreement with the results of PIXE analysis by Matsuda et al.⁶⁾ They reported that Zn and Fe contents in LEC liver had been very high compared with those in SD liver. Cobalt, Zn, Se and Y were highly accumulated in the kidney of LEC rats as shown in Fig. 2, although no abnormal accumulation of Sc and Mn in kidney was observed in contrast to the case of liver. Iron in kidney was not determined because of its weak radioactivity.

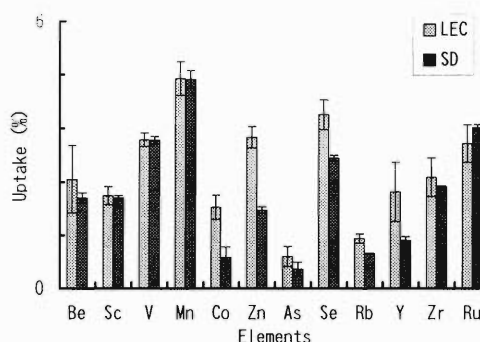


Fig. 2. Uptakes of various trace elements in kidney of LEC and SD rats.

Severe jaundice was observed for two of five LEC rats used, which means that the two LEC rats had developed acute hepatitis at that time. Suzuki et al. reported that Zn content in LEC liver decreased suddenly and Fe content increased following acute hepatitis.⁷⁾ Although this trend was not observed in the present tracer experiment, the abnormal metabolism of several elements was found in this work. Further work is planned to elucidate the behaviour of trace elements in LEC rats.

References

- 1) M. Yanaga et al.: *Appl. Radiat. Isot.*, in press.
- 2) S. Enomoto et al.: *J. Radioanal. Nucl. Chem.*, in press.
- 3) M. Sasaki et al.: *Rat News Lett.*, **14**, 4 (1985).
- 4) N. Takeichi: *CRJ Lett.*, **4**, 1 (1991).
- 5) Y. Li et al.: *J. Clin. Invest.*, **87**, 1858 (1991).
- 6) K. Matsuda et al.: *NMCC Ann. Rep.*, **1**, 94 (1993).
- 7) K. Suzuki et al.: *Toxicology*, **97**, 81 (1995).

* Department of Chemistry, The Jikei University School of Medicine

Studies on the Ion Exchange Adsorption Behavior of Strongly Acidic Resin Nafion and Its Application to Analytical Chemistry

A. Sekiguchi, N. Ito, N. Furusato, Y. Saito, K. Kimura, H. Maeda, S. Ambe, and F. Ambe

Radioactive multitracer solutions in a carrier and salt-free state, prepared from a gold foil irradiated with a ^{14}N beam of $135\text{ MeV/nucleon}^{1-5}$ were used for the titled study in a Nafion-HBr system after being converted to a hydrobromic acid solution. The Nafion-501 resin, manufactured by DuPont, is a perfluorinated polymer containing $\sim 5\text{ mmol/g}$ sulfonic acid groups. Because of the strong acidity of the resin, a comparison of its exchange behavior with that of common cation exchange resins attracts much attention.

The resin, commercially available as a cylindrical shape of ca. $1\text{ mm}\phi \times 3\text{ mm}$, was crushed with a stamp mill at liquid nitrogen temperature, passed through a 50–120 mesh screen, and used. Into a small polyethylene bottle, 0.1 ml of the multitracer solution and 2.4 g of the resin were introduced, and the acidity of the system was adjusted to 0.1, 0.3, 0.5, 1, 3, 5, and 8 M with hydrobromic acid and distilled water, thereby making the volume of the solution to 10 ml. The contents of the bottle were shaken vigorously at $25\text{ }^\circ\text{C}$ with an 8-mode shaker. Time of shaking was 75 hours. After filtration, γ -ray spectrometry was carried out for both phases.

The distribution ratios (D_v) of alkali metals, alkaline earth metals and rare earth elements were obtained (Fig. 1a). The ratios decrease as hydrobromic acid concentrations (C) increase and slopes on $\log D_v$ - $\log C$ plots increase with the valence number of cations. The behavior described above is the characteristic of the ion exchange resins. The ion exchange behavior of platinum group metals (Ru, Pt, and Ir) for HBr medium is somewhat different from that for HCl medium studied previously. In the case of the HCl medium, the slopes on $\log D_v$ - $\log C$ plots were flat. For the HBr medium, Ru and Ir showed the slopes of -2 and -1 , respectively, but Pt did not, as indicated in Fig. 1b.

Further, ion exchange separation using a Nafion resin column was carried out with 0.1 M HCl, and 0.3 and 0.5 M HBr eluents. Platinum group metals (Ru, Rh) were first eluted by 0.1 M hydrochloric acid without adsorption, corresponding to their lower D_v values. Alkaline earth and transition metals were eluted by 0.3 M hydrobromic acid and finally rare earth elements

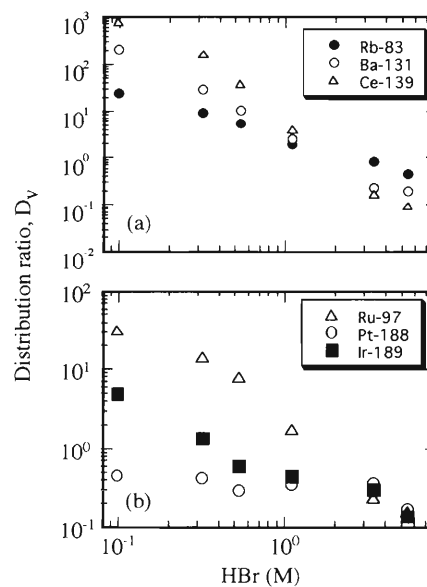


Fig. 1. Relationship between distribution ratios and hydrobromic acid concentrations.

were eluted by 0.5 M hydrobromic acid, according to the order of their D_v values.

References

- 1) S. Ambe, S. Y. Chen, Y. Ohkubo, Y. Kobayashi, M. Iwamoto, M. Yanokura, and F. Ambe: *RIKEN Accel. Prog. Rep.*, **25**, 95 (1991).
- 2) S. Ambe, S. Y. Chen, Y. Ohkubo, Y. Kobayashi, M. Iwamoto, M. Yanokura, and F. Ambe: *Anal. Sci.*, **7**, Suppl., 317 (1991).
- 3) S. Ambe, S. Y. Chen, Y. Ohkubo, Y. Kobayashi, M. Iwamoto, and F. Ambe: *RIKEN Accel. Prog. Rep.*, **24**, 73 (1990).
- 4) S. Ambe, S. Y. Chen, Y. Ohkubo, Y. Kobayashi, M. Iwamoto, M. Yanokura, and F. Ambe: *Chem. Lett.*, **1991**, 149.
- 5) T. Bamba, H. Harakawa, Y. Saito, K. Kimura, T. Yaita, S. Shibata, S. Ambe, Y. Ohkubo, M. Iwamoto, Y. Kobayashi, M. Yanokura, H. Maeda, and F. Ambe: *RIKEN Accel. Prog. Rep.*, **26**, 88 (1992).

Uptake Behavior of Multitracers in LEC Rats before Jaundice Development

S. Oishi,* R. Amano, A. Ando,* K. Ishimoto,* M. Naruse,* S. Enomoto, and F. Ambe

Unusual Cu accumulation in the liver of LEC (Long Evans Cinnamon) rats has been known to be involved in the development of jaundice, hepatic injury and hepatocellular carcinoma. Recently, the biodistribution of other essential trace elements (V, Cr, Mn, Fe, Co, Zn and Se) in the LEC rats has been of interest to get an insight into the pathogenesis of the disease. In this work, we are studying the uptake behavior of Sc, V, Mn, Zn, Se and Rb radioisotopes in the LEC rats before jaundice development by the use of radioactive multitracer technique, which was developed at RIKEN.

Male LEC rats at different ages (4, 7 and 11 weeks after birth) were purchased from Charles River Japan Inc. The LEC rats were then housed in plastic and steel cages in Laboratory for Experimental Animals, Kanazawa University, fed a standard laboratory diet and had free access to drinking water during 1 week prior to administration. Five LEC rats were used in each different age.

A no-carrier-added radioactive multitracer solution was obtained from an Ag (purity: more than 99.99%) target irradiated with 135 MeV/nucleon N-14 beam accelerated in RIKEN Ring Cyclotron. The preparation for a multitracer solution from the Ag target was carried out in Radioisotope Center, Kanazawa University, according to the method of Ambe et al.¹⁻³⁾ More than 35 radioisotopes of 19 elements (Be, Na, Sc, V, Mn, Fe, Co, Zn, Ga, As, Se, Rb, Sr, Y, Zr, Tc, Ru, Rh and Pd) can be observed in the solution for injection. Among these radioisotopes, 16 nuclides of 13 elements could be used as the tracers in the LEC rat experiments.

An appropriate amount of the final radioactive multitracer solution was intraperitoneally injected into the LEC rats. At 48 hr after injection of a radioactive multitracer solution, the LEC rats were killed under ether anesthesia. After this, brain, pectrales, cardiac muscle, lung, liver, spleen, pancreas, kidney and thymus were excised. These tissues were weighed immediately and freeze-dried. The dried samples were measured by gamma-ray spectrometry with pure Ge semi-conductor detectors against an appropriate standard to obtain the percentage of injected dose per gram of tissue (% dose/g) for different tracers.

In this work, no significant age-dependent changes in Rb uptake rates were observed in several tissues of LEC rats. In general, Rb is thought to be analogous to potassium and Rb tracer can penetrate membranes via potassium ion channels and pump to reach all regions as a substitute for the similar K ion. It is reasonable

to assume that no unusual behavior of endogenous K ions can be observed in the various organs in LEC rats before jaundice development.

Uptake behavior of Sc, V, Mn, Zn and Se was evaluated as the ratio of Sc/Rb, V/Rb, Mn/Rb, Zn/Rb and Se/Rb, respectively. Figure 1(a) compares easily their uptake behavior in the liver of LEC rats at 5, 8 and 11 weeks of age. No change in the ratios of V/Rb and Se/Rb was observed. On the other hand, the ratios of Mn/Rb and Zn/Rb increased and that of Sc/Rb decreased with aging before jaundice development of LEC rats. Recently, Sakurai et al. described that the unusual Cu accumulation was associated with the induction of metallothionein in the liver of the LEC rats rather than that of superoxide dismutase.^{4,5)} In Fig. 1(a), the age-dependent uptake of Zn is due to the corporation of Zn into metallothionein induced by endogenous excess Cu in the liver of LEC rats.

Figure 1(b) compares the uptake behavior of Sc, V, Mn, Zn and Se in the kidney of LEC rats at 5, 8 and 11 weeks of age before jaundice development. No significant change in the ratios of Sc/Rb and Mn/Rb was observed in the kidney of LEC rats. On the other hand, the ratios of V/Rb, Zn/Rb and Se/Rb increased with aging. Especially at 11 weeks old just before jaundice development of the LEC rats, the uptake behavior of Se-75 tracer was characteristic in the kidney. We think that Se may play a role in the excess Cu detoxification function. Further study is required to discuss the Se function in vivo in detail.

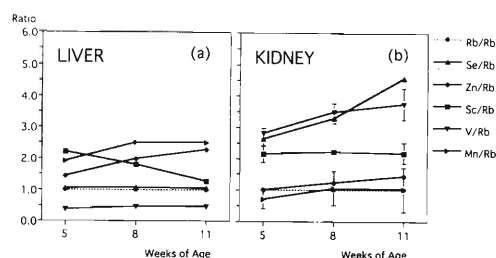


Fig. 1. Comparison of the uptake behavior of Sc, V, Mn, Zn, and Se in the liver (a) and in the kidney (b) of LEC rats at different age before jaundice development.

References

- 1) S. Ambe et al.: *Chem. Lett.*, **1991**, 149.
- 2) S. Ambe et al.: *Anal. Sci.*, **7**, Suppl., 317 (1991).
- 3) S. Ambe et al.: *J. Radioanal. Nucl. Chem.*, **195**, 297 (1995).
- 4) H. Sakurai et al.: *Biochem. Biophys. Res. Commun.*, **184**, 1393 (1992).
- 5) H. Sakurai et al.: *ibid.*, **185**, 548 (1992).

* School of Health Sciences, Faculty of Medicine, Kanazawa University

Biodistribution of Multitracers in Normal, Al-Overloaded and Cd-Overloaded Mice

R. Amano, S. Oishi,* M. Ihyou,* A. Kakunaga,* Y. Yoshida,* T. Ishizaki,* T. Suzuki,* S. Enomoto, and F. Ambe

Radioactive multitracer technique was applied to the simultaneous evaluation of biobehavior of many trace elements in normal, Al-overloaded and Cd-overloaded mice. Their tissue and subcellular distributions were examined in brain, cardiac muscle, lung, liver, spleen, pancreas, kidney and skeletal muscle by using a radioactive multitracer solution,¹⁻³⁾ which was prepared from an Ag target irradiated with 135 MeV/nucleon ¹⁴N beam accelerated in RIKEN Ring Cyclotron.

Male ddY mice weighing 20–30 g were used. Physiological saline solutions, Al³⁺ (1 mg Al/ml) and Cd²⁺ (0.5 mg Cd/ml) solutions were injected intraperitoneally (5 ml/kg) into three groups of mice, namely, the control group, Al-overloaded group and Cd-overloaded group, respectively. At 1 hr for Al-overloaded group, and at 3 hr for Cd-overloaded group after injection of the Al³⁺ or Cd²⁺ solution, 0.2 ml of the radioactive multitracer solution was intraperitoneally injected. At 48 hr after injection of the multitracers, the mice were sacrificed under ether anesthesia and the 8 tissues were excised, weighed and freeze-dried. The subcellular distribution for several tissues was determined according to the modified method of Hogeboom and Schneider. Radioactivities were measured using Ge γ -ray spectrometry.

Figure 1 compares the uptake rates of Sc, V, Mn, Co, Zn, Se, Rb, Y, Zr and Rh in liver at 48 hr after injection among the control, Al-overloaded and Cd-overloaded mice. The values of Sc, Y and Zr of Al-overloaded mice were substantially larger than those of control and Cd-overloaded mice. The values of Se and Zn of Cd-overloaded mice were slightly larger than those of control and Al-overloaded mice. Figure 2 shows the changes of subcellular distributions of a Y tracer (A) and a Zn tracer (B) in liver between control mice and

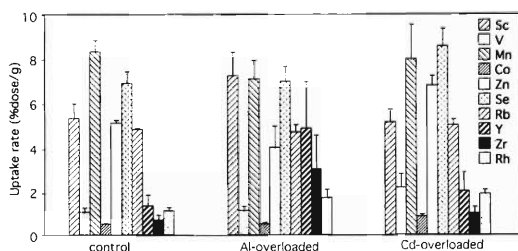


Fig. 1. Uptake rates of Sc, V, Mn, Co, Zn, Se, Rb, Y, Zr and Rh in liver at 48 hr after injection in control, Al-overloaded and Cd-overloaded mice.

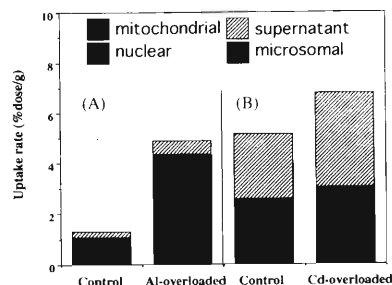


Fig. 2. Comparison of tissue and subcellular distributions in liver between control and metal-overloaded mice. (A): The change of subcellular percentages of Y tracer by Al-treatment; (B): The change of subcellular percentages of Zn tracer by Cd-treatment.

metal (Al or Cd)-overloaded mice. The uptake rate of the Y tracer in the mitochondrial fraction increased significantly by the Al-overloading treatment. The uptake rate of Zn tracer in the supernatant fraction increased slightly by the Cd-overloading treatment.

Al-induced synergistic interactions were significantly observed in the uptake rates of Sc, Y, and Zr tracers in liver. These tracers are known to be localized in the mitochondrial (containing lysosome) fraction.⁴⁾ In addition, the liver uptake of these tracers was increased in the mitochondrial fraction by the Al injection. A large amount of Al was also accumulated in the mitochondrial fraction of liver. Therefore, mitochondria and/or lysosomes play an important role in the accumulation of Sc, Y, and Zr tracers and the Al-induced co-uptake effects in liver. On the other hand, Cd-induced interactions were slightly observed in the liver uptake of Zn and Se tracers. These tracers are known to exist in the supernatant fraction mentioned above. Their liver uptakes in the supernatant fraction were considerably increased by the Cd treatment. The Cd-induced synergistic effect of Zn tracer can be explained as follows: metallothionein is freshly induced into the supernatant fluid and the content of metallothionein is increased there by the Cd-treatment, and then Zn tracer incorporated into cell encounters the metallothionein with high probability and is bound to the metallothionein.

References

- 1) S. Ambe et al.: *Chem. Lett.*, **1991**, 149.
- 2) S. Ambe et al.: *Anal. Sci.*, **7**, Suppl., p. 317 (1991).
- 3) S. Ambe et al.: *J. Radioanal. Nucl. Chem.*, **195**, 297 (1995).
- 4) A. Ando and I. Ando: *Appl. Radiat. Isot.*, **41**, 327 (1990).

* School of Health Sciences, Faculty of Medicine, Kanazawa University

Creating a New Design System Using a Cooled CCD Camera Multi Spectrum Imager

Y. Okamoto, Y. Miyagi-Okamoto,* S. Enomoto, and F. Ambe

The accelerator can produce many types of radioisotopes. In their application to biology, a method to analyze their density and distributions is essential. In the multitracer technique developed at RIKEN, a number of radioactive isotopes are simultaneously used to trace different elements.¹⁾ We design a new type of gamma camera called Multi Spectrum Imager (MSI). It has a new function to capture many types of radiation and also visual light. Combination and comparison data of the MSI and metabolic behavior of various elements revealed using the multitracer technique will enable us to determine the localization of various elements and the time dependent metabolism on various tissues of animals and plants.^{2,3)}

Figure 1 shows a diagram of the MSI. The object is located in front of a fluorescence screen and the CCD camera is at the back of the screen. The space from the screen to the camera is surrounded by lead blocks and its interior darkened. The camera is connected to a computer. The image data is downloaded to the computer and is analyzed by NIH Image 1.54 software. The camera catches the light from the fluorescence screen stimulated by the radiation energy. The camera also catches the visual light. The CCD camera that we use is a cooled type different from the conventional ones. It has an excellent S/N ratio and low dark current.⁴⁾ Using this character, the camera detects very weak light from the screen. Inserting different types of screens between the object and the camera, the system can be applied as a sensor yielding different spectra.

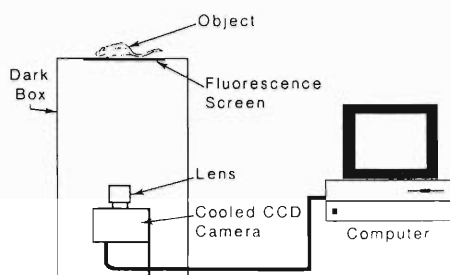


Fig. 1. System diagram of MSI.

The stepsamples were made from 4 mm ϕ paper disks and an Na^{99m}TcO₄ solution. Zero, 1, 2, 3, and 4 μ l of the solution were dropped onto each of the disks. Images of these disks were taken using both the MSI and BAS2000 (made by Fuji Photo Film Co., Ltd.). The ^{99m}Tc-MDP solution was also injected into a rat and the distribution image of this isotope was taken.^{5,6)}

Figure 2 shows ^{99m}Tc-grayscale for (a) MSI and

(b) BAS2000. For the γ ray, the MSI had the same sensitivity as the BAS2000, and the linearity was excellent. The visual-light image was only taken by the MSI. X-ray image was superimposed onto the γ -ray image easily (Fig. 3). All types of light and radiation passed through the MSI in the same light path.

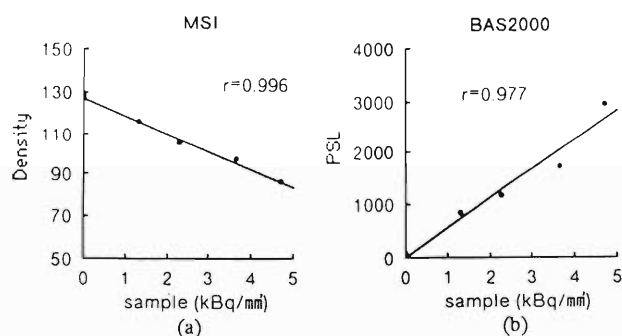


Fig. 2. (a) ^{99m}Tc-Grayscale (MSI), (b) ^{99m}Tc-Grayscale (BAS2000).

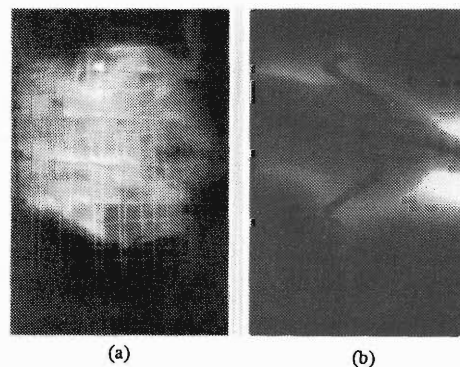


Fig. 3. (a) Visual-light image (MSI), (b) Superimposed image (γ ray and visual light).

We are planning the following four more experiments. First, we must find a suitable fluorescence screen for γ rays. Second, we will try to develop a screen the β ray. Third, we will combine a high pure germanium γ -ray spectrometer with MSI. And finally, we believe that this system can be applied to autoradiography and chromatography.

References

- 1) F. Ambe: *RIKEN Rev.*, No. 4, p. 31 (1994).
- 2) S. Ambe et al.: *J. Radioanal. Nucl. Chem.*, **195**, 305 (1995).
- 3) Y. Okamoto: *Oral. Surg. Oral. Med. Oral. Pathol. Oral. Radiol. Endod.*, **80**, 115 (1995).
- 4) Technical Manual of Astromed CCD Camera.
- 5) BAS2000 Technical Manual, p. 48.
- 6) Imager 2 Functional Index (1995).

* Kanagawa Dental College, Department of Oral and Maxillofacial Radiology

TDPAC of ^{99}Ru Arising from ^{99}Rh in $\alpha\text{-Fe}_2\text{O}_3$ and EuFeO_3

Y. Ohkubo, Y. Kobayashi, Y. Yanagida, T. Okada, K. Asai, and F. Ambe

Previously, we incorporated ^{99}Rh ions into Fe_3O_4 and measured the hyperfine magnetic fields H_{hf} at ^{99}Ru arising from ^{99}Rh by means of TDPAC and emission Mössbauer spectroscopy.¹⁾ The temperature dependence of H_{hf} and the isomer shift imply that the Ru ion exists as a mixed state of Ru^{2+} and Ru^{3+} and that the unpaired $4d$ electron of the Ru^{3+} ion itself contributes to H_{hf} in addition to the A - O - B supertransfer interaction. Several years ago, we also measured the hyperfine fields at ^{99}Ru in $\alpha\text{-Fe}_2\text{O}_3$ using the same techniques.²⁾ The isomer shift indicates that the Ru ion exists as Ru^{3+} . Figure 1 shows the temperature dependence of H_{hf} at ^{99}Ru in $\alpha\text{-Fe}_2\text{O}_3$ tentatively deduced from the frequency distributions of the TDPAC spectra. A comparison of it with that for ^{111}Cd in $\alpha\text{-Fe}_2\text{O}_3$ ³⁾ suggests that besides the supertransfer interaction, the magnetic moment of the Ru^{3+} ion also contributes to H_{hf} . However, the implied temperature dependence of the latter contribution is different from that for Fe_3O_4 . The H_{hf} produced by the Ru^{3+} ion in Fe_3O_4 is a monotonically decreasing function of the temperature, whereas that in $\alpha\text{-Fe}_2\text{O}_3$ seems to be most significant at about 200 K. This time, we measured the hyperfine field at ^{99}Ru in EuFeO_3 using TDPAC and report the results. EuFeO_3 takes the perovskite structure and is an antiferromagnet with $T_N = 662$ K.⁴⁾

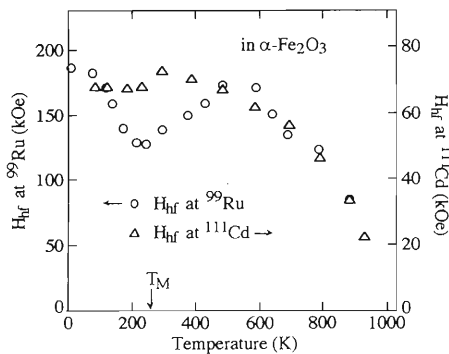


Fig. 1. Temperature dependence of the hyperfine magnetic field H_{hf} at ^{99}Ru ($\leftarrow^{99}\text{Rh}$) in $\alpha\text{-Fe}_2\text{O}_3$. Temperature dependence of H_{hf} at ^{111}Cd ($\leftarrow^{111}\text{In}$) in $\alpha\text{-Fe}_2\text{O}_3$ (Ref. 3) is also shown for comparison. T_M is the Morin temperature.

Isotopically enriched ^{99}Ru metal powder was irradiated with 13-MeV protons available from the RIKEN AVF cyclotron. The (p, n) reaction produces ^{99}Rh from ^{99}Ru . The irradiated ^{99}Ru powder was treated according to the chemical procedure described in Ref. 1 and $\alpha\text{-Fe}_2\text{O}_3(^{99}\text{Rh})$ was thereby obtained. Stoichiometric amounts of high-purity powder of Eu_2O_3 and

dried $\alpha\text{-Fe}_2\text{O}_3(^{99}\text{Rh})$ were milled and heated at 1300 °C for 5 h in air. The mixture was pressed into a pellet and heated at 1300 °C for 24 h in air to obtain $\text{EuFeO}_3(^{99}\text{Rh})$.⁴⁾

Figure 2 shows the measured TDPAC spectra of ^{99}Ru in EuFeO_3 and their corresponding frequency distributions. We see at 80 and 293 K two peaks, labeled **1** and **2**, due to hyperfine magnetic interactions: Peak **1** corresponds to the Larmor frequency ω_L and peak **2** to $2\omega_L$. Thus, there is a hyperfine magnetic field at ^{99}Ru . However, there is also a large broad peak, located below ω_L , hiding peak **1** at 376 K. We have not yet identified the origin of this peak. The peak seen at 717 K ($> T_N$) is due to a quadrupole interaction and is considered to be different from the unidentified one. Careful analysis of the TDPAC spectra for EuFeO_3 as well as for $\alpha\text{-Fe}_2\text{O}_3$ is in progress using a fitting program code written on visual basic.

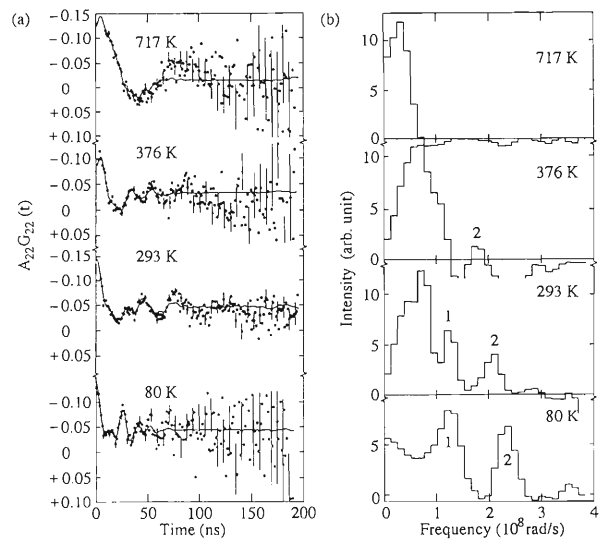


Fig. 2. (a) TDPAC spectra $A_{22}G_{22}(t)$ of ^{99}Ru ($\leftarrow^{99}\text{Rh}$) in EuFeO_3 measured at 80, 293, 376, and 717 K, and (b) their frequency distributions. The solid curves in (a) represent the time spectra reproduced from the frequency distributions in (b). Peaks **1** and **2** in part b correspond to the Larmor frequency ω_L and $2\omega_L$.

References

- 1) Y. Ohkubo, Y. Kobayashi, K. Asai, T. Okada, and F. Ambe: *Phys. Rev.*, **B47**, 11954 (1993).
- 2) Y. Ohkubo and F. Ambe: *RIKEN Accel. Prog. Rep.*, **23**, 75 (1989).
- 3) K. Asai, F. Ambe, S. Ambe, T. Okada, and H. Sekizawa: *Phys. Rev.*, **B41**, 6124 (1990).
- 4) C. Boekema, F. van der Woude, and G. A. Sawatzky: *Int. J. Magnetism*, **3**, 341 (1972).

Extraction of an Intense Slow Positron Beam Using He^{++} Beams from the AVF Cyclotron

Y. Itoh, K. Lee, A. Goto, N. Nakanishi, M. Kase, and Y. Ito

Until the last year we had been trying to extract slow positron beams by bombarding BN, Al, and Ni targets with p^+ beams, and bombarding Si_3N_4 , C, and SiO_2 targets with d^+ beams from the AVF cyclotron. The intensity of the extracted slow positron beam was very close to the values estimated from the known data of excitation functions of the nuclear reactions and of positron energies emitted from the produced nuclides, and from reasonable assumptions on the moderation efficiency, geometrical efficiency, and so on. The results show that about $(1\sim 1.5) \times 10^4$ slow positrons/sec can be extracted per μA of p^+ or d^+ . Comparing this value with the theoretical estimate, the intensity is expected to be increased by a factor of up to 5 by the improvement of geometries and moderator efficiency, but an increase by an order of magnitude is inaccessible.

With the hope for a still more intense slow positron beam we have searched for further possible targets that produce positron emitters by irradiation with He^{++} . As the candidate targets we selected Ni, Al, and Si, and the slow positron beam intensity was estimated theoretically and experimentally. For the theoretical estimation we used the ALICE program to obtain excitation functions, and the TRIM program to obtain depth-energy relationships. Other parameters necessary for the theoretical estimate, such as the branching ratio for positron emission per disintegration of the positron emitter, the maximum energy of positrons, and the absorption coefficient of positrons, were derived from a handbook. The conversion efficiency of the W moderator is taken to be 1×10^{-4} . Two different geometries have been considered (see Table 1).

Table 1. Various targets for slow positron beam.

Target (Thickness/ μm)	Nuclear Reaction	σ_{max} mb (MeV)	Calculated Slow e^+ ($10^4/\text{sec}/\mu\text{A}$)		Ratio of Transmission to Reflection	Measured Slow e^+ ($10^4/\text{sec}/\mu\text{A}$)
			Transmission	Reflection		
Ni (200)	$^{58}\text{Ni}(\alpha, \text{pn})^{60}\text{Cu}$	586 (27.0)	5.86	1.81	3.24	1.30
	$^{60}\text{Ni}(\alpha, \text{pn})^{62}\text{Cu}$	786 (29.0)				
Al (550)	$^{27}\text{Al}(\alpha, \text{n})^{30}\text{P}$	619 (11.0)	7.56	1.69	4.47	1.19
	$^{27}\text{Al}(\alpha, \alpha\text{n})^{26}\text{Al}$	177 (32.0)				
Si (600)	$^{28}\text{Si}(\alpha, \text{n})^{31}\text{S}$	117 (18.0)	9.41	2.40	3.92	(0.493)
	$^{28}\text{Si}(\alpha, \text{pn})^{30}\text{P}$	547 (28.0)				

In the reflection geometry, slow positrons are extracted at 30 degrees backward to the incident He^{++} beam, while in the transmission geometry slow positrons are extracted in the same direction as the incident He^{++} beam. In the latter geometry, the purely geometrical efficiency is larger by a factor of about 5, but the absorption of fast positrons in the target material is a little larger. The ratio of extraction efficiency is 2–5 as shown in the next-to-last column in the Table. Experiments were performed in the transmission ge-

ometry, and the results were $(1.2 \sim 1.3) \times 10^4$ slow positrons/sec/ μA of He^{++} . This agrees in the order of magnitude with the theoretical estimate. For Si the experimental results were far smaller than the theoretical estimate. This small intensity was caused by an accidental break of the Si target ($0.3 \mu\text{m} \times 2$) during the He^{++} beam irradiation. Since the Si target is expected to give the largest intensity of slow positrons, it is necessary to repeat the measurements.

Resistivity Dependence of Positron/Positronium Annihilation in Porous Silicon

Y. Itoh, H. Murakami, and A. Kinoshita*

The porous Si layer formed by anodization of single crystalline Si (c-Si) in HF solution contains a great amount of micro- and nano-meter pores. The positron/positronium annihilation method is a very useful tool for investigating the fundamental properties of porous silicon since positronium is formed at a relatively high rate in porous silicon.¹⁾ The interaction between positrons and electrons confined in surface layers should be an interesting subject for the application of positron annihilation, and for clarifying the property of electrons confined in the Si surface layers.

Two boron-doped silicon wafers (diameter = 76 mm, thickness = 400 μm) with the different resistivities of 1 (sample A) or 0.01 (sample B) $\Omega\cdot\text{cm}$, were used as starting materials. Aluminum was deposited on one side of the wafer surfaces (100), and annealed at 833 K for 15 min by current heating. The aluminum ohmic electrode was uniformly pressed onto a positive copper plate electrode mounted on a sample holder, and was set opposite to a platinum electrode in an anodization bath. The silicon wafer was anodized in HF solution of 55 wt.% under d.c. current density of 52 mA/cm^2 . The temperature fluctuation throughout the anodization was controlled within 3 K.

It is confirmed experimentally that the number density of pores on the anodized surface, n_p , is equal to the two-thirds power of their bulk concentration n_B in the starting materials.²⁾ The porosity P is obtained from weight loss Δw of the samples by anodization, and from the wafer thickness t as $P = \Delta w / (s \cdot t \cdot \sigma_{\text{Si}})$, where s is the anodization area and σ_{Si} is the density of bulk crystalline Si, 2.34 $\text{g}\cdot\text{cm}^{-3}$. If we assume that cylindrically shaped pores are oriented perpendicularly to the sample surface and penetrate the anodized layer, the pore diameter d is given by $2(P/\pi n_B^{2/3})^{1/2}$, and the internal surface area S per cm^3 is $\pi d n_B^{2/3}$. These quantities are listed in Table 1, where it is seen that

Table 1. Characteristics of porous silicon A and B.

Sample	A	B
Boron concentration [cm^{-3}] in starting bulk Si	1×10^{16}	6×10^{18}
Resistivity [$\Omega \cdot \text{cm}$] of bulk Si	1	0.01
Thickness [μm] pf porous Si	119	114
Porosity	0.50	0.35
Pore diameter [nm]	38	3.7
Internal surface area [$\text{cm}^2 \cdot \text{cm}^{-3}$]	5.5×10^5	3.7×10^6

* Tokyo Denki University

the internal surface area of the sample B is one order of magnitude larger than that of A.

The sample was cooled to temperatures ranging from 300 to 12 K in a chamber evacuated to 8×10^{-4} Pa. Three lifetime components of about 0.2, 0.5, and 35–45 ns were found for sample A, but only two of about 0.2 ns and 0.5 ns were found for sample B. The longest lifetime in sample A is attributed to the o-Ps annihilation. Figure 1(a) shows the temperature dependence of the longest lifetime τ_3 in sample A, which decreased from 45 to 34 ns with a rise in temperature from 12 to 300 K. Figure 1(b) shows the temperature dependence of τ_1 and τ_2 in sample B. The middle lifetime τ_2 and the shortest lifetime τ_1 were nearly independent of temperature up to 200 and 300 K, ($\tau_2 \cong 520$ ps, $\tau_1 \cong 241$ ps), respectively.

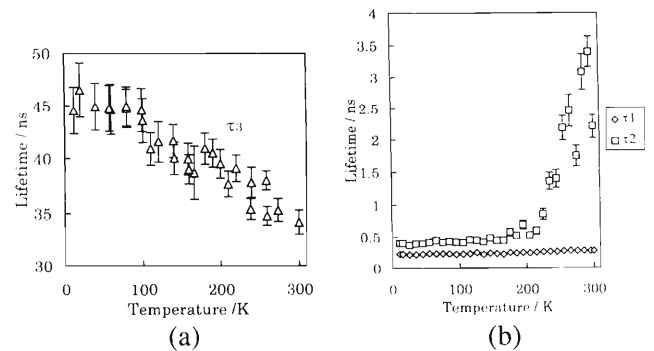


Fig. 1. (a): Temperature dependence of the longest lifetime of the sample A, (b): Temperature dependence of the shortest and middle lifetime components of the sample B.

Since the longest lifetime τ_3 could not be observed in Sample B, we believe that positronium is not formed. The specific internal surface area of the pores in sample B is one order larger than that in A, and the pore diameter in sample B is large enough to contain positronium. It means that there is sufficient condition to form positronium in sample B. Nevertheless, the result that positronium formation did not occur in sample B suggests that the physical and chemical properties of the pore surface are quite different from those in sample A. We are currently undertaking further investigations to clarify this point.

References

- 1) Y. Itoh et al.: *Appl. Phys. Lett.*, **63**, 2798 (1993).
- 2) A. Kinoshita et al.: *Trans. IEICE* (in Japanese), C-II, **J73-C-II**, No. 2, p. 129 (1990); H. Aoyagi et al.: *ibid.*, No. 4, p. 135 (1995).

Positron Annihilation Studies on the Interaction between Hydrogen and Defects in Nickel

Y. Itoh, Y. Wu, and Y. Ito

Positron annihilation was measured for Ni crystals containing different kinds of defects. The nickel crystals were annealed at 1173 K for 1 h and then slowly cooled to room temperature. The annealed sample was then cold-rolled to different degrees of deformation to introduce vacancies and dislocations. It was found that the lifetime spectrum could be fitted to a single component for annealed and cold-rolled nickels. The positron lifetime increased by the cold-rolling, and at a strain exceeding about 9% it reached a saturation value of 179 ± 1 ps (Fig. 1(a)), which is close to the value $\tau_{1v} = 180$ ps for positron trapping in a single vacancy. Hydrogen was then doped by the cathodic hydrogen charging method. The lifetime spectra of hydrogen-charged samples could be decomposed into two components with $\tau_1 = 179 \pm 1$ ps and $\tau_2 = 390 \pm 20$ ps and $I_2 = 5 \pm 1\%$. The longer lifetime component is attributed to the formation of vacancy clusters. In view of the appearance of a well separable long-lived component of about 390 ps, the hydrogen-vacancy composite can become the center of vacancy agglomeration. This is in accordance with the results of Johnson et al.¹⁾

In subsequent experiments the cold-rolled Ni was tempered at 473 K for 10 h to eliminate most of the vacancies but leaving the dislocation density unaffected. The absence of the effect of hydrogen-charging in tempered nickel clearly indicates that hydrogen does not react with dislocation. The interaction between hydrogen and vacancy-type defects may be the dominant reason for the increase of mean lifetime and S-parameter (Fig. 1) in the hydrogen-charged cold-rolled nickel.

It is concluded that hydrogen is trapped at vacancies and becomes a center of vacancy agglomeration, and that dislocation sites are not responsible for the forma-

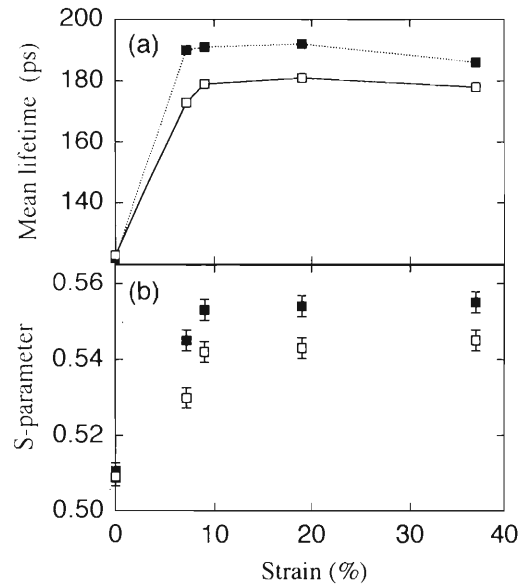


Fig. 1. The effect of hydrogen-charging on (a) the mean positron lifetime and (b) S-parameter for cold-rolled nickel samples. The strain introduced by cold-rolling is shown on the abscissa. Both vacancies and dislocations are thought to be present in the samples. □ : Cold-rolled Ni, ■ : hydrogen-charged cold-rolled Ni.

tion of larger vacancies. This observation is confirmed by measurements of the Doppler broadened annihilation radiation.

References

- 1) J. A. Johnson, P. S. Doubloon, and R. E. Smallmann: *Proc. Roy. Soc.*, **A315**, 231 (1970).

4. Radiation Chemistry and Radiation Biology

Track-Depth Resolved Dynamics of Excited States in Ion Irradiated Rare Gases near Condensed Phases

K. Kimura, W. Sekiguchi, Y. Yoshioka, T. Morita, M. Imura, and W. Hon

The radiation effects induced by ion irradiation have been mainly on the primary collisions in physics while product analysis have been major methods in chemistry and biology. As for the relevance between the two approaches, we can find very few studies. This study aims to elucidate the physico-chemical stages of ion irradiation by focusing on the dynamics of excited states along the ion track. This may be achieved by measuring the Bragg curve of the luminescence from the track in the condensed phase; for this, we developed a digital camera for the ion track, a track scope, composed of an imaging fiber mounted in a cryostat and a position sensitive photon counter. This allows us to obtain depth dependent luminescence spectra, efficiency, and decay. The depth can be converted into several parameters including derivatives of ion energy, stopping power, velocity, and relative excitation density. In our previous study of helium, we found that the luminescent states, upper level excimers, originate from the recombination between the lowest triplet excimers. The regeneration of upper level excimers increases along the Bragg curve, and near the Bragg peak, the reactions of the three excimers occur to result in the quenching. An extra Bragg peak caused by the Fano-type mechanisms was observed near the termination of the track.

Now the study are extended to other rare gases. With increasing atomic number, rare gases evolve in electronic properties such as excited states, the electronic conduction level in the condensed phase (V_0), and the electron mobility. These effects on the physico-chemical stage will be studied. We developed a modified track scope essentially composed of the same parts to the previous one but can pressurize gases up to 40 atm near the critical temperature, resulting in nearly condensed gases. The track length could therefore be adjusted by altering the pressure. This track scope is illustrated in Fig. 1. A capillary plate was used to transmit only the luminescence perpendicular to the track. Figure 2 shows the specific luminescence dL/dx vs. the track depth in Ar-ion irradiated dense argon-gas. The luminescence is vacuum ultra violet light originating from argon excimers. The dL/dx is damped earlier than the stopping power, which is quite different from the result in case of the helium sample. The high-density excitation can enhance the luminescence in helium while it is quenching in this case.

Figure 3 shows the luminescence efficiency (dL/dE) as a function of the velocity of ions; dL/dE rises toward the termination of the track. Similar results were observed for other rare gas samples. The results counter

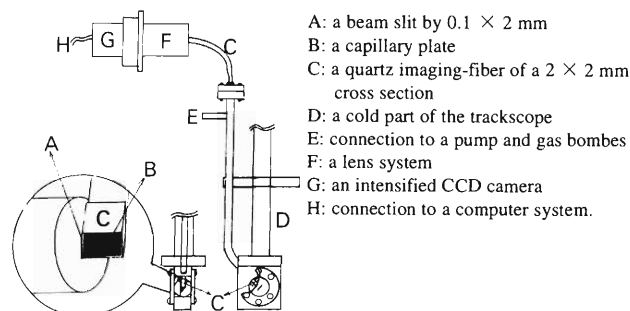


Fig. 1. A track scope.

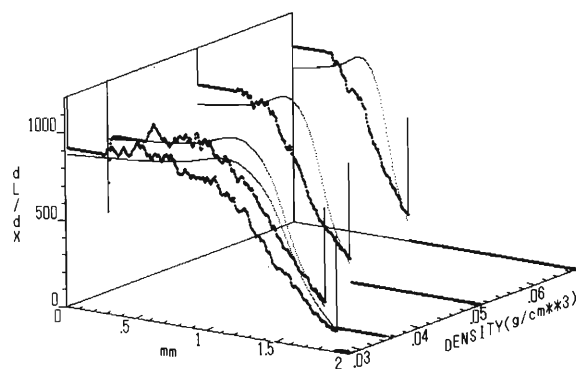


Fig. 2. The specific luminescence intensity dL/dx vs. the track depth of Ar-ion irradiated Ar gas.

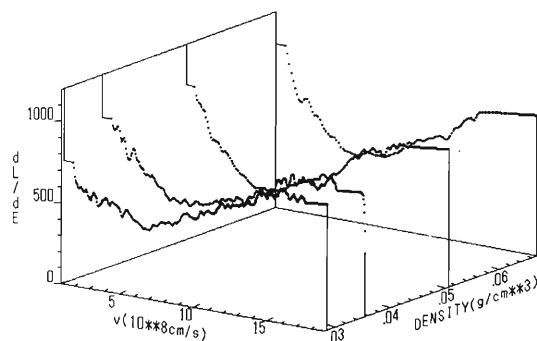


Fig. 3. The luminescence efficiency as a function of the ion velocity obtained by the conversion of data from Fig. 2.

to what scintillator theory and experiments have indicated. This may be explained by the charge exchange and direct excitation processes which were also important in the appearance of the 2nd Bragg peak in the helium sample.

References

- 1) K. Kimura: *Phys. Rev.*, **A47**, 327 (1993).

Unusual Temperature-Dependent Decay of Self-Trapped Excitons Formed at High Density in Ion Irradiated BaF₂

K. Kimura, Y. Yoshioka, W. Sekiguchi, T. Morita, M. Iimura, K. Ushida, and W. Hon

Recently, the luminescence of photoexcited BaF₂ and several alkali halide crystals have attracted interest not only as new scintillators for high energy physics but also as crystals that demonstrates the new exciton luminescence called Auger electron free luminescence (AEFL). We have studied the dynamics of exciton luminescence, induced by irradiation with several kinds of ions of low energies of about 2.0 MeV/nucleon, by developing techniques for fast luminescence decay measurements (SISP) of 100 ps resolution. Excitation-density dependent shortening of the lifetime of AEFL was found newly, which were reported already.¹⁾ The present report describes the effect of ion irradiation with temperature changes on the self-trapped exciton (STE). It was found previously²⁾ that at room temperature, the He-ion irradiation caused drastic lifetime shortening of the STE compared with the photo- and electron-irradiation, which is shown in Fig. 1. Heavier ions caused increased shortening of the STE lifetime. Under our condition of the high density excitation, which is intensified with increasing mass of the projectile ion, the STE decays according to the STE-STE exchange interaction in addition to the spontaneous process. The competition rate equations could be solved analytically. The instantaneous luminescence intensity, $I(t)$, can be expressed by the following equation:

$$I(t) = k/[(a + N(0)^{-1}) \exp(kt) - a] \quad (1)$$

where $N(0)$, k , and a stand for, respectively, the number density of STE at time 0, the rate constant of spontaneous luminescence of STE, and a constant dependent on the radii of the track and STE and on the critical exchange interaction. This equation could simulate the result fairly well (Fig. 2).

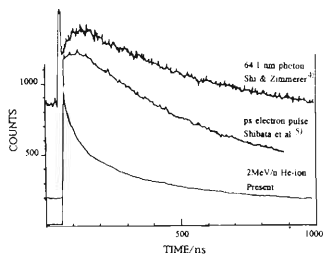


Fig. 1. A comparison of the decay of STE in BaF₂ induced by different sources.

Decreasing temperatures shortened the decay time from several ns to about 400 ps with no prominent change in its intensity.³⁾ This temperature effect was contrary to that for photoirradiation by synchrotron

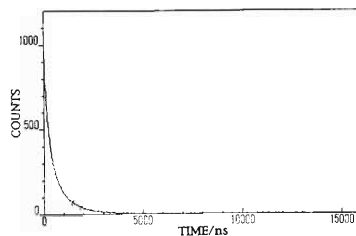


Fig. 2. Fitting of Eqn. (1) to the decay curve for He-ion BaF₂.

radiation which results in a lengthening of the decay time from about 1 μ s at room temperature to about 10 μ s at 50 K.⁴⁾ Both effects of temperatures and masses projectile ions are shown in Fig. 3 comprehensively. The results may be explained by the high-density excitation which is mentioned briefly in the following sentences. The slow rises in cases of photo- and electron-irradiation in Fig. 1 suggest that STE's can be regenerated through the recombination of holes (H-centers) and electrons (F-centers). The decrease in temperature should slow down the rate of these recombinations. By contrast, in case of the ion irradiation, the F- and H-centers are formed at such a high density that neither can localize separately and they are always able to recombine. Decreasing temperatures suppress the expansion of the volume covered by F- and H-centers so that the density of STE increases.

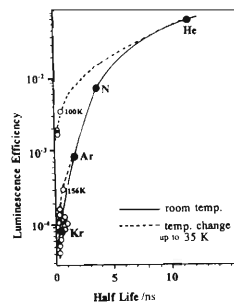


Fig. 3. Temperature and the mass of projectile dependencies of the luminescence efficiency and the half-life.

References

- 1) K. Kimura et al.: *Phys. Rev.*, **B48**, 15535 (1993).
- 2) K. Kimura: *Nucl. Instrum. Methods Phys. Res.*, **B90**, 100 (1993); K. Kimura and H. Kumagai: *Rad. Eff. Def. Solids*, **126**, 45 (1993).
- 3) K. Kimura: to be published on *Nucl. Instrum. Methods Phys. Res.*, **B** (1996) and *J. Elec. Spec. Re. Phenomena* (1996).
- 4) C. Shi et al.: *Physica Scripta*, **41**, 1022 (1990).
- 5) Shibata et al.: Private communication.

Effect of Heavy-Ion Beams during the Fertilization Cycle of Plants

T. Abe, S. Kumata, T. Torashima, S. Kitayama, and S. Yoshida

During the fertilization cycle of some plant species, there is an optimal period when certain chemicals can induce mutagenesis at a high frequency.¹⁾ An accelerated ion beam can also elicit mutagenesis when administered during the fertilization cycle and its effect can be made within extremely short time periods because of its relatively high LET compared to other energy beams such as γ - and X-rays; the irradiation area can be limited to a specific stage and organ avoiding undesired damage to other plant tissues.

In this study we examined the effectiveness of ion beams in inducing mutagenesis in the embryo of the tobacco plant (*Nicotiana tabacum* L. cv. BY-4). Sev-

eral ovaries at different developmental stages, 24–36, 48–60, 72–84 and 96–108 hrs after pollination, were irradiated with a N-ion beam (135 MeV/u). The M₁ seeds were harvested one month after irradiation, and then germinated in an 1/2 MS agar medium. After a two week incubation, we determined their germinating rates and observed the shapes of the M₁ seedlings.

A high irradiation dose at almost any developmental stage caused a decrease in germination percentage and an increase in the number of chlorophyll deficient plants (CDP). The stage at which ion beam treatment is most effective in causing the production of CDP is 72–84 hrs after pollination (Table 1). We are con-

Table 1. Frequency of chlorophyll deficient plants (CDP) induced with the ion-beam treatment at various flowering stages.

Stage of treatment	No. of treated flowers	Germination (%)	Seeds weight mg/100seeds	No. of M ₁ seedlings	No. of CDP	Frequency ($\times 10^{-1}$ %)
Control	4	97.8	7.7	2968	0	0.0
24–36 hrs	6	74.9	4.6	6051	8	1.3
48–60 hrs	6	78.3	3.7	6428	19	3.0
72–84 hrs	5	74.8	4.7	2728	17	6.2
96–108 hrs	4	85.4	6.2	2719	13	4.8

tinuing to monitor and analyze M₁ plants and their progeny. If ion beam treatments consistently result in a high mutation rate and a wide range of mutant phenotypes, this work will significantly contribute to

future studies of many subjects in molecular biology.

References

- 1) K. Kang and T. Kameya.: *Euphytica*, **69**, 95 (1993).

Enhanced Cell Inactivation at Nonpermissive Temperature

S. Kitayama, A. Tanaka, N. Shikazono, and N. Inabe

When DNA is damaged in living cells, many physiological changes such as the suspension of normal DNA replication, induced synthesis of protein etc. will be observed. However, almost all of the cells have repair capability for such lesions and can survive within the sublethal dose. However, many intracellular or environmental factors will influence their recovery process and consequently change the surviving fraction. The repair efficiency of DNA lesions depends on the type of damage, the cells genetically-controlled capability for repair, and, again, its physiological environment. Therefore, a comparison of repair efficiency under the same physiological condition will contribute to elucidate the difference in damages or repair process involved in the cell recovery.

Deinococcus radiodurans, the most radiation resistant bacterium, can survive even after the induction of many lesions in and various kinds of damage to DNA. The principal reason for this tolerance is an efficient and accurate repair mechanism for such DNA lesions.¹⁾ We have reported that the interruption of the recovery process reduced greatly the surviving fraction. Post-incubation at a nonpermissive temperature (42 °C) also reduces the cell survival following the physical or chemical treatments that cause DNA damage. Even the fragmented DNA by gamma irradiation are rejoined in the cells, their colony forming ability (survivor) was reduced by postincubation at 42

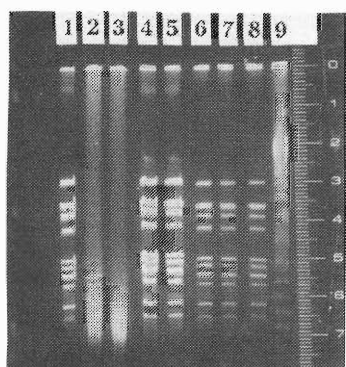


Fig. 1. Pulse field gel electrophoresis of DNA in the cells post-incubated at 30 °C or a nonpermissive temperature. Unirradiated control (lane 1), 1 kGy (lane 2), 1.5 kGy (lane 3), 1 kGy and postincubated at 30 °C (lane 4), 1.5 kGy and post-incubated (lane 5), unirradiated but incubated at 42 °C (lane 6), 1 kGy and postincubated at 42 °C (lane 7), 1.5 kGy and postincubated at 42 °C (lane 8), λ -ladder DNA marker (lane 9).

°C for 6 hours. In the previous experiments α -particles were used for the bombardment with accelerated particle and the changes of DNA molecular weight were analysed by sedimentation.²⁾ Since the bombardment with α -particles in a liquid phase is thought to include a substantial low LET fraction, Ne-ions (135 MeV/ μ) were used in this experiments. Pulse field gel electrophoresis (PFGE) was also used for these analyses (Fig. 1) because it has been recently become useful for the analysis of high molecular weight DNA.

As shown in Fig. 2 the enhanced lethal effects of incubation at 42 °C for 6 hrs following the sublethal doses of Ne-ion irradiation is lower than that with α -particles reported previously.²⁾ Therefore, comparative experiments using γ -ray irradiation or treatments with some radiomimetic chemicals will be carried out to obtain some conclusive evidence.

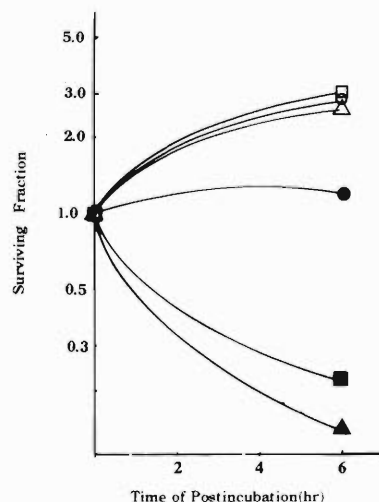


Fig. 2. Cell survivors after incubation at nonpermissive temperature following Ne-ion bombardment. Colony forming units of unirradiated cells (circle), irradiated with 1 kGy (square) or 1.5 kGy (triangle). Following the irradiation cells were postincubated at 30 °C (open symbols) or 42 °C (closed symbols) for 6 hrs and were plated on TGY-agar.

References

- 1) S. Kitayama and A. Matsuyama: *Biochem. Biophys. Res. Commun.*, **33**, 418 (1968).
- 2) S. Kitayama et al.: *Agric. Biol. Chem.*, **41**, 2297 (1977).

Effects of Ne Ion Beams on the Survival of *Arabidopsis thaliana*

N. Shikazono, A. Tanaka, Y. Yokota,* H. Watanabe,** S. Tano,**
T. Kanai, and S. Kitayama

The biological effects of heavy charged particles, measured by the relative biological effectiveness (RBE) on lethality as a function of linear energy transfer (LET), have been extensively studied in bacteria, yeast and mammalian cell cultures. However, the effects of heavy ions on multicellular organisms are still not fully understood. *Arabidopsis thaliana* (L.) Heynh. is a particularly suitable multicellular organism for studying the effects of heavy ions and other kinds of radiation because its seeds and plants are small, it produces a large number of seeds and plants, and its life cycle is short.¹⁾

We have investigated the effects of heavy ions on the survival of *Arabidopsis* using heavy ions with a LET of 17–549 keV/ μm , and found that the highest RBE value was obtained by Ar ion irradiation (LET 252 keV/ μm).²⁾ In addition, we determined the characteristic survival curve for Ne ions (LET 549 keV/ μm). The typical survival curve for other ions showed a shoulder at lower doses and a steep decline from the level obtained by a critical dose that depends on the kind of ion and its energy. In contrast, the survival curve for Ne ions with a LET of 549 keV/ μm consists of a gentle slope with no shoulder. This result cannot be simply interpreted as an “overkill effect”, since the survival curves for heavier ions with LETs higher than 549 keV/ μm still have shoulders.¹⁾ To further elucidate the dependence of RBE on LET, we used Ne ions of various LETs.

The dry seeds of *Arabidopsis thaliana* ecotype Columbia were used for these experiments. A monolayer of seeds sandwiched between kapton films (7.5 μm thickness) was exposed to Ne ions at the RIKEN Ring Cyclotron. The LETs for Ne ions were varied by placing an absorber in front of the irradiation site. The mean LETs were calculated by ELOSS code (modified OSCAR code). Seeds were irradiated by Ne ions of three different LETs (156, 275, 525 keV/ μm), and the plants were grown at 23 °C under continuous light (40 $\mu\text{E}/\text{m}^2/\text{s}$); the survival was measured one month after sowing. We scored plants with expanded rosette leaves as survivors.

The survival curves for Ne ions with LET 156, 275 and 525 keV/ μm are shown in Fig. 1. Ne ions with LET, 156 keV/ μm , had the largest shoulder, while

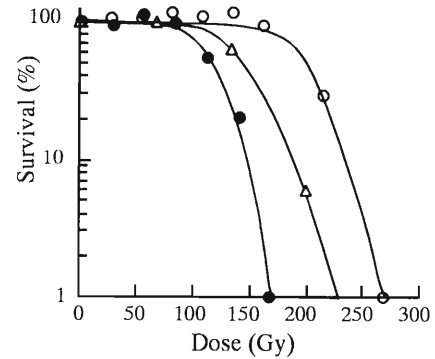


Fig. 1. Effects of Ne ion beams with different LETs on survival. ○: LET 156 keV/ μm , ●: LET 275 keV/ μm , △: LET 525 keV/ μm .

those with LET, 275 keV/ μm , had the smallest. The size of the shoulder with LET 525 keV/ μm was intermediate. These survival curves were typical and were not similar to the curve for Ne ions with LET 549 keV/ μm . Consequently, the condition of energy deposition accounting for the characteristic curve for Ne ions with LET, 549 keV/ μm , still remains unclear.

D_{37} for Ne ions with LET, 525 keV/ μm , was not significantly different from that for LET, 275 keV/ μm . This explains the relatively high RBE of survival when the Ne ions had LETs to 500 keV/ μm . In unicellular systems, ion beams with LETs more than 200 keV/ μm usually reduce the RBE value. The difference in how the LET values affect the RBE peak in unicellular systems and *Arabidopsis* might be explained by the existence of specific repair mechanisms which operate in multicellular organisms.

Further investigations using other particles with LETs of around 500 keV/ μm would be important to make clear the relationship between RBE and LET in *Arabidopsis* and to understand the underlying mechanism(s) of the characteristic survival curve.

References

- 1) U. Bork et al.: *Adv. Space Res.*, **9**(10), 117 (1989).
- 2) A. Tanaka et al.: 5th Workshop on Heavy Charged Particles in Biology and Medicine, GSI, Darmstadt, Aug. 23–25, p. 87 (1995).

* Beam Operation Co.

** Advanced Science Research Center, JAERI

Dependence of Interphase-Death Induction on the LET of Accelerated Neon-Ions in CHO Cells

H. Sasaki, F. Yatagai, T. Kanai, and F. Hanaoka

Cultured mammalian cells exposed to moderate doses of X-rays (< 10 Gy) usually die after dividing at least once (reproductive death). However, we previously found that HeLa cells frequently die before dividing (interphase death) after exposure to as low as 1–2 Gy of alpha particles from ^{241}Am .¹⁾ This suggests a predisposition to interphase death when cells are exposed to high LET radiations. The purpose of this study, which makes use of heavy-ions accelerated by the RIKEN Ring Cyclotron, is to verify this hypothesis. First, we observed HeLa cells exposed to 3 Gy of Ne-ions (135 MeV/u; 102 keV/ μm) using time-lapse photography and found that about 30% of the cells died after detaching from the plate as if they were entering mitosis. Since it was clear that this death process was apoptotic and involved DNA fragmentation, as also observed in other cell lines (CHO, FM3A), we employed an apoptois-induction assay (indirect method) to elucidate the effect of the LET of Ne-ions on the induction of the interphase death of CHO cells.

CHO cells, which were destined to undergo interphase death after irradiation, remained in the G2 phase for an extended period (> 24 h) and then became giant before dying by apoptosis. Caffeine induces apoptosis in these cells within a short period; the caffeine probably disturbs a check-point control mechanism in the G2 phase. In this study, cells were incubated for 24 h after exposure to graded doses of Ne-ions with different LETs (63–341 keV/ μm) and then treated with caffeine (10 mM) for 1 h. The fraction of cells undergoing interphase death was estimated by counting round cells (detaching apoptosis-initiated cells) which appeared after the addition of caffeine. The results in Fig. 1 indicate that the induction of interphase death-related apoptosis depends on the LET of Ne-ions. The maximum effect (RBE = 4.6) was observed at 228 keV/ μm for Ne-ions compared to X-rays at the half maximum level (35% induction). Evaluation of LET dependence for induction of interphase death by means of time-lapse observation (direct method) is now in progress and preliminary results are shown in Fig. 2. A similar RBE (4.2) was obtained for 228 keV/ μm Ne-ions.

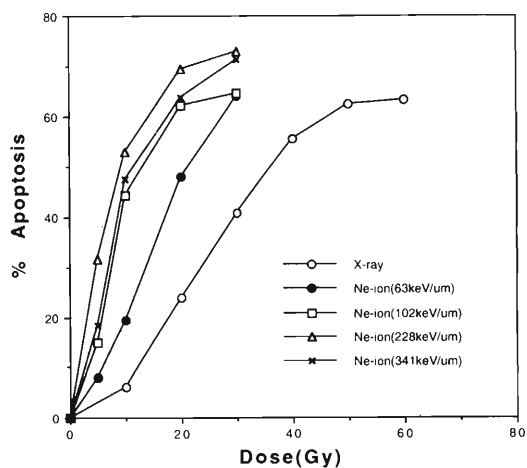


Fig. 1. Dose-response for apoptosis induction in CHO cells exposed to X-ray or accelerated neon-ions with different LET.

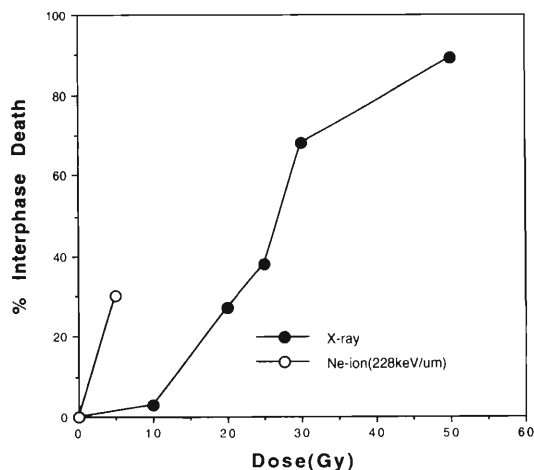


Fig. 2. Dose-response for interphase-death induction in CHO cells (Time-lapse observation).

References

- 1) H. Sasaki: *Radiat. Res.*, **99**, 311 (1984).

The Role of DNA Repair on Cell Killing by Neutron and Heavy-Ion Beams[†]

K. Eguchi-Kasai, M. Murakami, H. Itsukaichi, K. Fukutsu,* T. Kanai,
Y. Furusawa, K. Sato,** H. Ohara, and F. Yatagai

It has been suggested that initial double-strand breaks (dsb) in DNA correlate well with cell death induced by conventional radiations.¹⁾ However, this is not true for radiations with high linear energy transfer (LET). In these cases, the relative biological effectiveness (RBE) for cell killing is high, ranging from 2 to more than 10, but the RBE for dsb induction is approximately 1 for particles with LETs below 300 keV/ μm^2 .^{2,3)} or even smaller than unity for very high LET ions.^{4,5)}

Therefore, it can be deduced that it is not simple dsb, but non-reparable breaks that are responsible for the lethality of high LET radiation.⁶⁻⁸⁾ Here, we have examined the effectiveness of high LET radiations on causing cell death in 19 mammalian cell lines including radiosensitive mutants.

The radiations used in this work were fast neutrons from the NIRS cyclotron, and low (at NIRS, initial energy = 12 MeV/u) or high (RIKEN Ring Cyclotron, 135 MeV/u) energy charged particles.

Some of the radiosensitive cell lines, such as LX830, M10, V3, SX9, SX10 and L5178Y-S, are deficient in DNA dsb repair. In our experiments they showed lower values of RBE for fast neutron-beams compared to their parent cells. Their average RBE value was 1.23 ± 0.15 (mean \pm standard deviation) while that of their parent cell group was 1.86 ± 0.16 . The other cell lines, human ataxia-telangiectasia fibroblasts, irs 1, irs 2, irs 3 and irs 1SF, are also radiosensitive but known as proficient in dsb repair; their RBE measured a moderate 1.68 ± 0.15 . The RBE values for the three groups differ significantly ($p < 0.05$).

The RBE values varied depending on the radiation

quality and on the cell types. The RBE value was smaller for low LET He-ion beams and larger for high LET C- or Ne-ion beams, when both were compared to neutron-beams. Dsb repair deficient mutants demonstrated low RBE values close to unity for heavy ions; this was independent of the kind of ion beam or its energy. The inactivation cross sections of 2 dsb repair deficient cell lines (M10 and SL3-147) increased with increasing LET. They were always larger than those of their parents (L5178Y and LTA) for all the LET ranges tested up to 330 keV/ μm . With increasing LET, however, the difference in inactivation cross section between the mutants and their parents became smaller. This suggests that the DNA repair system is less effective in response to high LET radiations, even in DNA repair proficient cells. This is because the induction of repairable dsb decreases and the ratio of non-reparable dsb to total dsb increases with increasing LET.

Based on these findings, we suggest that the main cause of cell death induced by high LET radiations is non-reparable dsb, which are produced at a higher rate than when cells are exposed to low LET radiations.

References

- 1) L. R. Radford: *Int. J. Radiat. Biol.*, **49**, 611 (1986).
- 2) I. Furuno et al.: *ibid.*, **36**, 639 (1979).
- 3) T. J. Jenner et al.: *ibid.*, **61**, 631 (1992).
- 4) J. Heilmann et al.: *Radiat. Res.*, **135**, 46 (1993).
- 5) K. J. Weber and M. Flentje: *Int. J. Radiat. Biol.*, **64**, 169 (1993).
- 6) D. Blöcher: *ibid.*, **54**, 761 (1988).
- 7) K. Eguchi et al.: *ibid.*, **52**, 115 (1987).
- 8) M. A. Ritter et al.: *Nature*, **266**, 653 (1977).

[†] Condensed from the article in *Adv. Space Res.*, **18**, 109 (1996).

* Division of Radiobiology and Biodosimetry, National Institute of Radiological Sciences

** Deputy Director in General, National Institute of Radiological Sciences

Analysis of Mutations in the Human *HPRT* Gene Induced by Accelerated Heavy-Ion Irradiations (II)

F. Yatagai, N. Inabe, K. Eguchi-Kasai, Y. Furusawa, M. Suzuki, M. Watanabe, T. Kato,* and F. Hanaoka

Knowledge of the specificity of mutations induced by a variety of mutagens has enabled better understanding of the molecular mechanisms of mutagenesis. The mutations induced by various types of chemicals, and UV and conventional ionizing-radiation, have been analyzed extensively at the molecular level to gain insights into the induction mechanisms, but only a few studies have been published on the characteristics of heavy-ion-induced mutations. We have analyzed the hypoxanthine phosphoribosyltransferase (*HPRT*) mutations in human embryo (HE) cells induced by C-ions adjusted to different LETs (39, 68, 124, or 230 keV/ μ m).¹⁾

The deletion pattern of each exon region in the *hprt* locus is dependent on the LET, as revealed by the analysis of multiplex PCR products of genomic DNA in the mutants. Most of the mutations induced by 124 keV/ μ m C-ions showed deletion of almost the entire locus of the *hprt* gene. None of the mutations caused by 230 keV/ μ m C-ions involved such large deletions, despite the much greater energy deposition within their tracks. To characterize the 230 keV/ μ m mutations, the sequence alterations in a cDNA of the *hprt* gene were determined for 18 mutant clones.²⁾ The loss of exon 6 was the most frequent mutational event (10 clones), and that of both exons 6 and 8 was the next most frequent event (6 clones). In two cases, the mutations consisted of base substitutions. Further analysis of the intron regions on genomic DNA from mutants carrying exon losses support the possibility that the mutations were induced by aberrant mRNA splicing.

Is this characteristic specific to high-LET irradiation that exceeds the peak of RBE (Relative Biological Effectiveness)? We used the human lymphoblastoid cell lines, WI-L2-NS and TK6, to study this question. In this series of experiments, we adjusted the energy of ions to three different LETs, one at nearly the initial energy, one at the RBE-peak, and one at the level just before the stop of the ion. The survival curves for both C- and Ne-ions are shown in Fig. 1 and a comparison of the radiosensitivity with that for X-rays at D_{10} dose, the so-called "calculation of RBE", is made in Table 1. The expected LET effect on cell viability was observed with the WI-L2-NS cell line. The mutation frequencies at certain survival rates were also determined and listed in Table 2. Although the precise RBE cannot be estimated because of the small number of trials, the tendency of RBE seems to be similar to that for cell viability.

The data on TK6 cells is not yet complete enough

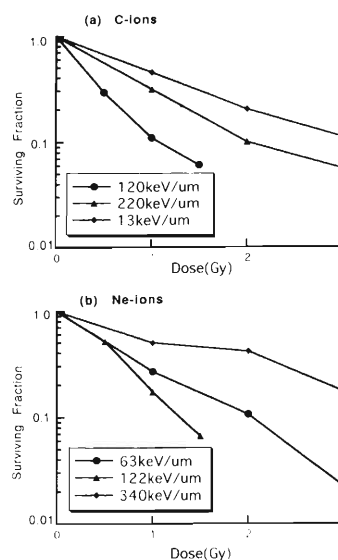


Fig. 1. Survival curves of WI-L2-NSs for C- and Ne-ions. Irradiation by 13 keV/ μ m of C-ions was performed at HIMAC.

Table 1. RBE Values for a lethal effect in WI-L2-NS cells.

Ion	C	C	C	Ne	Ne	Ne
LET (keV/ μ m)	13	122	220	63	120	340
RBE at D_{10}	1.0	3.0	1.5	1.5	2.4	1.0

Table 2. Mutation frequencies of WI-L2-NS cells.

Ion	—	C	Ne	Ne
LET (keV/ μ m)	—	13	120	340
Dose (Gy)	0	2.0	1.0	3.0
Surviving fraction	1.0	0.25	0.173	0.172
Mutat. freq. ($\times 10^{-6}$)	3.7	13	27	14

to judge such LET effects on them. The study of this cell line needs to continue, because a difference in both the type and level of p53 protein between these two cell lines has been reported to account for the differences in their radiosensitivities.³⁾ It is also important to analyze the isolated mutant clones at the DNA sequence level.

References

- 1) M. Suzuki, M. Watanabe, M. Kanai, Y. Kase, F. Yatagai, T. Kato, and S. Matsubara: *Adv. Space Res.*, **18**, 127 (1995).
- 2) Y. Kagawa, F. Yatagai, M. Suzuki, Y. Kase, A. Kobayashi, M. Hirano, T. Kato, M. Watanabe, and F. Hanaoka: *J. Radiat. Res.*, **36**, 185 (1995).
- 3) W. Zhen, C. M. Denault, K. Loviscek, S. Walter, L. Geng, and A. T. M. Vaughan: *Mutat. Res.*, **346**, 85 (1995).

* School of Medicine, Osaka University

Early Phase Histological Changes of Skin after Carbon Ion Slit-Beam Irradiation

H. Tatsuzaki, H. Takahashi, T. Okumura, and F. Yatagai

Heavy ion treatment of cancerous tumors increases the cure rate of other therapies. Although the cure rate increases as the dose of irradiation increases, the size of the prescribed dose is limited by the tolerance of normal tissue. That tolerance depends on many factors, including the LET and the volume of irradiation. We have shown that the smaller the volume, the greater the tolerance.¹⁾ We used the skin of the mouse to study more closely the effects of irradiation on normal tissue. The preliminary results were shown in this article.

We used twelve week old female C₃H/He Slc mice raised under Specific Pathogen Free (SPF) conditions. All the irradiation was performed at the RIKEN Ring Cyclotron using the entrance plateau portion of an original mono-peak beam from a 135 MeV/u C-ion beam. The LET value of the beam at the skin surface was around 22 keV/ μ .²⁾ The beams were collimated to a 25 or 5 mm width slit-shape to vary the volume irradiated.

Seven days before irradiation, the lower hind legs of the mice were shaved. The legs were then irradiated with 60 Gy while they were under anesthesia (65 mg/kg sodium pentobarbital, i.p. injection). The skin reaction typically progresses from erythema to dry desquamation, then moist desquamation and then healing. The reaction is most severe from 14 days to 25 days after irradiation.^{3,4)} Histological specimens were taken on the 13th, 17th, 21st, and 27th day after irradiation. At those time points, the mice were sacrificed by an overdose of inhaled ether. Before amputation, the extended irradiated legs were fixed to a wooden plate with pins to prevent the skin from shrinking. The legs were then amputated, fixed in 10% formalin solution together with the wooden plate, and embedded in paraffin. The sections were prepared in the longitudinal direction, perpendicular to the beam entrance surface. The specimens were stained by hematoxylin and eosin (H&E) and observed under a light microscope. Un-irradiated skin was used as controls.

After 5 mm slit irradiation the thickness of the epidermis markedly increases. It reaches its maximum thickness by the 17th to 19th day after irradiation and then decreases slightly. The changes in the thickness of the epidermis, measured at the middle of the irradiated area, are shown in Fig. 1. The measurement was taken at the point of the papilla dermis to avoid interference by hair follicles. We observed no defects in the epidermis. The thickness of the dermis shows the same tendency and becomes maximally large at the 13th day. The hair follicles measured 30 to 50 μ m in diameter in

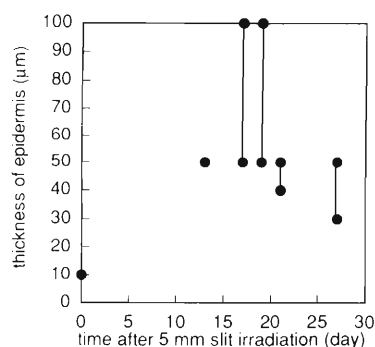


Fig. 1. The changes in the thickness of the epidermis after 5 mm slit carbon beam irradiation. The closed circles and vertical lines indicate the range of thicknesses. Day 0 shows the thickness of un-irradiated skin.

un-irradiated skin. By the 13th day after irradiation, their diameter reached 100 μ m. After the 17th day, the hair follicles gradually disappeared. Desquamation of the horny layer was evident on the 27th day.

A different profile emerged after 25 mm slit irradiation. By the 17th day, the epidermis had disappeared from almost the entire irradiated area. Thickening of the epidermis was seen only at the edge of the irradiated area and its length was around 1 mm. The dermis of the irradiated area thickened slightly to 200 μ m from a control thickness of 25 to 100 μ m, and the hair follicles were destroyed. Necrotic tissue was attached to the uncovered surface of the dermis and remained that way until the 27th day. The size of the thickened part of the epidermis at the edge of the irradiated area increased gradually to 3 mm by the 27th day.

This results suggest that smaller volume irradiation cause less injury to normal tissues. Thus, reduction of irradiated volume using the particle radiation therapy to cancers is important.

References

- 1) T. Tatsuzaki et al.: in Extended Abstracts. 4th Workshop on Heavy Charged Particles in Biology and Medicine, G. Kraft (ed.), Gesellschaft für Schwerionenforschung mbH, Darmstadt, Germany, p. G5 (1991).
- 2) T. Kanai et al.: Proc. 2nd Workshop on Physical and Biological Research with Heavy Ions, K. Ando and T. Kanai (eds.), Natl. Inst. of Radiol. Sci., Chiba, p. 1 (1992).
- 3) H. Aizawa: *Nippon Acta Radiol.*, **33**, 602 (1973).
- 4) A. E. Pearson and G. G. Steel: *Int. J. Radiat. Biol.*, **44**, 353 (1983).

Measurement of Potassium, Rubidium and Cesium Influx Rate into Rat Erythrocytes Using Multitracer Technique

N. Ito, I. Kunugiyama, A. Iwatsuki, S. Enomoto, S. Ambe, B. Liu, and F. Ambe

Since rubidium (Rb) and cesium (Cs) have physico-chemical properties similar to potassium (K), many biologists have been interested in the kinetics of these alkaline metal elements.¹⁾ Rubidium is present in mammalian tissues at a higher concentration than that in the external environment. However, it has been shown that Rb cannot completely substitute for K in mammals despite the two element's similarities.²⁾ We, therefore, studied qualitatively the discrimination by the potassium transport system (like $\text{Na}^+\text{-K}^+$ ATPase) between K and Rb, and between K and Cs using the Multitracer.

Erythrocyte samples withdrawn from Wistar rats under general anesthesia were used in these experiments. A multitracer solution was obtained from a gold foil target irradiated with a ^{14}N beam accelerated by the RIKEN Ring Cyclotron, then the tracer solutions, containing either ^{43}K , ^{83}Rb , ^{84}Rb or ^{129}Cs , were extracted from the multitracer solution by an ion exchange resin. The tracer solutions consisted of the tracer in phosphate buffered saline (PBS): K (3 mM-6 mM), Rb (0.3 μM -6 mM) and Cs (7 nM-6 mM). The range of potassium concentrations used was determined based on that found in rat plasma (from 3 mM to 6 mM). The lowest concentrations of Rb and Cs used match their abundance in nature, and the highest concentrations used were fixed at 6 mM, the highest concentration of K in rat plasma. Gamma-ray spectroscopy was performed using a HPGe detector and a multichannel PHA.

The erythrocyte samples were soaked in the tracer solutions, and incubated for one hour at 38 °C. The active transport rate was calculated from the difference in influx rate between a solution containing ouabain and a solution without ouabain. The passive transport rate was obtained from erythrocyte samples soaked in a solution containing ouabain.

Figure 1 shows the changes in the Rb and K influx rates in erythrocytes soaked in Rb tracer solution. The active transport rates of K and Rb were 3 to 4 times higher than the passive transport rates. The active transport rate of K decreased significantly as the Rb concentration increased. The rubidium influx rate matched the potassium influx rate when the Rb

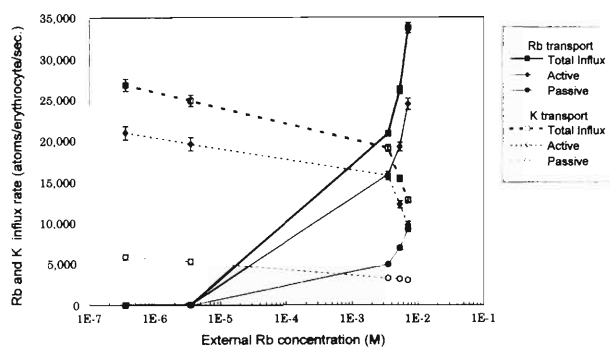


Fig. 1. Active and passive transport rate of rubidium and potassium into erythrocytes. K concentration is 4 mM.

concentration equaled the K concentration (3 mM, 4 mM and 6 mM). Figure 2 shows the changes in the Cs and K influx rates when the external tracer solution contained Cs. The active transport rate of Cs was very low, and lower than the passive transport rate. Potassium transport was not much influenced by Cs.

The potassium transport system doesn't seem to make a clear distinction between K and Rb. Hereafter, we plan to study the efflux rate of K, Rb and Cs from erythrocytes.

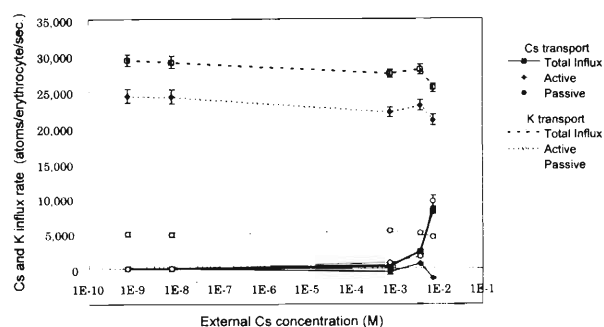


Fig. 2. Active and passive transport rate of cesium and potassium into erythrocytes. K concentration is 4 mM.

References

- 1) Mertz W.: Trace Elements in Human and Animal Nutrition, 5 ed., Academic Press (1986).
- 2) Follis R. H.: *Am. J. Physiol.*, **138**, 246 (1973).

Translocation of Radionuclides from Plant Leaf Surfaces

T. Watanabe, K. Matsumoto, S. Ambe, and I. Yamaguchi

The outermost surfaces of the aerial parts of growing plants are usually covered with cuticle which protects the plant against invasion by microbes and against non-specific penetration of foreign substances. In this study, we investigated the transcuticular uptake and translocation patterns of various radionuclides in plants. Ten μl of an aqueous solution containing the multitracer generated from Au and ^{137}Cs , which is deficient in the multitracer, was applied to the upper surface of the 2nd leaf of the Komatsuna plant (*Brassica Rape var. pervidis* cv. Seisen) and the mugwort at the 5th leaf stage. The plants were then grown for 15 days at 25 °C and 70% RH under the illumination of artificial solar light.

The uptake and translocation of the radionuclides throughout the plant were periodically assayed by examining the radioactivity of the surface residue, of the cuticle layer beneath the applied water droplet, of the leaf area outside the site of the applied water droplet, of the other aerial parts of the plant, and of root. The radionuclides in the various samples were detected by a Ge detector.

Most of the applied radionuclides were absorbed into the cuticle layer under the applied site, and then translocated through the cuticle to the inner tissue, and eventually to the other leaves, stems and roots. Figure 1 illustrates the time course of the uptake and translocation of Rb throughout the Komatsuna plant. However, the distribution and accumulation depends upon the characteristics of each radionuclide as demonstrated in Table 1.

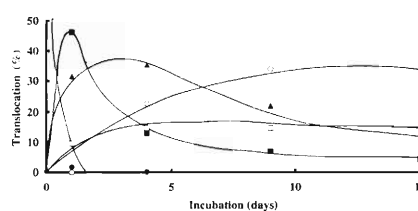


Fig. 1. Time course of the translocation of Rb in the Komatsuna plant (cv. Seisen) ● Residue on leaf surface, ■ Penetration into cuticle, ▲ Accumulation in the leaf area outside the applied site, ○ Accumulation in the leaves and stem other than the treated leaf, □ Root.

Table 1. Distribution of radionuclides in Komatsuna and Mugwort 15 days after application.

Radionuclide	Residue on leaf surface (%)		Penetration into cuticle (%)		Accumulation in the treated leaf outside the applied site (%)		Accumulation in the non-treated leaves and stem (%)		Root (%)	
	Komatsuna	Mugwort	Komatsuna	Mugwort	Komatsuna	Mugwort	Komatsuna	Mugwort	Komatsuna	Mugwort
Ca	98	100	2							
Te	97	96	3	4						
Be		78		22						
V	40	53	60	47						
Zn	68	73	32	27						
Ce	87	79	13	21						
Ir	19	49	81	51						
Mn	72	52	11	23	17	25				
As	8	52	85	33	7	15				
Sr	55	64	29	24	16	10				
Rh	50		20		30					
Ba	77	45	9	47	14	8				
Eu	74	85	22	15	4					
Gd	76	85	20	15	5					
Pt	11	43	71	57	18					
Re		18		33		49				
Co	55	34	4	31	16	6	20	10	5	19
Rb	2	47	5	9	14	10	59	13	20	21
Cs	4	3	31	28	19	22	26	29	20	18

From these results, one can discern a pattern of transcuticular uptake and translocation common to the two plants. Ca and Te remained on the leaf surfaces, without being absorbed into cuticle, Co, Rb and Cs were easily absorbed and then translocated and distributed to every part of the plant, and the others such as Be, Cr, Zn, Ce, Eu, Gd, Ir, and Pt tended to remain in the region close to the site of its application. These pat-

terns indicate the existence of mechanisms for selective transcuticular uptake, translocation and distribution of radionuclides within plant tissues.¹⁾

References

- 1) T. Watanabe et al.: Proc. 32th Ann. Meet. on Radioisotopes in the Physical Sciences and Industries, Tokyo, July, p. 129 (1995).

5. Instrumentation

Computer Environment around the Accelerator Facility

T. Ichihara, Y. Watanabe, and A. Yoshida

A general description of the data acquisition system at the RIKEN accelerator research facility can be found elsewhere.¹⁾ In this report, we will describe the recent improvement of the system.

(1) On-line data acquisition system

Currently, eight Micro VAX's are used for on-line experiments at the RIKEN accelerator research facility. The node names and locations are as follows:

RIKMOV1:: Micro VAX II (1F)
 RIKMOV2:: Micro VAX II (B2F E3)
 RIKMOV3:: Micro VAX II (Linac)
 RIKMOV4:: Micro VAX II (B2F RIPS)
 RIPS VX:: VAX 4000 (B2F RIPS)
 SMART:: VAX Station 3520 (B2F SMART)
 SMARTF:: VAX Server 3300 (B2F SMART)
 RIKLV2:: VAX Station 3100 M76 (1F)

Independent measurements and counter tests can be performed without interference. The current version of the data-taking program supports the CAMAC multi-crate parallel-readout using multi-J11's (starbursts). The throughput of the data acquisition is increased by using these parallel readout features. Digital audio tape (DAT) units of 2 GB capacity are used for the standard on-line data recording.

(2) Off-line data processing system-1

The following Alpha/VMS and VAX/VMS workstations are available for the off-line data analysis and for general purpose calculations.

RIKAXP:: Alpha server 5/250 (Ring 1F)
 RIKAX1:: DEC 3000-400 (Ring 1F)
 RIKAX2:: DEC 3000-400 (Ring 1F)
 RIKAX3:: DEC 3000-400 (Ring 2F)
 RIKAX4:: DEC 3000-300 (Linac lab.)
 RIKAX5:: DEC 3000-300 (Atomic lab.)
 RIKAX6:: DEC 3000-300 (Ring, nuclear theory)
 RIKAX7:: DEC 3000-300 (Radiation lab.)
 RIKEN:: (virtual node name of the VAX cluster)
 RIKVAX:: VAX-6610 (VAX boot server)
 RIKVS0:: VAX Station 4000-60 (Ring 1F)
 RIKVS2:: VAX Station 4000-60 (Ring 2F)
 RIKVS3:: VAX Station 4000-60 (Ring 1F)
 RIK835:: VAX Station 4000-60 (Radiation lab.)
 RIKLV1:: VAX Station 3100 M76 (Linac Lab.)
 RIKLV2:: VAX Station 3100 M76 (Linac Lab.)

Alpha server 5/250 consists of a dual CPU and a 512 MB memory and has been newly installed as a

home machine for the experimental user and also for a boot server. Seven Alpha workstations and seven VAX workstations are used for the data analysis, etc. These computers are connected by LAVC (Local Area VAX Clusters) via the FDDI or ethernet. They are also connected to the HEPnet (DECnet) and TISN and STA/IM Internet (IP/DECnet) and can be reached from all over the world.

(3) Off-line data processing system-2

Following FACOM VPP 500 Massive Parallel computers and DEC OSF/1 server and workstation groups have been also used for the off-line data analysis, simulations and theoretical calculation.

FACOM VPP 500 (RIKEN computation center)
 DEC 7000 (OSF/1) (RIKEN computation center)

These computers are connected to the Local Area Network(LAN) via the FDDI using TCP/IP protocols.

(4) Wide area computer network

The RIKEN accelerator research facility is connected to the world-wide network of HEPnet (High Energy Physics NETwork) / SPAN (Space Physics Analysis Network) as Area 40, which is a part of the DECnet Internet, and to the TISN and STA/IMnet which is a part of "the internet". In order to support these wide area network connections, following five leased lines are used.

1.5 Mbps to STA/IMnet
 512 kbps to TISN Tokyo NOC hub
 64 kbps to KEK, Tsukuba
 9.6 kbps to Tokyo Institute of Technology

(5) Address of the electric-mail

The address of the electric-mail for a general user of the RIKEN accelerator research facility is described as follows, where the userid should be replaced by a proper name.

(Internet)
 USERID@RIKAXP.RIKEN.GO.JP
 (HEPnet/DECnet)
 RIKAXP::USERID (or 41823::USERID)

References

- 1) T. Ichihara et al.: *IEEE Transaction on Nuclear Science*, **36-5**, 1628 (1989).

Data Acquisition System for Segment-Ge Detector

T. Morikawa, Y. Gono, M. Shibata, T. Maeda, K. Miyazaki, T. Kishida,
E. Ideguchi, and M. Ishihara

A new data acquisition system has been developed for a counter telescope of Ge detectors.^{1,2)} The telescope consists of a segmented ΔE detector and a clover detector. The ΔE detector consists of twenty-five pixels. It has individual cathode outputs and a common anode output, while the clover detector has four outputs. The energy and timing signals are handled separately, which gives a total number of sixty signals. For the design of the acquisition system, much effort has been paid to reduce the number of electronic modules such as ADC's necessary for these signals. A block diagram of the present system is given in Fig. 1.

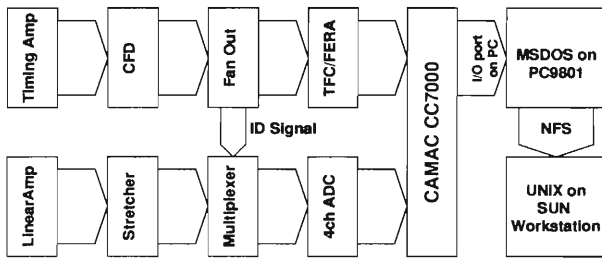


Fig. 1. A block diagram of the data acquisition system.

All energy signals are amplified separately by the integrated amplifiers,²⁾ and are fed into the multiplexer specially designed for the present system. The multiplexer has thirty linear energy inputs, thirty logic 'ID' inputs, one strobe input and one reset input. The logic 'AND' between the strobe signal and the logic ID signals gives the valid channels to be handled. Thus, the thirty energy signals are multiplexed into four inputs of the ORTEC ADC 413A; the average number of si-

multaneous hits has been estimated to be less than four. The separately handled CFD outputs are used as the ID inputs for the multiplexer. The CFD timing signals are also measured by LeCroy TFC 4303's and FERA ADC 4300B's, which gives the ID for the data of ADC 413A.

The crate controller CC7000 made of TOYO TECHNICA company interfaces the CAMAC modules, such as ORTEC 413A and LeCroy 4300B, and an MSDOS-based data-taking program running on an NEC PC9801. A trigger for the acquisition system is given by a LAM generator, which accepts a TTL signal for a valid event and gives a level to the LAM line in the station. Once the LAM is detected, the program sends a series of CAMAC commands to CC7000 to read the digitized data from the modules. By the data-taking program, the data are stored in the buffer allocated on a PC memory. When the buffer becomes full or high-water, the data is transferred to the disk file of the SUN workstation which is accessible from the PC by NFS mount via TCP/IP. The maximum data transfer rate is about 50–60 kbytes/sec.

On the SUN workstation, an online sorting program is waiting for the arrival of the data. When the data newly arrives, the program starts sorting and updates the histograms. The histograms can be analyzed online by using the program GF2.³⁾

References

- 1) E. Ideguchi et al.: *RIKEN Accel. Prog. Rep.*, **27**, 121 (1993).
- 2) Y. Gono et al.: *ibid.*, **28**, 122 (1995).
- 3) D. C. Radford: private communication.

Development of an On-line Laser Ion Source Using Resonance Ionization in an Ion Guide Chamber at RIKEN GARIS/IGISOL

M. Hies, T. Ariga, T. T. Inamura, W. G. Jin, K. Morita, T. Murayama, Y. Pu, and M. Wakasugi

At the RIKEN GARIS-IGISOL facility a new on-line Laser Ion Source (LIS) system has been constructed. The nuclear reaction products are separated from the primary beam by using the gas filled recoil separator GARIS¹⁾ (see Fig. 1). The reaction products are implanted through a thin entrance window of 5 μm Al in a thermalization chamber (see Fig. 1), where the highly charged recoils are thermalized and neutralized in the buffergas, typically a noble gas like helium or argon. The not neutralized single charged recoil ions are removed with the help of an electric field towards an electrode inside the thermalization chamber. The remaining recoil atoms are transported with the help of the helium gas flow to the laser ionization chamber, where the atoms are ionized through incident pulsed laser beams via a multi-step ionization scheme. The ions created via resonance ionization are now flushed out with the help of the gas flow through a nozzle and are transported via a SPIG (sextupole ion beam guide)²⁾ and a skimmer towards the extraction and acceleration electrodes. After passing through the dipole magnet the mass separated and element selected secondary radioactive beam can be transported to a detector or a further experimental set-up. The new three chamber set-up (thermalization, laser ionization and nozzle chamber) is constructed in modular design to adapt to experimental conditions and to have good testing possibilities in off-line experiments.

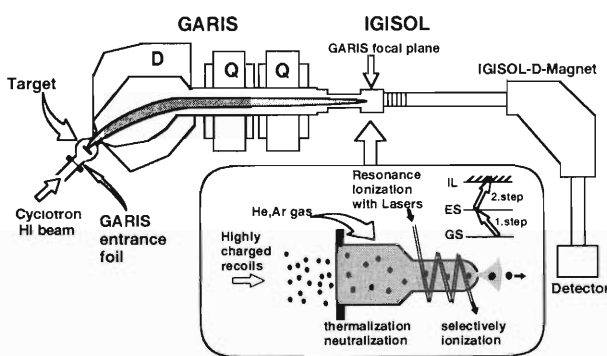


Fig. 1. On-line experimental setup.

First off-line experiments have been performed using stable hafnium. The atoms are produced via laser ablation when focussing a weak dye laser beam (0.3 mJ/pulse) on a Hf-plate in the thermalization chamber. The atoms are ionized via the two-colour-two-step excitation scheme as cited in Ref. 3. In Fig. 2 the ion count rate at the channeltron detector is shown

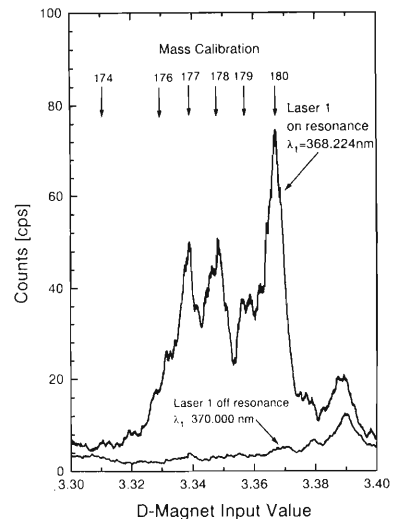


Fig. 2. Ion count rate at the detector position as a function of the D-magnet-current on laser resonance and off resonance. The arrows are marking the stable Hf isotope mass abundance. The laser repetition rate was set to 100 Hz and the second laser wavelength was fixed to an autoionizing transition at $\lambda_2=356.405$ nm.

as a function of the IGISOL-D-magnet current for the on resonance ($\lambda_1=368.224$ nm) and the off resonance case ($\lambda_1=370.000$ nm). The enhancement factor of ions with the mass 180 through laser ionization is about 15. The total transportation time was measured to 60 ms. However, only 1% of the Hf ions produced via laser ionization survive during the transportation with the gas flow towards the nozzle. The rest forms molecules like HfH_xO_y after collisions with impurities in the gas. To enhance the signal a further improvement in the gas purification and the vacuum conditions of the IGISOL chamber have to be done.

Beside using the new system as an ion source to provide highly selected radioactive ion beams, also laser spectroscopy experiments can be carried out by using the resonance ionization spectroscopy (RIS) to measure isotope shift and hyperfine structure of nuclei far from stability and determine their nuclear radii and nuclear moments.⁴⁾

References

- 1) K. Morita et al.: *Nucl. Instrum. Methods Phys. Res.*, **B70**, 220 (1992).
- 2) H. J. Xu et al.: *ibid.*, **A33**, 274 (1993).
- 3) M. Hies et al.: This report, p. 198.
- 4) E. W. Otten: *Treatise on HI- Sci.*, **8**, 517 (1989).

Operation and Status of the RIKEN EBIS (REBIS)

N. Watanabe, S. Kravis,* Y. Awaya, T. M. Kojima, K. Okuno, and M. Oura

Electron Beam Ion Source (EBIS) is widely used to study the physics of highly charged ions. The highly charged ions are formed by successive ionization by electron impact while ions are trapped inside the source using electric field which is produced radially by the space charge of the electron beam and axially by the applied dc potential. The EBIS has advantages that the pulsed ion beam operation which creates a higher charge state effectively, is available and the delivered ion beam has a low emittance and a low energy spread which enables one to carry out a high resolution experiment. We have constructed and operated a mini-size RIKEN EBIS (REBIS) based on Okuno's mini-EBIS.^{1,2)} This report presents the status of REBIS and some spectra obtained.

The REBIS is much smaller than typical EBISes which require liquid He for a superconducting solenoid and a residual gas trap. Adoption of the liquid nitrogen cooled solenoid, instead of the superconducting one, which can make enough magnetic field to pro-

duce bare ions with moderate Z species, enables us to reduce the size of REBIS. The existence of residual gas essentially restricts the performance of EBIS since the charge states of produced ions are easily decreased by the charge exchange with neutral atoms. In addition, since sample gas is normally introduced into the ionization region continuously, electron capture from neutral sample gas becomes a serious problem specially in the higher charge states. The REBIS is evacuated by two turbo molecular pumps and the non-evaporative getter (NEG) pump. The pumping system with an LN₂ trap can produce a vacuum in the low 10⁻¹⁰ torr range where the effect of charge exchange with residual gas is very small. Moreover, applying pulsed sample gas, the charge exchange with that was minimized and consequently the production rate of highly charged ions was significantly improved. Ions are extracted from a trap region after a given confinement time and charge analyzed by the time of flight (TOF) method. Figure 1 shows typical charge

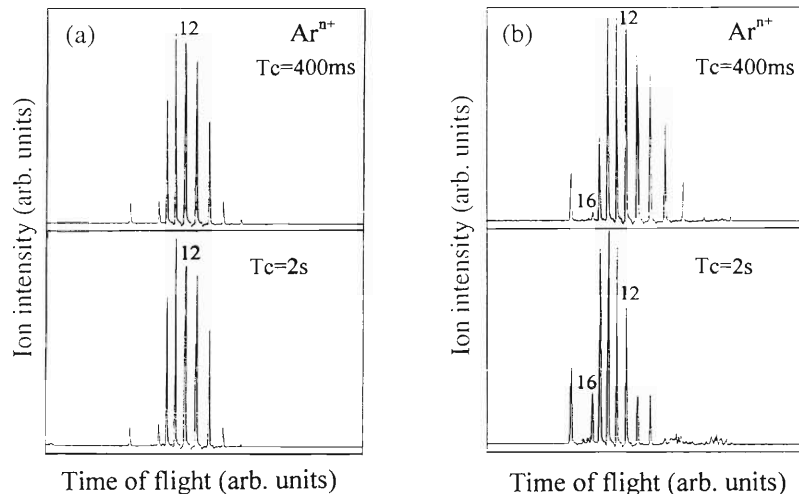


Fig. 1. TOF spectra for the continuous gas (a) and the pulsed gas operation (b), respectively. Tc represents a confinement time.

distributions for Ar ions extracted by 2 kV. The electron-beam current is normally only 5 mA. One can see that for the pulsed gas operation, the charge distribution shifts to higher states and a relative intensity of Ar¹⁶⁺ increases with the confinement time. On the other hand, for the continuous gas operation Ar¹⁶⁺ is not observable. Charge distribution for the continuous gas operation is almost saturated after 400-msec confinement, that is, the distribution does not change anymore in contrast to the pulsed gas case. The ion intensity is typically from 10 pA to 30 pA for

Ar¹¹⁺ for both the continuous and pulsed gas with 1-sec confinement. Ion current for the each charge state strongly depends on the operation condition, particularly the condition of the electron beam. Further tuning and characterizing the REBIS will be done.

References

- 1) K. Okuno et al.: *Nucl. Instrum. Methods Phys. Res.*, **B53**, 387 (1991).
- 2) S. Kravis et al.: *Rev. Sci. Instrum.*, **65**, 1066 (1994).

* Department of Physics, Kansas State University

Development of the Deuteron POLarimeter DPOL

S. Ishida, Y. Satou, H. Okamura, N. Sakamoto, H. Otsu, T. Uesaka, T. Wakasa, S. Fujita, T. Ohnishi, T. Nonaka, H. Sakai, T. Ichihara, T. Niizeki, N. Nishimori, and K. Hatanaka

We reported last year the construction and the first test experiment of a new vector and tensor Deuteron POLarimeter DPOL.¹⁾ In this year we slightly modified the configuration of DPOL to improve the performance.

A CH₂ block with 2.5 cm thickness was equipped as a scatterer to improve double scattering efficiency in addition to existing two plastic active scatterers described in Ref. 1. Thicknesses of the iron absorbers of the calorimeters CM1 and CM2 were also changed from 1.80 to 1.35 cm to cope with the increase of energy losses of particles in the thickened scatterer.

DPOL will mainly be used for spin transfer measurements in deuteron inelastic reactions at excitation energies up to 40 MeV with a deuteron polarized beam of 270 MeV. Therefore we have to know effective analyzing powers and efficiency of DPOL in the energy region from 230 to 270 MeV.

The calibration experiment was performed in this March with a 270 MeV polarized deuteron beam extracted from the RIKEN Ring Cyclotron. DPOL was installed in the second focal plane of the spectrograph SMART. The beam swinger magnet of SMART was set at 0° and the measurement was performed directly in the faint beam of about 5×10^4 deuterons/sec without any scattering in a primary target. DPOL was also calibrated at energies of 230 and 250 MeV. Such deuteron beams were obtained by using Al energy-degraders placed in the SMART target chamber. The depolarization effect by degrading the beam energy is

expected to be negligibly small.²⁾

Three combinations of the beam polarizations were used in this experiment and their ideal values of vector and tensor polarizations are $(p_z, p_{zz}) = (0, -2)$, $(0, 1)$ and $(2/3, 0)$, respectively.³⁾ The polarization axis was controlled with the Wien filter located at downstream of the ion source. The beam polarization was monitored by using the $d + p$ scattering at 270 MeV and typically 60–65% polarization of the ideal value was obtained throughout the experiment.

The cross sections corresponding to these polarized beams are written as follows :

$$\begin{aligned} \sigma(\theta, \phi) = \sigma_0(\theta) \times \\ \{1 + 2it_{11}iT_{11}(\theta) \cos \phi + t_{20}T_{20}(\theta) \\ + 2t_{21}T_{21}(\theta) \cos \phi + 2t_{22}T_{22}(\theta) \cos 2\phi\}, \end{aligned}$$

where it_{11} , t_{20} , t_{21} and t_{22} are beam polarizations and iT_{11} , T_{20} , T_{21} and T_{22} are effective analyzing powers of DPOL. Using the $\sigma(\theta, \phi)$ values corresponding to the polarized beams and the $\sigma_0(\theta)$ value obtained by an unpolarized beam, we can get all components of analyzing powers. The double scattering efficiency was also determined.

Figure 1 shows the preliminary result of the effective analyzing powers for the $^{12}\text{C}(d, d_0)$ reaction at $E_d = 270$ MeV. Large iT_{11} values are obtained.⁴⁾ The same data for the $^1\text{H}(d, ^2\text{He})$ reaction are shown in Fig. 2. In this reaction T_{20} and T_{22} have large values.⁵⁾ Thus DPOL can determine vector and tensor polarizations simultaneously by using the single polarimeter-system.

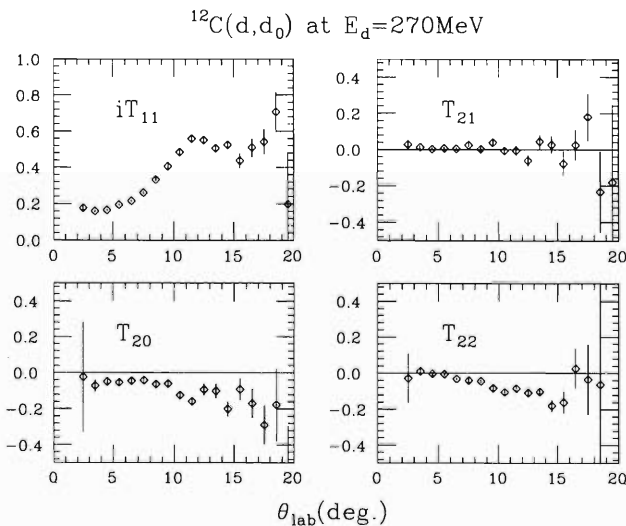


Fig. 1. Preliminary results of the effective analyzing powers of DPOL at $E_d = 270$ MeV for the $^{12}\text{C}(d, d_0)$ reaction.

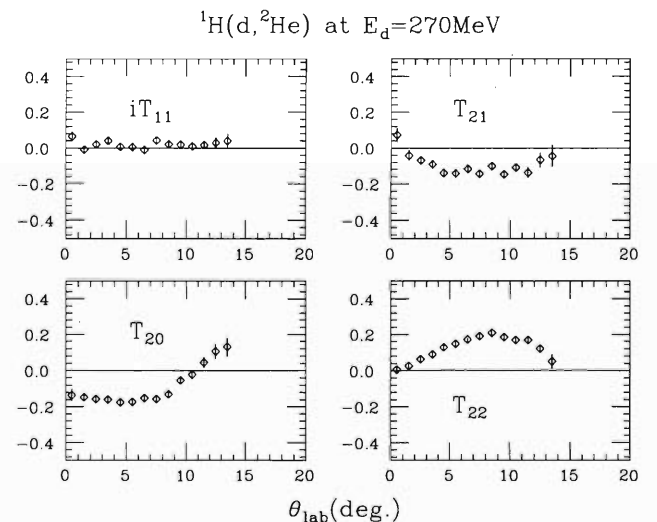


Fig. 2. The same as Fig. 1 for the $^1\text{H}(d, ^2\text{He})$ reaction. The excitation energy range of the pp pair is 0-4 MeV.

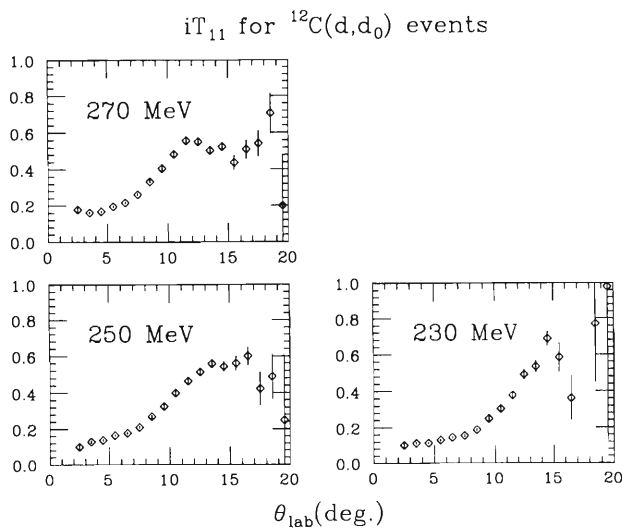


Fig. 3. Energy dependence of the iT_{11} values for the $^{12}\text{C}(d,d_0)$ reaction.

The double scattering efficiency is 1.2×10^{-2} for the $^{12}\text{C}(d,d_0)$ reaction and 0.9×10^{-3} for the $^1\text{H}(d, ^2\text{He})$ reaction.

Energy dependence of the performances of DPOL was also tested. For example, iT_{11} values for the $^{12}\text{C}(d,d_0)$ reaction at $E_d = 230, 250$ and 270 MeV are shown in Fig. 3. This result shows the stable performance of DPOL over an energy range from 230 to 270 MeV.

References

- 1) S. Ishida et al.: *RIKEN Accel. Prog. Rep.*, **28**, 125 (1995); *AIP Conf. Proc.*, **343**, 182 (1995).
- 2) S. Kato et al.: *Nucl. Instrum. Methods Phys. Res.*, **A238**, 453 (1985).
- 3) H. Okamura et al.: *RIKEN Accel. Prog. Rep.*, **28**, 148 (1995).
- 4) B. Bonin et al.: *Nucl. Instrum. Methods Phys. Res.*, **A288**, 389 (1990).
- 5) S. Kox et al.: *ibid.*, **A346**, 527 (1994).

Development of Polarized Xe Solid as a Means to Produce Spin Polarization in Stopped Unstable Nuclei

H. Sato, K. Mochinaga, M. Adachi, and K. Asahi

Recent results¹⁻⁴⁾ obtained at RIKEN Ring Cyclotron demonstrated that measurements of nuclear moments provide useful information on the microscopic structure of nuclei far from stability. In such experiments, producing spin polarization in the objective nuclei is a key technical ingredient. We are developing a new method to produce the polarization, which comprises the implantation of unstable nuclei in a highly polarized stopper and the subsequent transfer of the host nuclear polarization to them through dipole-dipole interaction. For the host material, we employ a ^{129}Xe solid for which a large spin polarization and a long relaxation time can be attained.⁵⁾ We started the study to polarize ^{129}Xe gas last year.

The ^{129}Xe nuclear spin is polarized by spin exchange with an optically polarized Rb atom. A cylindrical glass cell 4 cm long and 2.2 cm in diameter is filled with a natural Xe gas of a partial pressure p_{Xe} , an N_2 gas of 100 Torr, and a small amount of Rb vapor. The cell is illuminated by a circularly polarized light from a 2 W Ti:sapphire laser. Details of the principle of the method and of our apparatus have been described previously.⁶⁾

We studied the pressure dependence of the Xe polarization P_{Xe} by using several cells with different Xe gas pressures. The result is shown by dots in Fig. 1. A polarization as large as $P_{\text{Xe}} = 57.4\%$ is obtained at $p_{\text{Xe}} = 10$ Torr. P_{Xe} decreases with increasing p_{Xe} , but up to $p_{\text{Xe}} = 200$ Torr which amounts to the number of Xe atoms of 1.0×10^{20} , the polarization stays larger than 9%. In Fig. 1 are also shown theoretical curves which are derived from the rate equations describing the transfer of polarization among the laser photons, Rb atoms, Xe nuclei and a cell wall.⁷⁾ The theoretical P_{Xe} depends on the wall relaxation time T_w . For the cells used in this experiment, $T_w \approx 5$ min was obtained from the ^{129}Xe NMR signal amplitude measured as a function of time after the cell was cooled to room temperature. As shown in Fig. 1, the curve for $T_w = 5$ min indeed reproduces the data fairly well. Also, the curves indicate that a longer wall relaxation time will allow realization of a stopper with enhanced polarization and number of atoms. We are testing new glass cells whose

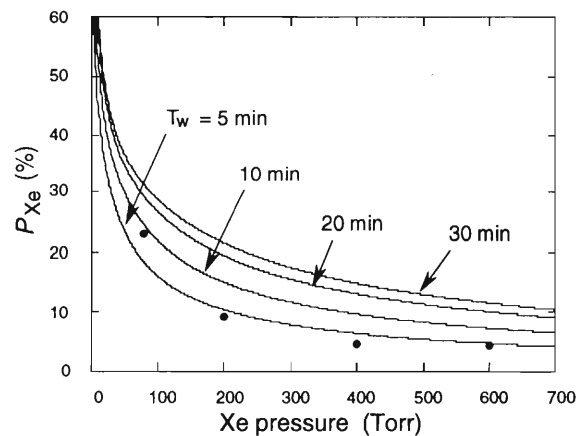


Fig. 1. Pressure dependence of P_{Xe} . The experimental data are shown by dots. Also shown are the theoretical curves obtained for several T_w .

inner surfaces are coated by dichlorodimethylsilane, with which T_w as long as 30 min is reported.⁸⁾

For a stopper to polarize implanted nuclei, a solid has to be produced from thus obtained polarized gas of Xe. A magnet to produce a 0.5 T field and an NMR system operated under this field were installed. This field is needed in order to lengthen the spin-lattice relaxation time of Xe in a solid phase. In order to solidify Xe gas, the cell is moved from the optical pumping setup to the high field region where the liquid N_2 bath to cool the cell is installed. We are investigating the condition for the adiabatic transport of the Xe sample so that the initial polarization is maintained during this process.

References

- 1) H. Okuno et al.: *Phys. Lett.*, **B354**, 41 (1995).
- 2) H. Izumi et al.: *ibid.*, **B366**, 51 (1996).
- 3) H. Ueno et al.: submitted to *Phys. Rev.*, **C**.
- 4) K. Asahi et al.: *Nucl. Phys.*, **A588**, 135c (1995).
- 5) M. Gatzke et al.: *Phys. Rev. Lett.*, **70**, 690 (1993).
- 6) H. Sato et al.: *RIKEN Accel. Prog. Rep.*, **28**, 128 (1995).
- 7) G. D. Cates et al.: *Phys. Rev.*, **A45**, 4631 (1992).
- 8) X. Zeng et al.: *Phys. Lett.*, **A96**, 191 (1983).

Development of the Detector for Sub-MeV β -Delayed Neutron

K. Yoneda, N. Aoi, H. Miyatake, H. Ogawa, Y. Yamamoto, E. Ideguchi, T. Kishida, T. Nakamura, M. Notani, H. Sakurai, T. Teranishi, S. S. Yamamoto, Y. Watanabe, A. Yoshida, and M. Ishihara

We developed a new type of a neutron detector in order to measure neutrons with energies as low as about 100 keV. The low-energy neutron detection is often required in studying structures of very neutron-rich nuclei via β -decay with neutron emission.

In our previous experiment on the β -decay of neutron drip-line nuclei ^{14}Be ,¹⁾ a prominent peak was found at the low neutron energy of 283 keV in the delayed-neutron spectrum. However, we could not deduce the branching ratio with sufficient accuracy due to the limitation of the low-energy neutron detection. The objective of developing new neutron detectors is primarily to determine precisely the branching ratio of the β -decay of ^{14}Be , and to apply the detectors to the similar cases in the future experiments.

The neutron detector used in the previous experiment was a plastic scintillator BC408 which has a rectangular shape with size of $6\text{ cm}^{(H)} \times 110\text{ cm}^{(W)} \times 6\text{ cm}^{(D)}$. We set the threshold at about 20 keV in electron equivalent energy, corresponding to about 200 keV for neutron energy. The threshold was calibrated with the energy of Compton edge of 662 keV γ -ray from a ^{137}Cs source. The detection efficiency for 283 keV neutron was only about 10%, and furthermore, the time-of-flight (TOF) spectrum of the delayed neutron might be distorted due to the rapidly changing function of neutron efficiency toward the lower neutron energy. These difficulties were attributed to the fact that the threshold was very close to the relevant peak energy. Further amplification of the light output by a photomultiplier tube (PMT) or by other electronic amplifying circuits cannot, by itself, lower the threshold, because of the fatal lack of initial photoelectrons in the PMT. In the measurement of 283 keV neutron, the number of scintillation photons that could reach the photocathode of the PMT was found to be less than 20 due to the small number of original photons and the poor transmission efficiency (about 8%) of the detector, and this implies that less than 5 photoelectrons could be emitted from the photocathode of the PMT. The only way to reduce the threshold is to increase the photon numbers impinging on the photocathode, which may be realized by making the detector with a shorter light path and thereby improving the transmission efficiency in the plastic scintillator.

We produced a plastic scintillation detector with size of $30.0\text{ cm}^{(H)} \times 4.5\text{ cm}^{(W)} \times 2.5\text{ cm}^{(D)}$. This short size of the detector enables us to obtain larger transmission efficiency, approximately 25%. In the case of detecting

283 keV neutron, about 70 scintillation photons may reach the photocathode and about 20 photoelectrons would be released from the photocathode, which would be enough for the 283 keV neutron measurement.

On the other hand, when we actually use this detector, the solid angle and the time resolution may cause a problem. We can overcome the decrease of solid angle due to the small size of this detector by making the neutron flight path shorter. However, a shorter flight path may cause worse resolution. As the optimum condition both for the solid angle and for the resolution, we set the neutron flight path 50 cm, one-fourth of the previous setup (2.0 m) so as to make the total solid angle to be 4.2% of 4π , which is comparable to that in the previous experiment. As for the time resolution, in the case of detecting 283 keV neutron, such a low energy allows us to obtain sufficiently long TOF even for the short flight path of 50 cm. In fact, the TOF is 68.3 ns for 283 keV neutron and the time resolution caused by the thickness of the detector is about 1.0 ns, corresponding to 1.5% for momentum resolution. This value is comparable to the resolution of the detectors which make the start signal of the TOF.

We applied this new neutron detector to the measurement of β -decay of ^{14}Be ²⁾ and ^{11}Li . The TOF spectrum of the β -delayed neutron of ^{14}Be is presented in the Ref. 2. The detection efficiency for 283 keV neutron detection was estimated to be about 50% from comparison between spectra of β -ray and neutron TOF, from each of which we can deduce the branching ratio. We were able to set the threshold at about 2 keV in electron equivalent energy (a few tens keV for neutron energy), which was calibrated with the low energy X-ray from a ^{133}Ba source and a ^{241}Am source. Such a low threshold enabled us to measure much lower energy neutrons, such as the β -delayed neutron of about 80 keV from ^{11}Li , which was not observed with the previous detector. The time resolution was deduced to be about 1.5 ns from the width of the prompt γ -ray peak in the spectrum. This resolution is to be improved by the further analysis. The peak width of a 283 keV neutron from ^{14}Be was found to be about 4 ns, much larger than the time resolution, implying that the resolution of the new detector is good enough to deduce the natural width of this state.

References

- 1) N. Aoi et al.: *RIKEN Accel. Prog. Rep.*, **28**, 38 (1995).
- 2) N. Aoi et al.: This report, p. 67.

Slew Correction for Timing Signals from NaI(Tl) Scintillators

T. Kikuchi, T. Motobayashi, S. Shimoura, and H. Murakami

Leading-edge discrimination is widely used to generate the timing logic signals, especially for fast signals from plastic scintillators etc. However, in using this type of discriminators, one encounters a famous *walk* effect. It is variation of the delay time of the output signals according to the amplitude of the incoming signal, which is caused by its finite rise time. So when the discriminators are used in coincidence experiments or TOF measurements, it is necessary to correct this effect in off-line analysis (slew correction) to improve the timing resolution.

For plastic scintillators, a simple method is often used for the slew correction,^{1,2)} that is $\Delta t = C/\sqrt{A}$, where Δt is the amount of the correction, A is the amplitude of the pulse and C is an adjustable parameter. An additional way is proposed²⁾ to take account of the pulse shape of the inputs directly. However, the authors concluded that it showed little difference from the former method in case of plastic scintillators.

We studied the walk effect for NaI(Tl) scintillators that gave slower signals than those of plastic scintillators. The results showed quite different features from the case of plastics, suggesting strong pulse shape dependence. We propose another method for the slew correction from the results.

We used a NaI(Tl) scintillator with a $6 \times 6 \times 12$ cm³ volume and the pulse shape was measured. It could be expressed as $V(t) = V_0(e^{-t/t_1} - e^{-t/t_2})$, with $t_1=230$ (ns) and $t_2=40$ (ns). For the triggering of leading-edge discriminators, the rise time t_2 is essentially important and the decay time is not. Another effect to be considered is the gaussian-like smearing that is caused by processes in the photo-tube and following circuits. By referring to the formula for plastic scintillators,²⁾ we can write down the effective pulse shape of NaI(Tl) as,

$$A_{th} = A(1 - e^{-t/\tau})^2, \quad (1)$$

where A is the amplitude of the pulse, A_{th} is the amplitude corresponding to the threshold, $\tau = t_{rise}/2.6$, and t_{rise} is the rise time of the pulse that is 40 ns in this case. Note that it gives the same correction as that with $\Delta t = C/\sqrt{A}$ at the limit of $t \ll \tau$. In the present slew correction, we improved further this formulation by replacing the second power in Eqn. (1) with the x -th power as a parameter. As a result, we got a new formula of slew correction as,

$$\Delta t = \tau \ln(1 - (\frac{A_{th}}{A})^x). \quad (2)$$

The power x should be adjusted for a given threshold level.

We applied this equation for the slew correction of the NaI(Tl) scintillators. The difference of the timing from the NaI(Tl) scintillator and a plastic scintillator was measured by detecting two γ rays from a ⁶⁰Co source in coincidence. Assuming constant timing for the plastic scintillator, we extracted the amount of walk for NaI(Tl) with some different settings of the threshold A_{th} . Examples of the results are shown by the two-dimensional spectrums in Fig. 1. The dots represent averaged time difference deduced from the experimental data at each amplitude, and the solid curves represent the slew correction using Eqn. (2). Adjusted values for the parameter x are 0.2 and 0.6 for A_{max}/A_{th} values of 60 and 5, respectively. The results show good agreements with the data in a wide range of amplitude. We tried also the method $\Delta t = C/\sqrt{A}$ for these data, which agreed only with the setting of very low thresholds. For the data of Fig. 1 (a), the achieved time resolution was much the same with both methods. However, for the data of Fig. 1 (b), the achieved time resolution was 5.5(ns) with the method $\Delta t = C/\sqrt{A}$, whereas that was 4.5(ns) with Eqn. (2).

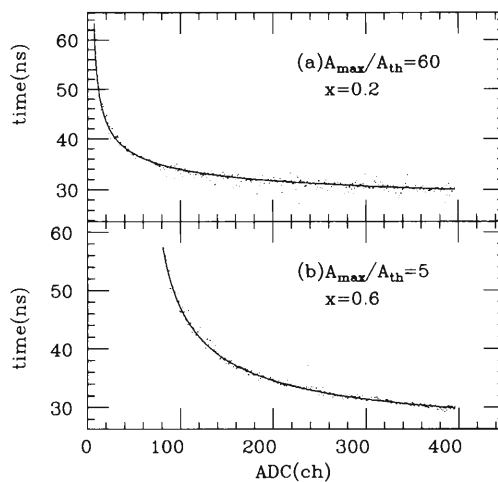


Fig. 1. Time difference between NaI(Tl) and plastic scintillators plotted versus ADC channel in cases of (a) a lower threshold and (b) a higher threshold.

References

- 1) T. Kobayashi and T. Sugitate: *Nucl. Instrum. Methods Phys. Res.*, **A287**, 389 (1990).
- 2) W. Braunschweig et al.: *Nucl. Instrum. Methods.*, **134**, 261 (1976).

NaI(Tl) Detector Assembly for Low Intensity Radiation (DALI)

T. Nishio, T. Motobayasi, K. Ieki, Y. Ando, H. Murakami, Y. Yanagisawa, Y. Iwata, T. Kikuchi, T. Uchibori, H. Fujiwara, T. Minemura, M. Suzuki, and S. Shimoura

A detector array DALI (Detector Assembly for Low Intensity radiation) has been constructed for measurements of γ ray from nuclear reactions with low yield. It consists of sixty four NaI(Tl) scintillators and six plastic scintillator plates. To achieve the high efficiency for γ rays, the detector should cover a large solid angle. An example of the geometry is shown in Fig. 1. The volume of NaI(Tl) scintillator is $6 \times 6 \times 12 \text{ cm}^3$. To reduce background contained between spectra due to cosmic rays, plastic scintillators of $1 \times 30 \times 90 \text{ cm}^3$

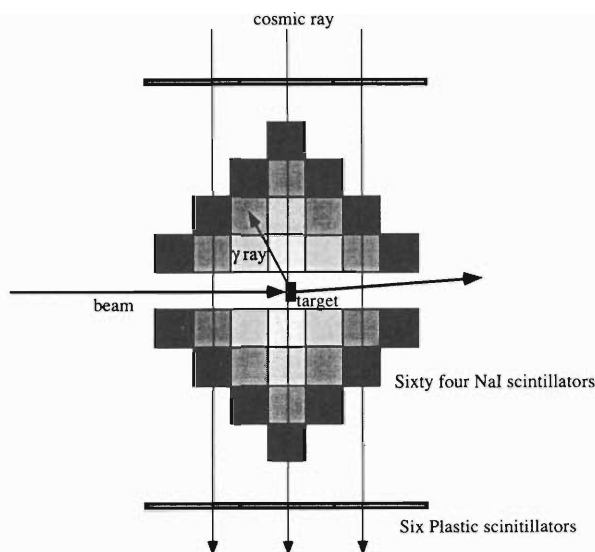


Fig. 1. The DALI setup by sixty four NaI scintillators and six plastic scintillators.

were set on the top and bottom of the NaI(Tl) scintillators as shown in the Fig. 1.

To gain fast signals suitable to trigger a fast discriminator, a timing filter amplifier (TFA) was developed. It amplifies the slow signals from the NaI(Tl) scintillator with a fixed gain and a fixed time constant of 22 ns. For the DALI setup, eight NIM-standard modules with eight parallel TFA units were fabricated.

The DALI has been used in the Coulomb excitation experiments with radioactive beams of 50–70 MeV/nucleon for the $^{208}\text{Pb}(^{32}\text{Mg}, ^{32}\text{Mg}\gamma)^{208}\text{Pb}^{1)}$ and $^{208}\text{Pb}(^{56}\text{Ni}, ^{56}\text{Ni}\gamma)^{208}\text{Pb}^{2)}$ reactions. The highly segmented structure of the DALI setup allows to correct a large Doppler shift caused by the fast ($v/c \sim 0.3$) production that emits γ rays. The total detection efficiency of the DALI for a full-energy peak was 20 and 9% for the 885 keV and 2.7 MeV γ rays, respectively, which are of interest in the above two experiments. This efficiency is for the events where one of the NaI(Tl) scintillators used with the DALI absorbs the entire γ -ray energy. The setup was used also in an experiment at Luvain-La-Neuve with a low energy (below 1 MeV/nucleon) radioactive ^{13}N beam. The 5.17 MeV γ ray from the $^1\text{H}(^{13}\text{N}, \gamma)^{14}\text{O}$ reaction was measured. The full-energy peak efficiency is estimated to be around 20%, if all possible combinations of energy deposited among the NaI(Tl) scintillators are allowed.

References

- 1) T. Motobayashi et al.: *RIKEN Accel. Prog. Rep.*, **28**, 37 (1995); *Phys. Lett.*, **B346**, 9 (1995).
- 2) Y. Yanagisawa et al.: This report, p. 76.

Summing Amplifiers for Heavy-Nucleus Search Experiments

T. Uchibori, T. Motobayashi, H. Murakami, M. Kurokawa, K. Morita,
Y. Pu, T. Nomura, and Y. Tagaya

In experiments of heavy-nucleus search, a detection system with high energy- and position-resolution is necessary to detect evaporation residues produced by fusion reactions. To identify the product, the energies of its successive α decays are measured.

For this purpose a system with a position sensitive detector has been developed¹⁾ and used in the experiment of $^{40}\text{Ar}+^{232}\text{Th}$ reaction.²⁾ Since the charge division method is employed to measure the position along a strip, signals from the two ends of the strip should be analyzed. In the experiment, the two signals are treated by two parallel amplifier systems independently and fed into peak-sensitive ADCs as shown in Fig. 1.

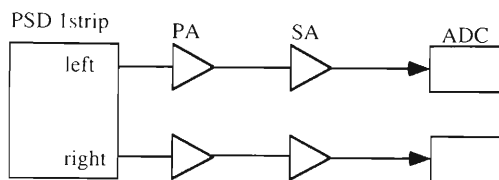


Fig. 1. The block diagram for a scheme without the summing amplifier.

The energy data are obtained by summing the two ADC outputs. This method, however, has a problem at low energies. The peak-sensitive ADC takes a maximum voltage during the gate duration. For low-energy α particles (below 1 MeV), this maximum can be due to a large thermal noise instead of the true energy signal, resulting in a wrong energy-sum datum. This thermal noise along the strip is mostly cancelled by integrating the charge from the two ends. This is achieved by summing the two signals as shown in Fig. 2 before analysis by the ADCs, and correct sum-energy signals are provided.

We developed an amplifier (SUM AMP) to realize

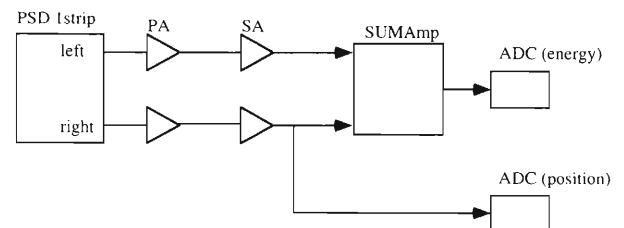


Fig. 2. The block diagram for a scheme with the summing amplifier.

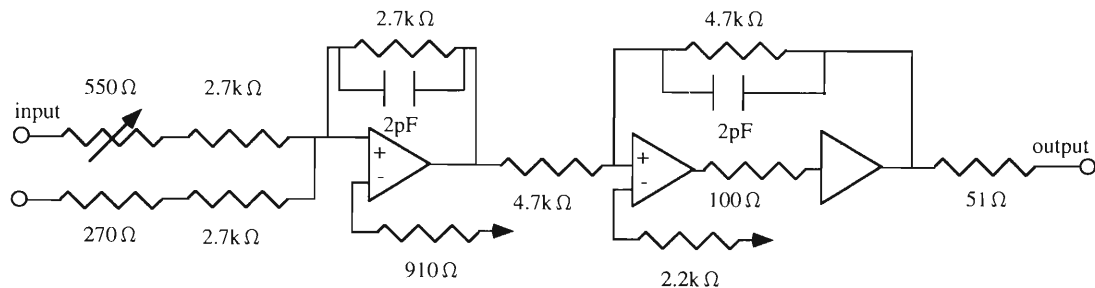


Fig. 3. The circuit diagram of the summing amplifier.

this analogue sum. A schematic diagram is shown in Fig. 3. By a variable resistance, fine adjustment of the gain is possible. This reduced much the time to calibrate all the channels for the 40 detector outputs. We fabricated NIM one-span modules that contain 8ch of the summing amplifier units.

Without the SUM AMP (Fig. 1), the energy resolution was measured to be 300-400 keV FWHM at energies lower than 1 MeV though it becomes 40-60 keV at energies higher than 6 MeV where the α decays from heavy nuclei are expected. When the SUM AMP is used (Fig. 2), the resolution in the low energy region was improved to about 100 keV. This

new system has been used in the $^{36}\text{Ar}+^{164}\text{Er}$ reaction experiment.³⁾ The present development improved the performance of the detection system especially for the α -decay escaped from the detector leaving a small energy signal.

References

- 1) M. Kurokawa et al.: Proc. Tours Symp. Nucl. Phys. II, Tours, France, Sept. 1994, World Scientific, Singapore, p. 428 (1995).
- 2) M. Kurokawa et al.: This report, p. 44.
- 3) Y. Pu et al.: This report, p. 43.

Test of a High-Rate MWDC for Heavy-Ion Detection

M. Yamagami, K. Miki, H. Utsunomiya, T. Yamagata,*¹ S. Kubono,
M. H. Tanaka, Y. Matsuyama,*² H. Sakurai, and T. Murakami*³

A high-rate coincident detection of α and ^{12}C is necessary for the study of Coulomb breakup of ^{16}O at the intermediate energy.¹⁾ We have built a prototype multi-wire drift chamber (MWDC) with the drift cell width of 5.0 mm in four planes (16 cm wide and 16 cm high) of X-X'-Y-Y' configuration. It was mounted behind the end of the beam line and was tested with beams of α and ^{12}C at 100 MeV/nucleon from the HIMAC at the National Institute of Radiological Sciences (NIRS). The chamber was operated with 50% He and 50% C_2H_6 mixture containing methylal as an additive. Helium-base gas mixture, instead of argon-base, was used to reduce the δ -ray contribution. We investigated the dependence of anode pulse-height distribution on the operating high voltage, δ -ray production, and the space charge effect with each beams. The number of beam particles was counted with fast signals from a plastic scintillator placed behind the MWDC. It was kept well below 10^3 particles per beam spill/cm(pps/cm), spill time being 0.4 second, for the pulse height study and was increased up to 10^5 pps/cm for studying the space charge effect.

Figure 1 shows pulse-height distributions of ^{12}C at cathode voltage (V_c) -1300 V. In this condition, the probability of firing of the neighboring wire by δ -rays was about 25%. The most probable pulse height of α and ^{12}C vs V_c (Fig. 2) and the space charge effect for

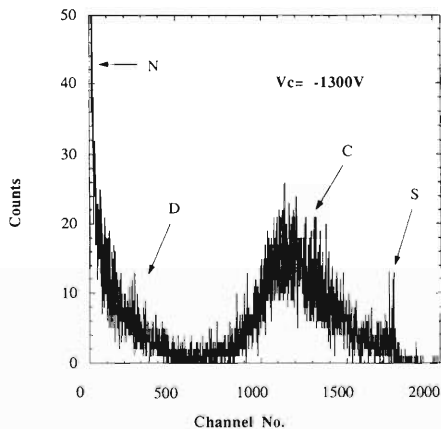


Fig. 1. Pulse-height distributions of ^{12}C at cathode voltage (V_c) -1300 V. Signals of ^{12}C (part C) are well separated from those of δ -rays occurred in neighboring cell (part D). Part S and N of the spectra are due to saturation of the signals and detector noises, respectively.

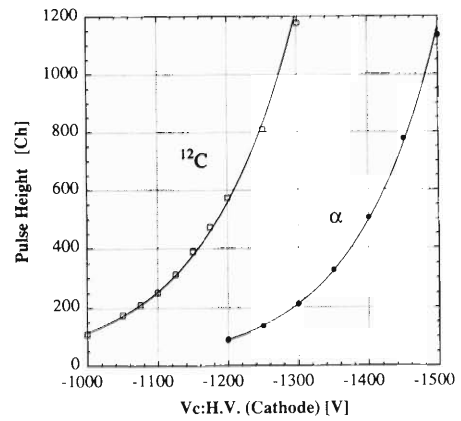


Fig. 2. Most probable pulse height of α and ^{12}C vs. V_c .

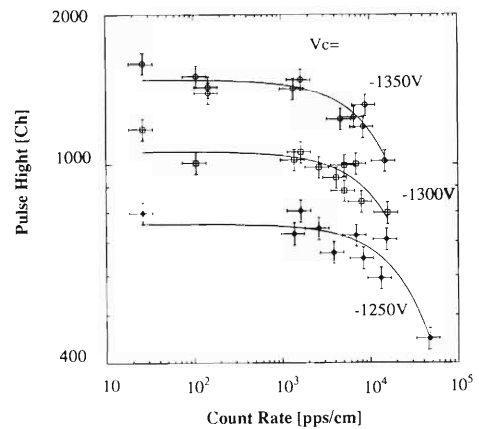


Fig. 3. Space charge effect for ^{12}C . The abscissas stands for the count rate in units of counts per second per cm for a wire.

^{12}C (Fig. 3) were presented. It was found that the MWDC works stably at the rate higher than 1×10^3 counts per second per cm for a wire, and have no sign of aging of wire after the test.

References

- 1) H. Utsunomiya, Y. Hirabayashi, M. Hirai, T. Ichihara, M. Kamimura, S. Kato, S. Kubono, T. Motobayashi, S. Okabe, H. Sakurai, and M. Yamagami: Proc. of Tours Symp. on Nucl. Physics II, H. Utsunomiya, M. Ohta, J. Galin, and G. Münzenberg (Eds.), World Scientific Publishing, Singapore, p. 126 (1995).

*¹ Department of Physics, Konan University

*² Institute for Nuclear Study, University of Tokyo

*³ National Institute of Radiological Science

Construction of a PPAC with High Position Resolution

H. Kumagai and K. Yoshida

A parallel plate avalanche counter (PPAC) with position resolution of less than 1 mm was developed as a focal-plane detector for the secondary beam separator RIPS.¹⁾ The existing PPAC was the one whose cathode had a strip structure with a 2 mm pitch. Figure 1 shows the position spectrum of the PPAC when the electrode was irradiated uniformly by α rays from ^{241}Am . The peaks seen in the figure correspond to the strips on the cathode. This is because the charge arising from the avalanche is collected with a few strips and hence, it is impossible to get the position resolution of less than 2 mm.

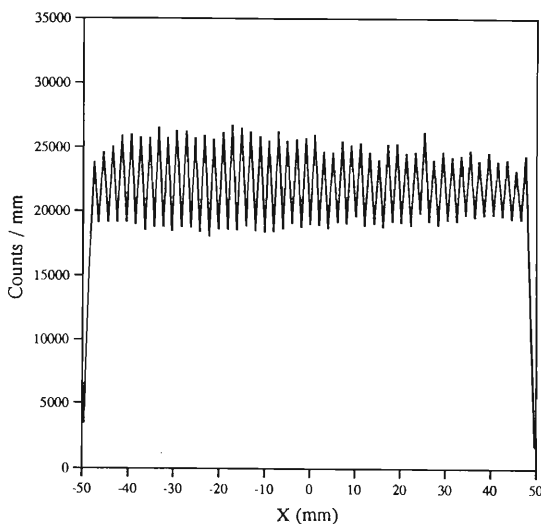


Fig. 1. The position spectrum for the PPAC with 2 mm strips uniformly irradiated by α rays of ^{241}Am .

In order to improve the position resolution, three types of PPACs with active areas of $50 \times 50 \text{ mm}^2$, $100 \times 100 \text{ mm}^2$, and $150 \times 100 \text{ mm}^2$ were constructed with an electrode with strips of 1 mm pitch. The strip was formed by evaporating gold on a polyester film with 0.8 mm width and 0.2 mm inter-strip gap. To make narrow strips on a wide area, we improved the support of the evaporation mask and the evaporation of gold was performed in a large vacuum chamber to avoid the thermal variation of the mask. The method to put resistor array on the electrode for the charge division read-out was also changed to make maintenance easy. Instead of the direct gluing of resistors, the board of resistor array was newly constructed and was attached to the electrode with an electric contact. Chip resistors of 150Ω were used as the resistor array for the PPAC with an active area of $150 \times 100 \text{ mm}^2$ and 200Ω was used for the others.

In Fig. 2 shown is the position spectrum with a new

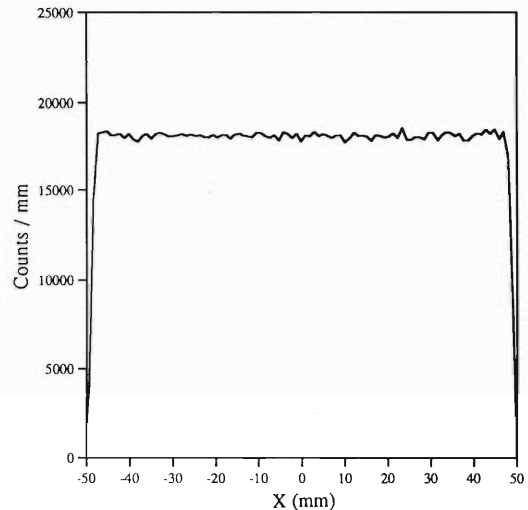


Fig. 2. The same figure as Fig. 1 except for the PPAC with 1 mm strips.

$100 \times 100 \text{ mm}^2$ PPAC irradiated uniformly by α rays from ^{241}Am . As seen, the position spectrum is almost flat and the peaks corresponding to the strips disappear. The differential linearity of the position is less than 2% for all types of the PPAC. The value of 2% corresponds to the error of the resistor used. The integral linearity of the position is shown in Fig. 3 for the case of a $100 \times 100 \text{ mm}^2$ PPAC. The linearity obtained is $\pm 0.1 \text{ mm}$ for the positions within $\pm 45 \text{ mm}$. For a PPAC with $150 \times 100 \text{ mm}^2$ active area, the value is $\pm 0.3 \text{ mm}$ for positions within $\pm 70 \text{ mm}$. The position resolution was measured by placing an aluminum slit

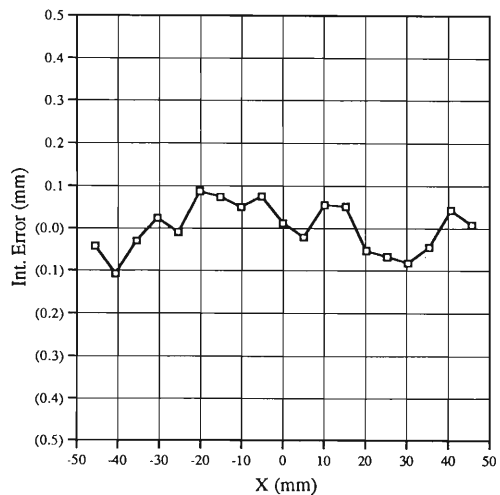


Fig. 3. Integral linearity of the PPAC with an active area of $100 \times 100 \text{ mm}^2$ and 1 mm strips.

with a 0.3 mm gap between the PPAC and the ^{241}Am source and was 0.3, 0.6, and 0.9 mm in FWHM for PPACs with active areas of $50 \times 50 \text{ mm}^2$, $100 \times 100 \text{ mm}^2$ and $150 \times 100 \text{ mm}^2$, respectively. These values correspond to the position resolution of 0.6% for all PPACs.

The PPAC with an $150 \times 100 \text{ mm}^2$ active area is now used as a focal plane detector of RIPS at F1. The PPACs with $100 \times 100 \text{ mm}^2$ are used at F2 and

F3. The PPAC with $150 \times 100 \text{ mm}^2$ is also used for the beam tracking for the radiation damage measurements of semiconductors at E3 experimental room.

References

- 1) T. Kubo, M. Ishihara, N. Inabe, H. Kumagai, I. Tanihata, K. Yoshida, T. Nakamura, H. Okuno, S. Shimoura, and K. Asahi: *Nucl. Instrum. Methods Phys. Res.*, **B70**, 309 (1992).

Heavy Ion Beam Test of Cosmic Ray Telescope for the First Brazilian Scientific Satellite

T. Kohno, H. Kato, I. Yamagiwa, and K. Nagata

We are promoting a joint collaboration program¹⁾ of solar and anomalous cosmic ray observation with United States group and Brazilian group aboard the first Brazilian scientific microsatellite. Assembling and integrating the telescope box with seven solid state detectors and charge sensitive pre-amplifiers are in charge of our Japanese group. We are now going to make an engineering model (EM) which will be tested by heavy ion beam exposure in addition to various environment tests such as vibration test, thermal vacuum test, and electromagnetic compatibility test. After clearing all these tests and confirming that there is no problem in the design of the overall system, we proceed to the integration of flight model (FM) using space specification parts and material.

The EM of the telescope box is now nearly completed. The main amplifiers, ADC board and the digital board which are in charge of US and Brazilian groups are not yet completed. Therefore we performed the first heavy ion beam experiment of our telescope system. The telescope structure is shown in Fig. 1.

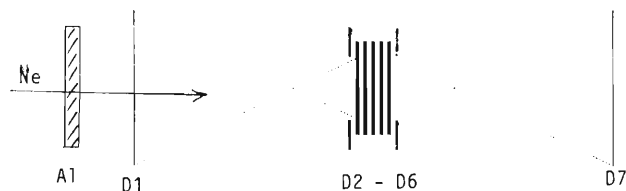


Fig. 1. Cross sectional view of the telescope and the beam arrangement.

The main amplifiers used in this experiment were our standard modules which we made using custom hybrid ICs. The design of this custom IC of pulse shaping main amplifier is basically identical to the hybrid IC which will be used in the flight model. The used beam was Ne-20 of 135 MeV/nucleon.

In order to examine the telescope response for a wide energy range, we took data for various Al thicknesses of an energy degrader which is shown in Fig. 1. We could confirm that each detector response to various energies of Ne beam is consistent with the expected value obtained by calculation. Here we show in Fig. 2 an example of scatter plots of D2 + D3 vs D2 + D3 + D4. The spread of the total energy seen in the abscissa comes from the energy loss straggling in the Al degrader with a thickness of 9.5 mm placed in front of D1. In addition to the main group of Ne, we can see the tracks of fragments from F to Be produced in the Al degrader.

Furthermore the isotopic tracks in each element can also be seen. Using $\Delta E - E$ method we made a histogram of atomic number distribution for this scatter plots, which is shown in Fig. 3. The mass resolution of $\sigma_m = 0.6$ in FWHM was obtained.

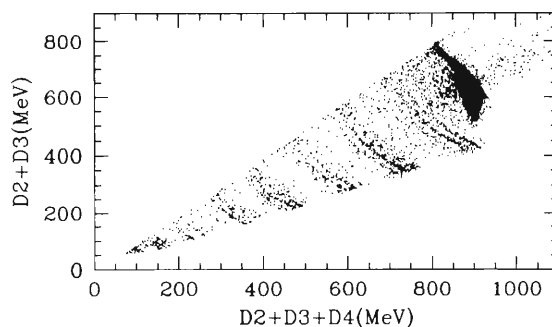


Fig. 2. Scatter plots of D2 + D3 vs D2 + D3 + D4 for the case of Al thickness of 9.5 mm. The condition for this plots is only events stopped at D4.

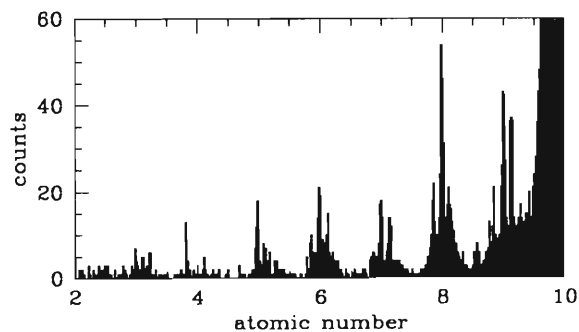


Fig. 3. The atomic number histogram for events shown in Fig. 2.

At the real observation in space, cosmic rays enter the telescope from various directions within the opening angle of 22° , degrading the resolution due to the pathlength dispersion in the ΔE detector. Therefore we cannot observe isotopic distribution. (Our purpose is elemental observation.) But by this experiment, we could confirm the mass resolution of the telescope for the parallel beam in addition to the general response of each detector.

References

- 1) T. Kohno et al.: *RIKEN Accel. Prog. Rep.*, **28**, 132 (1995).

Progress in Beam Optics for RIKEN-RAL Muon Facility

K. Ishida, T. Matsuzaki, I. Watanabe, and K. Nagamine

There has been major improvement in the muon beam size since the beam was first produced at the RIKEN-RAL Muon Facility in Rutherford Appleton Laboratory on Nov. 9th of 1994,¹⁾ although the muon beam intensity itself has not much changed. Also some basic characteristics of the beam line were measured.

1. Measurement of basic characteristics of the beam line by using surface muons

Surface muons are produced when the pions stop and decay into two-body in the production target. The momentum spectrum of the muons emitted from the target surface has a sharp high momentum cutoff at 29.8 MeV/c and a slope to the lower momentum side due to the various thicknesses that the muons have to penetrate to come out. In order to test the various characteristics of the beam line such as finite momentum acceptance, we measured how the muons with this spectrum are transported to the end of the beam line.

The muon beam intensity was measured as in Fig. 1 for various momentum settings. The horizontal axis is the center momentum of the beam line calculated from the magnetic field measurement. The position of the high momentum cutoff after correction of the energy loss in foils in the beam line was used for determining the real momentum-versus-setting relation, which was found to be in good agreement with that expected. The sharpness of the high momentum cutoff reflects the finite momentum bite of the beam line. The four lines in Fig. 1 are the result of calculation assuming Gaussian with standard deviations of 0, 1, 2, and 4%. The measurement coincides with the line of 2% in agreement with the optics design calculation. The measured slope at a low momentum side was

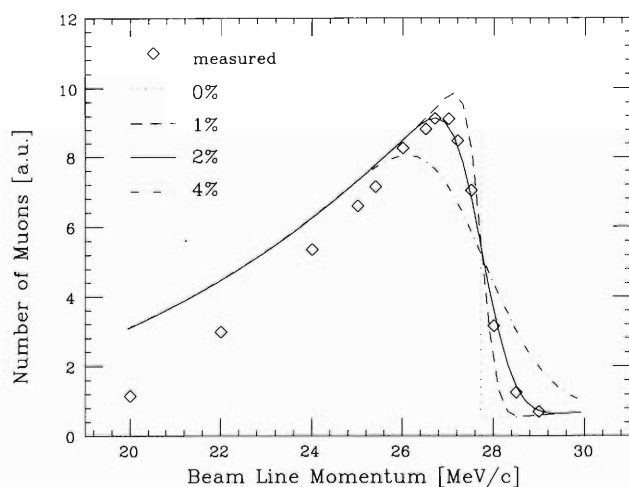


Fig. 1. The measured muon beam intensity versus beam line momentum. The four lines are the calculation with momentum bite of 0, 1, 2, and 4% (standard deviation).

sharper than the calculation probably due to the increased multiple scattering in the beam line foils. The measurement also indicates some muons existing above the cutoff momentum, although at much lower intensity, which is considered to come from the low energy pions decaying in flight around the production target.

2. Improvement of the beam size

As the μ SR method is applied to new materials such as high T_c superconductors, it has become increasingly common that these valuable samples are available only in a small quantity. Typical sample area is less than 20 mm by 20 mm and considerably smaller than the typical beam size. This could cause a serious problem. In a typical μ SR setup like in Fig. 2, the muons are focused to the sample and the positrons from muon decay are detected.²⁾ However, the muons which did not hit the sample may stop in surrounding materials such as cryostat windows, sample holder or detectors. The μ e decays from them may dilute the real signal from the sample or add complication to the interpretation of the μ SR signal. In order to avoid this, a collimator system made of lead is normally used to limit the beam size. However, the muons stopping in the collimator itself may become a source of background when the space restriction does not allow the collimator to be thick enough to stop the positrons produced. So there has been a great demand to make the beam size as small as possible.

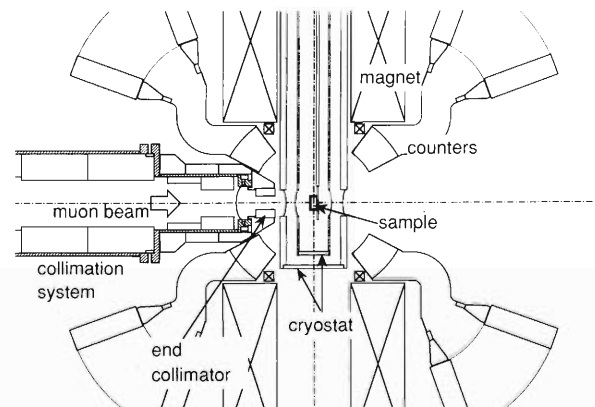


Fig. 2. Typical μ SR setup showing a basic collimator system with exchangeable end collimator, μ e detectors and sample in the cryostat.

Figure 3(a) shows the typical beam envelope for the part of the beam line from the solenoid exit to Port 2 where the μ SR setup is located. The beam line had been designed to obtain the maximal muon beam intensity. In that case the beam size was typically

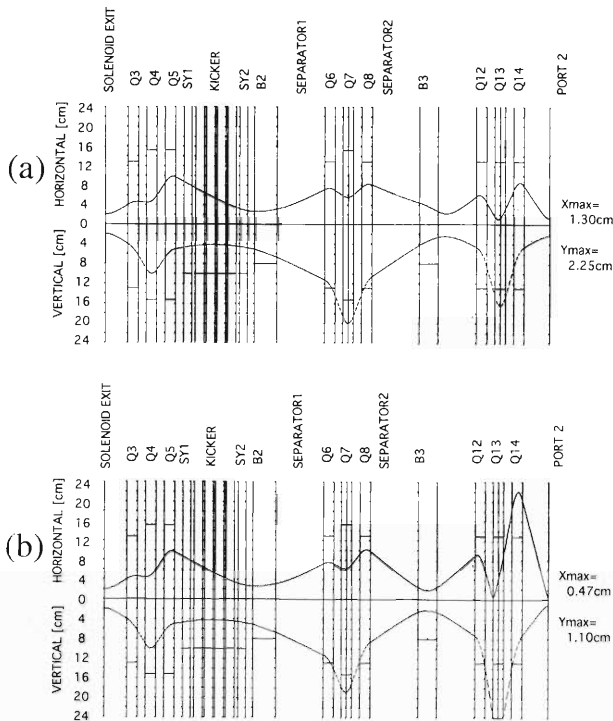


Fig. 3. (a) Calculated beam envelope for the original intensity-oriented beam line setting, and (b) that for the revised size-oriented settings.

around $40\text{ mm} \times 40\text{ mm}$. The design was changed recently aiming at obtaining a smaller beam size. Figure 3(b) shows the result of new calculation, where the beam size was minimized rather than maximizing the total beam intensity. Because of the principle of phase space conservation, we have to increase the beam divergence as we try to make the beam size smaller. This means that the beam becomes wider in the last quadrupole and more muons are lost there. However, these lost muons had been contributing mainly to the background and thus we do not lose too many signals.

This idea was tested recently. Figure 4 shows the number of μe decay for the original intensity-oriented setting and the new size-oriented setting. The μe

rate was measured for three typical sample conditions, namely “sample out”, “small sample ($20\text{ mm} \times 20\text{ mm}$)” and “large material ($50\text{ mm} \times 50\text{ mm}$)”. The subtraction of the first two gives the rate from the real sample and the subtraction of the last two gives the rate from the surrounding materials typically associated with a cryostat. We also tested placing a small end collimator to limit the beam size. The signal to noise ratio (S/N) was improved for the case with new size-oriented tuning and a smaller collimator size.

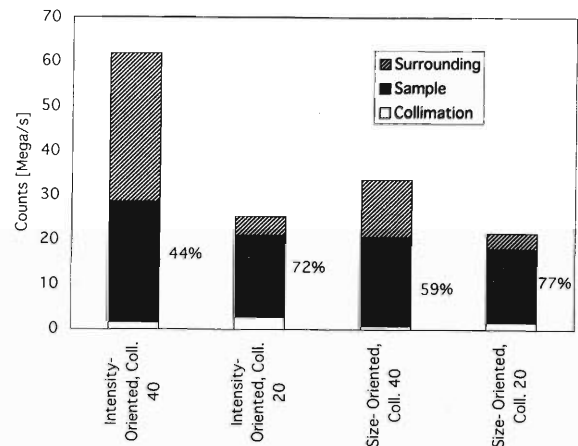


Fig. 4. Source of μe decay signals for two beam line settings and two sizes of end collimator hole. The fraction coming from a 20×20 sample was improved for size-oriented settings with the use of 20 mm end collimation.

This method may be applied also to the decay muon beam depending on whether the intensity or the S/N is important.

The authors thank Drs. G. H. Eaton, R. Kadono, and F. Pratt for the discussions on the improvement of the beam line.

References

- 1) K. Nagamine: *Hyperfine Interact.*, **87**, 1091 (1994).
- 2) R. Kadono et al.: This report, p. 196.

New Data Acquisition System for RIKEN-RAL μ CF Experiment

S. N. Nakamura and M. Iwasaki*

With the most powerful pulsed muon beam, a μ CF experiment is going to be carried out at RIKEN-RAL Muon Facility. In order to acquire a large number of data measured in this experiment, a new data acquisition system (*EXP95*) was designed. Following characteristics are required for the new system:

- A large number of data (1000 words/pulse = 50000 words/sec at maximum) can be acquired without serious dead time.
- Quality of obtained data can be checked during data acquisition.
- Off-line analysis can be performed by the the same software which is used for the on-line analysis.
- User-friendly graphical user interface is desirable.

To achieve above requirements, *EXP95* was designed. In the following section, the hardware and software configuration will be described.

(1) Hardware Configuration (see Fig. 1)

EXP95 system consists of two computers. One is a CAMAC Auxiliary Crate Controller (ACC: Kinetics

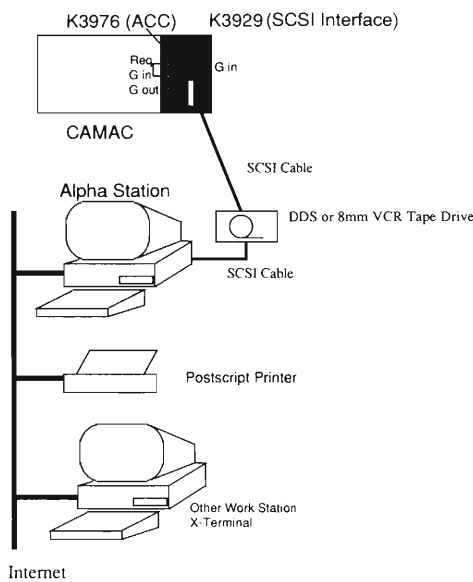


Fig. 1. Hardware configuration:

In the μ CF experiment at RIKEN-RAL Muon Facility, signals from detectors are converted to digital information by CAMAC modules. ACC K3976 reads module data and stores the data on its memory. These data will be transferred to the host computer (alpha station) via SCSI bus and stored on DDS/8 mm VCR tapes. On-line analysis results can be printed out by a postscript printer via network. On-line analysis results can be monitored from other workstations and X-terminals.

K3976) which concentrates on data taking. This computer has an MC68030 40MHz CPU with 1MB memory (upgradable to 4MB) and is able to access directly to the CAMAC modules which convert a detector signal to digital information. Typically, one word data acquisition takes 1.6 μ sec. When the memory of ACC becomes full, acquired data will be transferred to a host computer via CAMAC-SCSI interface (Kinetics K3929) by Direct Memory Access (DMA). Heavy tasks such as data analysis and data storage will be carried out by the host computer. Current *EXP95* system uses DEC alpha station as a host computer. The K3929 CAMAC-SCSI interface is also used at RIKEN Ring Cyclotron.¹⁾ The SCSI interface data transfer rate is not very fast (376 kword/sec in our case); however, DMA does not take place very frequently (typically less than once in every 30 sec) and it is not a serious problem. The advantage of SCSI interface is that it is widely used for workstations (WS) and personal computers (PC) and almost all WS/PC are equipped with it. Recently, the performance of computers increased very rapidly and the analysis software becomes heavier. When host computer becomes out of date, it can be easily replaced by a faster (less expensive) computer with SCSI interface.

(2) Software Configuration (see Fig. 2)

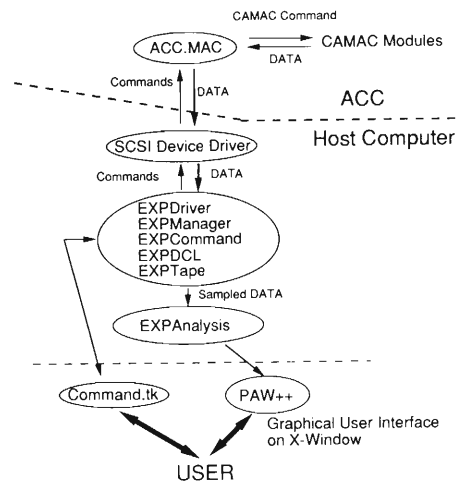


Fig. 2. Software configuration:

EXP95 software can be roughly categorized in three. The first one is MC68030 machine routine on ACC which handles CAMAC commands and DMA request. The second one is *EXP95* main routine which consists of six processes. They communicate with each other to accept user commands, receive data from ACC and store the data on a hard disk. The last software is *PAW++* developed at CERN. Some parts of the stored data are handed over to *PAW++* for on-line analysis.

* Meson Science Lab., School of Science, University of Tokyo

On ACC K3976, the program which manages CAMAC commands is running. This program is written by MC68030 assembly language. A user can easily write CAMAC commands sequence using Macro library without any knowledge on MC68030 CPU. MC68030 cross-assembler is prepared on the host computer and the machine code will be loaded to K3976 by just selecting one button on *EXP95* main window.

On the host computer, several processes are running on Open-VMS to receive data from ACC, store data on a hard disk, accept commands from user and so on. SCSI device driver was written using Queue I/O system with a help of Dr. E. Widmann (CERN). On-

line and off-line analyses were performed by *PAW++* software developed at CERN.²⁾ *EXP95* handed over some parts of acquired data to *PAW++* and the data quality can be checked during experiment. Acquired data will be stored on a hard disk and DDS (Digital Data Storage) device for off-line analysis. Stored data can be analyzed after the experiment with the same software used for the on-line analysis. *PAW* is working on many platforms (even on PC), thus alpha station is not necessary for the off-line analysis.

The user-friendly graphical user interface was constructed on X-Window system (Fig. 3). The X-Window system can open windows on the other work-

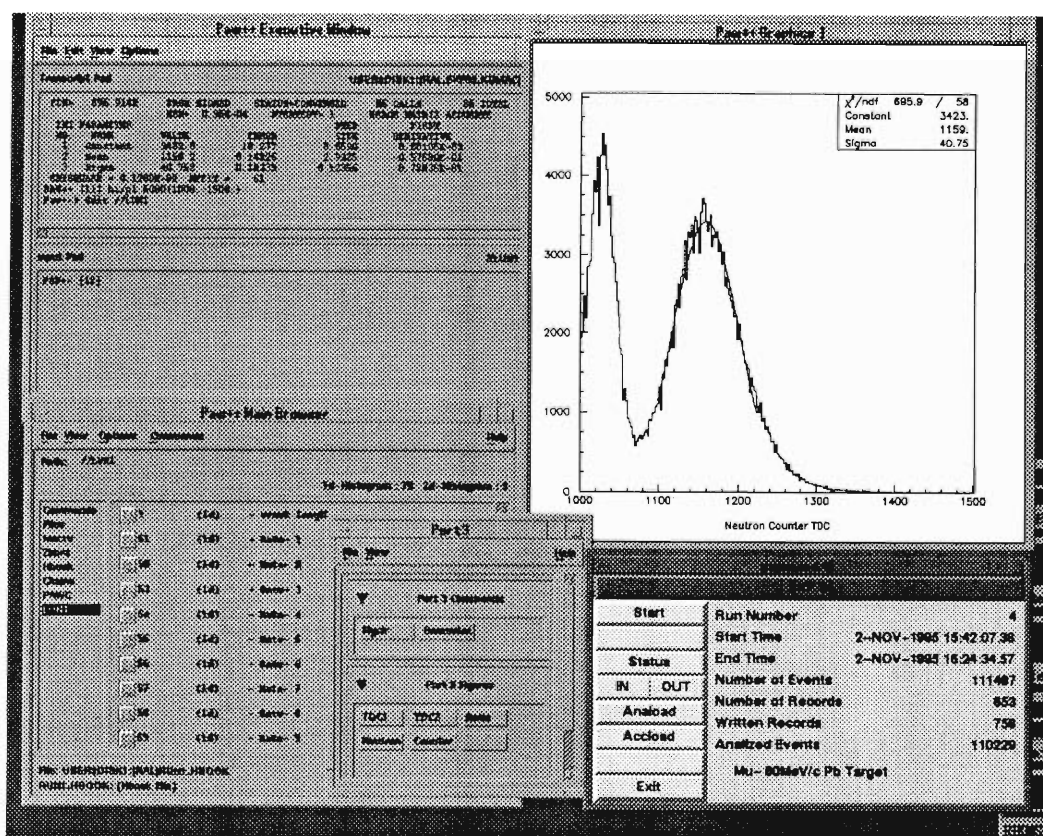


Fig. 3. *EXP95* User Interface:

Main window locates right-down; run information and command panels are displayed. Obtained data are analyzed by *PAW++*. Histogramming and data fitting can be easily done with *PAW++*.

station or X-terminal via network. Thus, it is possible to monitor the data taken in UK from the Wako campus though the response speed will be much affected by band width of the network.

As a host computer, a DEC alpha station with Open-VMS is now required. In the future, there is a plan to export *EXP95* to a less expensive PC. This data acquisition system was designed for the μ CF experiment at RIKEN-RAL Muon Facility; however, it

can be also used for μ SR experiments and nuclear experiments performed at RIKEN Ring Cyclotron and KEK-PS.

References

- 1) N. Aoi, Y. Doki, Y. Watanabe, T. Ichihara, and A. Yoshida: *RIKEN Accel. Rep.*, **26**, 113 (1992).
- 2) CERN Application Software Group: CERN Program Library, **Q121** (1995).

Installation of Tritium Gas Handling System for Muon Catalyzed Fusion Experiment at RIKEN-RAL Muon Facility

T. Matsuzaki, K. Ishida, I. Watanabe, K. Nagamine, M. Kato, K. Kurosawa,
M. Hashimoto, and M. Tanase

A tritium gas handling system (TGHS) has been constructed for the muon catalyzed fusion (μ CF) experiment at RIKEN Muon Facility of Rutherford Appleton Laboratory (RAL) in U.K. A high purity D_2/T_2 target gas is required in the experiment for a precise measurement of sticking probability in μ CF cycle. The purification system employing a palladium filter in the TGHS can produce a high purity D_2/T_2 gas without ^3He impurity-component which is a decay product of tritium and captures a negative muon to terminate the μ CF cycle. The mixing ratio of D_2/T_2 target gas can be adjusted in the system at the experiment site. The detailed design of the TGHS was described in a previous report.¹⁾

The construction has been completed after various tests and inspections to conform to a tritium gas handling system. In the factory test, the performance of purification device was investigated. The D_2 gas with ^3He impurity of 1% was purified by passing through the palladium filter and was analyzed by a gas chromatograph in the system. In Fig. 1, the component spectra are shown; (a) before and (b) after the purification process. It was proved that the ^3He impurity

component could be removed completely after the purification process.

The globe box containing the TGHS, secondary enclosure clean-up system (SECS) and experimental target were transported to RAL and reconstructed in port-1 experiment area of RIKEN Muon Facility. The whole system was placed on a mobile stand adjacent to a superconducting magnet to confine not only the muon beam to the target but also the decay electrons not to hit the detectors.²⁾ In Fig. 2, the glove box with the TGHS and SECS at Port-1 are shown. The superconducting magnet and muon beam line are seen behind the TGHS system.

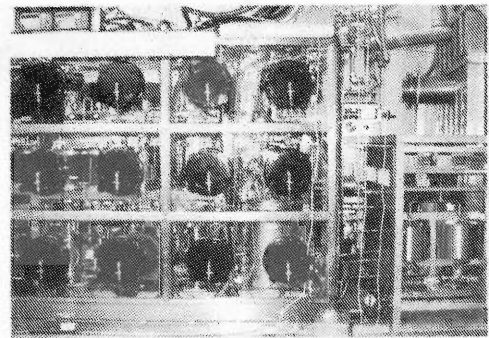


Fig. 2. Photograph of the TGHS for μ CF experiment at Port-1 experiment area of RIKEN Muon Facility.

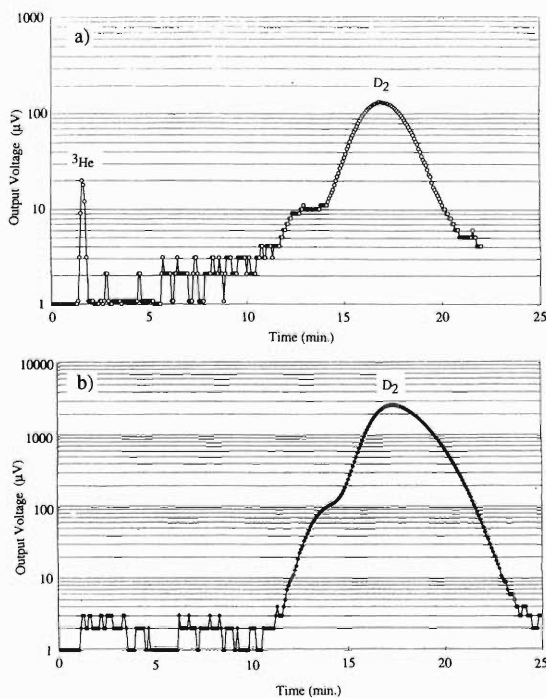


Fig. 1. Component spectra of the gas chromatograph are shown; (a) before and (b) after the purification process.

The various tests were conducted to confirm the integrity of the TGHS; helium leak, pneumatic and pressure tests for the tritium gas line and the pneumatic test for the glove box. Under the working magnetic field, normal operations of automatic valves, pressure gauges, thermometers, moisture gauge and oxygen meter were confirmed to investigate a possible magnetic field effect to the whole system operation. The electrometers for in-line tritium monitors were relocated to evade the leakage flux by extending triplex cables from the ion chamber which transmit a very weak current.

The operation tests for major components in the TGHS were conducted to approve their performance. The inner gas of the glove box (3.4 m^3) was replaced by argon gas. In order to confirm the performance of the SECS, the moisture and oxygen concentrations of the glove box gas, instead of the hydrogen component, were measured by circulating it through a ZrFe getter of the SECS, where the flow rate was 2 liter/sec. After two hours operation, the moisture and oxygen concentrations were reduced from 600 ppm and 17 ppm down

to 220 ppm and 1 ppm, respectively.

A tertiary house with a ventilation system, as the third enclosure, was built around the TGHS and superconducting magnet at Port-1. Two environmental tritium gas monitors are located in the house. A stack gas monitor and a bubbler system to measure a tritium water component are placed in the ventilation line.

The power control panel of the TGHS and electrometers for the in-line tritium monitors were placed in a separate room of the house. The electric power for the TGHS, SECS, tritium gas monitors and ventilation system is supplied from an unperturbed power supply which can last the power for 20 minutes to complete the shut down procedure of the whole system at a possible power failure.

Two independent safety interlock systems were constructed for a redundancy. For a safety approval to the whole system, a large number of discussions and document-preparation were done.

The performance test of the whole system will be conducted by using D₂ gas and then a low level activity test of tritium will be scheduled before the full activity operation.

References

- 1) T. Matsuzaki et al.: *RIKEN Accel. Prog. Rep.*, **28**,134 (1995).
- 2) K. Nagamine et al.: *Muon Catalyzed Fusion*, **1**, 121 (1987).

Development of a New μ SR Spectrometer ARGUS

R. Kadono, I. Watanabe, K. Ishida, T. Matsuzaki, and K. Nagamine

In the time-differential μ SR experiment with a pulsed muon beam, the pile-up of decay positron events due to the limited time resolution of the detection system leads to the distortion of time spectrum. This problem of distortion is already quite appreciable in the time spectra obtained by the spectrometers with multistop TDC's currently used at the existing pulsed muon facilities and gives rise to a bottleneck of data acquisition rate: The incoming muon rate is reduced by beam collimation so that the distortion may remain within an acceptable level. This constraint on the acceptable positron rate leads to the limitation of practical muon rate which is far below the highest intensity currently available from the muon sources at the Rutherford Appleton Laboratory (RAL).

One alternative to cope with this challenging muon (and positron) rate is to move on to the so-called *analog* technique¹⁾ in place of the established digital method,²⁾ where the analog output from the positron detectors is recorded/analysed assuming that the signal amplitude is proportional to the instantaneous number of positron events within a time bin. This technique, however, has uncertainty in the estimation of statistical errors. Another conservative choice is to increase both time resolution and detector segmentation in the conventional digital technique to cover the predicted event rates with acceptable level of pile-up distortion. The current RIKEN system is aimed at the latter solution, which is an important part of the new muon facility completed recently at the Rutherford Appleton Laboratory under RIKEN-RAL collaboration.³⁾

The new μ SR spectrometer ARGUS (Advanced Riken General-purpose μ SR Spectrometer) is designed to collect good μ -e decay events from 192 positron detectors covering more than 20% of the entire solid angle (see the schematic view in Fig. 1). This makes it no longer practical to select good events by the coincidence technique (i.e., to accept events occurred simultaneously in a pair of positron detectors aligned along the positron path). One of the major steps taken for the design of positron counter is to get a direction sensitivity without resorting to the coincidence technique. This has been accomplished by discrimination of light intensity in a planer scintillator which is dependent on positron trajectories. The drawing of scintillators with rigid light guides and photomultipliers is shown in Fig. 2a. The longer axes of the scintillators are aligned in the radial directions so that the positrons from the sample position penetrate through their longest path. The yield of scintillation light is proportional to the path length in the scintillator when the positron energy is near the minimal ionization regime (e.g., $10^{0\sim 1}$ MeV in lucite) and thereby the highest light yield (and ac-

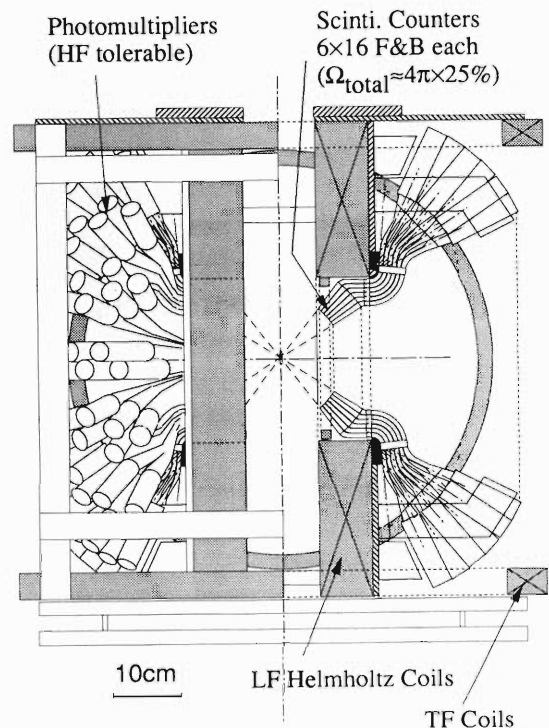


Fig. 1. A cross-sectional view of the ARGUS spectrometer. The muon beam axis is in the left-right direction.

cordingly the highest signal from the photomultiplier) is expected for the positrons emitted from the sample. Because of the short distance between the sample position and scintillators the bending of trajectory due to the magnetic field from a spectrometer magnet is negligible for high energy positrons. The discrimination level for the photomultiplier signal was determined so that the coincidence rate of the neighboring counters might be less than 10% of the single rates. An example of tuning result is shown in Fig. 2b where both the single and coincidence event rates are plotted as a function of discrimination level. Thus, it demonstrates that a reasonable direction sensitivity is established for the single counters by exploiting the character of minimal ionization. (However, we note that this method may not work efficiently for the discrimination of low energy positrons which tend to yield much higher signals to the single counter.)

Another major advent in the new detection system is the large scale application of high-field-tolerant photomultipliers (R5505, Hamamatsu Co.), with which we can remove the shielding of phototubes against fringe fields from experimental magnets. Although their gain is slightly low ($\sim 10^6$) compared with those for standard high energy physics experiments ($\sim 10^7$) the vari-

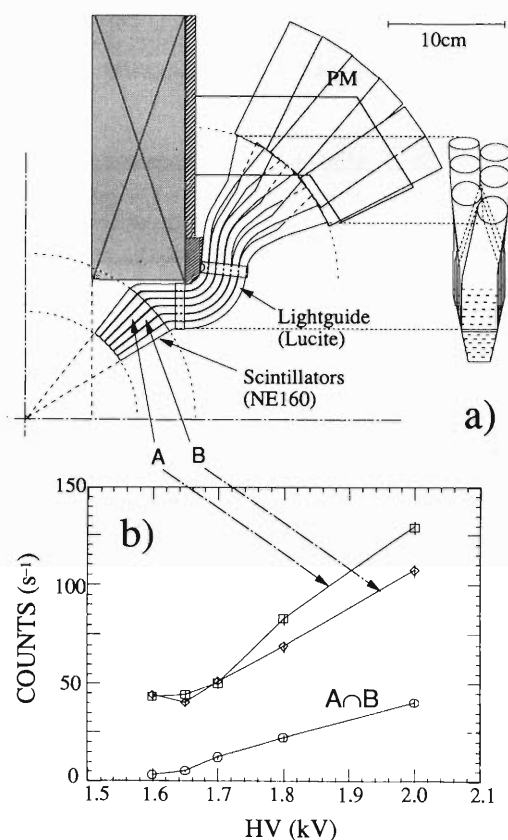


Fig. 2. a) Design of positron detectors for ARGUS spectrometer. One unit consists of six planer scintillators placed along the radial direction seen from the sample position. b) Single and coincidence rate for a neighboring pair of positron detectors as a function of photomultiplier cathode voltage, where the higher cathode voltage corresponds to the lower signal discrimination level.

ation of gain is less than 10% below 0.3 T (when the field is coaxial with the tube). This allows considerable flexibility for the compact design of the spectrometer. As shown in Figs. 1 and 2b the phototubes (1 inch dia., 90 mm long) are closely assembled near the magnet coils along with the fringe field direction and optically connected to the scintillators by rigid lightguides made of lucite.

The number of detector requires high-density TDC's, for which those developed either in UTMSL (single channel/CAMAC slot²) or in RAL (two channels/CAMAC slot) would not suffice: It should be

noted that any two of those 192 signals should not be OR'ed before recorded by TDC's, otherwise it would lead to the increase of pile-up probability in a TDC. In order to realize such a high-density system we have adopted a TDC (model 2277, LeCroy Co.) which has 32 input channels in a single slot device with multistop capability of up to 16 events within 64 μ s. The double pulse resolution of the model 2277 is 20 ns which is acceptable for the predicted event rate. Thus, using 6 TDC modules to cover 192 detectors, the system can tolerate 10^3 positron events per muon pulse (i.e., $\times 10^{4\sim 5}$ positron events per second at a rate of 50 Hz in RAL-ISIS facility). The estimated distortion due to the pile-up is less than 5×10^{-3} in routine μ SR experiments taking 3×10^7 events per hour.

The spectrometer magnets are designed for the conventional μ SR experiments with zero field (ZF), transverse field (TF), and longitudinal field (LF). The LF coils (water cooled) satisfy the Helmholtz condition with 110 mm gap to generate a maximal field of 0.4 T with relative homogeneity of 10^{-4} within 20 mm core radius at the sample position (i.e., the center between the coils). A pair of small correction coils are placed in the LF direction and used together with other coils to obtain zero field condition at the sample position. The vertical pair of coils are used also to generate a transverse field up to 4 mT. The fringe field from Helmholtz coils with maximal excitation is about 0.25 T at the position of photomultipliers and thereby the change of the gain is less than 10%. The positron detectors are assembled around the bored coils, leaving an aperture of 10 cm diameter along the beam direction. All the power supplies for these coils are controlled by a data acquisition program coherently with histogramming of μ SR data, which is useful for some particular measurements where the automatic progression of magnetic field is desirable (e.g., resonance experiments, etc.).

References

- 1) Y. Kawashima, Y. Watanabe, and T. Yamazaki: *Hyperfine Interact.*, **32**, 873 (1986); K.-H. Münch, A. Krazter, G. M. Kalvius, K. Maier, J. Major, M. Hampele, and T. Pfiz: *ibid.*, **87**, 1049 (1994).
- 2) F. Shimokoshi, Y. Kuno, K. Nagamine, and T. Yamazaki: *Nucl. Instrum. Methods Phys. Res.*, **A297**, 103 (1990).
- 3) K. Nagamine, T. Matsuzaki, K. Ishida, I. Watanabe, R. Kadono, G. H. Eaton, G. Thomas, H. J. Jones, and W. G. Williams: *Hyperfine Interact.*, **87**, 1091 (1994).

Development of a Resonance Ionization Buffer Gas Cell for Laser Spectroscopy of Refractory Elements and Actinides

M. Hies, T. Ariga, T. T. Inamura, W. G. Jin, T. Murayama, and M. Wakasugi

On-line laser spectroscopy experiments of refractory elements and actinides are planned at the RIKEN accelerator facility using a combination of resonance ionization spectroscopy (RIS) and ion guide technique (IGISOL).¹⁾ To optimize the laser excitation of such an on-line experiment, the excitation cross section and the spectral line profile in the buffer gas have to be investigated with stable isotopes in the case of refractory elements and with long-living isotopes in the case of actinides in a reference buffer gas cell.

The main part of the reference chamber is a 6-way UHV-CF63 stainless steel double cross filled with a noble gas like argon (purity 99.9999%) at a typical gas pressure of 30 mbar (see Fig. 1). The atoms are evaporated from a thin filament (25–50 μm thick) through thermal heating with a current of 10 to 20 A into the gas and are stored in the gas for the typical diffusion time of 50 ms. The stored atoms are then ionized with an overlapped pulsed laser beam (diameter 10 mm). The produced photoions are transported with the help of an electric field to a pick-up electrode (–200 V). The ion current is measured with a charge sensitive detector as a function of the detuning laser frequency.

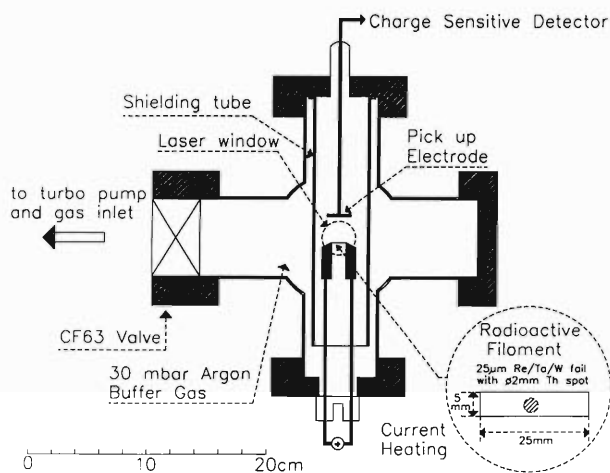


Fig. 1. Experimental setup of the buffer gas cell.

As a first candidate the refractory element hafnium (M.P.2227 °C) has been chosen. The filament was a 25 μm thick Hf-foil ($5 \times 20 \text{ mm}^2$). An excimer-dye-laser combination supplying laser pulse energies in the range of mJ/cm^2 was used to investigate the laser excitation. Typical two-photon two-color ionization with excitation in the ultra-violet spectral range are shown in Figs. 2(a) and (b). A lot of Rydberg states

and autoionization states have been discovered. From the pattern of the Rydberg states the ionization energy of Hafnium could be determined to $(55070 \pm 50) \text{ cm}^{-1}$. This value agrees with the calculated value²⁾ of $(54700 \pm 600) \text{ cm}^{-1}$, but disagrees with the previous value of $(53200 \pm 800) \text{ cm}^{-1}$ measured via electron impact method.³⁾

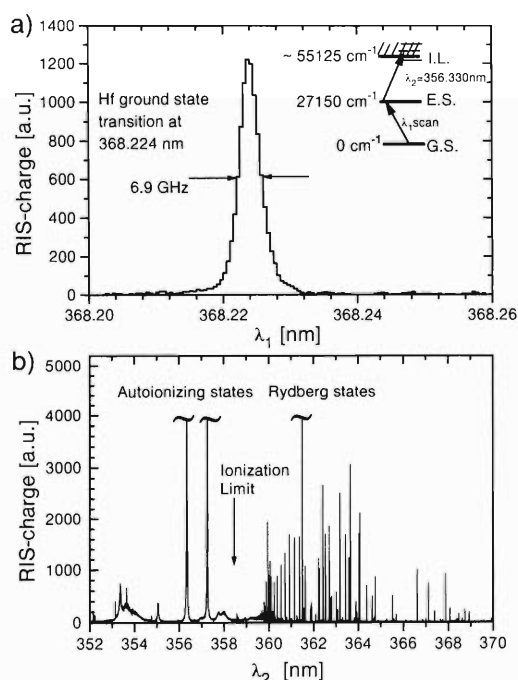


Fig. 2. (a) Laser detuning of the first excitation step over the hafnium ground state transition at 368.224 nm and (b) Laser detuning of the second step over the ionization limit. The excitation scheme is shown in the inlet of Fig. (a).

Further experiments on actinides are planned. Therefore special filaments have to be used, where long-living isotopes like ^{232}Th (total amount 10^{14} atoms, $3 \cdot 10^{-4}$ Bq) are electrodeposited with a spot diameter of 2–3 mm on a thin rhenium foil (25 μm thick) as described in Ref. 4.

References

- 1) M. Hies et al.: This report, p. 177.
- 2) W. F. Meggers: *NBS Monograph*, **153**, 3 (1976).
- 3) E. G. Rauh et al.: *J. Chem. Phys.*, **60**, 1396 (1974).
- 4) H. Wendeler et al.: *Nucl. Instrum. Methods Phys. Res.*, **A334**, 93 (1993).

A New Beam Line for Material Irradiations in the Ring Cyclotron

T. Kambara, M. Kase, M. Matsuda, T. Mitamura, and Y. Awaya

We report about a new setup for material irradiation installed at the Ring Cyclotron.

The radiation effects on materials like high-temperature superconductors have been studied with high-energy heavy ions (10^{10} to 10^{12} ions/cm²) from the Ring Cyclotron.¹⁾ Formerly a one-meter-diameter vacuum chamber on the E2b beam line has been used for the irradiation. Recently, along with the increase of demands for heavy-ion irradiation on materials, it has become necessary to handle more samples within limited beam time without spending too much time

for exchange of samples. It is also necessary to have a uniform distribution of the dose and measure the total dose precisely. Therefore a dedicated beam line with a setup for material irradiation was desired.

The setup is constructed at E5a beam line, which has been used for biological irradiation as well as E5b. This beam line is already equipped with a wobbler magnet system which enables one to get a uniform beam distribution. As shown in Fig. 1, the new setup consists of two parts, one for beam collimators and monitor systems and another for sample handling and irradiation.

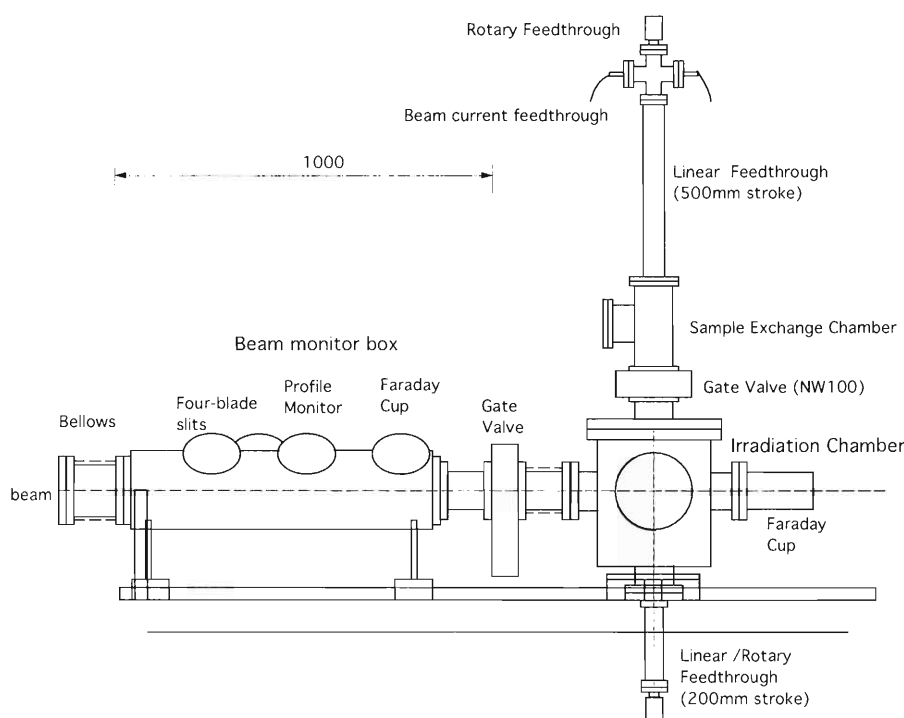


Fig. 1. Side view of the material irradiation set-up.

The beam from the accelerator which passes through the wobbler is shaped by a four-blade slit which can be remotely controlled. The spatial distribution and the intensity of the beam after the slits can be monitored with a beam profile monitor and a Faraday cup. Those equipments are mounted on the beam monitor box.

The irradiation chamber is equipped with a sample handling system and the second Faraday cup with large aperture and depth. Up to four samples can be mounted on a sample holder supported by a 50cm-stroke linear motion feed through. The position and the angle of the samples are fixed by another linear-

rotary motion feed through at the bottom of the chamber. The beam intensity at the sample has been normalized with the second Faraday cup.

When the samples are exchanged, the holder is moved to the sample exchange chamber and then the gate valve is closed. The sample exchange takes about 20 minutes including evacuation. The first irradiation with this setup was successfully performed in September 1995 with 26 MeV/nucleon Xe ions.

References

- 1) M. Terasawa et al.: *Physica C*, **235/240**, 2805 (1994).

6. Material Analysis

RBS Study of Tb-Implanted Sapphire (II)

M. Kumagai and M. Iwaki

A study has been made of the luminescence during Tb-implantation in Al_2O_3 . The substrates used were colorless and transparent single-crystal Al_2O_3 with the (0001) surface. The surfaces of all wafers were mechanically polished before ion implantation. The Tb^+ ion implantation was performed at an energy of 100 keV with doses between 10^{13} and 10^{17} Tb^+/cm^2 at room temperature. The beam current density was about $0.1 \mu\text{A}/\text{cm}^2$. The luminescence owing to Tb^{3+} from Tb-implanted Al_2O_3 was seen during Tb-implantation. The luminescence spectrum from Tb-implanted Al_2O_3 was green.

In order to clarify the mechanism of ion beam induced luminescence of Tb-implanted Al_2O_3 , the composition, damage and Tb-lattice sites in the Tb-implanted layers of Al_2O_3 have been estimated by Rutherford backscattering spectroscopy (RBS). RBS spectra have been measured at room temperature by using 1.5 MeV He^+ ions with a scattering angle of 150° .

Figure 1 shows random and (0001) aligned spectra for the specimens implanted with a dose of 1×10^{16} Tb^+/cm^2 . The Tb^+ depth profile in the random spectra of implanted specimen is of a Gaussian-type, and the Tb amount calculated from the spectra is in good agreement with the nominal value of the implanted dose. The standard deviation calculated from the FWHM of the Tb spectra is about 15.4 nm, which disagrees with the predicted value of about 6.2 nm by the TRIM-90 code. The depth (\bar{R}_p) corresponding to the Tb peak in the spectra is about 20.3 nm, which shows a smaller value than the projected range of Tb of about 23.4 nm predicted from the TRIM-90 calculation. These results are almost the same as that obtained for Tb implantation into (1 $\bar{1}$ 02) sapphire as shown in our precious report.¹⁾

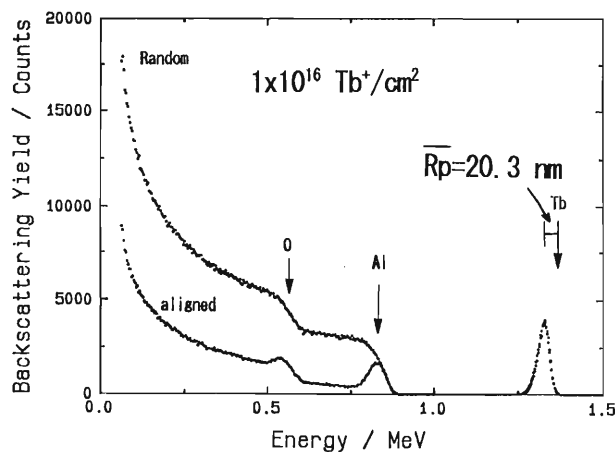


Fig. 1. Random and (0001) aligned spectra obtained for Tb-implanted Al_2O_3 with a dose of 1×10^{16} Tb^+/cm^2 .

The (0001) aligned spectrum of the implanted sapphire shows that the scattering yields of Al and O near the surface increase. The enhancement of the yields results from the radiation damage induced by Tb-implantation, but the spectrum shows that no amorphization takes place even at the high dose. The scattering yield from Tb in the (0001) aligned spectrum is identical with that for the random spectrum. The accordance of the two spectra reveals that most of the implanted Tb atoms may sit at the random sites.

The relationship between the surface characterization and luminescence is under investigation.

References

- 1) M. Kumagai and M. Iwaki: *RIKEN Accel. Prog. Rep.*, **28**, 142 (1995).

Sample Charging Effect on Satellite Spectra of Ion-Induced X Rays

K. Maeda and H. Hamanaka*

Abnormally strong characteristic X rays are emitted from some metal fluorides after their bombardment by accelerated ions.¹⁾ The enhancement of the X-ray yields has been ascribed to the charge build-up in insulating materials that is followed by discharge due to the production of high-flux energetic electrons. X-ray spectra induced by ions have strong satellite lines arising from multiple ionized states. On the other hand, the satellites in the electron-excited X-ray spectra are very weak compared to their parent diagram lines arising from single-vacancy states. Therefore, if energetic electrons produced by discharge are the true cause of the abnormal enhancement, sample charging must have effects not only on the yields of characteristic X rays but also on the fine structures of the X-ray spectra. In the present work we examine the above hypothesis by measuring the silicon $K\alpha$ satellite spectra of SiO_2 (fused quartz) bombarded by He ions under various experimental conditions.²⁾ Fused quartz was used as a target sample because it is a good insulating material and, moreover, the multiple-vacancy satellite structures of Si $K\alpha$ have already been extensively investigated.

X-rays spectra were excited by 1.5 MeV He^+ ions and measured with a high-resolution PIXE spectrometer of Hosei University. The spectrometer was equipped with an ADP (110) plane crystal and a position-sensitive proportional counter. Crystalline silicon was used as a reference non-insulating sample. A tungsten filament taken from an electric lamp was set in front of the sample target to spray electrons for neutralizing the positive charge built-up in the target. Figure 1 shows Si $K\alpha$ spectra of SiO_2 bombarded by 1.5 MeV He^+ ions under the following experimental conditions: (a) the vacuum in the scattering chamber [p] was 1×10^{-2} Pa and the power of the W filament [w] was 0 W; (b) $p = 1 \times 10^{-2}$ Pa, $w = 6$ W; (c) $p = 9 \times 10^{-2}$ Pa, $w = 0$ W; and (d) $p = 9 \times 10^{-2}$ Pa, $w = 23$ W.

The diagram line (KL^0) in Fig. 1(a) is very strong in comparison with the KL^n satellites. Here, KL^n denotes the initial state with single K and n L vacancies. The ratio of the integrated intensities of the KL^0 and KL^1 lines is 100 : 7, very similar to that of electron bombardment of 100 : 9. If this strong diagram line was induced by energetic electrons during the discharge, the elimination of the sample charging should weaken the diagram line and make the satellites evident. As expected, the satellites appeared prominently, as seen in Figs. 1(b) and 1(d), when electron showers were introduced in the system. The intensity distribution of the $KL^0 : KL^1 : KL^2 : KL^3$ lines is

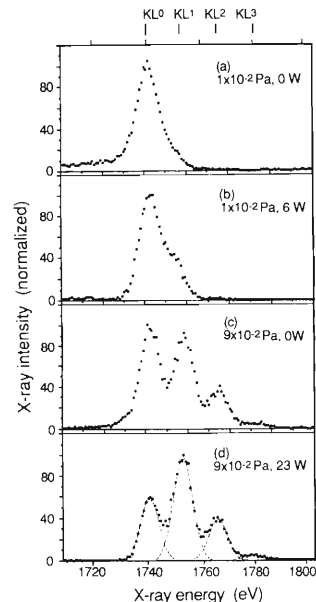


Fig. 1. Si $K\alpha$ spectra of a fused quartz bombarded by 1.5 MeV He^+ ions under different experimental conditions.

100 : 167 : 67 : 8, when an electron shower of high-flux is applied as shown in Fig. 1(d). This ratio is close to that of the silicon of 100 : 172 : 73 : 12. The intensity distributions of the satellite spectra in Figs. 1(b) and 1(c) are intermediate between those of Figs. 1(a) and 1(d). The electron flux in condition (b) is not sufficient to fully neutralize the positive charge in the sample. Under condition (c), charge leakage by way of residual gas has likely occurred because the vacuum in the chamber was not high.

The change of the intensity distribution of the satellite spectra shown in Fig. 1 leads to the conclusion that the characteristic X rays induced by sample charging is strong enough so that the multiple-vacancy satellites are obscured by the intense diagram line. Thus, by means of high-resolution measurements, we have proved the hypothesis¹⁾ that the enhancement of X-ray yields from insulating targets is caused by energetic electrons generated by charge build-up and subsequent discharge. The above argument was confirmed by results of experiments for ion-induced Ca $K\alpha$ spectra of CaF_2 and CaB_6 , in which the intensities of the KL^0 and KL^1 lines were measured as functions of the magnitude of the electron shower.³⁾

References

- 1) J. Kawai, K. Maeda, N. Sakauchi, and I. Konishi: *Spectrochim. Acta*, **B50**, L1 (1995).
- 2) K. Maeda and H. Hamanaka: *ibid.*, in press.
- 3) H. Hamanaka, K. Hasegawa, and K. Maeda: *Nucl. Instrum. Methods Phys. Res.*, in press.

* College of Engineering, Hosei University

Correlation between Seawater Temperature and Sr/Ca Ratios in Otoliths of Red Sea Bream *Pagrus major*

N. Arai, W. Sakamoto,* and K. Maeda

Fish otoliths, ear stones which function as a detector of acceleration and sound, are generally composed of aragonite crystals and continuously deposited from fish birth to its death. In addition, trace metals can enter the crystals of calcium carbonate and the amount of the metals seems to vary according to the environmental parameters such as temperature that fish has experienced. Especially strontium is well known as a good indicator of ambient temperature. An in-air PIXE was adopted to detect a small amount of strontium in otoliths of red sea bream *Pagrus major*. In a previous study,¹⁾ we indicated that the Sr concentration in the otoliths of red sea bream reared in different three sea areas that showed different seawater temperatures depended on the temperatures; Sr increased in the higher temperature condition. The object of this temperature controlled experiment is to examine the correlation between seawater temperature and Sr concentration and the other factors that affect the correlation.

The otolith samples were removed from juvenile red sea bream reared in two experiments. Forty-five individuals of 64 days old juveniles were kept in five tanks in the first experiment (Exp. 1) and 15 individuals of 119 days old were kept in the other experiment (Exp. 2). Seawater temperatures were controlled at 17, 20, 23, 26, and 29 °C. Fish were fed with a commercial assorted food three times a day.

Otoliths surfaces were not cut nor polished and bombarded in air by a 1.6 MeV proton beam generated in the RIKEN Tandatron accelerator. The proton beam was collimated with a carbon collimator with a 1-mm diameter hole and brought out from the vacuum system into air through a 6 μm thick Al foil, and traveled 10 mm to the target. Path lengths in air and the Al foil caused reduction in the proton energy to 1.16 MeV and also spread the beam spot about 1.2 mm in diameter.

X-rays emitted from the target were detected with an Si(Li) crystal made by EG&G Co. through a 74 μm Al absorber to attenuate CaK X-rays, since the otolith is almost composed of pure calcium carbonate. The distance was 26 mm between the top of the Si(Li)

crystal and the beam spot on the target. The detector position was kept at 135° with respect to the incident beam direction. PIXE spectra were measured by monitoring a beam current and accumulated for a total beam charge of 20 μC. Experimental errors were examined using a NIST standard argillaceous limestone SRM-1C.

Figure 1 shows the correlation between seawater temperature and Sr/Ca concentration ratios. The ratios in otoliths in smaller juveniles increase in proportion to temperature, while the ratios in larger juveniles are almost constant values. This result indicates that the ability of red sea bream juveniles to discriminate Ca from Sr depends on its body size as well as ambient seawater temperature.

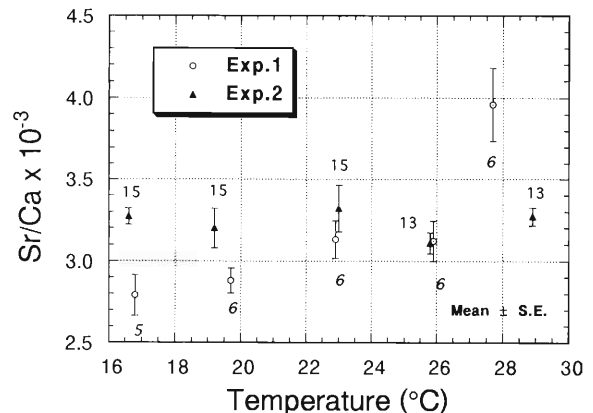


Fig. 1. Correlation between seawater temperature and Sr/Ca ratios in juvenile red sea bream otoliths. Fork length was ranging from 31 to 66 mm in the Exp. 1 and was ranging from 82 to 108 mm in the Exp. 2. Numerals under and above error bars are the number of specimens.

References

- 1) N. Arai, W. Sakamoto, and K. Maeda: *Fisheries Science*, **61**, 43 (1995).

* Faculty of Agriculture, Kyoto University

Whether Ion Beam Attracts Ions in Solutions or Not?

J. Kawai and K. Maeda

In our previous report,¹⁾ the x-ray intensity induced by accelerated charged particles was not proportional to the concentration of Cu^{2+} ion in aqueous solutions of nitrates. That is to say, the Cu $K\alpha$ intensity gradually increased with the increase of the total accumulated charge when the projectile intensity was constant. This increasing factor was more than ten for a 60 ppm Cu solution and the factor was decreased with the increase of concentration; the factor was two for a 600 ppm Cu solution and one for 6000 ppm. The experiment was performed with a horizontal 6-MeV He-ion beam. Thus the He beam interacted with the Cu solution through a thin Kapton window which separated the solution from the air. We have concluded that this nonlinear behaviour of x-ray intensity is due to the deposition of the solute elements on the Kapton surface.

We have constructed a vertical beam PIXE (Particle Induced X-ray Emission) beam line²⁾ at RILAC to measure solutions without using a window. On this beam line, we have tested whether He-ion beam, which was introduced into free aqueous so-

lution surface, could attract or concentrate ions or not. We measured 0.100 M KBr solution, 0.0020 M stearyltrimethylammonium bromide (STAB) solution, and 0.00021 M STAB solution. STAB is $\text{CH}_3(\text{CH}_2)_{17}\text{N}(\text{CH}_3)_3^+\text{Br}^-$, thus the Br^- ions are attracted at the solution surface,³⁾ and the concentration of Br^- at the surface was expected to be higher than that at a deeper place of solution. However, the present PIXE measurement indicates neither any nonlinear effect nor the high concentration of Br^- at free aqueous solution surface. This is because the PIXE analysis is not surface sensitive to detect the top few layers of solution.

References

- 1) K. Maeda and J. Kawai: *RIKEN Accel. Prog. Rep.*, **27**, 123 (1993).
- 2) J. Kawai and K. Maeda: *Int. J. PIXE*, **4**, 147 (1994).
- 3) H. Tanida, I. Watanabe, and H. Watarai: Book of Abstracts, 8th Int. Conf. on X-Ray Absorption Fine Structure, Berlin, Aug.-Sept. ThFr-16 (1994).

IV. NUCLEAR DATA

Status Report of the Nuclear Data Group

Y. Tendow, A. Yoshida, A. Hashizume,* and K. Kitao

The Nuclear Data Group has been continuing the data activities mentioned below since the previous year.¹⁾

This year, one of the staff (Y.T.) has retired reaching the age limit. But he is supposed to continue the data works as a non-regular member of the Institute for the continuity and completeness of nuclear data activities of the group.

(1) Nuclear reaction cross-section data (EXFOR)

Compilation of charged particle nuclear reaction cross sections has been continued. Cross sections to produce 20 radioisotopes of medical use: ^{11}C , ^{13}N , ^{15}O , ^{18}F , ^{28}Mg , ^{52}Fe , ^{67}Ga , ^{68}Ge , ^{74}As , ^{77}Br , ^{82}Br , ^{77}Kr , ^{81}Rb , $^{82\text{m}}\text{Rb}$, ^{111}In , ^{123}Xe , ^{127}Xe , ^{123}I , ^{124}I , and ^{125}I as well as old data which are not included in the EXFOR master file up to now and new data appeared in recent journals are continued to be collected and compiled into EXFOR files.

(2) Evaluated Nuclear Structure Data File (ENSDF)

We have been participating in the ENSDF compilation network coordinated by the Brookhaven National Nuclear Data Center (NNDC). The evaluation and compilation of $A = 118$ mass chain has been published this year.²⁾ The author post-review and galley for $A = 129$ evaluation has been completed and sent back to the NNDC for publishing. Mass chain $A = 127$ is now in the stage of review at the NNDC. $A = 120$ evaluation is now under progress.

(3) Nuclear Structure Reference file (NSR)

We are engaged in collecting and compiling secondary references (annual reports, conference proceedings, etc.) appeared in Japan since the previous year into the Nuclear Structure Reference (NSR) file and in sending it to NNDC.

The compilation of 1994 annual reports has been completed and sent to the NNDC. Japanese Secondary sources surveyed this year are as follows (in code name in NSR):

RIKEN (*RIKEN Accel. Prog. Rep.*),
 JAERI-TV (*JAERI Tandem & V.D.G.*),
 JAERI-TIARA (*JAERI Takasaki Ion Acc. Advanced Rad. Appl.*),

INS (*INS Univ. Tokyo*),
 UTTAC (*Univ. Tsukuba Tandem Accel. Center*),
 RCNP (*Res. Center Nucl. Phys. Osaka Univ.*),
 OULNS (*Osaka Univ. Lab. Nucl. Study*),
 KUTL (*Kyushu Univ. Tandem Acc. Lab.*),
 CYRIC (*Cyclo. Radioisot. Center, Tohoku Univ.*).
 (4) Others

The regular IAEA Technical Nuclear Reaction Data Centers (NRDC) Meeting was held at the IAEA Nuclear Data Section (NDS) in Vienna on 2–4 May 1995. The proposal for restructuring of the going worldwide cooperation network which had been proposed at the last IAEA meeting was continued to be discussed in this meeting, and a document of conclusion and agreement was reached and signed by all of the 11 center heads participating in the network. In the course of discussion, radical aspects in the original proposal for restructuring the network were rather toned down. The document only provides the purposes and functions of nuclear data network activities as well as the unique responsibilities and special expertise of each center. It was also recognized at the meeting that the most of leading data centers in the network were menaced with cutting down on the budget and decrease in man power.

A new PC program package “NUCHART for Windows” has been released from IAEA NDS. It provides an on-screen chart of nuclides which pops up various nuclear data of the nuclide clicked by the mouse. Another program package “VuENSDF for Windows” alpha test version has been released from LBL which displays decay scheme drawings on the basis of ENSDF inputs. An MS-DOS program “ENSDAT”, available from BNL, also provides a postscript file of decay scheme drawings like that in “Nuclear Data Sheets” from ENSDF inputs.

References

- 1) Y. Tendow, A. Yoshida, Y. Ohkubo, A. Hashizume, and K. Kitao: *RIKEN Accel. Prog. Rep.*, **28**, 145 (1995).
- 2) K. Kitao: *Nuclear Data Sheets*, **75**, 99 (1995).

* Japan Atomic Energy Relations Organization

Measurements of Activation Cross Sections of Energy Up to 110 MeV for Several Neutron-Induced Reactions

N. Nakanishi, S. Fujita, S. Nakajima, M. Watanabe,* and H. Ohishi*

Neutron activation cross sections for ^{12}C , ^{27}Al , ^{56}Fe , ^{59}Co , ^{58}Ni , ^{115}In , and ^{197}Au detectors (foils) were measured in the neutron energy range up to 110 MeV by the activation method. As well known, the method gives the activity which is represented as the product of an activation cross section and a neutron flux. Information on a neutron spectrum, therefore, is indispensable in order to obtain that of the activation cross section. Activity A is given by the following expression,

$$A = \int \phi(E) \cdot \sigma(E) dE,$$

where $\phi(E)$ and $\sigma(E)$ are an energy spectrum of neutron flux and an activation cross section, respectively. We adopt neutron spectra measured by Meier.¹⁾ These metal foils were irradiated by a neutron flux with a continuous energy spectrum which was produced by 113 MeV protons incident on thick C, and Fe targets. The gamma-rays from the reaction products in the foil were measured using a Ge-detector after irradiation.

The reactions which were studied are listed along with the half lives and energies of measured gamma-

Table 1. Studied reactions and physical properties of the gamma-ray transitions concerned.

Target	Reaction	Half-life	γ -ray energy (MeV)
C	$^{12}\text{C}(n,2n)^{11}\text{C}$	20.38 m	0.511
Al	$^{27}\text{Al}(n,\alpha)^{24}\text{Na}$	15.02 h	1.369
Fe	$^{56}\text{Fe}(n,p)^{56}\text{Mn}$	2.579 h	0.847
Co	$^{59}\text{Co}(n,2n)^{58}\text{Co}$	70.79 d	0.811
Co	$^{59}\text{Co}(n,\alpha)^{56}\text{Mn}$	2.579 h	0.847
Ni	$^{58}\text{Ni}(n,p)^{58}\text{Co}$	70.79 d	0.811
Ni	$^{58}\text{Ni}(n,2n)^{57}\text{Ni}$	35.94 h	1.378
In	$^{115}\text{In}(n,n')^{115m}\text{In}$	4.486 h	0.336
Au	$^{197}\text{Au}(n,4n)^{194}\text{Au}$	3.955 h	0.329
Au	$^{197}\text{Au}(n,2n)^{196}\text{Au}$	6.183 d	0.356
Au	$^{197}\text{Au}(n,\gamma)^{198}\text{Au}$	2.696 d	0.412

rays in Table 1. Activation cross sections are unfolded in the same algorithm as that of the Sand II. Calculated results by the ALICE code are used as initial guesses in unfolding processes. Typical examples of the neutron energy dependence of activation cross sections are shown in Fig. 1. In the $^{27}\text{Al}(n,\alpha)^{24}\text{Na}$ reaction, other reactions such as $(n,n\ ^3\text{He})$, $(n,2d)$, (n,upd)

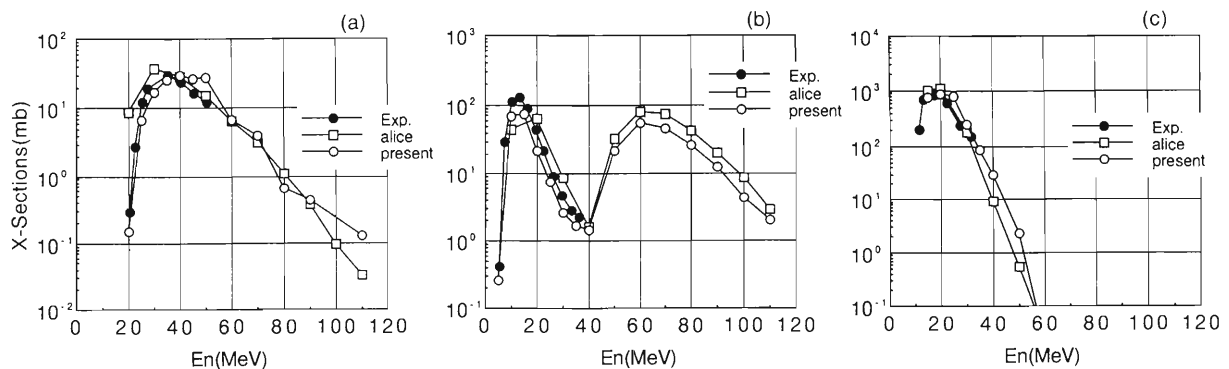


Fig. 1. Activation cross sections of typical examples; (a) $^{12}\text{C}(n,2n)^{11}\text{C}$, (b) $^{27}\text{Al}(n,\alpha)^{24}\text{Na}$ and (c) $^{59}\text{Co}(n,2n)^{58}\text{Co}$.

and $(n,2n2p)$ are also included. In the $^{59}\text{Co}(n,2n)^{58}\text{Co}$ reaction, the cross section becomes very small in a high energy region.

References

- 1) M. M. Meier et al.: *Nucl. Sci. Eng.*, **102**, 310 (1989) and private communication ('94).

* Faculty of Science and Technology, Chuo University

V. DEVELOPMENT OF ACCELERATOR FACILITIES

Status of RIKEN 10 GHz ECRIS

T. Nakagawa, T. Kageyama, M. Kase, A. Goto, and Y. Yano

For the experiments to search new isotopes, intense neutron rich beams, such as ^{50}Ti and ^{48}Ca , are strongly demanded. To produce such beams, it is effective to use enriched materials, because of the low natural abundance of the ions. As the enriched isotopes are normally sold as oxides, the method to produce highly charged ions from oxide materials described in Ref. 1 is one of the best ways. However, it is not advantageous to make a rod of oxide materials of the enriched isotopes from the point of view of cost performance. We tried to put the oxide powder into Al_2O_3 or SiO_2 tubes (2 mm in inside diameter, 4 mm in outside diameter) and insert them directly into the plasma.

At first we compared the beam intensities of ^{48}Ti by using 1) a tube (SiO_2 or Al_2O_3) filled with oxide powder of natural Ti and 2) an oxide rod. The condition of the ECRIS was kept same for both cases. Figure 1 shows the obtained beam intensity of ^{48}Ti ions for each charge state. The beam intensity produced by using the tube method is almost the same as that of the rod method.

Encouraged by this success, we have tried to produce ^{50}Ti ions from ^{50}TiO powder. As shown in Fig. 2, the

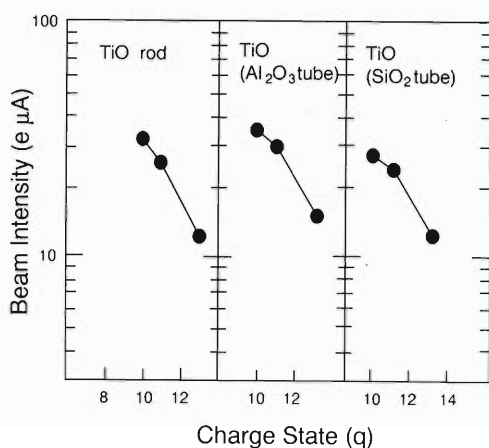


Fig. 1. Charge state distributions of Ti ions.

best result was obtained with using an Al_2O_3 tube. In this case, however, it is very difficult to distinguish $^{50}\text{Ti}^{13+}$ from $^{27}\text{Al}^{7+}$ which has almost the same value of $A/q = 3.85$ as that of $^{50}\text{Ti}^{13+}$, where A and q are the mass number and charge state of the ion. For this reason we have chosen a SiO_2 tube. The support gas was oxygen. The vacuums of the first, second, and extraction stages were 7.0×10^{-6} , 5×10^{-7} , and 8×10^{-8} Torr, respectively. The microwave power supplied in the second stage was 600 W. Figure 2 shows the charge state distribution as a function of the analyzing magnet current. The ECRIS was tuned for producing $^{50}\text{Ti}^{13+}$ ions. The ^{50}Ti ions were accelerated by the AVF-Ring Cyclotron complex up to 80 MeV/u. The beam intensity was 15 eμA from the ECRIS and 160 enA on the target. The consumption rate was 1.5 mg/h.

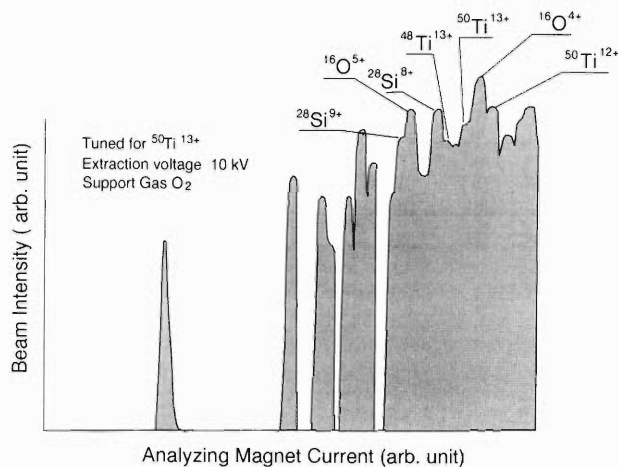


Fig. 2. Charge state distributions as a function of analyzing magnet current. The source was tuned for producing the $^{50}\text{Ti}^{13+}$ ions.

References

- 1) T. Nakagawa, T. Kageyama, A. Goto, M. Kase, and Y. Yano: *Jpn. J. Appl. Phys.*, **32**, L1335 (1993).

Present Status and Future Plans of RIKEN 14.5 GHz Caprice

Y. Kanai, Y. Nakai, K. Soejima, T. M. Kojima, T. Kambara, and Y. Awaya

We have installed a 14.5 GHz Caprice at RIKEN as an ion source of the low energy highly charged ion facility. With this facility, we are planning to study ion-atom collisions and ion-surface interactions. We have constructed the beam line from the middle of December in 1994 and started to operate the Caprice in the middle of January in 1995. Here, we show the present status of this facility and future plans.

We have constructed the beam lines as shown in Fig. 1. Our Caprice source uses a double wall chamber and a 1.2 Tesla hexapole magnet. Details of the Caprice itself are presented in separate papers.^{1,2)} The performance of the 14.5 GHz Caprice has been measured at Grenoble and also at RIKEN. Typical intensities of ions from the Caprice at RIKEN are shown in Table 1.

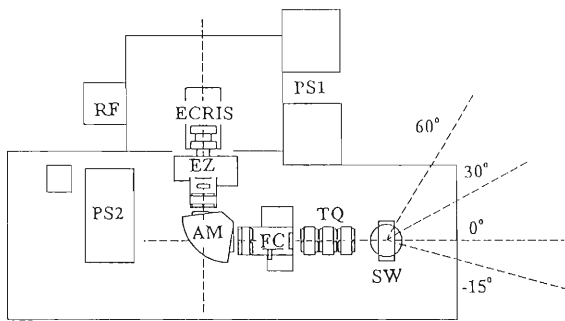


Fig. 1. Schematic drawing of low energy highly charged ion beam line. ECRIS: 14.5 GHz Caprice, EZ: einzel lens, AM: analyzing magnet, TQ: triplet quadrupole magnet, SW: switching magnet, FC: Faraday cup, 14.5 GHz rf generator, PS1: power supply for mirror coils, PS2: power supplies for beam transport magnets.

These ion currents were measured by a Faraday cup after an analyzing magnet, shown as FC in Fig. 1. These values are smaller than the maximum ion currents reported by Grenoble group. This may be due to the misalignment between the Caprice and the beam line.

We are planning to use the ion beam in the energy range of $1-20 \times q$ keV; q is the charge state of ions. To get lower energy ions ($1 \times q$ keV), we used such a method that the potential difference between a beam

Table 1. Typical ion currents from RIKEN 14.5 GHz Caprice.

Ion	Ion Currents(μA)															
	+1	+2	+3	+4	+5	+6	+7	+8	+9	+10	+11	+12	+13	+14	+15	+16
N	1000	1100	700	680	560	95	—									
O	1430	1310	1000	—	700	500	41									
Ar	360	162	—	39	15	5	2	—	0.05							

line and the plasma chamber, which means the extraction potential, is kept constant, and the potentials of the plasma chamber and a beam line are changed depending on the beam energy that we need.³⁾ To use this method, (1) we made the whole beam line between the Caprice and the point just after the switching magnet to be isolated from ground potential, and (2) we modified the insulator of the extraction part of the Caprice to isolate the beam line from the plasma chamber of the Caprice. Power supplies of the magnets for the beam transport system and the beam diagnostic system, which are isolated from ground, are controlled by using an optical fiber system. The various kinds of ions have been transported to the experimental chamber at the 30 degrees beam line with keeping the potential of the isolated beam line to ground potential. A test of the whole isolated system will be made in this winter.

For the first experiment, we are planning the electron spectroscopy of the doubly-excited ions produced by the multiple electron transfer processes.⁴⁾

References

- 1) D. Hitz et al.: *Nucl. Instrum. Methods Phys. Res.*, **B98**, 517 (1995).
- 2) D. Hitz et al.: Proc. 12th Int. Workshop on ECR Ion Sources, RIKEN, p. 126 (1995).
- 3) B. Martin et al.: Proc. 11th Int. Workshop on ECR Ion Sources, Groningen, p. 188 (1993).
- 4) Y. Kanai et al.: *Nucl. Instrum. Methods Phys. Res.*, **B98**, 81 (1995).

E-Field Injection for Extracting Much Faster Pulse Trains or for Enhanced CW Beams out of an ECRIS Potential-Well

M. Niimura, T. Kageyama, T. Nakagawa, A. Goto, and Y. Yano

An alternative upgrade technology was developed by applying the key physics identified as responsible for upgrading the ECRIS beam-current. The electric (\mathbf{E} -) field injection method proposed here can produce not only faster pulse trains than achievable by present techniques but also upgraded beam intensity at low emittance beyond the level of electron (e^-) beam method. The goal is a pre-bunched ECRIS injector usable for fast timing linacs as well as synchrotrons, yet operable in an efficient CW mode for cyclotrons. Here, we present its underlined physics and conceptual design, where an intensive ($\eta = 169$ at $Z = 15$), fast-pulsed (sub-microsecond), yet low-emittance ($\sim 10^{-7}$ m rad) beam can be expected.

Presently available pulsing techniques need to destruct the confinement of ECR-heated electrons by either turning off the RF field (afterglow mode) or pulsing the mirror magnetic field (PuMa mode). These techniques rely on the diffusion processes of charged particles for its extraction, thereby making the production of a fast pulse train unable nor of a short pulsewidth. E-field, on the other hand, can extract ions by the drift process, a faster transport than diffusion. The method won't perturb the electron confinement nor destruct the ECR potential-well.

Our idea is to increase the end-loss current, $I_b = I_o \exp\{-Ze\Delta\phi/kT_{iz}\}$, without lowering the potential barrier $\Delta\phi$. Petty¹⁾ has attempted to increase the end-loss or spill current of particular Z ions by raising its temperature T_{iz} via ion cyclotron resonance heating (ICRH); only 25% of beam enhancement was observed. This was, however, predictable since ICRH can increase the radial transport (to walls) of ions due to the increase of Larmor radius. Nevertheless, this experiment has indirectly confirmed the existence of an ion-trapping potential-well and prompted us to propose a new way of extraction. In our device, ions are supposedly accelerated only one-dimensionally by an axial electric field E_z without heating the T_{iz} , yet raising the directed energy enough to overcome the $\Delta\phi$. Then, the end-loss current may be described by $I_b = I_o \exp\{-Ze\Delta\phi/[kT_{iz} + ZeE_z l_p]\}$. An improved emittance can be expected because our method can extract even the $kT_{iz} = 0$ ions trapped in the bottom of potential-well. The technology needed here is to accelerate only the trapped ions without losing the resonantly heated hot electrons out of the ECR zone. In order to estimate such a proper range of E_z , following theoretical background was needed.

Forces on Electrons and Ions Inside the Mirror Magnetic Field (MMF): The force (eE_z) to be applied ex-

ternally with the purpose to extract only the ions has to be much smaller than the magnetic confinement force exerting on electrons, but has to be larger than that on ions inside the MMF. Consider an electron gyrating around the axisymmetric \mathbf{B} -field whose intensity increases gradually towards the direction of $+z$ axis. Then, in the cylindrical polar coordinates, there exists the radial component B_r since the field lines are gradually compressed towards $+z$ axis. The electrons with azimuthal velocity $v_{\theta e}$ interact with the B_r to experience an axial force: $F_z = -e[v_e \times \mathbf{B}]_z = ev_{\theta e} B_r$ since $B_{\theta} = 0$. The Maxwell equation, $\nabla \cdot \mathbf{B} = 0$, expressed in the axisymmetric system ($\partial/\partial\theta = 0$) is in the form: $rB_r = -\int r(\partial B_z/\partial z)dr$. This integral equation gives $B_r \approx -(r_{Le}/2)(\partial B_z/\partial z)$ for $r \leq r_{Le}$ if the $\partial B_z/\partial z$ can be assumed constant for r as large as the electron Larmor radius, $r_{Le} \equiv v_{\theta e}/\omega_{ce}$. Therefore, the magnetic confinement force on electrons is given by $F_z = -(ev_{\theta e} r_{Le}/2)(\partial B_z/\partial z)$. Since $\omega_{ce} \equiv eB/m$, the axial equation of motion is

$$m \frac{dv_{ze}}{dt} = -\mu_e \frac{\partial B_z}{\partial z}, \quad \mu_e \equiv \frac{mv_{\theta e}^2}{2B} (\geq 0). \quad (1)$$

Equation 1 states that the electrons in the region where $\partial B_z/\partial z \geq 0$ experience the force $F_z = -\mu_e(\partial B_z/\partial z)$ of $-z$ direction (towards the midplane, $z = 0$). The magnitude of F_z is proportional to the magnetic moment of gyrating electrons, μ_e . This means that the force exerted on electrons, $-eE_z$ should be much smaller than the electron confinement force $-\mu_e(\partial B_z/\partial z)$. Namely, their magnitudes should satisfy the condition:

$$eE_z \ll \mu_e (\partial B_z/\partial z). \quad (2)$$

Since $v_{ze} = dz/dt$, we can rewrite the equation of motion (1) as $(d/dt)(mv_{ze}^2/2) = -\mu_e(dB_z/dt)$, and the definition of μ_e as $mv_{\theta e}^2/2 = B_z\mu_e$. Therefore, the constraint of constant total kinetic energy, $dW/dt \equiv (d/dt)\{m(v_{ze}^2 + v_{\theta e}^2)/2\} = 0$ can be expressed as $-\mu_e(dB_z/dt) + (d/dt)(B_z\mu_e) = 0$. From this, the invariance of μ can be derived as $d\mu_e/dt = 0$. Since $W_z = 0$ at the turning point ($B = B_R$), the invariance of μ_e tells that $\mu_e = W/B_R$. This B_R should be equal to B_{ECR} which forms the ECR surface because the largest azimuthal energy $W_{\theta max}$ is generated at this surface. Should a particle move along the \mathbf{B} -field line to a location $B \geq B_{ECR}$, the magnitude of W_{θ} has to increase beyond that of $W_{\theta max}$ due to the invariance of μ_e , which is unlikely. Thus, electrons are magnetically confined by MMF, whose volume is called ECR-zone or -egg.

Let us evaluate Eq. (2) numerically. For a 10 GHz ECRIS, the \mathbf{B} -field at the turning point is $B_R \approx B_{ECR} = 3.57$ kG. So, if $B_{mirror} = 10$ kG we have the mirror ratio $M \geq (B_{mirror} - B_{ECR})/B_{ECR} = 1.80$

assuming $B_{\text{midplane}} \approx B_{\text{ECR}}$. We also assume the characteristic length of mirror field to be $\Delta z = 10$ cm, and the kinetic energy evaluated at $B = B_{\text{ECR}}$ to be $mv_e^2/2 = 500$ eV. Then, Eq. (2) gives the condition:

$$E_z \ll \frac{1}{2e} mv_e^2 \frac{\Delta B}{B_{\text{ECR}} \Delta z} = 90 \text{ V/cm} \quad (3)$$

On the other hand, the ions are usually not well confined inside of MMF because its Larmor radius r_{Li} is often too large. However, under ECRIS conditions, $r_{Li}/r_{Le} = (MT_i/mT_e)^{1/2}/Z \leq 10$ even for Ar ions because $T_i/T_e \leq 1$ and $Z \geq 10$ are typical. This implies the situation $r_{Li} \approx r_{Le}$. Then, $(\partial B_z/\partial z)$ can be constant for $r \leq r_{Li}$. This means that the axial force on ions is in a similar form:²⁾ $F_z = -\mu_i(\partial B_z/\partial z)$, where $\mu_i \equiv Mv_{\theta i}^2/2B \approx kT_i/B_{\text{ECR}}$. Obviously, $\mu_i/\mu_e \leq 1/10$ and this imbalance helps to extract the ions selectively with a small external force: $ZeE_z \geq \mu_i(\partial B_z/\partial z)$. The minimum E_z necessary to extract ions from MMF can be calculated by

$$E_z \geq \frac{1}{2Ze} Mv_{\theta i}^2 \frac{\Delta B}{B_{\text{ECR}} \Delta z} = 0.90 \text{ V/cm} \quad (4)$$

Here, $Mv_{\theta i}^2/2 = 50$ eV was assumed beside the conditions used above. The E_z not to disturb electron confinement is thus in the range:

$$0.90 \leq E_z \ll 90. \quad (\text{V/cm}) \quad (5)$$

Directed Energy Gain of Ions Inside an ECR Potential-Well: Beside satisfying the condition (5), the E_z needs to give enough energy for trapped ions to overcome the $\Delta\phi$ in its extraction:

$$E_z \geq \Delta\phi/Zl_p \approx 0.4[\text{V/cm}], \quad l_p \approx 5 \text{ cm} \quad (6)$$

For the numerical evaluation of Eq. (6) we have referred the e-beam injection experiment conducted at LBL.³⁾ The e-beam injection has lowered the height of the positive (or peripheral) plasma potential V_p (which is the electric potential measured with respect to the wall potential). It is equivalent to lower the height of barrier of the potential-well, $\Delta\phi$. They were successful to lower V_p or $\Delta\phi$ by approximately 10 eV, which implies that the e-beam potential was $\Delta\phi_{\text{eb}} = 10$ eV. Their experiments can be well explained if $Z = 10$ and $\Delta\phi = 20$ eV are assumed. Further, $l_p \approx 5$ cm was assumed in Eq. (6) as an effective acceleration length which corresponds to a half length of the typical ECR-zone.

As an appropriate E_z to satisfy the both conditions (5) and (6), we chose $E_z = 4$ V/cm. This number together with the values used above has been substituted into the formula of upgrading factor of the E-field injection:

$$\eta_E(Z) = \exp\left[-\frac{Ze\Delta\phi}{kT_{iz} + E_z l_p}\right] / \exp\left[-\frac{Ze\Delta\phi}{kT_{iz}}\right] \quad (7)$$

Figure 1 graphically shows the calculated η_E as a function of Z , together with the case of e-beam injection: $\eta_e(Z) = \exp(e\Delta\phi_{\text{eb}}Z/kT_{iz}) = \exp(0.2Z)$. A drastic improvement at higher Z 's is evident: $\eta_E = 24.5$ and 169 (whereas $\eta_e = 7.39$ and 19.9) at $Z = 10$ and 15, respectively.

Figure 2a shows a conceptual design of the new ECRIS injector. The E_z will be induced externally across the ECR potential-well via a betatron-like mechanism. In order to secure the low-emittance beam extraction a drift tube with a griddle front entrance will be used. The tailored electric field lines are to avoid electrons from entering the loss cone. In the CW mode of operation, an e-beam emitted from the biased-disk like cathode is used, but injected in the direction opposed to that of conventional e-beam injection. In this way the $\Delta\phi$ at the side of extraction electrode will be lowered, thereby mitigating the ion loss taken place during the transport. Figures 2a and 2b show the motions of charged particles inside of MMF and of potential-well, respectively.

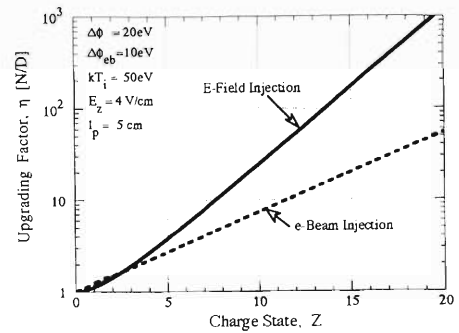


Fig. 1. Upgrading factors η achievable with E-field injection in reference to the case of e-beam injection.

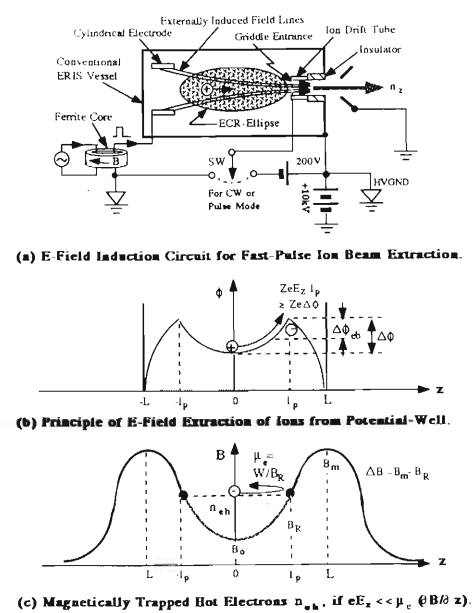


Fig. 2. A conceptual design of (a): E-field extracting, low-emittance pre-bunched ECRIS injector, where (b): only the ions are extracted out of ECR zone, whereas (c): the hot electrons are kept trapped inside of MMF.

References

- 1) C. C. Petty et al.: *J. de Physique*, **50**, C1-783 (1989).
- 2) A. Irani and N. Rostoker: *Particle Acc.*, **8**, 107 (1978).
- 3) Z. Q. Xie et al.: *Proc. ECR-11*, p. 996 (1993).

Supporting Evidences of the LLPB Concept to Explain Enhanced High-Charge State Ion Beam-Current in ECRIS

M. Niimura, T. Kageyama, T. Nakagawa, A. Goto, and Y. Yano

Progress was made in identifying various experimental evidences to support the concept of local lowering of potential barrier (LLPB) which can explain the beam-current upgrade mechanism in an ECR ion source (ECRIS). A threshold like behavior observable in the upgrade experiment was found due to the effect of the peripheral-plasma (PP) surrounding an ECR-plasma. This suggests two sources (peripheral and ECR plasmas) of producing ions in a single ECRIS device. The background theory was thus extended for the two-source model and was treated by a more realistic spherical (rather than cylindrical) model for simulating an ellipsoidal ECR-egg. Finding the non-trivial roles of PP, its parameters were estimated by applying an electrostatic probe theory on available experimental data. The PP electron temperature (T_{ec}) of RIKEN 10 GHz ECRIS was found to be 70 ~ 172 eV.

Extension of Background Theory: Here we introduce a spherical model followed by a theory of two sources. From the Gauss theorem, $\int_S \mathbf{E} \cdot \mathbf{ndS} = \Sigma q/\epsilon_0$, the \mathbf{E} -field induced by the uniform space charge ($\Sigma q \equiv \int \rho dv = 4\pi r^3 \rho/3$, where $\rho = -n_e e$) inside a spherical ECR-volume of radius “a” has the radial component, $E_r = \rho r/3\epsilon_0$ for $r \leq a$. Here, “a” is determinable by $(S/4\pi)^{1/2}$ using the surface area S of a real ECR-volume. The E_r is negative since the potential of spherical model is $\phi(r) = (r/a)^2 \Delta\phi$, which is parabolic like the case of a charged cylinder except the barrier height $\Delta\phi \equiv \phi(a) \equiv n_e e a^2/6\epsilon_0$ for the spherical model. While the resonant electrons are magnetically confined (due to the large perpendicular magnetic moment) to create the space charge, the ions are confined only by the space-charge potential (gradient) force, $-Zen_z \nabla_r \phi(r)$, inside the ECR-egg. Thus, the radial equation of motion of the trapped ion mass-density is

$$Mn_z \frac{dv_z}{dt} = -\nabla_r n_z(r) kT_{iz} - Zen_z \nabla_r \phi(r), \quad \nabla_r \equiv \partial/\partial r \quad (1)$$

Spatial integration of Eq. (1) at the steady-state (s-s) gives $n_z(r) = n_z(0) \exp[-Zc\phi(r)/kT_{iz}] \equiv n_z(0) \exp(-Kr^2)$. Here, $K \equiv Ze^2 n_e / 6\epsilon_0 kT_{iz}$ and $n_z(0)$ is the s-s ion peak density at the midplane ($r=0$, $\phi=0$). The $n_z(r)$ obtained right above indicates a Gaussian distribution of n_z . The ion density at the surface of ECR-volume is thus given by $n_z(a) = n_z(0) \exp[-Ze\Delta\phi/kT_{iz}] \equiv n_z(0) \exp(-Ka^2)$. The spill-flux, $\Gamma_a \equiv v_i n_z(a)$, crossing over the potential barrier $\Delta\phi$ is

$$\Gamma_a = v_i n_z(0) \exp\left(-\frac{Ze\Delta\phi}{kT_{iz}}\right), \quad v_i \equiv \sqrt{2kT_{iz}/\pi M}. \quad (2)$$

Here, the exponential term represents the probability for the ions of charge state Z and temperature kT_{iz} to cross (or spill) over the $\Delta\phi$. See, Fig. 1.

If n_z ions were produced only inside the ECR sphere [Single-Source Theory], the extracted beam-

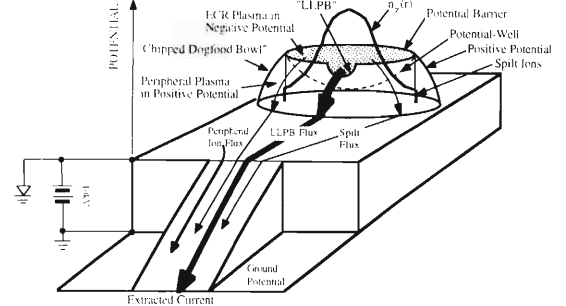


Fig. 1. A “chipped dogfood bowl” like potential distribution inside an ECRIS, illustrating the LLPB concept and the two sources for ion production.

current (I_{ext}) should be equal to the spill-current: $I_{ext} = I_a \equiv ZeS_a \Gamma_a$, where $S_a \equiv 4\pi a^2$. Since $n_z(r)$ has readily been derived from Eq. (1), the volume-averaged density is rigorously calculable. Here, however, the most simple-minded approximation, $\langle n \rangle \approx n_z(0)/2$, is used for simplicity. Then, the total number of ions contained inside the sphere is $N \equiv V_a \langle n \rangle \approx V_a n_z(0)/2$. Therefore, the continuity equation, $\partial N/\partial t + S_a \Gamma_a = Q$, gives $\partial n_z(0)/\partial t + 2S_a \Gamma_a/V_a = Q$; where Q is the supply term. Since Γ_a is given by Eq. (2) and $S_a/V_a = 3/a$ for the spherical model, we have

$$\frac{\partial n_z(0)}{\partial t} + \frac{n_z(0)}{(a/6v_i) \exp[Ze\Delta\phi/kT_{iz}]} = Q. \quad (3)$$

If $Q = 0$, the particle loss can not be offset. The homogeneous ($Q = 0$) solution of Eq. (3) gives the ion confinement time relevant for spherical ECR plasmas:

$$n_z(0) = n_{z0} \exp\left(-\frac{t}{\tau}\right), \quad \tau \equiv \frac{a}{6v_i} \exp\left(\frac{Ze\Delta\phi}{kT_{iz}}\right) \quad (4)$$

The spill-flux can then be written as $\Gamma_a = (a/6\tau)n_z(0)$; thus $\Gamma_a \rightarrow 0$ as $\tau \rightarrow \infty$ no matter how large the $n_z(0)$ is.

Two-Source Theory: Now we take the PP into consideration. As for its container, we assume a cylindrical magnetic bottle with length L_c (chamber length or magnetic mirror separation, whichever shorter) and volume V_c ($\gg V_a$). The non-resonant electrons as well as ions will diffuse out of the mirror magnetic field (MMF) if the pitch angle is smaller than $\theta_m \equiv \sin^{-1}(R_m^{-1/2})$, where R_m is the mirror ratio, thus creating a positive ambipolar potential (ϕ_A) in order to accelerate ions parallel to the MMF. Charged particles are lost only through the ends of cylinder whose area is $2S_{end}$. No cross-field diffusion is allowed throughout this paper. The ambipolar diffusion equation, $\partial n/\partial t = D_A \nabla^2 n$, can be solved by using the method of separation of variables to obtain $n_z(z, t) = n_z(0, 0) \exp(-t/\tau) \cos(\pi z/L_c)$ and $\tau = (L_c/\pi)^2/D_A$. Here, $D_A = (1 + T_e/T_i)D_i$ being

$D_i = kT_i/M\nu_{in}$. For the ECR pressure range ($\sim 10^{-6}$ Torr), the mean-free-path, $MFP \equiv v_i/n_{in}$, is much longer than $L_c/2$ so that the ion-neutral collision frequency is effectively $\nu_{in} = 2v_i/L_c$, thereby giving $D_i = v_i L_c/2$. Thus, we obtain the ion confinement time of PP as $\tau = 2(L_c/v_i)\pi^{-2}(1 + T_e/T_i)^{-1} \approx (L_c/10v_i)$ if $T_e/T_i \approx 1$. This gives $\tau = 3.2 \mu s$ being $v_i = (kT_i/M)^{1/2} = 1.55 \times 10^6$ cm/s if $T_i = T_e = 100$ eV for argon ions and $L_c = 50$ cm. However, $\tau = L_c/2v_i = 16 \mu s$ if the n_z distribution was uniform. Such τ is measurable in the afterglow mode from the signal delay time of the high charge state ions produced at the midplane.

The above study indicates that τ of PP is not a function of Z and rather short. Therefore, PP can produce only the LCS ions lower than $Z \leq Z_o$. Here, the critical Z_o is predictable as the maximum Z that PP at T_{ec} can produce by the time τ . In the domain $Z \leq Z_o$, the τ of ECR-plasma can be much smaller than that of PP due to the small Z and small "a" as seen in Eq. (4); thereby giving $I_{ext} \equiv I_a + I_{end} \approx I_{end}$. When the sheath edge of the extraction port locates at $z = s$ ($< L_c/2$), we can write $I_{end} = ZeS_s\Gamma_s$ and $\Gamma_s \equiv v_B n_s$, where $v_B \equiv (kT_e/M_i)^{1/2}$ is the Bohm velocity. Since $n_s \approx 0.61n_z$, we obtain $I_{end} = 0.61ZeS_s v_B n_z(a) \cos(\pi s/L_c)$. As for Γ_a of Eq. (2), only a half of the flux is directing towards $z = s$, and $I_a \gg I_{end}$ for $Z \geq Z_o$. Here,

$$I_a = 0.31 ZeS_s v_B n_z(0) \exp\left(-\frac{Ze\Delta\phi}{kT_{iz}}\right) \quad (5)$$

If the $\Delta\phi$ was lowered by the amount $\Delta\phi_{eb}$ due to, say, an e-beam injection, Eq. (5) gives

$$I_a = I_o \exp\left[-Ze\frac{\Delta\phi - \Delta\phi_{eb}}{kT_z}\right] \sim \exp(\Delta\phi_{eb}) \quad (6)$$

where $I_o \equiv 0.31ZeS_s v_B n_z(0)$. The upgrading factor defined by $\eta \equiv I_a(\Delta\phi_{eb} \neq 0)/I_a(\Delta\phi_{eb} = 0)$ is therefore scaled by

$$\eta = \frac{I_o(\Delta\phi_{eb} \neq 0)}{I_o(\Delta\phi_{eb} = 0)} \exp\left[\frac{Ze\Delta\phi_{eb}}{kT_{iz}}\right] \sim \exp[z] \quad (7)$$

for Z above the threshold, Z_o . Experimental data¹⁾ show a good fit with $\eta(Z) \sim \exp(Z - Z_o)$ in the domain $Z \geq Z_o$.

Experimental Evidences in Support of the LLPB Concept are: (A) Exponential growth of the extracted ion beam current observable in the plasma cathode and biased-disk experiments¹⁾; i.e., $I_b \sim \exp(V)$ at a fixed Z for the negative bias voltage V . This is a direct proof of the LLPB concept. Since the e-beam current extractable from the plasma cathode obeys Child-Langmuir law $I_e = \text{Const } V^{1.5}$, the electrostatic potential of e-beam can be expressed by $\Delta\phi_{eb} \equiv \text{Const } I_e/V^{0.5} = \text{Const } V$. Therefore, from Eq. (6), one should have $I_a \equiv I_b \sim \exp(\Delta\phi_{eb}) \sim \exp(V)$, thus confirming the lowering of potential by the amount of $\Delta\phi_{eb}$. (B) Existence of Z_o in the plot of $\eta(Z)$; i.e., $\eta \sim \exp(Z - Z_o)$. This indicates presence of two sources for ion production. No clear threshold in Z should be observable without a PP. (C) Good agreement of experimental data with the scaling laws; $\eta \sim \exp[Z]$ when $\Delta\phi_{eb}$ is fixed. This suggests that kT_{iz}

is independent of Z in the first order approximation. Further, the scaling law $\eta \sim \exp[\Delta\phi_{eb}]$ for fixed Z indicates that I_o won't change by $\Delta\phi_{eb}$. This means that $n_z(0)$ as well as T_{ec} is not disturbed by the injection of e-beams. This supports the localized event of the potential lowering; if it were not in the perturbation order, the $n_z(0)$ would deteriorate during the e-beam injection, thereby saturating $\eta(Z)$ curve prematurely.

Characteristics of PP: When a biased-disk or a cathode-plasma-supporting conductive-wall is biased by a negative potential (V) more negative than the floating potential (V_F), a forward electric-current is drained from the conductive surface as much as $I = I_{is} - I_{es} \exp -e(V_{es} - V)/kT_{ec}$. Here, the suffixes 'is' and 'es' denote the ion and electron saturations, respectively. Using the condition $I = 0$ at $V = V_F$, we obtain $\ln(I_{is} - I) = \ln I_{is} - e(V_F - V)/kT_{ec}$. We have converted the V-I data of biased disk and plasma cathode experiments¹⁾ into the $(V_F - V)$ vs. $\ln(I_{is} - I)$ data and replotted them on a semi-logarithmic graph. The T_{ec} has been calculated from the straight line obtained, since its tangent ought to be $-e/kT_{ec}$. We found $T_{ec} = 29.5$ eV and $v_B = 9.79 \times 10^5 [T_{ec}(\text{eV})/A]^{1/2} = 8.42 \times 10^5$ cm/s for argon ions in the PP of Mini-Mafios ion source.²⁾ Since $I_{is} \equiv ZeS_n \exp(-1/2)(kT_e/M)^{1/2}$ is experimentally observable, the ion density was calculable as $n_1(\text{cm}^{-3}) = 8.48 \times 10^{13} I_{is}(\text{Amp})/[T_e(\text{eV})]^{1/2}$ for $Z = 1$ argon ions assuming $S = 0.785$ cm². The n_1 gave the electron number density since $n_e \equiv \Sigma Z n_z$, with which the maximum e-beam current extractable from the PP plasma has been calculated as $I_{es} \equiv 0.25en_e S(8kT_e/\pi m)^{1/2} = 1.32 \times 10^{-12} n_e (\text{cm}^{-3}) [T_e(\text{eV})]^{1/2} [A]$. Figure 2 plots these parameters, together with the maximum ion beam-current (I_{bmax}) extracted,¹⁾ for RIKEN 10-GHz ECRIS. Rather high T_e is evident. Notice that all parameters are exhibiting the same pressure dependence in both domains if a jump between the domains of plasma-cathode and biased-disk is neglected.

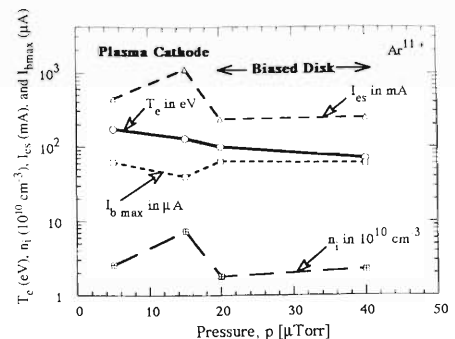


Fig. 2. Semi-experimental PP-parameters of an ECRIS.

References

- 1) T. Nakagawa et al.: *Jpn. J. Appl. Phys.*, **31**, L1129 (1992); *ibid.*, **32**, L1335 (1993).
- 2) B. Paul: *Patent, Int. Cl.* 9013232, Oct. 25 (1991); JP5-89792, Apr. 9 (1993).

Development of Polarized ^3He Gas Target

T. Uesaka, T. Wakui, and M. Wakasugi

With the test bench constructed last year,¹⁾ the polarized ^3He gas target that is produced by a spin exchange reaction with optically pumped Rb atoms has been studied.

The polarization of ^3He was observed with an adiabatic fast passage NMR polarimeter; the result is shown in Fig. 1. The experimental conditions are listed in Table 1.

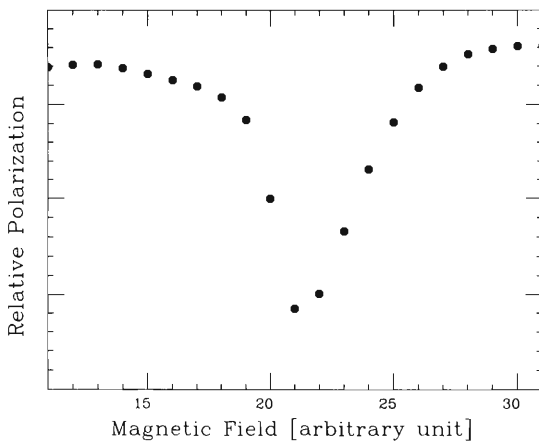


Fig. 1. Observed NMR signal.

Table 1. Experimental conditions. 1 amagat corresponds to 1 atm at 273 K.

Cell material	Corning1724
^3He density	3.3 amagats
N_2 density	~ 0.13 amagats
Cell temperature	180 $^\circ\text{C}$
Holding field	~ 25 gauss
RF frequency	82 kHz

Instead of measuring the absolute polarization, the spin relaxation time is used to evaluate the cell, because it is very difficult to calibrate the absolute polarization. To measure the relaxation time, time dependence of the polarization has to be measured. The

relaxation time, however, was too short to measure and the polarization disappeared in a few seconds. To solve this problem, two kinds of modifications to the target system were made.

One is for a glass material of the target cell. Corning1720 has been known to be a good material for the polarized ^3He target cells. However, it is no longer in production. Therefore at first we started with Corning1724 which is also aluminosilicate glass as Corning1720. KEK group and one of the authors tested Corning1724 cells at KEK Booster Synchrotron Facility. The result showed much shorter relaxation time for Corning1724 than for Corning1720. We thus gave up Corning1724 and then employed Corning7056, which was reported to show comparable relaxation time to Corning1720 by Michigan group.²⁾

The other is for the cell making apparatus. From the investigation performed in collaboration with KEK group, a gas purification method was found to play an important role to achieve long relaxation time.³⁾ Following this result, two chemical getter gas purifiers for ^3He and N_2 , SAES Getters GC50s, have been introduced. GC50's reduce almost all the impurities to less than 10 ppb.

In spite of these modifications, however, the relaxation time was still of the order of 10 seconds. This short relaxation time is considered to be due to a large surface-to-volume ratio of the cell. The problem will be reduced in the next target system with a larger target cell. Also the calibration of the polarization by the proton NMR method will be easier with the large cell.

Construction of the new system is now in progress. Measurement of the ^3He polarization is planned early in December 1995.

References

- 1) T. Uesaka et al.: *RIKEN Accel. Prog. Rep.*, **28**, 154 (1995).
- 2) K. P. Coulter et al.: *Int. Symp. Polarization Phenomena in Nuclear Physics*, Bloomington, U.S.A. (1994).
- 3) T. Uesaka et al.: *Proc. Int. Workshop on Polarized Beams and Polarized Gas Targets*, in press.

Development of a New Type of Single-Bunch Selector

N. Inabe, M. Kase, I. Yokoyama, A. Goto, and Y. Yano

A system to produce a single-bunched beam, which was reported in the last progress report,¹⁾ has been developed so as to increase intensity and quality of the beam. As concern to the quality, main purpose is to raise up purity that is a ratio of current of the desired bunch to total one including undesired bunches.

Figure 1 shows a method to produce the single-bunched beam. As shown in Fig. 1, the single-bunched beam can be produced by sweeping undesirable bunches transversally and/or longitudinally. In the old system only the transversal sweeping is done by a chopper with parallel plate electrodes. Because, in our method, sweeping is done for the continuous beam with a low energy from the ion source (extraction voltage < 10 kV), a base of the single-bunched beam, that is a remaining part which is not swept, has tails inevitably as shown in Fig. 1. Origins of the tail are a traveling time that the beam is passing through the electrodes with low velocity as well as a rise and fall time of the voltage supplied to it. In order to produce the pure single-bunched beam the tails should not overlap with the acceptance of the next bunch to the desired one. However, as it is difficult to shorten the tails for technical reasons, there is a limitation to produce the pure single-bunched beam in this way.

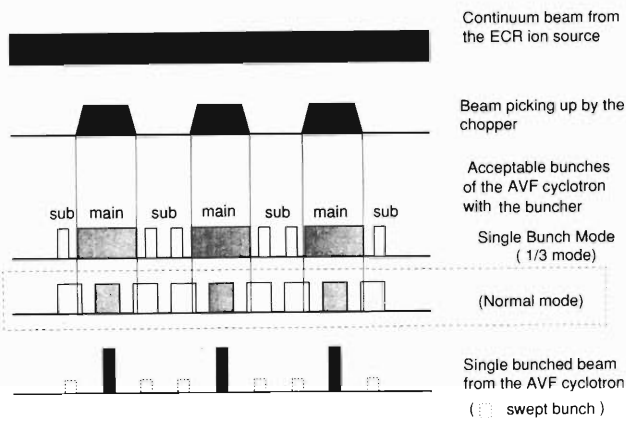


Fig. 1. Production mechanism of the single-bunched beam.

For the reason mentioned above longitudinal sweeping was also introduced in the system. The longitudinal sweeping can be done by making phase acceptance of the undesirable bunch at the buncher narrow. For the purpose, we used the buncher with sub-harmonic mode. Figure 2 shows the phase acceptance for the sub-harmonic mode and the normal one. For the sub-harmonic mode the phase is modulated by a sine-shaped wave that we used. As shown in Fig. 2, the acceptance is wide when the phase is compressed and

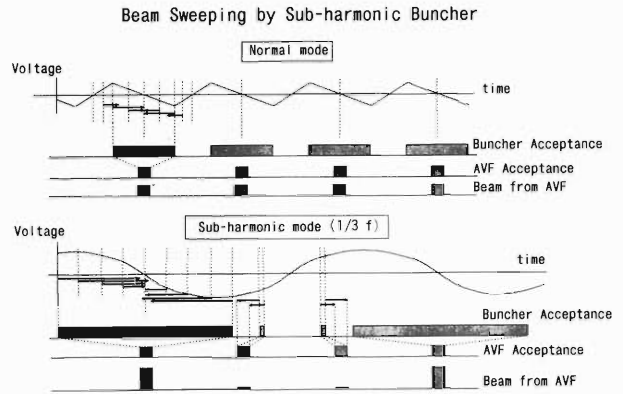


Fig. 2. Mechanism of phase compression by the buncher. Upper figure is for the normal mode and lower for the sub-harmonic mode ($f = 1/3$).

narrow when that is diverged. A ratio of the narrow acceptance to the wide one is a few percent. Moreover the intensity of the beam for the sub-harmonic mode becomes higher than that for the normal one because the compressed phase for the sub-harmonic mode is larger than that for the normal one. Of course, by using the part of the wide acceptance as the desired beam the single-bunched beam can be produced but the purity is not so high.

By combination of the two ways, clearly, the purity of the single-bunched beam can be raised up. Because the acceptance of the desired bunch is wide and the undesired one, narrow for the sub-harmonic mode, overlap between the tail and the acceptance of the undesired bunch becomes small. In principle, if the acceptance of the desired bunch becomes wide enough to include the tail, the single-bunched beam with the purity of 100% can be produced. In this way the highly intense and pure single-bunched beam can be produced by both the transversal and longitudinal sweeping.

We used the buncher that has been already installed.²⁾ In order to operate the sub-harmonic mode we must use the buncher at low frequency (4–8 MHz). For the purpose we made a new frequency divider whose amplifier and phase are controllable. A wave made by the divider is sent to the buncher via a wide-band amplifier.

A performance study of the system was carried out for the 10.0 KeV Ar¹¹⁺ beam from the ECR ion source which was accelerated to 5.2 MeV/nucleon by the AVF with an RF frequency of 14.05 MHz and to 95 MeV/nucleon by the Ring Cyclotron (RRC) with an RF frequency of 28.1 MHz. The setup is shown in Fig. 3. The voltage between the electrodes was switched off every 200 ns. Voltage of the electrodes was 200

V. The buncher was operated with the $(1/3)f$ mode. Time structures of the beam after the AVF and RRC were measured by using a time of flight (TOF) with the same method as shown in Ref. 1.

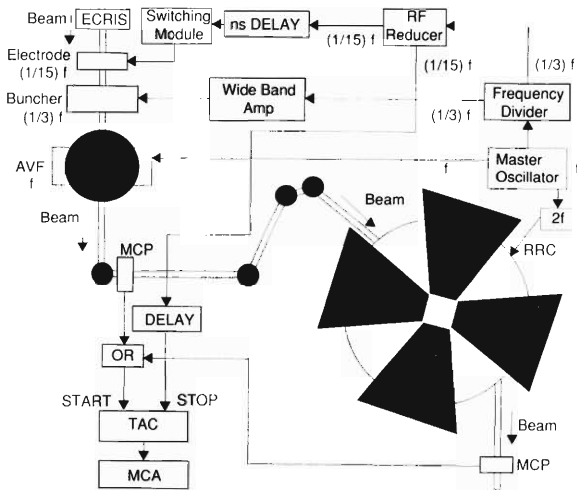


Fig. 3. Setup for a performance test of the single-bunch selector.

Figure 4 shows a typical example of the TOF spectrum of the AVF. As shown in Fig. 4, the purity of the single-bunched beam is almost 100%. Figure 5 shows an example of the TOF spectrum of the RRC. The main peak in Fig. 5 is made by the single-bunched beam to be extracted. The other peaks are originated from another turn of the RRC (a) and next main bunch (b). The production mechanism is shown in Ref. 1. By careful tuning of the RRC we can extract the beam with single turn. In fact, we supplied the single bunched beam of which purity was more than 99%. The current of the single bunched beam from the RRC is ~ 20 nA.

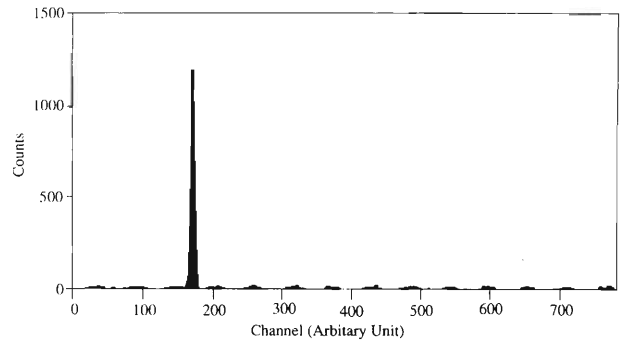


Fig. 4. An example of time spectra of the beam extracted from the AVF.

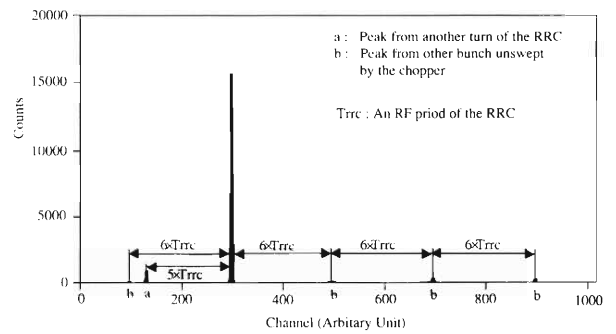


Fig. 5. An example of time spectra of the beam extracted from the RRC. T_{rrc} means the RF period of the RRC.

The obtained intensity is rather smaller than the estimated one. It might be due to bad transmission of the RRC because the electric injection channel did not work sufficiently. A detailed study will be performed.

References

- 1) N. Inabe et al.: *RIKEN Accel. Prog. Rep.*, **28**, 160 (1995).
- 2) K. Ikegami et al.: *ibid.*, **22**, 213 (1988).

Construction of a New Beam Line from the AVF Cyclotron

N. Inabe and M. Kase

A new beam line (E7E) has been constructed in the experimental room 7 (E7) for users of AVF cyclotron (AVF). Before the new construction, as shown in Fig. 1, the E7 room already had lines for beams from the AVF (E7C and E7D) other than those from the RIKEN Ring Cyclotron (RRC; E7A for SLOW and E7B for Large Ω). However, since the main space in the E7 room was used for the beam lines E7A and E7B, the experimental area of the beam lines E7C and E7D was very small. Especially, due to the small space, it was impossible to perform a newly proposed experiment of a polarized deuteron beam from the AVF.¹⁾ To solve a problem of the small space, it was needed that a new beam line with a large experimental area was to be constructed instead of the E7C. Recently experiments using the Large Ω have been finished. Under the situation, we removed the Large Ω and constructed the new beam line (E7E) in the area used for the Large Ω .

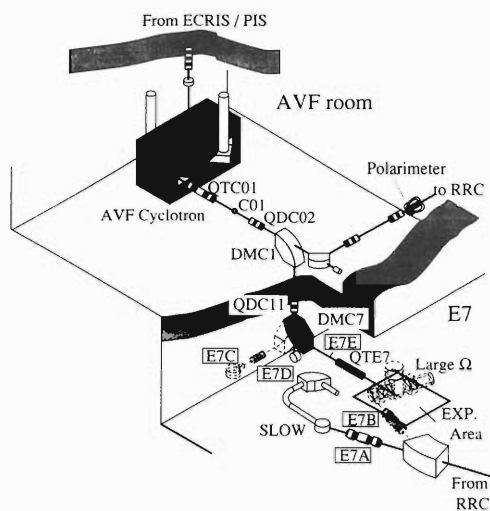


Fig. 1. Schematic drawing of the AVF and E7 room. The dark grey part is the new beam line and the dotted part is the old beam lines.

The newly constructed beam line is the downstream of the dipole magnet (DMC7) as shown with dark grey in Fig. 1. The DMC7, which has been used in the E7C, has been rotated by 90 degrees in counter-clockwise direction. The removed beam line of the E7B has been used in the E7E by adjusting the length of a beam duct in the upstream of the quadrupole magnet (QTE7). The new beam line has a Faraday cup and a profile monitor in the downstream of the QTE7 and steerer magnets in the upstream of the QTE7. The experimental area is now large enough to perform the experiment mentioned above.

Optics in the new beam line was calculated using the computer code TRANSPORT. A required beam-spot size is less than 4 mm. To meet the requirement we searched the parameters. In the calculation the emittance of the beam extracted from the AVF was assumed to be the one that had been measured.²⁾ The obtained values in the downstream of the DMC7 magnet are summarized in Table 1. The beam envelope is shown in Fig. 2.

Table 1. Parameters of the new beam line.

Drift length (m)	
DMC7 ~ 1st Q of the QTE7	2.7
1st ~ 2nd Q's of the QTE7	0.2
2nd ~ 3rd Q's of the QTE7	0.2
3rd Q of the QTE7 ~ target	2.0
Effective length (m)	
1st and 3rd Q of the QTE7	0.25
2nd Q of the QTE7	0.45
Max. field strength of Q (kG/cm)	
all three Q's	1.5

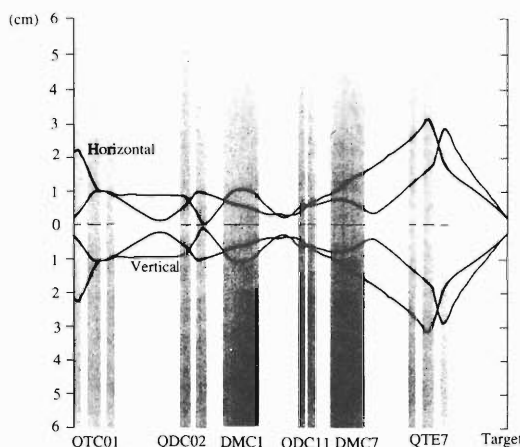


Fig. 2. Envelope of the beam in the new beam line.

Last April an 8 MeV polarized deuteron beam was firstly transported in the new beam line. The obtained beam-spot size was about 4 mm. Transmission of the beam from C01 to the target point was more than 80%.

Until now several users have done experiments in the E7E using not only the polarized deuteron but also other kinds of ions.

References

- 1) N. Nishimori et al.: This report, p. 58.
- 2) N. Inabe et al.: *RIKEN Accel. Prog. Rep.*, **28**, 158 (1995).

Improvement of the RF Control System for RILAC

S. Kohara, E. Ikezawa, M. Hemmi, T. Chiba, T. Aihara,* T. Ohki,* H. Hasebe,*
H. Yamauchi,* and Y. Miyazawa

The rf control system for six resonators of RILAC was improved to get easy maintenance and stable operation in this year. The amplitude controller and the automatic tuning circuit were newly designed, fabri-

cated and installed for each resonator of RILAC.

A block diagram of the rf control system is shown in Fig. 1. It consists of a three-stage power amplifier and the low level circuits.^{1,2)} The operational fre-

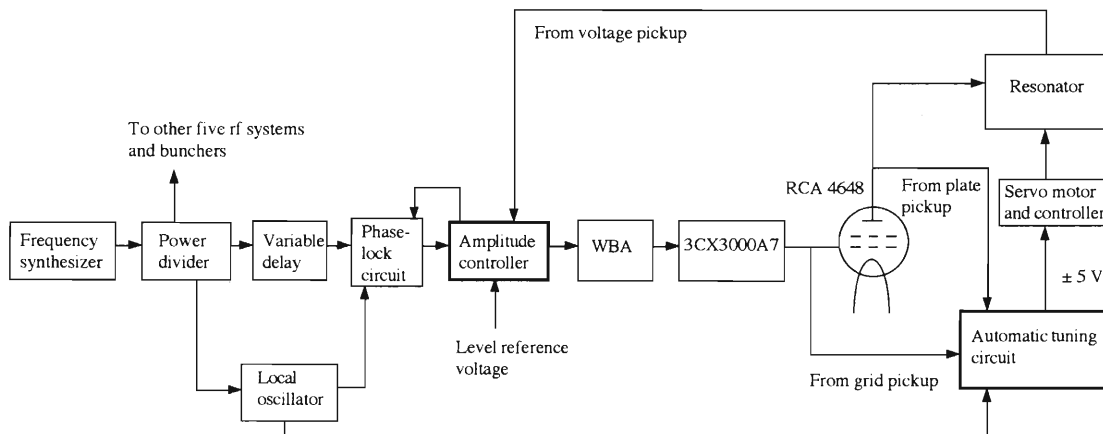


Fig. 1. Block diagram of the rf control system.

quency range of these controllers is from 17 to 45 MHz.

The amplitude controller operates to excite the resonator in the three modes; pulse, cw-pulse and cw. The pulse mode operation is employed to find a resonance condition of the resonator by moving a capacitive trimmer manually and to overcome the multipactoring phenomenon in the resonator tank. The pulse width and repetition cycle can be varied from 1 to 10 ms and from 0.5 to 10 Hz, respectively.

After the cw-pulse mode is selected, the pulse operation is automatically changed into the cw one when the accelerating voltage of the resonator reached more than 30 kV. The accelerating voltage is regulated with the amplitude controller by comparing the pickup voltage from the resonator and the level reference voltage. In this mode, the cw operation is automatically changed into the pulse one when the accelerating voltage is lost by the vacuum discharge which occur in the resonator. In order to easily recover the accelerating voltage the output level of the amplitude controller in the pulse mode operation is set about 1.2 times higher than that in the cw mode operation.

The cw mode operation is employed to adjust the impedance of the tuning circuit for the input and the output of the final amplifier (RCA 4648). The feedback signal of the accelerating voltage is fed to the phase-lock circuit via the amplitude controller.

The tuning of the resonator is maintained automatically by moving the capacitive trimmer with the auto-

matic tuning circuit. The automatic tuning is performed by comparing phases between the plate and the control grid voltages of the final amplifier. When the output circuit of the final amplifier is tuned to the resonator, the phase difference between the control grid and the plate voltages becomes 180°.

Output signal of the automatic tuning circuit is fed back to the servo motor to move the capacitive trimmer. When the accelerating voltage is lost in the resonator, its output voltage becomes zero to stop the capacitive trimmer. Maximum output voltage of the automatic tuning circuit is ±5 V DC.

A variable delay, which had been manually-adjusted delay lines, was replaced by a phase shifter equipped with the automatic tuning circuit. The phase shifter can be variable continuously more than ±180°. These controllers are connected to a computer in the control room.

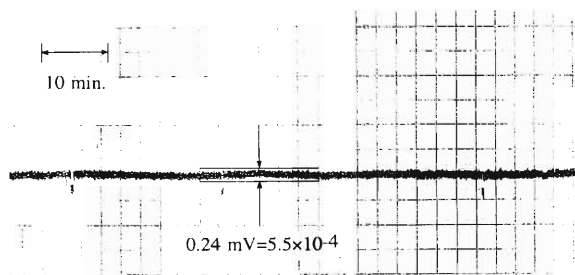


Fig. 2. Stability of the accelerating voltage measured at No. 5 resonator. The frequency and the voltage are 32 MHz and 230 kV, respectively.

* Sumijyu Accelerator Service, Ltd.

The resonator was easily excited with the cw-pulse mode (2.5 ms, 1.4 Hz) in the rf excitation test. The

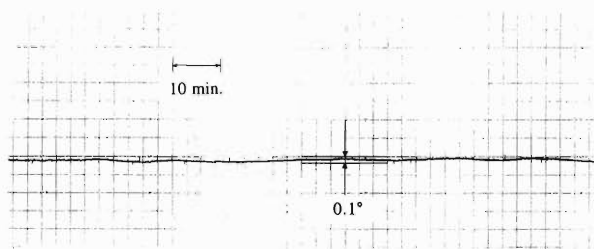


Fig. 3. Stability of the phase measured at No. 5 resonator. The frequency and the voltage are 28 MHz and 240 kV, respectively.

amplitude and the phase stability of the accelerating voltage were measured for six resonators under beam loading. Figures 2 and 3 show the typical results of the voltage and the phase stability for No. 5 resonator. Stability of the accelerating voltage and the phase are $< 5.5 \times 10^{-4}$ and $< 0.1^\circ$, respectively. The amplitude stability was improved by a factor of 5. The rf control system has been working well without serious troubles since the installation of the new circuits.

References

- 1) Y. Chiba: *RIKEN Accel. Prog. Rep.*, **14**, 120 (1980).
- 2) T. Kubo: *ibid.*, **16**, 166 (1982).

Status of a New Injector System for RILAC

A. Goto, Y. Miyazawa, M. Hemmi, O. Kamigaito, T. Nakagawa, M. Kase, T. Chiba, N. Inabe, S. Kohara, T. Kageyama, S. Numata, Y. Batygin, E. Ikezawa, and Y. Yano

Fabrication of a new injector system for RILAC was completed in the spring of 1995. We have made performance tests of the 18 GHz ECR ion source and the FC-RFQ linac as well as beam acceleration tests in the system. Details of the results are reported in Refs. 1 and 2. Figures 1 and 2 show the photographs of the 18 GHz ECR ion source and the FC-RFQ linac, respectively.

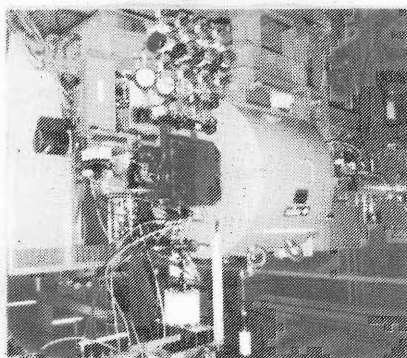


Fig. 1. Photograph of the 18 GHz ECR ion source.

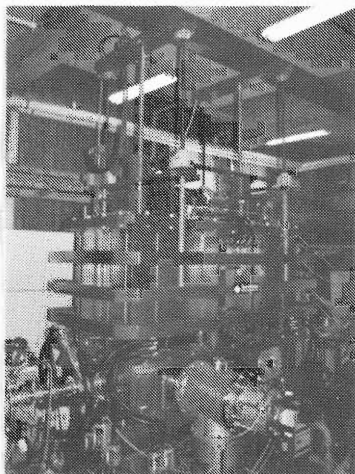


Fig. 2. Photograph of the FC-RFQ linac.

Ion beam intensity from the ECR ion source was measured for gaseous elements such as oxygen, argon and krypton with an extraction voltage of up to 15 kV. Obtained beam intensity of Ar^{11+} and that of O^{7+} ions, for example, were 160 and 130 $e\mu\text{A}$, respectively, with the RF power of about 600 W and an extraction voltage of 15 kV. The beam intensity from the 18 GHz ECR ion source was measured to be higher than that from NEOMAFIOS 8 GHz, now used for RILAC, by

one or two orders of magnitude. It is also noted that the beam intensity of, for example, Ar^{11+} ions was twice higher than that from CAPRICE 14.5 GHz when compared at the same RF power of 600 W. Pulse mode operation was also tested and a significant afterglow effect was seen particularly for heavy ions like krypton and high charge states: the ratio of the beam intensity in the pulse mode operation to that in the cw mode operation was 4 for Kr^{20+} ions. A rod for metallic ions and a plasma cathode have not yet been tested.

The vanes of the FC-RFQ linac have been three-dimensionally machined and assembled within the accuracy of $\pm 50 \mu\text{m}$, the value meeting the requirement for good beam transmission.³⁾ The surfaces of the vanes were polished with electrochemical buffing within the flatness of less than $1 \mu\text{m}$. The resonant frequency was measured to vary from 17.7 to 39.2 MHz. The measured Q-values and shunt impedances were about 60% of the MAFIA calculations. From the shunt impedance measurement, the required maximum RF power was found to be 26 kW (cw). We have encountered a serious problem on the ceramic pillars used for fixing the high voltage part on the base plate of the resonator; multipactoring occurred on the pillars at an intervane voltage below 15 kV, and heating due to dielectric losses in a local region of the pillars occurred at an intervane voltage above 35 kV. To fix this problem, the ceramic pillars were redesigned and are being newly fabricated.

Beam acceleration tests have been performed for Ar^{3+} , Ar^{6+} , Ar^{11+} , and O^{5+} ions at the frequencies of 17.7, 26.1, 34.4, and 39.2 MHz, respectively, and at the intervane voltage of about 20 kV. The beam velocity after acceleration, which was measured by the TOF technique using three capacitive pickup probes, was in agreement with the designed value within 1%. The beam transmission efficiency of 85% at the maximum through the FC-RFQ linac was obtained from the first tests. Beam emittance has not yet been measured in this test.

The performance tests including the beam acceleration tests showed that the beam intensity from the RILAC is expected to be increased by one or two orders of magnitude. The system is planned to be installed on site next year. A beam rebuncher will also be installed at that time between the FC-RFQ linac and the RILAC.

References

- 1) T. Nakagawa et al.: This report, p. 220.
- 2) O. Kamigaito et al.: This report, p. 221.
- 3) Y. Batygin et al.: This report, p. 223.

Development of RIKEN 18 GHz ECRIS

T. Nakagawa, Y. Miyazawa, M. Hemmi, T. Chiba, N. Inabe, M. Kase, T. Kageyama,
O. Kamigaito, E. Ikezawa, A. Goto, and Y. Yano

Recently, intense beams of medium mass heavy ions, mainly metallic ions, become one of the major requests in RIKEN Accelerator Research Facility. For satisfying such a request, a new ECRIS is demanded as an external ion source of the RILAC-Ring cyclotron accelerator complex. According to the scaling law proposed by R. Geller, the beam intensity increases with increasing microwave frequency and magnetic field strength.¹⁾ Therefore, the microwave frequency of 18 GHz has been chosen for the new RIKEN ECRIS. It is connected to a new RFQ linac and used as a new injector as described in Refs. 2 and 3. The design of RIKEN 18 GHz ECRIS was already described in Refs. 4 and 5. In this paper, we present the performance of producing multi-charged ions from gaseous elements.

Figure 1 shows the beam intensities of highly charged ions produced from a gaseous element. These results were obtained by using the gas mixing method.¹⁾ The typical gas pressure of plasma chamber and extraction stage was 1.0×10^{-6} , and 9×10^{-7} Torr, respectively. The extraction voltage was 15 kV. For example, beam intensities of Ar^{11+} and O^{7+} were 160 and $130 \text{ e}\mu\text{A}$, respectively. The distance between the orifice ($\phi = 10 \text{ mm}$) and the extraction electrode ($\phi = 13 \text{ mm}$) is also one of the important parameters to optimize the performance of ECRIS. It strongly depends on the condition of plasma, shape of extraction electrode, and charge state of extracted ions.⁶⁾ For RIKEN 18 GHz ECRIS, the best results for medium charge states of heavy ions (i.e., $\text{O}^{5+.6+}$, $\text{Ar}^{8+ \sim 11+}$)

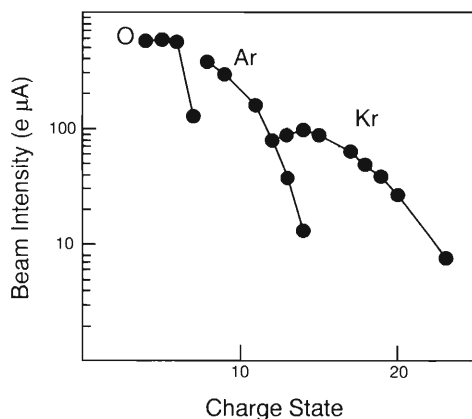


Fig. 1. Charge state distributions of O, Ar, and Kr ions.

could be obtained at the distance of about 30 mm.

Figure 2 shows the beam intensities of Ar^{11+} ions for 18 GHz ECRIS, CAPRICE (14.5 and 10 GHz) developed in Grenoble,⁷⁾ and ECRIS 4 (GANIL)⁸⁾ as a function of RF power. All of ECRISs has almost the same structure and the same volume of plasma chamber. The extraction voltage of RIKEN 18 GHz ECRIS was 13 kV. For other ECRISs the extraction voltage was 20 kV. In the figure B_{max} indicates the maximum field strength of the mirror magnetic field. At the same RF power, the beam intensity increases with increasing frequency of micro wave and magnetic field strength as described in Ref. 1.

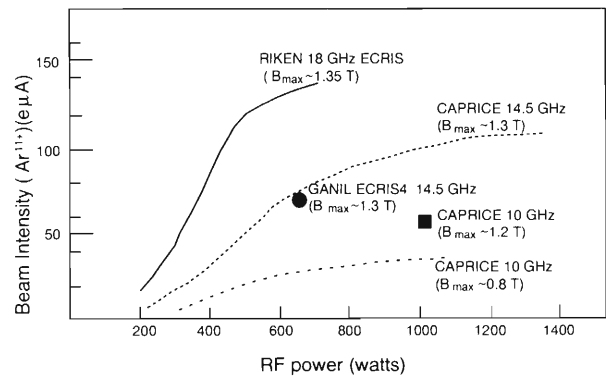


Fig. 2. Beam intensity of Ar^{11+} ion for various ion sources as a function of RF power.

References

- 1) R. Geller: *Ann. Rev. Nucl. Sci.*, **40**, 15 (1990) and references therein.
- 2) A. Goto et al.: This report, p. 219.
- 3) O. Kamigaito et al.: This report, p. 221.
- 4) T. Nakagawa et al.: *RIKEN Accel. Prog. Rep.*, **28**, 165 (1995).
- 5) T. Nakagawa et al.: Proc. of the 10th Symp. on Accel. Sci. Technol., JAERI-Conf. 95-021, Ibaraki, p. 224 (1995).
- 6) R. Leroy et al.: Proc. of 12th Int. Workshop on ECR Ion Source and their Application, M. Sekiguchi and T. Nakagawa (eds.), INS-J-182, Tokyo, p. 57 (1995).
- 7) D. Hiz et al.: *ibid.*, p. 126.
- 8) P. Sortais et al.: Proc. of 10th Int. Workshop on ECR Ion Sources, F. W. Meyer et al. (eds.) Ornl CONF-9011136, Oak Ridge, p. 35 (1991).

Development of a Variable-Frequency RFQ Linac for RILAC

O. Kamigaito, A. Goto, Y. Miyazawa, T. Chiba, M. Hemmi, S. Kohara,
M. Kase, Y. Batygin, and Y. Yano

A variable-frequency RFQ linac has been constructed as a new injector for the RILAC. This RFQ will accelerate ions with mass-to-charge ratios of 6 to 27 at up to 450 keV per charge by varying its resonant frequency from 17.7 to 39.2 MHz. The RFQ resonator, based on a folded-coaxial structure with a movable shorting plate, has the distinct features such as the compactness and the wide frequency-tunability.¹⁾

Figure 1 shows a schematic layout of the RFQ resonator whose details are described in Ref. 1. A detachable stem shown in Fig. 1 has been introduced considering the results of the cold test on a half-scale model.²⁾ This stem is used only in high-frequency operations where it is in electric contact with both the conductor tube and the base plate, while it is detached from the base plate in low-frequency operations. It is expected that the detachable stem reduces the power consumption because it shares the rf electric current with the upper stem.

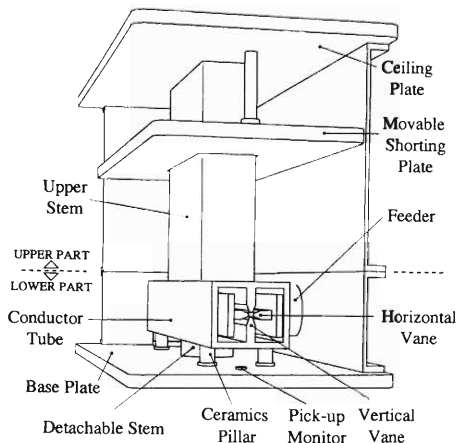


Fig. 1. Schematic drawing of the RFQ resonator. The inner volume is about 1700 mm (length) \times 700 mm (width) \times 1100 mm (height).

Channels for water cooling have been designed based on the heat analysis. Water for the horizontal vanes is supplied through the front and rear supports of the vanes. That for the vertical vanes and the rectangular tube is provided through the inside of the upper stem. The total water flow is 155 ℓ /min at 7 atm. Two turbomolecular pumps (1500 ℓ /s) are fixed on both sides of the resonator.

The vanes have been three-dimensionally machined within the accuracy of $\pm 50 \mu\text{m}$. The vane parameters have been determined by taking the results of a numer-

ical simulation into account.³⁾ Misalignment effects on the beam transmission have been also examined.⁴⁾

Figure 2 shows the measured resonant frequency along with the values calculated by the MAFIA program. The horizontal axis represents the gap distance between the top surface of the conductor tube and the bottom surface of the shorting plate. The resonant frequency varies from 17.7 to 39.2 MHz by changing the position of the shorting plate by a stroke of 790 mm.

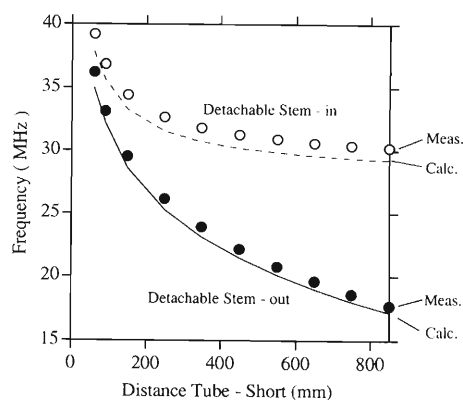


Fig. 2. Measured resonant frequency along with the MAFIA calculations. The closed circles and the solid curve represent the measured and the calculated values, respectively, when the detachable stem is out of the resonator. The open circles and the dashed curve represent the measured and the calculated values, respectively, when the stem is in the resonator.

Figure 3 shows the measured Q-values and shunt impedances. The corresponding MAFIA-calculation curves are shown in the figures as well. The shunt impedance R_s is defined by $V^2/(2P)$, where P is the rf power consumption and V is the intervane voltage. As expected, above 30 MHz the measured Q-values and shunt impedances with the detachable stem installed are larger than those without the detachable stem. The MAFIA calculations overestimate the measured values by about 50%. This is considered to result from the fact that the calculation does not realistically treat the roughness of the wall surface and the imperfection of the electric contact. The power losses estimated from the measured shunt impedances are 6 kW at 17.7 MHz and 26 kW at 39.2 MHz for the designed intervane voltage of 33.6 kV in the cw operation.

High power tests have been performed with an rf power source based on an Eimac 4CW50000E, which

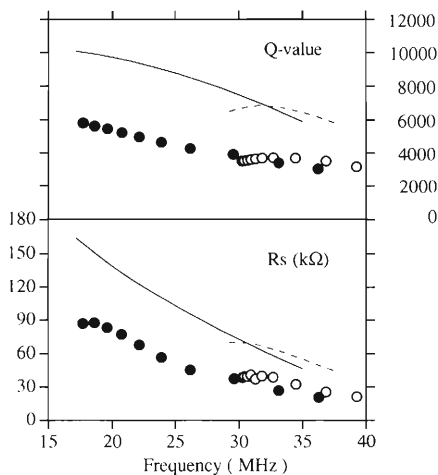


Fig. 3. Measured Q-values and the shunt impedances along with the MAFIA calculations. The data of symbols and curves are obtained under the same conditions as in Fig. 2.

has a cw power of 40 kW at maximum between 16.9 MHz and 40 MHz. Following results have been obtained: (1) The RFQ can be stably operated in the cw mode when the intervane voltage is between 15 kV and 30 kV. The vacuum stays in a range of $1 - 3 \times 10^{-7}$ Torr at the pump head. No temperature rise has been detected during the operation. (2) Emissions of blue-white glow are observed on the ceramic pillars when the intervane voltage is below 10 kV. This is considered to be caused by the multipactoring phenomena. (3) Emissions of red-white light are observed above the intervane voltage of 35 kV, which is due to the heat caused by the dielectric losses in the pillars.

In order to eliminate the drawbacks (2) and (3) described above, the shape of the pillars has been re-examined by use of the MAFIA code. Two different types of pillars, which have a smaller electric field within themselves, have been fabricated and will be tested soon.

Acceleration tests have been done using beams from an 18GHz-ECRIS.⁵⁾ The beam line from the ECRIS to the RFQ is described in Ref. 6. The velocity of the accelerated beams has been measured by means of the TOF method, using three capacitive pick-up probes settled in a diagnostic box which is located just after the RFQ.

The accelerated ions so far are Ar^{3+} , Ar^{6+} , Ar^{11+} , and O^{5+} at the frequencies of 17.7, 26.1, 34.4, and 39.2 MHz, respectively, and at the intervane voltage around 20 kV. The maximum transmission efficiency obtained from the first test was 85% with the beam intensity of 10–50 $e\mu\text{A}$. The velocity of the accelerated beam is in agreement with the designed value within 1%.

Measurements of the beam emittance and the acceleration tests with full-intensity beams from the ECRIS are in preparation.

References

- 1) O. Kamigaito et al.: *Jpn. J. Appl. Phys.*, **33**, L537 (1994).
- 2) O. Kamigaito et al.: *ibid.*, **34**, 5799 (1995).
- 3) Y. Batygin et al.: *RIKEN Accel. Progr. Rep.*, **28**, p. 172 (1995).
- 4) Y. Batygin et al.: This report, p. 223.
- 5) T. Nakagawa et al.: This report, p. 220.
- 6) N. Inabe et al.: *RIKEN Accel. Progr. Rep.*, **28**, p. 166 (1995).

Misalignment Effect of Vanes on Beam Transmission Efficiency in an RFQ Linac

Y. Batygin, A. Goto, O. Kamigaito, and Y. Yano

Beam transmission efficiency in an RFQ linac is affected by several reasons. Our previous study¹⁾ indicated significant sensitivity of beam dynamics on small systematic deviations of RFQ cell parameters from the original design. In this paper the effect of random vane errors on the beam transmission efficiency is examined to define the engineering tolerance for RFQ vane machining and alignment.

Random errors in manufacturing RFQ vane tips result in the amplitude growth of transverse and

longitudinal oscillations. Analytical treatment²⁾ shows monotonous enlargement of transverse oscillation amplitude r_{\max} and vertical size of separatrix $\langle \Delta g \rangle = \langle \Delta P \rangle / v_s$ after passing through the RFQ section with N cells:

$$\langle \delta r_{\max} \rangle^2 = 2N \left[\langle \delta r_o \rangle^2 + r_{\max}^2 \left(\left\langle \frac{\delta U}{U} \right\rangle^2 + 4 \left\langle \frac{\delta R_o}{R_o} \right\rangle^2 \right) \right], \quad (1)$$

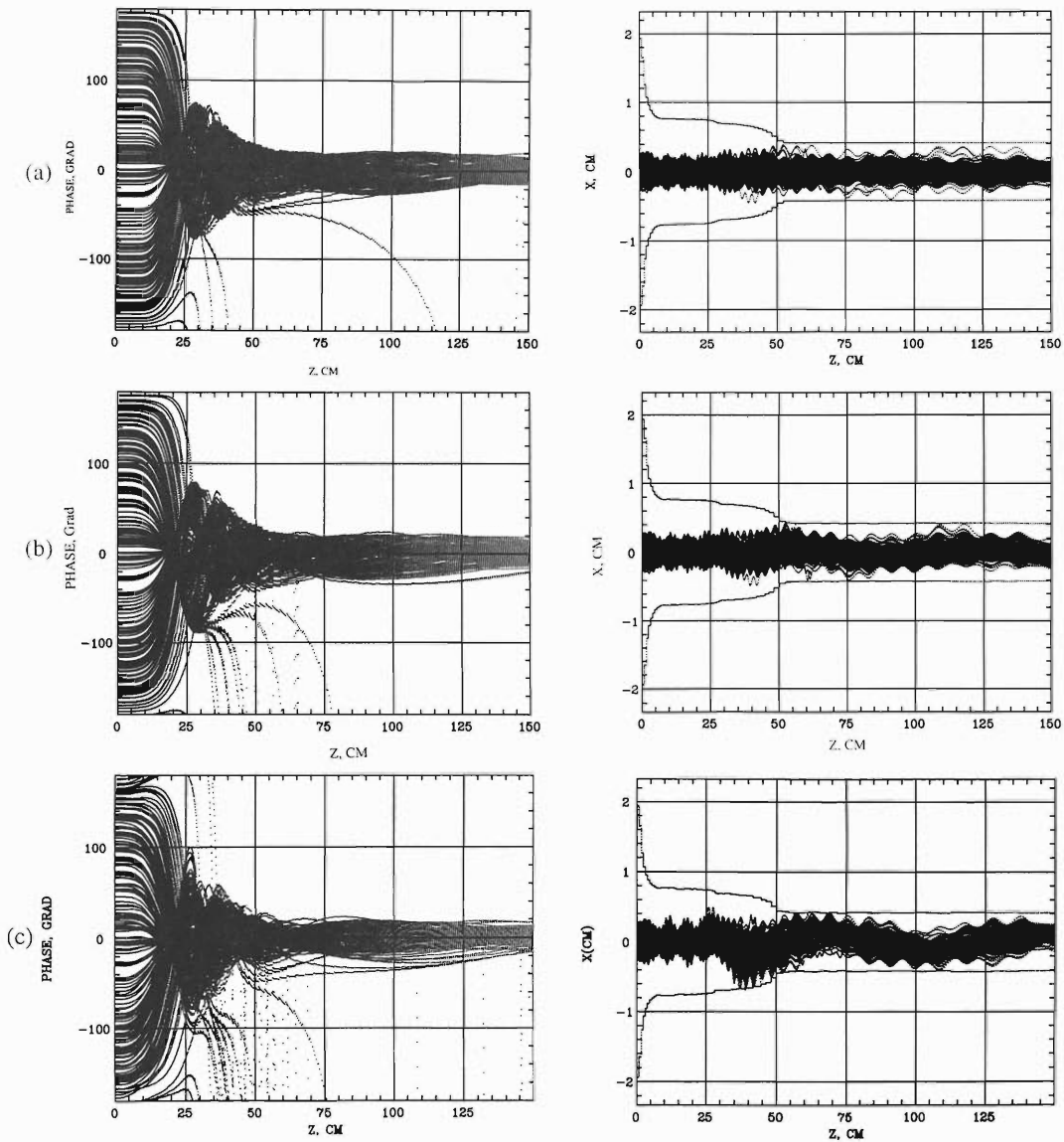


Fig. 1. Phase trajectories (left) and x-trajectories (right) of particles in the RFQ structure with various values of error in the vane fabrication: (a) 0 microns; (b) ± 50 microns; (c) ± 100 microns.

$$\langle \Delta g \rangle^2 = \pi^2 \left(\frac{\Omega_f}{\omega} \right)^2 \left(\frac{W_o}{\Delta W} + N \right) \left\{ \left(\frac{\Omega_f}{\omega} \right)^2 \text{ctg}^2 \varphi \right. \\ \cdot \left[1 - \sqrt{\frac{W_o}{W_f}} \left[\frac{\langle \delta A \rangle^2}{A^2} + \frac{\langle \delta U \rangle^2}{U^2} \right] \right. \\ \left. \left. + \frac{1}{3} \left[1 - \left(\frac{W_o}{W_k} \right)^{3/2} \right] \frac{\langle \delta L \rangle^2}{L^2} \right\}, \quad (2)$$

where δr_o is an axis displacement, δR_o an error in average radius of the structure $R_o = a/\sqrt{X}$, δL an error in cell length, δU an intervane voltage instability, Ω_f a longitudinal oscillation frequency, ω an RF frequency, W a particle energy, A an acceleration efficiency, φ a synchronous phase.

To obtain accurate estimation of this effect on the beam transmission efficiency, the computer simulation using code BEAMPATH³⁾ was done. The following parameters were randomly distributed at every cell within the maximum error $\pm\delta$: cell lengths L_i , aperture radius a_i , maximum distance from axis to electrodes ma_i , and axis displacement δr_{oi} . Results of simulation are presented in Table 1 and Fig. 1. Random errors in the RFQ geometry induce particle losses both in longitudinal and transverse directions. From the results of simulations it follows that the error of 50 microns does not create any serious degradation of the beam parameters while an error of 100 microns could cause notable decreasing of beam transmission efficiency.

Table 1. Change of beam transmission efficiency due to errors in the vane fabrication.

	δ , microns	I=0	I=1 mA
1.	0	0.94	0.87
2.	50	0.92	0.85
3.	100	0.80	0.70

Another possible source of particle losses is a disturbance of pure RFQ quadrupole symmetry due to a dipole field component. This effect was studied for the case when one of the RFQ electrodes is shifted from its ideal position at the distance Δ . It results in appearance of extra terms proportional to $\cos\theta$, $\cos 2\theta$, $\cos 3\theta$, ... in the RFQ potential expansion. The new lowest order RFQ potential is given by:

$$U(r, \theta, z) = -\frac{U_o}{2} \left[X \left(\frac{r}{a} \right)^2 \cos 2\theta + AI_o(kr) \sin(kz) \right. \\ \left. + A_{01} \frac{r}{a} \cos \theta + A_{11} I_1(kr) \cos \theta \sin(kz) \right]. \quad (3)$$

Coefficients A_{01} , A_{11} are defined by new boundary conditions where potential is kept constant at the surface of electrodes $U(r, \theta, z) = -U_o/2$:

$$U(x, y, z) = -U_o/2 \quad x = -a(z), \quad (4)$$

$$U(x, y, z) = -U_o/2 \quad x = a(z) + \Delta, \quad (5)$$

where $a(z)$ is the vane-tip profile of the modulated electrodes defined by equation:

$$X \left[\frac{a(z)}{a} \right]^2 + AI_o[ka(z)] \sin(kz) = 1. \quad (6)$$

From boundary conditions (4), (5) the expression for RFQ potential with a dipole component is given by:

$$U(r, \theta, z) = -\frac{U_o}{2} \left[X \left(\frac{r}{a} \right)^2 \cos 2\theta + AI_o(kr) \sin(kz) \right] \\ + \frac{U_o}{2} \frac{[x + a(z)]\Delta}{a^2} \left[X + \frac{A}{4} (ka)^2 \sin(kz) \right]. \quad (7)$$

The dipole component decreases the focusing strength of a pure RFQ field if the electrode is shifted outside the channel $\Delta > 0$ (and vice versa if $\Delta < 0$):

$$E_{\text{dipole}}^x = -\frac{U_o}{2} \frac{\Delta}{a^2} \left[X + \frac{A}{4} (ka)^2 \sin(kz) \right]. \quad (8)$$

The dipole component results in shifting of a stable oscillation point from the axis. From equation (7) the new stability point $E_x(x_o) = 0$ is defined as $x_o = \Delta/2$. Beam dynamics calculation performed for the electrode displacement of $\Delta = 50$ microns shows that the center mass of the beam oscillates around the new stability point $x_o = 25$ microns (see Fig. 2). In this case no significant changes of beam parameters were observed. Finally the engineering tolerance of 50 microns was thus adopted for the vane tips fabrication.

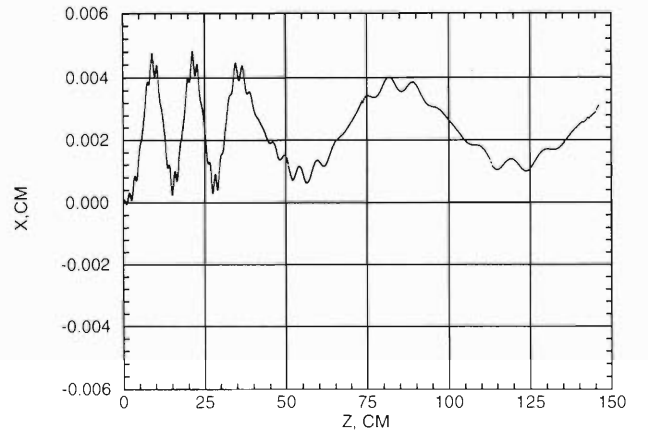


Fig. 2. Oscillation of the center mass of the beam due to vanes asymmetry of $\Delta = 50$ microns.

References

- 1) Y. Batygin, A. Goto, O. Kamigaito, Y. Yano: Proc. 10th Symp. on Accel. Science and Technology, Hitachinaka, p. 359 (1995).
- 2) I. M. Kapchinsky: Preprint IHEP 72-29, 72-30, Protvino (1972), in Russian.
- 3) Y. Batygin: Proc. 3rd European Particle Accelerator, Berlin, Germany, p. 822 (1992).

Design Study of Siberian Snake Magnet for RHIC-Spin Project

M. Okamura, T. Kawaguchi, K. Hatanaka, H. Sato, Takeshi Toyama, and T. Katayama

In Relativistic Heavy ion Collider (RHIC) Spin Project,¹⁾ it is intensively required to accelerate a proton beam to 250 GeV with high polarization. A device called Siberian Snake can overcome the depolarization spin resonance that occurs in a synchrotron. A design study of Siberian Snakes has been done at Brookhaven National Laboratory (BNL). In parallel with them, we also began to study about it.

A Siberian Snake is a kind of Spin rotators and the role of it is to rotate the spin by 180° precisely without any orbit displacement and any deflection. By inserting two Siberian Snakes on opposite sides of each of two RHIC rings, the depolarization from imperfection and intrinsic depolarizing resonance can be avoided up to the top energy of 250 GeV. The Snake magnet adopted for RHIC consists of four helical dipole magnets using superconductors twisted by 360° . This type of Snakes can rotate spin with smaller orbit excursion. In addition to the Siberian Snakes, spin rotators are required to be used at the intersection point where PHENIX is installed. To simplify the construction of spin rotators, the same structure as Snake magnets was adopted.

Two methods have already been suggested for winding of cables for actual magnets. The first method has been developed by Magnets Division at BNL. The cable is wound up along grooves on the cylinder. The other called "Direct Wire Technology" has been developed at SSC. In both methods, thin cables ($\phi = 1$ mm) comprise coils to reduce the heat leak through power feeds. However it is difficult to fix such thin cables so as not to cause quench. So, we have proposed to use Rutherford cables by considering their thickness with which the heat leak does not exceed the capacity of the cryogenic system, and have begun to design new Snake magnets.

To begin with, we calculated magnetic fields for the helical magnet designed at BNL. Two dimensional (2D) analysis was at first made because of complexity of the shape of magnet. However, it was difficult to estimate the fringe field and longitudinal component of the field using the 2D calculation. Then we calculated the three dimensional (3D) magnetic field using the computer code TOSCA. Figure 1 shows a total view of the helical dipole magnet. The coil consists of an inner layer and an outer layer. The inner and outer radii of the two-layer coil and the length of helical section are 50, 80, and 2200 mm, respectively. The inner and outer radii and the length of yoke used for the calcu-

lation are 90, 175 and 2200 mm, respectively. The results of 3D analysis for the magnetic fields at the center of the magnet are shown at Table 1. The magnetic field strength is 4 T. However, the longitudinal component of the magnetic field at the place 3 cm apart from the beam axis is more than 8% of the dipole field component. Uniformity of the dipole component is about 1%. It is necessary to optimize the coil geometry, in order to reduce the longitudinal component and get better uniformity of the dipole component.

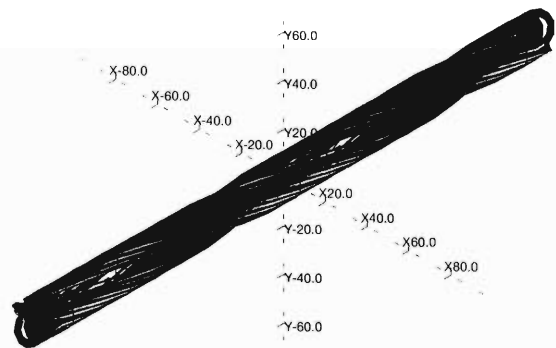


Fig. 1. A total view of the helical dipole magnet.

Table 1. Magnetic fields at the center of the magnet.

		without yoke	with yoke
Field strength on axis	T	2.83	3.98
Field strength of longitudinal component at $r=30$ mm	T	0.246	0.343
Field uniformity of dipole component at $r=30$ mm%		1.13	1.05
Current density	A/cm ²	21000	21000

We will analyze the beam orbit and spin motion of polarized protons in Siberian Snakes using the results of 3D calculation. The result of this research will be reflected to the design of our new Snake magnets with Rutherford cables.

The authors are grateful to Hitachi Co., Mitsubishi Electric Co. and Kyokuto Boeki Kaisha Co. for their collaboration.

References

- 1) H. En'yo et al.: This report, p. 80.

Progress of RIKEN RI Beam Factory Project

Y. Yano, A. Goto, and T. Katayama

The “RIKEN RI Beam Factory” is aimed at providing RI (Radioactive Isotope) beams over the whole atomic-mass range with the world-highest level of intensity in a wide energy range up to several hundreds MeV/nucleon. A very preliminary plan of the factory is illustrated in Fig. 1. The existing facility will be expanded to the adjacent site where a two-story building will be constructed underground.

The factory utilizes the “projectile fragmentation” to generate RI beams of intermediate energies. To enable the efficient generation are needed high-intensity primary heavy-ions, up to uranium ions, with the energies exceeding 100 MeV/nucleon. Such heavy-ions will be provided by a K2500-MeV superconducting ring cyclotron (SRC) which will be built for an energy booster of the existing K540-MeV ring cyclotron (RRC). RI

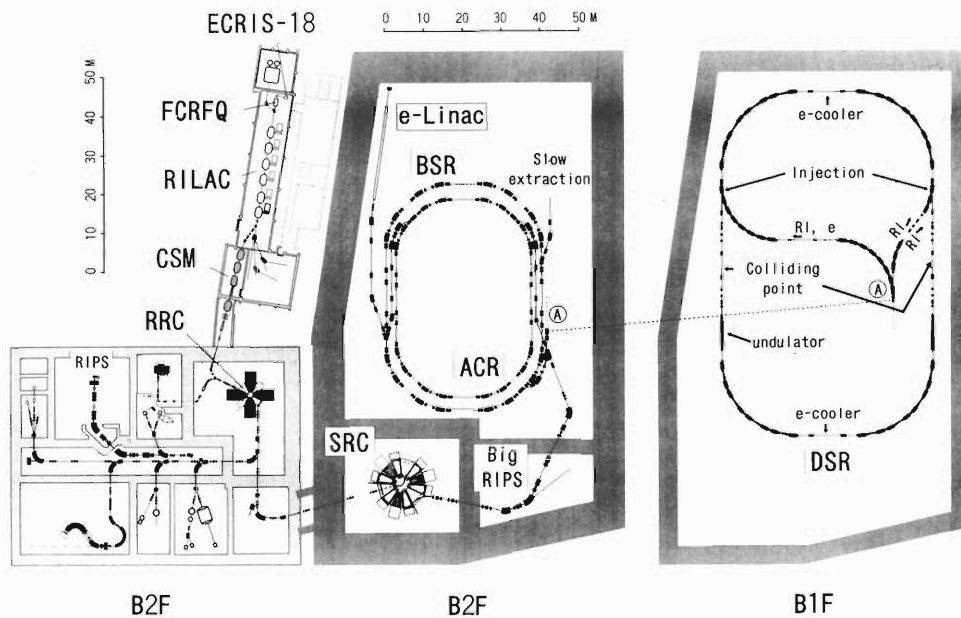


Fig. 1. Preliminary layout of the RIKEN RI Beam Factory. The SRC and the MUSES are housed in a two-story building underground. Experimental setups are not depicted.

beams will be generated by the Big RIPS. A new type of experimental installation called “MUSES” (Multi-Use Experimental Storage rings) will also be constructed. It consists of an accumulator cooler ring (ACR), a booster synchrotron ring (BSR) and double storage rings (DSR). With MUSES, various types of unique colliding experiments will become possible: ion-ion merging or head-on collisions; collisions of either electrons or X-rays with ion (stable isotope or RI) beams; internal target experiments; and atomic and molecular physics with cooler electron beams.

In 1995 fiscal year, the budget for the three-year R&D to design the details of the factory has been partially approved. This budget is to be invested to fabricate a test model of the SRC sector magnet.

Here we describe the revised parameters of the variable-frequency linacs-cyclotrons system which possesses such acceleration performance that a 100-MeV/nucleon uranium beam with the intensity over

1 μA is obtainable. On the other hand the revised parameters of MUSES are described by Katayama et al.¹⁾ The design study of each accelerator component is given in separate papers in this progress report.

RILAC serves as the initial-stage accelerator. We use the acceleration radio-frequencies between 18 and 38 MHz because this linac works stably in this frequency range. In order to upgrade the RILAC performance in the beam intensity by one or two orders of magnitude, its new pre-injector system consisting of a frequency-tunable folded-coaxial RFQ linac (FC-RFQ) equipped with an 18-GHz ECR ion source (ECRIS-18) has been developed.²⁾ In the recent test of this system, as for FC-RFQ, the variability of the resonant frequency was measured to cover from 17.7 to 39.2 MHz. In addition the beam transmission efficiency of 85% at the maximum was obtained.³⁾ This efficiency agrees well with the value calculated by the computer code BEAMPATH.⁴⁾ High-intensity highly-

charged ion beams have been obtained by ECRIS-18. Some results are given in the report on this source.⁵⁾ The pre-injector is scheduled to be installed in due site in the summer of 1996. It will be used jointly with the existing 450-kV Cockcroft-Walton accelerator.

The pre-accelerated beam is fully accepted and accelerated by RILAC.

A charge-state multiplier (CSM) consists of an accelerator, a charge stripper and a decelerator. Its functions are to produce higher charge states of ion beams by further increasing the stripping energy and to reduce their magnetic rigidity by decelerating them to the initial energy. With this device the magnetic rigidity of a most-probable charge-state beam can be reduced to the acceptable value of RRC even when the injection velocity into RRC is increased. The accelerator and decelerator are of a type of frequency-tunable IH linacs, whose operational radio-frequencies are twice as that of RILAC to double an acceleration gradient. Maximum gap voltages are set to be 350 kV for 62 cells of the accelerator and for 28 cells in the decelerator, and total lengths of each are 12.4 m and 5.5 m, respectively. Transmission efficiency through CSM depends only on charge state distributions behind the charge stripper foil. We estimate the yield of a given charge state in terms of Shima's formula.⁶⁾ A preliminary design of CSM is given in the report by Tomizawa et al.⁷⁾

For the present, we set the maximum beam energy of SRC to be 400 MeV/nucleon and this energy to be achieved at 38 MHz of the maximum rf frequency of RILAC. Consequently a velocity of RRC output beam is to be amplified by a factor of 2.26 by SRC. To this end, the mean extraction radius of SRC is taken to be 2.26 times the mean injection radius. We set this mean injection radius to be 2/3 times the mean extraction radius of RRC; accordingly mean injection and extraction radii of SRC are 2.37 m and 5.36 m, respectively. Then, to meet a good matching condition, the harmonic number in SRC becomes 6 as that in RRC is 9. The radio-frequency range of SRC is from 18 MHz to 38 MHz, which is the same as that of RRC.

The 6-sector SRC with the sector angle of 25 degrees has been investigated. The design details are described in the reports by Mitsumoto et al.⁸⁾ and by Kawaguchi et al.⁹⁾ The maximum field strength in the extraction region of SRC becomes 4.1 tesla.

We estimate the beam intensity expected to obtain from SRC for some typical gaseous elements and uranium ions, on the basis of the following assumptions: (1) the transmission efficiency through FC-RFQ is 85% irrespective of kinds of ion beams; and (2) from the

exit of FC-RFQ to the extraction beam line of SRC, the beam loss occurs only in the stripping process, i.e. this means that the transmission efficiency of both of RRC and SRC is 100% (this can be achieved by the off-centering acceleration technique which is routinely used for RRC). In Table 1 is given comparison of the ECR beam intensity (I^{ECR}) of a given charge state (q^{ECR}) required to obtain an ion beam of the energy (E^{SRC}) with the intensity (I^{SRC}) to the present performance of ECRIS-18 and 14.5 GHz CAPRICE.¹⁰⁾ Quite high beam intensity is expected to be provided especially for light ions, but use of such primary beams is not realistic from a viewpoint of the radiation-shielding-problem. We consider that primary-beam intensity of 1 μA is sufficient to generate RI beams with desirable intensity in the whole mass region: These primary beams will give us a possibility to create and identify as many as one thousand kinds of new isotopes. High current beams are used with a low duty factor of nearly 0.01% for MUSES.

Table 1. Comparison of the required beam intensity to the performance of the ECRIS-18 and the 14.5 GHz CAPRICE.

Ion	E^{SRC} MeV/u	I^{SRC} μA	q^{ECR}	I^{ECR} μA	I^{ECRIS18}			$I^{\text{CAPRICE14.5}}$		
					extrac. voltage		extrac. voltage	extrac. voltage		extrac. voltage
					10 kV	15 kV	20 kV	10 kV	15 kV	20 kV
$^{16}\text{O}^8$	400	100	6	700	550	610				800
$^{16}\text{O}^7$	400	100	7	820(1)	110					100
$^{40}\text{Ar}^{17}$	330	20	7	410						
			8	470	330	410			500	
$^{84}\text{Kr}^{30}$	300	2	14	120	90	110				120
$^{129}\text{Xe}^{38}$	200	1	15	100						80
$^{238}\text{U}^{85}$	200	0.02	28	16(2)						20
$^{238}\text{U}^{58}$	150	0.2	22	75(3)						25(*)
$^{238}\text{U}^{49}$	100	1	16	110						

(*): CAPRICE 10 GHz

(1): without stripper 1. (2) with stripper 2 (yield is estimated to be 30%). (3) yield for 58+ is 7% while that for 55+ (most probable) is 15%.

References

- 1) T. Katayama et al.: This report, p. 238 and 240.
- 2) A. Goto et al.: This report, p. 219.
- 3) O. Kamigaito et al.: This report, p. 221.
- 4) Y. Batygin et al.: This report, p. 223.
- 5) T. Nakagawa et al.: This report, p. 220.
- 6) K. Shima et al.: *Atomic Data and Nuclear Data Tables*, **51**, 174 (1992).
- 7) M. Tomizawa et al.: This report, p. 228.
- 8) T. Mitsumoto et al.: This report, p. 230.
- 9) T. Kawaguchi et al.: This report, p. 232.
- 10) Y. Kanai et al.: This report, p. 208.

Conceptual Design of a Frequency-Tunable IH Linac

M. Tomizawa

In the proposed “RIKEN RI Beam Factory”, the beam of the whole mass ranges up to uranium is accelerated up to several hundreds MeV/nucleon. To inject a heavy ion such as uranium into the RRC, it is necessary to increase the charge state of the beam from the RILAC. A charge-state multiplier (CSM) is proposed to increase the charge state of the heavy ion beam with unchanged velocity.¹⁾ The CSM consists of a linear accelerator, a charge stripper and a decelerator. For example, $^{238}\text{U}^{19+}$ beam is accelerated from 1.3 to 2.4 MeV/nucleon, charge-stripped to 41+ by the carbon foil, and decelerated to 1.3 MeV/nucleon by the decelerator. An interdigital H mode (IH) cavity is suitable for these linacs, because the IH cavity has a high acceleration gradient in the present velocity range. The frequency range is set to 36–76 MHz, which is twice as that of the RILAC to get a high accelerating gradient and to reduce the cavity size. The required mass to charge ratio is 7 to 28.

The designed CSM consists of three accelerator tanks and a decelerator tank. The main parameters of the tanks are shown in Table 1. Quadrupole triplets are placed between the tanks to focus the beam. In order to get a stable longitudinal beam motion, synchronous phases are set to -25 and 25 deg. in the accelerators and the decelerator, respectively. This acceleration scheme has been used in the IH linac to accelerate unstable nuclei at INS.²⁾ The length between tanks is chosen to be about 85 cm in which the quadrupole triplet is installed. The required field strength is less than 40 T/m at a bore radius of 2 cm. The multi-particle tracking on three dimensional phase space was performed. The effects due to the foil were neglected in this calculation except for the change of the charge state. Maximum longitudinal and transverse emittances at 100% transmission are 600π keV/nucleon-deg. ($f = 51$ MHz) and 1.6π mm·mrad (normalized), respectively. These are larger enough than those of the actual beam from the RILAC.

Table 1. Main parameters of the frequency tunable IH linac.

tank	energy (MeV/u)	cell length (m)	gap (cm)	bore rad. (cm)	Φ_s (deg.)	
acc.-1	1.312–1.657	18	2.98	8.2	1.5	-25
-2	1.657–2.003	18	3.31	9.1	1.5	-25
-3	2.003–2.390	20	4.03	9.9	1.5	-25
dec.	2.390–1.313	22	4.05	9.2	2.0	25

The rf characteristic of the IH cavity was analyzed by the MAFIA code. First, to see the reliability of the MAFIA calculation for the IH cavity, the calcu-

lated result was compared with the measured data of the IH linac (tank-4) constructed at INS. As a result, the MAFIA predicted a resonant frequency about 9% higher than measured one. The predicted resonant frequency increases with the mesh number. The shunt impedance and the gap voltage distribution are well reproduced by the calculation.

The schematic drawing of the frequency tunable IH cavity is shown in Fig. 1. In the present design, the cavity has a rectangular shape. The upper stems are connected on the wall directly, and the lower stems are put on the ridge. The frequency is tuned by moving a shorting plate in contact with the ridge and the wall. For impedance matching, the cell and end inductances are changed at the same time by this shorting plate. As a result, flat field distribution is obtained in the whole frequency range. The fine adjustment of the field distribution is performed by some capacitive tuners facing the ridge surfaces. Table 2 shows the calculated rf parameters of the decelerator cavity. The frequency is changed from 31 to 69 MHz by the 1.2 m stroke of the shorting plate. The shunt impedances are around 170 M Ω /m. It is not sensitive to the resonant frequency. The power consumption in the cavity is less than 65 kW. The rf current on the sliding contact between the ridge and the shorting plate is 63 A/cm(rms) at maximum. In such a high current density, the rf contact between the short plate and the ridge must be examined carefully. One of the candidates is the sliding contact using silver-graphite spheres supported by a flat spring via a thermal insulator.³⁾ In the

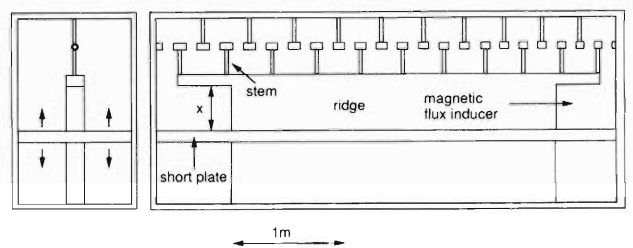


Fig. 1. Layout of the frequency-tunable IH linac designed as the decelerator of the CSM.

Table 2. Rf parameters obtained by the MAFIA. In the table, x shows the distance between the ridge and the shorting plate.

x (m)	f (MHz)	Z_s (M Ω /m)	P (kW)	J_{rms} (A/cm)
0.3	68.6	169	64	63
0.8	45.4	179	60	47
1.5	31.4	169	64	42

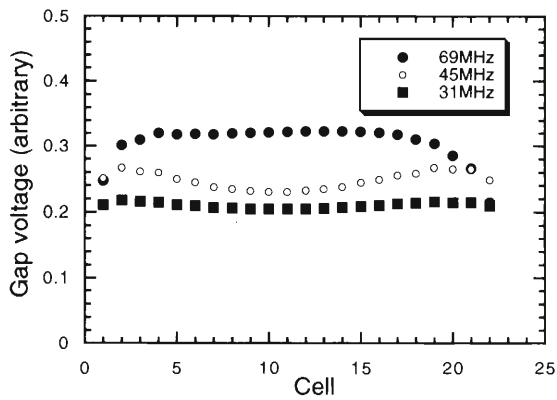


Fig. 2. Gap voltage distribution predicted by the MAFIA.

cavity using this contact, the rf current of 200 A/cm has been achieved at 50 MHz.

Figure 2 shows the gap voltage distributions calculated by the MAFIA. Except for the end cells at 68.6 MHz, flat distribution was obtained. The distribution is quite sensitive to the size of the magnetic flux inducer. Further optimization of the sizes is needed to get better field distribution.

References

- 1) Y. Yano et al.: Proc. 10th Symp. on Accelerator Science and Technology, Oct., Hitachinaka, p. 191 (1995).
- 2) M. Tomizawa et al.: *ibid.*, p. 457.
- 3) C. Pagani et al.: Proc. 11th ICC, Ionics Pub., Tokyo, p. 361 (1987).

Design Study of Sector Magnet of the Superconducting Ring Cyclotron (I)

T. Mitsumoto, A. Goto, T. Kawaguchi, Y. Tanaka, T. Kubo, H. Okuno,
T. Tominaka, S. Fujishima, and Y. Yano

The RIKEN Superconducting Ring Cyclotron (SRC) is one of the main accelerators of the "RIKEN RI Beam Factory."¹⁾ The SRC is expected to boost the energy of ion beams from the existing RIKEN Ring Cyclotron (RRC) up to 400 MeV/nucleon for light ions like carbon ions and 150 MeV/nucleon for very heavy ions like uranium ions. The sector magnets of the SRC have to be flexible enough to generate isochronous fields corresponding to a wide range of energies and for various q/A 's. In this report we describe the feature of the sector magnet together with magnetic field calculation and orbit analysis.

The maximum energies for typical ions are summarized in Table 1. Beam currents are expected to be 100 μA for 400 MeV/nucleon oxygen ions and about 0.2 μA for 150 MeV/nucleon uranium ions. The number of sectors for the SRC has been chosen to be 6, because in the case of 4 sectors, tune history of ions for 400 MeV/nucleon acceleration crosses a resonance line $\nu_r = 2$, which is known as N/2 stop band. Diameter of the SRC is 20 m. The pole length is longer than 3 m, the sector angle is around 25 deg., and the weight of one sector magnet is nearly 900 tons. From the matching condition with the RRC, the injection radius of the SRC has been selected to be 2/3 of the extraction radius of the RRC. Main parameters of the SRC are listed in Table 2.

Table 1. Required maximum energy of the SRC.

$^{16}\text{O}^{8+}$	400 MeV/nucleon
$^{84}\text{Kr}^{30+}$	300 MeV/nucleon
$^{238}\text{U}^{80+}$	150 MeV/nucleon

Table 2. Main parameters of the SRC.

Number of sectors	6
Harmonics	6
Average radii	injection 2.37 m
	extraction 5.36 m
RF Frequency	18-38 MHz

Isochronous field distributions for typical ions are shown in Fig. 1. The maximum required field in the sector magnet becomes nearly 4 T in the outer region. Field difference between the injection radius and extraction radius on the sector axis is 0.8 T for 400 MeV/nucleon ions and 0.1 T for energies below 100 MeV/nucleon ions. Therefore the main coil as well as trim coils for coarse fitting has to be superconducting.

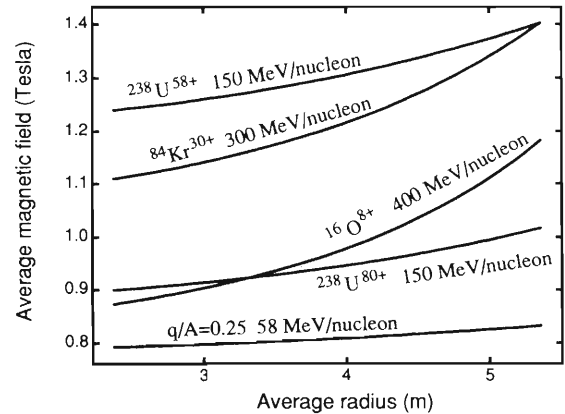


Fig. 1. Isochronous field for typical ions.

Magnetic fields and forces were calculated by a three-dimensional code TOSCA.²⁾ For the sector magnet only a quarter part of it was modeled because of its symmetry. For the coils a complete set of them in only one sector was taken into account in the calculation. Strictly speaking, TOSCA requires all conductors of the system to be taken into account. But owing to appropriate selection of the reduced potential region, good agreement of the magnetic field on the median plane can be obtained for both the system with six sets of coils placed rotational symmetry and the system with only one set. This method shortened the calculation time to be less than 25% of that of the six-set system.

Equilibrium orbits and betatron tunes were calculated by the computer program that had been originally developed for the RRC. Results of the field distributions by TOSCA were used in the orbit calculations.

Using the four sets of superconducting trim coils, we expect that the field generated with both the main coil and the superconducting trim coils can be fitted to the isochronous field within ± 0.01 T for all of the acceleration conditions. Further fine adjustment will be done with trim coils of room temperature.

Figures 2 and 3 show typical tune values in the cases that the sector angle is 23 deg. and 25 deg., respectively. In the case of 23 deg., all tune values are above $\nu_z = 1.0$. But the maximum magnetic field reaches 4.6 T. In the case of 25 deg., the tune history for $^{16}\text{O}^{8+}$ ions to 400 MeV/nucleon crosses $\nu_z = 1.0$. The maximum magnetic field, however, is reduced to be 4.1 T. In Fig. 3 are also shown the tune values for $^{16}\text{O}^{7+}$ ions. In this case the values are pushed above $\nu_z = 1.0$, but the beam intensity reduces by a factor of about 2 com-

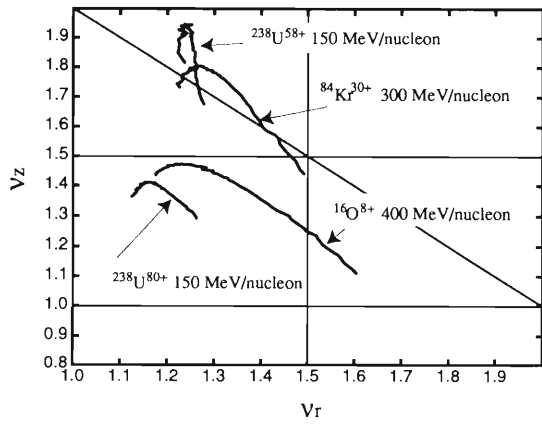


Fig. 2. Typical tune values in the case of 23 deg. sector angle.

pared with that of $^{16}\text{O}^{8+}$ ions. The final selection of the sector angle will be made after the evaluation of difficulty in producing a high field and of risk of crossing the resonance line.

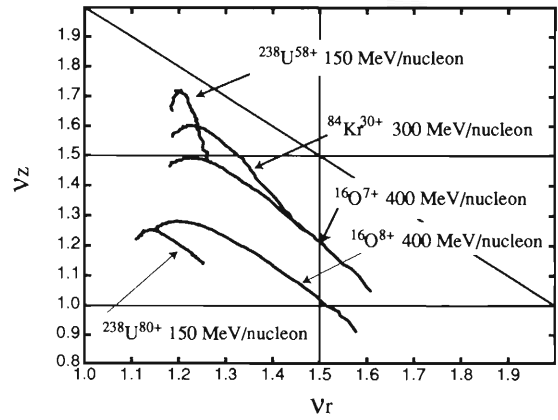


Fig. 3. Typical tune values in the case of 25 deg. sector angle.

References

- 1) Y. Yano et al.: 14th Int. Conf. on Cyclotrons and Their Applications, Cape Town, South Africa, Oct. (1995) to be published.
- 2) Vector Fields Limited, Oxford, England.

Design Study of Sector Magnet the Superconducting Ring Cyclotron (II)

T. Kawaguchi, T. Kubo, T. Mitsumoto, T. Tominaka, S. Fujishima, H. Okuno, Y. Tanaka, K. Ikegami, A. Goto, and Y. Yano

The superconducting ring cyclotron proposed for the RIKEN RI beam factory needs six units of superconducting sector magnets, each of which must generate a maximum magnetic field strength of 4 T in the beam orbital area. We use superconducting coils for the sector magnet to obtain compactness in size and to save electric power and cooling water. The yoke and pole made of magnetic soft iron are arranged in the sector magnet to reduce the ampere turns of the superconducting coils and to minimize the leakage magnetic flux.

Figure 1 shows an overview of the sector magnet. A cryostat is not drawn in this figure. The main components of the magnetic elements are superconducting coils, poles and a yoke. We use two kinds of superconducting coils: a pair of main coils and a group of trim coils. Both coils are located upper and lower sides with respect to the mid plane. We have studied two ways of arrangements for the pole. One is a warm pole system and the other a cold pole one. Figure 2 shows the both systems with a cryostat. In the cold pole system, the main superconducting coil is wound around the pole directly, so the cold mass consists of superconducting coils, poles and coil vessels. In view of the mechanical rigidity and magnetic force, we have decided to use the cold pole system. Figure 3 clearly shows the comparison of expanding forces on the straight section of the

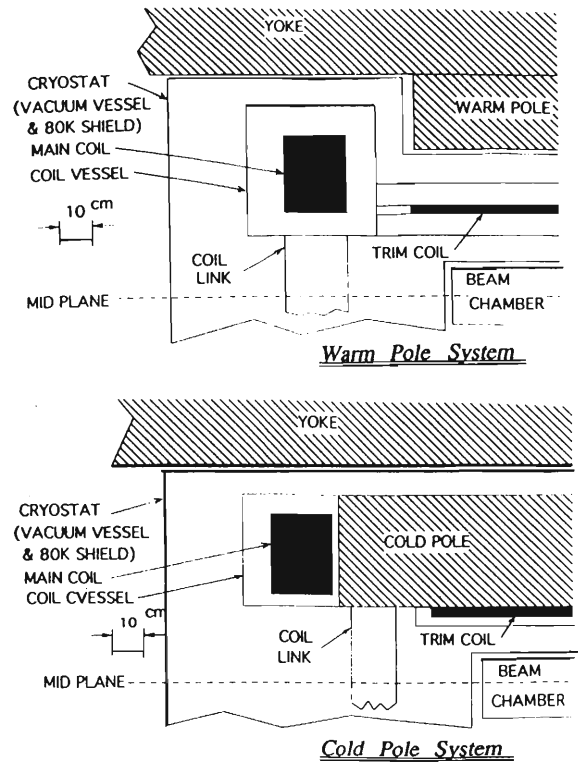


Fig. 2. Comparison of pole arrangements.

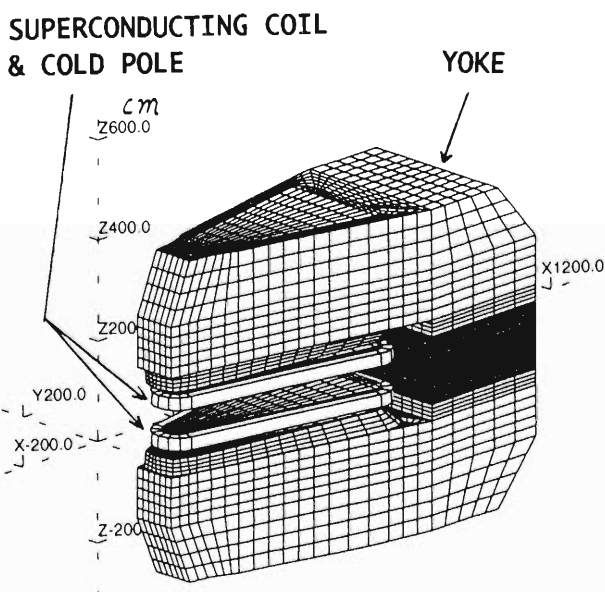


Fig. 1. Overview of superconducting sector magnet (for three dimensional magnetic field calculation).

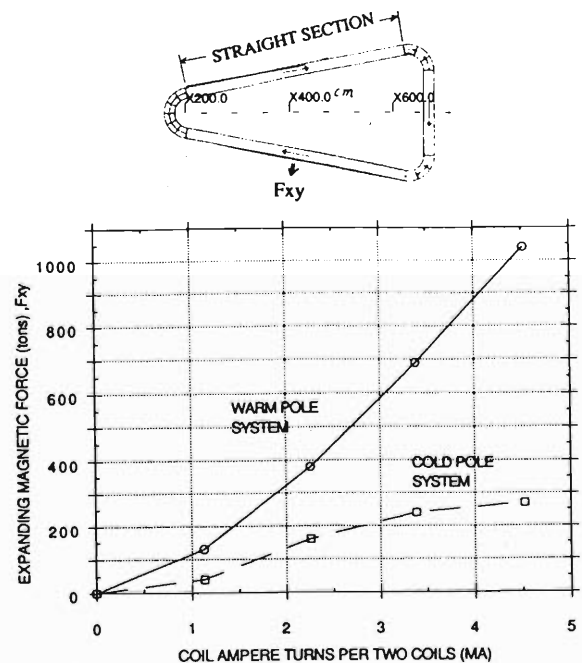


Fig. 3. Comparison of expanding magnetic forces on coil straight section.

main coil. The force in the cold pole system can be reduced to one-third of that in the warm pole system. This effect is due to the short distance between the main coil and the pole in the cold pole system. However, a serious problem in the cold pole system is the difference of thermal contraction between the pole and the coil vessel during the cooldown of the cold mass from 300 K to 4.5 K. We are currently investigating this problem.

Figure 4 shows the change of the maximum magnetic field (at a radius of 6 m on the median plane) and the magnetic forces F_x , F_z in the cold mass (consists of main coils and cold poles), as a function of the ampere turns of two (a pair of) main coils. The magnetic force F_z in the vertical direction is supported with two coil links which are arranged between the upper cold mass and lower one.

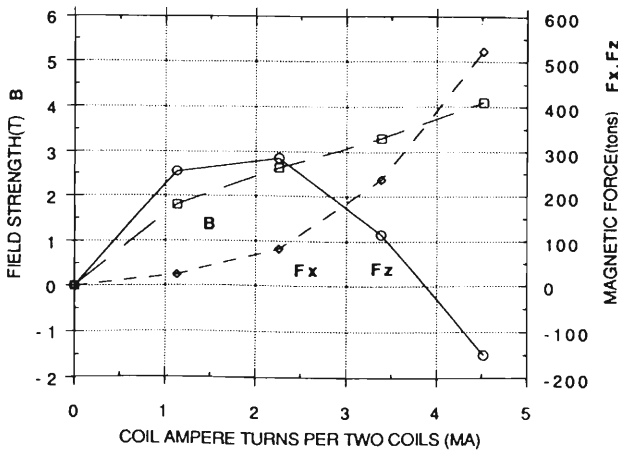


Fig. 4. Field strength and magnetic forces.

The force of 300 tons maximum causes a mechanical deflection of 4 mm maximum of the cold mass. The

magnetic force F_x in the radial direction is generated with a configuration of the six sector magnets. Each cold mass is pushed toward outer radius by the forces from sector magnets at both-side. The maximum force of F_x is estimated to reach about 500 tons per each magnet. It is very difficult to support this force by thermal insulating supports which locate in between the cold mass and the vacuum vessel. To support such a large F_x , we are investigating a cold ring of 2.6 m in diameter and 200 mm in thickness which connects the six cold masses in the central region of the ring cyclotron.

One of serious problems for a superconducting coil is coil quench which would be induced with wire movement in the coil under magnetic force. When the coil quench occurs, it is impossible to continue the normal operation, and the coil temperature rises spending magnetic stored energy, then we need re-cooldown of the coil. On the other hand, it is very hard to prevent coil's wire movement, particularly for the non-circular shape coil. Taking account of the above matter, we apply fully cryogenic-stable cooling for both the main coil and the trim coil adopting a method of conservative liquid-helium bath cooling, for preventing the coil quench. The operation currents of the main coil and trim coil are roughly set to be 5000 A and 500 A, respectively. In order to maintain the cryogenic stability, the average current densities of them should be less than 40 A/mm² and 50 A/mm², respectively.

The total heat leak of six magnets is roughly estimated to be 500 W at 4.5 K. A helium refrigerator having a capacity of 1 kW at 4.5 K stage will be used for six sector magnets and for the beam injection and extraction channels. An electric input power for the refrigerator will be 500 to 1000 kW. Weight of the total cold mass of six magnets is about 360 tons, and it will take almost one month for the cooldown of the cold mass from room temperature to 4.5 K by the helium refrigerator.

Design Study of the Injection System of the Superconducting Ring Cyclotron (III)

H. Okuno, T. Tominaka, T. Kubo, T. Mitsumoto, T. Kawaguchi, Y. Tanaka,
S. Fujishima, K. Ikegami, A. Goto, and Y. Yano

In the RI beam factory project,¹⁾ the Superconducting Ring Cyclotron (SRC)²⁾ is designed to boost the energy of the ion beams from the existing RIKEN Ring Cyclotron (RRC) up to 400 MeV/u for light ions such as carbon and 150 MeV/u for very heavy ions such as uranium. In this report, we describe the status of the design study of the injection system for the SRC.

Figure 1 shows one of injection trajectories now under consideration. The beam is injected through one of the valleys into the central region of the SRC and is radially guided to the 1st equilibrium orbit. The transport system consists of three bending magnets (BM1, BM2, BM3), two magnetic inflection channels (MIC1, MIC2) and an electrostatic inflection channel (EIC). The injection energies required to get the maximum output energies for three kinds of beams are shown in Table 1.

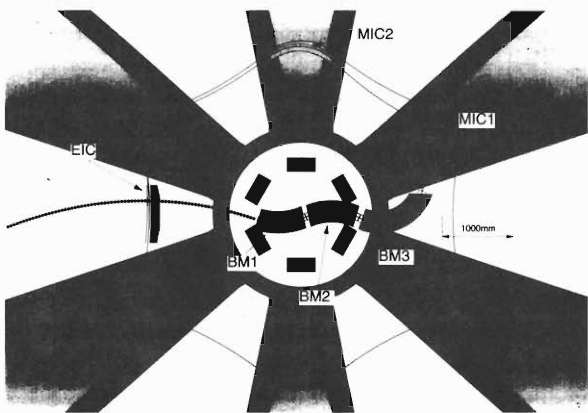


Fig. 1. The schematic layout of the SRC and an example of an injection trajectory.

Table 1. The energies of injected beams required for the maximum energy acceleration.

	Charge	E_{inj} (MeV/u)	E_{ext} (MeV/u)
^{16}O	8+	50.4	400
^{84}Kr	30+	41.7	300
^{238}U	80+	24.5	150

This radial injection method is most straightforward and is adopted widely in many ring cyclotrons. However, it is more difficult to apply the radial injection to the SRC than to the normal conducting ring cyclotron, because there exists strong negative fringe field in the

valley region and the beam trajectory there changes largely depending on the kind of acceleration condition. The bending angle in the valley region is estimated to be about 50 degrees at the maximum. Figure 2 shows an example of the difference of beam trajectories in the valley region between U and Kr ions.

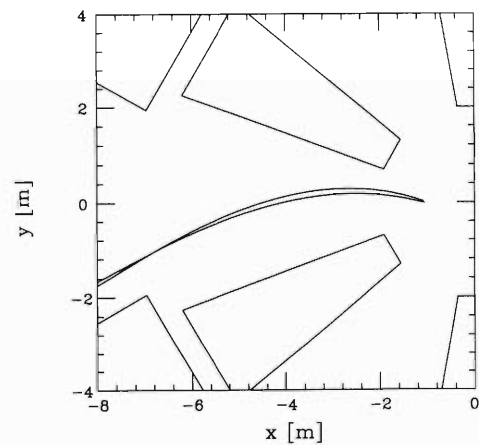


Fig. 2. Examples of beam trajectories in the valley region. The upper curve is a trajectory for U (150 MeV/u) acceleration and the lower is one for Kr (300 MeV/u).

The MICs are inserted between the poles of the sector magnets to increase the bending power of the sector field locally. The EIC is placed in the position where the injection trajectory is matched finally with the 1st equilibrium orbit. Characteristics of the injection elements are summarized in Table 2. The three bending magnets and MIC1 require to use superconducting coils to achieve the required fields. The sizes of the elements must be small enough so that they can be

Table 2. Characteristics of the injection elements.

(1) Bending magnets			
Element	θ (deg)	ρ (cm)	B (T)
BM1	39.4	80.0	4.55
BM2	52.5	85.0	3.40
BM3	100.6	63.5	3.61
(2) Inflection channels			
Element	θ (deg)	ρ (cm)	ΔB or ΔE (T or kV/cm)
EIC	11.96	383.9 – 623.6	81.2
MIC1	88.35	57.5	0.90
MIC2	88.46	63.5	0.33

placed within the limited available space in the SRC central region.

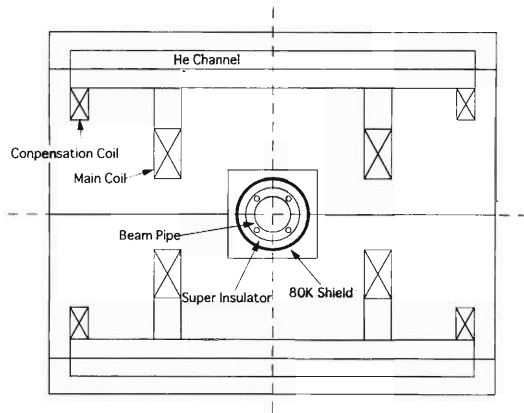


Fig. 3. A cross-section of the MIC1.

Figure 3 shows a cross-section of the MIC1 designed. The MIC1 contains a main coil and a compensation coil. This two-coil system provides the required field profile with an induction level up to 0.9 T in the bore of the inflection channel and with a small magnetic field disturbance in the acceleration region. The coils are indirectly cooled by 4.2 K liquid helium via the coil housing. The beam bore is also cooled by water in order to prevent the coils from quenching due to the beam losses. Required current densities for the coils are as high as about 300 A/mm². Analysis for the mechanical and cryogenic stability is in progress.

References

- 1) Y. Yano et al.: Int. Conf. on Cyclotrons and Their Applications, Cape Town, South Africa, 1995, in press.
- 2) T. Mitsumoto et al.: This report, p. 230.

Design of a Model Sector Magnet of the Superconducting Ring Cyclotron

T. Kubo, T. Kawaguchi, T. Mitsumoto, T. Tominaka, S. Fujishima, H. Okuno, J.-W. Kim, Y. Tanaka, K. Ikegami, A. Goto, and Y. Yano

An RI-beam factory based on the projectile fragmentation method has been proposed as an extension of RIKEN Ring Cyclotron (RRC).¹⁾ It is planned in this project to build a superconducting ring cyclotron (SRC) as a post accelerator of RRC. The SRC consists of six identical superconducting sector magnets whose sector angle is 25 degrees and maximum magnetic field is 4.1 T. The mean injection and extraction radii of SRC are 2.37 m and 5.36 m, respectively. The maximum energies are: e.g. 400 MeV/nucleon for light heavy ions like carbon, 300 MeV/nucleon for krypton ions, and 150 MeV/nucleon for uranium ions. Design studies of SRC are reported in this progress report.^{2,3)} Here we report on a design of a model magnet of the superconducting sector magnets.

We plan to build a full-scale model so that the design of the sector magnet can be made sure under the condition as close to the real one as possible. This is particularly important to see if the huge magnetic force due to the high magnetic field and current density³⁾ can be properly supported. We aim at generating a magnetic field higher than 4.1 T that is required in the current design of SRC.

Figures 1(a) and (b) show a schematic drawing of the model magnet. The cold-pole method has been adopted as described in Ref. 3. The pole pieces are separated from an iron yoke and cooled down together with main coils in a cryostat. The coil vessel that accommodates the main coil is attached to the side of the pole piece. The upper and lower pole pieces are linked each other. Such an arrangement allows the pole pieces to support the magnetic force exerted on the main coils. Furthermore it enables to reduce the magnetic force expanding the main coil, since the main coil can be placed very close to the pole.³⁾ Several support links are shown in Fig. 1; the horizontal ones support the shifting force and the vertical ones the weight of pole pieces and main coils. The cold-mass weight and the total magnet weight are estimated to be about 60 and 1000 tons, respectively.

We plan to use a cryogenically-stabilized superconductor in order to prevent the main coil from quenching.³⁾ The cooling is made by the liquid-helium bath-cooling method. The conductor to be used has a cross-sectional size of 7.5 mm × 14 mm and consists of a Rutherford-type NbTi cable and a stabilizer housing. The stabilizer material will be either copper or aluminum. The conductor is designed to be stable up to 6000 A when the magnetic field applied is 6 T and the cooling efficiency is assumed to be 50%. However

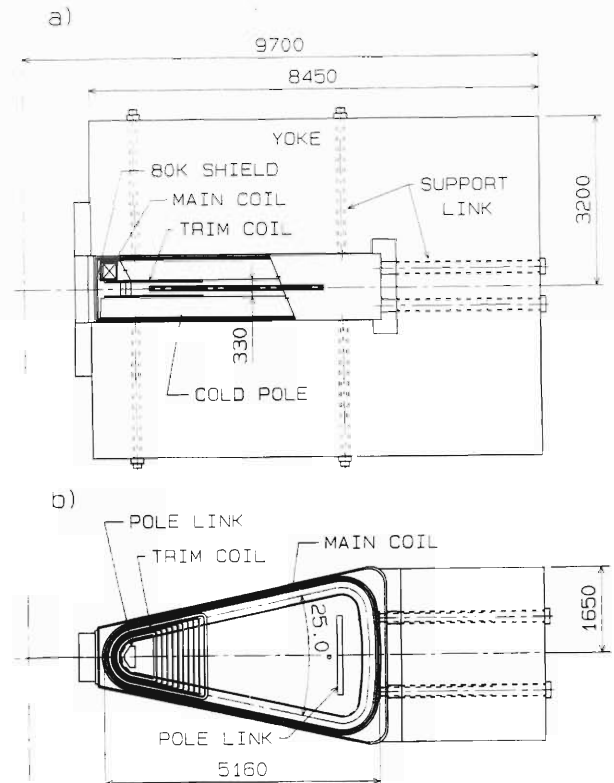


Fig. 1. A schematic drawing of the model sector magnet: (a) a side view; (b) a top view.

we plan to excite the main coil with currents lower than 5000 A, because the deterioration of cooling may happen in some parts of the coil. The current density at 5000 A is estimated to be about 40 A/mm², taking account of conductor gaps for the liquid helium and the insulation. The maximum stable current will be checked in the test operation of model magnet. The number of turns is taken to be 1200 so that the maximum ampere-turn can be 6 MA.

Figure 2 shows median-plane field distributions along the central line of sector which were calculated by the code TOSCA.⁴⁾ The solid line in the figure shows the distribution when the ampere-turn is 6 MA. The field is found to be around 5 T, which is well above the value required for SRC. The maximum field in the main coil is calculated to be 6.35 T, which is smaller than the stabilization limit at 5000 A. The stored energy is calculated to be 151 MJ.

Only the cold mass and cryostat will be first made

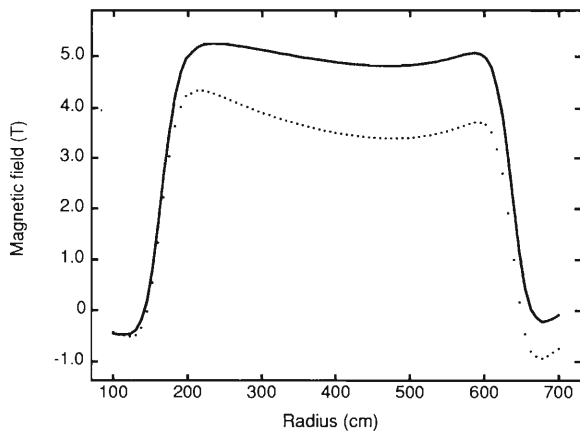


Fig. 2. Calculated median-plane field distributions along the central line of sector. The horizontal axis denoted as Radius gives the distance from the center of sector. The ampere-turn is taken to be 6 MA. The solid and dotted lines show the distributions with and without the iron yoke, respectively.

because of the limitation of budget and accommodation space. The iron yoke will be added later. We plan to operate the model magnet without the yoke for a

while. The dotted line in Fig. 2 shows the field distribution at 6 MA in the absence of the yoke. In this case the median-plane field is reduced by 20 to 30%. However the field strength in the main coil does not decrease that much. The decrease rate is calculated to be 5 to 10%. So the operation without the yoke would give us useful information.

The total heat load has been estimated to be about 140 W at 4.5 K. A liquid-helium refrigerator with a capacity of about 200 W at 4.5 K will be purchased.

We plan to test a prototype of superconducting trim coil by installing it onto the pole surface as shown in Fig. 1. The cryogenically-stable cooling will also be applied to the trim coil. We also plan to install and test a prototype of superconducting magnetic channel which will be used for the beam injection or extraction.

References

- 1) Y. Yano et al.: Int. Conf. on Cyclotrons and their Applications, Cape Town, South Africa, 1995, in press.
- 2) T. Mitsumoto et al.: This report, p. 230.
- 3) T. Kawaguchi et al.: This report, p. 232.
- 4) Vector Fields Limited, Oxford, England.

Double Storage Rings for MUSES

T. Katayama, Y. Batygin, N. Inabe, K. Ohtomo, T. Ookawa, M. Takanaka, M. Wakasugi, S. Watanabe, Y. Yano, K. Yoshida, J. Xia, Y. Rao, and Y. Yuan

A new type of experimental facility, MUSES (Multi-Use Experimental Storage rings), is proposed for RIKEN RI beam factory. It consists of an Accumulator Cooler Ring (ACR), a Booster Synchrotron Ring (BSR) and Double Storage Rings (DSR). This MUSES

is installed downstream from the Big RIPS (Fig. 1). The DSR permits various types of unique colliding experiments; ion-ion merging or head-on collisions; collisions of electron and ion (stable or RI) beams; internal target experiments; and atomic and molecular physics

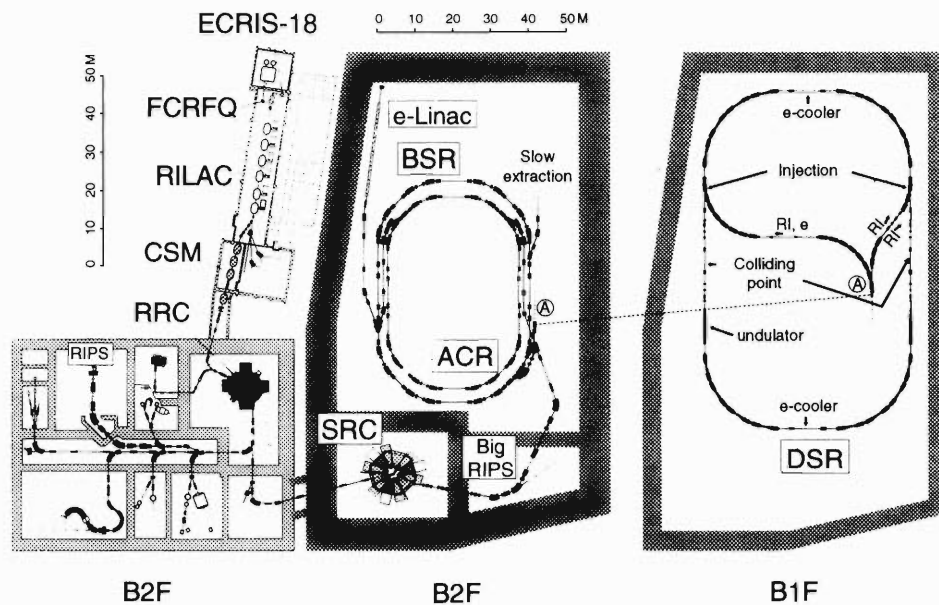


Fig. 1. Preliminary layout of the MUSES. The accelerators are housed in the 2-story building.

with cooler electron beams. On the other hand, the ACR functions exclusively for the accumulation and cooling of RI beams and the BSR works solely for the acceleration of ion and electron beams.

The DSR consists of vertically stacked two rings of the same specifications as shown in Table 1. Each lattice structure takes the form of a racetrack to accommodate two long straight sections. These straight sections of one ring vertically intersect those of the other ring at two colliding points. The ring circumference is 258.732 m, which is 46/6 times the extraction circumference of the Superconducting Ring Cyclotron (SRC), 5.363 m. It means that the harmonic number of DSR is 46 while that of SRC is 6. The maximum $B\rho$ -value becomes 14.6 Tm when the dipole field strength is 1.5 T at the maximum. The maximum energy is then, for example, 3.5 GeV for protons; 1.4 GeV/nucleon for light ions of $q/A = 0.5$; and 1.0 GeV/nucleon for U^{92+} ions. For electrons the BSR boosts them up to the maximum energy of 2.5 GeV from 300 MeV injector linac, and they are stored in the DSR. In the present lattice structure, the betatron tune values are 18.130

Table 1. Parameters of the DSR.

Circumference C (m)	258.732
Max. $B\rho$ (Tm)	14.60
Average radius R (m)	41.20
Max. beam energy (GeV/u)	
proton	3.50
ion ($q/A = 0.5$)	1.33
($q/A = 0.387$)	1.00
($q/A = 0.333$)	0.80
Betatron tune value (Q_x/Q_y)	18.130/10.197
Momentum compaction	0.00171
Transition γ	24.20
Max. betatron amplitude (β_x/β_y , m)	22.0/17.9
Max. dispersion function (D_x/D_y , m)	0.537/0.697
Betatron amplitude at Interaction point (β_x^*/β_y^* , m)	0.600/0.600
Length of field-free section at colliding section (m)	5.016
Natural chromaticity (Q'_x/Q'_y)	-45.59/-30.94

(horizontal) and 10.197 (vertical). The operating ion-beam energy is kept to be under the transition energy, since the transition gamma is as high as 24.20. At the colliding points the beta-function amplitudes are 0.6 m for both directions. The field-free section near the colliding points where experimental detector systems are installed, is 5.0 m in length. These two long straight sections are dispersion-free in horizontal and vertical directions.

One of the key researches planned at the DSR is the colliding experiment of an electron beam with an RI beam: 2.5 GeV electrons accumulated in one ring of the DSR collide with an RI beam stored in the other ring. The scientific aim of this experiment is to determine the charge and current distribution in the neutron- or proton-rich radio-active nuclei. To keep a

Table 2. Parameters of the stored electron beam.

Max. stored beam energy E_{max} (GeV)	2.5
Max. stored beam current I (A)	0.5
Max. stored No. of electrons N	2.7×10^{12}
Injection energy E_i (GeV)	2.5
Beam emittance at 2.5 GeV ($\varepsilon_x/\varepsilon_y$) (nm·rad)	8.5/25.5
Energy spread $\Delta E/E$	6.8×10^{-4}
Bunch length σ (cm)	0.50
RF voltage V_{RF} (MV)	2.0
Revolution frequency f_{rev} (MHz)	1.159
RF frequency f_{RF} (MHz)	498.2
Harmonic No. h	430
Number of bunch (typical)	23
Touschek lifetime at 2.5 GeV (s)	4.55×10^4
Synchrotron radiation loss at 2.5 GeV (keV/turn)	371.7

sufficiently long Touschek lifetime, the RF voltage of 2.0 MV is applied to the electron beam. The detailed specifications of stored electron beams in the DSR are given in Table 2. The number of stored electrons amounts up to 2.7×10^{12} particles, which is limited due to the longitudinal coupled bunch instability. The typical colliding luminosity for the electrons and RI ions is estimated to be 5.6×10^{26} cm²/s, provided that 1×10^7 particles of RI ions are stored and synchronously collide with electron bunches.¹⁾ In order to further improve the luminosity, the installation of a powerful pulsed heavy-ion source, e.g. a laser ion source or a metal-vapor ion source, should be considered.

Another envisaged experiment is the isotope shift of X-ray absorption by the Li-like or H-like unstable nuclei. To produce the short wavelength X-ray of 20-1000 eV energy, an undulator will be inserted in an electron ring.²⁾ To obtain the high flux mono-energetic X-ray, the emittance of stored electron beam should be as small as around 10 nano m-rad. The lattice structure of DSR is designed so as to give such a low emittance electron beam.³⁾

Other experiments such as ion-ion merging collisions at small angles are also envisaged. The luminosity is expected to be around 1×10^{26} cm²/s when the number of stored ions is assumed to be the space charge limit of 4×10^{12} particles and the colliding angle is 10 degrees.

References

- 1) K. Yoshida and T. Katayama: This report, p. 256.
- 2) M. Wakasugi, N. Inabe, and T. Katayama: This report, p. 257.
- 3) N. Inabe and T. Katayama: This report, p. 248.

Accumulator Cooler Ring and Booster Synchrotron Ring for MUSES

T. Katayama, Y. Batygin, N. Inabe, K. Ohtomo, T. Ookawa, M. Takanaka, M. Wakasugi, S. Watanabe,
Y. Yano, K. Yoshida, J. Xia, Y. Rao, and Y. Yuan

The Accumulator Cooler Ring (ACR) functions exclusively for the accumulation and cooling of RI beams. Taking the accumulation and cooling of an extremely neutron-rich $^{132}\text{Sn}^{50+}$ (a double-magic nucleus of 40 s in half-life) beam of 200 MeV/nucleon as an example, we give some specifications of the ACR. This RI beam is produced via the projectile fragmentation of a primary beam of ^{136}Xe ions with a peak current of 2 pμA. Typical beam characteristics are estimated as follows: the production rate is nearly 1×10^7 particles per second; the momentum spread is $\pm 0.1\%$; the phase width relative to RF frequency is ± 10 degrees; and the transverse emittance is 4.5π mm-mrad in both horizontal and vertical directions.

Firstly, the above RI beam is stored in the ACR with the conventional multi-turn injection method. About 1×10^1 particles are injected for each one turn revolution, because the orbit frequency is nearly 1 MHz. Provided that the acceptance of horizontal phase space of the ACR is designed to be 125π mm-mrad, and that the dilution factor during the multiturn injection is 1.25, the emittance of the stored beam becomes as large as the full acceptance after 22 turns injection. At this moment, the number of stored particles increases up to 2×10^2 particles.

Secondly, the stored particles are RF-stacked:¹⁾ The RF voltage of 24 kV is applied, and the frequency is swept from 30.30 MHz (corresponding to 200 MeV/nucleon) to 30.62 MHz. This frequency sweep brings about changes in the beam momentum and average radius by 1.8% and 17 mm, respectively. This multi-turn-injection plus RF-stacking process is repeated at 10 Hz ($1/\tau_{cool}$) where τ_{cool} is a longitudinal stochastic or electron cooling times. During this process the RF-stacked beam continuously undergoes the stochastic or electron cooling at the stacked top energy. Typical parameters of the stochastic cooling and electron cooler are tabulated in Tables 1 and 2. The longitudinal cooling time by the stochastic method is estimated to be as short as 0.1 s while the cooling time of electron cooler is several seconds.²⁾ After a sufficiently longer period than the intrinsic half-life, the number of coasting particles accumulated in the ACR amounts up to the equilibrium value of 1×10^5 . The momentum spread and emittance of the cooled stacked beams, become less than 0.15% and nearly 1π mm-mrad, respectively. This high-quality stored beam is adiabatically bunched with RF field. It is fast extracted, and is injected into the BSR by the one turn

Table 1. Parameters of the stochastic cooler.

Longitudinal cooling time	
(Number of Ions 1×10^8) (sec)	
U^{92+} (150 MeV/u)	0.06
C^{6+} (400 MeV/u)	0.01
Band width W (MHz)	2000
Ambient temperature T_n (K)	18
Atmospheric temperature T (K)	80
Total microwave power P (kW)	10
Pickup sensitivity Z_p (Ohm)	300

Table 2. Parameters of the electron cooler.

Maximum electron energy (keV)	300
Maximum cooled Ion energy (MeV/nucleon)	500
Maximum electron current (A)	10
Cathode diameter (mm)	5.81
Electron diameter at cooling section (mm)	50
Length of cooling section (m)	3.0
Cooling time (s) for 200-MeV/nucleon $^{132}\text{Sn}^{50+}$, initial $\Delta p/p = 0.5\%$ and emittance $\epsilon = 125\pi$ mm-mrad	5.4

injection method.

The Booster Synchrotron Ring (BSR) serves as a synchrotron to accumulate and accelerate electrons from a 0.3 GeV linac up to 2.5 GeV. The outline of the BSR is described elsewhere.³⁾ At the initial energy of 0.3 GeV the damping times are estimated to be 0.5 s for the transverse direction and 0.26 s for the longitudinal direction, which are short enough for the accumulation of electrons. The acceleration up to 2.5 GeV is done within 1 s.⁴⁾ This top-energy electron beam is fast extracted and injected into the DSR by the one turn injection method. The BSR will also be used for the acceleration of ion beams transferred from the ACR. The maximum $B\rho$ of the BSR is designed at 14.6 Tm which is matched with the DSR. The accelerated ion beams will be fast extracted and one turn injected into the DSR, and also slowly extracted for the experiments.

References

- 1) K. Ohtomo and T. Katayama: This report, p. 244.
- 2) K. Ohtomo and T. Katayama: This report, p. 246.
- 3) T. Ohkawa and T. Katayama: This report, p. 241.
- 4) S. Watanabe: This report, p. 242.

Design of Booster Synchrotron for MUSES

T. Ookawa and T. Katayama

The Booster Synchrotron Ring (BSR) is a part of Multi-Use Experimental Storage Rings (MUSES).¹⁾ The BSR follows the Accumulator-Cooler Ring (ACR). The BSR functions exclusively for acceleration of ion and electron beams. The accelerated ion and electron beams will be fast extracted and injected into the Double Storage Rings (DSR) that follow by one turn, and ion beams will be slowly extracted for experiments.

Layout of the BSR is shown in Fig. 1. The lattice structure takes the form to accommodate four long straight sections and four medium straight sections. The long straight sections are used for fast and slow extractions of ion and electron beams. In the medium straight sections, RF cavities and kicker magnets are inserted.

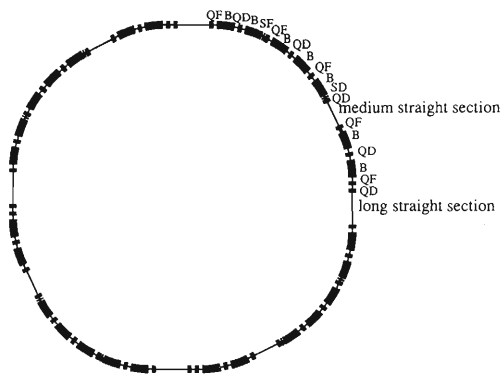


Fig. 1. Layout of the BSR.

Parameters of the BSR are given in Table 1. The ring circumference is 134.787 m, which is 4 times as large as the extraction circumference of the Superconducting Ring Cyclotron (SRC);²⁾ the harmonics of the BSR is 24 while that of the SRC is 6. The maximum $B\rho$ -value becomes 14.6 Tm when a dipole field strength is 1.524 T at the maximum. The maximum accelerating energy is then (to be) 3.54 GeV for protons, 1.45 GeV/nucleon for light ions of $q/A = 1/2$, and 800 MeV/nucleon for heavy ions of $q/A = 1/3$. For electron beams the BSR boosts them up to the

Table 1. Parameters of the BSR.

Circumference (m)	134.787
Max. magnetic field (Tm)	14.60
Average radius (m)	21.45
Radius of curvature (m)	9.58
Max. accelerating beam energy	
proton (GeV)	3.54
ion ($q/A = 1/2$) (GeV/nucleon)	1.45
ion ($q/A = 1/3$) (GeV/nucleon)	0.80
electron (GeV)	2.50
Betatron tune values (Q_x/Q_y)	5.438/4.867
Momentum compaction factor	0.218
Transition γ	4.579
Max. betatron amplitude (β_x/β_y , m)	18.12/21.97
Max. dispersion function (D_x/D_y , m)	2.52/0.0
Length of long straight section (m)	4.0
Length of medium straight section (m)	3.15

maximum energy of 2.5 GeV from the injection energy of 300 MeV. The acceleration up to the maximum energy is done within 1 s. The betatron tune values are 5.438 (horizontal) and 4.867 (vertical). The maximum energy is kept to be under the transition energy, since the transition gamma is as high as 4.58. Natural chromaticity values are -6.543 (horizontal) and -7.010 (vertical). The chromaticity is corrected by two families of sextupole magnets, one focusing and one defocusing. Taking the acceleration of $^{238}\text{U}^{92+}$ beam from 150 MeV/nucleon to 1 GeV/nucleon as an example, we give some RF parameters of the BSR. Typical beam characteristics are estimated as follows: The momentum spread is $\pm 0.1\%$; and the transverse emittances are 125π mm-mrad in horizontal direction and 5π mm-mrad in vertical direction. Provided that the dilution factor is 2, the maximum RF voltage is required to be about 200 kV, and the frequency to be modulated from 27.12 to 46.76 MHz.

Optimization of parameters of the BSR is under way.

References

- 1) T. Katayama: This report, p. 240.
- 2) Y. Yano et al.: This report, p. 226.

Computer Study of Magnet Power Supply for MUSES Booster Synchrotron (BSR)

S. Watanabe

MUSES-BSR is a booster synchrotron with a repetition rate of 1 Hz. In the BSR, electron and heavy ion beams are accelerated and fast extracted. Then they are injected into Double Storage Rings, DSR. The maximum energy of BSR is 2.8 GeV for protons and 350 MeV/u for $^{238}\text{U}^{58}$ beams. The magnetic optics of BSR is described precisely elsewhere in this progress report. The fundamental points of magnetic issues are as follows. The lattice structure of BSR is four FBDB-FBDB-FBDO-FBDB-FDO structures. Then the synchrotron magnet strings comprise 28 dipole magnets and 40 quadrupole magnets with four groups. In addition, one dipole magnet and four quadrupole magnets are needed to measure the magnetic field, which is used for a current feedback or B-block detection. A current excitation pattern has a flat bottom and a flat top field like the trapezoid wave form. Expected dipole magnet specifications are tabulated in Table 1. To reduce the inductance of a magnet coil, the excitation coil has a cross-section which is two times larger than that of hollow conductor.

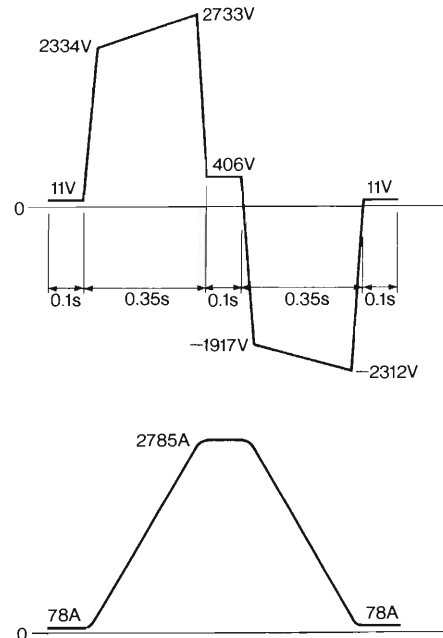


Fig. 1. Voltage and current patterns of BSR.

Table 1. Specifications of a dipole magnet of BSR.

Maximum field	1.5 T
Minimum field	0.042 T
Magnet length	1.8 m
Magnet width	1.0 m
Magnet height	0.7 m
Magnet gap height	0.07 m
Magnet gap width	0.272 m
Magnet ampere turn	83556.4 AT
Main coil turn number	30
Auxiliary coil turn number	12
Main coil inductance	8.532 mH
Main coil resistance	4.677 mΩ

The designed voltage and current patterns of the dipole magnet strings are shown in Fig. 1. The maximum time-derivative of dipole magnetic field in the beam acceleration phase is designed as large as 5.99 T/s. The estimated power consumption at the full excitation of dipole magnet system is 7.614 MW. The var component at the full-excitation is also estimated at 10.768 MVA. The flat top time will be expanded to a five or ten times longer than that in Fig. 1 in the case of slow extraction for the production of a long-spill beam. Figure 2 shows a schematic diagram of a power supply for BSR. The power supply comprises a thyristor, an LC filter, a dynamic filter and a current regulation loop. The current regulation loop comprises a voltage feed-forward, ACR and VCR loops. The feed-

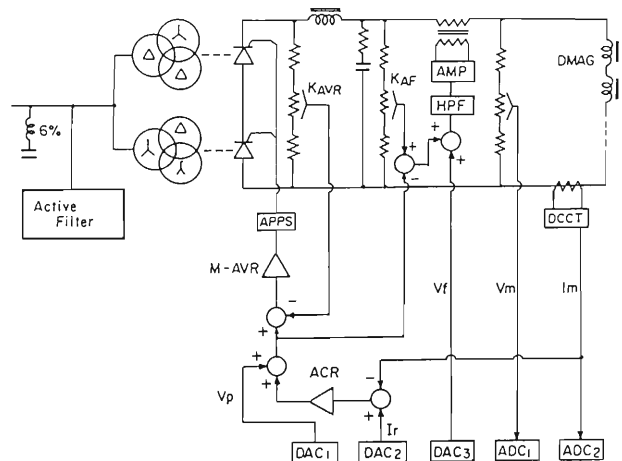


Fig. 2. Schematic structure of a bending power supply of BSR.

forward loop plays a role to boost the excitation current for an inductive load with a large time constant. A self-learning technique with a computer-feedback loop plays an important role so that the excitation-current error is to be minimized comparing with a reference current pattern.¹⁾ A computer study of dipole magnet power supply has been done to evaluate the accuracy, response and reliability in the operation mode of pulsed trapezoid wave form. The circuit model em-

ployed in the calculation, is similar to that of a synchrotron power supply of INS-TARN2.²⁾

The accuracy of excitation current is evaluated as a function of amplitude resolution of a current pattern generator, using a digital to analog converter. The current pattern at the acceleration phase comprises linear or quadratic time dependence. In the quadratic region, the current change appears suddenly because of a bit data change of the digital to analog converter. This step-wise current change must be smaller than 10^{-6} of the full excitation current.

The error of current pattern is exponentially decreased with the number of self-learning process. The computer study shows that a small change of circuit parameter is required to adapt the basic model to the MUSES-BSR power supply. The feed-forward time, gain of DCCT and the damping time of feed-back circuit have been searched to obtain high-precision current control up to 10^{-6} .

Figure 3 shows an example of the self-learning process. The vertical scale is a residual current defined as the subtraction of the reference current from a flowing current through the load magnet. For the check of the circuit parameter, firstly, we investigated the impulse response of the circuit to determine the delay time of the power supply circuit. The analysis of impulse response gave also the information on the component

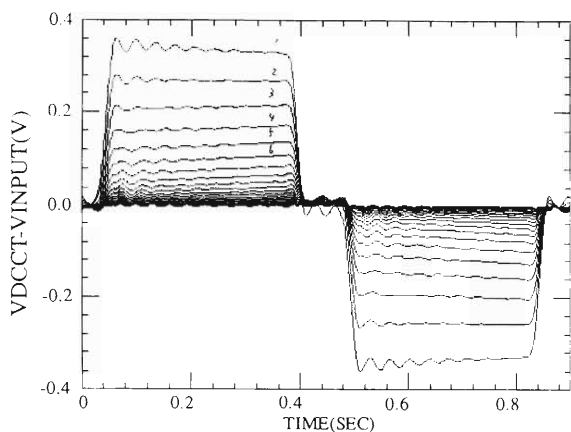


Fig. 3. Current pattern errors during the self-learning process.

of oscillations against rapid signal changing such as a step-wise reference signal from the digital to analog converter. Secondly, the delay time of the circuit was adjusted so as to reduce the ringing components appeared in the residual signal.

The magnet strings comprise π - π mode L-C network which has normal and common mode admittances.³⁾ These parameters are examined whether or not there are resonance phenomena due to the current ripples at a thyristor block. If the ripple current is coupled with resonance of these admittances, the error of magnetic field will be excited. Figure 4 shows the calculated normal mode admittance of dipole magnet strings. We can see that the resonance appears around the higher harmonics of 50 Hz component. The resonance frequency which coincides with higher harmonics of ripple current, must be shifted upward or downward by additional capacitance at the magnet component.

We are making a small model of magnet strings to evaluate the winding structure of magnet coils and the resonance detune method.

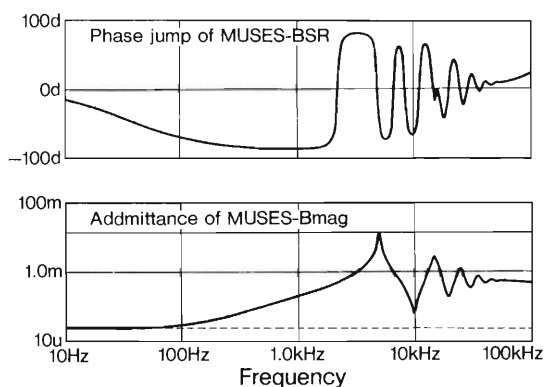


Fig. 4. Calculated normal mode admittance of BSR dipole magnet strings.

References

- 1) M. Takanaka and S. Watanabe: INS-T-456 [Accelerator-2] Mar. (1986).
- 2) S. Watanabe: INS-T-504 [Accelerator-13] July (1991).
- 3) S. Watanabe: INS-T-533 [Accelerator-20] Jan. (1995).

Simulation of RF Stacking Injection at Accumulator Cooler Ring for MUSES

K. Ohtomo and T. Katayama

The accumulator cooler ring (ACR) stacks the RI particles from the super conducting ring cyclotron (SRC) and cools them. The RF stacking technique^{1,2)} is generally used to stack the injected particles to a synchrotron ring effectively. To optimize the various parameters of the RF stacking, the stacking process has been simulated by solving the synchronous oscillation equations with the Runge-Kutta method.

The motion of an injected ion in the RF stacking process follows the equations:

$$\frac{d\varphi}{dt} = -\frac{\omega_{rev}h\eta}{\beta_s^2 E_s}(E - E_s),$$

$$\frac{dE}{dt} = \frac{\omega_{rev}eV_{acc}}{2\pi} \sin \varphi,$$

$$\eta = \frac{1}{\gamma^2} - \frac{1}{\gamma_t^2}.$$

Here subscript s represents the synchronous particle, φ and E are the phase and energy of a particle, ω_{rev} is the angular revolution frequency of the particle, h the harmonic number, V_{acc} an RF voltage, and γ_t the transition gamma. We have developed a computer program based on these equations and the 4-step 4th Runge-Kutta method. Parameters γ_t and h were fixed to be 4.875 and 24 given from the basic design of ACR. The spreads of energy and phase distributions (ΔE and $\Delta\varphi$) of injected particles were set to be ± 0.5 MeV/u and ± 10 degrees, respectively.

First, we calculated the one-cycle stacking process on trial to search the parameters. It was recognized that efficient stacking needed a large RF bucket at the injection and as small a suppression as possible of this RF bucket at the final stage of the stacking cycle. In order not to spill any particles from the RF bucket, the bucket height is required to be about 3 times larger than ΔE of injected particles and the RF voltage to be over 100 kV. But this voltage should be reduced suddenly to one third of the initial value after 30 μ sec which is quarter of the synchrotron oscillation period passed. This reduction prevents the emittance of the injected particles from increasing. The voltage reduction in the latter half of the stacking cycle is important to suppress the momentum spread of particles. Good results were obtained when the dilution factor was set to be 1.5 and the RF voltage at the final stage to be 3.6 kV. A typical pattern of time-dependent parameters is shown in Fig. 1.

In Fig. 2 is shown the motion of the injected particles in phase space during the one stacking cycle. In this case after 34 msec, 10% of the particles began to spill

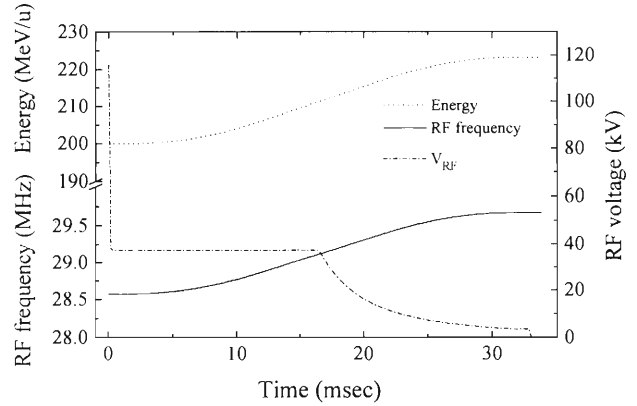


Fig. 1. RF frequency and voltage pattern.

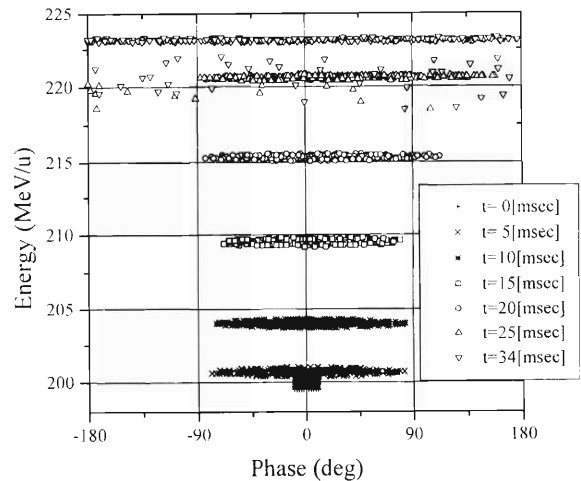


Fig. 2. Motion of the injected particles in phase space during one stacking cycle.

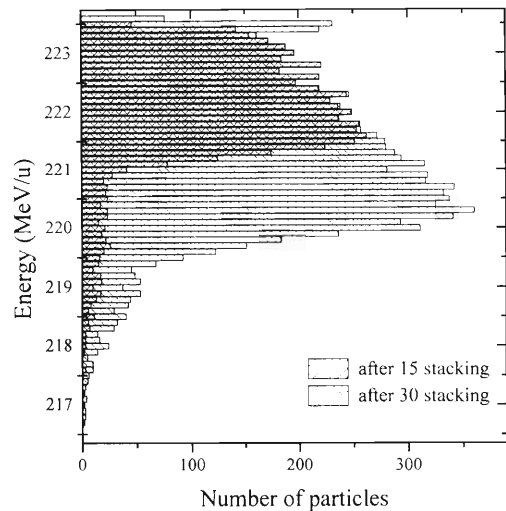


Fig. 3. Energy distributions of particles after 15- and 30-cycle stacking.

out from the stable area in phase space toward the lower energy.

Next, we calculated the multi-cycle stacking process. The energy distributions of all particles after 15 and 30 stacking cycles are shown in Fig. 3. About 10% of the particles were shifted to a low energy (less than 219.3 MeV/u) side during 30 stacking process. These particles are expected to be unable to receive the cooling force effectively, and thus expected to be spilled out.

In summary, it can be expected that the injection

efficiency is 90%. This value is acceptable for the stacking to ACR. As a next step we will take account of the cooling effect in this simulation.

References

- 1) E. Ciapala: Proc. CERN Accelerator School 85-19, 1, 195 (1985).
- 2) G. Bisoffi: "Radiofrequency Stacking: A Method to Reach High Intensities in the Storage Ring TSR", doctoral thesis (1989).

Electron Cooling at RI Beam Factory

K. Ohtomo and T. Katayama

The RI Beam Factory project demands very rapid cooling because of the short life time of RI. We have evaluated the cooling time at the Double Storage Ring¹⁾ (DSR) by using the technique of the electron cooling method.^{2,3)} The cooling time has been obtained by solving the kinetic equations of an ion with the cooling force.

An ion under the electron cooling process follows the equations:⁴⁾

$$\frac{d\theta}{dt} = -k \frac{\theta}{\left[\theta^2 + \frac{1}{\gamma^2} \left(\frac{\Delta p}{p} \right)^2 \right]^{3/2}}$$

$$\left[2(10 - \log Z) + 3 \frac{\theta^2 - \frac{2}{\gamma^2} \left(\frac{\Delta p}{p} \right)^2}{\theta^2 + \frac{1}{\gamma^2} \left(\frac{\Delta p}{p} \right)^2} \right],$$

$$\frac{d\frac{\Delta p}{p}}{dt} = -k \frac{\frac{\Delta p}{p}}{\left[\theta^2 + \frac{1}{\gamma^2} \left(\frac{\Delta p}{p} \right)^2 \right]^{3/2}}$$

$$\left[2(10 - \log Z) + 3 \frac{\theta^2}{\theta^2 + \frac{1}{\gamma^2} \left(\frac{\Delta p}{p} \right)^2} \right].$$

$$k = 2\pi r_e r_n \frac{j_e}{\beta^4 \gamma^5} \frac{Z^2 \ell}{A L}.$$

Here θ and $\Delta p/p$ are the transverse and longitudinal momentum deviations, Z is the charge state, A the mass number, r_e the classical electron radius, r_n the classical nucleon radius, j_e the electron flux density, ℓ the length of an electron cooler section, and L the circumference of a storage ring. To simulate the cooling process, we have developed a program in which these equations are solved by using the Runge-Kutta method.

In the present simulations, the ℓ and L are set to be 3 and 178.8 m, respectively, which are derived from the lattice design of the DSR. The initial value of θ is set to be 4.47 mrad, assuming that the beam emittance of ion is 100 mm·mrad and the beta function at the electron cooler is 5 m. The j_e is assumed to be 5000 A/m², considering the space charge effects.

Figure 1 shows an example of the simulation, in which 200-MeV/u $^{132}\text{Sn}^{+50}$ ions are selected as a test particle. The $\Delta p/p$ and θ of ions are plotted as a function of time. The simulation has been made for different initial value of $\Delta p/p$ ranging from 0.05 to 0.5%. The initial value of θ is fixed to be 4.47 mrad as mentioned above. The slope of the curves in the figure

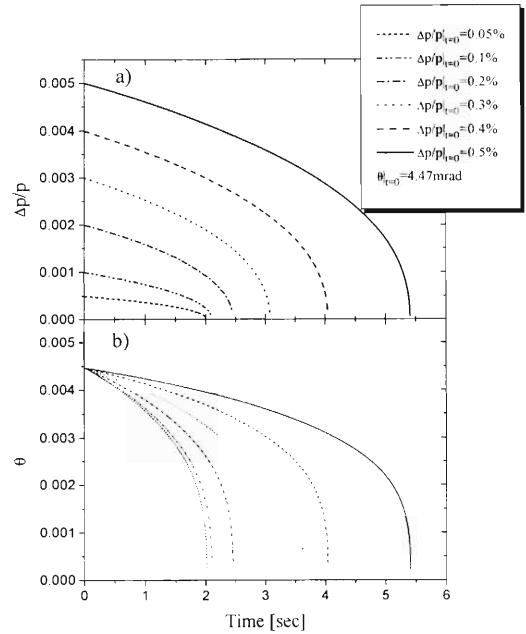


Fig. 1. Transient cooling process of 200 MeV/u $^{132}\text{Sn}^{+50}$ ions simulated for different initial values of $\Delta p/p$: a) the cooling of $\Delta p/p$; and b) the cooling of θ . The initial value of θ is taken to be 4.47 mrad. The cooling time is defined as an elapsed time before $\Delta p/p$ and θ get close to zero.

clearly indicates that the rate of cooling gets faster as the θ and $\Delta p/p$ decrease. This is a characteristic of the electron cooling. It is also shown that the cooling time decreases quadratically as the initial value of $\Delta p/p$ becomes smaller.

A contour plot in Fig. 2 shows the simulated cooling

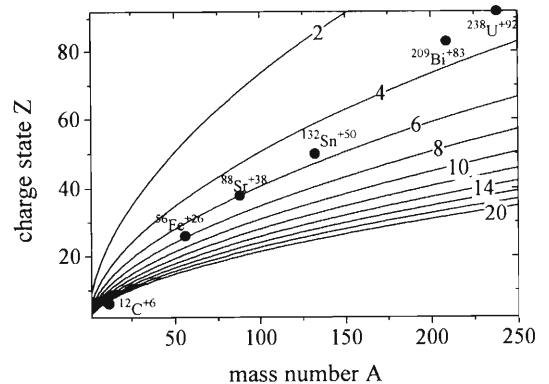


Fig. 2. A contour plot of cooling time given as a function of mass number and charge state number. The cooling times of typical ions are shown as closed circles in the figure.

time as a function of mass number and charge state number. The ion energy and the initial value of $\Delta p/p$ are taken to be 200 MeV/u and 0.5%, respectively. Most ions are fully-stripped at this energy. Very heavy ions such as bismuth are found to be cooled rapidly. The typical cooling time is about a few seconds. This will allow a large number of RI beams in this mass region to be cooled efficiently. On the other hand, light heavy ions are found to be cooled very slowly and their cooling times are much larger than life times of RI. For example, it takes about 25 seconds to cool $^{12}\text{C}^{+6}$ ions. The electron cooling cannot be used for most of RI beams in this mass region. The cooling time of medium heavy ions is found to be 6 to 10 seconds. In this case, RI beams far from the stability line cannot

be cooled efficiently.

It has been shown that the electron cooling is not applicable to all kinds of RI beams. We conclude that the stochastic cooling method needs to be used in addition to the electron cooling.

References

- 1) T. Katayama et al.: *RIKEN Accel. Prog. Rep.*, **28**, 180 (1995).
- 2) A. H. Sørensen and E. Bonderup: *Nucl. Instrum. Methods*, **215**, 27 (1983).
- 3) M. Bell et al.: *ibid.*, **190**, 237 (1981).
- 4) T. Katayama: "Electron Cooling at MUSES", internal report (1995) unpublished.

Design of a Lattice of the DSR

N. Inabe and T. Katayama

A new lattice of Double Storage Rings (DSR¹) has been designed to fulfill new requirements from experimenters who use X-rays radiated from stored electron beams in the ring. The requirements have two main points. One is to reduce natural emittance of the stored electron beam to about 1/30 of the old one in order to get X-rays with narrow widths of energy and size. The other is to insert an undulator with length of 5 m in a long straight section in order to produce X-rays. Since the required reduction can't be done for the old lattice, we changed the lattice configuration very much. As the result parameters of the new lattice such as circumference, tune and so on are much different from those of the old one. In addition to the two main changes, we changed the magnetic rigidity from 12.76 Tm to 14.60 Tm, which corresponds to its value of 800 MeV/u with $q/A = 1/3$.

Figure 1 shows a schematic drawing of the DSR. As shown in Fig. 1, the DSR is composed of four arcs, two long straight sections and two short straight sections. The long straight section consists of the undulator section and a colliding section. The short straight section is for cooling of ion beams.

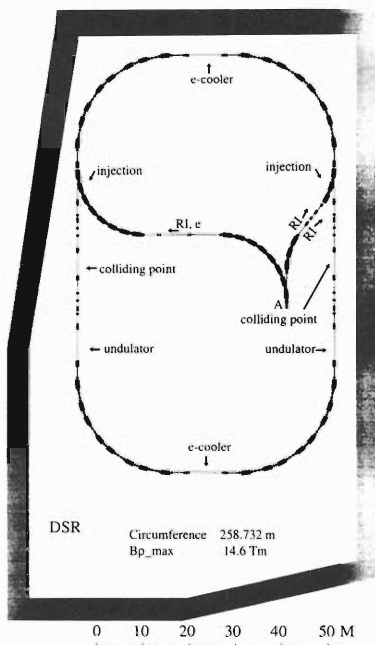


Fig. 1. Layout of the DSR.

The natural emittance is reduced by small dispersion in a dipole magnet in the arc.²⁾ We made the small dispersion by constructing a unit cell with a Double Bend Achromat (DBA) system. Figure 2 shows β and dispersion functions of the unit cell in the DSR. Although the DBA can be achieved only by the horizontal focus-

ing quadrupole magnet between the two dipole magnets (QFA), it is difficult to correct the natural chromaticity due to small dispersion between two dipole magnets. For this reason we introduce a horizontal defocusing quadrupole magnet (QDA) that enlarges the dispersion between the two dipoles and achieves the DBA by both the QFA and the QDA. Another horizontal focussing quadrupole magnet (QF) is introduced to fulfill the periodic condition of the cell. Each parameter shown in Table 1 is chosen so as to fulfill constraints that are the small natural emittance, easy chromaticity correction, small magnetic field strength of quadrupole magnets and short length of the cell.

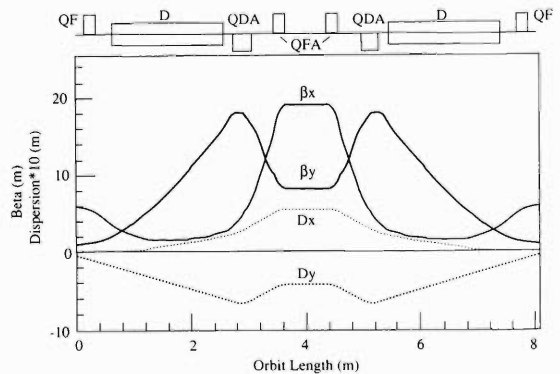


Fig. 2. β and dispersion functions of the unit cell in the DSR.

Table 1. Parameters of the unit cell in the DSR.

Drift length (m)	
QF~D	0.3
D~QDA	0.2
QDA~QFA	0.4
QFA's	0.7
QF's	0.3
Dipole radius (m)	
9.73	
Length of Q (m)	
QF	0.2
QFA	0.2
QDA	0.3
Field strength of Q ($1/m^2$)	
QF	3.356
QFA	4.172
QDA	-3.013

The arc consisted of four cells mentioned above. In order to reduce the natural emittance a large number of cells is suitable. However it is impossible to make the arc with many cells due to limitation of a construction area. The number, four, is maximum for the area.

In the undulator section small sized and parallel beams are required. The required value of Twiss parameter, β , is 5 m and that of α at the midpoint of the section is 0. To match emittance between the arc and the section a triplet quadrupole is inserted at the entrance of the section. Figure 3 shows the β function of the section.

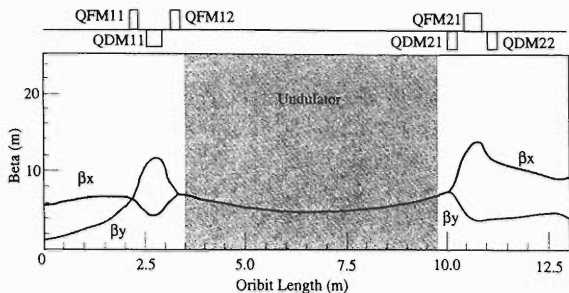


Fig. 3. β functions of the undulator section in the DSR.

The β -functions of the colliding section and the short straight section are the same as those of the old one.¹⁾ For the reason luminosity does not change from the old one. Matching with the connected section is achieved by a triplet quadrupole located at the entrance of the section. Figure 4 shows the β -functions of the colliding section (a) and the short straight section (b).

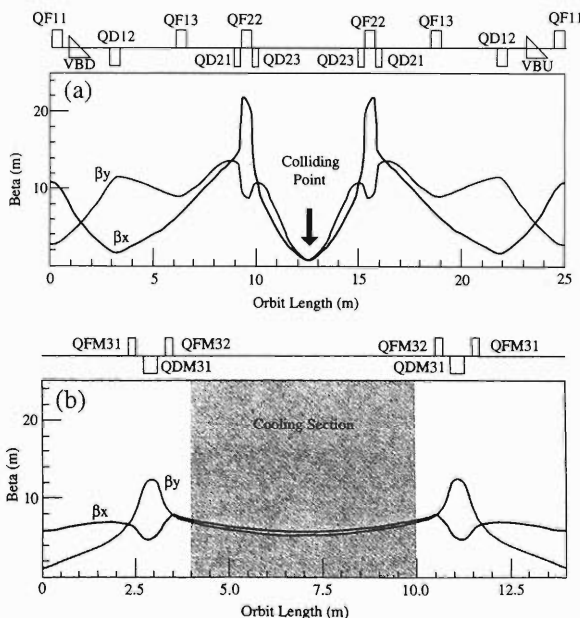


Fig. 4. β functions of the colliding (a) and cooling (b) sections in the DSR.

After matching all the sections we calculated several parameters of the DSR with a calculation code MAD.³⁾

These are summarized in Table 2. The circumference is 258.732 m, which is about 80 m larger than that of the old one. This is due to the long unit cell and insertion of the undulator section. The betatron tunes, 18.130 for horizontal and 10.197 for vertical, are much larger than those of the old one. The natural chromaticities are also very large. Enlargement of the tunes and the natural chromaticities are due to strong field strengths of the quadrupoles in the unit cell. Parameters of the stored electron beam are summarized in Ref. 4. The natural emittances for 2.5 GeV electron beam are 8.54 n m*rad for horizontal direction and 25.5 n m*rad for vertical one, both of which are much smaller than those of the old one. The values are small enough for the experimenters' requirement.

Table 2. Parameters of the DSR.

Circumference C (m)	258.732
Max. $B\rho$ (Tm)	14.60
Average radius R (m)	41.20
Max. beam energy (GeV/u)	
proton	3.50
ion ($q/A = 0.5$)	1.33
($q/A = 0.387$)	1.00
($q/A = 0.333$)	0.80
Betatron tune value (Q_x/Q_y)	18.130/10.197
Momentum compaction	0.00171
Transition γ	24.20
Max. betatron amplitude (β_x/β_y , m)	22.0/17.9
Max. dispersion function (D_x/D_y , m)	0.537/0.697
Betatron amplitude at Interaction point (β_x^*/β_y^* , m)	0.600/0.600
Length of field-free section at colliding section (m)	5.016
Natural chromaticity (Q'_x/Q'_y)	-45.59/-30.94

In the DSR several operation modes are required. For colliding electron and ion, a large emittance compared with that mentioned above is required for the electron beam. For ions the small natural chromaticity is required to enlarge a dynamic aperture. We are now searching different operation modes to meet the requirements.

References

- 1) T. Katayama et al.: *RIKEN Accel. Prog. Rep.*, **28**, 180 (1995).
- 2) A. Jackson.: *Particle Accelerators*, **22**, 111 (1987).
- 3) Hans Grote and F. Christoph Iselin: CERN/SL/90-13(AP) (User's Manual Version 8.1).
- 4) M. Wakasugi et al.: This report, p. 257.

Beam Current Limitations Due to Single-Beam Collective Effects at Double Storage Rings at MUSES

M. Takanaka and T. Katayama

The RIKEN Accelerator Research Facility group has been proposing "RIKEN RI Beam Factory" as a next project.¹⁾ Ion-electron colliding and ion-ion merging experiments are planned at Double Storage Rings (DSR) of Multi-USE-Experimental-Storage ring system (MUSES). These experiments require high luminosity with small momentum spread and emittances. For this purpose, an accumulator ring will be installed upstream the DSR where the intensity of ion beams is increased with a cooling-staking technique and the momentum spread and emittances are cooled down. The expected full momentum spread may become at most 10^{-3} and the transverse emittances 1×10^{-6} π mmrad. The improvement of beam qualities does not always mean the increase of luminosity, because it makes single-beam collective effects strong and hence limits the beam currents in the ring.

In this paper, limitations of ion beam current are estimated due to beam-beam effects during the collision, the direct space charge effects, and beam instability in the designed ion ring. The luminosity is evaluated for the threshold beam currents. Finally, a proposal is made to improve the luminosity. More detailed description has been given elsewhere.²⁾

In DSR bunched electron beams circulate in the one ring and ion beams circulate in the other ring which will collide at two interaction points with zero colliding angle. The stability of betatron motion of the ions in the ring, requires that the linear betatron tune shift due to the beam-beam effect should be less than about 0.05. From this point of view, the number of electrons per bunch is evaluated in Table 1 where the rms emittances of electron beams are assumed at 8×10^{-9} π mmrad for 300 MeV and at 530×10^{-9} π mmrad for 2500 MeV, respectively. On the other hand, the stored current of the electron beam is expected to be at least 300 mA, corresponding to the number of electrons of 7×10^{10} per bunch. Then the number of electrons at the low energy of electron beams is limited by the beam-beam effects on the ion beams.

In order to make an effective collision, the full bunch length of ion beams is required to be less than 40 cm,

Table 1. The threshold of electrons' number per bunch due to the beam-beam effect and the number per bunch for the 300 mA electron beam.

Ion \times electron	300 MeV e^-	2.5 GeV e^-	300 mA
400 MeV/u ${}^4\text{He}^{2+}$	3×10^9	2×10^{11}	
150 MeV/u ${}^{238}\text{U}^{92+}$	2×10^9	1×10^{11}	7×10^{10}

which corresponds to the bunching factor 1/15. The incoherent betatron tune shift due to the direct space charge is tolerable by $|\Delta\nu| = 0.2$, when resonance compensation is carried out completely. The space charge limits of ions' number per bunch are shown in Table 2.

Table 2. The threshold of ions' number per bunch due to the direct space charge.

400 MeV/u	${}^4\text{He}^{2+}$	1×10^9
150 MeV/u	${}^{238}\text{U}^{92+}$	7×10^6

The structure of vacuum chamber and numbers of elements have not yet determined in DSR. Here, the ion-beam coupling impedances with the chamber are estimated under a rough assumption as shown in Table 3. The longitudinal impedance of the RF cavity is assumed to be like that of a $\lambda/4$ coaxial cavity with the use of a perpendicular bias field on the ferrite.

Table 3. The imaginary parts of the longitudinal impedances $\text{Im}(Z_L/n)[\Omega]$ and those of the transverse ones $(Z_\perp)[\text{M}\Omega/\text{m}]$ of the ion ring of DSR at the low frequency.

Injection energy	150 MeV/u		400 MeV/u	
	Horizontal	Transverse	Horizontal	Transverse
Space charge	1900	6600	860	2300
Broad band	-3.2	-0.2	-4.0	-0.2

The microwave instability is undesirable, because it induces bunch lengthening when the ions' number per bunch goes beyond a threshold, and the lengthening decreases the luminosity. It is shown that the microwave instability does not occur for the ions' number less than the space charge limit with the momentum spread of 1×10^{-3} .

Single-bunch instability and multi-bunch instability are induced for the ions' number of space charge limit. The growth time of the most unstable coupled-bunch mode at each synchrotron mode is shown in Table 4, which is calculated with the program ZAP modified to be applicable to ion beams by the authors.

Transverse single-bunch instability is Landau damped because the coherent tune shift is less than the incoherent betatron tune shift by a factor of 3.

Transverse multi-bunch instability is induced through the resistive wall impedances and RF narrow band ones. Here, the growth times of instability just through the former are evaluated as shown in Table 5.

The electron cooling can be applied to damp the

Table 4. The growth times [s] of the most unstable mode(m,n) of the longitudinal single-bunch instability and multi-bunch instability in the n-th mode, where m shows the coupled-bunch mode and n the synchrotron one.

400 MeV/u		⁴ He ²⁺		150 MeV/u		²³⁸ U ⁹²⁺	
Single-bunch		Multi-bunch		Single-bunch		Multi-bunch	
Mode(1)	0.7	Mode(0,1)	0.02	Mode(1)	1	Mode(28,1)	0.07
Mode(2)	1	Mode(0,2)	0.05	Mode(2)	-0.3	Mode(27,2)	0.4
Mode(3)	10	Mode(0,3)	0.3	Mode(3)	-4	Mode(29,3)	0.3
Mode(4)	30	Mode(0,4)	0.9	Mode(4)	-0.8	Mode(28,4)	0.6

Table 5. The growth times [s] of the most unstable mode(m,n) of the transverse multi-bunch instability under the chromaticity of zero.

Energy	400 MeV/u	150 MeV/u
Ion	⁴ He ²⁺	²³⁸ U ⁹²⁺
Mode(23,0) or Mode (24,0)	1	3

longitudinal and transverse instability. The cooling time is required to be less than half the growth time;³⁾ $\tau_{cool} \leq 0.01$ [s].

In the presently designed ion ring of DSR, the longitudinal single-bunch instability and multi-bunch instability are induced at the number of ions at the space charge limit and the bunch length of 40 cm. The transverse multi-bunch instability may be induced, which is dependent on the chromaticity. The electron cooling with the cooling time of 0.01 s can damp the instability. As a result, the luminosity shown in Table 6 is determined by the space charge limit of ions and the limit of electrons' number. The luminosity for 150 MeV/u ²³⁸U⁹²⁺ is much less than 1×10^{27} cm⁻² s⁻¹. In order to improve the luminosity, the design of DSR

Table 6. The luminosity [cm⁻² s⁻¹] at the space charge limit of ions.

Ion×electron	300 MeV e ⁻	2.5 GeV e ⁻
400 MeV/u ⁴ He ²⁺	3×10^{27}	2×10^{28}
150 MeV/u ²³⁸ U ⁹²⁺	9×10^{24}	1×10^{26}

lattice should be modified as follows;

- (1) The beta function at the colliding point is reduced by one order,
- (2) The optics of the lattice of the electron ring is variable enough to increase the emittance of the 300 MeV electron beam up to around 0.5×10^{-6} π mrad in order that the beam-beam effects become weak,
- (3) The numbers of bunches of both beams are increased by a few times.

References

- 1) Y. Yano, A. Goto, and T. Katayama: RARF Accelerator Group, RIBF-A-1-1995 (1995).
- 2) M. Takanaka and T. Katayama: Proc. 10th Symp. on Accel. Sci. and Technol., p. 318 (1995).
- 3) S. Cocher and I. Hofmann: *Particle Accelerators*, **34**, 189 (1990).

Merging Beam-Beam Interaction at DSR

Y. Batygin and T. Katayama

Proposed Radioactive Isotope Beam Factory¹⁾ is aimed to be used for a wide range of experiments with unstable nuclear beams. Among variety of planning experiments the ion-ion merging collisions are very important. In this paper we analyze the luminosity constraints due to beam-beam interaction as a function of main parameters of the storage ring.

We consider two coasting merge ion beams with particle densities n_1 and n_2 and with beam velocities $\vec{v}_1 = c\vec{\beta}_1$ and $\vec{v}_2 = c\vec{\beta}_2$, colliding with angle α (see Fig. 1). Luminosity L is defined as a ratio of interaction rate to cross section for the particle interaction: $L = 1/\sigma \, dN/dt$. Using expression for invariant cross section²⁾ the number of collisions dN during the time dt is

$$\frac{dN}{dt} = \int_{\mathbf{v}} \sigma \sqrt{(\vec{v}_1 - \vec{v}_2)^2 - \frac{[\vec{v}_1 \times \vec{v}_2]^2}{c^2}} n_1 n_2 dV, \quad (1)$$

where integration is performed over the volume of interaction. It is convenient to express the luminosity as a function of collision angle α , number of particles per beam N_1 , N_2 , ring circumference $2\pi R$, and effective size of the beam h_{eff} at the interaction point:

$$L = \frac{\sqrt{\beta_1^2 + \beta_2^2 - 2\beta_1\beta_2 \cos \alpha - \beta_1^2\beta_2^2 \sin^2 \alpha} c N_1 N_2}{(2\pi R)^2 \sin \alpha h_{\text{eff}}}. \quad (2)$$

The numerical model for beam-beam interaction study includes a transfer matrix for particle revolution in the storage ring and particle-in-cell treatment of a space charge problem at the crossing point.³⁾ Linear approximation to the betatron tune shift is a scale parameter to define the strength of beam-beam collisions:

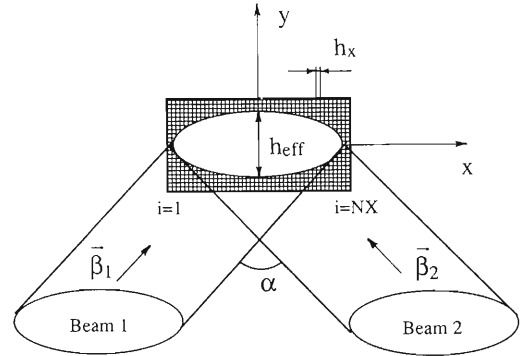


Fig. 1. Merge beam-beam interaction.

$$\xi = \frac{N r_0}{2\pi^2 \sigma \sin \alpha \beta^2 \gamma^3 Q}, \quad (3)$$

where $r_0 = q^2/4\pi\epsilon_0 mc^2$ is the value of classical radius of particle, N the number of particles per beam, σ the half size of the beam and Q the betatron tune.

The RI beam factory is supposed to have two colliding points; therefore the values of tune are half of betatron tunes in the ring: $Q_x/2 = 2.8815$; $Q_y/2 = 3.175$. For two coasting merge beams (see Fig. 1) only y -direction is responsible for degradation of beam luminosity because of compensation of the beam-beam kick in x -direction. The closest resonance value $mQ_y = n$ to a betatron tune value 3.175 is $6Q_y = 19$, i.e. the 6th order resonance is achieved for $Q_y = 19/6 = 3.16666$. Max tune shift from the working point to resonance is $\xi = 3.175 - 3.1666 = 0.00833$. In Table 1 the results of calculations for $\xi = 0.005$ (non-resonance case) and

Table 1. Results of PIC simulation of beam-beam effects.

Beam distribution	Distribution in real space	Tune ξ	Turns	Number of particles	Envelope growth (per 10^4 turns)	Emittance growth
Gaussian	$\rho(r) = \rho_0 \exp(-r^2/2\sigma^2)$	0.005	$4 \cdot 10^4$	10^3	1.0	1.0002
KV	$\rho(r) = \rho_0$	0.027	$2.5 \cdot 10^4$	$5 \cdot 10^3$	1.0	1.0 (no growth)
Water Bag	$\rho(r) = \rho_0 (1 - r^2/R_0^2)$	0.027	$2.5 \cdot 10^4$	$5 \cdot 10^3$	1.005	1.025
Parabolic	$\rho(r) = \rho_0 (1 - r^2/R_0^2)^2$	0.027	$2 \cdot 10^4$	$5 \cdot 10^3$	1.01	1.025
Gaussian	$\rho(r) = \rho_0 \exp(-r^2/2\sigma^2)$	0.027	10^4	$5 \cdot 10^3$	1.03	1.05

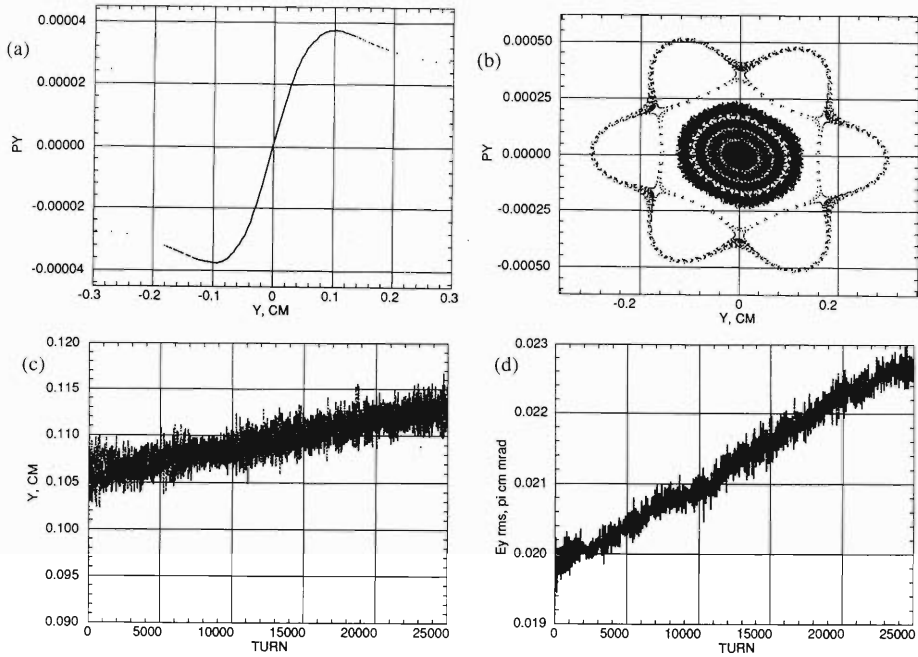


Fig. 2. (a) Momentum kick, (b) phase space trajectories, (c) beam envelope, and (d) RMS beam emittance for the beam-beam interaction of particles with Gaussian distribution: $Q_y = 3.175$, $Q_x = 2.8815$, $\xi_y = -0.027$, $N_{\text{particles}} = 5000$, mesh $NX \times NY = 64 \times 64$.

$\xi = 0.027$ (resonance case) for different particle distributions are presented. The results of simulation indicated that below the resonance threshold $\xi < 0.008$ beams were stable, i.e. no envelope and RMS emittance growth were observed. Under resonance conditions $\xi > 0.00833$ the beam-beam instability was observed (see Fig. 2).

Assuming $\xi_{\text{max}} = 0.008$, $\sigma_y = 10^{-3}\text{m}$, $\alpha = 10^\circ$, $\beta\gamma = 1.7$, $r_0 = 1.5 \cdot 10^{-18}\text{m}$ (proton) the limited number of particles due to beam-beam interaction is (see Eqn. (3)):

$$N < 2\pi^2 \frac{\xi_{\text{max}} Q_y \sigma_y \sin \alpha \beta^2 \gamma^3}{r_0} = 6 \cdot 10^{14}. \quad (4)$$

This value is larger than the space charge limited number of particles in a ring of radius $R = 28\text{m}$ due to the incoherent space charge tune shift (Laslett tune shift) $\Delta\nu_{\text{max}} = 0.25$:

$$N < 4\pi \frac{\Delta\nu_{\text{max}} Q_y \beta^2 \gamma^3 \sigma_y^2}{R r_0} = 3 \cdot 10^{12}. \quad (5)$$

Taking the limited number of particles $N_{\text{max}} = 3 \cdot 10^{12}$, $\alpha = 10^\circ$, $h_{\text{eff}} = 4 \cdot 10^{-3}\text{m}$ and assuming $\beta_1 = \beta_2 \approx 1$, the limitation in luminosity is (see Eqn. (2)):

$$L < \frac{N_{\text{max}}^2 c}{(2\pi R)^2 h_{\text{eff}}} \text{tg} \frac{\alpha}{2} = 2 \times 10^{26} \frac{1}{\text{sec cm}^2}. \quad (6)$$

From results of simulation we observed the increase of transverse beam size 1-3% per 10000 turns at the resonance conditions. If we assume that for serious degradation of luminosity the beam size is allowed to expand twice, the upper limit of beam lifetime in the resonance is

$$N_{\text{max}} = \frac{100\%}{2\%} 10000 = 5 \times 10^5 \text{ turns}. \quad (7)$$

If the resonance is avoided, the beam life time is limited by other reasons.

References

- 1) Y. Yano and T. Katayama: Present Status and Future Plan of RIKEN Accelerator Research Facility, Proc. EPAC94, London, p. 515 (1994).
- 2) L. Landau and E. Lifshitz: The Classical Theory of Fields, Pergamon Press (1975).
- 3) Y. Batygin and T. Katayama: Proc. 10th Symp. on Accelerator Science and Technology, Hitachinaka, p. 356 (1995).

Beam-Beam Interaction of Electrons and Ions at Double Storage Ring

Y. Batygin and T. Katayama

One of the main experiments at the new RI beam factory¹⁾ is a collision of 2.5 GeV electron beam with unstable ion beams. This experiment is intended to be used for determination of the charge and current distribution in the radio active nuclei. The physics of beam-beam interaction in the collision point is an important issue for determination of the value of collider luminosity.

The operating point of the Double Storage ring of RI beam factory is chosen to be $Q_x = 14.653$ and $Q_y = 16.283$. Because the ring is supposed to have two colliding points, the tune shift between sequence beam-beam interactions is equal to half of their values, $Q_x/2 = 7.3265$ and $Q_y/2 = 8.1415$.

Beam-beam interaction can be considered as an action of thin nonlinear lens at the interaction point. Influence of the opposite charged beams on each other results in increasing of betatron tune of particle oscillations. Because the electron beam is typically much stronger than the ion beam, it is enough for estimation to consider the behavior of ion beam in the unchanged field of the electron beam (strong-weak model). For the beam-beam interaction the linear part of the betatron tune shift ξ is a scale parameter, which defines the strength of the beam-beam interaction:²⁾

$$\xi = \frac{r_p \beta_x \frac{Z}{A} N_e (1 + \beta_e \beta_i)}{4\pi \gamma_i \beta_i^2 \sigma_e^2}, \quad (1)$$

where N_e is the number of electrons per bunch, β_x the beta-function at the interaction point, Z/A the charge-to-mass ratio of ion, β_e and β_i the velocities of electrons and ions, γ_i is the reduced ion energy, σ_e the half size of electron beam envelope and $r_p = e^2/4\pi\epsilon_0 mc^2 = 1.5 \cdot 10^{-18}$ m (classical radius of a proton). Limitation in ξ results in constraints of luminosity L , which is defined as follows:

$$L = \frac{f N_i N_e}{4\pi \sigma_e^2} N_{\text{bunch}}, \quad (2)$$

where $f = \omega_s/2\pi$ is the particle revolution frequency in a ring, N_i the number of ions per bunch and N_{bunch} the number of bunches per beam. To define the maximum value of betatron tune shift, the numerical calculations of ion trajectories in the collider ring including beam-beam interaction were done. Modulation of betatron tune due to coupling with synchrotron oscillations (synchro-betatron resonances) was taken into account as well. The beam-beam interaction model is a nonlinear four-dimensional map of the particle revolution in a ring with beam-beam kick $\Delta p_{x,y}$ arising

from Gaussian particle distribution:

$$\begin{aligned} x^{n+1} &= x^n (\cos 2\pi Q_x) + p_x^n \left(\frac{R \sin 2\pi Q_x}{p_s Q_x} \right), \\ p_x^{n+1} &= x^n \left(-\frac{p_s Q_x}{R} \sin 2\pi Q_x \right) + p_x^n (\cos 2\pi Q_x) + \Delta p_x, \\ Q_{x,y} &= \bar{Q}_{x,y} + A_S \sin(2\pi Q_S n), \\ \Delta p_x &= \frac{2r_p \frac{Z}{A} N_e (1 + \beta_i \beta_e)}{\beta_i} \frac{x}{r^2} \left[1 - \exp\left(-\frac{r^2}{2\sigma_e^2}\right) \right], \end{aligned} \quad (3)$$

analogously for y^{n+1} and p_y^{n+1} , where (x,y) are the particle position, p_x, p_y, p_s the reduced momentum of particles (divided by mc), R is the radius of ring, Q_s the betatron tune, $A_s = Q_s a_s/2\beta_x$ (depth of tune modulation³⁾), and a_s the bunch length.

Beam-beam interaction is a source of nonlinear resonances. Presence of betatron tune modulation increases the density of nonlinear resonances which obey the resonant condition (j, n, k and m are integers):

$$jQ_x + nQ_y + kQ_s = m. \quad (4)$$

The working area in phase space is covered by an infinite number of resonances for which the tune value is a rational fraction. If the resonances have sufficient width, they overlap in the tune space and the particle motion becomes unstable (stochastic motion).

General treatment of the stochastic problem⁴⁾ employs Hamiltonian which includes the betatron tune modulation:

$$\begin{aligned} H &= \left(Q_x + A_s \sin 2\pi Q_s t - \frac{p}{n} \right) J + \xi U(J) \\ &\quad + \xi V_n(J) \cos n\Psi, \end{aligned} \quad (5)$$

where J and Ψ are the action and angle variables, $\xi U'(J)$ is the amplitude dependent tune shift; $\xi V'(J)$ the 'resonance width', and n and p are integers. Functions $U(J)$ and $V(J)$ are defined by equations:

$$U'(J) = \frac{2}{J} [1 - e^{-J/2} I_0(J/2)], \quad (6)$$

$$V'_n(J) = (-1)^{n/2+1} \frac{4}{J} e^{-J/2} I_{n/2} \left(\frac{J}{2} \right). \quad (7)$$

Stochastic threshold (Chirikov criteria⁵⁾) for the linear tune shift expresses a condition that the separation of resonant islands should be larger than the width of resonances:

$$\xi \leq \frac{Q_s}{4nM} \sqrt{\frac{M^{1/2}}{U''(J)V_n(J)J_k \left(\frac{nA_s}{Q_s} \right)}}, \quad (8)$$

where n is the order of resonance, M is the number

of collisions per turn, and $J_k(x)$ the Bessel function of k -th order.

Figure 1 illustrates the mechanism of the beam stochasticity. Parameters of the problem were chosen as follows: $A/Z = 4$, $\beta_i \gamma_i = 1.7$, $\beta_x = 60$ cm, $a_s = 40$ cm, $Q_s = 0.01$ and $A_s = 0.01$. Depending on the combination of parameters, the behavior of particles can be either stable or chaotic (unstable). For small values of $\xi = 0.005 \dots 0.01$ the phase space trajectories are ellipses (see Fig. 1(a) and (b)). With increasing ξ until 0.03 the characteristic structure of the 7th and 14th order resonances at phase plane appears (Fig. 1(c)). With the further increase of ξ up to 0.05 the high order resonances overlap each other, which results in the stochastic behavior of particles (Fig. 1(d)).

From numerical simulation the stochastic threshold can be estimated as $\xi_{\max} = 0.01$. An analytical value

of the threshold, calculated from formula (8), shows the upper value of $\xi_{\max} = 0.00625$ (see Fig. 2). It is close to the experimentally observed values of $\xi_{\max} = 0.005 \dots 0.05$ in storage rings.

Taking the value $\xi_{\max} = 0.01$ as an upper limit for the betatron tune shift, $f = 1$ MHz, the limitation in luminosity is as follows (see Eqns. (1) and (2)):

$$L \leq \frac{f N_i N_{\text{bunch}} \gamma_i}{2 \beta_x r_p} \frac{A}{Z} \xi_{\max} \approx 5 \cdot 10^{17} \cdot N_i^{\text{total}} \frac{A}{Z} \approx 2 \cdot 10^{18} \cdot N_i^{\text{total}} \frac{1}{\text{cm}^2 \text{s}}, \quad (9)$$

where $N_i^{\text{total}} = N_i N_{\text{bunch}}$ (total number of stored ions in a ring), limited by the lifetime of unstable ions and finite value of acceptance of the ring.

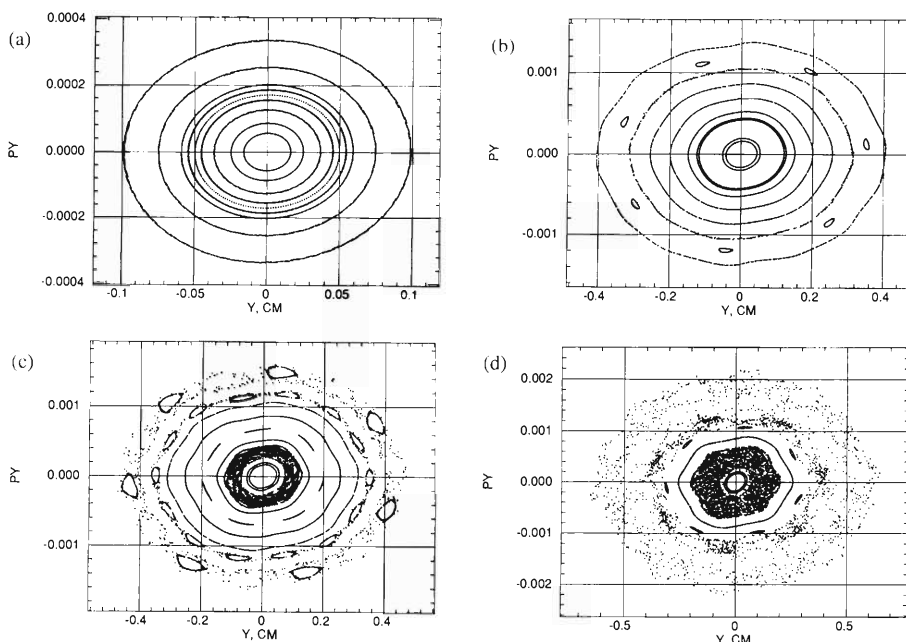


Fig. 1. Phase space trajectories of beam-beam interaction: $Q = 8.1415$, $Q_s = 0.01$, $A_s = 0.01$; (a) $\xi = 0.005$, (b) $\xi = 0.01$, (c) $\xi = 0.03$, (d) $\xi = 0.05$. Trajectories are plotted once per synchrotron period; the total number of turn is 200000.

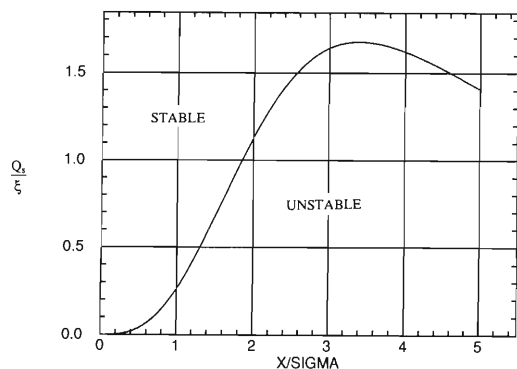


Fig. 2. Stochastic threshold (Chirikov criteria) as a function of amplitude for beam-beam resonance of the 7th order, $Q_s = 0.01$, $A_s = 0.01$.

References

- 1) Y. Yano, T. Katayama: Present Status and Future Plan of RIKEN Accelerator Research Facility, Proc. the EPAC94, London, p. 515 (1994).
- 2) E. Keil: "Theoretical Aspect of the Behavior of Beams in Accelerators and Storage Rings", CERN 77-13, Geneva, p. 314 (1977).
- 3) S. G. Peggs and R. M. Talman: *Ann. Rev. Nucl. Part. Sci.*, **36**, 287 (1986).
- 4) L. Evans: "The Beam-Beam Interaction", CERN 84-15, p. 319 (1984).
- 5) B. Chirikov: *Phys. Rep.*, **52**, 263 (1979).

Luminosity of Electron-Ion Collision in MUSES

K. Yoshida and T. Katayama

Luminosity for the head-on collision of electrons and unstable nuclei in the Double Storage Ring (DSR) of MUSES has been estimated.

Luminosity L of the head-on collisions is obtained by

$$L = n_1 n_2 N_c \frac{1}{h_{eff}} \frac{1}{w_{eff}} \operatorname{Erf} \left(\frac{(\beta_1 + \beta_2)d}{2\sqrt{2}\sqrt{\beta_1^2 \sigma_{z_2}^2 + \beta_2^2 \sigma_{z_1}^2}} \right),$$

$$h_{eff} = \sqrt{2\pi} \sqrt{\sigma_{y_1}^2 + \sigma_{y_2}^2}, \text{ and}$$

$$w_{eff} = \sqrt{2\pi} \sqrt{\sigma_{x_1}^2 + \sigma_{x_2}^2},$$

where $n_i (i=1,2)$ is the number of particles in one beam bunch in the DSR, β_i is the ratio of beam velocity to the speed of light, N_c is the number of collisions which occur in a unit time, σ_{x_i} , σ_{y_i} , σ_{z_i} are the bunch sizes of x, y, and z direction, and d is the length of the interaction region. Erf represents the error function. The bunch sizes will be $\sigma_x = \sigma_y = 0.774$ mm, and $\sigma_z = 50$ cm for unstable nuclei, and $\sigma_x = 0.651$ mm, $\sigma_y = 0.458$ mm, and $\sigma_z = 2.1$ cm for electrons. The number of electrons in a bunch is expected to amount up to 1.2×10^{12} which corresponds to the beam current of 500 mA.

The number of unstable nuclei in a bunch is estimated as follows. At RI Beam factory, RI beam will be produced through a projectile fragment process with primary heavy ion beams of 150–400 MeV/u from SRC, and will be momentum- and charge state-separated by the Big-RIPS. The production rates of RI beams are calculated with the code INTENSITY2 assuming the acceptance of the Big-RIPS as 10 mrad in angle and 1% in momentum. The primary beam and the thickness of the Be production target are optimized so as to obtain the maximum production rate. In the calculation, the intensity of the primary beam is assumed to be 100 particle μA .

RI beams separated by the Big-RIPS will be then stored in the Accumulator and Cooler Ring (ACR) of MUSES with the method of combination of multi-turn injection and RF stacking. Momentum cooling will be continuously applied to the stacked beam during the RF stacking process. The maximum intensity of the accumulated RI beam in the ACR is determined by the balance of intrinsic life time of RI beams and the injection rate. Since we will take the time interval of

the injection as the same as the momentum cooling time, the cooling time should be as short as possible to get the maximum intensity of stored beam.

Both of the electron cooling and the stochastic cooling were studied for the momentum cooling method. As a result, it is turned out that the stochastic cooling is always much faster than the electron cooling for the present case. The cooling time of the longitudinal stochastic cooling is calculated with the equation presented in Ref. 1.

The accumulated RI beam will be fast extracted from the ACR and injected into the Booster Synchrotron Ring (BSR) of MUSES. In the BSR, the beams will be accelerated to the energy required for the experiment within 0.5 sec, and then will be injected into the one ring of the DSR to collide with electrons stored in another ring. Since the RI beams are bunched by 30 pulses in the DSR, the maximum number of unstable nuclei in a bunch is obtained by dividing the maximum stored intensity in the ACR by the 30.

In Fig. 1, the calculated luminosity is plotted for various nuclei in an N-Z plane. Also shown in the Fig. 1 are the equi-life time lines. As seen, the luminosity $L \geq 10^{27}$ cm²/s, which is the minimum luminosity required to measure the charge distribution, is obtained for nuclei whose live times are longer than about 1 min.

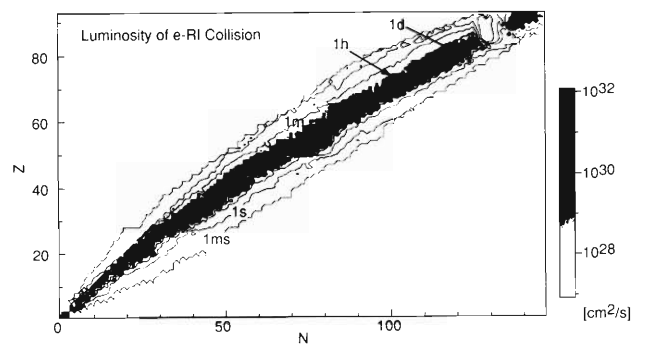


Fig. 1. The luminosity for the head-on collision of electrons and unstable nuclei in DSR.

References

- 1) T. Katayama and N. Tokuda: *Particle Accelerators*, **21** 99 (1987).

An Undulator and the Photon Flux at MUSES

M. Wakasugi, N. Inabe, and T. Katayama

Double storage rings (DSR) are planned to be constructed as the experimental tool in the MUSES which are proposed for the RI beam factory program.¹⁾ It can store not only an RI beam but also an electron beam. We have proposed the isotope shift measurement in atomic transitions of highly charged ion beams using the DSR to obtain systematically the mean square charge radii of radioactive isotopes far from a stability line which are produced with a projectile fragment separator (Big RIPS). The synchrotron radiation from one of the DSR in which the electron beam is stored with the energy of $E_e = 0.3\text{--}2.5$ GeV, is used to excite D1 and D2 transitions in a Li-like ion of a radioactive isotope which is stored in the other.

An undulator is designed to be inserted in the electron storage ring as a source of the radiation to make intense and narrow band X ray. The energy range of the X ray is from 30 to 2000 eV with the first harmonic radiation. The energy range was chosen to excite D1 and D2 transitions in Li-like ions with $Z > 40$. The energy resolution of the X ray is required to be $\Delta E_X/E_X < 2 \times 10^{-4}$ in the case of U^{89+} ($E_{D1} = 286$ eV) to resolve the isotope shift, and the photon flux of more than 10^{12} photons/s is required. The lattice of the DSR was also designed so as to make the emittance of electron beam as low as possible,²⁾ because the quality of the X ray from the undulator depends strongly on the emittance of electron beam in the DSR.

Parameters of the electron beam with an energy of $E_e = 2.5$ GeV in the DSR are shown in Table 1. There are short straight sections with 6.5 m in length close to the colliding section in the DSR for insertion of the undulator.²⁾ The values of the betatron function in both x and y directions are about 5 m and they are nearly constant in this section. The natural emittance

ϵ is made lower by adopting a double bend achromat lattice. The momentum compaction factor α and the dispersion η are nearly zero in this section. This means that a change of the envelope of the electron beam is quite small in the undulator. The size of the electron beam is about $120 \times 200 \mu\text{m}^2$.

Parameters of the undulator designed here are shown in Table 2. The X ray energy has to be tunable continuously to make a high resolution isotope shift measurement. This is realized with the tunability of the K value by changing the pole gap with a step of less than $5 \mu\text{m}$. The undulator should be of the in-vacuum type because the pole gap is too narrow to insert a vacuum chamber; the gap is changed from 1 to 3 cm which corresponds to the K values of from 2.0 to 0.3.

Table 2. Parameters of the undulator.

Length (m)	6.0
Length of one period (cm)	3.0
Number of periods	200
K value	0.3–2.0
Magnetic field at the pole tip (T)	1.3
Photon energy at $E_e = 1.0$ GeV, K = 1 (eV)	210.7
Photon flux at $E_e = 1.0$ GeV, K = 1 (photons/s mrad ² 0.1% b.w.)	8.6×10^{17}

The calculated photon flux (photons/s mrad² 0.1% b.w.) on the beam axis is shown in Fig. 1 for the cases of the electron beam energies of 1.0, 1.5, 2.0, and 2.5 GeV. In this calculation the electron beam current is taken to be 500 mA and the K value is fixed to unity. The maximum X ray energy of 2000 eV required here can be obtained with the smallest K value and the 2.5

Table 1. Parameters of the stored electron beam with $E_e = 2.5$ GeV.

Max. beam energy (GeV)	2.5
Max. beam current (A)	0.5
Max. stored number of electron	2.7×10^{12}
Beam emittance (ϵ_x/ϵ_y) (nmrad)	8.54/25.5
Energy spread ($\Delta E_e/E_e$)	6.84×10^{-4}
Bunch length (cm)	0.5
RF voltage (MV)	2.0
RF frequency (MHz)	498.2
Revolution frequency (MHz)	1.159
Harmonic number	430
Number of bunch (typical)	23
Touschek lifetime (s)	4.55×10^4
Synchrotron radiation loss (keV/turn)	371.7

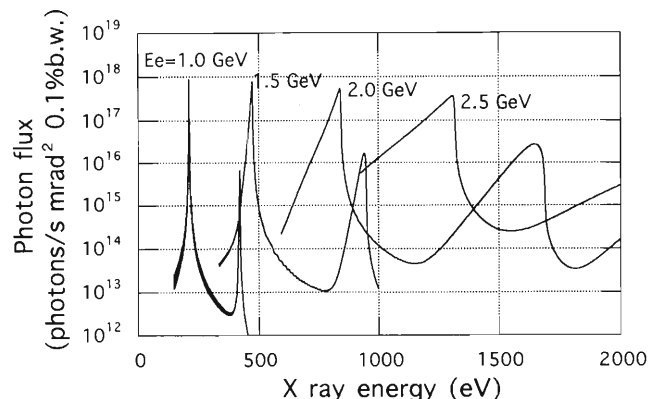


Fig. 1. Calculated photon fluxes on the beam axis from the undulator.

GeV electron energy. The flux can be reached to about 10^{18} photons/s mrad² 0.1% b.w. at the electron energy of $E_e = 1.0$ GeV and $K = 1$. The photon flux of about 10^{18} can be kept in the energy range of 100–2000 eV by adjusting the K value and the electron energy. The maximum photon flux is obtained at the electron energy of 1.2 GeV with fixed K value.

The X ray monochromized with an X ray spectrometer is used for the isotope shift measurement. The monochromization reduces the X ray yield to be 10% and the transmission efficiency of the monochrometer is assumed to be 1.0%. Then the effective photon flux, which has the required energy resolution for the isotope shift measurement, at the colliding point becomes

about 10^{12} photons/s if the spectrometer has an angular acceptance of 0.1 mrad. The required photon flux of 10^{12} photons/s is found to be satisfied from this calculation.

Energy loss of the electron due to the undulator is less than 2 keV at $0.5 \text{ GeV} < E_e < 2.5 \text{ GeV}$ and at $0.3 < K < 2.0$. The tune shift of the electron beam is $\Delta Q < 0.1$ in the same ranges of the electron energies and K values. These give no serious problem to the electron beam in the DSR.

References

- 1) T. Katayama: This report, p. 238.
- 2) N. Inabe et al.: This report, p. 248.

VI. RADIATION MONITORING

Leakage Radiation Measurements in the Ring Cyclotron Facility

S. Fujita, N. Nakanishi, S. Nakajima, M. Watanabe,* H. Ohishi,*
Y. Uwamino, and T. T. Inamura

The measurements of leakage radiation were carried out with five kinds of beams: 110, 113, and 135-MeV proton, 135-MeV/nucleon ^{14}N and 100-MeV/nucleon ^{18}O . The beam intensities were about 200 pA for protons, 20 pA for ^{14}N , and 10 pA for ^{18}O . The beams were stopped at an iron target in the beam distribution corridor.

Leakage radiation of neutrons from the corridor was measured with four neutron dose rate meters, TPS-451S's (Aloka). The beam current at the target was

read with a current integrator (ORTEC 439) and recorded with a personal computer. Figures 1(a), (b), and (c) show the target point and positions where leakage radiation was measured. The positions, 1Fc and B2c, are on the first floor and 2nd basement floor just right upper and under the target point, respectively. Leakage of neutrons was also detected at the several points outside of the building. Results are summarized in Table 1. Dose rates were normalized with respect to the beam intensity of $1 \mu\text{A}$.

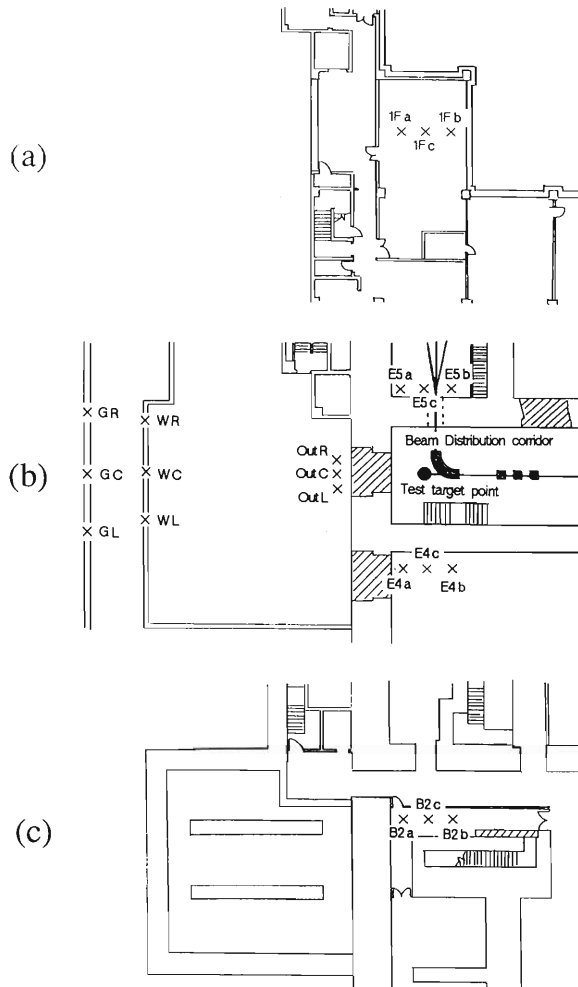


Fig. 1. Partial layout of the RIKEN Ring Cyclotron facility where the leakage radiation measurement was made. (a) Part of the 2nd basement floor; (b) Part of the 1st basement floor; (c) Part of the 1st floor. The target point is denoted by a closed circle. Leakage-radiation-dose measuring points are denoted by x.

* Faculty of Science and Technology, Chuo University

Table 1. Dose rates of neutron leakage radiation from a target placed in the beam distribution corridor. (see Figs. 1(a),(b),(c)). The unit of energy is MeV/nucleon. The notations of 1Fa - GL stand for measured positions shown in Fig. 1. The unit of dose rate is ($\mu\text{Sv/h}$)/($\text{p}\mu\text{A}$).

Measured date	Feb. 11, '95	Mar. 1, '95	Mar. 15, '95	Apr. 25, '95	June 28, '95
Accelerated particle	P	$^{14}\text{N}^{7+}$	$^{18}\text{O}^{8+}$	P	P
Energy	135	135	100	113	110
Position	Dose rate	Dose rate	Dose rate	Dose rate	Dose rate
1F a	7.43E-02	3.22E+00	1.61E+00	4.96E-02	2.05E-02
1F c	5.95E-02	1.56E+00	9.96E-01	4.01E-02	1.26E-02
1F b	1.90E-02	7.60E-01	1.02E+00	4.88E-02	1.86E-02
E5 a	2.44E+01	3.09E+02	1.38E+02	1.67E+01	1.95E+00
E5 c	1.57E+01	1.88E+02	1.60E+02	2.85E+01	3.35E+00
E5 b	5.43E+01	2.01E+02	2.04E+02	6.07E+01	1.71E+01
E4 a	7.50E+00	1.25E+02	5.70E+01	5.73E+00	2.32E+00
E4 c	4.14E+00	7.83E+01	4.52E+01	4.38E+00	1.45E+00
E4 b	1.57E+00	2.68E+01	3.21E+01	3.66E+00	4.28E-01
B2 a	1.93E+01	2.20E+02	1.35E+02	1.08E+01	7.00E+00
B2 c	1.30E+01	2.09E+02	1.33E+02	9.40E+00	4.94E+00
B2 b	7.00E+00	9.79E+01	9.37E+01	1.04E+01	4.17E+00
Out R	1.88E+01	1.16E+03	5.14E+02	4.86E+00	3.88E+00
Out C	2.37E+01	1.51E+03	6.65E+02	6.13E+00	4.98E+00
Out L	1.85E+01	1.12E+03	5.17E+02	4.94E+00	3.80E+00
WR	8.42E-01	4.48E+01	2.09E+01	3.45E-01	1.64E-01
WC	8.56E-01	4.85E+01	2.20E+01	3.54E-01	1.63E-01
WL	6.83E-01	3.73E+01	2.11E+01	3.34E-01	1.47E-01
GR	4.31E-01	2.21E+01	1.20E+01	1.59E-01	8.88E-02
GC	4.92E-01	3.08E+01	1.16E+01	2.08E-01	4.66E-01
GL	4.61E-01	2.53E+01	1.19E+01	2.05E-01	1.07E-01

Dose Rates Due to Residual Activities in the Ring Cyclotron Facility

S. Fujita, M. Watanabe,* H. Ohishi,* N. Nakanishi, Y. Uwamino, and T. T. Inamura

Dose rates due to residual radioactivities were measured at various points in the Ring Cyclotron facility. In the following we describe significant dose rates observed in the measurements.

The routine overhaul started just after the last beam time of the spring term, which was carried out with an $^{12}\text{C}^{6+}$ beam of 135 MeV/nucleon in the E6 experimental vault from Aug. 3 to 4. The dose rates in the Ring Cyclotron and the injector AVF cyclotron were measured on Aug. 23 and 24, during the overhaul period. The measured data of the Ring Cyclotron are shown in Fig. 1. Dose rates in the AVF cyclotron were

denote the places where the dose rates exceeded 50 $\mu\text{Sv/h}$. Table 1 summarizes the observed dose rates with the dates on which the measurements were performed. The maximum dose rate was found to be 11000 $\mu\text{Sv/h}$ at the target chamber, denoted by the point P in Fig. 3.

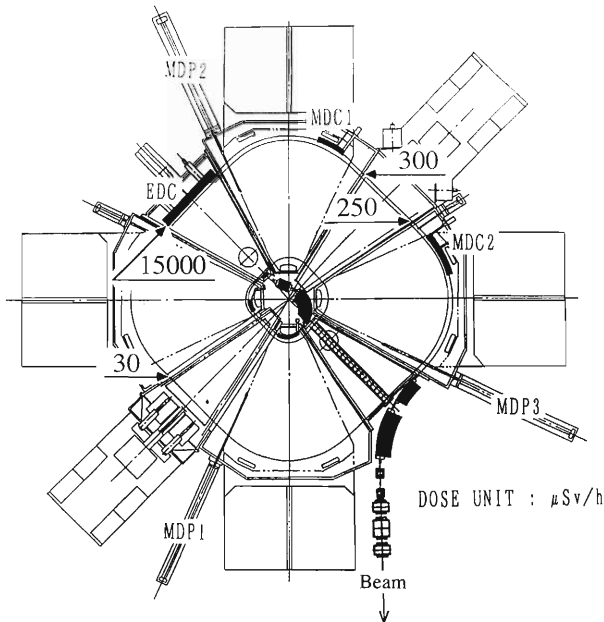


Fig. 1. Detection points around the RIKEN Ring Cyclotron: EDC, the electrostatic deflection channel; MDC1, the magnetic deflection channel 1; MDC2, the magnetic deflection channel 2; MDP1, the main differential probe 1; MDP2, the main differential probe 2; MDP3, the main differential probe 3. Indicated numerals are dose rates in units of $\mu\text{Sv/h}$.

also measured when its acceleration chamber was opened on May 29 because of a vacuum trouble. All the data are shown in Fig. 2.

In the period from Oct. 1, 1994 to Sept. 30, 1995, dose rates were measured along the beam lines after almost every beam time. The points a-t in Fig. 3

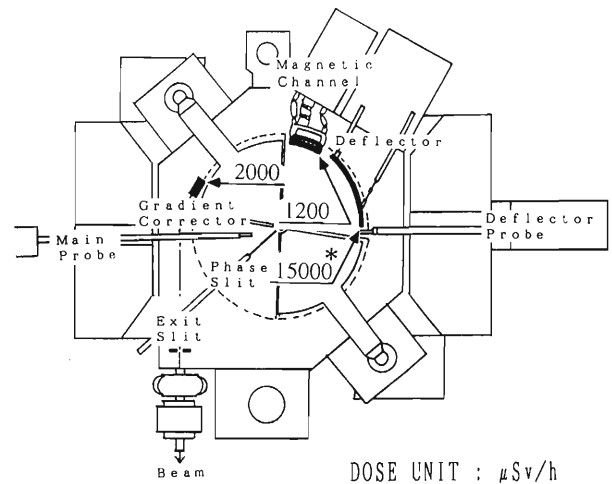


Fig. 2. Dose rates measured in the injector AVF cyclotron. They are given in units of $\mu\text{Sv/h}$; * indicates the data measured on May 29.

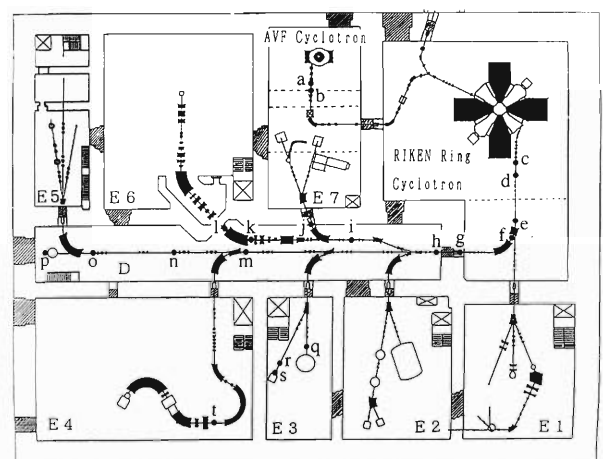


Fig. 3. Layout of the RIKEN Ring Cyclotron facility. Detection points of residual activities along the beam lines are denoted by a-t.

* Faculty of Science and Technology, Chuo University

Table 1. Summary of the dose rates measured along the beam lines with ionization-chamber survey meters. The points a-t indicate the detection points shown in Fig. 3.

Detection point	Measured dose rate ($\mu\text{Sv/h}$)	Date	Detection point	Measured dose rate ($\mu\text{Sv/h}$)	Date
a	1200	May 29, '95	k	2500	July 28, '95
b	300	Apr. 3, '95	l	300	Oct. 26, '94
c	400	Oct. 31, '94	m	140	Aug. 9, '95
d	230	Aug. 11, '95	n	50	June 7, '95
e	70	Oct. 31, '94	o	60	Oct. 26, '94
f	90	Aug. 11, '95	p	11000	Oct. 26, '94
g	50	May 2, '95	q	200	Mar. 23, '95
h	750	July 11, '95	r	800	June 12, '95
i	650	Oct. 26, '94	s	750	June 12, '95
j	300	Oct. 26, '94	t	70	July 21, '95

Routine Works for Radiation Safety in the Ring Cyclotron Facility

S. Fujita, N. Nakanishi, M. Watanabe,* H. Ohishi,* Y. Uwamino, and T. T. Inamura

The radiation safety control system has worked steadily this year, so as to enable us to make radiation monitoring continuously and automatically.

Figures 1(a), (b), and (c) show the trend graphs of

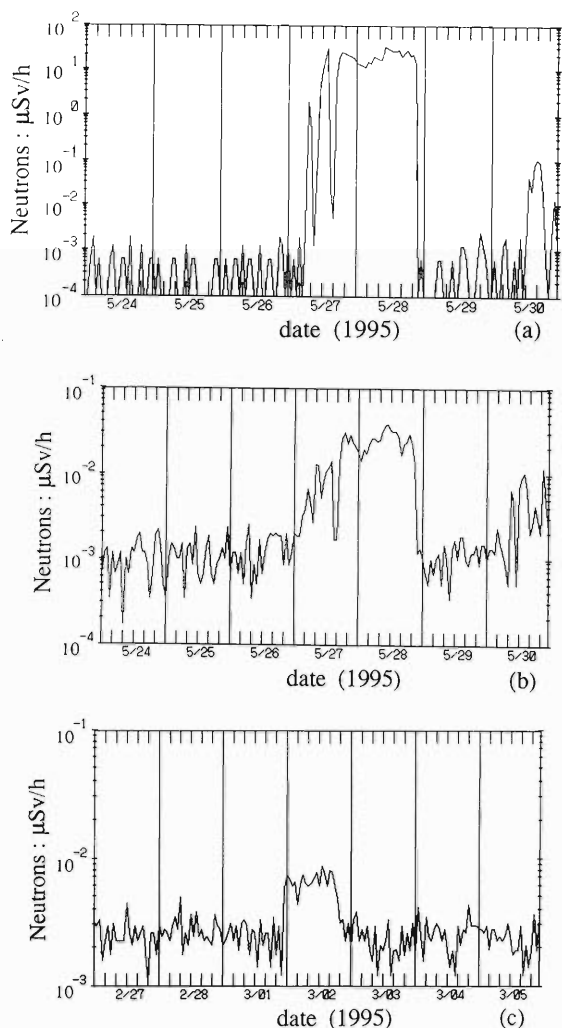


Fig. 1. Daily variation in the radiation level detected at the RIKEN Ring Cyclotron facility. Detectors are (a) a BF_3 counter in the experimental vault E4 of the controlled area, (b) a ^3He counter in the computer room, boundary of the controlled area, and (c) a ^3He counter at the boundary of the site.

neutron-radiation level during several days around the time when the maximum levels of this year were recorded at the three positions: E4 room in the controlled area, the computer room at the boundary of the controlled area, and outside at the boundary of the RIKEN site. Those radiation levels, however, are far less than the required safety limits for the controlled area (1 mSv/week), for the boundary of the controlled area (0.3 mSv/week), and for the boundary of the site (50 $\mu\text{Sv}/\text{year}$).

In this summer, all alarm lamps in each room inside the controlled area were changed to new ones, which show the same information as the radiation level indicators¹⁾ at the entrance of each room. Figure 2 shows the photograph of new lamps with neutron and γ -ray detectors.

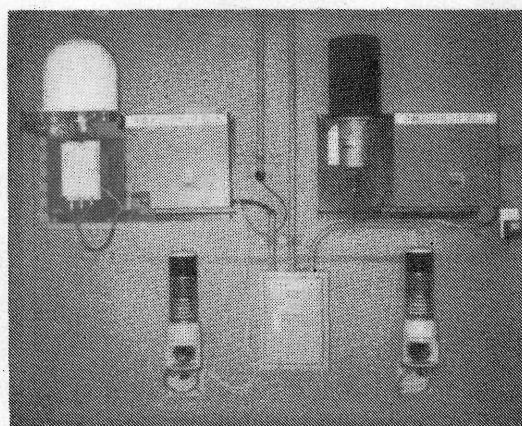


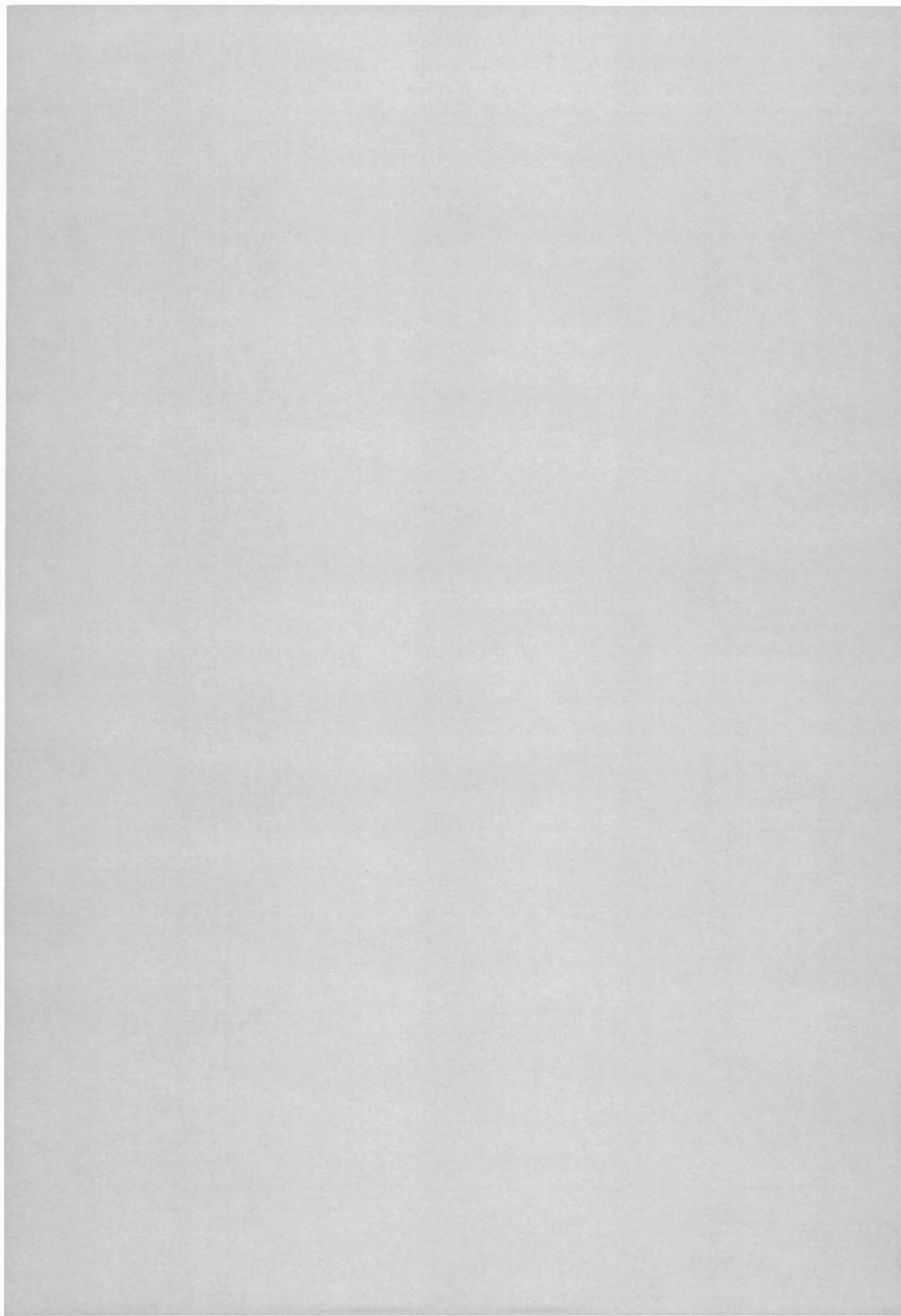
Fig. 2. The photograph of new lamps with neutron and γ -ray detectors.

We installed a new hand-foot-cloth monitor in front of the AVF cyclotron vault, in order to prevent contamination around the cyclotron from spreading to other places in the controlled area.

References

- 1) I. Sakamoto, S. Fujita, T. Wada, and H. Takebe: *RIKEN Accel. Prog. Rep.*, **20**, 206 (1986).

* Faculty of Science and Technology, Chuo University



VII. LIST OF PUBLICATIONS

1. Accelerator development and accelerator physics

T. Nakagawa, T. Kageyama, M. Kase, A. Goto, and Y. Yano: "Effect of Plasma-Cathode Method on Production of Highly Charged Ions from Oxide in RIKEN 10-GHz Electron-Cyclotron-Resonance Ion Source", *Jpn. J. Appl. Phys.*, **34**, 2463 (1995).

O. Kamigaito, A. Goto, Y. Miyazawa, T. Chiba, M. Hemmi, M. Kase, S. Kohara, and Y. Yano: "Improvement of Frequency Variability of the Folded-Coaxial Radio-Frequency Quadrupole Linac by Installing a Detachable Stem in Its Resonator", *ibid.*, pp. 5799–5800.

Y. Batygin, V. Kushin, and S. Plotnikov: "Uniform Target Irradiation by Circular Beam Sweeping", *Nucl. Instrum. Methods Phys. Res.*, **A363**, 128–130 (1995).

N. Nakanishi, T. Shikata, S. Fujita, and T. Kosako: "Calculated Shielding Characteristics of Eight Materials for Neutrons and Secondary Photons Produced by Monoenergetic Source Neutrons with Energies Less Than 400 MeV", *Nucl. Technol.*, **112**, 132–141 (1995).

Y. Batygin: "Nonlinear Potential Distribution for High Current Beam Transport without Emittance Growth", Proc. 17th Int. Linac Conf. (LINAC 94), Tsukuba, K. Takara et al. (eds.), Vol. 1, pp. 487–489 (1994).

Y. Batygin: "Density Uniforming of Large Momentum Spread Beam", *ibid.*, pp. 490–492.

O. Kamigaito, A. Goto, Y. Miyazawa, T. Chiba, M. Hemmi, S. Kohara, M. Kase, and Y. Yano: "Design of a New Type of Variable-Frequency RFQ Linac with a Folded-Coaxial Resonator", *ibid.*, pp. 701–703.

M. Niimura, T. Kageyama, T. Nakagawa, A. Goto, and Y. Yano: "Physics for ECRIS Beam-Current Upgrading Technologies Such as Electron Beam Injection, Wall Coating, and Gas Mixing", Proc. 12th Int. Workshop on ECR Ion Sources, M. Sekiguchi and T. Nakagawa (eds.), No. INS-J-182, pp. 141–147 (1995).

M. Niimura, H. Amemiya, A. Goto, and Y. Yano: "Averaged Excitation Rate Coefficient Calculation of HeI Up to $T_e = 1000$ eV and Plasma Potential Measurement Up to ECR-Heated Ellipsoid", *ibid.*, pp. 307–311.

T. Nakagawa, T. Kageyama, M. Kase, A. Goto, and Y. Yano: "Production of Highly Charged Ions from Oxide in RIKEN 10 GHz ECRIS", *ibid.*, pp. 314–316.

Y. Batygin, A. Goto, and Y. Yano: "Nonlinear Effect of Einzel Lens to the Beam Extracted from ECR Source", *ibid.*, pp. 317–320.

Y. Batygin: "Conservation of High Current Beam Emittance in Nonlinear Focusing Field", Proc. Int. Workshop on Particle Dynamics in Accelerators, S. Machida and K. Hirata (eds.), KEK Proc., No. 95–7, pp. 88–96 (1995).

O. Kamigaito, A. Goto, Y. Miyazawa, T. Chiba, M. Hemmi, S. Kohara, M. Kase, Y. Batygin, and Y. Yano: "Development of a Variable-Frequency RFQ Linac for the RILAC", Proc. 20th Linear Accelerator Meet. in Japan, Osaka, pp. 82–85 (1995).

T. Kubo, H. Okuno, K. Ikegami, T. Kawaguchi, T. Tominaka, T. Mitsumoto, S. Fujishima, A. Goto, and Y. Yano: "RI-beam Factory Project (I) — Superconducting Ring Cyclotron —", Proc. 54th Meet. on Cryogenics and Superconductivity, Nov., Akita, p. 62 (1995).

T. Kawaguchi, T. Mitsumoto, T. Kubo, T. Tominaka, H. Okuno, Y. Tanaka, S. Fujishima, K. Ikegami, A. Goto, and Y. Yano: "RI Beam Factory Project (II) — Superconducting Sector Magnet —", *ibid.*, p. 63.

T. Tominaka, H. Okuno, Y. Tanaka, T. Kubo, T. Mitsumoto, T. Kawaguchi, S. Fujishima, K. Ikegami, A. Goto, and Y. Yano: "RI Beam Factory Project (III) — Beam Injection and Extraction Systems —", *ibid.*, p. 64.

M. Kase, N. Inabe, A. Goto, T. Kageyama, I. Yokoyama, M. Nagase, S. Kohara, T. Nakagawa, K. Ikegami, O. Kamigaito, J. Fujita, and Y. Yano: "The Operation of RIKEN Ring Cyclotron", Proc. 10th Symp. on Accelerator Science and Technology, JAERI Conf., Oct., 1995, Hitachinaka, pp. 23–25 (1995).

T. Mitsumoto, A. Goto, T. Kawaguchi, Y. Tanaka, T. Kubo, H. Okuno, T. Tominaka, S. Fujishima, and Y. Yano: "Design Study of Sector Magnet for the RIKEN Superconducting Ring Cyclotron (I)", *ibid.*, pp. 124–126.

T. Kawaguchi, T. Kubo, T. Mitsumoto, T. Tominaka, S. Fujishima, H. Okuno, Y. Tanaka, K. Ikegami, A. Goto, and Y. Yano: "Design Study of Sector Magnet for the RIKEN Superconducting Ring Cyclotron (II)", *ibid.*, pp. 127–129.

N. Inabe, M. Kase, I. Yokoyama, A. Goto, and Y. Yano: "Development of a Single-Bunch Selector for RIKEN Ring Cyclotron", *ibid.*, pp. 165–167.

A. Goto, Y. Miyazawa, M. Hemmi, O. Kamigaito, T. Nakagawa, M. Kase, T. Chiba, N. Inabe, S. Kohara, T. Kageyama, Y. Batygin, and Y. Yano: "Construction of a New Pre-injector System for the RILAC", *ibid.*, pp. 188–190.

T. Nakagawa, Y. Miyazawa, M. Hemmi, T. Chiba, N. Inabe, M. Kase, T. Kageyama, O. Kamigaito, E. Ikezawa, A. Goto, and Y. Yano: "Development of RIKEN 18 GHz ECRIS", *ibid.*, pp. 224–226.

O. Kamigaito, A. Goto, Y. Miyazawa, T. Chiba, M. Hemmi, S. Kohara, M. Kase, Y. Batygin, and Y.

- Yano: "Development of a Variable-Frequency RFQ Linac for the RILAC", *ibid.*, pp. 236–238.
- M. Takanaka and T. Katayama: "Beam Current Limitations Due to Single-Beam Collective Effects in the Ion Storage Ring of RIKEN RI Beam Factory Project", *ibid.*, pp. 318–320.
- Y. Batygin, A. Goto, and Y. Yano: "Hollow Beam Formation in the Extraction Region of ECRIS", *ibid.*, pp. 353–355.
- Y. Batygin and T. Katayama: "Study of Incoherent Beam-Beam Effects at Radioactive Isotope Beam Factory", *ibid.*, pp. 356–358.
- Y. Batygin, A. Goto, O. Kamigaito, and Y. Yano: "Effect of Field Variation on Beam Parameters in RIKEN RFQ Linac", *ibid.*, pp. 359–361.
- N. Nakanishi, T. Shikata, S. Fujita, and T. Kosako: "Comparison of Calculated Shielding Effects for 8 Materials", *ibid.*, pp. 362–364.
- Y. Yano, A. Goto, T. Katayama, and RIBF Group: "RIKEN RI Beam Factory Project", *ibid.*, pp. 457–459.
- M. Niimura, T. Nakagawa, A. Goto, and Y. Yano: "Next-Step ECRIS and 2 m Length 4.52 GeV Advanced Accelerator: Novel Extraction of Trapped Ions and their Acceleration-Final Focusing by Non-neutral and Neutral Plasmas", *ibid.*, pp. 466–468.
- Y. Yano: "RIKEN Accelerator Research Facility (RARF), Its New Project 'RI Beam Factory', and Other Major Heavy-Ion Accelerator Facilities in Japan", Proc. Simposio Nipo-Brasileiro de Ciencia e Tecnologia, Brazil, pp. 194–202 (1995).
- ## 2. Nuclear physics and nuclear instrumentation
- S. Ishida, S. Fujita, Y. Hara, K. Hatanaka, T. Ichihara, K. Katoh, T. Niizeki, H. Okamura, H. Otsu, H. Sakai, N. Sakamoto, Y. Satou, T. Uesaka, T. Wakasa, and T. Yamashita: "Construction of the Deuteron POLarimeter DPOL at RIKEN", *AIP Conf. Proc.*, **343**, 182–186 (1995).
- K. Sumiyoshi, H. Suzuki, and H. Toki: "Influence of the Symmetry Energy on the Birth of Neutron Stars and Supernova Neutrinos", *Astron. Astrophys.*, **303**, 475–482 (1995).
- Y. Mochizuki and T. Izuyama: "Self-Trapping of Superfluid Vortices and the Origin of Pulsar Glitches", *Astrophys. J.*, **440**, 263–269 (1995).
- A. A. Korshennikov, M. V. Zhukov, M. Smedberg, and T. Kobayashi: "Neutron Momentum Distributions from Fragmentation of the Exotic Nucleus ${}^8\text{He}$ ", *Europhys. Lett.*, **29**, 359–364 (1995).
- S. A. Goncharov and A. A. Korshennikov: "Theoretical Analysis of Elastic and Inelastic Scattering ${}^8\text{He} + p$ at $E = 72 \text{ MeV/u}$ ", *ibid.*, **30**, 13–18 (1995).
- T. Kohno, A. A. Gusev, I. M. Martin, and G. I. Pugacheva: "The Trapped He Flux Dynamics Observed on the OHZORA Satellite during 1984–1987", *Geophys. Res. Lett.*, **22**, 877–880 (1995).
- M. Kurokawa, T. Motobayashi, K. Ieki, S. Shimoura, H. Murakami, Y. Ikeda, S. Moriya, Y. Yanagisawa, and T. Nomura: "Radiation Damage Factor for Ion-Implanted Silicon Detectors Irradiated with Heavy Ions", *IEEE Trans. Nucl. Sci.*, **42**, 163–166 (1995).
- S. Daté, K. Kumagai, O. Miyamura, H. Sumiyoshi, and X.-Z. Zhang: "A Study of Collision Frequency and Particle Density in Ultrarelativistic Nuclear Collisions by an Event Generator URASIMA", *J. Phys. Soc. Jpn.*, **64**, 766–776 (1995).
- K. Kitao: "A = 118 Update", *Nucl. Data Sheets*, **75**, 99–198 (1995).
- N. Nakao, T. Nakamura, M. Baba, Y. Uwamino, N. Nakanishi, H. Nakashima, and Sh. Tanaka: "Measurements of Response Function of Organic Liquid Scintillator for Neutron Energy Range Up to 135 MeV", *Nucl. Instrum. Methods Phys. Res.*, **A362**, 454–465 (1995).
- A. Warczak, and 13 others including T. Suzuki: "Radiative Double Electron Capture in Heavy-Ion Atom Collisions", *ibid.*, **B98**, 303–306 (1995).
- T. Ichihara, M. Ishihara, H. Ohnuma, T. Niizeki, T. Yamamoto, K. Katoh, T. Yamashita, Y. Hara, Y. Fuchi, S. Kubono, M. H. Tanaka, H. Okamura, S. Ishida, T. Uesaka, and Y. Satou: "Spin-Flip and Non-Spin-Flip Isovector Excitations Observed in the (${}^{12}\text{C}, {}^{12}\text{N}$) Reactions at $E/A = 135 \text{ MeV}$ and the (${}^{13}\text{C}, {}^{13}\text{N}$) Reactions at $E/A = 100 \text{ MeV}$ ", *Nucl. Phys.*, **A583**, 109c–114c (1995).
- T. Nakagawa, K. Yuasa-Nakagawa, K. Furutaka, K. Matsuda, K. Yoshida, Y. Futami, T. Mizota, Y. Honjo, S. Tomita, S. M. Lee, J. Kasagi, and W. Q. Shen: "Study of Pre-scission Evaporation for ${}^{84}\text{Kr} + {}^{27}\text{Al}$ at 10.6 MeV/u Using 3π -Phoswich Detector System", *ibid.*, 149c–152c.
- J. Chiba, D. Ashery, H. Ito, K. Kimura, Yu. T. Kiselev, S. Kouda, K. Miyano, T. Murakami, T. Nagae, Y. Nakai, M. Nomachi, H. Ochiishi, S. Sawada, M. Sekimoto, Y. Sugaya, T. Suzuki, K. H. Tanaka, M. K. Vlasov, Y. Yamanoi, K. Yasuda, and Y. Yoshimura: "Subthreshold Antiproton Productions in pA, dA, and α A Reactions", *ibid.*, pp. 633c–636c.
- S. Neumajer and 27 others including T. Suzuki: "Study of Nucleon Density Distribution of ${}^6\text{He}$ and ${}^8\text{He}$ by Proton Elastic Scattering in Inverse Kinematics", *ibid.*, pp. 799c–802c.
- M. V. Zhukov, A. A. Korshennikov, M. H. Smedberg, and T. Kobayashi: "Particle Momentum Distributions for ${}^8\text{He}$ in $\alpha + 4n$ Model", *ibid.*, pp. 803c–806c.
- A. Ozawa, I. Tanihata, T. Kobayashi, D. Hirata, O. Yamakawa, K. Omata, N. Takahashi, T. Shimoda, K. Sugimoto, D. Olson, W. Christie, and H. Wieman: "Interaction Cross Sections and Radii of ${}^{11}\text{C}$ and ${}^{12}\text{N}$ and Effective Deformation Parameters in Light Mirror Nuclei", *ibid.*, pp. 807c–810c.
- L. V. Chulkov, C. A. Bertulani, and A. A. Korshennikov: "Proton Scattering by ${}^8\text{He}$ and Neutron Halo Effects", *ibid.*, **A587**, 291–300 (1995).

- A. A. Korshennikov, D. V. Aleksandrov, N. Aoi, Y. Doki, N. Inabe, M. Fujimaki, T. Kobayashi, H. Kumagai, C.-B. Moon, E. Yu. Nikolskii, M. M. Obuti, A. A. Ogloblin, A. Ozawa, S. Shimoura, T. Suzuki, I. Tanihata, Y. Watanabe, M. Yanokura, and K. Yoshida: "Experimental Studies of Light Neutron Rich Nuclei", *ibid.*, **A588**, 23c–28c (1995).
- Y. Ogawa, Y. Suzuki, and K. Yabana: "Transverse Momentum Distributions of a ${}^9\text{Li}$ Fragment in the (${}^{11}\text{Li}$, ${}^9\text{Li}$) Reaction and Neutron Correlations", *ibid.*, pp. 77c–80c.
- A. Yoshida, N. Aoi, T. Fukuda, M. Hirai, M. Ishihara, H. Kobinata, Y. Mizoi, L. Mueller, Y. Nagashima, J. Nakano, T. Nomura, Y. H. Pu, F. Scarlassala, C. Signorini, and Y. Watanabe: "Measurement of Fusion Cross Section with Neutron Halo Nuclei", *ibid.*, pp. 109c–112c.
- W. von Oertzen, H. G. Bohlen, B. Gebauer, M. von Lucke-Petsch, A. N. Ostrovski, Ch. Seyfert, Th. Stolla, M. Wilpert, Th. Wilpert, D. V. Alexandrov, A. A. Korshennikov, I. Mukha, A. A. Ogloblin, R. Kalpakchieva, Y. E. Penionzhkevich, S. Piskor, S. M. Grimes, and T. N. Massey: "Nuclear Structure Studies of Very Neutron-Rich Isotopes of ${}^7\text{--}{}^{10}\text{He}$, ${}^9\text{--}{}^{11}\text{Li}$, and ${}^{12}\text{--}{}^{14}\text{Be}$ via Two-Body Reactions", *ibid.*, pp. 129c–134c.
- K. Asahi, H. Ueno, H. Izumi, H. Okuno, K. Nagata, H. Ogawa, Y. Hori, H. Sato, K. Mochinaga, M. Adachi, A. Yoshida, G. Liu, N. Aoi, T. Kubo, M. Ishihara, W.-D. Schmidt-Ott, T. Shimoda, H. Miyatake, S. Mitsuoka, and N. Takahashi: "Electromagnetic Moments of Unstable Nuclei Studied with Polarized Projectile Fragments", *ibid.*, pp. 135c–140c.
- M. Tohyama: " $E1$ and $E2$ Giant Resonance in ${}^{22}\text{O}$ ", *ibid.*, pp. 141c–146c.
- K. Matsuta, M. Fukuda, M. Tanigaki, T. Minamisono, Y. Nojiri, M. Mihara, T. Onishi, T. Yamaguchi, A. Harada, M. Sasaki, T. Miyake, S. Fukuda, K. Yoshida, A. Ozawa, T. Kobayashi, I. Tanihata, J. R. Alonso, G. F. Krebs, and T. J. M. Symons: "Magnetic Moment of Proton Drip-Line Nucleus ${}^9\text{C}$ ", *ibid.*, pp. 153c–156c.
- Y. Gono, T. Morikawa, T. Kishida, K. Moita, A. Odahara, E. Ideguchi, T. Murakami, M. Oshima, M. Sugawara, H. Kusakari, H. Kumagai, H. Tsuchida, M. Ogawa, M. Kidera, M. Shibata, K. Miyazaki, S. Mitarai, Y. H. Zhang, A. Ferragut, G. H. Liu, Y. Hatsukawa, J. C. Kim, S. A. Shin, and M. Ishihara: "Gamma-Ray Spectroscopy with High-Spin Isomer Beam", *ibid.*, pp. 241c–246c.
- H. Toki, D. Hirata, Y. Sugahara, K. Sumiyoshi, and I. Tanihata: "Relativistic Many Body Approach for Unstable Nuclei and Supernova", *ibid.*, pp. 357c–364c.
- A. Ozawa, G. Raimann, R. N. Botd, F. R. Chloupek, M. Fujimaki, K. Kimura, H. Kitagawa, T. Kobayashi, J. J. Kolata, S. Kubono, I. Tanihata, Y. Watanabe, and K. Yoshida: "Study of β -Delayed Neutron Emission of ${}^{19}\text{C}$ ", *ibid.*, **A592**, 244–256 (1995).
- K. Sumiyoshi, K. Oyamatsu, and H. Toki: "Neutron Star Profiles in Relativistic Brueckner-Hartree-Fock Theory", *ibid.*, **A595**, 327–345 (1995).
- T. Kandler, and 16 others including T. Suzuki: "Transition Selective Investigation of the Resonant Transfer and Excitation in $\text{U}^{90+} \rightarrow \text{C}$ Collisions", *Phys. Lett.*, **A204**, 274–280 (1995).
- X. Gu, R. N. Boyd, M. M. Farrell, J. D. Kalen, C. A. Mitchell, J. J. Kolata, M. Belbot, K. Lamkin, K. Ashktrab, F. D. Becchetti, J. Brown, D. Roberts, K. Kimura, I. Tanihata, K. Yoshida, and M. S. Islam: "The ${}^8\text{Li}(\alpha, n){}^{11}\text{B}$ Reaction and Primordial Nucleosynthesis", *ibid.*, **B343**, 31–35 (1995).
- A. A. Korshennikov, E. Yu. Nikolskii, T. Kobayashi, D. V. Aleksandrov, M. Fujimaki, H. Kumagai, A. A. Ogloblin, A. Ozawa, I. Tanihata, Y. Watanabe, and K. Yoshida: "Spectroscopy of ${}^{12}\text{Be}$ and ${}^{13}\text{Be}$ Using ${}^{12}\text{Be}$ Radioactive Beam", *ibid.*, pp. 53–58.
- J. A. Casado and S. Daté: "On the Systematic Behavior of the Chaoticity Parameter in HBT Analyses", *ibid.*, **B344**, 441–446 (1995).
- T. Motobayashi, Y. Ikeda, Y. Ando, K. Ieki, M. Inoue, N. Iwasa, T. Kikuchi, M. Kurokawa, S. Moriya, S. Ogawa, H. Murakami, S. Shimoura, Y. Yanagisawa, T. Nakamura, Y. Watanabe, M. Ishihara, T. Teranishi, H. Okuno, and R. F. Casten: "Large Deformation of the Very Neutron-Rich Nucleus ${}^{32}\text{Mg}$ from Intermediate-Energy Coulomb Excitation", *ibid.*, **B346**, 9–14 (1995).
- S. Shimoura, T. Nakamura, M. Ishihara, N. Inabe, T. Kobayashi, T. Kubo, R. H. Siemssen, I. Tanihata, and Y. Watanabe: "Coulomb Dissociation Reaction and Correlations of Two Halo Neutrons in ${}^{11}\text{Li}$ ", *ibid.*, **B348**, 29–34 (1995).
- T. Morikawa, Y. Gono, K. Morita, T. Kishida, T. Murakami, E. Ideguchi, H. Kumagai, G. H. Liu, A. Ferragut, A. Yoshida, Y. H. Zhang, M. Oshima, M. Sugawara, H. Kusakari, M. Ogawa, M. Nakajima, H. Tsuchida, S. Mitarai, A. Odahara, M. Kidera, M. Shibata, J. C. Kim, S. J. Chae, Y. Hatsukawa, and M. Ishihara: "Coulomb Excitation of ${}^{174}\text{Hf}$ K-Isomer. γ -Ray Spectroscopy with High-Spin Isomer Beam", *ibid.*, **B350**, 169–172 (1995).
- K. Yuasa-Nakagawa, T. Nakagawa, K. Furutaka, K. Matsuda, Y. Futami, K. Yoshida, J. Kasagi, S. M. Lee, T. Suomijärvi, W. Q. Shen, and T. Matsuse: "Entrance Channel Effect on the Pre-scission Time of Binary Decay for the Medium Mass Nuclei (Mass ~ 110)", *ibid.*, **B351**, 77–81 (1995).
- Ch. O. Bacri, B. Borderire, J. L. Charvet, D. Cussol, R. Dayras, O. Lopetz, A. Ouatizerga, M. F. Rivet, G. Auger, A. Bemkirance, J. Benlliure, B. Berthier, R. Bougault, R. Brou, P. Box, Y. Casagnou, A. Chibih, J. Colin, E. De Phillippo, A. Demeyer, D. Durand, P. Ecomard, P. Eudes, A. Genoux-Lubain, D. Gourio, D. Guinet, L. Lakehal-

- Ayat, P. Loutesse, L. J. Laville, L. Leberton, C. Lebrun, J. F. Lecolley, A. LeFevre, R. Legrain, M. Louvel, M. Mahi, M. Marie, V. Metivier, L. Napas, T. Nakagawa, M. Prolog, J. Peter, E. Plagnol, E. Pollacco, A. Rahmani, R. Regimbart, T. Reponseur, E. Rosato, F. Saint-Laurent, M. Sualli, J. C. Steckmeyer, B. Tamain, L. Tassan-Got, E. Vient, C. Volant, J. P. Wieleczko, A. Wieloch, and K. Yuasa-Nakagawa: "Onset of Vaporization for Ar + Ni System", *ibid.*, **B353**, 27–31 (1995).
- H. Okuno, K. Asahi, H. Ueno, H. Izumi, H. Sato, M. Adachi, T. Nakamura, T. Kubo, N. Inabe, A. Yoshida, N. Fukunishi, T. Shimoda, H. Miyatake, N. Takahashi, W.-D. Schmidt-Ott, and M. Ishihara: "Measurement of the Magnetic Moments of ^{14}B and ^{15}B Using Projectile Fragmentation Spin Polarization", *ibid.*, **B354**, 41–45 (1995).
- T. Horibata, M. Oi, and N. Onishi: "Signature Splitting of Tilted-Axis Rotational States", *ibid.*, **B355**, 433–438 (1995).
- T. Suzuki, T. Otsuka, and A. Muta: "Magnetic Moment of ^{11}Be ", *ibid.*, **B364**, 69–74 (1995).
- W. G. Jin, M. Wakasugi, T. T. Inamura, T. Murayama, T. Wakui, H. Katsuragawa, T. Ariga, T. Ishizuka, and I. Sugai: "Laser-rf Double-Resonance Spectroscopy of $^{177,179}\text{Hf}$ ", *Phys. Rev. A*, **52**, 157–164 (1995).
- A. Ono and H. Horiuchi: "Flow of Nucleons and Fragments in $^{40}\text{Ar} + ^{27}\text{Al}$ Collisions Studied with Antisymmetrized Molecular Dynamics", *Phys. Rev. C*, **51**, 299–309 (1995).
- K. Sugawara-Tanabe, A. Arima, and N. Yoshida: "Resurrection of the L-S Coupling Scheme in Superdeformation", *ibid.*, pp. 1809–1818.
- E. Liénard, D. Baye, Th. Delbar, P. Descouvemont, P. Duhamel, W. Galster, M. Kurokawa, P. Leleux, I. Licot, P. Lipnik, C. Michotte, T. Motobayashi, A. Ninane, J. Vanhorenbeeck, and J. Vervier: "Comparative Experimental Study of the Mirror $^{13}\text{N} + ^{12}\text{C}$ and $^{13}\text{C} + ^{12}\text{C}$ Elastic Scatterings", *ibid.*, **52**, 775–783 (1995).
- K. Varga and Y. Suzuki: "Precise Solution of Few-Body Problems with Stochastic Variational Method on Correlated Gaussian Basis", *ibid.*, pp. 2885–2905.
- A. Mengoni, T. Otsuka, and M. Ishihara: "Direct Radiative Capture of p -Wave Neutrons", *ibid.*, pp. R2334–R2338.
- R. A. Kryger, A. Azhari, M. Hellström, J. H. Kelley, T. Kubo, R. Pfaff, E. Ramakrishna, B. M. Sherrill, M. Toennessen, and S. Yokoyama: "Two-Proton Emission from the Ground State of ^{12}O ", *Phys. Rev. Lett.*, **74**, 860–863 (1995).
- T. Suzuki, H. Geissel, O. Bochkarev, L. Chulkov, M. Golovkov, D. Hirata, H. Irnich, Z. Janas, H. Keller, T. Kobayashi, G. Kraus, G. Münzenberg, S. Neumaier, F. Nickel, A. Ozawa, A. Piechaczek, E. Roeckl, W. Schwab, K. Suemmerer, K. Yoshida, and I. Tanihata: "Neutron Skin of Na Isotopes Studied via Their Interaction Cross Sections", *ibid.*, **75**, 3241–3244 (1995).
- H. Irnich and 18 others including T. Suzuki: "Half-Life Measurements of Bare, Mass-Resolved Isomers in a Storage-Cooler Ring", *ibid.*, pp. 4182–4186.
- T. Nakagawa, K. Yuasa-Nakagawa, Y. Futami, K. Furutaka, K. Matsuda, K. Yoshida, T. Mizota, Y. Honjo, S. Tomita, T. Suomijärvi, W. Q. Shen, J. Kasagi, T. Matsuse, and S. M. Lee: "Pre- and Post-scission Charged Particle Multiplicity in Binary Decay Process for Medium Mass Nuclei", Proc. 3rd IN2P3-RIKEN Symp. on Heavy Ion Collisions, T. Motobayashi et al. (eds.), World Scientific, Singapore, pp. 139–147 (1995).
- K. Furutaka, J. Kasagi, K. Yoshida, A. Yajima, Y. Akeboshi, K. Matsuda, T. Murakami, T. Nakagawa, K. Yuasa-Nakagawa, Y. Futami, G. Bizard, and A. Galonsky: "Excitation Energy and Temperature of Hot Nuclei Produced in Incomplete Fusion Reactions", *ibid.*, pp. 180–188.
- A. Ono and H. Horiuchi: "Flow of Nucleons and Fragments Studied with AMD", *ibid.*, pp. 219–228.
- S. Shimoura: "Nuclear Responses of Neutron Drip-Line Nuclei", *ibid.*, pp. 259–268.
- H. Kurasawa and T. Suzuki: "Macroscopic Model of Giant Resonance States in Neutron-Rich Nuclei", *ibid.*, pp. 269–282.
- H. Kurasawa and T. Suzuki: "Quasielastic Electron Scattering", Proc. Korea-Japan Joint Symp. on Recent Development of Nuclear Study Using Electron and Photon Beams, Il-Tong Cheon (ed.), Global Publications Services, Singapore, pp. 39–46 (1995).
- T. Wada: "Dissipative Dynamics of Nuclear Fission", Proc. Tours Symp. on Nuclear Physics II, H. Utsunomiya et al. (eds.), World Scientific, Singapore, pp. 470–479 (1995).
- A. Mengoni, T. Otsuka, and M. Ishihara: "Halo Structure of Nuclear Excited States and the Neutron Radiative Capture Process", Proc. Workshop on Experimental Perspectives with Radioactive Nuclear Beams, Padova, 14–17 Nov., 1994, C. Signorini (ed.), pp. 175–185 (1995).
- M. Tohyama: "Correlated Ground State and $E2$ Giant Resonance Built on It", *Prog. Theor. Phys.*, **94**, L147–L150 (1995).
- S. Takagi, T. Nakamura, T. Kohno, and F. Makino: "Flux Distribution and Modulation of Charged Particles in the Radiation Belt Observed with AKEBONO", *Rep. Institute of Space and Astronautical Science*, **80**, 1–24 (1995).
- T. Kohno, H. Kato, and K. Nagata: "Anomalous and Solar Cosmic Ray Observations with the First Brazilian Scientific Microsatellite", *RIKEN Rev.*, No. 10, pp. 33–34 (1995).
- H. Kurasawa and T. Suzuki: "Effects of Antinucleon-Degrees of Freedom on Quasielastic Electron Scattering", *Soryusiron Kenkyu* (in Japanese), **91**, c61–c65 (1995).

- W. Schwab and 16 others including T. Suzuki: "Observation of a Proton Halo in ^8B ", *Z. Phys.*, **A350**, 283–284 (1995).
- K. Morita, Y. H. Pu, J. Feng, M. G. Hies, K. O. Lee, A. Yoshida, S. C. Jeong, S. Kubono, T. Nomura, Y. Tagaya, M. Wada, M. Kurokawa, T. Motobayashi, H. Ogawa, T. Uchibori, K. Sueki, T. Ishizuka, K. Uchiyama, Y. Fujita, H. Miyatake, T. Shimoda, T. Shinozuka, H. Kudo, Y. Nagai, and S. A. Shin: "New α -decaying Neutron Deficient Isotopes ^{197}Rn and ^{200}Fr ", *ibid.*, **A352**, 7–8 (1995).
- ### 3. Atomic and solid-state physics
- N. Toshima and J. Eichler: "Relativistic Generalizations of Distorted-Wave Capture Theories", *Comm. Atom. Mol. Phys.*, **31**, 109–122 (1995).
- K. Kumagai, K. Kawano, I. Watanabe, K. Nishiyama, and K. Nagamine: " μSR and NMR Investigations on Electronic and Magnetic State around $x = 0.12$ in $\text{La}_{2-x}\text{Ba}_x\text{CuO}_4$ and $\text{La}_{2-x}\text{Sr}_x\text{CuO}_4$ ", *Hyperfine Interact.*, **86**, 473–480 (1994).
- I. Watanabe, K. Nishiyama, K. Nagamine, K. Kawano, and K. Kumagai: "Observation of Magnetic Order of Cu-Moment around $x = 0.12$ in $\text{La}_{2-x}\text{Ba}_x\text{CuO}_4$ and $\text{La}_{2-x}\text{Sr}_x\text{CuO}_4$ by $\mu^+\text{SR}$ ", *ibid.*, pp. 603–608.
- M. Sataka, M. Imai, Y. Yamazaki, K. Komaki, K. Kawatsura, Y. Kanai, K. Tawara, D. R. Schultz, and C. O. Reinhold: "Projectile Charge State Dependence of Binary Electron Production for 1 MeV $u^{-1}\text{Au}^{q+}$ ($q = 12 - 37$) Ion Impact on He", *J. Phys. B: At. Mol. Opt. Phys.*, **27**, L171–L177 (1994).
- L. P. Presnyakov, H. Tawara, I. Yu. Tolstikhina, and D. B. Uskov: "Double Ionization of Atomic Helium under Heavy Ion Impact", *ibid.*, **28**, 785–793 (1995).
- B. D. DePaola, Y. Kanai, P. Richard, Y. Nakai, T. Kambara, T. M. Kojima, and Y. Awaya: "Binary Encounter Electron Production at Relativistic Velocities", *ibid.*, pp. 4283–4290.
- T. Kambara, J. Z. Tang, Y. Awaya, B. D. DePaola, O. Jagutzki, Y. Kanai, M. Kimura, T. M. Kojima, V. Mergel, Y. Nakai, H. Schmidt-Böcking, and I. Shimamura: "Three-Dimensional Recoil-Ion Momentum Analyses in 8.7 MeV O^{7+} -He Collisions", *ibid.*, pp. 4593–4606.
- M. Hacke and E. Yagi: "Annealing Behaviour of Kr Atoms in Kr-Implanted Aluminium", *J. Phys. Soc. Jpn.*, **64**, 800–808 (1995).
- Q. Hui, J. L. Persson, J. H. M. Beijersbergen, and M. Takami: "Laser Spectroscopy of Neutral Atoms in Superfluid Helium: New Environment for Spectroscopy and Chemistry", *Laser Chem.*, **15**, 221–228 (1995).
- E. Yagi: "Solid Bubble Formation in Metals Implanted with Inert Gas Ions", *Materia Japan* (in Japanese), (Bull. Jpn. Inst. Metals), **34**, 971–972 (1995).
- T. Mizogawa, M. Sato, and Y. Awaya: "Application of the "MBWC" Two-Dimensional Position Read-out Technique to a Multiwire Proportional Counter", *Nucl. Instrum. Methods Phys. Res.*, **A366**, 129–136 (1995).
- R. Hutton, S. Huldt, B. Nyström, I. Martinson, K. Ando, T. Kambara, Y. Kanai, Y. Nakai, and Y. Awaya: "Beam-Foil Studies of Highly Ionized Nb", *ibid.*, **B98**, 48–52 (1995).
- Y. Kanai, T. Kambara, Y. Awaya, H. Ida, Y. Matsui, T. Takayanagi, K. Wakiya, N. Nakamura, M. Koide, S. Kitazawa, and S. Ohtani: "Ejected Electron Spectra from Triplet States of Doubly-Excited O^{4+} and Ne^{6+} ", *ibid.*, pp. 81–84.
- L. P. Presnyakov, H. Tawara, and D. B. Uskov: "Double Electron Removal from H^- in Collisions with Highly Charged Ions", *ibid.*, pp. 332–334.
- Y. Zou, Y. Awaya, C. P. Bhalla, T. Kambara, Y. Kanai, M. Oura, Y. Nakai, K. Ando, A. Hitachi, and S. Kravis: "L-Subshell Vacancy Production of Fast Argon Ions in Solids", *ibid.*, **B99**, 1–3 (1995).
- R. Hutton, S. Huldt, B. Nyström, I. Martinson, K. Ando, T. Kambara, Y. Kanai, Y. Nakai, Y. Awaya, and J. Sugar: "Experimental Lifetimes for the $3p^2P$ Levels in Na-Like $\text{Nb}(\text{Nb}^{30+})$ ", *Phys. Rev. A*, **51**, 143–146 (1995).
- M. F. V. Lundsgaard, N. Toshima, and C. D. Lin: "Electron Capture from Circular Rydberg Atoms", *ibid.*, pp. 1347–1350.
- Y. Zou, Y. Awaya, C. P. Bhalla, T. Kambara, Y. Kanai, M. Oura, Y. Nakai, K. Ando, A. Hitachi, and S. Kravis: "Inner-Shell Vacancy Distribution in Energetic Ar Ions by Penetration in Solids", *ibid.*, pp. 3790–3798.
- J. Z. Tang, C. D. Lin, B. Zhou, and I. Shimamura: "Resonances in Photodetachment of $\text{H}^-(2p^2\ ^3P^e)$ ", *ibid.*, pp. 4694–4698.
- J. Z. Tang and I. Shimamura: "High-Lying Doubly Excited Resonances in the Photodetachment of H^- ", *ibid.*, pp. R1738–R1741.
- Y. Kino, M. R. Harston, I. Shimamura, E. A. G. Armour, and M. Kamimura: "Normalization of the Asymptotic Form of Three-Body $(d\mu)^+$ and $(dd\mu)^+$ Wave Functions", *ibid.*, **52**, pp. 870–873 (1995).
- S. Kravis, H. Saitoh, K. Okuno, K. Soejima, M. Kimura, I. Shimamura, Y. Awaya, Y. Kaneko, M. Oura, and N. Shimamura: "Single- and Double-Charge-Exchange Cross Sections for $\text{Ar}^{q+} + \text{H}_2$ ($q = 6, 7, 8, 9$, and 11) Collisions from 6 eV to 11 keV", *ibid.*, pp. 1206–1212.
- J. L. Persson, Q. Hui, M. Nakamura, and M. Takami: "Optical Spectra of Metal Dimers and Trimers in Superfluid Helium", *ibid.*, pp. 2011–2015.
- B. D. DePaola, M.-T. Huang, S. Winecki, M. P. Stöckli, Y. Kanai, S. R. Lundeen, C. W. Fehrenbach, and S. A. Arko: "Absolute Cross Sections for Charge Capture from Rydberg Targets by Slow Highly Charged Ions", *ibid.*, pp. 2136–2140.
- J. Z. Tang and I. Shimamura: "Double Photoionization of Helium at Low Photon Energies", *ibid.*, pp.

R3413–R3416.

- E. Karlsson, R. Wäppling, S. W. Lidström, O. Hartmann, R. Kadono, R. F. Kiefl, R. Hempelmann, and D. Richter: “Quantum Diffusion and Localization of Positive Muons in Superconducting Aluminium”, *ibid.*, pp. 6417–6423.
- K. Kumagai, K. Kawano, H. Kagami, G. Suzuki, Y. Matsuda, I. Watanabe, K. Nishiyama, and K. Nagamine: “Magnetic Order and Suppression of Superconductivity around $x = 0.12$ in $\text{La}_{2-x}\text{Ba}_x\text{CuO}_4$ and $\text{La}_{2-x}\text{Sr}_x\text{CuO}_4$ ”, *Physica*, **C235/240**, 1715–1716 (1994).
- Q. Hui, J. L. Persson, J. H. M. Beijersbergen, and M. Takami: “Spectroscopy and Dynamics of Neutral Atoms in Superfluid Helium”, *Z. Phys.*, **B98**, 353–357 (1995).
- #### 4. Radiochemistry, radiation chemistry, and radiation biology
- K. Eguchi-Kasai, M. Murakami, H. Itsukaichi, K. Fukutsu, T. Kanai, Y. Furusawa, K. Sato, H. Ohara, and F. Yatagai: “The Role of DNA Repair on Cell Killing by Charged Particles”, *Adv. Space Res.*, **18**, 109–118 (1995).
- Y. Itoh, K. H. Lee, H. Murakami, and R. Iwata: “Defect Study of Proton-Irradiated Liquid-Encapsulated Czochralski GaAs Using the Positron-Annihilation”, *Appl. Phys.*, **A60**, 57–60 (1995).
- Y. Itoh, K. H. Lee, T. Nakajyo, A. Goto, N. Nakanishi, M. Kase, M. Kanazawa, Y. Yamamoto, N. Oshima, and Y. Ito: “Slow Positron Production Using the RIKEN AVF Cyclotron”, *Appl. Surf. Sci.*, **85**, 165 (1995).
- S. Ambe and F. Ambe: “Mössbauer Emission Spectra of ^{119}Sn in Binary Compounds of Antimony and Tellurium”, *Bull. Chem. Soc. Jpn.*, **68**, 1935–1940 (1995).
- S. Enomoto, B. Liu, R. Amano, S. Ambe, and F. Ambe: “*In Vivo* Behavior of Various Rare Earth Elements in Lipogenous Diabetes Model Mice by Using the Multitracer Technique”, *J. Inorg. Biochem.*, **59**, 353 (1995).
- R. Hirunuma, S. Enomoto, M. Yanaga, R. Amano, K. Endo, S. Ambe, and F. Ambe: “Multitracer Studies of Behavior of Trace Elements in Rats and Mice”, *ibid.*, p. 354.
- F. Ambe, Y. Ohkubo, S. Ambe, Y. Kobayashi, T. Okada, Y. Yanagida, J. Nakamura, K. Asai, Y. Kawase, and S. Uehara: “Local Structure and Valence of Impurity Ions in Oxides by TDPAC and Mössbauer Emission Spectroscopy”, *J. Radioanal. Nucl. Chem.*, **190**, 215–224 (1995).
- S. Ambe and F. Ambe: “Mössbauer Study of Defect ^{119}Sn Atoms with Ligands from Silver to Iodine”, *ibid.*, pp. 425–430.
- S. Ambe, S. Y. Chen, Y. Ohkubo, Y. Kobayashi, H. Maeda, M. Iwamoto, M. Yanokura, N. Takematsu, and F. Ambe: “‘Multitracer’ A New Tracer Technique —Its Principle, Features, and Application”, *ibid.*, **195**, 297–303 (1995).
- S. Ambe, Y. Ohkubo, Y. Kobayashi, M. Iwamoto, H. Maeda, and M. Yanokura: “Multitracer Study on Transport and Distribution of Metal Ions in Plants”, *ibid.*, pp. 305–313.
- Y. Ohkubo, Y. Kobayashi, K. Harasawa, S. Ambe, T. Okada, F. Ambe, K. Asai, and S. Shibata: “Time-Differential Perturbed-Angular-Correlation and Emission Mössbauer Studies on ^{99}Ru Dispersed in $\text{YBa}_2\text{Cu}_3\text{O}_{6.8}$ and $\text{YBa}_2\text{Cu}_3\text{O}_6$ ”, *J. Phys. Chem.*, **99**, 10629–10634 (1995).
- Y. Itoh, H. Murakami, and A. Kinoshita: “Positronium Formation and Annihilation in Porous Silicon”, *Mater. Sci. Forum*, **175/178**, 173–176 (1995).
- H. Kusawake, T. Saito, A. Yokoyama, K. Takesako, N. Takahashi, H. Baba, Y. Ohkubo, and A. Shinohara: “Angular-Momentum Effect in the Fusion Reaction of ^{141}Pr with ^{40}Ar Projectiles”, *Radiochim. Acta*, **69**, 65–75 (1995).
- Y. Itoh: “The Study on Porous Silicon by Means of Positron Annihilation”, *Radioisotopes*, **14**, 759–760 (1995).
- #### 5. Material analysis
- J. Kawai, S. Hayakawa, F. Esaka, S.-Y. Zhen, Y. Kitajima, K. Maeda, H. Adachi, Y. Gohshi, and K. Furuya: “Depth Selective Chemical State Analysis of Fine Particle Using X-Ray Absorption”, *Anal. Chem.*, **67**, 1526–1529 (1995).
- N. Arai, W. Sakamoto, and K. Maeda: “Analysis of Trace Elements in Otoliths of Red Sea Bream *Pagrus Major*”, *Fish. Sci.*, **61**, 43–47 (1995).
- N. Arai, W. Sakamoto, and K. Maeda: “PIXE Analysis of Otoliths from Several Species of Teleost Fish”, *Int. J. PIXE*, **4**, 123–129 (1994).
- J. Kawai and K. Maeda: “Vertical Beam PIXE for *in situ* Analysis of Liquids”, *ibid.*, pp. 147–154.
- K. Maeda and J. Kawai: “Water Analysis by Particle Induced X-Ray Emission (PIXE)”, *Genshikaku Kenkyu* (in Japanese), **39**, No. 4, pp. 9–26 (1994); *IONICS*, **20**, No. 11, pp. 3–21 (1994).
- K. Maeda: “Application of Particle Induced X-Ray Emission (PIXE) to Liquid Samples”, Proc. Symp. Research and Development of Beam Engineering at 62nd Spring Meet. Electrochemical Soc. Jpn. ‘Advanced Material-Processing Beam-Technology’, S. Masaki (ed.), *Ionics*, pp. 39–42 (1995).
- J. Kawai, K. Maeda, K. Nakajima, and Y. Gohshi: “Reply to ‘Comment on ‘Relation between Copper L X-Ray Fluorescence and 2p X-Ray Photoelectron Spectroscopies’”, *Phys. Rev. B*, **52**, 6129–6131 (1995).
- J. Kawai, K. Maeda, N. Sakauchi, and I. Konishi: “Strong X-Ray Emission from Electrified Material”, *Spectrochim. Acta*, **50B**, L1–L4 (1995).

VIII. LIST OF PREPRINTS

1995

RIKEN-AF-NP

- 184 M. Yokoyama, T. Otsuka, and N. Fukunishi: “Giant Quadrupole Excitation in Nuclei with Neutron Skin”
- 185 T. Otsuka, M. Yokoyama, N. Fukunishi, and K. H. Kim: “Structure and Excitation of Nuclei Far from Stability”
- 186 I. Tanihata: “Nuclear Structure Studies from Reaction Induced by Radioactive Nuclear Beams”
- 187 A. A. Korshennikov, D. V. Aleksandrov, N. Aoi, Y. Doki, N. Inabe, M. Fujimaki, T. Kobayashi, H. Kumagai, C.-B. Moon, E. Yu. Nikolskii, M. M. Obuti, A. A. Ogloblin, A. Ozawa, S. Shimoura, T. Suzuki, I. Tanihata, Y. Watanabe, M. Yanokura, and K. Yoshida: “Experimental Studies of Light Rich Nuclei”
- Y. Suzuki, K. Arai, Y. Ohbayashi, and K. Varga: “Study of Halo Structure in Light Nuclei with a Multi-cluster Model”
- M. Ishihara: “Current Topics on Light Neutron-Rich Nuclei”
- Y. Ogawa, Y. Suzuki, and K. Yabana: “Transverse Momentum Distributions of a ${}^9\text{Li}$ Fragment in the (${}^{11}\text{Li}$, ${}^9\text{Li}$) Reaction and Neutron Correlations”
- T. Nakamura, S. Shimoura, T. Kobayashi, T. Teranishi, K. Abe, N. Aoi, Y. Doki, M. Fujimaki, N. Inabe, K. Katori, T. Kubo, H. Okuno, T. Suzuki, I. Tanihata, Y. Watanabe, A. Yoshida, and M. Ishihara: “Coulomb Dissociation of a Halo Nucleus ${}^{11}\text{Be}$ and Direct Breakup Mechanism”
- Ka-Hae Kim, T. Otsuka, and M. Tohyama: “Transfer and Fusion Reactions of Unstable Nuclei”
- T. Otsuka, A. Muta, M. Yokoyama, N. Fukunishi, and T. Suzuki: “Structure of Nuclei Far from Stability”
- K. Varga, Y. Suzuki, and I. Tanihata: “Microscopic Multicluster Description of the ${}^7\text{Li}$ - ${}^7\text{Be}$, ${}^8\text{Li}$ - ${}^8\text{B}$, and ${}^9\text{Li}$ - ${}^9\text{C}$ Mirror Nuclei”
- I. Tanihata: “RI Beam Factory Project”
- H. Toki, D. Hirata, Y. Sugahara, and I. Tanihata: “Relativistic Many Body Approach for Unstable Nuclei and Supernova”
- 188 A. Muta and T. Otsuka: “Deformed Woods-Saxon Potential Approach to the Structure of ${}^{11}\text{Be}$ ”
- 189 H. Okuno, K. Asahi, H. Ueno, H. Izumi, H. Sato, M. Adachi, T. Nakamura, T. Kubo, N. Inabe, A. Yoshida, N. Fukunishi, T. Shimoda, H. Miyatake, N. Takahashi, W.-D. Schmidt, and M. Ishihara: “Measurement of the Magnetic Moments of ${}^{14}\text{B}$ and ${}^{15}\text{B}$ Using Fragment Spin Polarization”
- 190 K. Varga and Y. Suzuki: “Precise Solution of Few-Body Problems with the Stochastic Variational Method”
- 191 T. Horibata, M. Oi, and N. Onishi: “Signature Splitting in Tilted Axis Rotating States”
- 192 T. Kobayashi, K. Yoshida, and H. Kitagawa: “Recent Progresses at RIKEN Accelerator Facility”
- 193 K. Yuasa-Nakagawa, T. Nakagawa, K. Furutaka, K. Matsuda, Y. Futami, K. Yoshida, J. Kasagi, S. M. Lee, T. Suomijärvi, W. Q. Shen, and T. Matsuse: “Entrance Channel Effect on the Pre-scission Time of Binary Decay for the Medium Mass Nuclei (Mass ~ 110)”
- 194 T. Horibata and N. Onishi: “Theory, Self-Consistent Three-Dimensional Cranking Calculation Based on HFB I. Energy Surface and Gamma-Deformation for ${}^{182}\text{Os}$ ”
- 195 K. Sumiyoshi, H. Suzuki, and H. Toki: “Theory, Influence of the Symmetry Energy on the Birth of Neutron Stars and Supernova Neutrinos”

- 196 E. Ideguchi, Y. Gono, S. Mitarai, T. Morikawa, A. Odahara, M. Kidera, M. Shibata, H. Tsuchida, K. Miyazaki, M. Oshima, Y. Hatsukawa, S. Hamada, H. Imura, M. Shibata, T. Ishii, T. Murakami, H. Kusakari, M. Sugawara, T. Kishida, K. Morita, H. Kumagai, and M. Ishihara: “High-Spin States in ^{148}Tb ”
- 197 M. Honma, T. Mizusaki, and T. Otsuka: “Diagonalization of Hamiltonians for Many-Body Systems by Auxiliary Field Quantum Monte Carlo Technique”
- 198 K. Sumiyoshi, K. Oyamatsu, and H. Toki: “Neutron Star Profiles in the Relativistic Brueckner Hartree Fock Theory”
- 199 Y. Mochizuki, K. Oyamatsu, and T. Izuyama: “Nuclear Lattice Deformation Inside Neutron Stars and the Origin of Pulsar Glitches”
- 200 T. Ariga, K. Uchiyama, S. Ozawa, K. Osada, M. Hirai, A. Yamashita, A. Yoshimi, K. Kodaka, and H. Okuno: “Heisei 6nen Gakui Ronbun Happyokai”
- 201 A. Mengoni, T. Otsuka, and M. Ishihara: “Direct Radiative Capture of P-Wave Neutrons”
- 202 A. Ono and H. Horiuchi: “Improvement of the Nucleon Emission Process and the Statistical Property in Molecular Dynamics”
- 203 H. Izumi, K. Asahi, H. Ueno, H. Okuno, H. Sato, K. Nagata, Y. Horii, M. Adachi, N. Aoi, A. Yoshida, G. Liu, N. Fukunishi, and I. Tanihara: “Electric Quadrupole Moments of Neutron-Rich Nuclei ^{14}B and ^{15}B ”
- 204 T. Suzuki, H. Geissel, O. Bochkarev, L. Chulkov, M. Golovkov, D. Hirata, H. Irnich, Z. Janas, H. Keller, T. Kobayashi, G. Kraus, G. Munzenberg, S. Neumaier, F. Nickel, A. Ozawa, A. Piechaczek, E. Roeckl, W. Schwab, K. Suemmerer, K. Yoshida, and I. Tanihata: “Neutron Skin of Na Isotopes Studied via the Interaction Cross Sections”
- 205 K. Varga and Y. Suzuki: “Precise Solution of Few-Body Problems with Stochastic Variational Method on Correlated Gaussian Basis”
- 206 S. Kim and S. Ohta: “Light Hadron Masses with 4 GeV Cutoff and $L = 2.4 \text{ fm}$ ”
- 207 S. Ohta: “Self-Test Monte Carlo Method”
- 208 H. Hofmann, F. A. Ivanyuk, and S. Yamaji: “On the Nature of Nuclear Dissipation, as a Hallmark for Collective Dynamics at Finite Excitation”
- 209 H. Kurasawa and T. Suzuki: “Macroscopic Model of Giant Resonance States in Neutron-Rich Nuclei”
- 210 H. Kurasawa and T. Suzuki: “Quasielastic Electron Scattering”
- 211 H. Kurasawa and T. Suzuki: “A Sum-Rule Constraint on the Soft Dipole Mode”
- 212 H. Kurasawa and T. Suzuki: “The Mean Energy, Strength and Width of the Double Giant Dipole States”
- 213 I. Tanihata: “Neutron Halo Nuclei”
- 214 A. Ono and H. Horiuchi: “Statistical Properties of Antisymmetrized Molecular Dynamics for Non-Nucleon-Emission and Nucleon-Emission Processes”
- 215 A. A. Korshennikov, E. Yu. Nikolskii, T. Kobayashi, A. Ozawa, S. Fukuda, E. A. Kuzmin, S. Momota, B. G. Novatakii, A. A. Ogloblin, V. Pribora, I. Tanihata, and K. Yoshida: “Spectroscopy of the Halo Nucleus ^{11}Li by an Experimental Study of $^{11}\text{Li} + p$ Collisions”
- 216 H. Ueno, K. Asahi, H. Izumi, K. Nagata, H. Ogawa, A. Yoshimi, H. Sato, M. Adachi, Y. Hori, K. Mochinaga, H. Okuno, N. Aoi, M. Ishihara, A. Yoshida, G. Liu, T. Kubo, N. Fukunishi, T. Shimoda, H. Miyatake, M.

Sasaki, T. Shirakura, N. Takahashi, S. Mitsuoka, and W.-D. Schmidt: “Magnetic Moments of ^{17}N and ^{17}B ”

217 M. Honma, T. Mizusaki, and T. Otsuka: “Quantum Monte Carlo Diagonalization Method for Realistic Shell”

IX. PAPERS PRESENTED AT MEETINGS

1. Accelerator development and accelerator physics

- T. Uesaka, T. Wakui, M. Wakasugi, A. Minoh, Y. Yano, H. Sato, K. Sakai, and Y. Masuda: "Development of Polarized ^3He Gas Target at RIKEN", 1995 Spring Meet. Phys. Soc. Jpn., Yokohama, Mar. (1995).
- M. Niimura, T. Kageyama, T. Nakagawa, A. Goto, and Y. Yano: "Physics for ECRIS Beam-Current Upgrading Technologies Such as Electron Beam Injection, Wall Coating, and Gas Mixing", 12th Int. Workshop on ECR Ion Sources, Wako, Apr. (1995).
- T. Nakagawa, T. Kageyama, M. Kase, A. Goto, and Y. Yano: "Production of Highly Charged Ions from Oxide in RIKEN 10 GHz ECRIS", *ibid.*
- Y. Batygin, A. Goto, and Y. Yano: "Nonlinear Effect of Einzel Lens to the Beam Extracted from ECR Source", *ibid.*
- M. Niimura, H. Amemiya, A. Goto, and Y. Yano: "Averaged Excitation Rate Coefficient Calculation of HeI up to $T_e = 1000$ eV and Plasma Potential Measurement up to ECR-Heated Ellipsoid", *ibid.*
- Y. Batygin, A. Goto, and Y. Yano: "Hollow Beam Profile in the Extraction System of ECR Ion Source", Particle Accelerator Conf., Dallas, U.S.A., May (1995).
- Y. Batygin: "Invariability of Intense Beam Emittance in Nonlinear Focusing Channel", *ibid.*
- D. Bruhwiler and Y. Batygin: "Beam Transport for Uniform Irradiation: Nonlinear Space Charge Forces and the Effect of Boundary Conditions", *ibid.*
- T. Uesaka, T. Wakui, M. Wakasugi, A. Minoh, Y. Yano, H. Sato, K. Sakai, and Y. Masuda: "Development of Polarized ^3He Gas Target at RIKEN", Int. Workshop on Polarized Beams and Polarized Gas Targets, Koeln, Germany, June (1995).
- Y. Yano: "RIKEN Accelerator Research Facility (RARF), Its New Project 'RI Beam Factory', and Other Major Heavy-Ion Accelerator Facilities in Japan", Simposio Nipo-Brasileiro de Ciencia e Tecnologia, São Paulo, Brazil, Aug. (1995).
- O. Kamigaito, A. Goto, Y. Miyazawa, T. Chiba, M. Hemmi, S. Kohara, M. Kase, Y. Batygin, and Y. Yano: "Development of a Variable-Frequency RFQ Linac for the RILAC", 20th Linear Accelerator Meet. Jpn., Osaka, Sept. (1995).
- M. Kase, N. Inabe, A. Goto, T. Kageyama, I. Yokoyama, M. Nagase, S. Kohara, T. Nakagawa, K. Ikegami, O. Kamigaito, J. Fujita, and Y. Yano: "The Operation of RIKEN Ring Cyclotron", 10th Symp. on Accelerator Science and Technology, Hitachinaka, Oct. (1995).
- M. Niimura, T. Nakagawa, A. Goto, and Y. Yano: "Next-Step ECRIS and 2 m Length 4.52 GeV Advanced Accelerator: Novel Extraction of Trapped Ions and their Acceleration-Final Focusing by Non-neutral and Neutral Plasmas", *ibid.*
- T. Mitsumoto, A. Goto, T. Kawaguchi, Y. Tanaka, T. Kubo, H. Okuno, T. Tominaka, S. Fujishima, and Y. Yano: "Design Study of Sector Magnet for the RIKEN Superconducting Ring Cyclotron (I)", *ibid.*
- T. Nakagawa, Y. Miyazawa, M. Hemmi, T. Chiba, N. Inabe, M. Kase, T. Kageyama, O. Kamigaito, E. Ikezawa, A. Goto, and Y. Yano: "Development of RIKEN 18 GHz ECRIS", *ibid.*
- O. Kamigaito, A. Goto, Y. Miyazawa, T. Chiba, M. Hemmi, S. Kohara, M. Kase, Y. Batygin, and Y. Yano: "Development of a Variable-Frequency RFQ Linac for the RILAC", *ibid.*
- Y. Yano, A. Goto, T. Katayama, and RIBF Group: "RIKEN RI Beam Factory Project", *ibid.*
- M. Kase, N. Inabe, I. Yokoyama, A. Goto, and Y. Yano: "Applications of MCP Phase Monitor to Operations of RIKEN Heavy Ion Accelerators", 14th Int. Conf. on Cyclotron and Their Applications, Cape Town, South Africa, Oct. (1995).
- T. Mitsumoto, T. Kawaguchi, T. Kubo, H. Okuno, T. Tominaka, Y. Tanaka, S. Fujishima, K. Ikegami, A. Goto, and Y. Yano: "Design Study of Sector Magnets of Superconducting Ring Cyclotron for the RIKEN RI Beam Factory", *ibid.*
- Y. Yano, A. Goto, T. Katayama, and RIBF Group: "The RIKEN RI Beam Factory Project", *ibid.*
- A. Goto, Y. Miyazawa, M. Hemmi, O. Kamigaito, T. Nakagawa, M. Kase, T. Chiba, N. Inabe, S. Kohara, T. Kageyama, Y. Batygin, E. Ikezawa, and Y. Yano: "Construction of a New Pre-injector System for the RILAC", *ibid.*
- T. Kubo, H. Okuno, K. Ikegami, T. Kawaguchi, T. Tominaka, T. Mitsumoto, S. Fujishima, A. Goto, and Y. Yano: "RI-Beam Factory Project(I)-Superconducting Ring Cyclotron", 1995 Fall Meet. Cryogenics and Superconductivity, Akita, Nov. (1995).
- T. Kawaguchi, T. Mitsumoto, T. Kubo, T. Tominaka, H. Okuno, Y. Tanaka, S. Fujishima, K. Ikegami, A. Goto, and Y. Yano: "RI Beam Factory Project (II) — Superconducting Sector Magnet—", *ibid.*
- T. Tominaka, H. Okuno, Y. Tanaka, T. Kubo, T. Mitsumoto, T. Kawaguchi, S. Fujishima, K. Ikegami, A. Goto, and Y. Yano: "RI Beam Factory Project(III) —Beam Injection and Extraction Systems—", *ibid.*
- T. Kawaguchi, T. Kubo, T. Mitsumoto, T. Tominaka, S. Fujishima, H. Okuno, Y. Tanaka, K. Ikegami, A. Goto, and Y. Yano: "Design Study of Sector Magnet for the RIKEN Superconducting Ring Cyclotron (II)", 10th Symp. on Accelerator Science and Technology, JAERI Conf., Hitachinaka, Oct. (1995).
- N. Inabe, M. Kase, I. Yokoyama, A. Goto, and Y. Yano: "Development of a Single-Bunch Selector for

- RIKEN Ring Cyclotron”, *ibid.*
- A. Goto, Y. Miyazawa, M. Hemmi, O. Kamigaito, T. Nakagawa, M. Kase, T. Chiba, N. Inabe, S. Kohara, T. Kageyama, Y. Batygin, and Y. Yano: “Construction of a New Pre-injector System for the RILAC”, *ibid.*
- M. Takanaka and T. Katayama: “Beam Current Limitations Due to Single-Beam Collective Effects in the Ion Storage Ring of RIKEN RI Beam Factory Project”, *ibid.*
- Y. Batygin, A. Goto, and Y. Yano: “Hollow Beam Formation in the Extraction Region of ECRIS”, *ibid.*
- Y. Batygin and T. Katayama: “Study of Incoherent Beam-Beam Effects at Radioactive Isotope Beam Factory”, *ibid.*
- Y. Batygin, A. Goto, O. Kamigaito, and Y. Yano: “Effect of Field Variation on Beam Parameters in RIKEN RFQ Linac”, *ibid.*
- N. Nakanishi, T. Shikata, S. Fujita, and T. Kosako: “Comparison of Calculated Shielding Effects for 8 Materials”, *ibid.*
- Y. Batygin: “On Space Charge Dominated Beam Transport without Emittance Growth”, 8th ICFA Workshop on Space Charge Dominated Beams, Indiana, U.S.A., Oct. (1995).
- ## 2. Nuclear physics and nuclear instrumentation
- C. Signorini: “Fusion at the Barrier with Stable and Radioactive Nuclei: Present and Future”, Tours Symp. on Nucl. Phys. II, Tours, France, Aug. (1994).
- H. Kurasawa and T. Suzuki: “Macroscopic Model of Giant Resonance States in Neutron-Rich Nuclei”, 3rd IN2P3-RIKEN Symp. on Heavy Ion Collisions, Wako, Oct. (1994).
- Y. Ogawa, Y. Suzuki, and K. Yabana: “Transverse Momentum Distributions of a ${}^9\text{Li}$ Fragment in the (${}^{11}\text{Li}$, ${}^9\text{Li}$) Reaction and Neutron Correlations”, Int. Symp. on Physics of Unstable Nuclei, Niigata, Oct.–Nov. (1994).
- H. Kurasawa and T. Suzuki: “Quasielastic Electron Scattering”, Korea-Japan Joint Symp. on Recent Development of Nuclear Study using Electron and Photon Beams, Seoul and Pohang, Korea, Dec. (1994).
- H. Sato, Y. Hori, K. Mochinaga, M. Adachi, and K. Asahi: “Development of Polarized ${}^{129}\text{Xe}$ Stopper as a Polarizer for Unstable Nuclei”, Symp. on Science with Radioactive Nuclear Beams, Tanashi, Jan. (1995).
- Y. Mochizuki, K. Oyamatsu, and T. Izuyama: “Effects of Deformed Nuclei on Neutron Star Glitches”, *ibid.*
- A. Ozawa, T. Kobayashi, D. Hirata, I. Tanihata, O. Yamakawa, K. Sugimoto, D. Olson, W. Christie, and H. Wieman: “Interaction Cross Sections and Radii of the Light Proton Rich Nuclei”, *ibid.*
- K. Sumiyoshi: “Influence of the Symmetry Energy on the Cooling of Protoneutron Stars and Supernova Neutrinos”, *ibid.*
- Y. Mochizuki: “Abnormal Braking Indices as a Indicator of Glitching Pulsars”, Winter School on Nuclear Astrophysics, Sponsored by Science of Short-Lived Nuclear Beams, Shiozawa, Feb. (1995).
- T. Horibata: “Calculation of Signature Splitting”, RIKEN Symp. on Recent Progress at Accelerator Facility, Wako, Mar. (1995).
- T. Kohn: “Radiation Observation in Space”, Workshop on Space Environment Monitoring from Space, Nagoya, Mar. (1995).
- A. Ono and H. Horiuchi: “Improvement of the Nucleon-Emission Process in AMD and Its Statistical Property”, 50th Ann. Meet. Phys. Soc. Jpn., Yokohama, Mar. (1995).
- H. Sato, Y. Hori, K. Mochinaga, M. Adachi, and K. Asahi: “Polarization of Xe Nuclear Spin by Using the Optical Pumping Method II”, *ibid.*
- N. Aoi: “ β -decay of Light Neutron Rich Nuclei”, *ibid.*
- T. Horibata, M. Oi, and N. Onishi: “Calculation of Signature Splitting”, *ibid.*
- Y. Sugaya, D. Ashery, J. Chiba, H. Ito, K. Kimura, Yu. T. Kiselev, S. Kouda, K. Miyano, T. Murakami, T. Nagae, Y. Nakai, M. Nomachi, H. Ochiishi, S. Sawada, M. Sekimoto, T. Shibata, T. Suzuki, K. H. Tanaka, M. K. Vlasov, Y. Yamanoi, K. Yasuda, and Y. Yoshimura: “Subthreshold Anti Proton Production Nucleus Collision with p , d , and α Particle”, *ibid.*
- T. Teranishi, M. Ishihara, H. Sakurai, M. Hirai, T. Motobayashi, S. Shimoura, H. Murakami, Y. Ando, N. Iwasa, T. Nishio, S. Moriya, Y. Yanagisawa, T. Kikuchi, T. Uchibori, Y. Watanabe, and T. Nakamura: “Charge Exchange Reactions of ${}^{11}\text{Li}$ ”, *ibid.*
- H. Koura, M. Uno, T. Tachibana, Y. Shigeta, and M. Yamada: “Semi-Empirical Shell Energy and Atomic Mass Formula II”, *ibid.*
- Y. Sugahara, K. Sumiyoshi, and H. Toki: “Study of the Light Nuclei in the Relativistic and the Non-Relativistic Models”, *ibid.*
- N. Nakanishi, S. Nakajima, S. Fujita, T. Minemura, Y. Kangyou, M. Watanabe, and H. Ohishi: “Measurements of Eleven Neutron Activation Cross Sections Using 113 MeV Proton Beams”, *ibid.*
- S. Takahara, N. Onishi, and N. Tajima: “Deformed Hartree-Fock Calculation of $Z \geq 82$ Nuclei (I)”, *ibid.*
- Y. Aoki, R. Sasaki, T. Ohtsuki, J. Kasagi, K. Furutaka, Y. Futami, K. Matsuda, K. Yuasa-Nakagawa, T. Nakagawa, K. Yoshida, and T. Suomijarvi: “Giant Dipole Resonances at $E_x \sim 150$ MeV Observed in Heavy Ion Fusion Reactions”, *ibid.*
- H. Ogawa, N. Aoi, M. Ito, K. Asahi, H. Ueno, H. Izumi, K. Nagata, A. Yoshida, H. Okuno, G. Liu, S. Mitsuoka, M. Adachi, and M. Ishihara: “Measurements of Branching Ratio for the Unique First Forbidden Beta Decay of ${}^{14}\text{B}$ ”, *ibid.*
- K. Sumiyoshi, K. Oyamatsu, and H. Toki: “Equation of State and Neutron Stars in the Relativistic Brueckner Hartree Fock Theory”, *ibid.*

- A. A. Korshennikov: "Experimental Studies of Light Exotic Nuclei", 15th Nuclear Physics Division Conf. on LEND 95 of European Physical Society, St. Petersburg, Russia, Apr. (1995).
- A. A. Korshennikov: "Experimental Studies of Light Neutron-Rich Nuclei", 2nd RIKEN/INFN(Italy) Joint Symp., Wako, May (1995).
- A. Yoshida: "Measurement of Fusion Cross Section with Neutron Rich RI Beam", *ibid.*
- C. Signorini: "Fusion and Break-Up Around the Coulomb Barrier with Halo/Loosely Bound Unstable Nuclei", *ibid.*
- A. Ono and H. Horiuchi: "Nucleon Flow and Fragment Flow in Heavy Ion Collisions Studied with AMD," *ibid.*
- M. Wakasugi: "Laser Spectroscopy on Radioactive Isotopes of Refractory Elements", *ibid.*
- T. Wada, Y. Aritomo, M. Ohta, Y. Abe, and S. Yamaji: "Fission as Dissipative Process", *ibid.*
- K. Yuasa-Nakagawa, T. Nakagawa, Y. Futami, K. Furutaka, K. Matsuda, K. Yoshida, T. Mizota, Y. Honjo, S. Tomita, T. Suomijärvi, W. Q. Shen, J. Kasagi, T. Matsuse, and S. M. Lee: "Angular Momentum Dependence of Pre-Scission Time for Binary Decay in Medium Mass Nuclei", YITP Symp. on Similarities and Differences of Microcluster and Nucleus, Kyoto, June (1995).
- T. Motobayashi: "Experimental Study of Nuclear Reactions Related to Solar Neutrino Production", 4th Int. Symp. on Weak and Electromagnetic Interaction in Nuclei (WEIN'95), Osaka, June (1995).
- A. A. Korshennikov: "Experimental Studies of Light Exotic Nuclei", Int. Conf. on Exotic Nuclei and Atomic Masses ENAM'95, Arles, France, June (1995).
- M. Uno, H. Koura, T. Tachibana, and M. Yamada: "Nuclear Shell Energies and Deformations in Mass Formulas", *ibid.*
- S. Shimoura: "Spectroscopy of Neutron-Rich Nuclei via Direct Reactions using Secondary Nuclear Beams at Several Tens of MeV Per Nucleon", *ibid.*
- K. Matsuta, M. Tanigaki, M. Fukuda, T. Minamisono, Y. Nojiri, M. Mihara, T. Onishi, T. Yamaguchi, A. Harada, M. Sasaki, T. Miyake, K. Minamisono, T. Fukao, K. Sato, Y. Matsumoto, T. Ohtsubo, S. Fukuda, S. Momota, K. Yoshida, A. Ozawa, T. Kobayashi, I. Tanihata, J. R. Alonso, G. F. Krebs, and T. J. M. Symons: "Magnetic Moments of Proton Drip-Line Nuclei", *ibid.*
- T. Motobayashi, N. Iwasa, T. Kikuchi, Y. Ando, M. Kurokawa, S. Moriya, H. Murakami, T. Nishio, J. Ruan(Gen), S. Shimoura, S. Shirato, T. Uchibori, Y. Yanagisawa, N. Inabe, M. Ishihara, T. Kubo. Y. Watanabe, M. Hirai, T. Nakamura, H. Sakurai, T. Teranishi, M. Gai, R. H. France III, K. I. Hahn, Z. Zhao, Y. Futami, K. Furutaka, Th. Delbar, C. Michotte, and P. Lipnik: "Coulomb Dissociation of ^8B and Sonar Neutrino Problem", *ibid.*
- T. Ichihara, M. Ishihara, H. Ohnuma, T. Niizeki, T. Yamamoto, K. Katoh, T. Yamashita, Y. Hara, Y. Fuchi, S. Kubono, M. H. Tanaka, H. Okamura, S. Ishida, T. Uesaka, and Y. Satou: "Spin-Flip and Non-Spin-Flip Isovector Excitations Observed in the ($^{12}\text{C},^{12}\text{N}$) and ($^{13}\text{C},^{13}\text{N}$) Reactions at $E/A=100\text{--}135$ MeV", Groningen Conf. on Giant Resonances, Groningen, The Netherlands, June–July (1995).
- Y. Okamoto, K. Endo, and R. Hirashima: "Try to Make a New Type Gamma Camera Using Cooled CCD Camera", 32nd Ann. Meet. on Radioisotopes in the Physical Sciences and Industries, Tokyo, July (1995).
- Y. Itoh, T. Kakizaki, K. Tanaka, A. Goto, N. Nakanishi, M. Kase, N. Oshima, T. Suzuki, I. Kanazawa, T. Nakajyo, and Y. Ito: "Slow Positron Production Using RIKEN AVF Cyclotron II", *ibid.*
- S. Kim and S. Ohta: "Light Hadron Masses with 4-GeV Cutoff and $L=2.4$ fm", Int. Symp. Lattice Field Theories 95, Melbourne, Australia, July (1995).
- K. Sumiyoshi: "Unstable Nuclei and Relativistic EOS for Neutron Stars and Supernovae", RCNP Workshop on Structure and Reaction of Unstable Nuclei, Osaka, July (1995).
- Y. S. Mochizuki, K. Oyamatsu, and T. Izuyama: "Nuclear Deformation Induced by Superfluid Vortices in the Neutron Star Crusts", *ibid.*
- T. Teranishi, M. Ishihara, H. Sakurai, M. Hirai, T. Motobayashi, S. Shimoura, H. Murakami, Y. Ando, N. Iwasa, T. Nishio, S. Moriya, Y. Yanagisawa, T. Kikuchi, T. Uchibori, Y. Watanabe, and T. Nakamura: "Charge Exchange Reactions of ^{11}Li ", *ibid.*
- Y. Ogawa, K. Arai, K. Varga, and Y. Suzuki: "Structure of the ^9Be and ^{10}Be Nuclei in a Microscopic Multicenter Model", *ibid.*
- T. Nakamura: "Coulomb Excitation of ^{11}Be ", *ibid.*
- K. Oyamatsu: "Symmetry Energy and Nuclei in Neutron Stars", *ibid.*
- T. Nakagawa, K. Yuasa-Nakagawa, K. Yoshida, K. Furutaka, K. Matsuda, Y. Futami, T. Mizota, Y. Honjo, S. Tomita, S. M. Lee, J. Kasagi, T. Suomijärvi, W. O. Shen, and T. Matsuse: "Angular Momentum Effect on the Pre-Scission Time and Mass Equilibration from Medium Mass Nuclei", Int. Nucl. Phys. Conf., INPC'95, Beijing, China, Aug. (1995).
- K. Sugawara-Tanabe: "Magnetic Properties in a Superdeformed Nucleus", *ibid.*
- A. Ono and H. Horiuchi: "Fragmentation Reactions at Medium Energies Studied with Antisymmetrized Molecular Dynamics", *ibid.*
- A. Mengoni, T. Otsuka, and M. Ishihara: "The Direct Radiative Capture Process and the Neutron Halo Structure of Nuclear Excited States", *ibid.*
- C. Signorini: "Heavy Ion Reaction Around the Coulomb Barrier", *ibid.*

- Y. Watanabe: "Effects of Break-Up in the Fusion of ^{11}Be with ^{209}Bi ", *ibid.*
- H. Izumi, K. Asahi, H. Ueno, H. Okuno, H. Sato, K. Nagata, Y. Hori, M. Adachi, N. Aoi, A. Yoshida, G. Liu, N. Fukunishi, and M. Ishihara: "Measurements of Electric Quadrupole Moments of Neutron-Rich Nuclei ^{14}Be and ^{15}B ", 10th Int. Conf. on Hyperfine Interactions, Leuven, Belgium, Aug. (1995).
- K. Matsuta, T. Minamisono, M. Tanigaki, M. Fukuda, Y. Nojiri, M. Mihara, T. Onishi, T. Yamaguchi, A. Harada, M. Sasaki, T. Miyake, K. Minamisono, T. Fukao, K. Sato, Y. Matsumoto, T. Ohtsubo, S. Fukuda, S. Momota, K. Yoshida, A. Ozawa, T. Kobayashi, I. Tanihata, J. R. Alonso, G. F. Krebs, and T. J. M. Symons: "Magnetic Moments of Proton Drip-Line Nuclei ^{13}O and ^9C ", *ibid.*
- M. Tanigaki, K. Matsuta, M. Fukuda, T. Minamisono, Y. Nojiri, M. Mihara, K. Minamisono, T. Fukao, K. Sato, Y. Matsumoto, T. Ohtsubo, S. Fukuda, S. Momota, K. Yoshida, A. Ozawa, T. Kobayashi, I. Tanihata, J. R. Alonso, G. F. Krebs, and T. J. M. Symons: "Quadrupole Moment of Proton Dripline Nucleus ^{13}O ($I^\pi = 3/2^-, T_{1/2} = 8.6$ ms)", *ibid.*
- K. Matsuta, M. Fukuda, M. Tanigaki, T. Minamisono, Y. Nojiri, H. Akai, T. Izumikawa, M. Nakazato, M. Mihara, T. Yamaguchi, A. Harada, M. Sasaki, T. Miyake, T. Onishi, K. Minamisono, T. Fukao, K. Sato, Y. Matsumoto, T. Ohtsubo, S. Fukuda, K. Yoshida, A. Ozawa, S. Momota, T. Kobayashi, I. Tanihata, J. R. Alonso, G. F. Krebs, and T. J. M. Symons: "Hyperfine Interaction of ^{13}O and ^{23}Mg Implanted in Pt", *ibid.*
- A. Ono and H. Horiuchi: "Fragmentation Described by the Improved Antisymmetrized Molecular Dynamics", 2nd Int. Symp. on Heavy Ion Physics and Its Applications, Lanzhou, China, Aug. (1995).
- T. Kakizaki, Y. Itoh, K. H. Lee, K. Tanaka, A. Goto, N. Nakanishi, M. Kase, and Y. Ito: "Generation of Slow Positron Beam from Short Lifetime Positron Emitters", 56th Meet. Jpn. Soc. Appl. Phys., Kanazawa, Aug. (1995).
- Y. S. Mochizuki and T. Izuyama: "A Model for the Physical Origin of Neutron Star Glitches", Int. Workshop on Elementary Processes in Astrophysical Dense Matter, Aspen, U.S.A., Aug.-Sept. (1995).
- Y. S. Mochizuki: "A Expected Glitch in PSR B1757-24", *ibid.*
- T. Kohno, A. Turtelli Jr., T. Kohno, U. B. Jayanthi, J. H. Adams Jr., I. M. Martin, A. A. Gusev, G. I. Pugacheva, H. Kato, K. Nagata, A. J. Tylka, and P. R. Boberg: "Anomalous and Solar Cosmic Ray Observations with the First Brazilian Scientific Microsatellite", 24th Int. Cosmic Ray Conf., Rome, Italy, Sept. (1995).
- Y. Itoh, H. Murakami, and A. Kinoshita: "Positron/Positronium Annihilation in Low Dimensional Silicon Materials", Int. Symp. on Si Heterostructures, Crete, Greece, Sept. (1995).
- K. Tanaka, Y. Itoh, K. H. Lee, T. Kakizaki, A. Goto, N. Nakanishi, M. Kase, and Y. Ito: "Development of the Targets for Online Spin-Polarized Slow Positron Beam", *ibid.*
- Y. Sugahara, K. Sumiyoshi, and H. Toki: "Comparison of the Relativistic and the Non-Relativistic Models for Properties of Unstable Nuclei", 1995 Fall Meet. Phys. Soc. Jpn., Kasugai, Sept. (1995).
- N. Hasebe, Y. Mishima, M. Kobayashi, M. Kondo, J. Hamada, T. Doke, J. Kikuchi, T. Hayashi, N. Hemmi, T. Takashima, T. Kashiwagi, T. Yanagimachi, A. Nakamoto, H. Hurukami, T. Kohno, K. Munakata, C. Kato, K. Maezawa, Y. Muraki, T. Koi, A. Nishida, T. Terasawa, S. Yanagita, K. Nagata, and B. Wilken: "Observation of CIR Events with GEOTAIL Satellite II", *ibid.*
- N. Fukunishi and I. Tanihata: "Magnetic Moment of the Mirror Nuclei ^9C and ^9Li ", *ibid.*
- K. Sugawara-Tanabe and K. Tanabe: " C_4 Symmetry in a Superdeformed State", *ibid.*
- K. Oyamatsu, K. Sumiyoshi, and Y. Mochizuki: "Symmetry Energy and Nuclei in the Inner Crust of Neutron Stars", *ibid.*
- K. Arai, Y. Ogawa, Y. Suzuki, and K. Varga: "Structure of the $A=9$ System with Microscopic Cluster Model", *ibid.*
- A. Mengoni: "Neutron Capture Reaction Rates for Nuclear Astrophysics", *ibid.*
- Y. Watanabe, T. Fukuda, A. Yoshida, Y. Watanabe, Y. Mizoi, J. Nakano, M. Hirai, Y. Sakurai, H. Kobinata, Y. Pu, K. Kimura, and M. Ishihara: "Measurement of Fusion Cross Section of Neutron-Rich Nuclei ^{29}Al , ^{31}Al ", *ibid.*
- A. Ono and H. Horiuchi: "Application of AMD with the Wave Packet Spread Effect to Heavy Ion Reactions", *ibid.*
- K. Sumiyoshi, D. Hirata, Y. Sugahara, H. Toki, and I. Tanihata: "A Systematic Study of Deformed Nuclei in the Relativistic Mean Field Theory", *ibid.*
- H. Koura, M. Uno, T. Tachibana, Y. Shigeta, and M. Yamada: "Semi-Empirical Shell Energy and Atomic Mass Formula IIP", *ibid.*
- T. Horibata and N. Onishi: "Tilting Mechanism and the Quasiparticle Energy", *ibid.*
- M. Oi, T. Horibata, and N. Onishi: "Angular Momentum Projection of Tilted Axis Rotating States", *ibid.*
- Y. S. Mochizuki, K. Oyamatsu, and T. Izuyama: "Nuclear Deformation Induced by Superfluid Vortices in the Neutron Star Crusts", *ibid.*
- H. Kitagawa and T. Hatsuda: "Gluon Distribution Functions Using QCD Sum Rule", *ibid.*
- S. Ishida: "Development of the Deuteron POLarimeter DPOL at RIKEN I", *ibid.*
- Y. Satou: "Development of the Deuteron POLarimeter DPOL at RIKEN II", *ibid.*
- T. Teranishi, M. Ishihara, H. Sakurai, M. Hirai, T. Motobayashi, S. Shimoura, H. Murakami, Y. Ando, N. Iwasa, T. Nishio, S. Moriya, Y. Yanagisawa,

- T. Kikuchi, T. Uchibori, Y. Watanabe, and T. Nakamura: "Charge Exchange Reactions of ^{11}Li ", *ibid.*
- K. Mochinaga, H. Sato, M. Adachi, and K. Asahi: "Development of Polarized Xe Solid for Polarizing Unstable Nuclei", *ibid.*
- Y. Aoki, R. Sasaki, T. Ohtsuki, J. Kasagi, K. Furutaka, Y. Futami, K. Matsuda, K. Yuasa-Nakagawa, T. Nakagawa, K. Yoshida, and T. Suomijarvi: "Giant Dipole Resonances at $E_x \sim 150$ MeV Observed in $^{40}\text{Ar} + ^{92}\text{Mo}$, ^{116}Sn , $^{\text{nat}}\text{Ni}$ Fusion Reactions", *ibid.*
- S. Takahara, N. Onishi, and N. Tajima: "Deformed Hartree-Fock Calculation of $Z \geq 82$ Nuclei (II)", *ibid.*
- Y. Ogawa, K. Arai, K. Varga, and Y. Suzuki: "Structure of the ^9Be and ^{10}Be Nuclei in a Microscopic Multicluster Model", *ibid.*
- M. Yamagami, H. Utsunomiya, T. Yamagata, and K. Miki, S. Kubono, M. H. Tanaka, Y. Fuchi, Y. Matsuyama, K. Omata, and H. Sakurai: "Test of a High-Rate MWDC for Heavy-Ion Detection", *ibid.*
- Y. Ohbayasi, K. Varga, and Y. Suzuki: "Stochastic Variational Method for Few-Nucleon Systems with Realistic Forces", *ibid.*
- M. Notani, H. Sakurai, N. Aoi, M. Hirai, H. Kobinata, Y. Watanabe, T. Nakamura, A. Yoshida, Y. Watanabe, T. Kubo, T. Nakagawa, N. Inabe, H. Kumagai, A. Goto, and M. Ishihara: "Search for New Neutron Rich Nuclei Far from Stability ($Z = 10 \sim 13$)", *ibid.*
- T. Suzuki: "Radii of Na Isotopes and a Neutron Skin", *ibid.*
- T. Ichihara, M. Ishihara, H. Ohnuma, T. Niizeki, T. Yamamoto, K. Katoh, T. Yamashita, Y. Hara, Y. Fuchi, S. Kubono, M. H. Tanaka, H. Okamura, S. Ishida, T. Uesaka, and Y. Satou: "Spin-Flip and Non-Spin-Flip Isovector Excitations Observed in the ($^{12}\text{C}, ^{12}\text{N}$) Reactions at $E/A=135$ MeV and the ($^{13}\text{C}, ^{13}\text{N}$) Reactions at $E/A=100$ MeV", *ibid.*
- Y. S. Mochizuki, K. Oyamatsu, and T. Izuyama: "Nuclear Deformation Induced by Superfluid Vortices Inside Neutron Stars and the Origin of Glitches", Fall Meet. Astronomical Soc. Jpn., Niigata, Oct. (1995).
- T. Kohno: "Current and Future Data Available in Japan", Int. Workshop on Radiation Belts, Models and Standards, Brussel, Belgium, Oct. (1995).
- T. Nakamura, E. Kim, A. Konno, M. Imamura, N. Nakao, T. Shibata, Y. Uwamino, N. Nakanishi, Su. Tanaka, H. Nakashima, Sh. Tanaka, and M. Baba: "Activation Cross Section Measurements using Quasi-Monoenergetic Neutron Field from 20 to 150 MeV", OECD/NEA, 2nd Specialists' Meet. on Shielding Aspects of Accelerators, Targets and Irradiation Facilities, CERN, Geneva, Switzerland, Oct. (1995).
- K. Oyamatsu: "Symmetry Energy at Subnuclear Densities and Its Implications on Unstable Nuclei and Non-spherical Nuclei in the Neutron-Star Crust", RCNP Workshop on Relativistic Approaches in Nuclear Structure and Reactions, RCNP, Osaka, Nov. (1995).
- A. Mengoni: "Direct Radiative Capture Mechanisms and the Structure of Light Nuclei", Ann. Meet. on Nuclear Data, JAERI, Tokai, Nov. (1995).
- T. Suzuki: "Radii of Sodium Isotopes", Invited talk at Int. Chem. Congr., Hawaii, U.S.A., Dec. (1995).

3. Atomic and solid-state physics

- J. Z. Tang and I. Shimamura: "Calculations of Photodetachment from H^- by the Hyperspherical Close-Coupling Method II", Fall Meet. Phys. Soc. Jpn., Shizuoka, Sept. (1994).
- M. Kimura, I. Shimamura, and M. Inokuti: "Double and Single Ionization of He and H_2 by Slow Protons and Antiprotons", US-Mexico Workshop on Atomic Physics, San Juan del Rio, Mexico, Dec. (1994).
- J. Z. Tang and I. Shimamura: "Resonances in the Photodetachment of H^- ", Symp. on Atomic and Molecular Processes in the Space, Sagami-hara, Dec. (1994).
- I. Shimamura: "Recent Topics on the Theory of Antiprotonic Helium", 3rd RIKEN Symp. on the Theory of Atomic and Molecular Processes, Wako, Feb. (1995).
- Y. Kanai, Y. Nakai, T. Kambara, T. M. Kojima, M. Oura, and Y. Awaya: "Impact Parameter Dependence of Double-Electron Capture Processes in Low-Energy Highly-Charge Ion Collisions", Symp. on the Physics of Highly-Charged Ions, Tokyo, Feb. (1995).
- B. DePaola: "Binary Encounter Electron Production at Relativistic Collision Velocities", RIKEN Symp. on Researchers on Solid State Physics and Materials, Atomic Physics, Nuclear Chemistry, Biological and Material Medical Sciences Using RIKEN Ring Cyclotron VIII, Wako, Feb. (1995).
- I. Shimamura: "Theory of Muon-Catalyzed Fusion", Symp. on Elementary Atomic Processes for the Developments of Nuclear Reactors, Tokaimura, Mar. (1995).
- T. Yoshida, N. Jiang, and D. M. Schrader: "Chemically Stable Compounds of Positrons with Ordinary Atoms and Molecules", Meet. American Physical Society, Milwaukee, U.S.A., Mar. (1995).
- I. Shimamura: "Recent Topics on Muon-Catalyzed Fusion Theory", RIKEN Symp. on Muon Sciences '94/UTMSL Users' Meet., Wako, Mar. (1995).
- Y. Awaya: "X-ray Emitted by Electronic Transition in Muonic Atoms", *ibid.*
- T. Okada, Y. Noro, H. Kitazawa, Y. Kobayashi, and F. Ambe: " ^{61}Ni Mössbauer in Spinel Chromites II", 50th Meet. Phys. Soc. Jpn., Yokohama, Mar. (1995).
- R. Kadono, A. Matsushita, R. M. Macrae, K. Nishiyama, and K. Nagamine: "Muonium Centers in Si and Ge under Photo-Excitation", *ibid.*
- Q. Hui, J. L. Persson, M. Nakamura, and M. Takami: "Highly Excited Atoms in Liquid Helium", *ibid.*

- T. Fujita, N. Nishimori, F. Wakamatsu, K. Maeda, H. Akiyoshi, A. Motoshima, H. Nakamura, K. Sagara, and T. Nakashima: "Production of Polarized Neutron Beam Around 12 MeV and Precise Determination of Polarization", *ibid.*
- J. Z. Tang and I. Shimamura: "Calculation of Angular Distribution of Photoelectrons from He", *ibid.*
- J. Z. Tang: "One-Photon Double Ionization of He", *ibid.*
- M. Kimura and I. Shimamura: "Difference in the Mechanisms of Double Ionization by Low-Energy Protons and Antiprotons", *ibid.*
- Y. Bitoh, H. Suzuki, A. Itoh, M. Imai, N. Imanishi, Y. Nakai, T. Kambara, Y. Kanai, T. M. Kojima, and Y. Awaya: "Incident Ion Dependence of the Fragmentation of C₆₀", *ibid.*
- M. Oura, Y. Itoh, T. Koizumi, T. M. Kojima, M. Gonno, M. Sano, T. Sekioka, H. Yamaoka, N. Watanabe, and Y. Awaya: "Ionization of Eu⁺ Ions Due to 5p Photoexcitations", *ibid.*
- H. Schmidt-Böcking: "He Double Ionization Investigated by Cold Target Recoil Ion Momentum Spectroscopy", *ibid.*
- B. D. DePaola: "Experimental Absolute Charge Capture Cross Sections for Highly Charged Xenon on a Rydberg Target", *ibid.*
- I. Shimamura: "Cross Sections for Collisions of Molecules with Subexcitation Electrons", Workshop on Electron Degradation Processes, Cambridge, Massachusetts, U.S.A., Apr. (1995).
- Y. Kanai, Y. Nakai, K. Soejima, T. M. Kojima, T. Kambara, and Y. Awaya: "Present Status and Future Plans of RIKEN 14.5 GHz Caprice", 12th Int. Workshop on ECR Ion Sources, Wako, Apr. (1995).
- S.F.C.O' Rourke, I. Shimamura, and D.S.F. Crothers: "CDW-EIS Recoil DCS for Single Ionization in Proton-Helium Collisions", European Conf. on Atomic and Molecular Physics, Edinburgh, U.K., Apr. (1995).
- H. Kageyama, K. Kawatsura, R. Takahashi, S. Arai, H. Takeshita, Y. Aoki, S. Yamamoto, P. Geoppelt-Langer, H. Naramoto, T. Kambara, M. Oura, T. Papp, Y. Kanai, Y. Awaya, H. Horino, Y. Mokuno, and K. Fujii: "L X-ray Spectra of Fe and Cu by 0.75 MeV/u H, He, Si, and Ar Ion Impacts", 3rd Int. Symp. on Swift Heavy Ions in Matter, Carn, France, May (1995).
- K. Sagara: "Precise Experiments on N-d Scattering and Capture Reaction", Recent Progress in Nuclear Reaction Study, Tokyo, May (1995).
- H. Saitoh, K. Soejima, S. Kravis, K. Okuno, and N. Kobayashi: "Single and Multiple Electron Capture Cross Sections in Low-Energy Multiply Charged Ion-Atom Collisions", 1995 Joint Meet. on the Mass Spectrometry, Hachioji, May (1995).
- I. Shimamura and M. Kimura: "Molecular Theory of Antiprotonic and Other Exotic Helium", Int. Symp. on Muon Catalyzed Fusion and Physics of Exotic Atoms and Molecules, Dubna, Russia, June (1995).
- M. Kimura and I. Shimamura: "Double and Single Ionization of He and H₂ by Proton and Antiproton Impact", *ibid.*
- A. Igarashi, T. Shirai, N. Toshima, and I. Shimamura: "Muon-Transfer Reaction $d\mu(n = 2) + t \rightarrow d + t\mu(N = 2)$ ", *ibid.*
- Y. Nakai: "Fragmentation of C₆₀ in Fast Ion-C₆₀ Collision", YITP Symp. on the Similarity and Difference between Nuclei and Microclusters, Kyoto, June (1995).
- K. Kawatsura, H. Kageyama, R. Takahashi, Y. Nakai, D. Hamaguchi, S. Arai, Y. Aoki, S. Yamamoto, P. Geoppelt-Langer, H. Takeshita, H. Naramoto, T. Kambara, M. Oura, T. Papp, Y. Kanai, and Y. Awaya: "L X-ray Emission Spectra of Fe and Cu Induced by Heavy Ions", 4th TIARA Res. Rev. Meet., Tokyo, June (1995).
- J. Z. Tang and I. Shimamura: "Differential Cross Sections for Photoionization of He", Int. Symp. on Atomic and Molecular Dynamics in Photoionization, Quebec, Canada, July (1995).
- E. Yagi: "Channelling Study on the Behaviour of Kr Atoms Implanted in Aluminium", 16th Int. Conf. on Atomic Collisions in Solids, Linz, Austria, July (1995).
- M. Oura, Y. Awaya, M. Gonno, Y. Itoh, M. Kimura, T. Koizumi, T. M. Kojima, M. Sano, T. Sekioka, N. Watanabe, and H. Yamaoka: "Photoionization of Eu⁺ in the Region of 5p Excitation", 19th Int. Conf. on the Physics of Electronic and Atomic Collisions (XIX ICPEAC), Whistler, Canada, July-Aug. (1995).
- T. M. Kojima, Y. Awaya, M. Gonno, Y. Itoh, M. Kimura, T. Koizumi, M. Oura, M. Sano, T. Sekioka, N. Watanabe, and H. Yamaoka: "Photoionization of Eu⁺ in the 4d Giant Resonance Region", *ibid.*
- M. Sano, Y. Awaya, M. Gonno, Y. Itoh, T. Koizumi, T. M. Kojima, S. D. Kravis, M. Oura, T. Sekioka, N. Watanabe, and A. Yagishita: "Photoion Yield Spectroscopy in the 4d Shell of Xe⁺", *ibid.*
- T. Kambara, Y. Awaya, Y. Kanai, T. M. Kojima, Y. Nakai, O. Jagutzki, V. Mergel, H. Schmidt-Böcking, B. D. DePaola, J. Z. Tang, M. Kimura, and I. Shimamura: "Momentum Distribution of Recoil Ions from 8.7 MeV O⁷⁺-He Collisions", *ibid.*
- Y. Itoh, T. Koizumi, S. D. Kravis, M. Oura, M. Sano, T. Sekioka, and Y. Awaya: "Photoionization of Sr⁺ Ions in 3d Ionization Region", *ibid.*
- M. Oura, Y. Awaya, M. Gonno, Y. Itoh, M. Kimura, T. Koizumi, T. M. Kojima, M. Sano, T. Sekioka, N. Watanabe, and H. Yamaoka: "Photoionization of Eu⁺ in the Region of 5p Excitation", *ibid.*
- A. Igarashi: "Calculation of Ionization Cross Sections in Positron-Hydrogen Scattering", *ibid.*
- J. Z. Tang and I. Shimamura: "Double Photoionization of He by the Hyperspherical Close-Coupling

- Method”, *ibid.*
- J. Z. Tang and I. Shimamura: “Angular Distributions of Photoelectrons from Helium”, *ibid.*
- A. Itoh, Y. Bitoh, Y. Nakai, H. Suzuki, M. Umezawa, M. Imai, N. Imanishi, T. Kambara, and Y. Awaya: “Projectile Dependence of C₆₀-Fragmentation by the Impacts of MeV Energy H, Li, C, Si, and Au Ions”, *ibid.*
- Y. Nakai, A. Itoh, T. Kambara, Y. Bitoh, and Y. Awaya: “Coincidence Measurement of Fragment Ions with Final Charge State of Projectile Ion in Fast Carbon Ion-C₆₀ Collision”, *ibid.*
- M. Kimura and I. Shimamura: “Double and Single Ionization of H₂ by Proton and Antiproton Impact at 10 keV”, *ibid.*
- J. F. McCann, I. Shimamura, and T. Watanabe: “Muon Capture by Helium and Molecular Hydrogen”, *ibid.*
- Y. Kino, M. R. Harston, I. Shimamura, E. A. G. Armour, and M. Kamimura: “Normalization of the Asymptotic Form of Three-Body (*dtμ*)⁺ and (*ddμ*)⁺ Wave Functions”, *ibid.*
- S. F. O. O’ Rourke, I. Shimamura, and D. S. F. Crothers: “CDW-EIS Recoil DCS for Single Ionization of Helium by Proton Impact”, *ibid.*
- B. D. DePaola, M.-T. Huang, S. Winecki, M. P. Stöckli, Y. Kanai, S. R. Lundeen, C. W. Fehrbach, and S. A. Arko: “Absolute Cross Sections for Charge Capture from Rydberg Targets by Slow Highly Charged Ions”, *ibid.*
- B. D. DePaola, Y. Kanai, P. Richard, Y. Awaya, T. Kambara, and Y. Nakai: “Binary Encounter Electron Production at Relativistic Collision Velocities”, *ibid.*
- K. Sagara, A. Motoshima, T. Fujita, H. Akiyoshi, N. Nishimori, and K. Maeda: “A Blow-In Type Windowless Gas Target”, Int. Nucl. Phys. Conf., Beijing, China, Aug. (1995).
- N. Nishimori, K. Sagara, T. Fujita, H. Akiyoshi, K. Maeda, H. Nakamura, and T. Nakashima: “Production of Low-Energy Polarized Neutron Beam”, *ibid.*
- J. Z. Tang and I. Shimamura: “Differential Cross Sections for Photoionization of He”, 11th Int. Conf. on Vacuum Ultraviolet Radiation Physics, Tokyo, Aug. (1995).
- T. Kambara, Y. Awaya, A. Igarashi, Y. Kanai, T. M. Kojima, Y. Nakai, O. Jagutzki, V. Mergel, and H. Schmidt-Böcking: “Electron Capture and Transfer Ionization in 8.7 MeV O⁷⁺ - He Collisions”, 14th Int. Seminar on Ion-Atom Collisions, Seattle, U.S.A., Aug. (1995).
- T. Koizumi, Y. Awaya, M. Gonno, Y. Itoh, M. Kimura, T. M. Kojima, S. Kravis, M. Oura, M. Sano, T. Sekioka, N. Watanabe, H. Yamaoka, and F. Koike: “4d Photoionization of Singly-Charged Xe, Ba, and Eu Ions”, Int. Conf. on Vacuum Ultraviolet Radiation Physics, Tokyo, Aug. (1995).
- I. Shimamura: “Exotic Atoms and Molecules”, Meet. of the Meson Science Association, Wako, Aug. (1995).
- R. Kadono, R. M. Macrae, A. Matsushita, K. Nishiyama, and K. Nagamine: “Bistability of Muonium Centers in Crystalline Si and Ge Proved by Photo-Induced μ SR”, 9th Int. Conf. Hyperfine Interactions, Leuven, Belgium, Aug.-Sept. (1995).
- Y. Kobayashi, T. Okada, Y. Noro, H. Kitazawa, and F. Ambe: “Giant Magnetic Hyperfine Field of Ni²⁺ Ions in Spinel Chromites”, 1995 Int. Conf. on Applications of Mössbauer Effect, Rimini, Italy, Sept. (1995).
- J. Nakamura, Y. Kobayashi, K. Asai, N. Yamada, and F. Ambe: “⁵⁷Fe Mössbauer Spectroscopy of Fe_{1+x}Sb”, *ibid.*
- R. Kadono: “Bistability of Muonium Centers in Crystalline Si and Ge Probed by Photo-Induced μ SR”, Invited Talk at the Autumn Meet. of the British Radiofrequency Spectroscopy Group, Oxford, U.K., Sept. (1995).
- K. Kawatsura, R. Takahashi, H. Kageyama, Y. Nakai, D. Hamaguchi, A. Nishihata, S. Arai, T. Kambara, M. Oura, T. Papp, Y. Kanai, Y. Awaya, Y. Aoki, S. Yamamoto, H. Takeshita, P. Goppelt-Langer, H. Naramoto, Y. Horino, Y. Mokuno, and K. Fujii: “Fine Structure of L X-Ray Emission Spectra of Fe and Cu”, 13th PIXE Symp., Tokyo, Sept. (1995).
- J. Z. Tang and I. Shimamura: “Hyperspherical Close-Coupling Approach to Single and Double Photoionization of Two-Electron Systems”, Oji Int. Seminar on Atomic and Molecular Photoionization, Tsukuba Sept. (1995).
- N. Nishimori, K. Sagara, T. Fujita, F. Wakamatsu, H. Akiyoshi, H. Nakamura, K. Maeda, and T. Nakashima: “Precise Measurement of Analyzing Powder of D(\bar{n}, n) Scattering at 12 MeV”, 1995 Fall Meet. Phys. Soc. Jpn., Kasugai, Sept. (1995).
- T. Okada, Y. Noro, H. Kitazawa, Y. Kobayashi, and F. Ambe: “Relation between Hyperfine Magnetic Field at ⁶¹Ni and Ligand Distortion”, 1995 Fall Meet. Phys. Soc. Jpn., Sakai, Sept. (1995).
- R. Kadono, R. F. Kiefl, W. A. MacFarlane, and S. R. Dunsiger: “Diffusion and Localization of Muonium in KCl:Na”, *ibid.*
- T. Okada, Y. Noro, H. Kitazawa, Y. Kobayashi, J. Nakamura, and F. Ambe: “Magnetization and ⁶¹Ni Mössbauer on Spinel Rhodites”, *ibid.*
- K. Ishii, Y. Kimura, T. Nishida, and K. Ando: “Beam-Foil Spectra of Highly Charged Neon Ions”, *ibid.*
- K. Hamada, M. Ohsawa, E. Kajiro, W. G. Jin, H. Uematsu, T. Minowa, and H. Katsuragawa: “Measurement of Isotope Shifts of Fe by Resonance Ionization Spectroscopy”, *ibid.*
- Q. Hui, J. L. Persson, M. Nakamura, and M. Takami: “LIF Spectra of Ag-He Complex in Liquid Helium”, *ibid.*

- M. Nakamura, J. L. Persson, Q. Hui, and M. Takami: "LIF Spectra of Ag-He Complex in Cold Helium Gas", *ibid.*
- T. Kambara: "Future Projects of RIKEN Accelerator Research Facility", 19th Ann. Meet. of the Society for Atomic Collision Research, Tokyo, Oct. (1994).
- J. Z. Tang and I. Shimamura: "Photoionization of He from an Excited State", Int. Workshop on Photoionization, San Francisco, U.S.A., Oct. (1994).
- Y. Kobayashi, T. Okada, Y. Noro, H. Kitazawa, and F. Ambe: " ^{61}Ni Mössbauer Spectroscopy of Ni Oxides with Spinel Structure", 39th Symp. Radiochemistry, Niigata, Oct. (1995).
- Y. Kobayashi, Y. Yoshida, H. Häßlein, K. Yukihiro, K. Hayakawa, Y. Watanabe, A. Yoshida, T. Nakamura, M. Ishihara, N. Inabe, M. Kase, A. Goto, Y. Yano, and F. Ambe: "Development of In-Beam Mössbauer Spectroscopy at RALF", *ibid.*
- J. Z. Tang and I. Shimamura: "Hyperspherical Close-Coupling Approach to High-Lying Double Excited States of He and H^- ", 5th Int. Workshop on Autoionization Phenomena in Atoms (AIS-95), Dubna, Russia, Dec. (1995).
- E. Yagi: "Perspectives of Accelerator-Using Analysis-RBS", 4th Nucl. Res. Center of Univ. Tokyo Symp., Tokyo, Dec. (1995).
4. Radiochemistry, radiation chemistry, and radiation biology
- T. Abe, S. Yoshida, T. Sakamoto, T. Kameya, S. Kitayama, N. Inabe, M. Kase, A. Goto, and Y. Yano: "Is Irradiation of Heavy Ion Beams at Specific stages of the Fertilization Cycle of Plants Effective for Mutagenesis?", Japan-U.S.A. Workshop on Modification of Gene Expression and Non-Mendelian Inheritance, Tsukuba, Jan. (1995).
- S. Yamago, H. Tokuyama, E. Nakamura, K. Kikuchi, K. Sueki, S. Kaneko, M. Nakahara, S. Enomoto, and F. Ambe: "In Vivo Biological Behavior of Water-Miscible Fullerenes. ^{14}C -Labeling, Absorption, Distribution, Excretion and Acute Toxicity", 8th Symp. of Fullerenes, Kyoto, Jan. (1995).
- S. Enomoto, M. Yanaga, R. Hirunuma, K. Endo, S. Ambe, and F. Ambe: "Bio-Trace Elemental Research Using the Multitracer Technique (1)", RIKEN Symp. on Studies on Condensed Matter Physics, Atomic Physics, Nuclear Chemistry, and Biology and Medicine Using RIKEN Ring Cyclotron VII, Wako, Feb. (1995).
- S. Enomoto and F. Ambe: "Study of Bio-Trace Element Using a Muon X-ray Technique", *ibid.*
- M. Iwamoto, S. Ambe, S. Enomoto, H. Maeda, and F. Ambe: "Preparation of a Multitracer by Heating under a Reduced Pressure a Tin Target Irradiated with Heavy Ions", 69th Natl. Meet. Chem. Soc. Jpn. (Spring), Kyoto, Mar. (1995).
- A. Shinohara, S. Kiryu, K. Soga, T. Muroyama, M. Furukawa, S. Kojima, Y. Ohkubo, F. Ambe, K. Mukai, A. Yokoyama, T. Saito, and H. Baba: "Differential Recoil Ranges of Reaction Products in the Cu^{+40}Ar , ^{14}N Nuclear Reactions", *ibid.*
- M. Yanaga, S. Enomoto, K. Miyabayashi, R. Hirunuma, K. Endo, S. Ambe, M. Tozawa, and F. Ambe: "Study on Uptake and Distribution of Various Elements in Rats using the Multitracer Technique (3) Distribution and Behaviour of Trace Elements Produced from Au Target", *ibid.*
- M. Yanaga, R. Hirunuma, H. Minami, K. Endo, S. Enomoto, S. Ambe, M. Tozawa, and F. Ambe: "Study on Uptake and Distribution of Various Elements in Rats using the Multitracer Technique (4) Distribution and Behaviour of Trace Elements Produced from Ge Target", *ibid.*
- Y. Takahashi, Y. Minai, S. Ambe, S. Enomoto, M. Iwamoto, H. Maeda, F. Ambe, and T. Tominaga: "Influence of Humic Acid on Adsorption of Ions on Kaolinite or Silica Gel -Application of Multitracer Technique-", *ibid.*
- K. Mukai, A. Yokoyama, T. Saito, H. Baba, Y. Ohkubo, A. Shinohara, and M. Furukawa: "Incomplete Fusion in the Intermediate Energy Region", *ibid.*
- T. Shinonaga, S. Ambe, S. Enomoto, H. Maeda, M. Iwamoto, T. Watanabe, and I. Yamaguchi: "The Absorption of Various Elements into Plant in Atmosphere-Plant System, The Application of the Multitracer", *ibid.*
- S. Ambe and F. Ambe: "Emission and Absorption Mössbauer Spectra of Tin with Ligands from Silver to Iodine", *ibid.*
- K. Endo, R. Hirunuma, M. Yanaga, M. Tozawa, S. Enomoto, S. Ambe, and F. Ambe: "Behavior of Trace Elements in Rats Using the Multitracer Technique (1) Absorption and Distribution of Trace Elements by Oral Administration", 115th Ann. Meet. Pharm. Soc. Jpn., Sendai, Mar. (1995).
- S. Enomoto, S. Ambe, F. Ambe, K. Endo, R. Hirunuma, and M. Yanaga: "Behavior of Trace Elements in Rats Using the Multitracer Technique (2) Tissue Distribution of Trace Elements in Zinc Deficient Rats", *ibid.*
- R. Hirunuma, K. Endo, M. Yanaga, S. Enomoto, S. Ambe, and F. Ambe: "Behavior Trace Elements in Rats Using the Multitracer Technique (3) Tissue Distribution of Trace Elements in Vitamin D Overloaded Rats", *ibid.*
- T. Ozaki, S. Enomoto, Y. Minai, S. Ambe, F. Ambe, and T. Tominaga: "Distribution of REE in Ferns", 12th Symp. on Rare Earth Element, Tokyo, May (1995).
- Y. Takahashi, Y. Minai, S. Ambe, M. Iwamoto, S. Enomoto, H. Maeda, N. Takematsu, F. Ambe, and T. Tominaga: "Evaluation of Environmental Behavior of Trace Metal Elements by Multitracer Tech-

- nique: Influence of Humate Formation”, 56th Conf. Analytical Chemistry, Osaka, May (1995).
- S. Enomoto, B. Liu, R. Amano, S. Ambe, and F. Ambe: “Biodistribution of Rare Earth Elements in Diabetes Model Mice 2”, 4th Ann. Meet. of the Rare Earth Soc. Jpn., Tokyo, May (1995).
- S. Enomoto, M. Yanaga, R. Hirunuma, K. Endo, S. Ambe, and F. Ambe: “Metabolism and Behaviour of Various Rare Earth Elements in Rats Using the Multitracer Technique”, *ibid.*
- F. Ambe: “The Multitracer”, CHRT Forum’95 Tokyo, Tokyo, May (1995).
- T. Shinonaga, S. Ambe, S. Enomoto, H. Maeda, M. Iwamoto, T. Watanabe, and I. Yamaguchi: “Multitracer Study on Behavior of Various Elements in Atmosphere-Plant System”, Int. Conf. on Isotopes’95, Beijing, China, May (1995).
- S. Ambe, M. Iwamoto, H. Maeda, and F. Ambe: “Multitracer Study on Adsorption of Metal Ions on α - Fe_2O_3 ”, *ibid.*
- S. Enomoto, M. Yanaga, R. Hirunuma, K. Endo, S. Ambe, and F. Ambe: “Multitracer Study on Distribution of Carrier-Free Radioactive Isotopes in Organs of Rats”, *ibid.*
- Y. Takahashi, Y. Minai, T. Ozaki, S. Ambe, M. Iwamoto, H. Maeda, F. Ambe, and T. Tominaga: “Multitracer Study on the Effect of Humate Formation on the Adsorption Behavior of Metal Ions on Kaolinite and Silica Gel”, *ibid.*
- S. Enomoto, S. Ambe, and F. Ambe: “Usefulness of the Multitracer Technique in Research of Bio-Trace Elements”, 7th Symp. on Roles of Metals in Biological Reactions, Biology and Medicine, Hamamatsu, June (1995).
- S. Enomoto, R. Amano, S. Ambe, and F. Ambe: “Biobehavior of Various Rare Earth Elements in Diabetes Mellitus Mice”, *ibid.*
- R. Hirunuma, K. Endo, M. Yanaga, S. Enomoto, S. Ambe, and F. Ambe: “Behavior of Various Trace Elements in Vitamin D Overloaded Rats Using Multitracer Technique”, *ibid.*
- S. Enomoto, S. Ambe, and F. Ambe: “Significance of the Bio-Trace Elemental Research in Metabolic Physiology on Space Field: Metabolism in Bio-Organisms on Non-Gravitational Field by Using the Multitracer Technique”, 12th Space Utilization Symp., Tokyo, July (1995).
- S. Ambe, R. Hirunuma, S. Enomoto, M. Yanaga, R. Amano, K. Endo, and F. Ambe: “Radioactive Multitracer Technique for the Study of Trace Elements in Rats and Mice”, 5th COMTOX Symp. on Toxicology and Clinical Chem. of Metals, Vancouver, Canada, July (1995).
- R. Hirunuma, K. Endo, M. Yanaga, S. Enomoto, S. Ambe, and F. Ambe: “Study on Distribution of Trace Elements in Vitamin D Overloaded Rats Using the Multitracer Technique”, *ibid.*
- S. Enomoto, M. Yanaga, R. Hirunuma, K. Endo, S. Ambe, and F. Ambe: “Distribution and Behavior of Trace Elements in Zinc Deficient Rats Using the Radioactive Multitracer Technique”, *ibid.*
- H. Yasuda, S. Uchida, S. Ambe, B. Liu, H. Maeda, S. Enomoto, and F. Ambe: “Distribution Coefficient between Soil Solid and Liquid Phase Obtained by Multitracer Technique”, 32nd Ann. Meet. on Radioisotopes in the Physical Sciences and Industries, Tokyo, July (1995).
- T. Ozaki, S. Enomoto, Y. Minai, S. Ambe, F. Ambe, and T. Tominaga: “Study on Accumulation of Lanthanides in *Dryopteris erythrosora* by Multitracer Technique”, *ibid.*
- Y. Takahashi, Y. Minai, S. Ambe, M. Iwamoto, H. Maeda, F. Ambe, and T. Tominaga: “Multitracer Study on Distribution of Metal Ions between Solid and Aqueous Phases in the Environment”, *ibid.*
- Y. Itoh, T. Kakizaki, K. Tanaka, A. Goto, N. Nakanishi, M. Kase, N. Oshima, T. Suzuki, I. Kanazawa, T. Nakajyo, and Y. Ito: “Slow Positron Production using RIKEN AVF Cyclotron II”, *ibid.*
- B. Liu, S. Ambe, S. Enomoto, and F. Ambe: “Application of Radioactive Multitracer to the Study of Labelling of Antibody”, *ibid.*
- T. Watanabe, K. Matsumoto, S. Ambe, and I. Yamaguchi: “Translocation of Radionuclides from Plant Leaf Surfaces”, *ibid.*
- T. Kakizaki, Y. Itoh, K. H. Lee, K. Tanaka, A. Goto, N. Nakanishi, M. Kase, and Y. Ito: “Generation of Slow Positron Beam from Short Lifetime Positron Emitters”, 56th Meet. Jpn. Soc. Appl. Phys., Kanazawa, Aug. (1995).
- K. Eguchi-Kasai: “Radiation Quality and the Relationship among Cellular Radiosensitivity, DNA Repair and RBE”, 10th Int. Natl. Congr. Radiat. Res., Wuerzburg, Germany, Aug. (1995).
- F. Ambe: “Multitracer-A Versatile Tracer Technique Developed from Heavy Ion Physics”, 2nd Int. Symp. on Heavy Ion Physics and Its Applications, Lanzhou, China, Aug. (1995).
- Y. Yanagida, J. Nakamura, K. Asai, N. Yamada, Y. Ohkubo, S. Ambe, T. Okada, F. Ambe, and S. Uehara, and Y. Kawase: “Studies on Structural Phase Transition of Barium-Ruthenium Metal Oxides by ^{117}In -TDPAC”, 10th Int. Conf. on Hyperfine Interactions, Leuven, Belgium, Aug.-Sept. (1995).
- K. Tanaka, Y. Itoh, K. H. Lee, T. Kakizaki, A. Goto, N. Nakanishi, M. Kase, and Y. Ito: “Development of the Targets for Online Spin-Polarized Slow Positron Beam”, 1995 Fall Meet. Phys. Soc. Jpn., Sakai, Sept. (1995).
- M. Iwata, S. Ambe, Y. Iijima, M. Iwamoto, H. Maeda, and F. Ambe: “Study of Adsorption of Metal Ions on α - Fe_2O_3 Using a Multitracer”, 39th Symp. on Radiochemistry, Shizuoka, Sept. (1995).
- R. Hirunuma, S. Enomoto, M. Yanaga, R. Amano, K. Endo, B. Liu, S. Ambe, and F. Ambe: “Multi-

- tracer Studies of Behavior of Trace Elements in Rats and Mice", 7th Int. Conf. on Bioinorganic Chemistry, Lübeck, Germany, Sept. (1995).
- S. Enomoto, B. Liu, R. G. Weginwar, R. Amano, S. Ambe, and F. Ambe: "In Vivo Behavior of Various Rare Earth Elements in Lipogenous Diabetes Model Mice by Using the Multitracer Technique", *ibid.*
- T. Ozaki, S. Enomoto, Y. Minai, S. Ambe, F. Ambe, and T. Tominaga: "Determination of Lanthanides and Other Trace Elements in Ferns by Instrumental Activation Analysis", 9th Int. Conf. on Modern Trends in Activation Analysis, Seoul, Korea, Sept. (1995).
- Y. Okamoto, S. Enomoto, and R. Hirashima: "Try to Make a Gamma Camera Using Cooled CCD", Jpn. Soc. Nucl. Med., 35th Ann. Meet., Yokohama, Oct. (1995).
- T. Abe, T. Sakamoto, S. Kumata, T. Torashima, and S. Yoshida: "New Mutation Method using Specific Stages of the Fertilization Cycle of Plants", 30th Ann. Meet. Soc. Chem. Regul. Plants, Utsunomiya, Oct. (1995).
- N. Ito, I. Kunugiyama, A. Iwatsuki, M. Ito, S. Ambe, S. Enomoto, and F. Ambe: "Measurement of Potassium, Rubidium and Cesium Influx Rate into Erythrocyte using Multitracer Technique", 39th Symp. on Radiochemistry, Niigata, Oct. (1995).
- K. Mukai, A. Yokoyama, T. Saito, H. Baba, Y. Ohkubo, S. Kiryu, C. Murata, T. Muroyama, A. Shinohara, and M. Furukawa: "Heavy-Ion Reactions for the $^{14}\text{N}+^{165}\text{Ho}$ and the $^{40}\text{Ar}+^{141}\text{Pr}$ Systems at Intermediate Energies", *ibid.*
- A. Shinohara, S. Kiryu, K. Mukai, T. Muroyama, J. Kurachi, S. Kojima, T. Saito, A. Yokoyama, Y. Ohkubo, M. Furukawa, and F. Ambe: "Angular Distribution of Fission Fragments in the Heavy-Ion Reaction of Gold in the Intermediate Energy Range", *ibid.*
- B. Liu, S. Ambe, S. Enomoto, H. Maeda, R. Weginwar, and F. Ambe: "Group Separation of a Multitracer from a Gold Target Irradiated by High-Energy Heavy Ions", *ibid.*
- R. G. Weginwar, Y. Kobayashi, S. Ambe, B. Liu, S. Enomoto, and F. Ambe: "Separation of a Multitracer from an Au Target Irradiated by Heavy Ions", *ibid.*
- B. Liu, S. Enomoto, S. Ambe, and F. Ambe: "Biodistribution Study of Antibodies Labelled with Multitracer in Mice", *ibid.*
- A. Sekiguchi, N. Ito, N. Furusato, Y. Saito, K. Kimura, H. Maeda, S. Ambe, and F. Ambe: "Studies on the Ion Exchange Adsorption Behavior of Strongly Acidic Resin Nation and its Application to Analytical Chemistry", *ibid.*
- S. Enomoto, B. Liu, R. G. Weginwar, H. Maeda, S. Ambe, and F. Ambe: "Physiological and Biochemical Investigations of Bio-Trace Elements in Various Disease Model Animals", *ibid.*
- T. Ozaki, S. Enomoto, Y. Minai, S. Ambe, F. Ambe, and T. Tominaga: "Activation Analysis Study on Distribution of Trace Elements in Ferns", *ibid.*
- R. Hirunuma, K. Endo, S. Enomoto, M. Yanaga, B. Liu, S. Ambe, and F. Ambe: "Distribution of Trace Elements in Vitamin D Overloaded Rats Using the Multitracer Techniques", *ibid.*
- M. Yanaga, R. Endo, S. Enomoto, R. Hirunuma, B. Liu, K. Endo, S. Ambe, M. Tozawa, H. Nakahara, and F. Ambe: "Application of the Multitracer Technique for a Study on Distribution of Trace Elements, in LEC Rats", *ibid.*
- M. Yanaga, R. Yamamoto, S. Enomoto, S. Futatsugawa, R. Hirunuma, K. Endo, M. Tozawa, and F. Ambe: "Determination of Trace Elements in Organs of Rats by PIXE and Neutron Activation Analysis", *ibid.*
- H. Sasaki, F. Yatagai, Y. Furusawa, T. Kanai, F. Hanaoka, and W. G. Zhu: "Dependence of Interphase Cell-Death Induction on LET Values of Accelerated Heavy-Ions", 38th Ann. Meet. Jpn. Radiation Res. Soc., Chiba, Nov. (1995).
- S. Kitayama, K. Narumi, M. Kikuchi, and H. Watanabe: "Construction of Cosmid Library of *Deinococcus radiodurans*", *ibid.*
- I. Narumi, H. Watanabe, A. B. M. M. Hossain, A. Tanaka, and S. Kitayama: "Cloning and Base Sequence of Radiation Induced Catarase of *Deinococcus radiodurans*", *ibid.*
- Y. Minai, Y. Takahashi, T. Ozaki, S. Enomoto, S. Abe, B. Liu, F. Ambe, and T. Tominaga: "Multitracer Study on the Environmental Behavior of Trace Elements", 1995 Ann. Meet. Geochem. Soc. Jpn., Shimizu, Nov. (1995).
- Y. Takahashi, Y. Minai, S. Ambe, H. Maeda, F. Ambe, and T. Tominaga: "Formation of Humate Complexes with Various Metal Ions -Application of Multitracer Technique", 11th Meet. on Humic Substances, Tokai, Nov. (1995).
- K. Narumi, H. Watanabe, and S. Kitayama: "Comparative Studies of Thermotolerance of RecA Proteins of *Deinococcus* and *Thermus*", 18th Ann. Meet. Jpn. Mol. Biol. Soc., Nagoya, Dec. (1995).
- A. Yokoyama, K. Mukai, K. Takesako, T. Saito, H. Baba, Y. Ohkubo, A. Shinohara, and M. Furukawa: "Recoil Properties of the Products in the Heavy-Ion Reactions at Intermediate Energy", 1995 Int. Chem. Congr. Pacific Basin Soc., Honolulu, U.S.A., Dec. (1995).

5. Material analysis

- K. Maeda: "Application of Particle Induced X-Ray Emission (PIXE) to Liquid Samples", 62nd Spring Meet. Electrochemical Soc. Jpn., Tokyo, Apr. (1995).
- N. Arai, Y. Nagata, W. Sakamoto, K. Maeda, and K. Yoshida: "Correlation between Trace Elements

- in Red Sea Bream Otoliths and Ambient Temperature”, 1995 Spring Meet. Jpn. Soc. Fish. Sci., Tokyo, Apr. (1995).
- N. Arai, W. Sakamoto, and K. Maeda: “An Attempt to Analyze Fish Otoliths by In-Air PIXE”, 7th Int. PIXE Conf., Padova, Italy, May (1995).
- H. Hamanaka, K. Hasegawa, and K. Maeda: “Study of Sample Charging Effects on Satellite Peaks by Means of High Resolution PIXE”, *ibid.*
- J. Kawai, K. Maeda, N. Sakauchi, and I. Konishi: “Strong X-Ray Emission Due to Electrification”, *ibid.*
- M. Kumagai and M. Iwaki: “Luminescence of Al₂O₃ Implanted with Rare Earth Element (IV)”, 56th Autumn Meet. Jpn. Soc. Appl. Phys., Nonoichi, Aug. (1995).
- J. Kawai, S. Hayakawa, Y. Kitajima, K. Maeda, and Y. Gohshi: “Total Reflection X-Ray Photoelectron Spectroscopy of Ag”, 1995 Fall Meet. Phys. Soc. Jpn., Sakai, Sept. (1995).
- Y. Ikeda, N. Arai, W. Sakamoto, T. Murayama, K. Maeda, and K. Yoshida: “Trace Element Analysis of Japanese Common Squid Statoliths”, 1995 Autumn Meet. Jpn. Soc. Fish. Sci., Kyoto, Sept. (1995).
- Y. Ikeda, N. Arai, W. Sakamoto, T. Murayama, K. Maeda, and K. Yoshida: “Trace Elemental Analysis of Hard Tissues of Marine Lives: In the Case of Squids”, 13th PIXE Symp., Tokyo, Sept. (1995).
- N. Arai, N. Takai, W. Sakamoto, K. Yoshida, and K. Maeda: “Trace Elemental Analysis of Fish Otoliths-III”, *ibid.*

X. LIST OF SYMPOSIA

(Jan.–Dec. 1995)

- 1) Structure Functions of Nucleons and Nuclei
17–18 Jan., Wako, RIKEN, Cyclotron Lab.
- 2) 8th Symp. on Solid State Physics and Materials, Atomic Physics, Nuclear Chemistry, and Biology and Medicine Using RIKEN Ring Cyclotron
6 Feb., Wako, RIKEN, Muon Science Lab., Atomic Physics Lab., Nuclear Chemistry Lab., and Cellular Physiology Lab.
- 3) Theory of Atomic and Molecular Processes III
17–18 Feb., Wako, RIKEN, Atomic Physics Lab.
- 4) Muon Science '94
6–7 Mar., Wako, RIKEN, Muon Science Lab.
- 5) Application of Nuclear Hyperfine Techniques to Physics and Chemistry '95
22 Mar., Wako, RIKEN, Nuclear Chemistry Lab.
- 6) Recent Progress at RIKEN Accelerator Facility
23–24 Mar., Wako, RIKEN, Linear Accelerator Lab.
- 7) 2nd RIKEN/INFN Joint Symp. on Perspectives in Heavy-Ion Physics
22–26 May, Wako, RIKEN, Radiation Lab.
- 8) Int. Symp. on Molecular Mechanisms of Mutation Induction
12–14 July, Tokyo, Cellular Physiology Lab. and Radioisotope Technology Div.
- 9) Symp. on Radiation Protection at RIKEN RI Beam Factory
8 Sept., Wako, RIKEN, Safety Center, Cyclotron Lab., and Radioisotope Technology Div.
- 10) Electron Scattering and Unstable Nuclei
1 Dec., Wako, RIKEN, Linear Accelerator Lab.
- 11) Basics and Application of Spin-Polarized Positron Beam
14 Dec., Wako, RIKEN, Nuclear Chemistry Lab.
- 12) Spin Structure of the Nucleon
18–19 Dec., Wako, RIKEN, Radiation Lab. and Cyclotron Lab.
- 13) Structure of Medium and Heavy Nuclei
26–27 Dec., Wako, RIKEN, Cyclotron Lab. and Radiation Lab.

XI. LIST OF SEMINARS

(Jan.–Dec. 1995)

Radiation Lab., Cyclotron Lab., and
Linear Accelerator Lab.

- 1) K. Takayanagi, Tokyo Denki University (Saitama), 20 Jan.
“Response Function in Extended RPA Theory”
- 2) N. Ohnishi, University of Tokyo (Tokyo), 30 Jan.
“Magnetization of Ferromagnetic Clusters”
- 3) K. Sugawara-Tanabe, Otsuma Women’s University (Tokyo), 13 Feb.
“M1 Transitions and Resurrection of LS-Coupling in Superdeformation”
- 4) I. T. Cheon, Yonsei University (Korea), 15 Feb.
“Physical Phenomena in Limited Space”
- 5) M. Tomizawa, INS (Tokyo), 31 Mar.
“On the IH Linac at INS”
- 6) H. Sato, RIKEN (Saitama), 10 Apr.
“Systematics of Alpha Q-value: Potential Dependence of Alpha Decay Life Time”
- 7) S. Kuyucak, Australian National University (Australia), 21 Apr.
“High-Spin States in Boson Models with Applications to Actinide Nuclei”
- 8) A. Ono, RIKEN (Saitama), 24 Apr.
“Heavy Ion Reactions Studied with Antisymmetrized Molecular Dynamics”
- 9) Yuko S. Mochizuki, RIKEN (Saitama), 8 May
“Nuclear Lattice Deformation Inside Neutron Stars and the Origin of Pulsar Glitches”
- 10) A. Mengoni, RIKEN (Saitama), 9 May
“The Direct Radiative Capture Process and the Halo Structure of Nuclear Excited States”
- 11) M. Hara, RIKEN (Nishi-Harima), 10 May
“RF System of SPring-8”
- 12) R. G. Lovas, Institute of Nuclear Research of the Hungarian Academy of Sciences (Hungary), 15 May
“Antisymmetrization in Cluster Decay”
- 13) Valery V. Burov, Bogoliubov Laboratory of Theoretical Physics (Russia), 31 May
“Hadron Form Factors in Relativistic Harmonic Oscillator Model”
- 14) S. Ozaki, Brookhaven National Laboratory (U.S.A.), 1 June
“On the RHIC Project”
- 15) G. Munzenberg, GSI (Germany), 5 June
“The Heaviest Elements 110 and 111: Results and Future Experiments”
- 16) R. Warner, Oberlin College (U.S.A.), 12 June
“Proton Halo in ${}^8\text{B}$? Reaction Cross Sections of It and Other Light Nuclei”
- 17) X. Ji, MIT (U.S.A.), 20 June
“Theoretical Aspects of RHIC Spin Physics”
- 18) N. Dikansky, Novosibirsk (Russia), 26 June
“Collective Phenomena in Electron Cooling”
- 19) C. Samanta, Saha Institute of Nuclear Physics (India), 26 June
“Deuteron Breakup at Extreme Forward Angle: Evidence of Coulomb Dissociation?”
- 20) M. Okamura, RIKEN (Saitama), 29 June
“Siberian Snake at RHIC”
- 21) Z. Yizhong, Institute of Atomic Energy (China), 10 July
“Some Aspects of Relativistic Heavy Ion Collisions by Including Delta Degrees of Freedom”
- 22) A. Goto, RIKEN (Saitama), 14 July
“Review of Beam Orbit Simulations for the RARF Accelerators”
- 23) T. Watanabe, INS (Tokyo), 19 July
“Profile Beam Monitor and Orbit Correction at TARN II”
- 24) H. Kunz, University of Mainz (Germany), 19 July
“Optical Isotope Shift and Hyperfine Structure Measurements at Fission Isomers”
- 25) D. H. Wilkinson, Sussex University (U.K.), 24 July
“Structure of the Nucleon”
- 26) R. Nagaoka, Sincrotrone Trieste (Italy), 1 Aug.
“Commissioning and Operation of ELETTRA”
- 27) H. D. Luc, Institute of Nuclear Science and Technique Vietnam Atomic Energy Commission (Vietnam), 9 Aug.
“On the Accelerators in Vietnam”

- 28) T. Suda, Tohoku University (Sendai), 9 Aug.
“Recent Results of the ${}^3\text{He}(e,e'\pi)$ Measurement at MAMI, MAINZ”
- 29) M. Honma, Aizu University (Fukushima), 21 Aug.
“Quantum Montecarlo Diagonalization Method in Nuclei and Its Application”
- 30) J. S. Chai, KAERI (Korea), 22 Aug.
“Status of KAERI AVF Cyclotron”
“Proton Beam Energy Measurement of KAERI Cyclotron at 25.89 MHz”
- 31) H. Backe, Institute fuer Kernphysik (Germany), 30 Aug.
“X-ray Radiation from a Low Emittance 855 MeV Electron Beam”
- 32) J.-Y. Zhang, Institute of Modern Physics (China), 4 Sept.
“Tilted Cranking Model: TAC Solutions in Odd-Odd Nuclei”
- 33) K. Varga, ATOMKI (Hungary), 7 Sept.
“Precise Solution of Few-Body Problems with Stochastic Variational Method on Correlated Gaussian Basis”
- 34) A. Bonasera, INFN, Catania (Italy), 11 Sept.
“Quantum Dynamics in Phase Space”
- 35) M. Przyrembel, University of Mainz (Germany), 13 Sept.
“The Mainz Neutrino Mass Experiment”
- 36) Q. Shen, Shanghai Institute of Nuclear Research, Chinese Academy of Science (China), 18 Sept.
“Research on ${}^{40}\text{Ar} + {}^{27}\text{Al}$ Collision below 100 MeV/u: Experimental Results and BUU, QMD Calculations; Azimuthal Distribution and Reaction Plane Dispersion for ${}^{84}\text{Kr} + {}^{197}\text{Au}$ Reaction at E_{Lab}/A between 35 and 400 MeV/u”
- 37) M. Tomizawa, INS (Tokyo), 20 Sept.
“Variable Frequency IH Linac for RIKEN RI Beam Factory”
- 38) L. Westerberg, The Svedberg Laboratory in Uppsala (Sweden), 21 Sept.
“An Overview of Experimental Programs, the Gustaf Werner Synchro Cyclotron and the CELSIUS Storage Ring, at The Svedberg Laboratory in Uppsala”
- 39) K. Ikeda, Niigata University (Niigata), 2 Oct.
“Structure of Bound and Resonance States of Light Nuclei Far from Stability”
- 40) K. Kumar, Tennessee Technological University (U.S.A.), 6 Oct.
“Semiclassical Field Theory of Fundamental Interactions”
- 41) E. Ormand, University of Tennessee (U.S.A.), 16 Oct.
“Nuclear Structure at the Proton-Drip Line: Some Things to Do with Radioactive Beams”
- 42) D. A. Kosower, Service de Physique Theorique, Centre d’Etudes de Saclay (France), 19 Oct.
“Cutting and Sewing One-Loop Amplitudes in QCD”
- 43) D. A. Kosower, Service de Physique Theorique, Centre d’Etudes de Saclay (France), 24 Oct.
“Physics with Jets”
- 44) T. Nakatsukasa, Chalk River Laboratory (Canada), 6 Nov.
“Rotational Alignment, Breakdown and Damping of Octupole Vibrations in Rapidly Rotating Nuclei”
- 45) S. Watanabe, INS (Tokyo), 7 Nov.
“DCCT for Power Supply of Magnet”
- 46) D. Dean, Oak Ridge National Laboratory (U.S.A.), 10 Nov.
“Shell Model Monte Carlo Studies of Nuclei”
- 47) M. Borden, Los Alamos (U.S.A.), 13 Nov.
“Introduction to the Los Alamos Neutron Science Center”
- 48) Y. D. Devi, RIKEN (Saitama), 14 Nov.
“New Signature for g-Bosons in the Magnetic Dipole Strength Distribution of Odd Mass Nuclei”
- 49) V. Yu. Denisov, Institute for Nuclear Research, Kiev (Ukraine), 20 Nov.
“Giant Resonances in a Semiclassical Approximation”
- 50) K. Kaki, Shizuoka University (Shizuoka), 4 Dec.
“Relativistic Impulse Approximation for Nucleon-Nucleus Elastic Scattering”
- 51) T. Udagawa, University of Texas (U.S.A.), 5 Dec.
“Longitudinal and Transverse Spin Response in the Gap and Delta Resonance Regions”
- 52) R. Seki, The California Institute of Technology (U.S.A.), 12 Dec.
“Effects of Nuclear Correlation on High-Energy”

Atomic Physics Lab.

- 1) T. Åberg, Helsinki Univ. Tech. (Finland), 13 Jan.
“Electron Capture by Strong Dynamic Electromagnetic Fields”
- 2) J. H. McGuire, Tulane Univ. (U.S.A.), 1 Mar.
“Dynamics of Matter, Antimatter and Light Interacting with Atoms, Molecules and Solids”
- 3) H. Shiromaru, Dept. Phys., Tokyo Metrop. Univ. (Tokyo), 16 Mar.
“Molecular Coulomb Explosion”
- 4) A. M. Ermolaev, Univ. Durham (U.K.), 16 Mar.
“Some Theoretical Studies Suggested by the Current Program of JET Experiments (Oxford)”
- 5) J.-P. Connerade, Imperial College (U.K.), 8 Sept.
“Giant Resonances in Atomic Photoionization”
- 6) Yu. N. Demkov, St. Petersburg Univ. (Russia), 19 Sept.
“Different Aspects of the Exchange Processes”
- 7) M. Zhan, The Chinese Academy of Sciences (China), 8 Dec.
“Coherent Control of Molecular Motions by Laser”

Nuclear Chemistry Lab.

- 1) R. G. Weginwar, College of Engineering, Chandrapur (India), 8 June
“Trace Elemental Determination in Biological and Environmental Samples by Neutron Activation Analysis”
- 2) R. Sielemann, Hahn-Meitner-Institut Berlin (Germany), 19 July

“Detection of Defects in Semiconductors by Mössbauer Spectroscopy and PAC”

- 3) M. Kojima, Washington Univ. (U.S.A.), 19 Sept.
“Diamonds, Noble Gas and Geohistory”
- 4) M. Katayama, Univ. Osaka Pref., 27 Sept.
“Arsenic Metabolism in Living Cells”
- 5) M. Hasegawa, Tohoku Univ., 9 Nov.
“Study on Defect and its Electron Structure of Si and SiO₂ Glasses by Means of Positron Annihilation”

Seminars on Physics at the RI Beam Factory

- 1) I. Tanihata, RIKEN (Saitama), 17 May
“The RI Beam Factory Project, Present Status”
- 2) M. Uno, Ministry of Education, Science, Sports and Culture (Tokyo), 5 June
“Mass Formulas in the Region of Unstable Nuclei”
- 3) H. Izumi, Tokyo Inst. Tech. (Tokyo), 23 Oct.
“Measurement of Deformation Parameter for Unstable Nuclei by Means of Spin-Aligned Radioactive Beam”
- 4) N. Aoi, Univ. Tokyo/RIKEN (Tokyo/Saitama), 13 Nov.
“Beta-Decay of Nuclei Very Far from the Stability Line”
- 5) T. Suzuki, Nihon Univ. (Tokyo), 13 Nov.
“Comments upon Effects of Halo on Beta-Decay”
- 6) A. Korshennikov, RIKEN (Saitama), 4 Dec.
“Measurements under Inverse Kinematical Conditions with Radioactive Beams”

XII. LIST OF PERSONNEL

RIKEN Accelerator Research Facility

ISHIHARA Masayasu 石原正泰 (Facility Director)

AWAYA Yohko 粟屋容子 (Vice Facility Director)

YANO Yasushige 矢野安重 (Vice Facility Director)

Linac Division

CHIBA Toshiya 千葉利哉

IKEZAWA Eiji 池沢英二

KOHARA Shigeo 小原重夫

HEMMI Masatake 逸見政武

KASE Masayuki 加瀬昌之

MIYAZAWA Yoshitoshi 宮沢佳敏*¹

Ring Cyclotron Division

FUJITA Jiro 藤田二郎

IKEGAMI Kumio 池上九三男

KAGEYAMA Tadashi 影山正

KASE Masayuki 加瀬昌之

KUBO Toshiyuki 久保敏幸

NAKAGAWA Takahide 中川孝秀

OKUNO Hiroki 奥野広樹

GOTO Akira 後藤彰*¹

INABE Naohito 稲辺尚人

KAMIGAITO Osamu 上垣外修一

KOHARA Shigeo 小原重夫

NAGASE Makoto 長瀬誠

OGIWARA Kiyoshi 荻原清

YOKOYAMA Ichiro 横山一郎

Experimental Support Division

ICHIHARA Takashi 市原卓

KANAI Yasuyuki 金井保之

KUMAGAI Hidekazu 熊谷秀和

MORITA Kosuke 森田浩介

WATANABE Yasushi 渡邊康

KAMBARA Tadashi 神原正*¹

KOBAYASHI Toshio 小林俊雄

MATSUZAKI Teiichiro 松崎禎市郎

OKUBO Yoshitaka 大久保嘉高

YATAGAI Fumio 谷田貝文夫

Radioisotope Facilities Division

AMBE Fumitoshi 安部文敏*¹

KOBAYASHI Yoshio 小林義男

IWAMOTO Masako 岩本正子

Radiation Protection Group

FUJITA Shin 藤田新

NAKANISHI Noriyoshi 中西紀喜*¹

NAKAJIMA Shunji 中島諄二

UWAMINO Yoshitomo 上藁義朋

Secretariat

NAKAMURA Toshiko 中村とし子

YOSHIDA Tohru 吉田徹*²

NUMATA Shigeo 沼田茂男

Steering Committee

AMBE Fumitoshi 安部文敏

AWAYA Yohko 粟屋容子

HANAOKA Fumio 花岡文雄

INOUE Yorinao 井上頼直

KAMBARA Tadashi 神原正

KOBAYASHI Toshio 小林俊雄

MATSUOKA Masaru 松岡勝

MIYAZAWA Yoshitoshi 宮沢佳敏

TAKAMI Michio 高見道生

YAGI Eiichi 八木栄一

YOSHIDA Shigeo 吉田茂男

AONO Masakazu 青野正和

GOTO Akira 後藤彰

INAMURA Takashi T. 稲村卓

ISHIHARA Masayasu 石原正泰

KATSUMATA Koichi 勝又紘一

KUMAGAI Noritaka 熊谷教孝

MATSUZAKI Teiichiro 松崎禎市郎

NAGAMINE Kanetada 永嶺謙忠

TANIHATA Isao 谷畑勇夫*³

YANO Yasushige 矢野安重

*¹ Group Leader, *² Manager, *³ Chairperson

Scientific and Engineering Personnel

Cosmic Radiation Laboratory

KATO Hiroshi 加藤 博

KOHNO Tsuyoshi 河野 毅

(Visitors)

HASEBE Nobuyuki 長谷部信行 (Fac. Gen. Educ., Ehime Univ.)

KASHIWAGI Toshisuke 柏木利介 (Fac. Eng., Kanagawa Univ.)

KATO Chihiro 加藤千尋 (Fac. Sci., Shinshu Univ.)

MUNAKATA Kazuoki 宗像一起 (Fac. Sci., Shinshu Univ.)

MURAKAMI Hiroyuki 村上浩之 (Fac. Sci., Rikkyo Univ.)

NAGATA Katsuaki 永田勝明 (Fac. Eng., Tamagawa Univ.)

NAKAMOTO Atsushi 中本 淳 (Fac. Sci., Rikkyo Univ.)

YANAGIMACHI Tomoki 柳町朋樹 (Fac. Sci., Rikkyo Univ.)

(Students)

ITO Tomoyuki 伊藤朋行 (Fac. Sci. Eng., Waseda Univ.)

ITSUMI Norifumi 逸見憲史 (Fac. Sci. Eng., Waseda Univ.)

SHINO Tomoaki 篠智彰 (Fac. Sci. Eng., Waseda Univ.)

YAMAGIWA Iwao 山際 巖 (Grad. Sch. Sci. Eng., Saitama Univ.)

Cyclotron Laboratory

FUJITA Jiro 藤田二郎

GOTO Akira 後藤 彰*¹

INABE Naohito 稲辺尚人

JIN Wei-Guo 金 衛国

KAMIGAITO Osamu 上垣外修一

KATAYAMA Takeshi 片山武司*²

KOHARA Shigeo 小原重夫

MORITA Kosuke 森田浩介

NAKAGAWA Takahide 中川孝秀

NAKANISHI Noriyoshi 中西紀喜

OKUNO Hiroki 奥野広樹

OTSUKA Takaharu 大塚孝治*²

SUGANUMA Hideo 菅沼秀夫

UESAKA Tomohiro 上坂友洋

YAMAJI Shuhei 山路修平*¹

YOKAYAMA Ichiro 横山一郎

FUJITA Shin 藤田 新

IKEGAMI Kumio 池上九三男

ISHIDA Satoru 石田 悟

KAGEYAMA Tadashi 影山 正

KASE Masayuki 加瀬昌之

KITAGAWA Hisashi 北川 尚

KUBO Toshiyuki 久保敏幸

NAGASE Makoto 長瀬 誠

NAKAJIMA Shunji 中島諄二

OGIWARA Kiyoshi 荻原 清

ONO Akira 小野 章

PU Yuehu 蒲 越虎

SUZUKI Toshio 鈴木敏男*²

WAKASUGI Masanori 若杉昌徳

YANO Yasushige 矢野安重*³

*¹ Senior Scientist, *² Senior Visiting Scientist, *³ Chief Scientist

(Visitors)

ABE Yasuhisa 阿部恭久 (Yukawa Inst. Theor. Phys., Kyoto Univ.)

AKUTSU Takao 阿久津亮夫 (NASDA)

AOKI Jiro 青木司郎 (NASDA)

ARAI Eiichi 新井栄一 (Res. Lab. Nucl. React., T. I. T.)

ARAKAWA Kazuo 荒川和夫 (JAERI, Takasaki)

BABA Shinji 馬場信次 (NASDA)

BATYGIN Yuri (Elect. Phys. Dept., Moscow Eng. Phys. Inst., Russia)

CHA Shin 錢 興 (Peking Univ., China)

DATÉ Schin 伊達 伸 (JASRI)

DEY Ranadhir (Variable Energy Cycl. Cent.)

EJIRI Hiroyasu 江尻宏泰 (Fac. Sci., Osaka Univ.)

EN'YO Hideto 延与秀人 (Fac. Sci., Kyoto Univ.)

FUJIOKA Manabu 藤岡 学 (Cyclotron Radioisot. Cent., Tohoku Univ.)

FUJISAWA Takashi 藤沢高志 (Denki Kogyo Co. Ltd.)

FUJISHIMA Shiro 藤島史郎 (I. H. I.)
 FUJITA Yoshitaka 藤田佳孝 (Fac. Sci., Osaka Univ.)
 FUJIWARA Mamoru 藤原守 (RCNP, Osaka Univ.)
 FUKUDA Mitsuhiro 福田光宏 (JAERI, Takasaki)
 FUKUMOTO Sadayoshi 福本貞義 (KEK)
 FURUNO Kohei 古野興平 (Tandem Accel. Cent., Univ. Tsukuba)
 FUTAMI Yasuyuki 二見康之 (N.I.R.S.)
 HADA Takashi 羽田尚志 (NASDA)
 HAMA Hiroyuki 浜広幸 (I.M.S.)
 HARADA Yuu 原田融 (Sapporo Gakuin Univ.)
 HASHIMOTO Osamu 橋本治 (Inst. Nucl. Study, Univ. Tokyo)
 HATANAKA Kichiji 畑中吉治 (RCNP, Osaka Univ.)
 HATSUKAWA Yuichi 初川雄一 (JAERI, Tokai)
 HATTORI Toshiyuki 服部俊幸 (Res. Lab. Nucl. React., T.I.T.)
 HAYANO Ryugo 早野龍五 (Fac. Sci., Univ. Tokyo)
 HEIGUCHI Kazuhiko 平口和彦 (Sch. Medicine, Niigata Univ.)
 HIES Markus G. (Dept. Phys., Mainz Univ., Germany)
 HIRAO Yasuo 平尾泰男 (N.I.R.S.)
 HIRASAWA Shokichi 平沢正吉 (Former Staff of RIKEN)
 HONMA Mitio 本間道雄 (Aizu Univ.)
 HONMA Toshihiro 本間寿広 (Cyclotron Radioisot. Cent., Tohoku Univ.)
 HORIBATA Takatoshi 堀端孝俊 (Fac. Eng., Aomori Univ.)
 HORIGUCHI Takayoshi 堀口隆良 (Fac. Sci., Hiroshima Univ.)
 HORIUCHI Hisashi 堀内昶 (Fac. Sci., Kyoto Univ.)
 HOSONO Kazuhiko 細野和彦 (RCNP, Osaka Univ.)
 IGARASHI Toshio 五十嵐敏雄 (NASDA)
 IKEDA Akitu 池田秋津 (Shizuoka Inst. Sci. & Tech.)
 IKEDA Nobuo 池田伸夫 (Inst. Nucl. Study, Univ. Tokyo)
 IKEDA Kiyomi 池田清美 (Fac. Sci., Niigata Univ.)
 IKEZOE Hiroshi 池添博 (JAERI, Tokai)
 IMAI Kenichi 今井憲一 (Fac. Sci., Kyoto Univ.)
 IMAMURA Mineo 今村峯雄 (Inst. Nucl. Study, Univ. Tokyo)
 INOUE Makoto 井上信 (Inst. Chem. Res., Kyoto Univ.)
 ISHII Takayuki 石井孝幸 (NASDA)
 ISHIZUKA Takeo 石塚武男 (Fac. Sci., Saitama Univ.)
 IWAMOTO Akira 岩本昭 (JAERI, Tokai)
 IWASHITA Yoshihisa 岩下芳久 (Inst. Chem. Res., Kyoto Univ.)
 IZUMOTO Toshiaki 泉本利章 (Coll. Sci., Rikkyo Univ.)
 JEONG S. C. (Inst. Nucl. Study, Univ. Tokyo)
 JIN Wei-Guo 金衛国 (Fac. Sci., Tohou Univ.)
 JYAN Donshin 江棟興 (Peking Univ., China)
 KAMIMURA Masayasu 上村正康 (Fac. Sci., Kyushu Univ.)
 KANAZAWA Mitsutaka 金沢光隆 (N.I.R.S.)
 KANMURI Tetsuo 冠哲夫 (Fac. Sci., Osaka Univ.)
 KANNO Toru 菅野徹 (NASDA)
 KATAYAMA Ichiro 片山一郎 (Inst. Nucl. Study, Univ. Tokyo)
 KATAYAMA Takeshi 片山武司 (Inst. Nucl. Study, Univ. Tokyo)
 KATO Kiyoshi 加藤幾芳 (Fac. Sci., Hokkaido Univ.)
 KATO Shohei 加藤昌平 (Fac. Sci., Osaka Univ.)
 KATORI Kenji 鹿取謙二 (Fac. Sci., Osaka Univ.)
 KATSURAGAWA Hidetsugu 桂川秀嗣 (Fac. Sci., Tohou Univ.)
 KAWAGUCHI Hideo 川口秀夫 (Tokyo Denshi Co., Ltd.)
 KAWAGUCHI Takeo 川口武男 (Mitsubishi Electric Co., Ltd.)
 KAWAI Mitsuji 河合光路 (Fac. Sci., Kyushu Univ.)
 KITAGAWA Hisashi 北川尚 (Inst. Phys., Univ. Tsukuba)
 KOHAMA Akihisa 小濱洋央 (Fac. Sci., Univ. Tokyo)
 KOHMOTO Toshiro 河本敏郎 (Fac. Sci., Kyoto Univ.)
 KONDO Michiya 近藤道也 (RCNP, Osaka Univ.)

KOSAKO Toshiso 小佐古敏莊 (Atomic Energy Res. Cent., Univ. Tokyo)
 KOTAJIMA Hisaya 古田島久哉 (Fac. Eng., Tohoku Univ.)
 KUBOYAMA Satoshi 久保山智司 (NASDA)
 KUDO Hisaaki 工藤久昭 (Fac. Sci., Niigata Univ.)
 LEE Kong Ok 李康玉 (Rika Women's College)
 LEE Sang Mu 李相茂 (Inst. Phys., Univ. Tsukuba)
 LIN Ching-Liang 林清涼 (Taiwan Univ., People's Republic of China)
 MAEDA Kazuhide 前田和秀 (Fac. Sci., Kyushu Univ.)
 MARUMORI Toshio 丸森寿夫 (Fac. Sci. Tech., Sci. Univ. Tokyo)
 MATSUDA Sumio 松田純夫 (NASDA)
 MATSUI Yoshiko 松井芳子 (Fac. Tech., Tokyo Univ. Agr. Tech.)
 MATSUKI Seishi 松木征史 (Inst. Chem. Res., Kyoto Univ.)
 MATSUSE Takehiro 松瀬丈浩 (Dept. Phys., Shinshu Univ.)
 MATSUYANAGI Kenichi 松柳研一 (Fac. Sci., Kyoto Univ.)
 MATSUZAKI Kazuhiro 松崎一浩 (NASDA)
 MIAKE Yasuo 三明康郎 (Inst. Phys., Univ. Tsukuba)
 MIDORIKAWA Shoichi 緑川章一 (Fac. Eng., Aomori Univ.)
 MINAMISONO Tadanori 南園忠則 (Fac. Sci., Osaka Univ.)
 MITSUMOTO Toshinori 密本俊典 (Sumitomo Heavy Industries, Ltd.)
 MIURA Iwao 三浦岩 (RCNP, Osaka Univ.)
 MIYAMURA Osamu 宮村修 (Dept. Phys., Hiroshima Univ.)
 MIYATAKE Hiroari 宮武宇也 (Fac. Sci., Osaka Univ.)
 MIZOTA Takeshi 溝田武志 (Inst. Phys., Univ. Tsukuba)
 MIZUNO Yoshiyuki 水野義之 (RCNP, Osaka Univ.)
 MIZUSAKI Takahiro 水崎高浩 (Fac. Sci., Univ. Tokyo)
 MOCHIKI Kouiti 持木幸一 (Dept. Phys., Musashi Inst. Technol.)
 MORI Yoshiharu 森義治 (Inst. Nucl. Study, Univ. Tokyo)
 MUKHOPADHTAY M. (Variable Energy Cycl. Cent., India)
 MURAKAMI Tetsuya 村上哲也 (Fac. Sci., Kyoto Univ.)
 MURAYAMA Toshiyuki 村山利幸 (Tokyo Univ. Mercantile Marine)
 MUROTANI Shin 室谷心 (Sch. Sci. & Eng., Waseda Univ.)
 MUTO Kazuo 武藤一雄 (Fac. Sci., T.I.T.)
 NAGAI Yasuki 永井泰樹 (Fac. Sci., T.I.T.)
 NAITO Ichiro 内藤一郎 (NASDA)
 NAKADA Hitoshi 中田仁 (Coll. Art & Sci., Chiba Univ.)
 NAKAHARA Hiromichi 中原弘道 (Fac. Sci., Tokyo Metrop. Univ.)
 NAKAI Koji 中井浩二 (KEK)
 NAKAJIMA Masato 中島真人 (NASDA)
 NAKAMURA Hiroyuki 中村裕之 (Fac. Sci., Kyushu Univ.)
 NAKAMURA Masao 中村正夫 (NASDA)
 NAKAMURA Ichiro 中村市郎 (Fac. Sci., Saitama Univ.)
 NAKAMURA Takashi 中村尚司 (Cyclotron Radioisot. Cent., Tohoku Univ.)
 NAKAO Noriaki 中尾徳晶 (Inst. Nucl. Study, Univ. Tokyo)
 NEMOTO Norio 根本規生 (NASDA)
 NIIMURA Masanobu 新村正信 (Sch. Sci. & Eng., Waseda Univ.)
 NODA Akira 野田章 (Inst. Chem. Res., Kyoto, Univ.)
 NODA Kouji 野田耕司 (N.I.R.S.)
 NOMURA Toru 野村亨 (Inst. Nucl. Study, Univ. Tokyo)
 OGAWA Kengo 小川健吾 (Fac. Educat., Chiba Univ.)
 OHIRA Hideharu 大平秀春 (NASDA)
 OKAMURA Hiroyuki 岡村弘之 (Fac. Sci., Univ. Tokyo)
 OKAMURA Masahiro 岡村昌弘 (Fac. Sci., T.I.T.)
 OKUMURA Susumu 奥村進 (JAERI, Takasaki)
 ONISHI Naoki 大西直毅 (Coll. Art Sci., Univ. Tokyo)
 OOKAWA Tomohiro 大川智宏 (Mitsubishi Heavy Industries)
 OSUGA Toshiaki 大須賀敏明 (Coll. Art & Sci., Chiba Univ.)
 OTSUKI Tsutomu 大槻勤 (Lab. Nucl. Sci., Tohoku Univ.)
 OURA Akio 大浦昭夫 (NASDA)

OYA Jiro 大矢次郎 (NASDA)
 QUAN Zhuo-Shu 全卓樹 (Coll. Eng., Hosei Univ.)
 ROA Yi Nong (Inst. Modern Phys., Academia Sinica, China)
 SAGARA Kenji 相良建至 (Fac. Sci., Kyushu Univ.)
 SAKAI Hideyuki 酒井英行 (Fac. Sci., Univ. Tokyo)
 SAKATA Fumihiko 坂田文彦 (Inst. Nucl. Study, Univ. Tokyo)
 SATO Kenichi 佐藤憲一 (Dept. Phys., Tohoku Coll. Pharm.)
 SATO Kenji 佐藤健次 (N.I.R.S.)
 SATO Yukio 佐藤幸夫 (N.I.R.S.)
 SEBE Takashi 瀬部孝 (Coll. Eng., Hosei Univ.)
 SEKINE Hiroataka 関根弘隆 (Former Staff of RIKEN)
 SEKINE Toshiaki 関根俊明 (JAERI, Tokai)
 SHIBATA Tokushi 柴田徳思 (Inst. Nucl. Study, Univ. Tokyo)
 SHIKAZONO Naoki 鹿園直基 (JAERI, Tokai)
 SHIMANO Yousuke 嶋野洋介 (NASDA)
 SHIMIZU Akira 清水昭 (RCNP, Osaka Univ.)
 SHIMOMURA Koichiro 下村浩一郎 (Meson Sci. Lab., KEK Branch, Univ. Tokyo)
 SHIN Kazuo 秦和夫 (Fac. Eng., Kyoto Univ.)
 SHIN Seung Ai 辛承愛 (Rika Women's Coll.)
 SHINOZUKA Tsutomu 篠塚勉 (Cyclotron Radioisot. Cent., Tohoku Univ.)
 SHIRAI Toshiyuki 白井敏之 (Yukawa Inst. Theor. Phys., Kyoto Univ.)
 SUEKI Keisuke 末木啓介 (Fac. Sci., Tokyo Metrop. Univ.)
 SUGAI Isao 菅井勲 (Inst. Nucl. Study, Univ. Tokyo)
 SUGIYAMA Hiroki 杉山大樹 (NASDA)
 SUMIYOSHI Hiroyuki 住吉広行 (Matsusho-Gakuen Junior Coll.)
 SUZUKI Toshio 鈴木敏夫 (Fac. Eng., Fukui Univ.)
 SUZUKI Toshio 鈴木俊夫 (Coll. Sci. Tech., Nihon Univ.)
 TAGISHI Yoshihiro 田岸義宏 (Tandem Accel. Cent., Univ. Tsukuba)
 TAJIMA Naoki 田嶋直樹 (Coll. Art Sci., Univ. Tokyo)
 TAKANAKA Masao 高伸政雄 (INS., Univ. Tokyo)
 TAKEMASA Tadashi 武政尹士 (Kyoto Univ. Education)
 TAKEUCHI Suehiro 竹内末広 (JAERI, Tokai)
 TAKIGAWA Noboru 滝川昇 (Fac. Sci., Tohoku Univ.)
 TAMAGAKI Ryoza 玉垣良三 (Fac. Sci., Kyoto Univ.)
 TAMURA Takashi 田村高志 (NASDA)
 TANABE Kazuko 田辺和子 (Otsuma Women's Coll.)
 TANAKA Jinichi 田中仁市 (Inst. Nucl. Study, Univ. Tokyo)
 TANAKA Kazuhiro 田中和廣 (Fac. Sci., Hiroshima Univ.)
 TANAKA Yasushi 田中保志 (Kyokuto Boeki Kaisha, Ltd.)
 TANIKAWA Masashi 谷川勝至 (Fac. Sci., Univ. Tokyo)
 TOHYAMA Mitsuru 遠山満 (Kyorin Univ.)
 TOMIMASU Takio 富增多喜夫 (FEL Res. Inst. Inc.)
 TOMINAKA Toshiharu 冨中利治 (Hitachi, Ltd.)
 TOMITANI Takehiro 富谷武浩 (N.I.R.S.)
 TOMIZAWA Masato 富澤正人 (Inst. Nucl. Study, Univ. Tokyo)
 TOMOTA Toshiaki 友田敏章 (Fac. Eng., Aomori Univ.)
 TORIYAMA Tamotsu 鳥山保 (Dept. Phys., Musashi Inst. Technol.)
 TSUNEMOTO Hiroshi 恒元博 (N.I.R.S.)
 UESUGI Masato 上杉正人 (NASDA)
 UTSUNOMIYA Hiroaki 宇都宮弘章 (Fac. Sci., Konan Univ.)
 UWAMINO Yoshitomo 上藁義朋 (Inst. Nucl. Study, Univ. Tokyo)
 WADA Michiharu 和田道治 (Inst. Nucl. Study, Univ. Tokyo)
 WADA Ryoiti 和田良一 (Texas A & M Univ., U.S.A.)
 WADA Takahiro 和田隆宏 (Fac. Sci., Konan Univ.)
 WAKAI Masamichi 若井正道 (Fac. Sci., Osaka Univ.)
 WAKUTA Yoshihisa 和久田義久 (Fac. Eng., Kyushu Univ.)
 WATANABE Shiniti 渡辺伸一 (Inst. Nucl. Study, Univ. Tokyo)
 WEI Baowen 魏宝文 (Inst. Modern Phys., Academia Sinica, China)

XIA Jiawen 夏佳文 (Inst. Modern Phys., Academia Sinica, China)
 YABANA Kazuo 矢花一浩 (Fac. Sci., Niigata Univ.)
 YAMADA Taiichi 山田泰一 (Coll. Eng., Kanto Gakuin Univ.)
 YAMANOUCHI Mikio 山内幹雄 (Inst. Phys., Univ. Tsukuba)
 YAMAZAKI Takashi 山崎魏 (RCNP, Osaka Univ.)
 YAMAZAKI Hirohito 山崎寛仁 (Lab. Nucl. Sci., Tohoku Univ.)
 YE Feng 叶峰 (Inst. Modern Phys., Academia Sinica, China)
 YOSHIDA Nobuaki 吉田宣章 (Fac. Sci., Univ. Tokyo)
 YOSHIDA Shiro 吉田思郎 (Dept. Phys., Ishinomaki Senshu Univ.)
 YOSHINAGA Naotaka 吉永尚孝 (Fac. Sci., Saitama Univ.)
 YOSHIOKA Yasuhiro 吉岡康弘 (NASDA)
 YOSHIZAWA Yasukazu 吉沢康和 (Fac. Eng., Kyushu Univ.)
 YUAN You-Jin (Inst. Modern Phys., Academia Sinica, China)
 ZHANG Li 張立 (Inst. Modern Phys., Academia Sinica, China)

(Students)

AKABORI Taisuke 赤堀泰祐 (Dept. Phys., Musashi Institute of Technology)
 AKAZAWA Takashi 赤澤貴 (Fac. Sci., Saitama Univ.)
 AKIYOSHI Hiromiti 秋吉啓充 (Fac. Sci., Kyushu Univ.)
 AOKI Yuka 青木由香 (Lab. Nucl. Sci., Tohoku Univ.)
 ARIGA Takehiro 有賀健博 (Fac. Sci., Saitama Univ.)
 FUJITA Ken 藤田建 (Fac. Sci., Kyushu Univ.)
 FUTAMI Yasuyuki 二見康之 (Inst. Phys., Univ. Tsukuba)
 HONJYOU Yoshio 本城義夫 (Inst. Phys., Univ. Tsukuba)
 HONMA Hiroyuki 本間裕之 (Fac. Sci., T.I.T.)
 ITAGAKI Shohei 板垣松平 (Fac. Sci., Saitama Univ.)
 KANGYO Yoshitsugu 観行愛嗣 (Coll. Sci., Chuo Univ.)
 KIM Eun Ju (Fac. Sci., Tohoku Univ.)
 KURATOMI Kouiti 倉富弘一 (Dept. Phys., Musashi Inst. Technol.)
 KURIHARA Kaori 栗原香 (Inst. Phys., Univ. Tsukuba)
 KURITA Tetsuro 栗田哲郎 (Inst. Sci., Univ. Tsukuba)
 KUROSAWA Tadahiro 黒沢忠弘 (Fac. Sci., Tohoku Univ.)
 LIU Xin (Peking Univ., China)
 MABUCHI Hideyuki 馬淵英之 (Fac. Sci., Konan Univ.)
 MATSUMOTO Norihiro 松本典洋 (Fac. Sci., Konan Univ.)
 MIURA Takashi 三浦崇 (Inst. Phys., Univ. Tsukuba)
 NAKAGAWA Keiko 中川恵子 (Fac. Sci., Tohoku Univ.)
 NISHIMORI Nobuyuki 西森信行 (Fac. Sci., Kyushu Univ.)
 ODA Ayato 織田彩人 (Tokyo Univ. Mercantile Marine)
 OI Makito 大井万紀人 (Coll. Art Sci., Univ. Tokyo)
 ONO Shinji 小野慎二 (Fac. Eng., Kyoto Univ.)
 OOTUKA Takahiro 大塚崇広 (Dept. Phys., Musashi Inst. Technol.)
 OZAWA Shuichi 小澤修一 (Coll. Sci., Rikkyo Univ.)
 RYU Shin (Inst. Phys., Univ. Tsukuba)
 SASAHARA Takafumi 笹原孝文 (Coll. Sci., Chuo Univ.)
 SASAKI Reiji 佐々木玲仁 (Fac. Sci., Tohoku Univ.)
 SEINO Satoshi 清野聡 (Fac. Sci., T.I.T.)
 TAGAYA Yu 多加谷裕 (Fac. Sci., Univ. Tokyo)
 TOMITA Shigeo 富田成夫 (Inst. Phys., Univ. Tsukuba)
 TOMOHISA Yasuhiko 友久保彦 (Inst. Phys., Univ. Tsukuba)
 UTIYAMA Koji 内山浩志 (Fac. Sci., Saitmam Univ.)
 WAKAMATU Fumihiko 若松文彦 (Fac. Sci., Kyushu Univ.)
 WAKUI Takashi 湧井崇志 (Fac. Sci., Toho Univ.)
 YAMAGAMI Munetaka 山上宗隆 (Fac. Sci., Konan Univ.)
 YAMASHITA Ayako 山下亜矢子 (Fac. Sci., Toho Univ.)
 YODA Tetsuhiko 依田哲彦 (Lab. Nucl. Sci., Tohoku Univ.)
 YUKI Hideyuki 結城秀行 (Fac. Sci., Tohoku Univ.)

Linear Accelerator Laboratory

CHIBA Toshiya 千葉利哉	FUJIMAKI Masaki 藤巻正樹
FUKUDA Moichi 福田茂一*1	HEMMI Masatake 逸見政武
IKEZAWA Eiji 池沢英二	ITO Sachiko 伊藤祥子*1
KASE Masayuki 加瀬昌之	KOBAYASHI Toshio 小林俊雄*2
KORSHENINNIKOV Alexei	KUMAGAI Hidekazu 熊谷秀和
MIYAZAWA Yoshitoshi 宮沢佳敏	MOCHIZUKI Yuko 望月優子*1
MOMOTA Sadao 百田佐多生*1	OGAWA Yoko 小川洋子*1
OZAWA Akira 小沢顕	SUGAHARA Yuichi 菅原雄一*3
SUZUKI Takeshi 鈴木健	TANIHATA Isao 谷畑勇夫*4
TONUMA Tadao 戸沼正雄	YANOKURA Minoru 矢野倉実
YOSHIDA Koichi 吉田光一	

*1 Special Postdoctoral Researcher, *2 Senior Scientist, *3 Postdoctoral Researcher,
*4 Chief Scientist

(Visitors)

ALEKSANDROV D. V. (Kurchatov Inst., Russia)
ARATANI Michi 荒谷美智 (Inst. Environmental Sci.)
BOLBOT Michael D. (Notre Dame Univ., U.S.A.)
BOYD Richard (Ohio State Univ., U.S.A.)
BROCKMANN Rolf (Inst. Phys., Univ. Mainz, Germany)
CARLSON Brett (CTA, Inst. Estudos Avancados, Brasil)
CHLOUPEK Frank (Ohio State Univ., U.S.A.)
DEMYANOVA Alla S. (Kurchatov Inst. Atomic Energy, Russia)
FUJIWARA Mamoru 藤原守 (RCNP, Osaka Univ.)
FURUYA Keiichi 古谷圭一 (Fac. Sci., Sci. Univ. Tokyo)
HONG Wang 洪完 (Fac. Sci., Univ. Tokyo)
ITO Noriaki 伊藤憲昭 (Dept. Cryst. Mater., Nagoya Univ.)
IZUYAMA Takeo 伊豆山健夫 (Dept. Phys., Toho Univ.)
KANAZAWA Kenichi 金澤健一 (KEK)
KATORI Kenji 鹿取謙二 (Fac. Sci., Osaka Univ.)
KIKUCHI Jun 菊池順 (Sci. Eng. Res. Lab., Waseda Univ.)
KIMURA Kikuo 木村喜久雄 (Fac. Eng., Nagasaki Inst. Appl. Sci.)
KOLATA James (Notre Dame Univ., U.S.A.)
MATSUTA Kensaku 松多健策 (Fac. Sci., Osaka Univ.)
MATUOKA Nobuyuki 松岡伸行 (Res. Cent. Nucl. Phys., Osaka Univ.)
MOCHIZUKI Keiko 望月圭子 (Fac. Sci., Osaka Univ.)
MURAOKA Mitsuo 村岡光男 (Coll. Arts Sci., Chiba Univ.)
NIKOLSKI Evgenini Y. (Kurchatov Inst., Russia)
NOJIRI Yoichi 野尻洋一 (Fac. Sci., Osaka Univ.)
OGAWA Kengo 小川建吾 (Coll. Arts Sci., Chiba Univ.)
OGLOBLIN Alexei A. (Kurchatov Inst., Russia)
OJIMA Minoru 小嶋稔 (Fac. Sci., Osaka Univ.)
OMATA Kazuo 小俣和夫 (Inst. Nucl. Study, Univ. Tokyo)
OYAMATSU Kazuhiro 親松和浩 (Dept. Energy Eng. Sci., Nagoya Univ.)
PETRASCU Horia (Inst. Phys. Nucl. Eng., Romania)
PETRASCU Marius (Inst. Phys. Nucl. Eng., Romania)
RAIMANN Gerhard (Ohio State Univ., U.S.A.)
SAGAWA Hiroyuki 佐川弘幸 (Fac. Sci., Univ. Tokyo)
SAKAI Hideyuki 酒井英行 (Fac. Sci., Univ. Tokyo)
SATO Kazuhiro 佐藤和広 (Tokyo Fire Dept.)
SUDA Toshimi 須田利美 (Fac. Sci., Tohoku Univ.)
SUGAWARA Masahiko 菅原昌彦 (Fundam. Sci., Chiba Inst. Technol.)
SUZUKI Yasuyuki 鈴木宣之 (Fac. Sci., Niigata Univ.)
TOKI Hiroshi 土岐博 (Fac. Sci., Tokyo Metrop. Univ.)
VARGA Kalman (Inst. Nucl. Res. Hungarian Acad. Sci., Hungary)
WADA Takahiro 和田隆宏 (Osaka Dentist Univ.)

YAMAGUCHI Hiromi 山口裕美 (Sci. Eng. Res. Lab., Waseda Univ.)
ZAHAR Mohamed (Dept. Phys., Notre Dame Univ., U.S.A.)

(Students)

HARADA Akihiko 原田昭彦 (Fac. Sci., Osaka Univ.)
IZUMIKAWA Takuji 泉川卓司 (Fac. Sci., Osaka Univ.)
KANOU Kenji 叶健治 (Fac. Sci., Univ. Tsukuba)
KIUCHI Hiroshi 木内宏 (Fac. Sci., Saitama Univ.)
MATSUSHITA Kenichi 松下健一 (Fac. Sci., Sci. Univ. Tokyo)
MIHARA Mototsugu 三原基嗣 (Fac. Sci., Osaka Univ.)
MIKI Keitarou 三木敬太郎 (Fac. Sci., Konan Univ.)
MIYAKE Toru 三宅徹 (Fac. Sci., Osaka Univ.)
MIYAMOTO Shinya 宮本真哉 (Fac. Sci., Tokyo Metrop. Univ.)
NAKAZATO Masahisa 中里真久 (Fac. Sci., Osaka Univ.)
ONISHI Takashi 大西崇 (Fac. Sci., Osaka Univ.)
SASAKI Makoto 佐々木誠 (Fac. Sci., Osaka Univ.)
SHIMOOKA Masaaki 下岡正明 (Fac. Sci., Kyoto Univ.)
TANIGAKI Minoru 谷垣実 (Fac. Sci., Osaka Univ.)
YAMAGUCHI Takayuki 山口貴之 (Fac. Sci., Osaka Univ.)

Radiation Laboratory

FUKUNISHI Nobuhisa 福西暢尚	GAI Moshe* ¹
GONO Yasuyuki 郷農靖之* ²	HAHN Kevin I.* ³
ICHIHARA Takashi 市原卓	IDEUCHI Eiji 井手口栄治
IMAI Kenichi 今井憲一* ²	ISHIHARA Masayasu 石原正泰* ⁴
IZUMO Koichi 出雲光一	KISHIDA Takashi 岸田隆
MENGGONI Alberto* ⁵	NOTANI Masahiro 野谷将広
OKAMURA Masahiro 岡村昌宏	SAITO Naohito 齋藤直人* ³
SAKURAI Hiroyoshi 櫻井博儀	TALMI Igal* ¹
TENDOW Yoshihiko 天道芳彦	WATANABE Yasushi 渡邊康
YOSHIDA Atsushi 吉田敦	

*¹ Eminent Scientist, *² Senior Visiting Scientist, *³ Special Postdoctoral Researcher,
*⁴ Chief Scientist, *⁵ Visiting Researcher

(Visitors)

ABE Yasuhisa 阿部恭久 (Yukawa Inst. for Theoretical Phys., Kyoto Univ.)
ADACHI Minoru 足立實 (Fac. Sci., Tokyo Inst. Technol.)
ANDO Yoshiaki 安藤嘉章 (Coll. Sci., Rikkyo Univ.)
ASAHI Koichiro 旭耕一郎 (Fac. Sci., Tokyo Inst. Technol.)
BECK F. A. (Groupe RSN, Strasbourg, France)
BROGLIA R. (Univ. Milano & INFN, Italy)
CASTEN Rick (Phys. Dept., Brookhaven Natl. Lab., U.S.A.)
DEVI Yelamanchili Durga (Saha Inst. Nucl. Phys., India)
DOOI Makoto 堂井真 (Univ. Tsukuba)
ENYO Hideto 延与秀人 (Fac. Sci., Kyoto Univ.)
FLOCARD Hubert (Division de Physique Theorique, Inst. Phys. Nucl., Orsay, France)
FUCHI Yoshihide 渊好秀 (Inst. Nucl. Study, Univ. Tokyo)
FUJIOKA Manabu 藤岡学 (Cyclotron and Radioisot. Center, Tohoku Univ.)
FUKUDA Mitsunori 福田光順 (Fac. Sci., Osaka Univ.)
FUKUDA Tomokazu 福田共和 (Inst. Nucl. Study, Univ. Tokyo)
FURUTAKA Kazuyoshi 古高和禎 (JAERI)
HAMAGAKI Hideki 浜垣秀樹 (Inst. Nucl. Study, Univ. Tokyo)
HASEGAWA Takeo 長谷川武夫 (Fac. Eng., Miyazaki Univ.)
HATSUDA Tetsuo 初田哲男 (Univ. Tsukuba)
HAYASHI Naoki 林直樹 (School Sci., Nagoya Univ.)
HOSAKA Masahito 保坂将人 (Inst. Nucl. Study, Univ. Tokyo)

ICHIMURA Munetake 市村宗武 (Coll. Arts and Sci., Univ. Tokyo)
 IEKI Kazuo 家城和夫 (Coll. Sci., Rikkyo Univ.)
 KASAGI Jirota 笠木治郎太 (Lab. Nucl. Sci., Tohoku Univ.)
 KATAYAMA Ichiro 片山一郎 (Inst. Nucl. Study, Univ. Tokyo)
 KATO Seigo 加藤静吾 (Fac. Ed., Yamagata Univ.)
 KATORI Kenji 鹿取謙二 (Fac. Sci., Osaka Univ.)
 KAWAKAMI Hirokane 川上宏金 (Inst. Nucl. Study, Univ. Tokyo)
 KAWASHIMA Hideo 川島英雄 (Inst. Nucl. Study, Univ. Tokyo)
 KIM Jong Chan (Dept. Phys., Seoul Natl. Univ., Korea)
 KITAO Kensuke 喜多尾憲助 (Data Engineering Inc.)
 KOIKE Yuji 小池裕司 (Niigata Univ.)
 KOSOWER David A. (Service de Physique Theorique Centre d'Etudes Saclay, France)
 KUBONO Shigeru 久保野茂 (Inst. Nucl. Study, Univ. Tokyo)
 KUSAKARI Hideshige 草刈英榮 (Fac. Ed., Chiba Univ.)
 LEE Sang Mu 李相茂 (Inst. Phys., Univ. Tsukuba)
 LIU Guanhua 劉冠華 (Inst. Mod. Phys., Acad. Sin., China)
 MAEDA Kazushige 前田和茂 (Coll. Gen. Ed., Tohoku Univ.)
 MATSUYANAGI Kenichi 松柳研一 (Fac. Sci., Kyoto Univ.)
 MIN Byung-Joo 閔丙珠 (Korea Atomic Energy Res. Inst., Korea)
 MITARAI Shiro 御手洗志郎 (Fac. Sci., Kyushu Univ.)
 MITSUOKA Shinichi 光岡真一 (Res. Center for Nucl. Phys., Osaka Univ.)
 MIYACHI Takashi 宮地孝 (Inst. Nucl. Study, Univ. Tokyo)
 MIYATAKE Hiroari 宮武宇也 (Coll. Gen. Ed., Osaka Univ.)
 MORIKAWA Tsuneyasu 森川恒安 (Fac. Sci., Kyushu Univ.)
 MORINOBU Shunpei 森信俊平 (Fac. Sci., Kyushu Univ.)
 MOTOBAYASHI Toru 本林透 (Coll. Sci., Rikkyo Univ.)
 MOTTELSON Ben R. (NORDITA, Copenhagen, Denmark)
 MUELLER Ludwig (Univ. Padova, Italy)
 MURAKAMI Takeshi 村上健 (Natl. Inst. Radiol. Sci.)
 NAGAI Yasuki 永井泰樹 (Fac. Sci., Tokyo Inst. Technol.)
 NAGASHIMA Yasuo 長島泰夫 (Inst. Phys., Univ. Tsukuba)
 NAKAJIMA Mitsuo 中島充夫 (Graduate School Nagatsuta, Tokyo Inst. Technol.)
 NAKAMURA Shogo 中村正吾 (Fac. Ed., Yokohama Nat. Univ.)
 NAKAMURA Takashi 中村隆司 (Fac. Sci., Univ. Tokyo)
 NAKAYAMA Shintaro 中山信太郎 (Coll. Gen. Ed., Tokushima Univ.)
 NIIZEKI Takashi 新関隆 (Fac. Sci., Tokyo Inst. Technol.)
 NORO Tetsuo 野呂哲夫 (Res. Center Nucl. Phys., Osaka Univ.)
 ODAHARA Atsuko 小田原厚子 (Fac. Sci., Kyushu Univ.)
 OGAWA Masao 小川雅生 (Graduate School Nagatsuta, Tokyo Inst. Technol.)
 OKAMURA Hiroyuki 岡村弘之 (Univ. Tokyo)
 ONUMA Hajime 大沼甫 (Fac. Sci., Tokyo Inst. Technol.)
 ORIHARA Hikonojyo 織原彦之丞 (Cyclotron and Radioisotope Center, Tohoku Univ.)
 OSHIMA Masumi 大島真澄 (JAERI)
 OTSUKA Takaharu 大塚孝治 (Fac. Sci., Univ. Tokyo)
 OYAIZU Michihiro 小柳津充広 (Inst. Nucl. Study, Univ. Tokyo)
 RUAN (GEN) Jian-Zhi 阮建治 (Coll. Sci., Rikkyo Univ.)
 SAGAWA Hiroyuki 佐川弘幸 (Center Mathematical Sci., Univ. Aizu)
 SAKAGUCHI Harutaka 坂口治隆 (Fac. Sci., Kyoto Univ.)
 SAKAI Kenji 酒井健二 (Fac. Sci., Tokyo Inst. Technol.)
 SAKAI Mitsuo 坂井光夫 (Inst. Nucl. Study, Univ. Tokyo)
 SAKURAGI Hiroyuki 櫻木弘之 (Fac. Sci., Osaka City Univ.)
 SATO Hikaru 佐藤皓 (Natl. Lab. High Energy Phys.)
 SATO Hiroshi 佐藤竝 (Seikei Univ.)
 SCHMIDT-OTT Wolf-Dieter (II Physicalisches Inst., Univ. Goettingen, Germany)
 SHIBATA Toshiaki 柴田利明 (Fac. Sci., Tokyo Inst. Technol.)
 SHIMIZU Hajime 清水肇 (Fac. Ed., Yamagata Univ.)
 SHIMIZU Yoshifumi 清水良文 (Fac. Sci., Kyushu Univ.)
 SHIMODA Tadashi 下田正 (Coll. Gen. Ed., Osaka Univ.)

SHIMOURA Susumu 下浦 享 (Coll. Sci., Rikkyo Univ.)
 SHIRATO Syoji 白土 鈔二 (Coll. Sci., Rikkyo Univ.)
 SIGNORINI Cosimo (Phys. Dept., Inst. Nazionale di Fisica Nucl., Italy)
 SUGAWARA Masahiko 菅原昌彦 (Chiba Inst. Technol.)
 SUZUKI Masayo 鈴木昌世 (Jpn. Synchrotron Rad. Res. Inst.)
 SUZUKI Yasuyuki 鈴木宜之 (Fac. Sci., Niigata Univ.)
 TAKADA Eiichi 高田栄一 (Natl. Inst. Radiol. Sci.)
 TAKAHASHI Noriaki 高橋憲明 (Coll. Gen. Ed., Osaka Univ.)
 TAKAHASHI Tadayuki 高橋忠幸 (Fac. Sci., Univ. Tokyo)
 TAKAKU Seisaku 高久清作 (Inst. Nucl. Study, Univ. Tokyo)
 TAKIGAWA Noboru 滝川 昇 (Fac. Sci., Tohoku Univ.)
 TANAKA Masahiko 田中雅彦 (Inst. Nucl. Study, Univ. Tokyo)
 TANOKURA Atsushi 田野倉 敦 (Fac. Sci. Technol., Sophia Univ.)
 TERAOKA Atsuki 寺川貴樹 (Cyclotron and Radioisotope Center, Tohoku Univ.)
 TOKI Hiroshi 土岐 博 (Res. Center Nucl. Phys., Osaka Univ.)
 TOYAMA Takeshi 外山 毅 (Natl. Lab. High Energy Phys.)
 TOYOKAWA Hidenori 豊川秀訓 (Res. Center Nucl. Phys., Osaka Univ.)
 UENO Hideki 上野秀樹 (Fac. Sci., Osaka Univ.)
 UNO Masahiro 宇野正宏 (Ministry Ed., Sci. Culture)
 WU Heyu 吳 和宇 (Inst. Mod. Phys., Acad. Sin., China)
 YAMAMOTO Sukeyasu 山本祐靖 (Fac. Sci. Technol., Sophia Univ.)
 YAMANISHI Teruya 山西輝也 (Res. Center Nucl. Phys., Osaka Univ.)
 YAMAYA Takashi 山屋 堯 (Fac. Sci., Tohoku Univ.)
 YOSHINAGA Naotaka 吉永尚孝 (Coll. Liberal Arts, Saitama Univ.)
 YOSOI Masaru 與曾井 優 (Fac. Sci., Kyoto Univ.)

(Students)

AOI Nori 青井 考 (Fac. Sci., Univ. Tokyo)
 AOKI Kohji 青木宏治 (Coll. Sci., Rikkyo Univ.)
 CHAE Soo Joh 蔡 洙祚 (Dept. Phys., Seoul Natl. Univ., Korea)
 EBIHARA Minoru 海老原 稔 (Fac. Sci., Univ. Tokyo)
 FUJITA Satoshi 藤田哲史 (Fac. Sci., Univ. Tokyo)
 FUJIWARA Hideki 藤原秀樹 (Coll. Sci., Rikkyo Univ.)
 HARA Yosuke 原 洋介 (Fac. Sci., Tokyo Inst. Technol.)
 HARADA Masaki 原田昌樹 (Fac. Sci., Tokyo Inst. Technol.)
 HIRAI Masaaki 平井正明 (Fac. Sci., Univ. Tokyo)
 HISANAGA Isamu 久永 勇 (Coll. Sci., Rikkyo Univ.)
 HORI Junichi 堀 順一 (Coll. Sci., Rikkyo Univ.)
 HORI Masaki 堀 正樹 (Fac. Sci., Univ. Tokyo)
 HORI Yoichi 堀 陽一 (Fac. Sci., Tokyo Inst. Technol.)
 HOSOMICHI Kazuo 細道和夫 (Fac. Sci., Univ. Tokyo)
 IINO Hayato 飯野勇人 (Coll. Sci., Rikkyo Univ.)
 INOUE Masahiro 井上昌宏 (Coll. Sci., Rikkyo Univ.)
 ISHIDA Satoru 石田 悟 (Fac. Sci., Univ. Tokyo)
 ITO Kazuya 伊藤和也 (Cyclotron and Radioisotope Center, Tohoku Univ.)
 ITO Mikihiro 伊藤幹彦 (Fac. Sci., Tokyo Inst. Technol.)
 IWAMOTO Susumu 岩本 晋 (Coll. Sci., Rikkyo Univ.)
 IWASA Naohito 岩佐直仁 (Coll. Sci., Rikkyo Univ.)
 IWATA Yoshiyuki 岩田佳之 (Coll. Sci., Rikkyo Univ.)
 IZUMI Hideaki 出水秀明 (Fac. Sci., Tokyo Inst. Technol.)
 KANEDA Naoya 金田直也 (Fac. Sci., Kyushu Univ.)
 KATO Kenichi 加藤健一 (Fac. Sci., Tokyo Inst. Technol.)
 KATO Toshiyuki 加藤俊幸 (Sci. Eng. Res. Lab., Waseda Univ.)
 KIDERA Masanori 木寺正憲 (Fac. Sci., Kyushu Univ.)
 KIKUCHI Tadashi 菊地 正 (Coll. Sci., Rikkyo Univ.)
 KOBAYASHI Misaki 小林美咲 (Sci. Eng. Res. Lab., Waseda Univ.)
 KOBINATA Hideo 小日向秀夫 (Fac. Sci., Univ. Tokyo)
 KOMIYAMA Tatsuto 込山立人 (Sci. Eng. Res. Lab., Waseda Univ.)

KUBO Madoka 久保 円 (Fac. Sci. Technol., Sophia Univ.)
KUROKAWA Meiko 黒川明子 (Coll. Sci., Rikkyo Univ.)
KUROKAWA Nobuo 黒河暢雄 (Fac. Sci., Tokyo Inst. Technol.)
MATSUZAKI Keiichi 松崎恵一 (Fac. Sci., Univ. Tokyo)
MICHEL Xavier (Orsay Univ., France)
MINEGISHI Junichi 峰岸純一 (Coll. Sci., Rikkyo Univ.)
MINEMURA Toshiyuki 峯村俊行 (Coll. Sci., Rikkyo Univ.)
MIYACHI Takahiko 宮地岳彦 (Inst. Nucl. Study, Univ. Tokyo)
MIYAZAKI Kousuke 宮崎光介 (Fac. Sci., Kyushu Univ.)
MIZOI Yutaka 溝井 浩 (Inst. Nucl. Study, Univ. Tokyo)
MOCHINAGA Kensuke 持永建介 (Fac. Sci., Tokyo Inst. Technol.)
MORIYA Shingo 守屋真吾 (Coll. Sci., Rikkyo Univ.)
MURATA Tomoki 村田知樹 (Fac. Sci. Technol., Sophia Univ.)
NAGATA Kazuhiko 長田和彦 (Fac. Sci., Tokyo Inst. Technol.)
NAGATA Kazuhiro 永田和広 (Fac. Sci., Univ. Tokyo)
NAITO Yutaka 内藤 豊 (Fac. Sci., Univ. Tokyo)
NAKAMAE Shigefumi 中前茂文 (Fac. Sci., Univ. Tokyo)
NAKAMURA Tadashi 中村 正 (Sci. Eng. Res. Lab., Waseda Univ.)
NAKANO Jo 中野 讓 (Inst. Nucl. Study, Univ. Tokyo)
NARATO Masayuki 榑戸雅之 (Fac. Sci., Tokyo Inst. Technol.)
NISHIO Teiji 西尾禎治 (Coll. Sci., Rikkyo Univ.)
NONAKA Takamasa 野中敬正 (Fac. Sci., Univ. Tokyo)
OGAMI Hiroshi 尾上博司 (Fac. Sci., Tokyo Inst. Technol.)
OGAWA Hideto 小川秀人 (Coll. Sci., Rikkyo Univ.)
OGAWA Hiroshi 小川博嗣 (Fac. Sci., Tokyo Inst. Technol.)
OGURA Toshiyuki 小倉俊幸 (Coll. Sci., Rikkyo Univ.)
OKADA Hiroyuki 岡田宏之 (Sci. Eng. Res. Lab., Waseda Univ.)
OONISHI Tetsuya 大西哲哉 (Fac. Sci., Univ. Tokyo)
OTSU Hideaki 大津秀暁 (Fac. Sci., Univ. Tokyo)
OTSUKA Takanori 大塚貴徳 (Fac. Sci., Univ. Tokyo)
OZAWA Ryozi 小沢亮二 (Coll. Sci., Rikkyo Univ.)
SAITO Yoshitaka 齋藤芳隆 (Fac. Sci., Univ. Tokyo)
SAKAMOTO Naruhiko 坂本成彦 (Fac. Sci., Univ. Tokyo)
SASAKI Mitsuru 佐々木 充 (Fac. Sci., Osaka Univ.)
SATO Hiromi 佐藤広海 (Fac. Sci., Tokyo Inst. Technol.)
SATO Masaaki 佐藤真揚 (Coll. Sci., Rikkyo Univ.)
SATO Masaru 佐藤 優 (Sci. Eng. Res. Lab., Waseda Univ.)
SATO Yoshiteru 佐藤義輝 (Fac. Sci., Univ. Tokyo)
SHIBATA Masataka 柴田雅隆 (Fac. Sci., Kyushu Univ.)
SHIMURA Masakatsu 志村正勝 (Fac. Sci. Technol., Sophia Univ.)
SHINODA Morihiko 篠田守彦 (Sci. Eng. Res. Lab., Waseda Univ.)
SHIRAKURA Tetsuya 白倉徹也 (Fac. Sci., Osaka Univ.)
SHIZUMA Toshiyuki 静間俊行 (Fac. Sci., Kyushu Univ.)
SUZUKI Masataka 鈴木正恭 (Coll. Sci., Rikkyo Univ.)
TAJIMA Yasuhisa 田島靖久 (Fac. Sci., Tokyo Inst. Technol.)
TAKEUCHI Satoshi 武内 聡 (Coll. Sci., Rikkyo Univ.)
TANAKA Eiichi 田中英一 (Coll. Sci., Rikkyo Univ.)
TERANISHI Takashi 寺西 高 (Fac. Sci., Univ. Tokyo)
TERASAWA Kazuhiro 寺沢和洋 (Sci. Eng. Res. Lab., Waseda Univ.)
TERUNUMA Takashi 照沼貴史 (Coll. Sci., Rikkyo Univ.)
TSUCHIDA Naohiko 土田有彦 (Fac. Sci., Univ. Tokyo)
TSUDA Masaki 津田理樹 (Fac. Sci., Tokyo Inst. Technol.)
TSUZUKI Yutaka 都筑 豊 (Coll. Sci., Rikkyo Univ.)
TUCHIDA Hideo 土田英夫 (Fac. Sci., Kyushu Univ.)
UCHIBORI Takeshi 内堀武司 (Coll. Sci., Rikkyo Univ.)
WAKASA Tomotsugu 若狭智嗣 (Fac. Sci., Univ. Tokyo)
WATANABE Akira 渡辺 明 (Sci. Eng. Res. Lab., Waseda Univ.)
WATANABE Hiroshi 渡邊 寛 (Fac. Sci., Kyushu Univ.)

WATANABE Yutaka 渡辺 裕 (Fac. Sci., Univ. Tokyo)
 YAMAMOTO Yoshifumi 山本佳史 (Fac. Sci., Osaka Univ)
 YAMASHITA Toshiyuki 山下利幸 (Fac. Sci., Tokyo Inst. Technol.)
 YANAGISAWA Yoshiyuki 柳沢善行 (Coll. Sci., Rikkyo Univ.)
 YONEDA Kenichiro 米田健一郎 (Fac. Sci., Univ. Tokyo)
 YOSHIDA Takuji 吉田拓司 (Coll. Sci., Rikkyo Univ.)
 YOSHIMI Akihiro 吉見彰洋 (Fac. Sci., Tokyo Inst. Technol.)

Atomic Physics Laboratory

· ANDO Kozo 安藤剛三	AWAYA Yohko 粟屋容子*1
BENGTSSON Peter*2	IGARASHI Akinori 五十嵐明則
KAMBARA Tadashi 神原 正*3	KANAI Yasuyuki 金井保之
KOJIMA Takao M. 小島隆夫	NAKAI Yoichi 中井陽一
NISHIDA Masami 西田雅美	OURA Masaki 大浦正樹
SCHMIDT-BÖCKING Horst*4	SHIMAMURA Isao 島村 勲*3
SOEJIMA Kouichi 副島浩一	TANG Jian-Zhi 唐 建志
YOSHIDA Takashi 吉田高志	WATANABE Naoki 渡部直樹

*1 Chief Scientist, *2 Visiting Researcher, *3 Senior Scientist, *4 Eminent Scientist

(Visitors)

AZUMA Toshiyuki 東 俊行 (Coll. Arts Sci., Univ. Tokyo)
 DANJO Atsunori 壇上篤徳 (Dept. Phys., Niigata Univ.)
 DEPAOLA Brett D. (Kansas State Univ., U.S.A.)
 DÖRNER Reinhard (Inst. Kernphysik, Univ. Frankfurt, Germany)
 ENGSTRÖM Lars (Univ. Lund, Sweden)
 FUJIMA Kazumi 藤間一美 (Fac. Eng., Yamanashi Univ.)
 FUKUDA Hiroshi 福田 宏 (Sch. Administration and Informatics, Univ. Shizuoka)
 HARA Shunsuke 原 俊介 (Dept. Gen. Educ., Tsukuba Coll. Technol.)
 HARSTON Michael R. (Dept. Math., Univ. Nottingham, U.K.)
 HINO Ken-ichi 日野健一 (Dept. Appl. Phys. Chem., Univ. Electro-Commun.)
 HIRAYAMA Takato 平山孝人 (Dept. Phys., Gakushuin Univ.)
 HULDT Sven (Univ. Lund, Sweden)
 HUTTON Roger (Univ. Lund, Sweden)
 ICHIMURA Atsushi 市村 淳 (Inst. Space and Astronautical Science)
 ISHII Keishi 石井慶之 (Dept. Eng. Sci., Kyoto Univ.)
 ISOZUMI Yasuhito 五十棲泰人 (Inst. Chem. Res., Kyoto Univ.)
 ITO Shin 伊藤 真 (Radioisot. Res. Cent., Kyoto Univ.)
 ITOH Akio 伊藤秋男 (Fac. Eng., Kyoto Univ.)
 ITOH Yoh 伊藤 陽 (Fac. Sci., Josai Univ.)
 KAWATSURA Kiyoshi 川面 澄 (Fac. Eng. Design, Kyoto Inst. Technol.)
 KIMURA Masahiro 木村正廣 (Fac. Sci., Osaka Univ.)
 KIMURA Mineo 季村峯生 (Argonne Natl. Lab., U.S.A.)
 KINK Ilmar (Univ. Lund, Sweden)
 KOBAYASHI Nobuo 小林信夫 (Dept. Phys., Tokyo Metrop. Univ.)
 KOHARA Takao 小原孝夫 (Fac. Sci., Himeji Inst. Technol.)
 KOIKE Fumihito 小池文博 (Sch. Med., Kitasato Univ.)
 KOIZUMI Tetsuo 小泉哲夫 (Dept. Phys., Rikkyo Univ.)
 KOMAKI Ken-ichiro 小牧研一郎 (Coll. Arts Sci., Univ. Tokyo)
 KUROKI Kenro 黒木健郎 (Natl. Res. Inst. Police Sci.)
 MARTINSON Indrek (Univ. Lund, Sweden)
 MATSUO Takashi 松尾 崇 (Dept. Pathol., Tokyo Med. Dent. Univ.)
 MATSUZAWA Michio 松澤通生 (Dept. Appl. Phys. Chem., Univ. Electro-Commun.)
 MERGEL Volker (Inst. für Kernphysik, Germany)
 MITAMURA Tohru 三田村 徹 (Fac. Eng., Himeji Inst. Technol.)
 MIZOGAWA Tatsumi 溝川辰巳 (Nagaoka Coll. Technol.)
 MOKLER Paul (GSI, Germany)

MUKOYAMA Takeshi 向山 毅 (Inst. Chem. Res., Kyoto Univ.)
 NISHIDA Nobuhiko 西田信彦 (Fac. Sci., Tokyo Inst. Technol.)
 NYSTRÖM Bosse (Univ. Lund, Sweden)
 OHTANI Shunsuke 大谷俊介 (Inst. Laser Sci., Univ. Electro-Commun.)
 OKUNO Kazuhiko 奥野和彦 (Dept. Phys., Tokyo Metrop. Univ.)
 SAKATA Hideaki 坂田英明 (Fac. Sci., Tokyo Inst. Technol.)
 SAKURAI Makoto 桜井 誠 (Fac. Sci., Kobe Univ.)
 SATO Hiroshi 佐藤浩史 (Fac. Sci., Ochanomizu Univ.)
 SATOH Kazuhiko 佐藤一彦 (Fac. Sci., Tokyo Inst. Technol.)
 SATOH Yukinori 佐藤幸紀 (Res. Inst. Sci. Measurements, Tohoku Univ.)
 SEKIOKA Tsuguhisa 関岡嗣久 (Fac. Eng., Himeji Inst. Technol.)
 SHIBATA Hiromi 柴田裕実 (Res. Cent. Nucl. Sci., Univ. Tokyo)
 SHIMA Kunihiko 島 邦博 (Tandem Accel. Cent., Univ. Tsukuba)
 SHIMAKURA Noriyuki 島倉紀之 (Fac. Sci., Niigata Univ.)
 SUZUKI Isao 鈴木 功 (Electrotechnical Laboratory)
 TAKAYANAGI Toshinobu 高柳俊暢 (Dept. Phys., Sophia Univ.)
 TAWARA Hiroyuki 俵 博之 (Natl. Inst. Fusion Sci.)
 TERASAWA Mititaka 寺澤倫孝 (Fac. Eng., Himeji Inst. Technol.)
 TOSHIMA Nobuyuki 戸嶋信幸 (Inst. Appl. Phys., Tsukuba Univ.)
 WAKIYA Kazuyoshi 脇谷一義 (Dept. Phys., Sophia Univ.)
 WATANABE Shinichi 渡辺信一 (Dept. Appl. Phys. Chem., Univ. Electro-Commun.)
 YAGISHITA Akira 柳下 明 (Natl. Lab. High Energy Physics)
 YAMAZAKI Yasunori 山崎泰規 (Coll. Arts Sci., Univ. Tokyo)
 YODA Jun 依田 潤 (National Research Laboratory of Metrology)
 YOSHINO Masuhiro 吉野益弘 (Lab. Phys., Shibaura Inst. Technol.)
 ZOU Yaming 邹 亚明 (Jiao Tong Univ., China)

(Students)

BITO Yasunori 尾藤康則 (Fac. Eng., Kyoto Univ.)
 CHIBA Daisuke 千羽大介 (Dept. Phys., Sophia Univ.)
 FUJIWARA Masamichi 藤原正満 (Dept. Eng. Sci., Kyoto Univ.)
 KAGAWA Makoto 香川 真 (Dept. Phys., Sophia Univ.)
 KAGEYAMA Hiroyoshi 影山拓良 (Fac. Eng. Design, Kyoto Inst. Technol.)
 KANEKO Shinichi 金子真一 (Fac. Sci., Tokyo Inst. Technol.)
 KIMURA Yasuyuki 木村恭之 (Dept. Eng. Sci., Kyoto Univ.)
 NAKAI Yoshihiro 中居由博 (Fac. Eng. Design, Kyoto Inst. Technol.)
 NISHIDA Tetsuo 西田哲朗 (Dept. Eng. Sci., Kyoto Univ.)
 OKUMA Ryuji 大熊隆次 (Dept. Phys., Rikkyo Univ.)
 SANO Mutsumi 佐野 睦 (Dept. Phys., Rikkyo Univ.)
 SAWADA Hirokazu 澤田浩和 (Fac. Sci., Tokyo Inst. Technol.)
 SUZUKI Hajime 鈴木 一 (Fac. Eng., Kyoto Univ.)
 TAKAHASHI Ryohei 高橋竜平 (Fac. Eng. Design, Kyoto Inst. Technol.)
 TAKEUCHI Hiroko 竹内浩子 (Dept. Phys., Ochanomizu Univ.)
 TAMAGAWA Yoshihisa 玉川祥久 (Dept. Phys., Sophia Univ.)
 TANABE Kunihiko 田辺邦浩 (Dept. Phys., Sophia Univ.)
 TSUCHIDA Hidetsugu 土田秀次 (Fac. Eng., Kyoto Univ.)
 YAMAMOTO Reiko 山元玲子 (Dept. Phys., Sophia Univ.)

Muon Science Laboratory

ISHIDA Katsuhiko 石田勝彦	KADONO Ryosuke 門野良典
KOYAMA Akio 小山昭雄	MATSUZAKI Teiichiro 松崎禎市郎*
NAGAMINE Kanetada 永嶺謙忠**	NAKAMURA Satoshi 中村 哲
WATANABE Isao 渡邊功雄	YAGI Eiichi 八木栄一*

* Senior Scientist, ** Chief Scientist

(Visitors)

AKIMITSU Jun 秋光 純 (Coll. Sci. Eng., Aoyama Gakuin Univ.)
ASAI Kichizo 浅井吉蔵 (Univ. Electro-Commun.)
BRIERE Tina Marie (Dept. Phys., State Univ. New York, Albany, U.S.A.)
DAS Prasad Tara (Dept. Phys., State Univ. New York, Albany, U.S.A.)
HASHIMOTO Masashi 橋本雅史 (JAERI)
KATO Mineo 加藤岑生 (JAERI)
KINO Yasushi 木野康志 (Fac. Sci., Tohoku Univ.)
KUROSAWA Kiyoyuki 黒沢清行 (JAERI)
MACRAE Roderick M. (JSPS Fellowship)
MATSUSHITA Akira 松下 明 (Contract Researcher)
NISHIDA Nobuhiko 西田信彦 (Fac. Sci., Tokyo Inst. Univ.)
NISHIYAMA Kusuo 西山樟生 (Fac. Sci., Univ. Tokyo)
PONOMAREV Leonid (Kurachatov Inst., Russia)
PRATT Francis Laurence (Dept. Phys., Univ. Oxford, U.K.)
SHIMOMURA Koichiro 下村浩一郎 (Fac. Sci., Univ. Tokyo)
STRASSER Patrick (Nucl. Phys. Div., Inst. Nucl. Study, Univ. Tokyo)
TANASE Masakazu 棚瀬正和 (JAERI)
TORIKAI Eiko 鳥養映子 (Fac. Eng., Yamanashi Univ.)
YONEDA Akira 米田 晃 (Messege Co., Ltd.)

(Students)

DAWSON Wayne (Fac. Sci., Univ. Tokyo)

Magnetic Materials Laboratory

KATSUMATA Koichi 勝又 紘一^{*1}
MATSUDA Masaaki 松田雅晶

OKADA Takuya 岡田卓也^{*2}
TATARA Gen 多々良 源^{*3}

^{*1} Chief Scientist, ^{*2} Senior Scientist, ^{*3} Special Postdoctoral Researcher

Plasma Physics Laboratory

OYAMA Hitoshi 大山 等

YANO Katsuki 矢野勝喜

Microwave Physics Laboratory

MINOH Arimichi 箕曲在道

Semiconductor Laboratory

(Visitors)

AONO Keiko 青野桂子 (Coll. Liberal Arts, Kitasato Univ.)

Inorganic Chemical Physics Laboratory

AMBE Shizuko 安部 静子
MATSUO Yukari 松尾由賀利

MAEDA Kuniko 前田邦子
TAKAMI Michio 高見道生*

* Chief Scientist

(Visitors)

ARAI Nobuaki 荒井修亮 (Dept. Fisheries, Kyoto Univ.)
ISHII Keizo 石井慶造 (Cyclotron Radioisot. Cent., Tohoku Univ.)
KAWAI Jun 河合 潤 (Dept. Metallurgy, Kyoto Univ.)

Nuclear Chemistry Laboratory

AMBE Fumitoshi 安部文敏*

ITOH Yoshiko 伊東芳子

KOBAYASHI Yoshio 小林義男

OHKUBO Yoshitaka 大久保嘉高

ENOMOTO Shuichi 榎本秀一

IWAMOTO Masako 岩本正子

MAEDA Haruka 前田はるか

* Chief Scientist

(Visitors)

AMANO Ryohei 天野良平 (Fac. Med., Kanazawa Univ.)

ASAI Kichizo 浅井吉蔵 (Univ. Electro-Commun.)

BABA Hiroshi 馬場宏 (Fac. Sci., Osaka Univ.)

ENDO Kazutoyo 遠藤和豊 (Showa Coll. Pharm. Sci.)

FURUKAWA Michiaki 古川路明 (Fac. Sci., Nagoya Univ.)

FURUSATO Naohisa 古里直久 (Coll. Sci. Eng., Aoyamagakuin Univ.)

HARAKAWA Hiroaki 原川裕章 (Coll. Sci. Eng., Aoyamagakuin Univ.)

HIRUNUMA Rieko 蛭沼利江子 (Showa Coll. Pharm. Sci.)

HULETT D. Lester (Oak Ridge Natl. Lab., U.S.A.)

HSIA Yuanfu 夏元復 (Dept. Phys., Nanjing Univ., China)

ITO Nobuhiko 伊藤伸彦 (Sch. Veter. Med. Animal Sci., Kitasato Univ.)

ITO Yasuo 伊藤泰男 (Res. Cent. Nucl. Sci., Univ. Tokyo)

KANAZAWA Ikuzo 金沢育三 (Fac. Educ., Tokyo Gakugei Univ.)

KATAYAMA Masayuki 片山眞之 (Fac. Agr., Univ. Osaka Pref.)

KIMURA Kan 木村幹 (Coll. Sci. Eng., Aoyamagakuin Univ.)

KOJIMA Sadao 小島貞男 (Nucl. Med. Cent., Aichi Medical Univ.)

KOMURA Kazuhisa 小村和久 (Fac. Sci., Kanazawa Univ.)

KUNUGIYAMA Iwao 櫛山巖 (Sch. Veter. Med. Animal Sci., Kitasato Univ.)

LIU Bin 劉斌 (Dept. Tech. Phys., Peking Univ., China)

MINAI Yoshitaka 菜袋佳孝 (Fac. Sci., Univ. Tokyo)

MURAKAMI Hideoki 村上英興 (Fac. Educ., Tokyo Gakugei Univ.)

NAKAMURA Jin 中村仁 (Univ. Electro-Commun.)

NASU Saburo 那須三郎 (Fac. Eng. Sci., Osaka Univ.)

OKAMOTO Yoichi 岡本洋一 (Showa Coll. Pharm. Sci.)

PENG Zhilin 彭治林 (Wuhan Univ., China)

SAITO Tadashi 齋藤直 (Fac. Sci., Osaka Univ.)

SHIBATA Sadao 柴田貞夫 (Natl. Inst. Radiol. Sci.)

SHIBATA Seiichi 柴田誠一 (Inst. Nucl. Study, Univ. Tokyo)

SHINOHARA Atsushi 篠原厚 (Fac. Sci., Nagoya Univ.)

SHINONAGA Taeko 篠永妙子 (Fac. Sci., Tokyo Metropol. Univ.)

TANAKA Akira 田中彰 (Showa Coll. Pharm. Sci.)

WEGINWAR Rajiv G. (Chandrapur Coll. Eng., India)

YANAGA Makoto 矢永誠人 (Jikei Univ. Sch. Med.)

YASUDA Hiroshi 保田浩志 (Natl. Inst. Radiol. Sci.)

YOKOTA Yuko 横田裕子 (Coll. Sci. Eng., Aoyamagakuin Univ.)

YOKOYAMA Akihiko 横山明彦 (Fac. Sci., Osaka Univ.)

YOSHIDA Yutaka 吉田豊 (Shizuoka Inst. Sci. Technol.)

(Students)

DAIRAKU Tomohisa 大樂知久 (Fac. Sci., Nagoya Univ.)

ENDO Rieko 遠藤理枝子 (Fac. Sci., Tokyo Metropol. Univ.)

HAGIWARA Tetsuya 萩原徹也 (Fac. Sci. Eng., Tokyo Denki Univ.)

HANYU Takafumi 羽生貴文 (Showa Coll. Pharm. Sci.)

IJIMA Yoshihide 飯島由英 (Fac. Sci., Toho Univ.)

IMAIZUMI Manabu 今泉学 (Fac. Sci. Eng., Tokyo Denki Univ.)

INOUE Takakazu 井上貴和 (Fac. Sci., Osaka Univ.)

INOUE Takashi 井上高志 (Fac. Sci. Eng., Tokyo Denki Univ.)

ITOH Masahiro 伊藤昌宏 (Shizuoka Inst. Sci. Tech.)

ITOH Naoya 伊藤直弥 (Coll. Sci. Eng., Aoyamagakuin Univ.)

ITOU Mayu 伊藤麻由 (Sch. Veter. Med. Animal Sci., Kitasato Univ.)
IWATA Maki 岩田真紀 (Fac. Sci., Toho Univ.)
IWATSUKI Akira 岩月 晶 (Sch. Veter. Med. Animal Sci., Kitasato Univ.)
KAKIZAKI Takahiro 柿崎孝弘 (Fac. Sci., Sci. Univ. Tokyo)
KATAYAMA Osamu 片山 修 (Fac. Sci., Toho Univ.)
KAWASAKI Yuko 川崎祐子 (Fac. Sci., Toho Univ.)
KAWASHIMA Yasuko 川島康子 (Sch. Hygien. Sci., Kitasato Univ.)
KASUGA Ryouichi 春日良一 (Fac. Sci., Osaka Univ.)
KIKUCHI Yasuhisa 菊池泰久 (Fac. Sci. Eng., Tokyo Denki Univ.)
KIRYU Shigetoshi 桐生繁利 (Fac. Sci., Nagoya Univ.)
KOBAYASHI Kanako 小林香奈子 (Fac. Sci., Tokyo Metropol. Univ.)
KUWABARA Kazunori 桑原和憲 (Shizuoka Inst. Sci. Technol.)
MASUDA Yasuhisa 増田泰久 (Shizuoka Inst. Sci. Tech.)
MINAMI Hiroshi 南 浩 (Showa Coll. Pharm. Sci.)
MIYABAYASHI Kyoko 宮林京子 (Showa Coll. Pharm. Sci.)
MORIMOTO Shinya 森本真哉 (Fac. Sci., Osaka Univ.)
MUKAI Kazuhiko 向 和彦 (Fac. Sci., Osaka Univ.)
MURATA Chihiro 村田千裕 (Fac. Sci., Nagoya Univ.)
MUROYAMA Toshiharu 室山俊浩 (Fac. Sci., Nagoya Univ.)
NAKAGAWA Akihiro 中川彰宏 (Shizuoka Inst. Sci. Technol.)
NAKAJO Terunobu 中條晃伸 (Tokyo Gakugei Univ.)
ODA Hiroataka 小田寛貴 (Fac. Sci., Nagoya Univ.)
ODA Kaori 小田香織 (Showa Coll. Pharm. Sci.)
OIKAWA Shinji 及川真司 (Fac. Sci., Kanazawa Univ.)
ONIZUKA Nobuyuki 鬼塚信之 (Tokyo Gakugei Univ.)
OSHIMA Nagayasu 大島永康 (Tokyo Gakugei Univ.)
OTSU Yoko 大津庸子 (Tokyo Gakugei Univ.)
OZAKI Takuo 尾崎卓郎 (Fac. Sci., Tokyo Univ.)
SASAKI Jin 佐々木 仁 (Tokyo Gakugei Univ.)
SATO Hisayuki 佐藤久行 (Shizuoka Inst. Sci. Technol.)
SAWADA Naoto 澤田直人 (Shizuoka Inst. Sci. Technol.)
SEKIGUCHI Akiko 関口明子 (Coll. Sci. Eng., Aoyamagakuin Univ.)
SOGA Kyoko 曾我恭子 (Fac. Sci., Nagoya Univ.)
SOTOGAKU Naoki 外角直樹 (Showa Coll. Pharm. Sci.)
SUZUKI Akihiro 鈴木章浩 (Shizuoka Inst. Sci. Technol.)
TAKAHASHI Yoshio 高橋嘉夫 (Fac. Sci., Univ. Tokyo)
TANAKA Kenya 田中研也 (Fac. Sci. Technol., Chuo Univ.)
TSUKAHARA Kazuhiro 塚原和弘 (Shizuoka Inst. Sci. Technol.)
UEDA Mikiko 上田三紀子 (Dept. Botany, Stockholm Univ., Sweden)
YAMAMOTO Chie 山本智枝 (Shizuoka Inst. Sci. Tech.)

Chemical Dynamics Laboratory

KIMURA Kazuie 木村一宇

USHIDA Kiminori 丑田公規

(Visitor)

KAZAMA Shigeo 風間重雄 (Dept. Phys., Chuo Univ.)

(Students)

HON Wan 洪 完 (Dept. Chem., Tokyo Univ.)

IIMURA Munefumi 飯村宗史 (Dept. Phys., Chuo Univ.)

MORITA Toshio 森田敏夫 (Dept. Phys., Chuo Univ.)

SEKIGUCHI Wataru 関口航 (Dept. Phys., Chuo Univ.)

YOSHIOKA Yoshiki 吉岡良樹 (Dept. Phys., Chuo Univ.)

Cellular Physiology Laboratory

HANAOKA Fumio 花岡文雄*

KITAYAMA Shigeru 北山 滋

YATAGAI Fumio 谷田貝文夫**

* Chief Scientist, ** Senior Scientist

(Visitors)

ANDO Koichi 安藤興一 (Natl. Inst. Radiol. Sci.)
FUKUMURA Akifumi 福村明史 (Natl. Inst. Radiol. Sci.)
FURUSAWA Yoshiya 古澤佳也 (Natl. Inst. Radiol. Sci.)
HAMA Yoshimasa 浜 義昌 (Sci. Eng. Res. Lab., Waseda Univ.)
HASHIMOTO Shozo 橋本省三 (Fac. Med., Keio Univ.)
HOSHINO Kazuo 星野一雄 (Natl. Inst. Radiol. Sci.)
IIZUKA Masayuki 飯塚正之 (Natl. Inst. Radiol. Sci.)
ITO Hisao 伊東久夫 (Fac. Med., Keio Univ.)
ITOH Hiroko 伊藤浩子 (Natl. Inst. Radiol. Sci.)
ITSUKAICHI Hiromi 五日市ひろみ (Natl. Inst. Radiol. Sci.)
KANAI Tatsuaki 金井達明 (Natl. Inst. Radiol. Sci.)
KASAI Kiyomi 笠井清美 (Natl. Inst. Radiol. Sci.)
KAWACHI Kiyomitsu 河内清光 (Natl. Inst. Radiol. Sci.)
KIKUCHI Masahiro 菊地正博 (JAERI, Takasaki)
KIMOTO Masafumi 木元正史 (Natl. Inst. Radiol. Sci.)
KOBAYASHI Yasuhiko 小林泰彦 (JAERI, Takasaki)
KOHNO Toshiyuki 河野俊之 (Natl. Inst. Radiol. Sci.)
KOIKE Sachiko 小池幸子 (Natl. Inst. Radiol. Sci.)
KOJIMA Eiichi 小島栄一 (Natl. Inst. Radiol. Sci.)
KOSAKA Toshifumi 小坂俊文 (Dept. Vet. Radiol., Nihon Univ.)
KUBOTA Nobuo 窪田宜夫 (Fac. Med., Yokohama City Univ.)
MATSUFUJI Naruhiro 松藤成弘 (Natl. Inst. Radiol. Sci.)
McINTYRE Cindy L. (Radiobiol. Unit, Med. Res. Counc., U.K.)
MINOHARA Shinichi 箕原伸一 (Natl. Inst. Radiol. Sci.)
MIYAHARA Nobuyuki 宮原信幸 (Natl. Inst. Radiol. Sci.)
MURAIISO Chidori 村磯知採 (Natl. Inst. Radiol. Sci.)
MURAKAMI Masahiro 村上正弘 (Natl. Inst. Radiol. Sci.)
NAKAI Hirokazu 中井弘和 (Dept. Agric., Shizuoka Univ.)
OHARA Hiroshi 大原 弘 (Dept. Gen. Cult., Okayama Univ.)
OKUMURA Toshiyuki 奥村敏之 (Fac. Med., Univ. Tsukuba)
SASAKI Hiroshi 佐々木 弘 (Fac. Med. Kyushu Univ.)
SHIKAZONO Naoya 鹿園直哉 (JAERI, Takasaki)
SOGA Fuminori 曾我文宣 (Inst. Nucl. Study, Univ. Tokyo)
SUDO Michio 須藤美智雄 (Natl. Inst. Radiol. Sci.)
TAGUCHI Yasuko 田口泰子 (Natl. Inst. Radiol. Sci.)
TAKATUJI Toshihiro 高辻俊宏 (RI Cent., Nagasaki Univ.)
TANAKA Atsushi 田中 淳 (JAERI, Takasaki)
TANAKA Kaoru 田中 薫 (Natl. Inst. Radiol. Sci.)
TATSUZAKI Hideo 立崎英夫 (Fac. Med., Univ. Tsukuba)
TOMURA Hiromi 外村浩美 (Natl. Inst. Radiol. Sci.)
TSUBOI Atsushi 坪井 篤 (Natl. Inst. Radiol. Sci.)
TSUBOUCHI Susumu 坪内 進 (Suzuka Med. Technol. Univ.)
WATANABE Hiroshi 渡辺 宏 (JAERI, Takasaki)
WATANABE Masami 渡辺正己 (Fac. Pharm., Nagasaki Univ.)
YAMASHITA Shoji 山下昌次 (Natl. Saitama Hospital)

(Students)

FUJI Hiroshi 藤 浩 (Fac. Med., Univ. Tsukuba)
KAWASHIMA Mitsuhiko 河島光彦 (Fac. Med., Univ. Tsukuba)
TAKAHASHI Hideyuki 高橋英幸 (Fac. Med., Univ. Tsukuba)

Plant Functions Laboratory

ABE Tomoko 阿部知子

YOSHIDA Shigeo 吉田茂男*

* Chief Scientist

(Students)

KUMATA Shuji 熊田秀治 (Coll. Agr. Vet. Med., Nihon Univ.)

TORASHIMA Takashi 寅嶋 崇 (Coll. Agr. Vet. Med., Nihon Univ.)

Microbial Toxicology Laboratory

YAMAGUCHI Isamu 山口 勇*

* Chief Scientist

(Visitors)

WATANABE Tadakazu 渡部忠一 (Agro-Kanesho Co. Ltd.)

(Students)

MATSUMOTO Ken-ichi 松本健一 (Shimane Univ.)

Safety Center

HARASAWA Kaoru 原沢 薫

INOUE Yoshio 井上義夫

KATOU Hiroko 加藤博子

UWAMINO Yoshitomo 上 蓑義朋

INAMURA Takashi T. 稲村 卓*

KAGAYA Satoru 加賀屋 悟

MIYAGAWA Makoto 宮川真言

* Head

Division of Surface Characterization

IWAKI Masaya 岩木正哉*

KUMAGAI Makoto 熊谷 信

* Head

Radioisotope Technology Division

NAKANO Kazushiro 中野和城

YATAGAI Fumio 谷田貝文夫*

* Head

(Visitors)

IJIRI Kenichi 井尻憲一 (Radioisot. Cent., Univ. Tokyo)

ISHIKAWA Masanobu 石川雅紀 (Tokyo Univ. Fisheries)

KAGAWA Yasuhiro 香川康浩 (Toray Research Center Inc.)

KASE Youko 加瀬陽子 (Natl. Inst. Radiol. Sci.)

MAEZAWA Hiroshi 前澤 宏 (Fac. Med., Tokai Univ.)

OGURA Koichi 小倉紘一 (Coll. Ind. Technol. Nihon Univ.)

OHARA Hiroshi 大原 弘 (Dept. Gen. Cult., Okayama Univ.)

SUZUKI Masao 鈴木雅雄 (Fac. Pharm., Nagasaki Univ.)

YATO Osamu 矢頭 治 (Kagoshima Agr. Exp. Stn.)

(Students)

HAMANAKA Kenichi 浜中健一 (Fac. Sci. Eng., Waseda Univ.)

MATSUMOTO Hideya 松本英哉 (Fac. Sci. Eng., Waseda Univ.)

AUTHOR INDEX

- ABE Ryo 阿部 亮 3
 ABE Tomoko 阿部知子 165
 ABE Yasuhisa 阿部恭久 33
 ADACHI Minoru 足立 實 61, 62, 63, 181
 AIHARA Toshimitsu 藍原利光 6, 217
 AKAGI Hiroyasu 赤木宏安 3
 AKAI Hisazumi 赤井久純 109
 AKEBOSHI Yoshihiro 明星慶洋 54
 AKIYOSHI Hiromichi 秋吉哲充 58
 AKUTSU Takao 阿久津亮夫 121
 ALONSO Jose R. 60, 109
 AMANO Ryohei 天野良平 144, 145, 155, 156
 AMBE Fumitoshi 安部文敏 111, 112, 115, 127, 131,
 132, 134, 135, 136, 137,
 138, 139, 140, 141, 142,
 143, 144, 145, 146, 147,
 148, 149, 150, 151, 152,
 153, 154, 155, 156, 157,
 158, 172
 AMBE Shizuko 安部静子 130, 131, 132, 133, 134, 135,
 136, 137, 138, 139, 140, 141,
 142, 143, 144, 145, 146, 148,
 149, 150, 151, 152, 153, 154,
 172, 173
 ANDO Atsushi 安東 醇 155
 ANDO Kozo 安藤剛三 100, 101, 102, 103
 ANDO Yoshiaki 安藤嘉章 72, 73, 76, 184
 AOI Nori 青井 考 50, 51, 62, 63, 64, 67, 76, 182
 AOKI Jiro 青木司郎 121
 AOKI Yuka 青木由香 52
 ARAI Kouji 新井好司 8
 ARAI Nobuaki 荒井修亮 203
 ARIGA Takehiro 有賀健博 43, 45, 46, 177, 198
 ARKO A. Scott 106
 ASAHI Koichiro 旭 耕一郎 61, 62, 63, 64, 181
 ASAI Kichizo 浅井吉蔵 115, 158
 AWAYA Yohko 粟屋容子 98, 99, 100, 101, 102, 104,
 105, 122, 123, 178, 199, 208
 BABA Hiroshi 馬場 宏 128, 129
 BALBES Mark J. 65
 BATYGIN Yuri 219, 221, 223, 238, 240, 252, 254
 BENGTTSSON Peter 100, 101, 102
 BERTULANI Carlos A. 71
 BITOH Yasunori 尾藤康則 98
 BIZARD Guy 54
 BOCHKAREV Oleg 77
 BOYD Richard N. 65
 BUENKER R. J. 86, 90, 94
 CHANTRANUPONG L. 86
 CHIBA Toshiya 千葉利哉 6, 217, 219, 220, 221
 CHRISTIE William 78
 CHULKOV Leonid 77
 COQUARD Marie-Pierre 124
 DALGARNO A. 90
 DANG Nguyen Dinh 阮 廷燈 25
 DATÉ Schin 伊達 伸 38
 DELBAR Thierry 73
 DEPAOLA Brett D. 99, 106
 DILLON M. A. 86
 EGUCHI-KASAI Kiyomi 江口(笠井)清美 169, 170
 ENDO Kazutoyo 遠藤和豊 142, 143, 148, 149, 150, 153
 ENDOH Yasuo 遠藤康夫 122
 ENGSTRÖM Lars 100, 101, 102
 ENOMOTO Shuichi 榎本秀一 130, 131, 132, 134, 135,
 136, 137, 138, 139, 140,
 141, 142, 143, 144, 145,
 146, 148, 149, 150, 153,
 155, 156, 157, 172
 EN'YO Hideto 延与秀人 80, 81
 FEHRENBACH W. Charles 106
 FENG Jun 馮 軍 42, 65
 FLASCHIN Susanne 118
 FORTUNE Terry 79
 FRANCE III Ralph H. 73
 FUCHI Yoshihide 渕 好秀 59
 FUJIMAKI Masaki 藤卷正樹 65, 66
 FUJIOKA Manabu 藤岡 学 44
 FUJISHIMA Shiro 藤島史朗 230, 232, 234, 236
 FUJITA Jiro 藤田二郎 3
 FUJITA Satoshi 藤田哲史 56, 57, 179
 FUJITA Shin 藤田 新 47, 206, 259, 261, 263
 FUJITA Tatsuru 藤田 建 58
 FUJITA Yoshitaka 藤田佳孝 42, 44
 FUJIWARA Hideki 藤原秀樹 184
 FUKAO Tetsuhiro 深尾哲宏 60, 109
 FUKUDA Mitsunori 福田光順 60, 109
 FUKUDA Shigekazu 福田茂一 60, 66, 69, 70, 109
 FUKUDA Tomokazu 福田共和 68
 FUKUNISHI Nobuhisa 福西暢尚 9, 61, 62
 FUKUSHIMA Nobutsugu 福島伸次 89
 FUKUTSU Kumiko 福津久美子 169
 FURUKAWA Michiaki 古川路明 127, 128, 129
 FURUSATO Naohisa 古里直久 154
 FURUSAWA Yoshiya 古澤佳也 169, 170

- FURUTAKA Kazuyoshi 古高和禎 52, 53, 54
 FUTAMI Yasuyuki 二見康之 52, 53, 54
 GAI Moshe 73
 GALONSKY Aaron 54
 GEISSEL Hans 77
 GOLOVKOV Mikhael 77
 GONO Yasuyuki 郷農靖之 48, 176
 GOTO Akira 後藤 彰 3, 50, 51, 121, 159, 207, 209,
 211, 214, 219, 220, 221, 223,
 226, 230, 232, 234, 236
 GRUND Thomas 111
 GU J. P. 90
 HACKE Marcus 125
 HADA Takashi 羽田尚志 121
 HAHN Kevin I. 73
 HAMADA Kenji 濱田賢二 108
 HAMADA Shingo 濱田真悟 48
 HAMANAKA Hiromi 浜中廣見 202
 HANAOKA Fumio 花岡文雄 168, 170
 HASEBE Hiroo 長谷部裕雄 6, 217
 HASHIMOTO Masashi 橋本雅史 194
 HASHIZUME Akira 橋爪 朗 205
 HATANAKA Kichiji 畑中吉治 55, 57, 80, 179, 225
 HATSUKAWA Yuichi 初川雄一 48
 HEMMI Masatake 逸見政武 6, 217, 219, 220, 221
 HIES Markus 42, 43, 45, 46, 107, 177, 198
 HINO Ken-ichi 日野健一 89, 97
 HIRAI Masaaki 平井正明 50, 51, 68, 72, 73
 HIRATA Daisy 15, 77
 HIROSE Takayuki 広瀬孝幸 121
 HIRSCH G. 86, 90, 94
 HIRUNUMA Rieko 蛭沼利江子 142, 143, 148, 149, 150,
 153
 HOFMANN Helmut 32
 HOMMA Takayuki 本間隆之 3
 HON Wan 洪 完 163, 164
 HONMA Michio 本間道雄 19
 HORI Yoichi 堀 陽一 62
 HORIBATA Takatoshi 堀端孝俊 27, 28, 29
 HORIUCHI Hisashi 堀内 昶 30, 31
 HOSOYA Shoichi 細谷正一 122
 HUANG Ming-Tie 106
 HUI Patrick 79
 HUI Qin 惠 秦 124
 HULDT Sven 101, 102
 HUTTON Roger 100, 101, 102
 ICHIHARA Takashi 市原 卓 57, 59, 80, 81, 175, 179
 ICHIKAWA Ryuji 市川龍二 3
 IDEGUCHI Eiji 井出口栄治 48, 49, 67, 176, 182
 IEKI Kazuo 家城和夫 76, 184
 IGARASHI Akinori 五十嵐明則 96
 IHYOU Miki 井表美樹 156
 IIMURA Hideki 飯村秀紀 48
 IIMURA Munefumi 飯村宗史 163, 164
 IKEDA Nobuo 池田伸夫 44
 IKEGAMI Kumio 池上九三男 3, 232, 234, 236
 IKEZAWA Eiji 池沢英二 6, 217, 219, 220
 IMAI Kenichi 今井憲一 80, 81
 IMAMURA Mineo 今村峯雄 47
 INABE Naohito 稲辺尚人 3, 50, 51, 61, 74, 121, 166,
 170, 214, 216, 219, 220, 238,
 240, 248, 257
 INAMURA Takashi T. 稲村 卓 45, 46, 177, 198, 259,
 261, 263
 INOKUTI Mitio 井口道生 95
 IRNICH Hartmut 77
 ISHIDA Katsuhiko 石田勝彦 119, 190, 194, 196
 ISHIDA Satoru 石田 悟 55, 56, 57, 59, 179
 ISHIHARA Masayasu 石原正泰 11, 12, 48, 49, 50, 51,
 59, 61, 62, 63, 67, 68,
 72, 74, 75, 76, 80, 81,
 176, 182
 ISHII Keishi 石井慶之 103
 ISHII Tetsuro 石井哲朗 48
 ISHIMOTO Katsumi 石本勝巳 155
 ISHIZAKI Tikako 石崎千夏子 156
 ISHIZUKA Takeo 石塚武男 42, 45
 ISSHIKI Hiroshi 一色 博 3
 ITO Mikihiko 伊東幹彦 63
 ITO Naoya 伊藤直弥 154
 ITO Nobuhiko 伊藤伸彦 172
 ITO Sachiko 伊藤祥子 66
 ITO Yasuo 伊藤泰男 159, 161
 ITOH Akio 伊藤秋男 98
 ITOH Yoshiko 伊東芳子 159, 160, 161
 ITSUKAICHI Hiromi 五日市ひろみ 169
 IVANYUK Fedor A. 32
 IVIE Rex 79
 IWAKI Masaya 岩木正哉 5, 201
 IWAMOTO Masako 岩本正子 130, 147
 IWASA Naohito 岩佐直仁 72, 73
 IWASAKI Masahiko 岩崎雅彦 192
 IWATA Yoshiyuki 岩田佳之 44, 76, 184
 IWATSUKI Akira 岩月 晶 172
 IZUMI Hideaki 出水秀明 61, 62, 63, 64
 IZUYAMA Takeo 伊豆山健夫 37
 JAGUTZKI Ottmar 99
 JAKUBEK Zygmunt 124

- JANAS Zennon 77
- JEONG Sunchan 鄭 淳讚 42, 44
- JIN Wei Guo 金 衛国 45, 46, 107, 108, 177, 198
- KADONO Ryosuke 門野良典 116, 117, 118, 119, 120, 196
- KAGEYAMA Hiroyoshi 影山拓良 104
- KAGEYAMA Tadashi 影山 正 3, 207, 209, 211, 219, 220
- KAKUNAGA Atsushi 角永敦史 156
- KALVIUS G. Michael 118
- KAMBARA Tadashi 神原 正 98, 99, 100, 101, 102, 104, 105, 122, 123, 199, 208
- KAMIGAITO Osamu 上垣外修一 3, 219, 220, 221, 223
- KANAI Tatsuki 金井達明 167, 168, 169
- KANAI Yasuyuki 金井保之 99, 100, 101, 102, 104, 106, 208
- KANEKO Shin-ichi 金子真一 123
- KASAGI Jirohta 笠木治郎太 52, 53, 54
- KASAI Yasuko 笠井康子 124
- KASE Masayuki 加瀬昌之 3, 121, 159, 199, 207, 214, 216, 219, 220, 221
- KATAYAMA Ichiro 片山一郎 44
- KATAYAMA Masayuki 片山眞之 140
- KATAYAMA Takeshi 片山武司 80, 225, 226, 238, 240, 241, 244, 246, 248, 250, 252, 254, 256, 257
- KATO Hiroshi 加藤 博 189
- KATO Mineo 加藤峯生 194
- KATO Takeshi 加藤武司 170
- KATOH Kenichi 加藤健一 59
- KATSUMATA Koichi 勝又紘一 122
- KATSURAGAWA Hidetsugu 桂川秀嗣 45, 107, 108
- KAWAGUCHI Takeo 川口武男 225, 230, 232, 234, 236
- KAWAI Jun 河合 潤 204
- KAWATSURA Kiyoshi 川面 澄 104, 105
- KELLER Horst 77
- KIDERA Masanori 木寺正憲 48
- KIKUCHI Tadashi 菊地 正 44, 72, 73, 76, 183, 184
- KIM Eunjoo 金 琅珠 47
- KIM Jong-Won 金 鐘元 236
- KIM Seyong 金 世容 40
- KIMURA Kan 木村 幹 154
- KIMURA Kazuie 木村一字 163, 164
- KIMURA Kikuo 木村喜久雄 65, 68
- KIMURA Mineo 季村峯生 86, 87, 88, 90, 93, 94, 95, 99
- KIMURA Yasuyuki 木村恭之 103
- KINK Ilmar 100
- KINOSHITA Akira 木下 彬 160
- KISHIDA Takashi 岸田 隆 48, 49, 67, 176, 182
- KITAGAWA Hisashi 北川 尚 39
- KITAO Kensuke 喜多尾憲助 205
- KITAYAMA Shigeru 北山 滋 165, 166, 167
- KITAZAWA Hideaki 北澤英明 110, 112
- KOBAYASHI Toshio 小林俊雄 60, 65, 66, 69, 70, 74, 77, 78, 79, 109
- KOBAYASHI Yoshio 小林義男 110, 111, 112, 138, 158
- KOBINATA Hideo 小日向秀夫 50, 51, 68
- KOHARA Shigeo 小原重夫 3, 6, 217, 219, 221
- KOHNNO Tsuyoshi 河野 毅 121, 189
- KOIKE Yasuro 小池康郎 55
- KOJIMA Sadao 小島貞男 127
- KOJIMA Takao M. 小島隆夫 99, 100, 101, 102, 105, 178, 208
- KONNO Atsuko 紺野敦子 47
- KORSHENINNIKOV Alexei 65, 69, 70, 71
- KOURA Hiroyuki 小浦寛之 17, 18
- KRAJCAR-BRONIC Ines 87
- KRATZER Andreas 118
- KRAUS Gerald 66, 77
- KRAVIS Scott 178
- KREBS Gary F. 60, 109
- KUBO Toshiyuki 久保敏幸 50, 51, 61, 74, 230, 232, 234, 236
- KUBONO Shigeru 久保野 茂 42, 44, 59, 65, 73, 186
- KUDO Hisaaki 工藤久昭 42, 44
- KUMAGAI Hidekazu 熊谷秀和 48, 50, 51, 91, 187
- KUMAGAI Ken-ichi 熊谷健一 114
- KUMAGAI Kenji 熊谷健二 38
- KUMAGAI Makoto 熊谷 信 201
- KUMATA Shuji 熊田秀治 165
- KUNUGIYAMA Iwao 櫛山 巖 172
- KUNZ Henning 46
- KURASAWA Haruki 倉沢治樹 21, 22, 23, 34
- KUROKAWA Meiko 黒川明子 42, 44, 185
- KUROSAWA Kiyoyuki 黒沢清行 194
- KUSAKARI Hideshige 草刈英榮 48
- KUZMIN Evgenii A. 69, 70
- LEE Kang Ok 李 康玉 42, 43
- LEE Keunho 李 根浩 159
- LEE Sang Moo 李 相茂 53
- LI Y. 86, 94
- LIN Chii-Dong 83, 92
- LIPNIK Peter 73
- LIU Bin 劉 斌 134, 135, 136, 137, 138, 139, 140, 141, 144, 145, 149, 150, 153, 172

- LIU Guanhua 劉冠華 62, 63, 64
LUNDEEN R. Steve 106
LUNDSGAAD Morten F. V. 92
MACEK Joseph H. 97
MACRAE Roderick M. 120
MAEDA Haruka 前田はるか 130, 134, 135, 139, 146,
147, 151, 152, 154
MAEDA Kazuhide 前田和秀 58
MAEDA Kuniko 前田邦子 202, 203, 204
MAEDA Toyokazu 前田豊和 176
MAIE Takeshi 真家武士 3
MARTINSON Indrek 100, 101, 102
MASAIKE Akira 政池明 80, 81
MATSUDA Kiyohide 松田清秀 53, 54
MATSUDA Masaaki 松田雅昌 122, 199
MATSUDA Sumio 松田純夫 121
MATSUMOTO Ken-ichi 松本健一 173
MATSUMOTO Yasuhiro 松本康寛 60, 109
MATSUO Takashi 松尾崇 91
MATSUSE Takehiro 松瀬丈浩 53
MATSUTA Kensaku 松多健策 60, 109
MATSUYAMA Yoshitaka 松山芳孝 186
MATSUZAKI Teiichiro 松崎禎市郎 190, 194, 196
MATSUZAWA Michio 松澤通生 89
MENGONI Alberto 11, 12
MERGEL Volker 99
MICHOTTE Carrine 73
MIHARA Mototsugu 三原基嗣 60, 109
MIKI Keitaro 三木敬太郎 186
MINAI Yoshitaka 薬袋佳孝 131, 132, 151, 152
MINAMISONO Kei 南園啓 60, 109
MINAMISONO Tadanori 南園忠則 60, 109
MINEMURA Toshiyuki 峯村俊行 43, 184
MINOWA Tatsuya 箕輪達哉 107, 108
MITAMURA Tohru 三田村徹 122, 199
MITARAI Shiro 御手洗志郎 48
MITSUMOTO Toshinori 密本俊典 230, 232, 234, 236
MITSUOKA Shimichi 光岡真一 63
MIYAGI-OKAMOTO Yayoi 宮城(岡本)弥生 157
MIYAMURA Osamu 宮村修 38
MIYATAKE Hiroari 宮武宇也 42, 44, 61, 64, 67, 182
MIYAZAKI Kousuke 宮崎光介 48, 176
MIYAZAWA Yoshitoshi 宮沢佳敏 6, 217, 219, 220, 221
MIZOI Yutaka 溝井浩 68
MIZUSAKI Takahiro 水崎高浩 19
MOCHINAGA Kensuke 持永建介 181
MOCHIZUKI Yuko S. 望月優子 35, 36, 37
MOMOTA Sadao 百田佐多生 60, 66, 69, 70, 109
MONKMAN Andrew 119
MORIKAWA Tsuneyasu 森川恒安 48, 176
MORISHITA Toru 森下享 89
MORITA Kosuke 森田浩介 42, 43, 44, 46, 48, 177,
185
MORITA Toshio 森田敏夫 163, 164
MORIYA Shingo 守屋真吾 72, 73, 76
MOTOBAYASHI Tohru 本林透 42, 43, 44, 72, 73,
75, 76, 183, 184,
185
MUKAI Kazuhiko 向和彦 127, 129
MÜNZENBERG Gotfried 66, 77
MURAKAMI Hideoki 村上英興 160
MURAKAMI Hiroyuki 村上浩之 44, 72, 73, 183, 184,
185
MURAKAMI Masahiro 村上正弘 169
MURAKAMI Takeshi 村上健 48, 54, 186
MURAYAMA Toshiyuki 村山利幸 45, 46, 177, 198
MUROYAMA Toshiharu 室山俊浩 127
MUTA Atsushi 牟田淳 10
NAGAI Yasuki 永井泰樹 42, 44
NAGAI Yuki 永井由紀 121
NAGAMINE Kanetada 永嶺謙忠 113, 114, 115, 116,
117, 118, 119, 120,
190, 194, 196
NAGASE Makoto 長瀬誠 3
NAGATA Katsuaki 永田勝明 189
NAGATA Kazuhiko 長田和彦 62, 63
NAKAGAWA Takahide 中川孝秀 3, 50, 51, 52, 53, 54,
207, 209, 211, 219,
220
NAKAHARA Hiromichi 中原弘道 44, 153
NAKAI Yoichi 中井陽一 98, 99, 100, 101, 102, 105, 208
NAKAJIMA Junji 中島諄二 47
NAKAJIMA Satoru 中島理 113
NAKAJIMA Shunji 中島諄二 206, 259
NAKAMURA Hiroyuki 中村裕之 58
NAKAMURA Jin 中村仁 110, 111, 112, 115
NAKAMURA Masato 中村仁音 124
NAKAMURA Satoshi N. 中村哲 192
NAKAMURA Takashi 中村隆司 47, 50, 51, 61, 67, 72,
73, 74, 75, 76, 182
NAKANISHI Noriyoshi 中西紀喜 47, 159, 206, 259,
261, 263
NAKANO Jou 中野譲 68
NAKAO Noriaki 中尾徳晶 47
NAKASHIMA Takao 中島孝夫 58
NARUSE Miho 成瀬美帆 155
NEUMAIER Sigurt 77
NICKEL Frank 77

- NIIMURA Masanobu 新村正信 209, 211
 NIIZEKI Takashi 新関 隆 55, 57, 59, 179
 NIKOLSKII Evgenii Yu. 65, 69, 70
 NISHIDA Nobuhiko 西田信彦 123
 NISHIDA Tetsuo 西田哲朗 103
 NISHIMORI Nobuyuki 西森信行 57, 58, 179
 NISHIO Teiji 西尾禎二 72, 73, 76, 184
 NOJIRI Yoichi 野尻洋一 60, 109
 NOMURA Toru 野村 亨 42, 43, 44, 185
 NONAKA Takamasa 野中敬正 56, 57, 179
 NORO Yoshihiko 野呂良彦 110, 112
 NOTANI Masahiro 野谷将広 50, 51, 67, 76, 182
 NOVATSKII Boris 69, 70
 NUMATA Shigeo 沼田茂男 219
 NYSTRÖM Bo 100, 101, 102
 ODAHARA Atsuko 小田原厚子 48
 OGAWA Hideto 小川秀人 42
 OGAWA Hiroshi 小川博嗣 63, 64, 67, 182
 OGAWA Yoko 小川洋子 8
 OGIWARA Kiyoshi 荻原 清 5
 OGLOBLIN Alexei A. 69, 70
 OHARA Hiroshi 大原 弘 169
 OHBAYASI Yoshihide 大林由英 7
 OHIRA Hideharu 大平秀春 121
 OHISHI Hidenori 大石英典 206, 259, 261, 263
 OHKI Tomonori 大木智則 6, 217
 OHKUBO Yoshitaka 大久保嘉高 127, 128, 129, 158
 OHNISHI Tetsuya 大西哲哉 56, 57, 179
 OHNUMA Hajime 大沼 甫 59
 OHTA Shigemi 太田滋生 40
 OHTOMO Kiyotaka 大友清隆 238, 240, 244, 246
 OHTSUBO Takashi 大坪 隆 60, 109
 OHTSUKI Tsutomu 大槻 勤 52
 OI Makito 大井万紀人 28, 29
 OISHI Shigeo 大石茂雄 155, 156
 OKADA Takuya 岡田卓也 110, 112, 158
 OKAMOTO Yoichi 岡本洋一 157
 OKAMURA Hiroyuki 岡村弘之 55, 56, 57, 59, 179
 OKAMURA Masahiro 岡村昌宏 80, 225
 OKUMURA Toshiyuki 奥村敏之 171
 OKUNO Hiroki 奥野広樹 61, 62, 63, 230, 232, 234,
 236
 OKUNO Kazuhiko 奥野和彦 178
 OLSON Douglas 78
 OMATA Kazuo 小俣和夫 78
 ONISHI Naoki 大西直毅 20, 27, 28, 29
 ONO Akira 小野 章 30, 31
 OOKAWA Tomohiro 大川智宏 238, 240, 241
 OSHIMA Masumi 大島真澄 48
 OTSU Hideaki 大津秀暁 55, 56, 57, 179
 OTSUKA Takaharu 大塚孝治 10, 11, 12, 19
 OURA Masaki 大浦正樹 104, 105, 178
 OYAMATSU Kazuhiro 親松和浩 35, 37
 OZAKI Takuo 尾崎卓郎 131, 132
 OZAWA Akira 小沢 顕 14, 60, 65, 66, 69, 70, 77, 78,
 109
 PAPP Tibor 104, 105
 PERSSON John L. 124
 PÉTER Jean 76
 PIECHACZECK Andreas 77
 PRATT Francis L. 117, 119, 120
 PRIBORA Vasilii 69, 70
 PU Yuehu 蒲 越虎 42, 43, 44, 46, 68, 177, 185
 RAINMANN Grery 65
 RAO Yinoug 238, 240
 ROECKL Arnst 77
 RUAN Jian-Zhi 阮 健治 45
 SAGARA Kenshi 相良建至 58
 SAITO Naohito 齋藤直人 80, 81
 SAITO Tadashi 齋藤 直 127, 128, 129
 SAITO Yuko 齋藤裕子 154
 SAKAI Hideyuki 酒井英行 55, 56, 57, 179
 SAKAMOTO Naruhiko 坂本成彦 55, 56, 57, 179
 SAKAMOTO Wataru 坂本 亘 203
 SAKATA Fumihiko 坂田文彦 25
 SAKATA Hideaki 坂田英明 123
 SAKEMI Yasuhiro 酒見泰寛 80, 81
 SAKURAI Hiroyoshi 櫻井博儀 50, 51, 67, 68, 72, 73,
 75, 76, 182, 186
 SASAKI Hiroshi 佐々木 弘 168
 SASAKI Mitsuru 佐々木 充 64
 SASAKI Reiji 佐々木玲仁 52
 SATO Hikaru 佐藤 皓 80, 225
 SATO Hiromi 佐藤広海 61, 62, 181
 SATO Hiroshi 佐藤 竝 13, 16
 SATO Kazunori 佐藤和則 60, 109
 SATO Koki 佐藤弘毅 169
 SATOH Kazuhiko 佐藤一彦 123
 SATOU Yoshiteru 佐藤義輝 55, 56, 57, 59, 179
 SAWADA Hirokazu 沢田浩和 123
 SCHMIDT-BÖCKING Horst W. 99
 SCHMIDT-OTT W.-D. 61
 SCHWAB Wolfgang 77
 SEEGER Alfred 111
 SEKIGUCHI Akiko 関口明子 154
 SEKIGUCHI Wataru 関口 航 163, 164
 SHEN Wen Qing 53
 SHIBATA Masamichi 柴田理尋 48

- SHIBATA Masataka 柴田雅隆 48, 176
 SHIBATA Tokushi 柴田徳思 47
 SHIBATA Toshi-aki 柴田利明 80, 81
 SHIKAZONO Naoya 鹿園直哉 166, 167
 SHIMAKURA Noriyuki 島倉紀之 93
 SHIMAMURA Isao 島村 勲 83, 84, 85, 87, 93, 95, 96,
 99
 SHIMODA Tadashi 下田 正 42, 44, 61, 64
 SHIMOURA Susumu 下浦 享 72, 73, 74, 75, 76, 183,
 184
 SHIN Seung-Ai 42, 43
 SHINOHARA Atsushi 篠原 厚 127, 128, 129
 SHINONAGA Taeko 篠永妙子 130
 SHINOZUKA Tsutomu 篠塚 勉 42, 44
 SHIRAI Toshizo 白井稔三 96
 SHIRAKURA Tetsuya 白倉徹也 64
 SIELEMANN Rainer 111
 SIEMSEN Rolf H. 74
 SMITH Dovercas 79
 SOEJIMA Kouichi 副島浩一 208
 STÖCKLI P. Martin 106
 SUEKI Keisuke 末木啓介 42, 43, 44
 SUEMMERER Klaus 77
 SUGAHARA Yuichi 菅原雄一 14, 15, 78
 SUGAI Isao 菅井 勲 45
 SUGANUMA Hideo 菅沼秀夫 41
 SUGAWARA Masahiko 菅原昌彦 48
 SUGAWARA-TANABE Kazuko 菅原和子 26
 SUGIMOTO Kenzo 杉本健三 78
 SUMIYOSHI Hiroyuki 住吉広行 38
 SUMIYOSHI Kohsuke 住吉光介 14, 15, 35
 SUOMIJÄRVI Tiina 52, 53
 SUZUKI Masao 鈴木雅雄 170
 SUZUKI Masataka 鈴木正恭 184
 SUZUKI Takeshi 鈴木 健 66, 77
 SUZUKI Tomono 鈴木智乃 156
 SUZUKI Toshio 鈴木俊夫 10, 21, 22, 23, 34
 SUZUKI Yasuyuki 鈴木宜之 7, 8
 SYMONS T. James M. 60, 109
 TACHIBANA Takahiro 橘 孝博 17, 18
 TAGAYA Yu 多加谷 祐 42, 43, 44, 185
 TAJIMA Naoki 田嶋直樹 20
 TAKAHARA Satoshi 高原哲士 20
 TAKAHASHI Hideyuki 高橋英幸 171
 TAKAHASHI Katsuhiko 高橋克彦 3
 TAKAHASHI Noriaki 高橋憲明 61
 TAKAHASHI Ryohei 高橋竜平 104
 TAKAHASHI Yoshio 高橋嘉夫 151, 152
 TAKAMI Michio 高見道生 124
 TAKANAKA Masao 高仲政雄 238, 240, 250
 TANABE Kosai 田辺孝哉 26
 TANAKA Atsushi 田中 淳 166, 167
 TANAKA Kazuhiro 田中和廣 79
 TANAKA Masahiko 田中雅彦 59, 186
 TANAKA Yasushi 田中保志 230, 232, 234, 236
 TANASE Masakazu 棚瀬正和 194
 TANG Jian-Zhi 唐 建志 83, 84, 85, 99
 TANIGAKI Katsumi 谷垣勝巳 120
 TANIGAKI Minoru 谷垣 実 60, 109
 TANIHATA Isao 谷畑勇夫 9, 14, 15, 60, 65, 66, 69, 70,
 71, 74, 77, 78, 109
 TANIKAWA Masashi 谷川勝至 44
 TANO Shigemitsu 田野茂光 167
 TATARA Gen 多々良 源 122
 TATSUZAKI Hideo 立崎英夫 171
 TAWARA Hiroyuki 俵 博之 91
 TENDOW Yoshihiko 天道芳彦 205
 TERANISHI Takashi 寺西 高 67, 72, 73, 75, 76, 182
 TERASAWA Mititaka 寺澤倫孝 122
 TOHYAMA Mitsuru 遠山 満 24
 TOKI Hiroshi 土岐 博 14, 15, 35, 41
 TOMINAGA Takeshi 富永 健 131, 132, 151, 152
 TOMINAKA Toshiharu 富中利治 230, 232, 234, 236
 TOMIZAWA Masahito 富澤正人 228
 TONUMA Tadao 戸沼正雄 91
 TORASHIMA Takashi 寅嶋 崇 165
 TOSHIMA Nobuyuki 戸嶋信幸 92, 96
 TOYAMA Takeshi 外山 毅 225
 TOZAWA Machiko 戸澤満智子 148, 153
 TSUCHIDA Hideo 土田英夫 48
 TSUKIORI Noritoshi 月居憲俊 3
 UCHIBORI Takeshi 内堀武司 42, 43, 44, 72, 73, 76,
 184, 185
 UCHIDA Shigeo 内田滋夫 133
 UCHIYAMA Koji 内山浩志 42
 UEMATSU Haruko 植松晴子 107, 108
 UENO Hideki 上野秀樹 61, 62, 63, 64
 UESAKA Tomohiro 上坂友洋 55, 56, 57, 59, 179, 213
 UMISEDO Sei 海勢頭 聖 41
 UNO Masahiro 宇野正宏 17, 18
 URAI Teruo 浦井輝夫 5
 USHIDA Kiminori 丑田公規 164
 UTSUNOMIYA Hiroaki 宇都宮弘章 186
 UWAMINO Yoshitomo 上袁義朋 47, 259, 261, 263
 VANDEGRIF John 65
 VARGA Kálmán 7, 8
 WADA Michiharu 和田道治 42, 44
 WADA Takahiro 和田隆宏 33

- WAKAMATSU Fumihiko 若松文彦 58
- WAKASA Tomotsugu 若狭智嗣 55, 56, 57, 179
- WAKASUGI Masanori 若杉昌徳 45, 46, 177, 198, 213,
238, 240, 257
- WAKUI Takashi 涌井崇志 45, 213
- WATANABE Hiroshi 渡辺 宏 167
- WATANABE Isao 渡邊功雄 113, 114, 115, 116, 117,
118, 119, 190, 194, 196
- WATANABE Masaki 渡辺眞樹 206, 259, 261, 263
- WATANABE Masami 渡辺正己 170
- WATANABE Naoki 渡部直樹 178
- WATANABE Shin-ichi 渡辺伸一 238, 240, 242
- WATANABE Shinichi 渡辺信一 89
- WATANABE Tadakazu 渡部忠一 130, 173
- WATANABE Yasushi 渡邊 康 50, 51, 67, 68, 72, 73,
74, 80, 81, 175, 182
- WATANABE Yutaka 渡辺 裕 50, 51, 68
- WEGINWAR Rajiv G. 134, 135, 137, 138, 139, 140, 141,
144, 145
- WIEMAN Haward 78
- WINECKI Slawek 106
- WU Heyu 49, 80
- WU Yichu 161
- XIA Jiawen 238, 240
- YAGI Eiichi 八木栄一 5, 111, 125
- YAJIMA Akira 矢嶋 亨 54
- YAMADA Kazuyoshi 山田和芳 122
- YAMADA Masami 山田勝美 17, 18
- YAMAGAMI Munetaka 山上宗隆 186
- YAMAGATA Tamio 山県民穂 186
- YAMAGIWA Iwao 山極 巖 189
- YAMAGUCHI Isamu 山口 勇 130, 173
- YAMAJI Shuhei 山路修平 32, 33
- YAMAKAWA Osamu 山川 修 78
- YAMAMOTO Sukeyasu Steve 67, 182
- YAMAMOTO Yoshifumi 山本佳史 67, 182
- YAMAUCHI Hiromoto 山内啓資 6, 217
- YANAGA Makoto 矢永誠人 142, 143, 145, 148, 149,
150, 153
- YANAGIDA Yasuo 柳田保雄 158
- YANAGISAWA Yoshiyuki 柳澤善行 72, 73, 75, 76, 184
- YANO Yasushige 矢野安重 3, 121, 207, 209, 211, 214,
219, 220, 221, 223, 226,
230, 232, 234, 236, 238,
240
- YASUDA Hiroshi 保田浩志 133
- YATAGAI Fumio 谷田貝文夫 168, 169, 170, 171
- YOKOTA Yukihiko 横田幸彦 167
- YOKOYAMA Akihiko 横山明彦 127, 128, 129
- YOKOYAMA Ichiro 横山一郎 3, 214
- YONEDA Ken-ichiro 米田健一郎 67, 182
- YOSHIDA Atsushi 吉田 敦 42, 43, 44, 50, 51, 61, 62,
63, 64, 67, 68, 175, 182,
205
- YOSHIDA Koichi 吉田光一 52, 53, 54, 60, 65, 66, 69,
70, 77, 109, 187, 238, 240,
256
- YOSHIDA Shigeo 吉田茂男 165
- YOSHIDA Yukiyo 吉田幸世 156
- YOSHIDA Yutaka 吉田 豊 111
- YOSHIOKA Yoshiki 吉岡良樹 163, 164
- YOSOI Masaru 与曾井 優 80, 81
- YUAN Youjin 238, 240
- YUASA-NAKAGAWA Keiko 湯浅(中川) 恵子 52, 53,
54
- ZHANG Xiao-Ze 38
- ZHOU Bin 83

RIKEN Accelerator Progress Report Vol. 29

理化学研究所加速器年次報告 第29巻 (1996)

印刷 平成8年(1996)3月23日

発行 平成8年(1996)3月31日

発行者 理化学研究所

代表者 有馬朗人

〒351-01 埼玉県和光市広沢2番1号

電話 (048) 462-1111

編集者 理化学研究所加速器研究施設
運営委員会

印刷所 株式会社ユニバーサル・アカデミー・プレス
〒113 東京都文京区本郷6丁目16番2号 BR本郷5ビル

定価5,000円

(消費税別)

理化学研究所

埼玉県 和光市 広沢